CORA Cork Open Research Archive
Cartlann Taighde Oscailte Chorcaí

Title	Impurity distributions in pharmaceutical solids
Authors	Bourke, Timothy
Publication date	2022-04-01
Original Citation	Bourke, T. 2022. Impurity distributions in pharmaceutical solids. PhD Thesis, University College Cork.
Type of publication	Doctoral thesis
Rights	© 2022, Timothy Bourke. - https://creativecommons.org/licenses/by-nc-nd/4.0/
Download date	2026-11-16 15:03:36
Item downloaded from	https://hdl.handle.net/10468/13652



Ollscoil na hÉireann, Corcaigh

National University of Ireland, Cork



Impurity Distributions in Pharmaceutical Solids

Thesis presented by

Timothy Bourke B.Sc.

for the degree of

Doctor of Philosophy

University College Cork

School of Chemistry

Head of School: Dr. Humphrey Moynihan

Supervisor: Dr. Humphrey Moynihan

April 2022

Contents

ABSTRACT **1**
ABBREVIATIONS **3**
INTRODUCTION **5**
1.1 IMPURITIES IN THE PHARMACEUTICAL INDUSTRY 6
1.1.1 Impurity Management Strategies *7*
1.1.2 Purification-Resistant Impurities *9*
1.1.3 Quantification of Impurity Behaviour during Crystallisation *11*
1.2 CRYSTALS AND CRYSTALLISATION 14
1.2.1 The Crystal *14*
1.2.2 Crystallisation *16*
1.2.2.1 Nucleation 16
1.2.2.2 Crystal Growth 20
1.2.2.3 Methods of Crystallisation 22
1.2.3 Crystal Morphology and Habit *28*
1.2.4 Polymorphism *30*
1.3 ADDITIVES AND IMPURITIES 32
1.3.1 Means of Impurity and Additive Incorporation *33*
1.3.1.1 Physical Mixtures 33
1.3.1.2 Surface Adsorption and Deposition 34
1.3.1.3 Inclusions and Agglomerations 35
1.3.1.4 Other Means of Incorporation 35
1.3.2 Phase Behaviour *36*
1.3.2.1 Single-Component 36
1.3.2.2 Two-Component Systems 37
1.3.2.3 Construction of Phase Diagrams by Thermal Analysis 38
1.3.2.4 Types of Two-Component Phase Diagrams 39
1.3.2.5 Three-Component Systems 48
1.4 RESEARCH AIMS 49
1.4.1 Relevant Previous Work *51*
1.5 CHOICE OF HOST MATERIAL 53
1.5.1 Flufenamic Acid *54*
1.5.1.1 Compound Details 54
1.5.1.2 Benefits for Current Work 55
1.5.1.3 Polymorphism 56
1.5.1.4 Form III and Form I 56

1.6 PRIMARY MEANS OF ANALYSIS 57
1.6.1 High-Performance Liquid Chromatography (HPLC) *57*
1.6.2 Powder X-Ray Diffraction (PXRD) *58*
1.6.3 Differential Scanning Calorimetry (DSC) *59*
1.6.4 Thermogravimetric Analysis (TGA) *60*
METHOD DEVELOPMENT 61
2.1 INTRODUCTION 62
2.2 FLUFENAMIC ACID AND ADDITIVE SELECTION 63
2.2.1 Flufenamic Acid *63*
2.2.2 Choice of Additives *63*
2.2.2.1 Purpose of Additives 63
2.2.2.2 Principles of Additive Structure 64
2.2.3 Crystal Behaviour of FFA and Additives *65*
2.2.3.1 Crystal Behaviour of FFA 65
2.2.3.2 Potential Impact of Additives on FFA Crystal Behaviour 67
2.2.4 Structurally Similar Additives *69*
2.2.4.1 Descriptions of Additives 70
2.2.5 Additive Crystal Structures *74*
2.3 HPLC METHOD DEVELOPMENT 76
2.3.1 Uses of HPLC Analysis *76*
2.3.2 Method Development *77*
2.3.2.1 Method 1 77
2.3.2.2 Method 2 78
2.3.2.3 Method 3 82
2.3.2.4 Method 4 83
2.3.2.5 Minimising the Retention Times of Analytes 85
2.3.3 Final HPLC Method Evaluation *88*
*2.3.4 Chromatograms of FFA Doped with Compounds **15 - 19*** *89*
2.4 CALIBRATION CURVES 93
2.4.1 Standard Solution Preparation *93*
2.4.2 Plotting Data Points and Regression Analysis *94*
2.4.3 Overview of Constructed Calibration Curves *97*
2.5 SOLUBILITY TESTS 99
2.5.1 FFA Solubility Tests *100*
2.5.1.1 Solubility Determination of FFA at Room Temperature 100
2.5.1.2 Solubility Determination of FFA at Higher Temperatures 102
2.5.2 Solubility Determination of Additives *104*
2.5.2.1 Determining the Solubility of Additives in Pure Solvents 105
2.5.2.2 Pure-Component Relative Solubility (α^0) 107

2.6 CRYSTALLISATION METHOD DEVELOPMENT 109
2.6.1 Methods of Crystal Production 110
2.6.1.1 Crystallisation by Slow Evaporation 110
2.6.1.2 Crystallisation by Liquid-Liquid diffusion 118
2.6.1.3 Crystallisation by Slow Cooling 119
2.6.1.4 Alternative Methods of Crystal Production 121
2.6.1.5 Summary of Developed Methods of Crystal Production 124
2.6.2 Analysis of FFA Crystal Properties 125
2.6.2.1 Polymorphism of FFA 125
2.6.2.2 DSC Analysis of Form III FFA 128
2.6.2.3 Controlling the Phase Behaviour of Form III FFA 130
2.6.2.4 TGA Analysis of FFA 134
2.7 CONCLUSION 135
2.8 EXPERIMENTAL 137
2.8.1 HPLC 137
2.8.1.1 Instrument Specifications 137
2.8.1.2 Method Details 137
2.8.2 Calibration Curves 138
2.8.2.1 Standard Solution Preparation 138
2.8.2.2 Standard Solution Analysis 138
2.8.3 Solubility Tests 139
2.8.3.1 Sample Preparation 139
2.8.3.2 Solubility Analysis 139
2.8.4 Crystallisation 140
2.8.4.1 Preliminary Slow Evaporation Studies 140
2.8.4.2 Liquid-Liquid diffusion 141
2.8.4.3 Crystal Production Procedures 141
2.8.5 PXRD 143
2.8.6 Polymorphic Transformation Studies 143
2.8.6.1 Production of Form I FFA 143
2.8.6.2 Production of Form IV FFA 144
2.8.7 DSC 144
2.8.7.1 Instrument Specifications 144
2.8.7.2 Initial Experiments and Heat-Cool-Heat 144
2.8.7.3 Heating Rate Study 145
2.8.7.4 Effect of Sample Grinding Study 145
2.8.8 TGA 145
SYNTHESIS AND CHARACTERISATION 146
3.1 INTRODUCTION 147
3.2 SYNTHETIC ROUTES IN THE PRODUCTION OF FLUFENAMIC ACID 148

3.2.1 Ullmann-Goldberg Condensation 148
3.2.2 Buchwald-Hartwig Amination 152
3.2.3 Methods of Purification 156
3.2.4 Characterisation of FFA Products 157
3.2.4.1 IR Analysis 157
3.2.4.2 Proton NMR 158
3.2.4.3 Carbon NMR 160
3.2.4.4 PXRD 161
3.3 SYNTHETIC ROUTES IN THE PRODUCTION OF STRUCTURALLY SIMILAR FFA ANALOGUES 162
3.3.1 Characterisation of FFA Analogues 163
3.3.1.1 Me-FA **15** 163
3.3.1.2 Cl-FA **16** 168
3.3.1.3 DF-FA **17** 172
3.3.1.4 MF-FA **18** 176
3.3.1.5 t-Bu-FA **19** 180
3.4 INVESTIGATION INTO IMPURITY OBSERVED DURING SYNTHESIS OF FFA 186
3.4.1 Observation of Impurity Occurrence 186
3.4.2 Isolation and Analysis of Impurity 187
*3.4.3 Targeted Synthesis of Diacid Triaryl Compound **25** 190*
*3.4.4 Comparison of Isolated Impurity and Synthesised Compound **25** 191*
3.4.5 Possible Alternative Structure of Isolated Impurity 195
3.5 CONCLUSION 198
3.6 EXPERIMENTAL 199
3.6.1 Instrument Details and Analytical Methodologies 199
3.6.1.1 High-Performance Liquid Chromatography (HPLC) 199
3.6.1.2 Nuclear Magnetic Resonance (NMR) 199
3.6.1.3 Infrared (IR) Analysis 200
3.6.1.4 Mass Spectrometry (MS) 200
3.6.1.5 Powder X-Ray Diffraction (PXRD) 200
3.6.1.6 Differential Scanning Calorimetry (DSC) 200
3.6.1.7 Thermogravimetric Analysis (TGA) 201
3.6.2 Synthetic Methodologies 201
3.6.2.1 Ullmann-Goldberg Condensation 1 201
3.6.2.2 Ullmann-Goldberg Condensation 2 202
3.6.2.3 Buchwald-Hartwig Amination 1 202
3.6.2.4 Buchwald-Hartwig Amination 2 203
3.6.3 Purification Techniques 203
3.6.3.1 Recrystallisation 203
3.6.3.2 Column Chromatography 203

3.6.4 Compound Characterisation *204*
3.6.4.1 Flufenamic Acid **14** (FFA) 204
3.6.4.2 2-(*m*-Tolylamino)benzoic acid **15** (Me-FA) 205
3.6.4.3 *N*-(3-Chlorophenyl)anthranilic acid **16** (Cl-FA) 206
3.6.4.3 2-[3-(Difluoromethyl)anilino]benzoic acid **17** (DF-FA) 207
3.6.4.5 2-[3-(Fluoromethyl)anilino]benzoic acid **18** (MF-FA) 208
3.6.4.6 2-((3-(*tert*-Butyl)phenyl)amino)benzoic acid **19** (t-Bu-FA) 209
3.6.4.7 2,2'-((3-(Trifluoromethyl)phenyl)azanediyl)dibenzoic acid **25** 210
BEHAVIOUR OF DOPED SYSTEMS 211
4.1 INTRODUCTION 212
4.2 CREATING DOPED SYSTEMS 213
4.2.1 HPLC Response Factor Correction *214*
4.3 CRYSTAL INCORPORATION LEVELS OF ADDITIVES 216
4.3.1 Results *217*
4.3.1.1 Systems Doped with Me-FA **15** 218
4.3.1.2 Systems Doped with Cl-FA **16** 221
4.3.1.3 Systems Doped with DF-FA **17** and MF-FA **18** 225
4.3.1.4 Systems Doped with t-Bu-FA **19** 226
4.3.1.5 Systems Doped with Diacid Triaryl Compound **25** 228
4.3.1.6 Influence of Substituent Size and Relative Solubility on Additive Incorporation 230
4.4 ADDITIVE RESISTANCE TO PURIFICATION BY RECRYSTALLISATION 232
4.4.1 Results *234*
4.4.1.1 Systems Doped with 2% Additive 234
4.4.1.2 Systems Doped with 45% Me-FA **15** 237
4.4.1.3 Systems Doped with 42% Cl-FA **16** 239
4.5 CRYSTALLISATION BEHAVIOUR OF DOPED FFA 242
4.5.1 Appearance and Growth of Doped FFA Crystals *242*
4.5.2 Polymorphic Form *248*
4.5.2.1 Effect of Inclusion of Each Additive Type 248
4.5.2.2 Effect of Additive Inclusion on Crystallisation Methods 250
4.5.2.3 Effect of Increasing Doping Levels of Me-FA **15** 251
4.5.2.4 Effect of Increasing Doping Levels of Cl-FA **16** 253
4.5.2.5 Analysis of Crystals with Problematic Morphologies 254
4.6 PHASE BEHAVIOUR OF DOPED SYSTEMS 256
*4.6.1 FFA **14** / Me-FA **15** Systems* *256*
4.6.1.1 Polymorphic Behaviour 256
4.6.1.2 Interpretation of DSC Data 262
*4.6.2 FFA **14** / Cl-FA **16** Systems* *268*
4.6.2.1 Polymorphic Behaviour 268

4.6.2.2 Observations of FFA **14** / Cl-FA **16** System Behaviour 271
4.6.2.3 Nature of Hypo-Eutectic Region Behaviour 273
4.6.2.4 Interpretation of DSC Data 277
*4.6.3 Discussion of FFA **14** / Me-FA **15** and FFA **14** / Cl-FA **16** Systems 281*
4.6.4 Discussion into Other Additive Systems 282
4.6.4.1 FFA **14** / DF-FA **17** Systems 282
4.6.4.2 FFA **14** / MF-FA **18** Systems 283
4.6.4.3 FFA **14** / t-Bu-FA **19** Systems 285
4.7 INVESTIGATION INTO THE BEHAVIOUR OF T-BU-FA **19** AS AN ADDITIVE 286
*4.7.1 t-Bu-FA **19** System Observations 286*
4.7.2 Ruling out Types of Additive Inclusion 287
4.7.2.1 Physical Mixtures, Solvent Agglomerations, and Inclusions 288
4.7.2.2 Surface Deposition or Adsorption 291
4.7.2.3 Eutectic or Solid Solution 292
*4.7.3 Discussion of Possible Lattice Interactions of FFA **14** Doped with t-Bu-FA **19** 293*
*4.7.4 Discussion of Possible Lattice Interactions of FFA **14** Doped with Other Additives 295*
4.7.4.1 FFA **14** / Me-FA **15** Interactions 295
4.7.4.2 FFA **14** / Cl-FA **16** Interactions 296
4.7.4.3 FFA **14** / DF-FA **17** and FFA **14** / MF-FA **18** Interactions 297
4.8 CONCLUSION 298
4.9 EXPERIMENTAL 300
4.9.1 Preparation of Doped Systems 300
4.9.2 Response Factor Correction 300
4.9.3 Crystallisation Behaviour 301
4.9.4 Incorporation Tests 302
4.9.5 Impurity Rejection Tests 302
4.9.6 Phase Behaviour 303
4.9.6.1 FFA **14** / Me-FA **15** System 304
4.9.6.2 FFA **14** / Cl-FA **16** System 305
4.9.6.3 FFA **14** / DF-FA **17** System 307
4.9.6.4 FFA **14** / MF-FA **18** System 307
4.9.6.5 FFA **14** / t-Bu-FA **19** System 307
*4.9.7 t-Bu-FA **19** Inclusion Studies 308*
4.9.7.1 TGA 308
4.9.7.2 Partial Dissolutions 308
METHODS OF DETERMINING THE DISTRIBUTION OF IMPURITIES 309
5.1 INTRODUCTION 310

5.2 PARTIAL DISSOLUTIONS 311
5.2.1 PD Method Development *314*
5.2.1.1 Primary Development 314
5.2.1.2 Secondary Development 319
5.2.2 Application of Partial Dissolution Method to Different Systems *332*
5.2.2.1 Effect of Increased Sample Size 332
5.2.2.2 Effect of Different Additive Types and Levels 338
5.2.2.3 Effect of Crystal Size and Morphology 346
5.2.2.4 Studies on Single Prismatic Crystals 351
5.2.3 Crystal Systems with Problematic Morphologies *360*
5.2.3.1 Type A 363
5.2.3.2 Type B 368
5.2.3.3 Type C 375
5.2.3.4 Type D 380
5.2.3.5 Discussion of Studies on Crystal Systems with Problematic Morphologies 383
5.2.4 Discussion of Partial Dissolution Technique *384*
5.3 SEGMENTATION ANALYSIS 388
5.3.1 Background and Technique Description *388*
5.3.2 Segmentation Analysis Study Results *391*
5.3.3 Discussion of Segmentation Analysis Technique *393*
5.4 DISCUSSION OF PATTERNS OF ADDITIVE INCORPORATION 395
5.5 EXPERIMENTAL 398
5.5.1 Partial Dissolutions *398*
5.5.1.1 Primary Development 398
5.5.1.2 Secondary Development 399
5.5.1.3 Test of Anti-Flocculating Agent for Prismatic Crystals 401
5.5.1.4 Test of Anti-Flocculating Agent for Crystals with Problematic Morphologies 401
5.5.1.5 Data Processing Methods 402
5.5.2 Segmentation Analysis *403*
CONCLUSION **404**
APPENDIX **411**
7.1 SPACE-FILL DIAGRAMS OF COMPOUNDS **14** – **19** 412
7.2 HPLC ANALYSIS 415
*7.2.1 FFA **14** doped with different levels of Compounds **15** – **19*** *415*
*7.2.2 FFA **14** vs. Synthetic Starting Materials* *418*
7.3 CALIBRATION CURVES 419
*7.3.1 Me-FA **15** Calibration Curve* *419*
*7.3.2 Cl-FA **16** Calibration Curve* *421*
*7.3.3 DF-FA **17** Calibration Curve* *423*

*7.3.4 MF-FA **18** Calibration Curve* *425*
*7.3.5 t-Bu-FA **19** Calibration Curve* *427*
7.4 PXRD Analysis 429
7.5 DSC Analysis 433
7.6 TGA Analysis 434
7.6.1 TGA Curves of Pure Materials *434*
7.6.2 TGA Curves of Doped Materials *436*
7.7 Synthetic Method Development 438
*7.7.1 DF-FA **17** Additional NMR Analysis* *438*
*7.7.2 MF-FA **18** Additional NMR Analysis* *440*
*7.7.3 Compound **27** (Diacid Triaryl Synthesis Ester Intermediate) Analysis* *442*
*7.7.4 Diacid Triaryl Compound **25** Synthetic Product Analysis* *444*
7.8 Isolated Synthetic Impurity Analysis 446
7.8.1 HPLC Trace of Isolated Impurity *446*
*7.8.2 Spectra Assigned to Structure of Compound **25*** *447*
*7.8.3 Spectra Assigned to Structure of Compound **28*** *450*
7.9 Partial Dissolution Plots 454
7.9.1 Additional Additive Distribution Plots *454*
7.9.2 Distribution Coefficient Plots Collected by Additive *457*
7.9.3 Size Distribution Plots of PD Studies *460*
7.9.4 Box Plots of Crystal Sample Surface Areas *464*
7.9.5 Microscope images of Crystals with Problematic Morphologies *466*
7.9.5.1 Type A Systems 466
7.9.5.2 Type B Systems 469
7.9.5.3 Type C Systems 472
7.9.5.4 Type D Systems 474
REFERENCES **475**

This is to certify that the work I am submitting is my own and has not been submitted for another degree, either at University College Cork or elsewhere. All external references and sources are clearly acknowledged and identified within the contents. I have read and understood the regulations of University College Cork concerning plagiarism and intellectual property.

Acknowledgements

Firstly, I would like to thank Dr. Humphrey Moynihan for the opportunity to take on this project. I have been learning from you for almost a decade and I wouldn't be at this point without your guidance and support. Thanks to Dr. Dan McCarthy, Dr. Lorraine Bateman, and Dr. Denis Lynch for NMR services, Dr. Nuala Maguire and Dr. Tom O'Mahony for HPLC support, Dr. Michael Cronin for DSC and TGA services, and Dr. Florence McCarthy and Mick O'Shea for mass spectrometry. I'd also like to thank the technical staff at UCC for all their support of the course of the project, including Tina Kent, Denis Duggan, Noel Browne, Dr. Ian O'Connor, Dr. Francis Harrington, Will Daly, and everyone in the Chemistry office.

Special thanks to Denis Lynch for help with some particularly stubborn compound characterisation as well as general guidance and advice, and Nuala for her endless cheerful support. Thanks to Dr. Simon Lawrence and Dr. Florence McCarthy, my internal examiners, for asking the right questions and setting my research on a better path. I would like to acknowledge the SSPC for their assistance and the Irish Research Council and Alkermes for their financial support, with special thanks to Dr. Renato Chiarella for his guidance and the opportunity for a valuable work experience. Thank you to Alexandra Elbakyan for unlocking so many doors. Thanks to everyone on the 4th floor of the Kane and 2nd floor of the Cavanagh, and all members of the HAM group past and present: Louise, Olga, and Declan for their mentorship, Keith for the chats, and Áine and Michael for their friendship and company in what would otherwise have been a very lonely lab!

I want to say thanks to my parents and my sister Eva for the bottomless love and support you've given me over the years, I can honestly say I wouldn't have made it through without it. Big thanks to Alex, Will, and Lil, the original 12:30 lunch crew, even though those days seem like a very long time ago now. Thanks to Shane, my best bud, no matter how far away you try to move you'll never escape my friendship. To Molly, the couple of lines I'm giving you here cannot possibly express how much I appreciate everything you've done for me, from your terrible jokes to your valiant efforts to understand my research. You've been there with me through the highs, lows, and the strangeness of the last few years, and I love you for it. Finally, to the friends and family and everyone else I haven't mentioned here, I am endlessly grateful but if I listed you all this thesis would need another volume. Thank you.

“Shapes on shapes, wasted time

Pointless points along a line

Head down, straight on, you’ll be fine”

- Jonathan Coulton

Abstract

The management of impurities in batches of drug products is a continual challenge facing the pharmaceutical industry. While the inclusion of many synthetic and process impurities can be reduced to safe levels by common techniques such as crystallisation, others are not so simple to remove, persisting through multiple purification attempts. In these cases, more targeted impurity rejection techniques are required. In turn, information on the nature of the impurities and their distribution within a batch of crystalline product is vital to designing an effective impurity management strategy. This research focuses on the development of techniques for determining the distribution of purification-resistant impurities within crystalline pharmaceutical products. These techniques have been shown to be applicable to systems with a range of different impurity types and levels, as well as different crystal morphologies, and require no specialised equipment to perform.

Chapter one provides a summary of the impact of pharmaceutical impurities and strategies surrounding their management, background into crystal structure and morphology, and the relationship between an impurity/additive and its host material. Flufenamic acid (FFA) is introduced as the active pharmaceutical ingredient (API) basis for impure systems of study, upon which distribution determination methods can be developed. Some methods of analysis that will be used in the research are also discussed.

Chapter two focuses on the selection of appropriate additives for the impure systems and the development of the analytical techniques required to characterise their behaviour. The development of a robust high-performance liquid chromatography (HPLC) method will be described, as well as the construction of calibration curves,

measurement of solubility data, and the determination of effective methods of crystal production. The polymorphic behaviour of FFA is also explored.

Chapter three details the development of a reliable synthetic method for the production of FFA and the selected additives, as well as detailed spectroscopic characterisation of each. An investigation into the characterisation of an impurity observed in the synthesis of FFA will also be described.

Chapter four is concerned with exploring the relationship between FFA and each of the chosen additives within doped systems. To this end, the incorporation behaviour, resistance to purification, and phase behaviour of the doped system is examined. Binary phase diagrams are constructed for two of the systems. The unexpected behaviour of one of the systems is also examined in more detail.

The development of the aforementioned methods of determining impurity distributions is described in chapter five. This is focused primarily on the development of a robust partial dissolution technique and its application to a wide variety of systems with different properties. A second technique designed for acicular crystals is also described.

A short summary of the conclusions of the research is provided in chapter six, followed by an Appendix in chapter seven. Experimental details are presented at the end of each results chapter.

Abbreviations

2-CBA	2-Chlorobenzoic Acid **20**
ANOVA	Analysis of Variance
API	Active Pharmaceutical Ingredient
Cl-FA	*N*-(3-Chlorophenyl)anthranilic Acid **16**
COSY	Correlation Spectroscopy
CSD	Cambridge Structural Database
d	Doublet
DCM	Dichloromethane
dd	Doublet of Doublets
ddd	Doublet of Doublet of Doublets
DF-FA	2-[3-(Difluoromethyl)anilino]benzoic Acid **17**
DMF	*N*,*N*-Dimethylformamide
DSC	Differential Scanning Calorimetry
EHE	2-(2-Ethylhexyloxy)ethanol
ESI	Electrospray Ionization
EtOAc	Ethyl Acetate
EtOH	Absolute Ethanol
FFA	Flufenamic Acid **14**
HPLC	High-Performance Liquid Chromatography
HRMS	High Resolution Mass Spectrometry
ICH	International Council for Harmonisation of Technical Requirements for Pharmaceuticals for Human Use
IPA	Isopropyl Alcohol
IR	Infrared
m	Multiplet
m.p.	Melting Point
MeCN	Acetonitrile
Me-FA	2-(*m*-Tolylamino)benzoic Acid **15**

MeOD	Deuterated Methanol
MeOH	Methanol
MF-FA	2-[3-(Fluoromethyl)anilino]benzoic Acid **18**
mol	Moles
MS	Mass Spectrometry
MTBE	Methyl *tert*-Butyl Ether
n	Number of data points
NMR	Nuclear Magnetic Resonance
NSAID	Non-Steroidal Anti-Inflammatory Drug
PD	Partial Dissolution
ppm	Parts Per Million
PXRD	Powder X-Ray Diffraction
rac-BINAP	Racemic 2,2′-Bis(diphenylphosphino)-1,1′-binaphthyl
RF	Response Factor
RRF	Relative Response Factor
RRT	Relative Retention Time
RT	Retention Time
s	Singlet
SD	Standard Deviation
t	Triplet
t-Bu-FA	2-((3-(*tert*-Butyl)phenyl)amino)benzoic Acid **19**
T_E / T_{EU}	Eutectic Melting Temperature
TFA	Trifluoroacetic Acid
TGA	Thermogravimetric Analysis
THF	Tetrahydrofuran
T_O	Peak Onset Temperature
TOF-SIMS	Time-Of-Flight Secondary Ion Mass Spectrometry
T_P	Peak Maximum Temperature
UHPLC	Ultra-High-Performance Liquid Chromatography

Introduction

1.1 Impurities in the Pharmaceutical Industry

The presence of impurities in intermediates and products is an unfortunate reality of pharmaceutical drug manufacturing. An impurity, defined by The International Council for Harmonisation of Technical Requirements for Pharmaceuticals for Human Use (ICH), is "any component of the drug product that is not the chemical entity defined as the drug substance or an excipient in the drug product."[1] Such components can be classified as organic impurities, inorganic impurities, and residual solvents. Organic impurities often arise during the manufacturing process, and refer to any unreacted starting materials, intermediates, by-products, products of degradation, or other organic reagents or catalysts not removed during product work-up and isolation. Similarly, inorganic products can consist of catalysts, residual metals, salts, or other inorganic materials. Residual solvent, both organic and inorganic, can also be present in an impure product.

The presence of impurities in pharmaceutical products can significantly influence the drug's pharmacological performance, affecting its efficacy, dosage, and side effect profile, as well as its shelf-life, regulatory compliance, and overall safety. In many cases their inclusion can cause toxicological effects in patients, causing harmful and in some cases fatal results. Genotoxic impurities, mutagenic impurities, and carcinogens are of particular concern.[2–4] As such, strict guidelines are in place to minimise unwanted impurities in pharmaceutical products. For new drug products with a maximum daily dose of ≤ 2g, any impurity content higher than 0.1% (or 1.0 mg per day intake, whichever is lower) needs to be identified and its safety profile explored. This threshold drops to 0.05% for any drug with a higher daily dose. If the impurity is expected to be especially toxic or

potent, this limit does not apply, and identification is needed at any level. After characterisation, impurity levels can be reduced to a safe level based on the nature of the impurity. If no safety literature exists, toxicity studies may need to be carried out.

1.1.1 Impurity Management Strategies

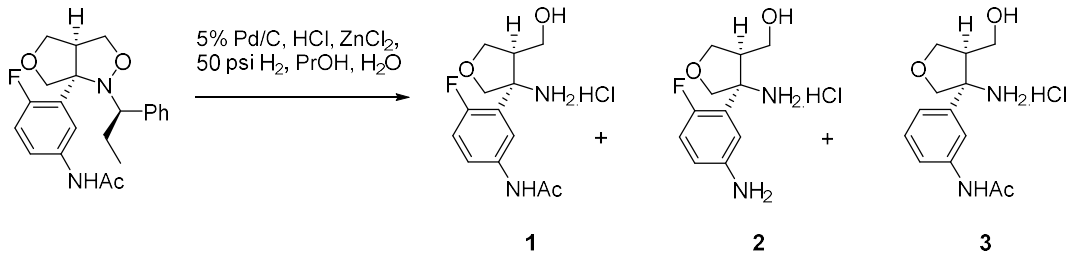
Many strategies exist for the management and reduction of impurities to safe levels, foremost among them being crystallisation. Crystallisation relies on the tendency of molecules to form repeating patterns during solidification, either by precipitation from solution or freezing, and the preference of those molecules for others with similar chemical and structural properties. This generally results in the formation of crystals of pure material and the selective rejection of impurities from the solid phase. This inherent selectivity is extremely advantageous for the production of purified material on both small and large scale. In addition, as the majority of pharmaceutical products are marketed in a crystalline form,[5] crystallisation is an important tool in the formulation of pharmaceutical products. Crystallisation of a product can be achieved in a number of ways: by the cooling of a supersaturated solution of the material, isothermal evaporation of a solvent, precipitation of the material *via* the addition of an antisolvent, liquid or vapour diffusion of an antisolvent into a solution, or sublimation, to name a few. Cooling crystallisation is by far the most common method due to the level of control afforded, as well as its efficiency in terms of time and material.[6]

Purification of products can also be achieved through other means. Slurrying and washing of freshly crystallised products is an effective way of removing impurities that

are included in the outer layers of crystals or adsorbed to the surface of the particles through deposition of mother liquor material.[7] A slurry is a dense suspension of solid particles in a liquid medium, often used in the pharmaceutical industry as a means of purification, transporting product, and controlling crystal form and particle size. Distillation is a common technique of separating pure liquid-phase products from mixed solutions, as well as the recovery of solvent and unreacted starting materials for recycling.[8,9] Liquid-liquid extraction, taking advantage of differences in solubility between components in two immiscible solvents, and various forms of chromatography are also widely used;[10–12] however, the scale at which these need to be performed often introduces significant complications in terms of safety and cost. In situations where other purification methods prove unsuccessful, often solid-state phase transformations can be an effective way of facilitating impurity rejection by altering the crystal lattice structure and/or polymorphic form of the crystalline product. This is especially useful for phase impurities such as solvents, the inclusion of which are dependent on the packing structure of a crystal lattice.[13] However, altering the phase of a solid drug product has an impact on the physical and chemical properties of the material, potentially impacting the formulation, dosage, solubility, and bioavailability amongst other properties of the drug. In many cases, when all purification efforts are exhausted, methodological changes are needed in the synthetic stage to minimise the generation of impurities.[14–16] All the approaches mentioned above have uses depending on the circumstances of the impure systems. As such, knowledge about the nature and distribution of impurities within batches of drug products is vital to informing the most appropriate and effective purification method.

1.1.2 Purification-Resistant Impurities

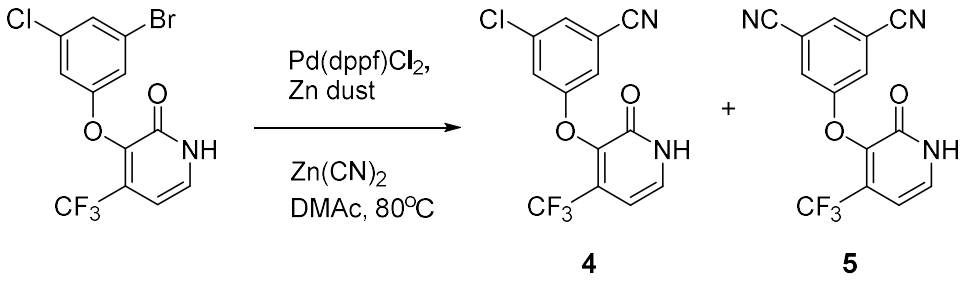
While the large majority of impure crystal products can be purified to safe levels by crystallisation, there have been many reported cases of impurities that are resistant to rejection in this way. For example, in one stage in the synthetic route to forming the *β*-amyloid cleaving enzyme inhibitor LY2886721 (Scheme 1.1), researchers reported the formation of two impurities alongside the primary product (compound **1**).[14] Purification of compound **1** by crystallisation from a solution of water and 1-propanol succeeded in purging the "des-Ac" compound **2**, but not the "des-F" compound **3**. Efforts to reject the des-F impurity **3** resulted in an unsatisfactory level of purity both of compound **1** and later downstream products. Ultimately a change in the synthetic method was necessary, performing the reaction under more acidic conditions to limit the formation of compound **3** to < 0.1%. This resulted in an increased formation of the des-Ac impurity **2**, which could be satisfactorily rejected by crystallisation.



Scheme 1.1. Reductive ring-opening stage in the synthesis of LY2886721, showing the formation of the main product **1** as well as the des-Ac impurity **2** and des-F impurity **3**.[14,17]

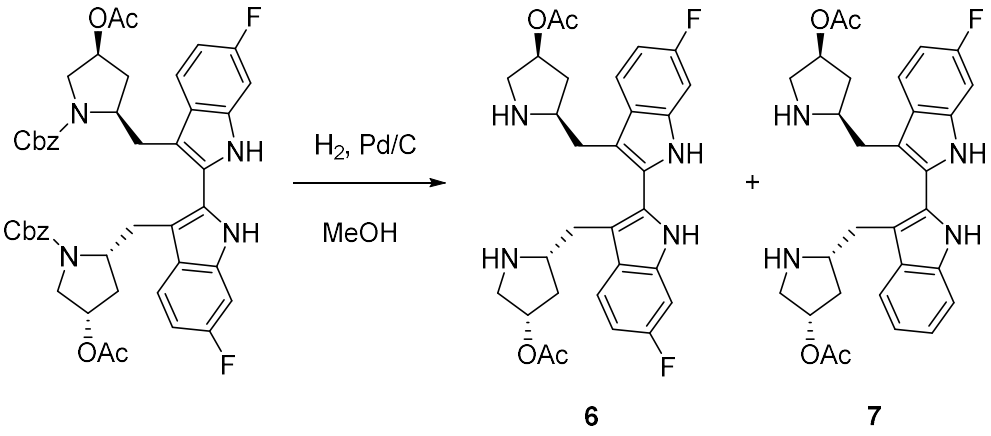
Similarly, while researching a kilo-scale synthesis of the HIV-treatment drug Doravirine, a bis-cyanation impurity **5** was discovered to be forming during the

production of the pyridone intermediate **4** (Scheme 1.2).[15] This impurity proved highly resistant to purification by crystallisation, and once again necessitated a change to the reaction conditions to prevent its formation; this time employing copper(I) cyanide in *N*-methyl-2-pyrrolidone and using an iodo-substituted starting material in the place of the original bromo-substituted species. This resulted in a high-yielding conversion to compound **4** with no formation of the bis-cyano impurity observed.



Scheme 1.2. Cyanation reaction step in the synthesis of Doravirine, forming the mono-cyanation primary product **4** and the bis-cyanation impurity **5**.[15,17]

In a final example of purification-resistant impurities, one was discovered during the deprotection hydrogenation step in the synthesis of birinapant (Scheme 1.3), involved in certain cancer treatments.[16] This impurity (compound **7**) was unable to be purged from the product (compound **6**) by recrystallisation at this or subsequent stages in the synthesis. The solution took the form of alternative hydrogenation conditions; use of hydrogen bromide and acetic acid in the place of hydrogen gas and palladium on carbon was found to produce similar yields of compound **6** with no observable formation of compound **7**.



Scheme 1.3. Deprotection step in the synthesis of birinapant, showing the formation of the product **6** and a purification-resistant des-F impurity **7**.[16,17]

1.1.3 Quantification of Impurity Behaviour during Crystallisation

The quantification of impurity level reduction over the course of a crystallisation is an important metric for gauging the effectiveness of the process and the resistance of impurity species to purification. In situations where the response factors of both the host drug and relevant impurities are known, and, as such, the impurity proportions as determined by high-performance liquid chromatography (HPLC) can be measured with a high degree of precision, a series of simple molar fraction calculations like those described by Urwin *et al*. can be used to measure impurity rejection by crystallisation.[18] An evolution of a metric of quantifying additive incorporation described by Hendrikson *et al*.,[19] the process is presented as a step in a larger approach of managing impurities during industrial crystallization development.

In the Urwin *et al*. approach, the level of resistance to rejection of an impurity in a system is quantified by its selectivity coefficient (α_1), calculated by a series of two successive formulae shown below (Formula 1.1 and Formula 1.2). The impure system is subjected to a recrystallisation process. The experimental distribution coefficient for a component (K_c) is determined by dividing the mole fraction of that component in the post-crystallisation solid phase (X_s^c) by the mole fraction of the component in the post-crystallisation liquid phase (X_l^c) (Formula 1.1). This is used to determine the distribution coefficient for both the impurity component (K_i) and the active pharmaceutical ingredient (API) host component (K_A). The selectivity coefficient (α_1) for the impurity in that system is defined as the ratio between those two values (Formula 1.2). The α_1-value for a system usually falls between 0 and 1. A low α_1-value implies that the impurity is well rejected from the system through recrystallisation, whereas a value closer to 1 suggests a high resistance of the impurity to rejection. If the α_1-value is greater than 1, the impurity content of the system can be said to increase after the recrystallisation process.

Formula 1.1. $$K_c = \frac{X_s^c}{X_l^c}$$

Formula 1.2. $$\alpha_1 = \frac{K_i}{K_A}$$

At this point it is worth clarifying the distinction between three similar terms used over the course of this text that may otherwise cause confusion. As discussed above, as well as in more detail in Section 4.4, the selectivity coefficient value which quantifies the

resistance of an impurity species to rejection from an impure system is denoted by the symbol α_1. A similar symbol (α_2) is introduced in Section 5.2.1.2 to describe the distribution coefficient, a measure of the distribution of additives or impurities within a crystal that corrects for the doping level of the system. Finally, a third similar but distinct symbol (α^0) is employed in Section 2.5.2.2 as the pure-component relative solubility. This is a comparative measure of the solubility of two compounds in a solvent and has uses in predicting levels of additive or impurity incorporation. The symbol α is used in the literature to describe each of these expressions and hence has been retained here with the use of superscripts and subscripts to distinguish between them. The distinction between these three terms is reiterated in each section of the text in which they are discussed.

Aside from the Urwin *et al.*, a number of other means of quantifying the behaviour of impurities during crystallisation exist, with unique advantages in different situations. For example, Caspi *et al*. propose a similar method of analysing the effectiveness of impurity rejection during crystallisation as Urwin *et al.*, but using mass-based formulae to eliminate the need of determining response factors for each analyte.[20] Alternatively, Teasdale *et al*. developed a more comprehensive means of analysing the behaviour of a genotoxic impurity in a synthetic process.[21] This method assigns a "purge factor" to the impurity, that quantifies its ease of removal from an impure batch based on a wide range of factors specific to the process that can influence such a removal, including the reactivity, solubility, volatility, and ionisablility of the species.

1.2 Crystals and Crystallisation

1.2.1 The Crystal

A crystalline solid is a material whose components are arranged in an organised structure which extends in a repeating pattern so that the internal structure (lattice) is highly regular.[22] The components can consist of atoms, molecules, or ions, which occupy specific positions in the lattice, known as lattice points. The regularity of the lattice gives rise to a characteristic supramolecular structure, with smooth faces and defined angles. This regularity also sets crystals apart from amorphous solids, like glass, which have no defined pattern between their constituents. A crystal lattice can be broken down into its simplest unit, known as the unit cell. The components at each lattice point in a unit cell are repeated along the translational vectors throughout the crystal.

The means by which the components at each point in the lattice are bonded depends on the nature of the components. Covalent crystals are often encountered in mineralogy, and consist of single atoms at each lattice point linked by covalent bonds.[23] The strength of these bonds makes covalent crystals extremely stable with very high melting points. Carbon-based crystals such as graphite or diamond would fall under this categorisation. Inorganic salts such as sodium chloride (NaCl) would be classified as ionic crystals, with ionic bonds linking charged components. Again, these crystals have a high melting point due to the strength of these bonds, but they are generally highly soluble in aqueous solvents.[24] Metallic crystals, such as the ones formed by a wide variety of elemental metals such as gold, copper, and iron, are linked by bonds between the cationic

metal species and the surrounding cloud of delocalised electrons.[25] Finally, molecular crystals are collections of polyatomic molecules, locked in patterns of defined orientation and repeating units by hydrogen bonding and weak van der Waals attractions. These weaker bonds contribute to lower melting points being recorded for these crystals than other types. Naturally, most pharmaceutical crystals fall into this category.[26]

A unit cell can be characterised by certain lattice parameters, namely the unit length along each translational vector (*a*, *b*, and *c*) and the angles between the vectors (*α*, *β*, and *γ*).[22] These parameters are illustrated on a unit cell model in Figure 1.1. Based on the combination of lattice parameters observed in the unit cell of a crystal, that crystal can be categorised into one of seven lattice systems; the systems and their requirements are listed in Table 1.1. Each system can be subdivided further into space groups based on the symmetry of the unit cell amongst other factors. Crystal systems with the same space group and unit cell dimensions are said to be isomorphous.[27]

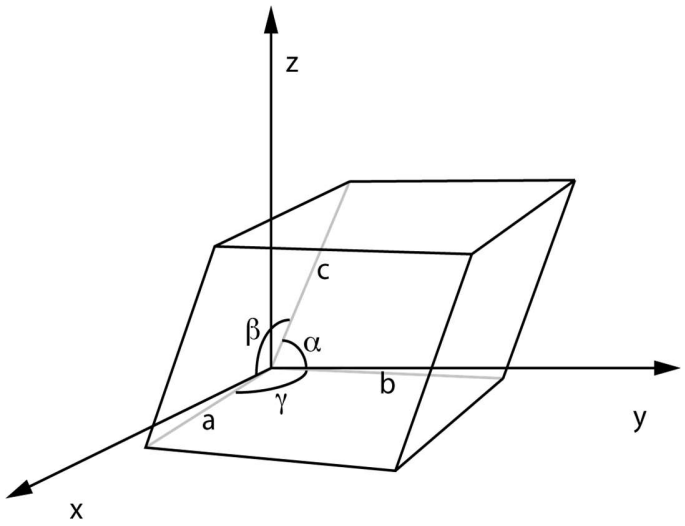


Fig 1.1. Model of a basic crystal unit cell, including the lengths along each edge (*a*, *b*, and *c*), and the angles between them (*α*, *β*, and *γ*).[28]

Table 1.1. The seven lattice system categories under which a unit call can be classified, and the cell length and cell angle relationships that define them.

Lattice System	Cell Length Relationship	Cell Angle Relationship
Cubic	$a = b = c$	$\alpha = \beta = \gamma = 90^o$
Tetragonal	$a = b \neq c$	$\alpha = \beta = \gamma = 90^o$
Orthorhombic	$a \neq b \neq c$	$\alpha = \beta = \gamma = 90^o$
Monoclinic	$a \neq b \neq c$	$\alpha = 90^o, \beta \neq 90^o, \gamma = 90^o$
Triclinic	$a \neq b \neq c,$	$\alpha \neq 90^o, \beta \neq 90^o, \gamma \neq 90^o$
Hexagonal	$a = b \neq c,$	$\alpha = \beta = 90^o, \gamma = 120^o$
Rhombohedral	$a = b = c$	$\alpha = \beta = \gamma$
	$a' = b' \neq c'$	$\alpha' = \beta' = 90^o, \gamma' = 120^o$

1.2.2 Crystallisation

1.2.2.1 Nucleation

The formation of crystalline material from solution takes place in two stages: the nucleation of the first solid material from the solution, followed by crystal growth on the nucleated material.[29] Nucleation can be described as a phase change of a critical number of molecules from a supersaturated solution to an organised crystal body. This can be induced with the use of seeding crystals, which provide an anchor for crystal generation to begin, or it can occur spontaneously; these routes are described by many researchers as secondary and primary nucleation respectively.[30–32] In turn, primary nucleation can be induced heterogeneously by foreign nucleation points other than seeding crystals, such as

the surface of the crystallisation vessel, or homogenously, in which the generation of crystals happens in solution and independent of external nucleation induction sites. Nucleation as a process is defined by an element of randomness. In two identical supersaturated solutions, the nucleation of crystals has been demonstrated to occur at different times.[33,34] As such, secondary nucleation and heterogeneous primary nucleation are beneficial as they afford more control over the growth and the morphology of crystals.[35]

The saturation of a solute in solution for a system can be plotted as a function of concentration and temperature (e.g. Figure 1.2). The solubility curve (blue) marks the concentration that the solution becomes saturated at a given temperature; at concentrations lower than this point the solute will stay in solution. The red line denotes the metastable limit, concentrations above this enter the labile zone where the solution is so supersaturated that crystallisation is certain to occur under normal circumstances. The area between these two curves is known as the metastable zone or the metastable zone width (MSZW); a system that falls in this zone is supersaturated but may remain in solution or crystallise spontaneously. Crystallisation can be induced by forcing the system closer to the labile zone, and so increasing the probability of spontaneous nucleation. This can be achieved by increasing the concentration of the solute (e.g. solvent evaporation), lowering the temperature of the system (i.e. cooling), or otherwise decreasing the solubility of the solute in the solvent system (e.g. addition of an antisolvent). The saturation plot is highly dependent on the system being studied; the addition of foreign species such as additives or impurities can significantly alter the crystallisation behaviour

of a system. The relative metastable behaviour of each species in a system can also affect the extent and pattern of their incorporation into crystals grown from that system.

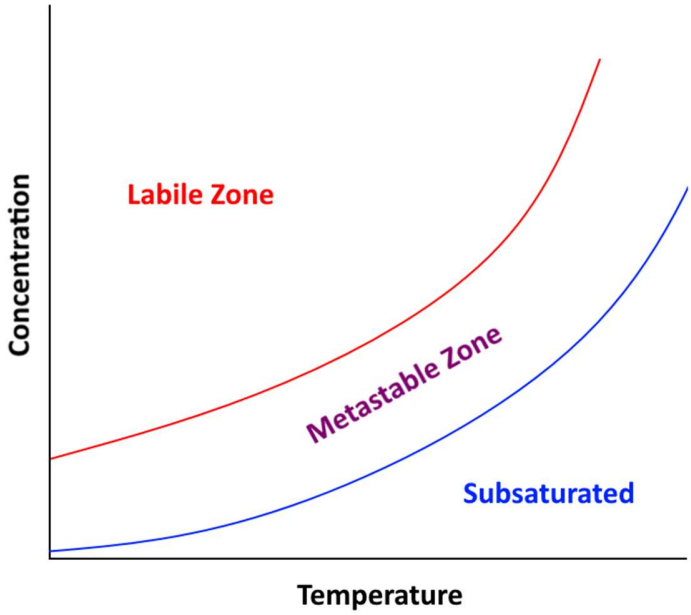


Fig 1.2. Illustration of the saturation behaviour and metastable zone for a hypothetical system of solute in solution.

The concentration within a supersaturated solution fluctuates with the movement of dissolved particles, giving rise to clusters of pre-nucleation solute. There is debate as to whether these solute clusters exist as pockets of high-concentration solution before crystal growth begins, as suggested by the two-step nucleation theory, or as ordered subcritical groups of solute molecules closer to the regular crystal structure they would subsequently form, as per classical nucleation theory.[36] The disorder of the liquid of described by two-step nucleation theory could contribute to the appreciable incorporation

of additive or impurity molecules observed at the core of many of the crystals studied as part of this project (see Chapter 5).

Nucleation is often considered as a competition between free energies, defined in its simplest form by Formula 1.3 below.[30,37] The total free energy change required for the formation of a crystal from one of these clusters (ΔG) is the sum of the free energy change for the phase transformation, ΔG_v, and the free energy change for the formation of a surface, ΔG_s. ΔG_v describes the spontaneous tendency of the solute to precipitate out of a supersaturated solution. Since the solid form is lower in energy than the liquid form, this free energy change is negative, and favours nucleation. ΔG_s is the balancing factor and takes into account the energy required to introduce a solid-liquid interface. The formation of this type of interface is thermodynamically unfavourable, driving the free energy of the system up and favouring dissolution. The relative magnitudes of these energy terms are dependent on the size of the cluster; as cluster size increases, ΔG_v increases and ΔG_s decreases. Therefore, smaller clusters dissolve and larger clusters nucleate. This also means there is a critical size (r_c) at which the ΔG_v value becomes larger than the ΔG_s. This causes the overall ΔG to become negative, resulting in the spontaneous nucleation of solid crystals. The relationship between the size of the cluster nucleus and free energy change can be seen on the free energy diagram in Figure 1.3.

Formula 1.3. $$\Delta G = \Delta G_v + \Delta G_s$$

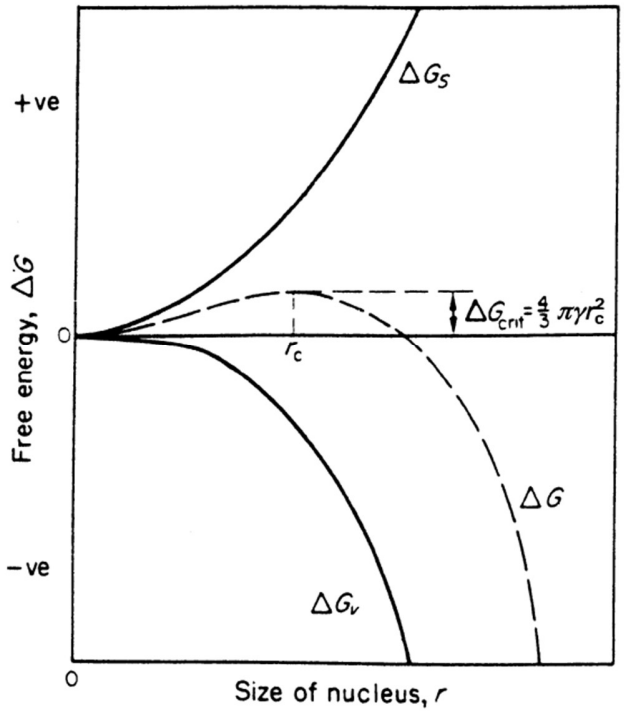


Fig 1.3. Plot of the free energy factors affecting a cluster of solute in solution, and the critical difference in free energy required for crystal nucleation to occur, according to classical nucleation theory.[30]

1.2.2.2 Crystal Growth

Once a nucleus of solid crystal is formed from a cluster of solute in solution, further molecules of solute diffuse out of the supersaturated solution and organise themselves on the surface of the nucleus, growing the crystal body in the repeating manner described previously.[29] While the mechanisms of continuous crystal growth have been extensively studied and are better understood than those of nucleation, the process is complex. Crystallisation is driven by supersaturation and the tendency of constituents to adhere to kinked or uneven sites on the crystal surface rather than smooth faces.[38,39] An

early explanation of the process by Gibbs suggested that molecules arrange themselves on a crystal in a manner that results in the lowest possible surface energy.[37] This theory was based on similar factors influencing the shape of a droplet of liquid. The theory has been adopted and adjusted in the years since but today is not generally accepted, as it fails to account for empirical effects of supersaturation and solution agitation on the rate of crystal growth.[29]

A wide range of other theories exist that attempt to explain the mechanisms by which crystal growth proceeds. Volmer suggested that rather than adhering directly to the crystal, solute molecules diffuse from solution into a highly-concentrated liquid layer near the surface of the crystal, migrating across it until a suitable site for attachment is found.[40] As mentioned, this site is most likely at a kink and/or ledge of atoms, where the newly affixed molecule would have the most interactions and, thus, the highest stability. In this way the crystal bulk expands in a layered fashion, and higher-index faces are favoured. Noyes and Whitney considered crystallisation as a diffusional process, acting as the reverse of dissolution, so that the driving force of the process is rooted in the difference between solute concentration at the crystal surface and in the solution bulk.[41] These and other theories are useful in understanding aspects of the observed behaviour of materials during crystallisation, and the process as a whole is likely the result of a combination of many mechanisms acting simultaneously.[29] Our means of controlling crystallisation are still primarily empirical, and a large number of techniques have been developed for influencing the growth rate, size, morphology, and polymorphic form of crystal products. The rate of crystallisation has a significant effect on the extent of crystal growth, as well as its shape and purity. A crystal grown rapidly tends to expand primarily on a single face,

often producing needle-like crystals, and foreign species are more easily uptaken into the crystal body. Slow crystallisation on the other hand tends to produce larger crystals with more even growth on all faces, and the slow addition of molecules to the growing crystal surface restricts the number of impurities incorporated.

1.2.2.3 Methods of Crystallisation

Evaporative Crystallisation

The growth of crystals can be achieved in a number of ways. Each has advantages and disadvantages, and the choice of crystallisation method and conditions is best tailored based on the chemical species and the intended nature of the crystals produced. A common method is crystallisation through solvent evaporation. This is an isothermal process by which an undersaturated solution of the material in a volatile solvent is allowed to evaporate under ambient conditions, driving the solution to supersaturation and inducing crystallisation. Evaporative crystallisation is a slow process, which is advantageous for the growth of well-developed crystals.[42,43] The rate of evaporation can be altered by choosing solvents with different volatilities, or by limiting the contact area of the solution surface to the surroundings, e.g., through the use of a perforated film or lid. The sporadic nature of nucleation means that little control is afforded over the growth of crystals by this method. As such, the resulting crystals can sometimes be of poor quality and possess unfavourable morphologies. These drawbacks often are mitigated by careful control of temperature, agitation, and the inclusion of seed crystals.[44] While crystallisation by evaporation has many benefits in small-scale research, it is uncommon in a

pharmaceutical process setting due to the time and solvent required to perform it on a larger scale.[43]

Cooling Crystallisation

The technique most commonly used for the crystallisation of large-scale batches of product is cooling crystallisation.[6,45] This is achieved by heating a suspension of the solid material in the crystallisation solvent to the point that the solubility of the material is sufficiently high and the solid is fully dissolved. The solution is then cooled, lowering the solubility of the material, and causing the solution to become supersaturated. In this supersaturated solution nucleation occurs, and further cooling encourages the growth of crystals.

The same control issues discussed in evaporation crystallisation are also encountered in this method, and can be mitigated in similar ways, by the use of seed crystals and careful control of agitation and cooling rate. Cooling crystallisation is more favoured by the pharmaceutical industry as it is time-efficient and requires less solvent than other processes such as evaporation.

Antisolvent Crystallisation

For certain systems and situations, evaporation and cooling can be problematic ways of inducing crystallisation. In some cases, the material to be crystallised has an unfavourable solubility curve or is unstable at or sensitive to high temperatures.[46,47] In such cases, crystallisation by precipitation can be used. This is commonly achieved through use of an antisolvent, addition of which lowers the solubility of the material in

solution, driving the system to supersaturation and inducing nucleation and crystal growth. This approach is often used in conjunction with cooling and seeding. In general, the high rate of crystallisation instigated by the precipitation process results in the production of very small crystal particles.[48] However, in situations where diffraction-quality crystals are not required, the efficiency of precipitation crystallisation methods make them an attractive option.

Reactive Crystallisation

In certain situations, a reactive additive can be included in the solution to encourage precipitation instead. This additive, known as a precipitant, often alters the chemical nature of the crystallisation material, thus changing its solubility in the solvent. Formulation of drug products as salts, e.g., by the addition of hydrochloric acid (HCl), is a common method of isolating crystalline product from solution.[49]

Crystallisation by Diffusion

Diffusion-based techniques work on a basis similar to antisolvent precipitation reactions but are designed for much slower crystal growth. As a result, they are widely used in the growth of large, single crystals suitable for study *via* single-crystal X-ray diffraction, though they are generally unsuitable for process-scale crystallisation.[50–52] There are two primary methods of diffusion crystallisation: liquid-liquid diffusion and vapour diffusion. Liquid-liquid diffusion is the process of carefully layering an antisolvent on a miscible solution of the material to be crystallised, so that an interface is formed between the two. The two layers slowly mix together *via* diffusion, reducing the solubility

and inducing crystal formation at the interface. In vapour diffusion, a vessel containing a solution of the crystallisation material is placed inside a larger vessel containing a larger volume of a miscible, more volatile anti-solvent precipitant. The larger vessel is sealed and left undisturbed. The anti-solvent vapours diffuse into the solution in the smaller vessel, reducing the solubility of the solvent and inducing crystallisation in the solution. Both techniques are illustrated in Figures 1.4 and 1.5 for liquid-liquid diffusion and vapour diffusion respectively.

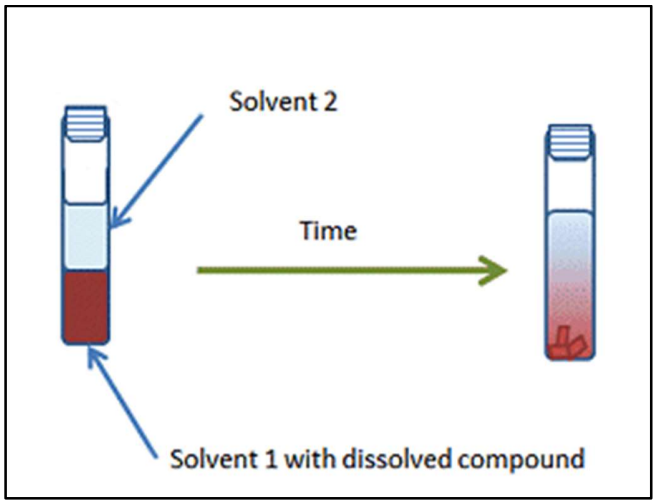


Fig 1.4. Illustration of the process of crystallisation by liquid-liquid diffusion.[53]

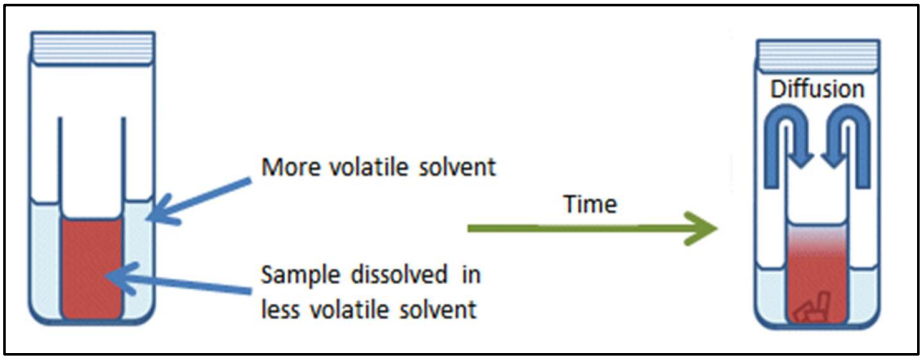


Fig 1.5. Illustration of the process of crystallisation by vapour diffusion.[53]

Crystallisation by Sublimation

Sublimation describes a phase change of a material from vapour to solid, without the usual transitional liquid phase.[54,55] This type of phase change can be employed for the growth of crystals. Solid material is heated under reduced pressure until it vaporises, rising in the vessel before crystallising either on the vessel walls or on a "cold finger" through which cool liquid or gas flows to create a low-temperature crystallisation point. An example of a sublimation set-up is illustrated in Figure 1.6. This process can be used to crystallise a solid material without the use of a solvent. Not only are solvent-free processes safer, greener, and more cost-effective, crystallising in this manner eliminates the solvent-solute interactions that often have a significant influence on crystal growth, a characteristic that can be advantageous to crystallisation control.[55] However, the technique is complex and non-scalable, risks thermal decomposition of material, and generally does not produce high quality crystals.[53,56] Also, a solid-to-vapour phase transition of the material would need to occur at accessible temperatures and pressures. As such, sublimation is not the first choice for crystal production in most situations.

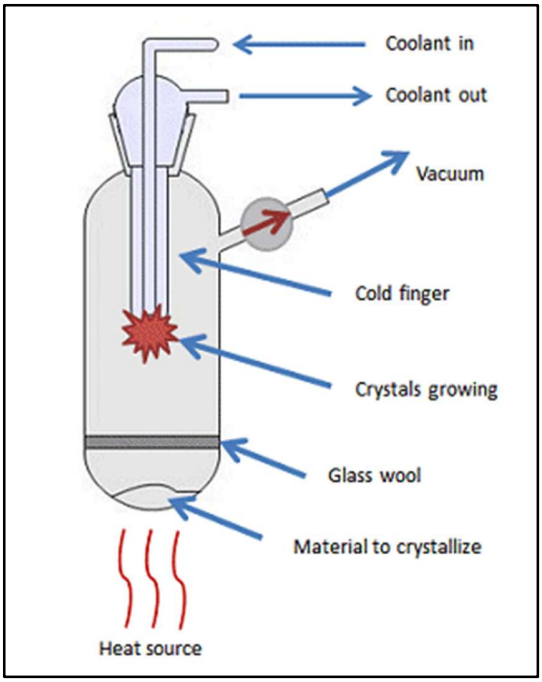


Fig 1.6. Illustration of the process of crystallisation by sublimation, using a cold finger crystallisation site.[53]

Crystallisation from the Melt

The term "melt" refers to an undissolved or neat material in its liquid phase; this can be used to refer to materials that exist as an oil or other fluid at room temperature.[57] These can be induced to crystallise by cooling and/or the addition of seed crystals; this can be useful for formulation or purification purposes, perhaps as an alternative to distillation for heat-sensitive products. Alternatively, solid material can be heated to above its melting point, then cooled to induce crystallisation. This is sometimes used to isolate metastable polymorphic forms; as described in Ostwald's Rule of Stages, the often metastable kinetic polymorph of a material is preferentially formed during cooling, transforming to the thermodynamically stable form over time.[58,59]

1.2.3 Crystal Morphology and Habit

The morphology of a crystal is a descriptor set of faces of a crystal that are dependent on the polymorphic form, habit and defects.[60] The habit of a crystal refers just to the characteristic external shape of the crystal.[61] The descriptors "habit", "shape", and "morphology" are often used interchangeably when referring to the appearance of crystalline material. While the morphology of a crystal is largely defined by which of the seven families of lattice structures it belongs to, it is also heavily influenced by the extent of growth experienced by each of the faces of the crystal. In mineralogy, there are many different classifications of crystal habit reflecting the wide array of diverse forms characteristic to different inorganic materials.[62] In pharmaceutics, however, crystals can generally be classified as one of three forms: tabular, prismatic, and acicular.[63] Illustrations of the three forms for a crystal belonging to the hexagonal family are shown in Figure 1.7. When relatively even growth occurs across all faces, a prismatic crystal (b) is formed. These crystals can be large, with the highest degree of circularity of the three. As such, they are the ideal crystals for diffraction studies, and are often described as "high-quality" in this context.[53,64] If growth is stunted in one dimension, the flatter tabular crystal (a) is produced. If this stunting is excessive, extremely thin flake-like crystals can be produced. Finally, if the growth of a crystal in one direction is significantly more developed than the others, elongated acicular crystals (c) are grown. Widely referred to as needles, these fragile crystals tend to taper to a point at the tip.

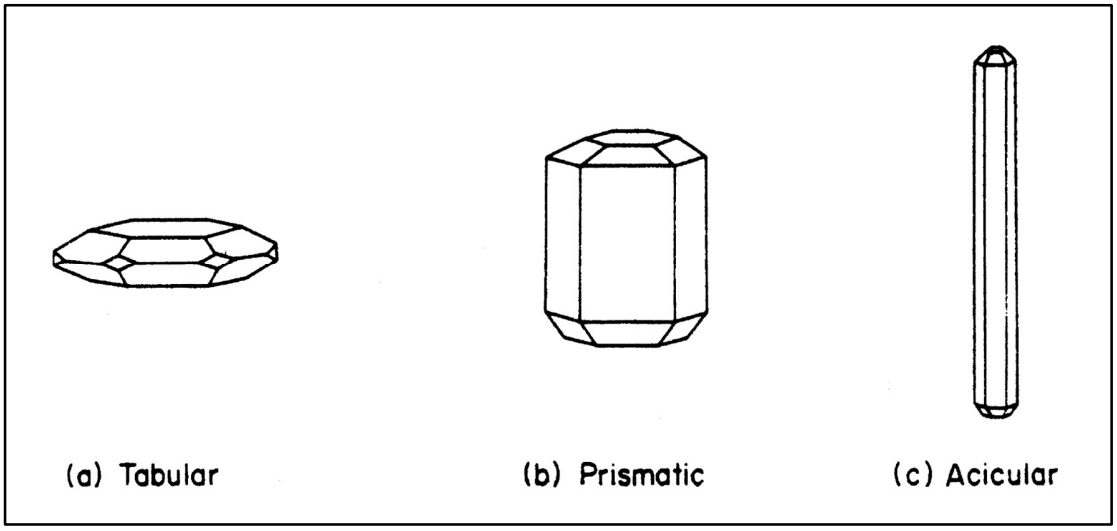


Fig 1.7. Illustration of tabular (a), prismatic (b), and acicular (c) habits of a hexagonal crystal.[63]

There are a number of factors that can influence the morphology of a crystal. Different polymorphic forms of the same material often crystallise into different habits.[65,66] The rate of crystallisation is important; rapid crystal formation, e.g. by rapid cooling or the addition of a precipitant, often results in small acicular crystals, while larger prismatic crystals generally require long periods of undisturbed growth to produce.[63,67] Use of different solvents in the crystallisation solution can lead to different solvent-solute interactions, altering the crystallisation behaviour of the dissolved material. The supersaturation level of the solution at the time of nucleation can also have a large influence, as can the agitation of said solution. Finally, the presence of impurities or additives in the growing crystal often disrupts the development of certain crystal faces, increasing the likelihood that tabular or acicular habits will be formed over prismatic ones.

1.2.4 Polymorphism

Polymorphism (or allotropy for crystal systems involving elemental material) is the phenomenon in which the same chemical compound exhibits different crystal structures.[68] Substances with the same chemical make-up can form crystals that fall under different family and lattice group classifications; as such, they can exhibit significantly different crystal habits, colours, and physical properties.[69] The formation of one polymorph over another can be the result of a variety of factors during crystallisation: e.g., crystallisation temperature, solvent choice, or the inclusion of certain seeds or polymeric heteronuclei.[70]

In general, a material has a single polymorphic form that is the most thermodynamically stable at a given temperature and pressure. The formation of other polymorphs of that material can often be kinetically favoured under many crystallisation conditions. These polymorphs are known as metastable forms and can be obtained under those conditions despite not being the thermodynamically stable forms. In fact, as mentioned in Section 1.2.2.3, Ostwald's rule of stages suggests that the less thermodynamically stable, kinetically favoured polymorph is the first to form during the crystallisation of a substance.[58,59] These metastable polymorphs often subsequently rearrange themselves over time into a more stable form, either by re-dissolution and re-nucleation of the material or *via* a solid-state transformation from one form to another.[59,71] This can sometimes be problematic as polymorphic transformations often are accompanied by a volume change; e.g., ammonium nitrate can potentially burst from metal storage containers when the Form II material transforms to Form III at ambient temperatures.[63] The thermodynamically stable form of a material can also vary based on

the temperature and/or pressure; e.g., again in the case of ammonium nitrate, the salt has five polymorphs, each the stable form in a different temperature range between −18 °C and 125 °C (Figure 1.8).[63,72] Ammonium nitrate can reversibly interconvert between these polymorphic forms with changing temperature; in this way the forms are known as enantiotropic.[73] Should the transitions from one form to another be irreversible, the system would be considered monotropic.

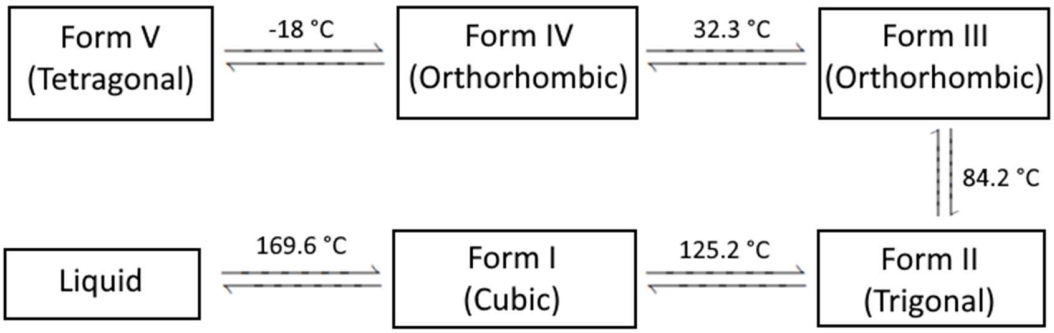


Fig 1.8. The transition temperatures between liquid ammonium nitrate and its five polymorphic forms, as well as the lattice systems of those forms.

As mentioned, the polymorphic form of a material can affect its melting point, solubility profile, and density, amongst other physical properties. The formation of metastable polymorphs is often desirable if that metastable form exhibits more favourable physical properties than the stable form. This is especially relevant in the pharmaceutical industry, where producing a drug product with a suitable solubility and bioavailability is a high priority. As such, the polymorphic form of a drug can have significant influence on the effectiveness and marketability of the product. For example, two polymorphic forms exist of the antiretroviral drug Ritonavir: the originally developed Form I and the more stable, less soluble, and less bioavailable Form II (increased stability is usually

associated with lower solubility).[74,75] Discovery of this second form forced the removal of the drug from the market and the reformulation of the original capsule to a refrigerated gel-cap to ensure only Form I Ritonavir was present in the product. A landmark legal case allowed Glaxo to extend its patent on Ranitidine, the active ingredient of Zantac, through the use of a different polymorphic form of the drug.[76]

It has been suggested that "the number of forms known for a given compound is proportional to the time and money spent in research on that compound."[77] Despite this, the occurrence of polymorphism in single component compounds was found to be just 37% in the Cambridge Structural Database (CSD).[78,79] Generally, materials known to be polymorphic have two or three reported forms, known as dimorphic or trimorphic materials respectively. Some compounds are more prone to polymorphism than others. For example, for many years the benchmark of polymorphic behaviour was 5-methyl-2-[(2-nitrophenyl)amino]-3-thiophenecarbonitrile, dubbed ROY, with twelve characterised forms,[80] while triacetone-tiperoxide (TATP) has been found to form at least six.[81]

1.3 Additives and Impurities

There is an important distinction to be made between the concepts of "additives" and "impurities" in the context of multi-component systems. Both are forms of substance that are foreign to the host material, and can affect the physical, chemical, and pharmacological properties of that material. However, the difference lies in the intent; "impurities" is the name given to foreign species, mostly unwanted, that are introduced unintentionally during a chemical process, e.g. synthesis.[1] Additives, on the other hand,

are foreign species added deliberately to a host system.[60] Additives often have many of the same effects on the host material as impurities, but these effects are generally intentional and targeted. The inclusion of such additives to a material is known as doping. Use of the term "doping" generally implies that the additive is intended to alter or generate specific properties of the material.[82] In the context of the current work however, the descriptor will be also used to refer to the inclusion of additives in a host material in situations where affecting the material's properties is not the primary goal.

The various types of impurities encountered in the pharmaceutical industry have been discussed previously in Section 1.1. In pharmaceutics, additives can be a form of excipient, and are generally included in drug material during the formulation stage of product development. In this function, they include preservatives to prolong shelf-life, glidants to enhance powder flowability, and emulsifying agents.[83] Additives can also be included during the crystallisation stage of product development. Crystallisation inhibitors can be tailored to promote growth on certain crystal faces over others, thus, producing crystals with a different habit than those produced with no additive.[84,85] Similar additives can also be used to promote the preferential formation of specific polymorphs in some cases.[86]

1.3.1 Means of Impurity and Additive Incorporation

1.3.1.1 Physical Mixtures

There are a number of different ways an additive or impurity can be present in an otherwise pure crystalline system, some of which are illustrated in Figure 1.9. The

simplest is as a physical mixture, where solid particles of the two components are intermingled with no chemical interaction between them, for example, the addition of colloidal silica to a drug product to enhance the flow of the formulation.[87] The chemical distinction between the two species is clear by most methods of analysis, and separation of the materials is often achievable with little difficulty.

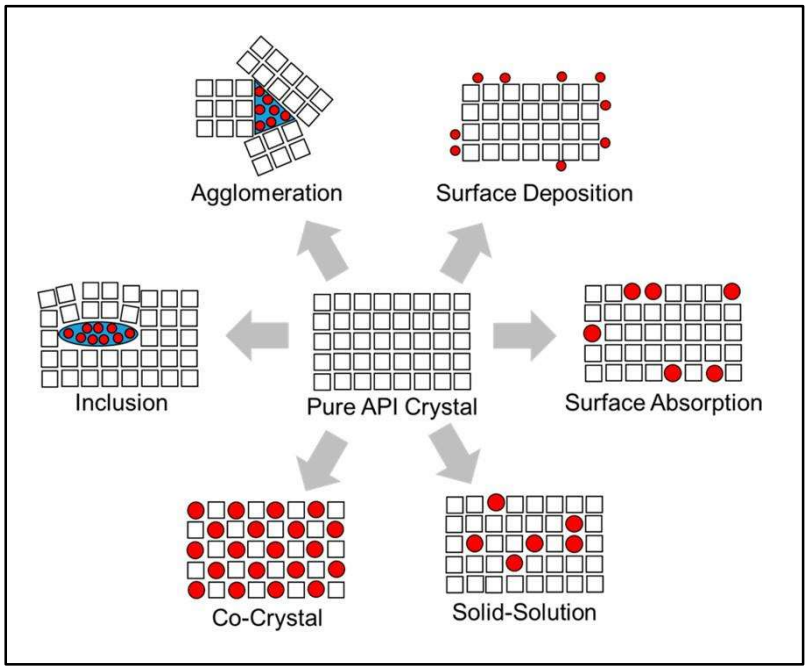


Fig 1.9. Illustration of some of the different means by which a foreign species (red circle) and solvent (blue) can be present in a crystal of pure active pharmaceutical ingredients (white squares).[18]

1.3.1.2 Surface Adsorption and Deposition

Sometimes an impurity or additive can be incorporated in the surface layer of a crystal, either by deposition or adsorption.[88,89] Deposition can occur when crystals growing from a solution containing a foreign species are removed from that solution, the

residual solvent on the crystal surface evaporating and depositing material.[90] Adsorption is similar, but a certain level of incorporation within the surface layers of a crystal is present. This is less disruptive to the overall crystal structure than surface-to-centre incorporation, especially with an impurity that is structurally and morphologically distinct from the host. As impurities included in this way are focused closer to the surface, washing and slurrying are often effective purification techniques.[91]

1.3.1.3 Inclusions and Agglomerations

In certain situations, relatively large pockets of impurity-rich mother liquor can be incorporated into the body of a crystal particle during growth. Known as impurity inclusions, they can be caused by rapid growing conditions, solvent-solute interactions, crystal attrition, or any combination of those factors.[92,93] Similar pockets of solvent can also become trapped between agglomerated crystal particles, rather than within single crystals.[94] Impurities incorporated in this manner may be rejected by recrystallisation, but changes in the crystallisation process may also be required.[29,95] Ultrasound processing has also proved effective in limiting the incorporation of impurities by agglomeration.[96,97]

1.3.1.4 Other Means of Incorporation

Other means of additive and impurity incorporation include solid solutions, eutectic mixtures, and co-crystals. These three types of system are discussed alongside their phase behaviour in the next section.

1.3.2 Phase Behaviour

A phase is a state of matter that is uniform throughout, not only in chemical composition but also in physical state.[98] As such, any system in a single homogenous state, be it solid, liquid, or vapour, is considered to consist of a single phase. This is true for single or multi-component systems, so long as the components are fully miscible, such as a solute fully dissolved in a solvent. Introduction of heterogeneous material that is not miscible, i.e., such that an interface forms between phases, classifies the system as containing two or more phases. Depending on the system, the number of phases present can be changed by adjusting one or more of (usually) three variables: composition, temperature, and pressure.

1.3.2.1 Single-Component

The most effective and versatile way of visualising phase behaviour is through the construction of a phase diagram. This is a chart upon which the most stable phase of a system can be visualised with regard to two or more of the aforementioned variables. In single-component systems, phase changes are tracked as a function of temperature and pressure, as composition is not a valid variable in such a system. For example, the phase behaviour of water is plotted on the diagram in Figure 1.10. The three phases in which water exists, liquid (water), solid (ice), and vapour (steam), are depicted along with phase boundaries marking the points at which the system transitions from one to the other. The triple point of water, the temperature and pressure conditions at which the three phases can coexist, is labelled *B*. The polymorphic behaviour of a single-component material can

also be visualised on a temperature-pressure phase diagram; despite having the same chemical make-up, in most cases different polymorphic forms qualify as different phases.

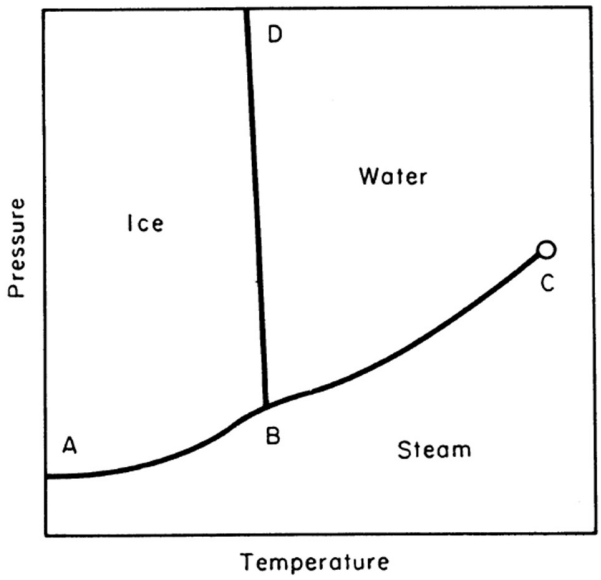


Fig 1.10. One-component phase diagram of water showing the transitions between three phases (ice, water, and steam) with changing temperature and pressure.[99]

1.3.2.2 Two-Component Systems

Adding a second component (including additives and impurities) allows for the use of composition as a variable in the phase diagram of a system. As such, three binary diagrams can be constructed for a single two-component system, describing the phase behaviour in relation to temperature-pressure, temperature-composition, and composition-pressure. Alternatively, a space model can be constructed for the system with three perpendicular axes representing each of the variables. However, most crystal processes are performed at atmospheric pressure, and, as such, that variable is usually

kept constant (isobaric conditions). Additionally, unless working with sublimation crystallisations, interest is often limited to systems in the liquid and solid phase. As such, two-component systems are generally presented in the form of binary temperature-composition phase diagrams focused on the behaviour of the system over these two phases. Different methods of additive and impurity inclusion naturally give rise to different phase behaviours. In particular, co-crystals, solid solutions, and eutectic systems have distinctive phase behaviours that, when plotted on such a diagram, can help characterise a system and the relationship between the two components.

1.3.2.3 Construction of Phase Diagrams by Thermal Analysis

Construction of phase diagrams was once a much more imprecise and laborious process, relying on observations from sample cooling or time-consuming isothermal experiments.[100,101] Sometimes the characterisation of an unknown system relied on the extrapolation of the phase behaviour of a related, known system as an estimation that could be adjusted to fit experimental data.[102,103] More recent calorimetric techniques such as differential thermal analysis (DTA) and differential scanning calorimetry (DSC) have allowed for the faster and more accurate determination of the thermal events used to construct phase diagrams. The latter technique, DSC, is the method by which the systems in this research will be analysed and phase diagrams examining their solid-state behaviour constructed.

1.3.2.4 Types of Two-Component Phase Diagrams

Physical Mixtures

For the sake of contrasting with the plots of other systems, an illustration of the expected binary phase diagram of a physical mixture of two components *A* and *B* is shown below in Figure 1.11. On the diagram, the dotted line represents the onset melting temperature of the lower-melting material, while the solid line represents the melting of the higher-melting material. There is a slight decrease in the melting temperature of the higher melting-point (m.p.) component with increasing *A* or *B* composition, characteristic of any impure material.[104] The defining attribute of a physical mixture is that both phases behave completely independently of each other at all compositions. This relationship is reasonably rare; most materials exhibit some level of more complex behaviour.

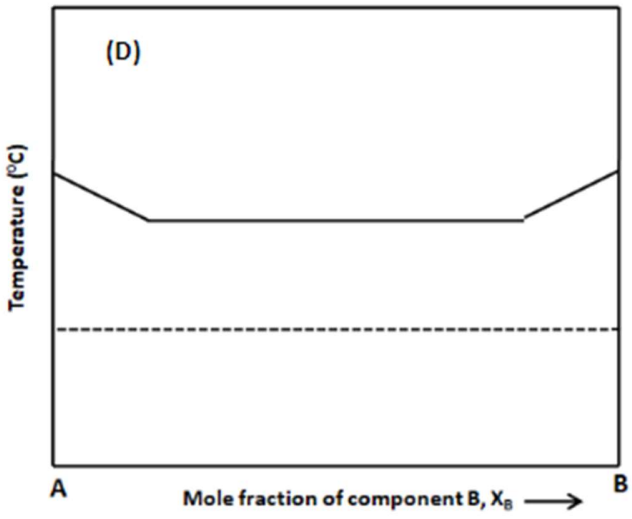


Fig 1.11. Two-component phase diagram of a physical mixture of components *A* and *B*.[105]

Solid Solutions

Solid solutions are mixtures of two components, usually isomorphous or isostructural, which do not precipitate individually when solidified, instead precipitating simultaneously as a single phase.[18,106] In substitutional solid solutions, one component, commonly known as the solute, is dispersed throughout the other (solvent or host) replacing a molecule of the host within the crystal lattice structure. Less commonly, the solute occupies a void between molecules in the host lattice forming an interstitial solid solution. In both these systems the solute is dispersed relatively evenly throughout the crystal structure of the host, which remains unaltered. Some solid solutions are continuous, maintaining the behaviour of the system at any ratio of the two components. Others, known as partial or terminal solid solutions, reach a miscibility limit at some proportion of solute inclusion, above which the behaviour of the system can be observed to change.

In substitutional solid solutions, units of the solute compounds interchange so easily with units of the host they often are resistant to purging by recrystallisation, redispersing within the host lattice during crystal growth. As such, crude batches of pharmaceutical products in which the impurities exhibit solid solution-like behaviour with the product are problematic in terms of purification.[14,17,107] In this way, the purification-resistant impurities discussed in Section 1.1.2 share many of the characteristics of solid solutions.

The homogeneous nature of an ideal, continuous two-component solid solution can be visualised on a binary phase diagram as seen in Figure 1.12. Two phases are represented on the diagram, that of the solid solution at lower temperatures and that of the

melted liquid at higher temperatures. In Figure 1.12, the unbroken line marks the boundary between the two phases (the liquidus), while the dotted line marks the temperature at which the solid material begins to melt (the solidus).

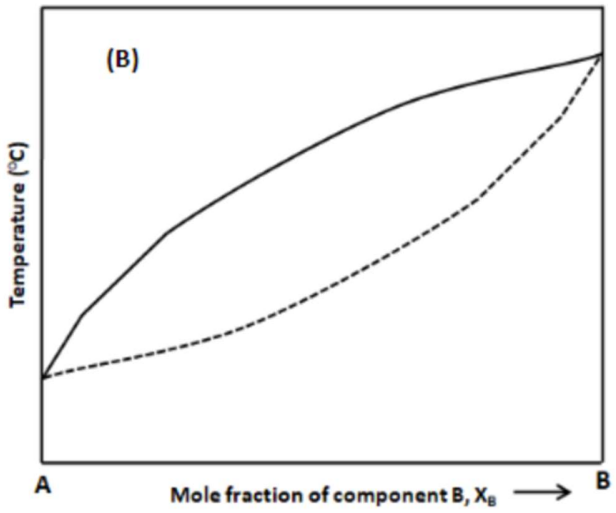


Fig 1.12. Two-component phase diagram of a continuous ideal solid solution of components *A* and *B*.[105]

When collecting thermal data by DSC, solid solutions can be recognised by the expression of a single endothermic peak representing the melting of the homogeneous material.[99] In an ideal continuous solid solution, the melting endotherm can be observed to widen with increasing levels of the second component (relative to the pure material melting peaks) and shift in temperature towards the m.p. of that component. The phase diagram boundary lines are plotted by measuring the onset point and the maximum of these peaks, as illustrated in Figure 1.13(c).

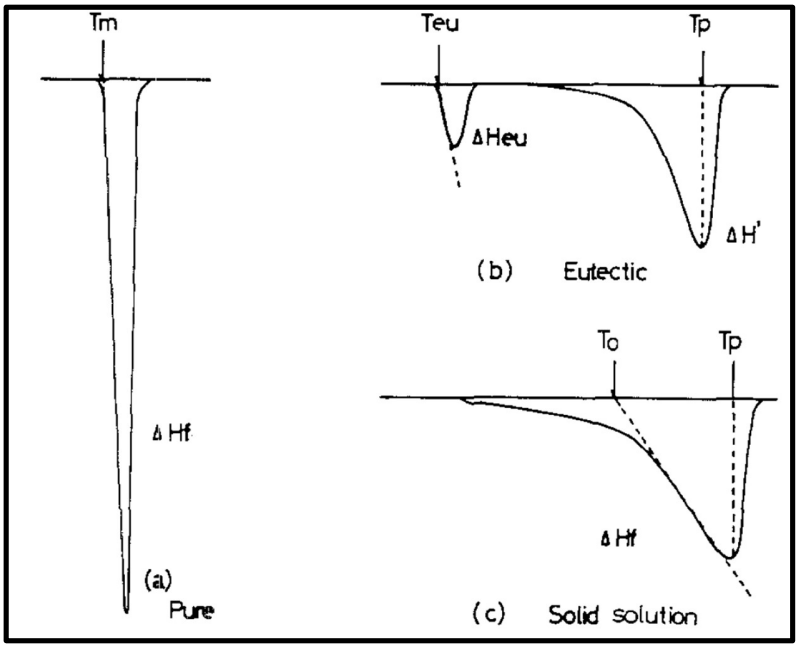


Fig 1.13. The types of DSC melting endotherm signal(s) expected from a pure material **(a)**, a eutectic system **(b)**, and a solid solution **(c)**, as well as temperature values used to construct phase diagrams of each (T_m = melting point; T_e = eutectic point; T_o = onset temperature; T_p = peak temperature).[99]

The shape of some continuous solid solution phase diagrams can deviate from that of Figure 1.13 above. In these cases, known as non-ideal solid solutions, the phase diagram of the system resembles that of Figure 1.14. Non-ideal solid solution systems can have a minimum point *M* at which the solidus and liquidus curves approach. The melting endotherm of the material at this point can be similarly narrow and sharp to those of the pure materials (Figure 1.13(a)). Additionally, the melting point of the solid solution material dips towards the minimum point, which is a lower temperature than the m.p. of either of the pure materials. In rare cases, a similar maximum point is instead observed on the diagram.

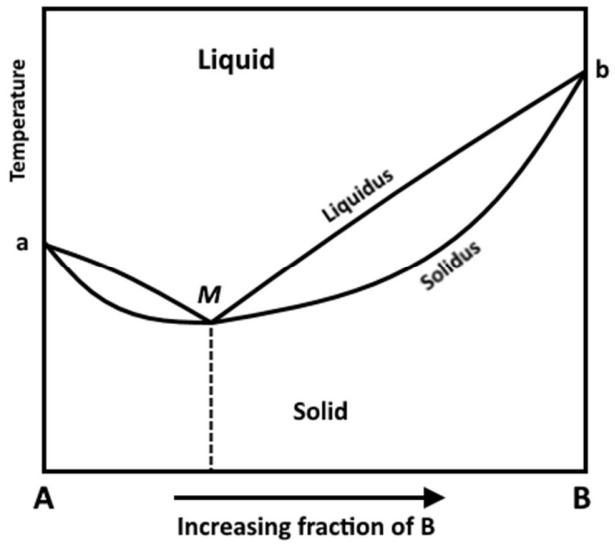


Fig 1.14. Example two-component phase diagram of a continuous non-ideal solid solution of *A* and *B* with minimum point *M*. *a* and *b* represent the pure melting temperatures of components *A* and *B* respectively.

Eutectics

Another means in which additives and impurities are incorporated is by way of a eutectic system. Eutectics are usually defined by a decrease in melting temperature of the mixed material compared to either pure component, and by the converging binary phase diagram discussed later in this section.[108,109] On a molecular level, a eutectic mixture is in fact a conglomeration of the two different components, or two solid solutions with different compositions of the two components in the system.[110] The components are usually too different structurally to form a true solid solution at the eutectic composition, so these two solid solutions form at the miscibility limits of each. Layers of the two solid solutions can often form lamellar arrangements, like in the tin-lead alloy system shown in Figure 1.15; these layers are held together by weak interphase boundaries. A combination of these bonds, the inherent strain of the constituent solid solutions, and imperfect atomic

arrangements contribute to the characteristic depressed melting temperature of the material.[111] A formal eutectic is composed of a defined ratio of the two components; a eutectic system made up of a different ratio of those components will in fact be a mixture of eutectic and solid solution material.

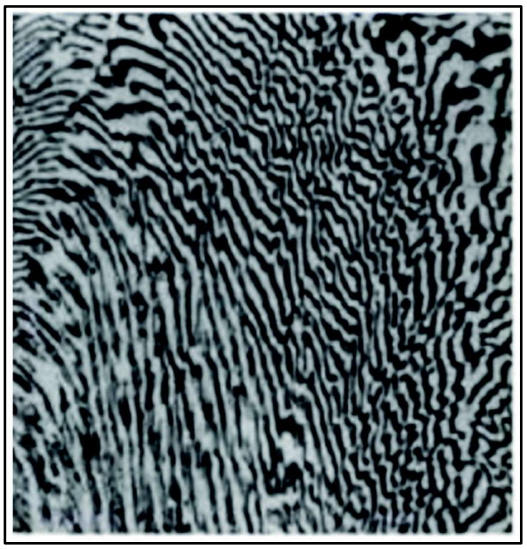


Fig 1.15. Photomicrograph of lead–tin eutectic material, showing the lamellar arrangement of two solid solutions of different component proportions in the eutectic solid.[110]

A sample from a simple eutectic system, the composition of which differs from that of the eutectic point, exhibits a characteristic second endothermic peak on a DSC curve. This is due to the solid sample being a mixture of the eutectic material and whichever component is in excess in relation to the eutectic point composition. An example of such a system is displayed in Figure 1.16. The endotherm with the lower melting point on the curve is the eutectic melt, represented by the line *cd* in Figure 1.16. The higher endotherm is the melt of the component present in excess of the eutectic composition, which drops in temperature as it approaches the eutectic point (*E*) as is

represented by the liquidus curves *aE* and *Eb*. This decrease in melting point is a characteristic feature of a eutectic system, though not an exclusive one; as mentioned previously, the melting points of certain non-ideal solid solutions can also decrease toward a minimum point. The area of the diagram to the left of the eutectic point is known as the hypoeutectic region, while to the right is called the hypereutectic region. This assignment is strictly arbitrary, dependant on which component is assigned to either extreme of the composition axis. A DSC curve of a sample with eutectic point composition appears as a single endotherm. Eutectic phase diagrams are constructed from DSC data by determining the temperature of the onset point of the eutectic endotherm and that of the peak maximum on the pure melt (Figure 1.13(b)).

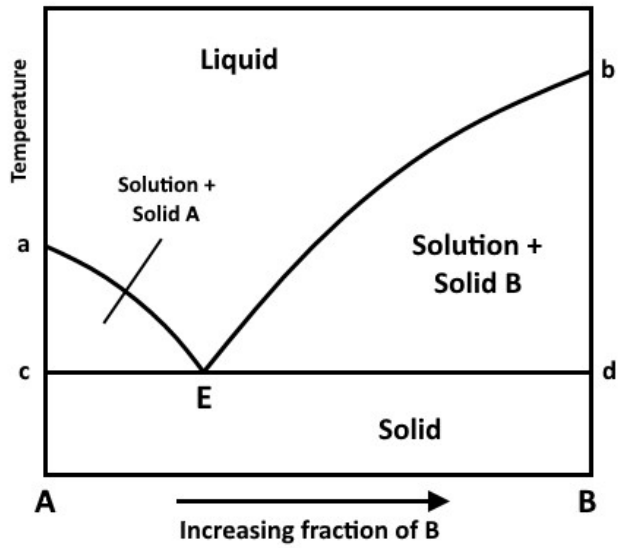


Fig 1.16. Example two-component phase diagram of a simple eutectic mixture of components *A* and *B*, including the eutectic point *E*. *a* and *b* represent the pure melting temperatures of components *A* and *B* respectively, while *c* and *d* represent the temperature of the eutectic solidus melt.

Not all systems exhibiting eutectic behaviour are simple eutectics. Often a system will exhibit regions of solid solution-like behaviour at each extreme of the composition axis. These systems, known as terminal or partial solid solutions, act as solid solutions up to a certain miscibility limit composition, after which the system reorganises as eutectic. An illustration of this can be seen in Figure 1.17. The solid solution regions for solute *B* in solvent *A* (α) and for solute *A* in solvent *B* (β) can be seen on either side of the diagram. The miscibility limits for α and β are labelled *c* and *d* respectively; compositions of *A* and *B* between these limits instead form a eutectic system.

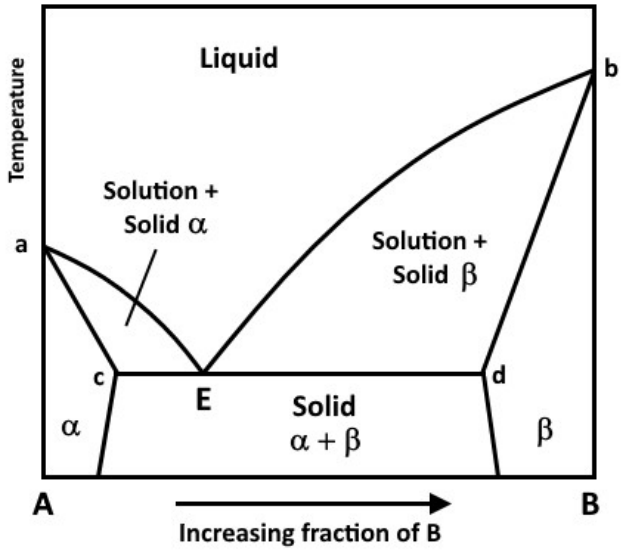


Fig 1.17. Two-component phase diagram of a eutectic mixture of components *A* and *B* with terminal solid solutions α and β at low compositions of each component. *a* and *b* represent the pure melting temperatures of components *A* and *B* respectively, while *c* and *d* represent the miscibility limits of each solid solution.

Co-Crystals

The final systems that will be discussed are those which form co-crystals. A co-crystal is defined as a "neutral crystalline single phase material composed of two or more different molecular and/or ionic compounds generally in a stoichiometric ratio which are neither solvates nor simple salts."[112] This material forms a homogeneous crystal structure that is distinct from the crystal structures of the pure components, and as a result can have significantly different physicochemical and pharmaceutical properties.[113] The components of co-crystals are solid at room temperature. Co-crystals have emerged as a promising area of pharmaceutical research in recent years, crystallising APIs with additives as a means of improving the properties of drug products.[114–116] In rare cases, unintended co-crystals can form between a material and an impurity forming a separate co-crystallised impurity phase; these can sometimes prove difficult to purify by recrystallisation.[117]

Co-crystals can be identified by a characteristic "W"-shaped liquidus curve (Figure 1.18). Systems capable of forming co-crystals have two eutectic points (T_{E1} and T_{E2}). At a composition between the eutectic points, marked *C* on the diagram, a co-crystal can form. On a DSC curve, the co-crystal is usually represented by a single endothermic melting peak, representing the homogenous co-crystalline phase, but can sometimes appear alongside endotherms representing the eutectic and/or pure material(s).[105]

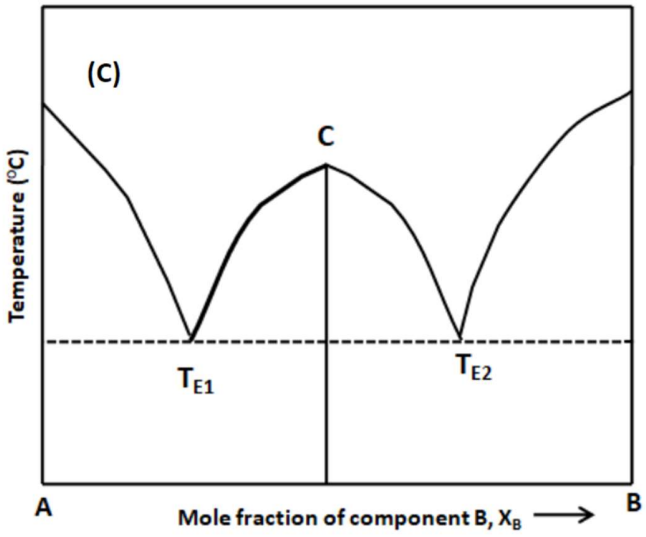


Fig 1.18. Two-component phase diagram of a simple co-crystal (*C*) of components *A* and *B*, including the two eutectic points T_{E1} and T_{E2}.[105]

1.3.2.5 Three-Component Systems

Although the interest of most crystallisation work, and, as such, this research, is limited to two-component binary phase diagrams, there are certain more complex systems that fall within the scope of the project. By introducing the crystallisation solvent as a component in a solid solution system, for example, a triangular three-component phase diagram can be constructed, such as the one in Figure 1.19. A diagram such as this can be used to gain insight into the composition of a system during the crystallisation process. This type of phase diagram is described in more detail in Section 5.2.1.2 when discussing patterns of additive distribution throughout solid solution crystals.

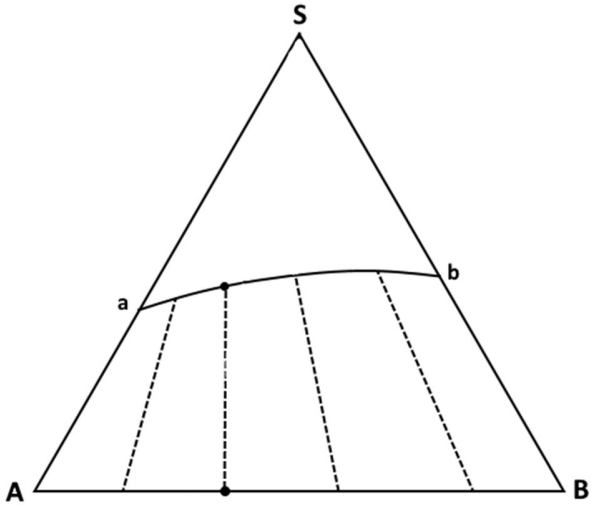


Fig 1.19. Three-component phase diagram of a continuous solid solution of components *A* and *B*, along with the crystallisation solvent *S* as the third component. Points *a* and *b* represent the solubilities of *A* and *B* in *S* respectively.

1.4 Research Aims

The issues surrounding purification-resistant impurities have been discussed earlier in the chapter. Pharmaceutical products containing impurities must be purified so the levels of those impurities are reduced to below a safe threshold before commercialisation.[1] If the impurities prove to be resistant to purification by crystallisation this can be problematic, as crystallisation is the most important means of process-scale impurity rejection.[6,17] Many alternative means of impurity limitation exist, ranging from washing and slurrying to phase transformations to changes in process.[7,13–16] However, design of a targeted and effective purification strategy requires detailed knowledge not only of the impurities themselves, but also of the nature of their incorporation into batches of crystalline drug product.

As such, this research aims to develop methods of determining the distribution of impurities and additives within a crystalline host. These methods are intended to be robust and provide detailed and meaningful data into impurity distributions while requiring no specialised equipment to perform. By employing these methods, a researcher should be able to gain insight into the distribution of an impurity within crystals of a drug product, and, hence, design an appropriate impurity management strategy. For example, if an impurity was found to be disproportionately present near the surface of a crystal, a wash or partial dissolution stage could be sufficient to reduce the levels of that impurity to below a safe threshold. Should even incorporation be observed throughout the crystal, a phase transformation or adjustment to the synthetic method may be required.

To develop such methods, an appropriate model of study must be selected. This model should reflect the types of purification-resistant impure systems encountered in the pharmaceutical industry. As such, the host for the model, representing the drug product itself, should also be an API. This API host would be doped with additives, representing process impurities, to produce the model of study for the work. To effectively mimic the type of purification-resistant impurities that the distribution methods are intended to investigate, these additives would also need to be highly resistant to rejection by recrystallisation. This requires additives that are designed specifically to exhibit this quality. It has been established previously in the chapter that crystal systems exhibiting solid solution-like behaviour share characteristics with purification-resistant impure products, namely that of appreciable solute incorporation and the consistent re-incorporation of those solute molecules during recrystallisation. As such, doped systems of additive and host that exhibit solid solution-like behaviour, would be appropriate

models to represent those purification-resistant impure products, even if they do not strictly qualify as solid solutions. Solid solutions are known to form between components which are isomorphous and/or isostructural.[27,110,118] Therefore, the additives would need to be selected to exhibit one or both of these qualities in relation to the host material. This selection process is discussed in detail in Section 2.2.2.

1.4.1 Relevant Previous Work

Previous research in UCC and elsewhere indicated useful approaches. The examples of purification-resistant impurities in process reactions described in Section 1.1.2 were collected by group researchers as part of a project on the rational morphology design of crystalline pharmaceutical solids.[17] As part of that work, an investigation was carried out on the impact of impurity incorporation on the crystallisation behaviour of phenacetin (compound **8**, Figure 1.20).[119] Phenacetin samples were doped with low levels of two process impurities: the side-product *N*-ethylparacetamol (compound **9**), and the synthetic starting material paracetamol (compound **10**). It was observed that while *N*-ethylparacetamol **9** was effectively rejected by crystallisation, paracetamol **10** proved resistant to the same purification steps. A stepwise dissolution study was performed on single crystals of phenacetin **8** doped with paracetamol **10**, analysing the impurity content of the crystal on a surface-to-centre basis. The direction and techniques of this study was suggested by an investigation into L-asparagine monohydrate / L-aspartic acid systems by Addadi *et al.*[91]

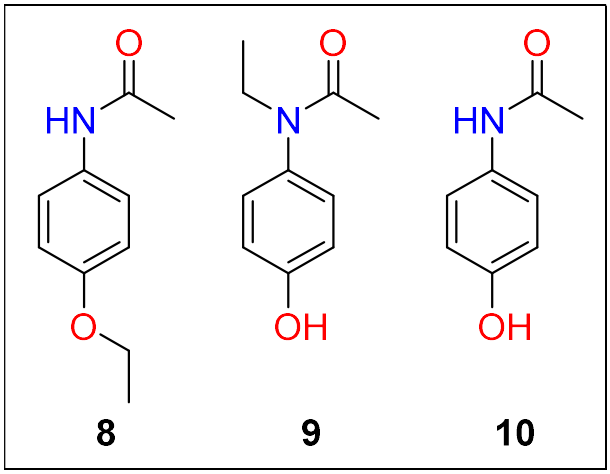


Fig 1.20. Phenacetin **8**, the process by-product *N*-ethylparacetamol **9**, and the synthetic starting material paracetamol **10**.[119]

Later, similar work would be performed on crystals of 2-nitro-4-trifluoromethylacetanilide (compound **11**, Figure 1.21) doped with low levels of 4-methyl-2-nitroacetanilide (compound **12**) and 4-chloro-2-nitroacetanilide (compound **13**) as additives.[90] **12** and **13** are structurally similar to the host **11** and had previously been demonstrated to exhibit appreciable levels of incorporation.[120] Using these compounds as a model of study, the stepwise dissolution method previously used to analyse the additive content in phenacetin was further developed to achieve multiple controlled dissolution levels on both single crystals and larger samples. In this way the incorporation levels of **12** and **13** within crystals of the host **11** could be tracked. Development of media that would inhibit the flocculation and aggregation of crystal particles during dissolution was also carried out.[121]

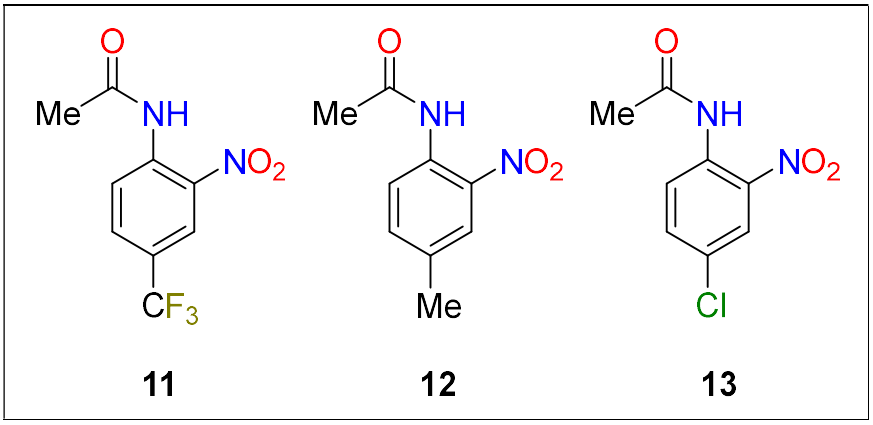


Fig 1.21. 2-nitro-4-trifluoromethylacetanilide **11**, alongside the additives 4-methyl-2-nitroacetanilide **12** and 4-chloro-2-nitroacetanilide **13**.[90]

The current work aims to further develop the partial dissolution method for application to pharmaceutical products, both in a laboratory and process development environment.

1.5 Choice of Host Material

The choice of host compound with which to produce the model of study was carefully considered. Some of these considerations are described above in Section 1.4. Firstly, it was decided to use an API with known pharmaceutical effects as the system host to better represent the types of systems encountered in process chemistry. The material should have a stable crystalline form, preferably with well-documented crystallisation behaviour available in the literature. Literature information regarding other material properties and known synthetic routes to the material would also be advantageous. Lastly, the material should be conducive to the design and synthesis of

additives; in other words, an aspect of the original structure could be changed while preserving the majority of the chemical structure of the host. In this way an additive could be designed that is structurally similar, if not isomorphous, to the host compound, and, as such, facilitate solid solution-like behaviour between the two materials.

1.5.1 Flufenamic Acid

1.5.1.1 Compound Details

Taking these considerations into account, the material chosen to act as the host material in this research is flufenamic acid (FFA, compound **14**), shown below in Figure 1.22. Flufenamic acid **14** is a non-steroidal anti-inflammatory drug (NSAID) belonging to the class of anthranilic acid derivatives, or fenamates in their ester form.[122] The structure of the compound consists of two aryl rings bridged by a secondary amine. One ring is substituted with a carboxylic acid ortho to the amine, while the other has a trifluoromethyl (-CF_3) group in the meta position.

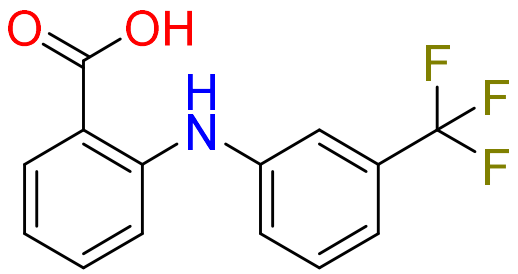


Fig 1.22. Structure of flufenamic acid **14** (FFA).

FFA is a known API. Its pharmaceutical benefits were originally discovered by Claude Winder in 1963 under the Parke Davis Co. in Detroit, identifying it and other anthranilic acid derivatives as inhibitors of UV erythema.[123] FFA is a cyclooxygenase inhibitor, reducing the activity of the prostaglandin-F synthase enzyme and activating the TRPC6 gene.[124] Originally marketed as a pain relief remedy in the treatment of arthritis, it and other members of the anthranilic acid derivatives (such as mefenamic acid) fell out of use due to a high incidence of adverse gastrointestinal effects.[125]

1.5.1.2 Benefits for Current Work

FFA was chosen as the API host material for a number of reasons. First of all, there is a large amount of literature documentation available relating to synthetic routes to the material,[126–129] physical properties,[130,131] and crystallisation behaviour.[65,71,132,133] The lattermost information is particularly relevant and will be discussed in more detail later in this section as well as in other chapters. Also of interest is the $-CF_3$ side chain on one of the aryl rings. $-CF_3$ has a relatively large van der Waal radius of 2.15 Å; this bulk makes it a useful replacement for smaller groups with similar electronegativities (like -Cl or -F) in drug design as a bioisostere.[134,135] In theory, an analogue of FFA in which the structure is preserved, save for the $-CF_3$ side chain being exchanged for a smaller group, would be an ideal candidate for a solid solution-like relationship. The formation of solid solution-like systems between trifluoromethyl-substituted compounds and alternatively-substituted analogues has been established, as discussed in Section 1.4.1.[90,120,121] Similar principles will be followed in the design of structurally similar analogues of FFA for use as purification-resistant additives.

1.5.1.3 Polymorphism

An important characteristic to note in relation to the crystallisation behaviour of FFA is its polymorphism. The polymorphic nature of FFA has been known for nearly 50 years, with the first form (Form III) being characterised in 1973 and the second (Form I) less than a decade later.[136,137] In the intervening years, a total of nine polymorphic forms of FFA have been identified, eight of which have been isolated and structurally characterised.[65] In Section 1.2.4, some of the benefits and challenges associated with polymorphic materials were discussed, particularly surrounding the different physical and chemical properties exhibited by each form. FFA is no different, and while the extent of the differences between forms has not been fully explored, the changes in crystal behaviour have been well observed. As such, care will need to be taken to ensure polymorphic consistency between experiments involving solid-state FFA throughout the entirety of the research.

1.5.1.4 Form III and Form I

The work in this project was almost exclusively focused on Form III and Form I. These are the most commonly encountered, and most widely commercially available, polymorphic forms of FFA.[71] Form III is the thermodynamically stable form at room temperature (*c.* 20 °C). Form I is kinetically stable at that temperature, transforming into Form III in the solid phase over a period of days. However, Form I becomes the thermodynamically stable form at temperatures above 39 – 42 °C.[138,139] Form III does not transform into Form I at this temperature in the same way that Form I transforms into

Form III at room temperature; such a polymorphic transformation does not occur below a temperature of 115 °C.[71,140] This hysteresis effect is hypothesised to be the result of the high energy barrier required to transition from Form III to Form I, even at a temperature at which Form I is the thermodynamically stable polymorph. The transformation between the two polymorphs can be observed during heating by DSC analysis (see Section 2.6.2.2). Form III and Form I are enantiotropically linked; amongst other attributes this means the transformation between the two polymorphs is reversible.[71,139,141,142]

1.6 Primary Means of Analysis

1.6.1 High-Performance Liquid Chromatography (HPLC)

HPLC is an analytical technique that relies on chromatography to separate analytes. A dissolved sample is passed through a column containing a solid adsorbent such as silica (stationary phase) at high pressure along with an eluent (mobile phase). Each analyte in the sample interacts with the stationary phase to a slightly different extent, separating the components in the column. The time at which each analyte leaves the column (retention time) is recorded by a detector, along with a signal intensity proportional to the concentration of the analyte in the sample. HPLC is a broad area of analysis, with many options in terms of column, detector, and data output type. Reversed-phase HPLC (the most common variation of HPLC used in pharmaceutical chemistry) works on the basis of the hydrophobic character of the analyte, employing an aqueous, polar mobile phase and a non-polar silica-based stationary phase.[60,143]

As this is an impurities-based project, HPLC is a central method of analysis. For one, comparison of retention times between sample traces allows for qualification and quantification of synthetic products more accurately than nuclear magnetic resonance (NMR), thin-layer chromatography (TLC), or other common analytical techniques. Peak area values from HPLC traces of doped samples can be used to accurately determine additive levels after doping, crystal growth, purification attempts, and partial dissolution stages, to name a few. HPLC also has quantitative use in synthesis as a measure of product purity.

1.6.2 Powder X-Ray Diffraction (PXRD)

PXRD is a form of analysis that provides certain information on crystal form and phase.[144] It achieves this by directing X-rays through a rotating powder-form sample of crystalline material. Interaction between the rays and the lattice geometry of the material results in diffraction of the beam in accordance with Bragg's Law. Constructive interference is recorded by the detector in the form of an intensity peak. The incidence angle of the beam (2θ) is altered throughout the scan to produce a pattern of peaks. Each pattern is unique to an individual crystal lattice, and, thus, can be compared to a reference for the purpose of unknown species or polymorph identification.

As FFA is a highly polymorphic material, PXRD is an important tool for this research. PXRD patterns of crystalline FFA samples can be compared to literature patterns of known polymorphic forms to identify the form of the sample material.[65,136,137] In this way, the effects of crystallisation conditions and additive/impurity inclusion on

polymorphic form can be observed. It can also ensure that a consistent form is maintained across all samples of crystalline FFA to limit variability between experiments.

1.6.3 Differential Scanning Calorimetry (DSC)

DSC analysis is a technique that measures the amount of heat required to raise the temperature of a solid sample in relation to a blank reference.[99,145] As such, it can be used to identify the nature of any thermal events that the sample undergoes as well as the temperature at which they occur. These events can be exothermic or endothermic in nature, and include melts, solidifications, polymorphic transformations, and glass transitions.

DSC is primarily used in this research to determine the melting points of the materials produced by noting the temperatures of the endothermic signals corresponding to the melting of the material. As such, the effect of additive inclusion on this melting temperature can be observed. Alongside HPLC, DSC can be used to investigate the phase behaviour of the doped systems created as a part of this research. This is vital in determining the nature of the solid-state relationship between the host and additive materials, and subsequently constructing phase diagrams, as described in Section 4.6. DSC is also the primary method of analysis used in the work for investigating the polymorphic transformations between Form III and Form I FFA.

1.6.4 Thermogravimetric Analysis (TGA)

In TGA, the changing mass of a sample is measured as a function of increasing temperature.[146] As such, any thermal event involving a change in sample mass is recorded, such as phase transitions, thermal decomposition, and certain chemical reactions (e.g. oxidation or reduction). In the context of this work, TGA is mainly used to help determine the nature of the solid-state relationships between two components in a doped system. The TGA curve of a doped sample can be compared against those of the pure components to observe similarities and differences that might indicate the type of the system present. TGA can also identify the presence of hydrates, solvates, and salts in both doped and pure material samples.

Method Development

2.1 Introduction

This chapter is focused on developing methods of analysing the materials of interest to the project, starting with the selection of the additives with which samples of flufenamic acid **14** (FFA) will be doped. These additives are intended to be resistant to purification by traditional means when included in crystal samples of FFA, mimicking the behaviour of the purification-resistant impurities introduced in Section 1.1.2. The development of methods of analysis for FFA and these additives is a necessary undertaking ahead of the research into the nature and behaviour of the doped systems, and, subsequently, the development of methods to determine the distribution of additives within those systems.

In addition to additive choice, this chapter includes the construction of calibration curves, by regression analysis of a series of standard solutions of compounds **14** – **19**. These are used for determining response factors by HPLC and in the calculation of proportional additive levels in a doped sample. Solubility tests are performed on compounds **14** – **16**, determining the saturation point of the materials across a range of solvents and temperatures. The development of methods for the crystallisation of FFA **14** is described. These methods will be used to produce pure and doped crystalline material for use in the research described in this chapter as well as Chapters 4 and 5. Finally, the crystal properties of FFA **14** will be analysed by PXRD, DSC, and TGA analysis, and the polymorphic behaviour of the material will be investigated.

2.2 Flufenamic Acid and Additive Selection

2.2.1 Flufenamic Acid

FFA was the compound chosen to act as the host in the impure systems being produced as a part of this project. As discussed previously in Section 1.5.1, FFA is a known NSAID in the fenamate or anthranilic acid derivative class of drugs. As a well-studied API, it is a suitable case study upon which to apply and further develop methods of impurity distribution determination, with a wide array of literature available describing its physical properties, behaviour, and synthetic routes.[65,71,126–133] This literature proved to be an invaluable resource when developing many of the methods described in this and later chapters.

2.2.2 Choice of Additives

2.2.2.1 Purpose of Additives

The design of the additives intended to act as purification-resistant impurities was based on the structure of FFA. Many of the impurities of this type encountered in process cases were determined to be exhibiting solid solution-like behaviour.[14,17,107] As such, the additives were selected with the intent that they would form solid solutions, or solid solution-type relationships, with FFA as a crystalline host. Historically, solubility in the solid phase and, thus, the formation of solid solutions has been considered a phenomenon unique to isomorphous components: those that share the same space group and unit cell

parameters.[147,148] However, further study over the years has proved this criterion too restrictive, presenting examples of immiscible isomorphous materials,[106,149,150] as well as non-isomorphous compounds which exhibit high levels of solubility.[151] As such, the limitations have since been relaxed to include both isomorphous and isostructural components.[27,110,118] Unlike isomorphous species, isostructural compounds need only share a close structural similarity without necessarily requiring the same cell dimensions or unit cell composition.[152] Any additives intended to be soluble in the host in the solid phase, therefore, would have to be structurally similar to FFA even if they do not exhibit the same crystallisation behaviour in their pure forms. The guiding principle for additive selection was to preserve as much of the structural form of FFA as possible to maintain that similarity, and any portion that needed to be altered should be reduced in size to prevent steric disruption of the crystal lattice.

2.2.2.2 Principles of Additive Structure

Aside from the pharmaceutical interest of the material and the large amount of information available surrounding it, the choice to use FFA as the crystal host material was made in a large part according to this principle. As is discussed in Section 1.5.1.2, the trifluoromethyl (-CF_3) substituent on one of the aryl rings has a van der Waal radius of 2.15 Å.[134] In theory, an analogue of FFA in which the structure is preserved, save for the -CF_3 substituent being exchanged for a smaller group, has potential for the formation for a solid solution-like relationship with FFA. This concept has been demonstrated in similar work previously in the literature, in which compounds substituted with methyl (-CH_3) and chloro (-Cl) groups respectively demonstrated appreciable levels of

incorporation into crystals of a structurally-similar material substituted with a -CF_3 group.[90,120,121]

2.2.3 Crystal Behaviour of FFA and Additives

2.2.3.1 Crystal Behaviour of FFA

Before selecting analogues of FFA based on the above research, the crystalline behaviour of the host material must be considered. Specifically, the role of the -CF_3 group in terms of the space it inhabits in the unit cell and the stabilising interactions in which it participates are of particular importance, as these attributes will influence the impact the replacement of the group will have on the crystal structure. As has been discussed in Section 1.5.1.3, FFA is a highly polymorphic material, with nine reported crystal forms.[65] For the majority of this project however, only two polymorphs will be considered, Form I and Form III, on the basis that they were the two forms almost exclusively encountered. The difference between the forms in terms of physical properties and crystal behaviour has been well reported.[71,133,153,154] Therefore, it is imperative that all experiments involving solid-state FFA maintain the same polymorphic form as to not introduce unwanted variability into the work as a whole. Form I FFA is the commercially available polymorph but is metastable at room temperature, converting to the stable Form III slowly in the solid phase, or upon recrystallisation from most solvents.[71] As such, Form III was selected as the primary polymorph of interest for the project. This decision will be explored in more detail as part of an empirical investigation into the polymorphism of FFA in Section 2.6.2.

The implication of this for the current topic is that it is the packing structure of Form III FFA that will be examined to evaluate the impacts of additive selection, as opposed to any other polymorphic form. The structure was examined on a molecular level using files downloaded from the CSD.[79,133] Form III FFA crystallises in the monoclinic C2/c space group. Molecules form dimers in the crystal lattice, linked *via* O−H···O interactions between the acid groups (1.75 ± 0.01 Å). Each pair of dimers are linked to others in the lattice *via* C^4–H···F (2.59 ± 0.01 Å) and C^5–H···π (2.79 ± 0.01 Å) interactions along the *c* axis, and C^9–H···π (2.68 ± 0.01 Å) interactions along the *b* axis to stabilise the skeleton and form the extended lattice (Figure 2.1).[132] Atoms are labelled as they are automatically assigned to FFA III in Mercury software (Figure 2.2).[155]

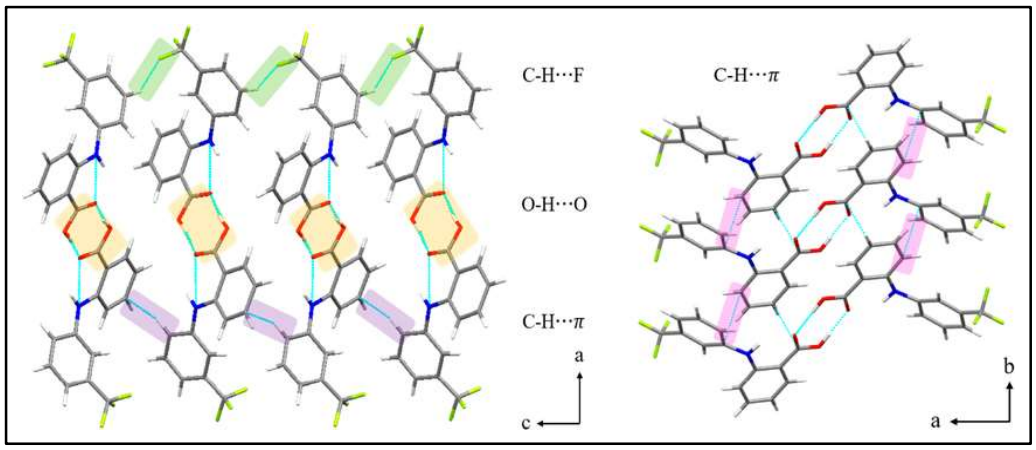


Fig 2.1. Crystal packing of Form III FFA including the main intermolecular stabilising interactions.[132]

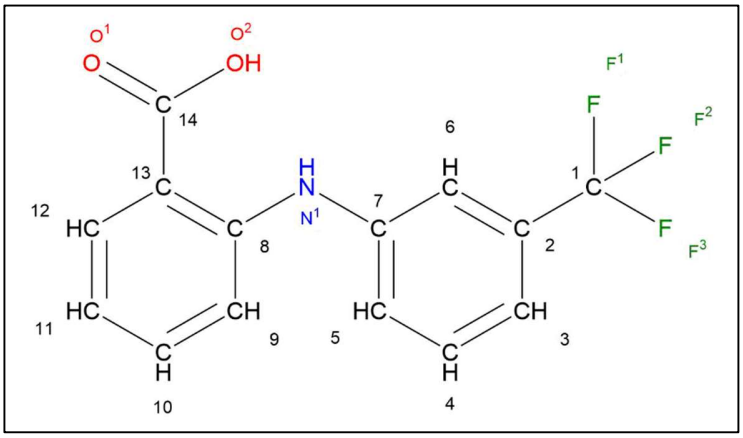


Fig 2.2. Chemical structure of a molecule of FFA with atom labels assigned automatically by Mercury software.

2.2.3.2 Potential Impact of Additives on FFA Crystal Behaviour

The only defined intermolecular stabilising interaction in the unit cell in which the -CF_3 group participates is a 2.590 Å hydrogen bond between one of the fluoro atoms and the C^4 proton. The orientation of the -CF_3 side chain is such that two of these groups are positioned facing each other in the crystal lattice at a distance of 4.156 Å (C···C) or 3.038 Å (F···F). The separation between the groups means that neither attractive nor repulsive forces are experienced to any significant degree.[133] This stands in contrast to Form I FFA, the conformation of which places the -CF_3 group of one molecule within the van der Waal radius of another, a factor which contributes to the lower stability of the form in comparison to Form III. The closest distances between atoms in the -CF_3 group and atoms on other molecules of Form III FFA are displayed in Figure 2.3. Aside from the stabilising C_4–H···F interaction, only two other distances are shorter than 3 Å. This suggests that the space around the -CF_3 group in Form III FFA is such that the group has little impact on the structure of the crystal lattice of the material. As such, replacing the group with one

that is smaller than -CF_3 should not significantly or detrimentally affect the formation of the lattice, even if that group has a different electronegativity than -CF_3. A certain level of stability will be sacrificed with the loss of the C^4–H···F interaction. This could potentially have an influence on the miscibility limit of FFA and the additive, as that destabilisation will become more impactful at higher levels of additive incorporation. However, as the group only participates in a single interaction per molecule of FFA, and the doping levels of systems being studied in the majority of the project will be low, the impact of the destabilisation will most likely be minimal.

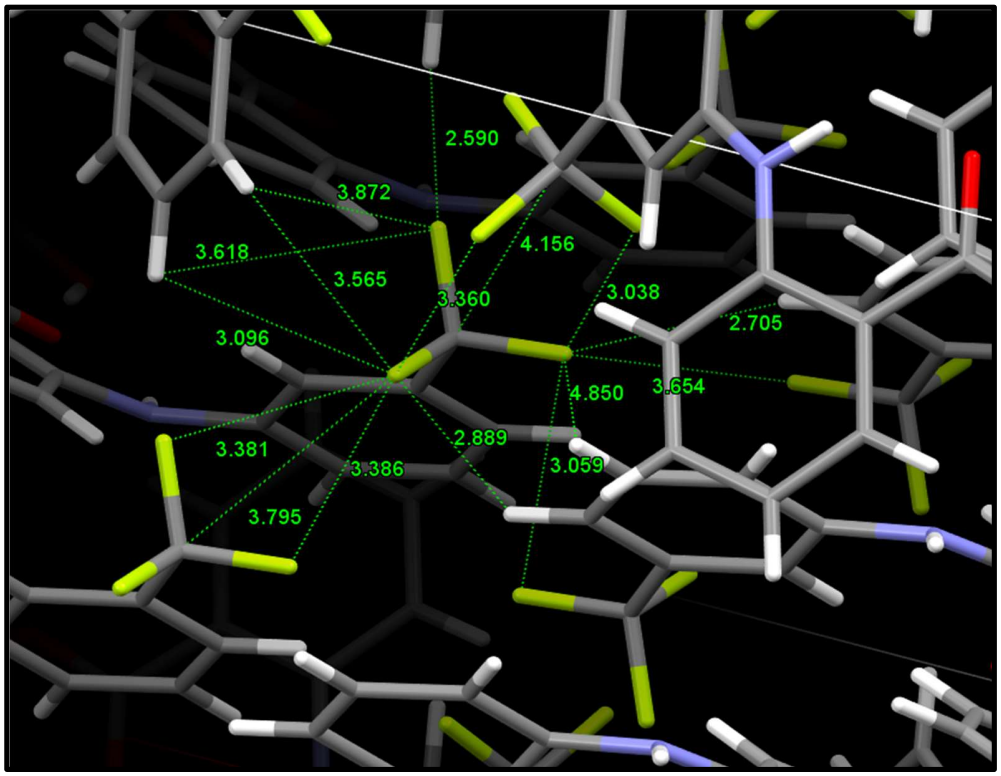


Fig 2.3. Closest distances between the -CF_3 group of FFA and neighbouring atoms in the Form III crystal lattice.[133]

It should be noted that this speculation into the solid-state interactions between FFA and potential additives is not the principle by which those additives were chosen. The choice of additive structure was guided primarily by the size and electronegativities of various substituents, along with the results of previous work on the subject.

2.2.4 Structurally Similar Additives

Five analogues of FFA were selected based on these principles. All five of these analogues preserve the fenamic acid skeleton of the original, but with the $-CF_3$ group on the C^2 atom replaced with a different substituent for each new compound. On this principle they can be considered isostructural (or at least structurally similar) to FFA, and, as such, are good candidates for lattice incorporation. The structures of all five compounds can be found in Figure 2.4. Space-fill diagrams of FFA and each of these additives can be found in Appendix Figures 7.1 – 7.6 respectively as a way of visualising the size of their respective substituents relative to $-CF_3$. These diagrams were constructed in Chem3D software.[156]

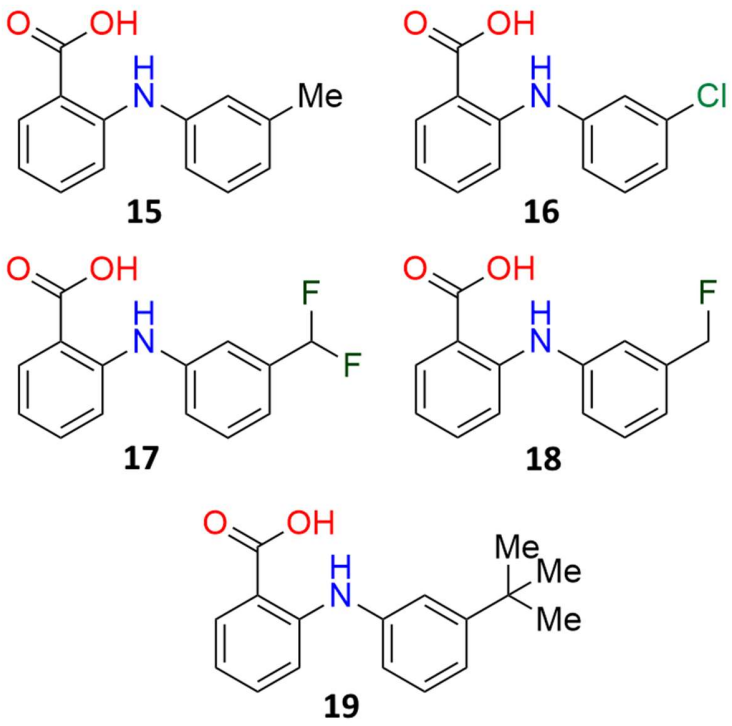


Fig 2.4. Analogues of FFA **14** selected as purification-resistant additives: (top left to bottom right) 2-(*m*-tolylamino)benzoic acid **15** (Me-FA), *N*-(3-chlorophenyl)anthranilic acid **16** (Cl-FA), 2-[3-(difluoromethyl)anilino]benzoic acid **17** (DF-FA), 2-[3-(fluoromethyl)anilino]benzoic acid **18** (MF-FA), and 2-((3-(*tert*-butyl)phenyl)amino)benzoic acid **19** (t-Bu-FA).

2.2.4.1 Descriptions of Additives

Me-FA **15** and Cl-FA **16**

The first two analogous additives are 2-(*m*-tolylamino)benzoic acid **15** (Me-FA), *N*-(3-chlorophenyl)anthranilic acid **16** (Cl-FA). The design of these additives, substituted with a methyl and chloro group respectively in the place of -CF_3, was based on the work carried out by He *et al*. and Armstrong *et al*. as described in Section 1.4.1.[90,120,121] These researchers both reported appreciable levels of solid miscibility between structurally similar compounds substituted with -CF_3, -CH_3, and -Cl groups. The reported van der

Waal radii of the -CH_3 and -Cl confirm the groups are smaller than -CF_3 (2.00 Å, 1.80 Å, and 2.15 Å respectively).[134] Therefore, even with the difference in group electronegativities (2.30 eV, 3.03 eV, and 3.35 eV respectively)[157] the available lattice space for the additive substituents to occupy should allow for minimal disruption to the crystal structure.

These compounds are not novel and have been studied previously in other areas of research. For example, Me-FA **15** was trialled in research surrounding the treatment of genetic diseases characterised by unstable mRNA under the name 2-(3-toluidino)benzoic acid (3TBA).[158] Cl-FA **16** has been shown to have its own anti-inflammatory effect, and, furthermore, has been used as a ligand in a titanium complex to enhance this effect and reduce toxicity.[159] Crystallographic data is available on both of these compounds; Me-FA **15** is not considered to be polymorphic, but Cl-FA **16** has three reported forms.[126,160] It will be important to determine the form of the material produced in this research to determine its relationship to the FFA **14** polymorphs in terms of crystal structure; however, all three forms are reported to crystallise in the triclinic P-1 space group, as is Me-FA **15**.

Me-FA **15** and Cl-FA **16** will be the foremost additives of study for this work. This is primarily due to the previous work carried out on materials with the same substituents: -CH_3 and -Cl respectively.[90,121] Me-FA **15** and Cl-FA **16** can be produced in larger quantities than the other additives due to the comparative availability of the precursor materials. This allows for a wider array of experimentation to be carried out, resulting in more accurate solubility and calibration data, amongst others. Additionally, it allows for the production of systems doped with higher levels of additive, providing more

information into the incorporation behaviour of the additives as well as the potential to construct phase diagrams.

DF-FA **17** and MF-FA **18**

Compounds **17** and **18** replace the trifluoromethyl group of FFA **14** with a difluoromethyl (-CHF_2) and fluoromethyl (-CH_2F) substituent respectively. These additives, 2-[3-(difluoromethyl)anilino]benzoic acid **17** (DF-FA) and 2-[3-(fluoromethyl)anilino]benzoic acid **18** (MF-FA), were intended to accomplish the same goal as Me-FA **15** and Cl-FA **16**, substitutional lattice incorporation, but with side chains more similar to (but still smaller in size than) that of FFA **14**. Van der Waal radii of these groups are unavailable in the literature, but their sizes can be compared to those of FFA **14** and the other additives through their Bondi volumes, a measure of molecular volume that accounts for both the van der Waal radii of atoms and the distances of the covalent bonds between them.[161,162] The Bondi volumes for the -CHF_2 and -CH_2F groups are 18.8 and 16.0 $cm^3\ mol^{-1}$ respectively, smaller than the -CF_3 volume of 21.3 $cm^3\ mol^{-1}$.[163] The groups are larger than -CH_3 and -Cl, which have Bondi volumes of 13.7 and 12.0 $cm^3\ mol^{-1}$ respectively. Comparisons of level of incorporation that the four additives achieve could provide insight into the impact of available lattice space on additive substitution.

DF-FA **17** and MF-FA **18** appear much more sparsely in the literature than FFA **14** or Me-FA **15** and Cl-FA **16**. They likely have been produced as side-products or impurities in previous research surrounding FFA **14**, but if so, they are not well reported. A PubChem search for DF-FA **17** returns no results at the time of writing, while MF-FA **18** only appears in a single patent.[164] As such, no polymorphic or other crystallographic

information is available with which to compare either the crystal structures of either additive with FFA **14**. The materials required to synthesise DF-FA **17** and MF-FA **18** are extremely costly. As a result, experimentation carried out on these materials will be more limited than Me-FA **15** and Cl-FA **16**, mainly involving systems doped with low levels of the additives. Comprehensive characterisation of these compounds was performed as part of the research and is described in detail in Section 3.3.1.

t-Bu-FA **19**

The final additive selected as part of this project was t-Bu-FA, 2-((3-(*tert*-butyl)phenyl)amino)benzoic acid **19**. As with the previous four compounds, the structure of FFA **14** was preserved but the -CF_3 group replaced, this time with a *tert*-butyl group. However, unlike the other additives, this compound was intended to be less likely to display solid solution-like behaviour with FFA **14**. With a van der Waal radius of between 2.43 and 3.15 Å (compared to the 2.15 Å radius of -CF_3), the relative bulk of the *tert*-butyl group of t-Bu-FA **19** was intended to be sterically unfavourable when it came to replacing a molecule of FFA **14** in the crystal lattice.[165,166] In theory, this should result in an impure system in which the additive exhibits low levels of inclusion, little-to-no solid solution-like miscibility, and facile rejection by recrystallisation compared to the other additives. In this way, t-Bu-FA **19** was intended to act as a sterically demanding control against which the effectiveness of the other additives could be judged.

The material is much more well documented than DF-FA **17** and MF-FA **18**, with crystal structures and synthetic methods available in the literature.[126] Much like Me-FA **15**, t-Bu-FA **19** is reported to be monomorphic, crystallising solely in the triclinic P-1

space group. The material has also been reported to have medicinal benefits, for example recently in the preparation of medicine for treating acute leukemia.[167]

2.2.5 Additive Crystal Structures

The crystal system and space group for each material and form as reported in the literature are listed below in Table 2.1. Eight polymorphs of FFA **14** are included; Form IX has not yet been fully characterised.[65] Each of the additives for which crystallographic information is available crystallises in the triclinic P-1 space group. On the other hand, Form III FFA, the chosen polymorph for experiments involving solid-state FFA in this work, crystallises in the monoclinic C2/c space group. As crystal materials must share a space group to be considered isomorphous, none of the additives selected as part of this study can be considered isomorphous to Form III FFA.[27] This holds true with the metastable Form I FFA also, which crystallises in the monoclinic $P2_1/c$ space group. However, as the additives bear such a structural similarity to FFA, it is appropriate to consider all six of the compounds isostructural, and, thus, potential candidates for solid solution formation.

Table 2.1. Crystal systems and space groups of each polymorphic form of FFA and the selected additives.

Material	Polymorphic	Crystal System	Space Group
Flufenamic Acid **14** (FFA)	I	Monoclinic	$P2_1/c$
	II	Monoclinic	$P2_1/c$
	III	Monoclinic	C2/c
	IV	Triclinic	P-1
	V	Monoclinic	$P2_1/c$
	VI	Triclinic	P-1
	VII	Monoclinic	$P2_1/c$
	VIII	Triclinic	P-1
Me-FA **15**	-	Triclinic	P-1
Cl-FA **16**	I	Triclinic	P-1
	II	Triclinic	P-1
	III	Triclinic	P-1
DF-FA **17**	-	Unknown	Unknown
MF-FA **18**	-	Unknown	Unknown
t-Bu-FA **19**	-	Triclinic	P-1

The space-fill diagrams of FFA **14** and compounds **15** – **19** constructed using the Chem3D software (Appendix Figures 7.1 – 7.6 respectively) may also provide some insight in this context.[156] This software allows for 3D modelling of small molecules, as well as the use of an energy minimisation function, which calculates the conformation which results in the minimal steric energy of a structure. This allows a researcher to

predict the conformation that a compound is most likely to adopt. When these calculations were applied to compounds **15** – **19**, they all adopted a very similar conformation to that of FFA **14**. This similarity in supramolecular conformation may also be of benefit when forming solid solution-like systems. However, as Chem3D does not account for interactions between molecules in the solid phase, this may not be representative of the behaviour of these compounds in a crystal lattice.

In-lab testing of doped systems of host and additive are required to definitively determine the nature of the relationships between FFA **14** and compounds **15** – **19**, specifically *via* HPLC, PXRD, DSC, and TGA. Such work will be discussed in Chapter 4.

2.3 HPLC Method Development

2.3.1 Uses of HPLC Analysis

As this is an impurities-based project, HPLC is a central method of analysis. The principles and uses of HPLC are discussed in Section 1.6.1. To effectively use HPLC as a mode of analysis, an appropriate method must be developed that is suitable for the systems of study. In general, a good method should result in sufficient separation between potential analytes, ideally outputting peaks that are sharp, narrow, and have minimal fronting or tailing, and with reasonably low retention times to minimise scan durations.

2.3.2 Method Development

2.3.2.1 Method 1

Development of a HPLC method suitable for analysing the materials of study was one of the earliest sections of work carried out as part of the project. The starting point for the development (Method 1) was based on a literature method describing the HPLC analysis of FFA as part of a study of the drug's pharmacokinetic properties in rats.[168] The method was used as reported, save for the injection volume which was lowered from 20 to 5 μL. An outline of this initial method is described in Section 2.8.8.2. At this stage no additives had been synthesised, so this method was trialled on the crude product of an FFA synthesis process in which the FFA was approx. 87% pure. ~12% of the product consisted of a single major impurity, and the remaining ~1% were other trace impurities. This method produced a trace with very narrow and sharp peaks with low retention times, but without sufficient separation between the analytes in the sample (Figure 2.5). As can be seen from the peak area percentage values in the figure, this resulted in the impurity peak being underrepresented in terms of sample proportion. The ratio of the two solvents was adjusted a number of times without any significant improvement to peak separation.

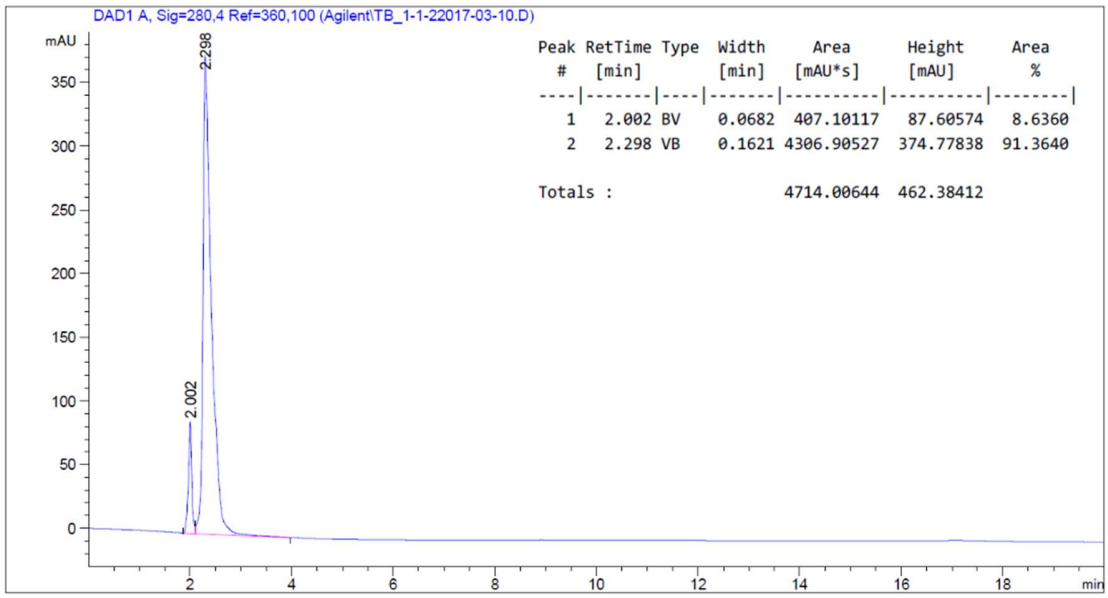


Fig 2.5. HPLC trace of crude FFA as analysed using Method 1; mobile phase 77:23 methanol / water, collected at 280 nm.

2.3.2.2 Method 2

Despite the coelution observed in Method 1, the peaks were sharp, narrow, and otherwise ideal. For that reason, it was decided to preserve all Method 1 parameters for Method 2 bar the mobile phase composition. That was changed from methanol (MeOH) / water to acetonitrile (MeCN) / water, beginning at a middle-ground ratio of 50:50 to gauge which direction to adjust. The first test using these parameters produced the trace in Figure 2.6. On first appearance, most of the peaks in this trace appear unreadable. However, considering the shape of the peak at 17.69 min, it seems that there was simply a large amount of peak fronting occurring; this resulted in a high number of smaller peaks with similar retention times to coelute. With the proper Gaussian peak shape, the majority of these peaks could elute with better separation. Peak fronting of this magnitude is often caused by overloading the column as a result of high sample concentrations.[169] The

sample was diluted and retested a number of times until the trace in Figure 2.7 was produced.

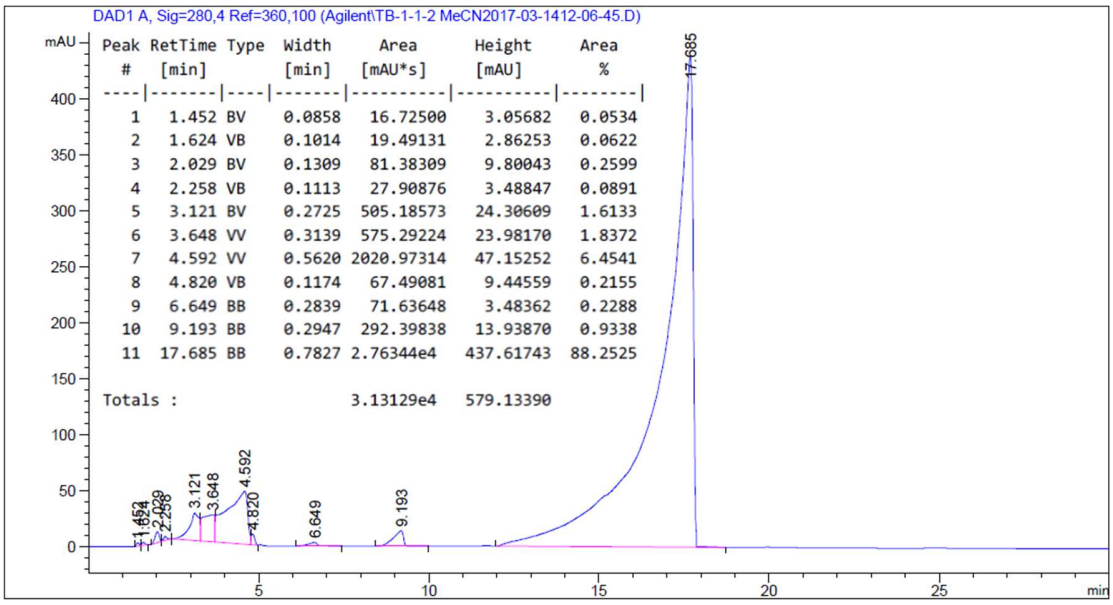


Fig 2.6. HPLC trace of crude FFA as analysed using Method 2; high sample concentration, collected at 280 nm.

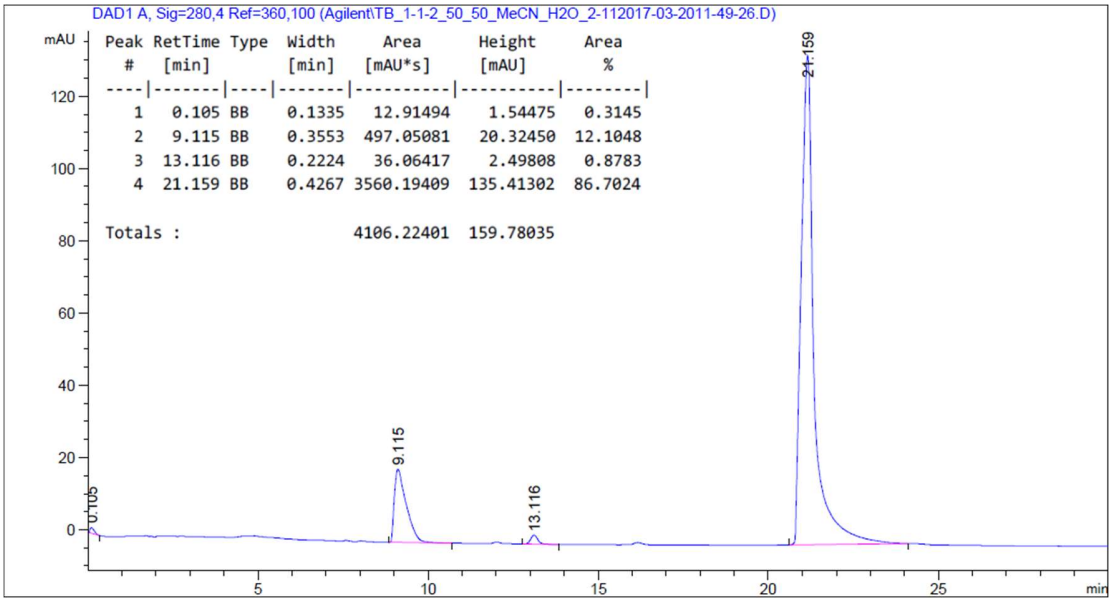


Fig 2.7. HPLC trace of crude FFA as analysed using Method 2; reduced sample concentration, collected at 280 nm.

The sample dilution resolved many of the issues observed in the Figure 2.6 trace. The analyte peaks were now much narrower with good levels of separation and no coelution. There was a small amount of tailing present on the samples, which while not a concern in the current traces could cause peak overlap for potential analytes with similar retention times. Before addressing the tailing, however, it was hypothesised that an adjustment to the mobile phase ratio could reduce the otherwise high retention times of the analytes. While not necessary for data collection, reduced scan times could increase efficiency and allow for multiple runs of single samples for the purpose of quantitative data accuracy. The same sample was run at a ratio of 90:10 MeCN / water and 75:25 MeCN / water (Figures 2.8 and 2.9 respectively). In both scans, although the peaks were extremely narrow and sharp with low retention times, there was a large amount of peak coelution in both samples. It was decided that, based on these traces, the separation observed in the 50:50 MeCN / water sample was more desirable than the low retention times provided by the other mobile phase ratios.

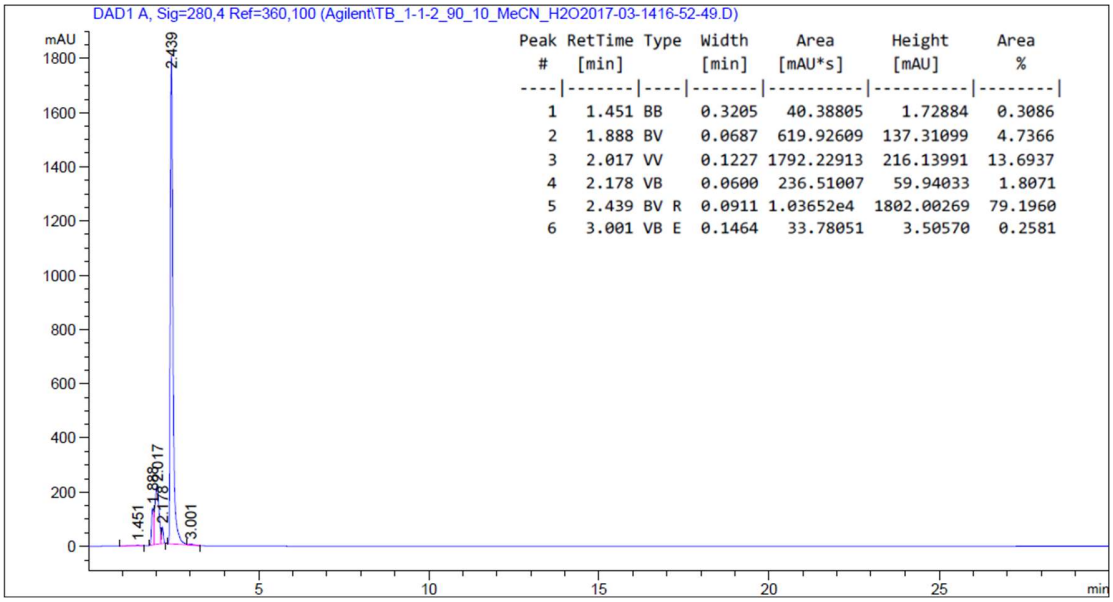


Fig 2.8. HPLC trace of crude FFA as analysed using Method 2; mobile phase 90:10 MeCN / water, collected at 280 nm.

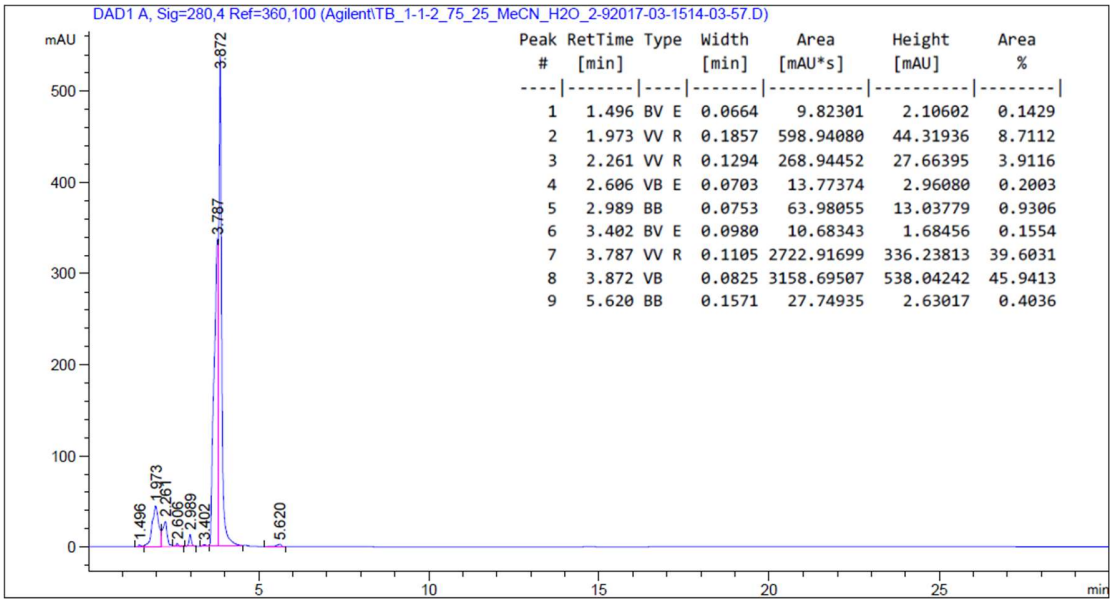


Fig 2.9. HPLC trace of crude FFA as analysed using Method 2; mobile phase 75:25 MeCN / water, collected at 280 nm.

Unless the issue is mechanical (blocked column frit, etc). tailing such as that observed in the Figure 2.7 trace is often the result of improper mobile phase pH. For analytes with acidic groups, such as FFA, too high a pH can cause ionisation of some molecules in the mobile phase. This can result in retention variability in analytes of the same species, characterised by peak broadening and tailing. Reducing the pH of the mobile phase can be a solution to this issue. This pH reduction is achieved by the use of an aqueous buffer, normally formic acid.[170] FFA also contains an amino group, which can have a similar reaction to low pH mobile phases. For amines, a higher pH buffer such as triethylamine (TEA) is used. However, pH levels above 8 increase the solubility of the silica stationary phase, decreasing the lifespan of the column, so this is not recommended unless necessary.[171] For this reason, and the prediction that the carboxylic acid of FFA would likely have the greater impact in terms of peak tailing, a low pH buffer was selected over one with a higher pH. The presence of the amino group could potentially result in a certain level of unavoidable peak broadening and/or tailing under certain conditions, however.

2.3.2.3 Method 3

For Method 3, the aqueous portion of the mobile phase was changed from pure water to a 0.1% v/v aqueous solution of formic acid, still in a 50:50 ratio with MeCN. The other method parameters were kept the same. The HPLC trace of the impure FFA sample collected using this method is presented in Figure 2.10.

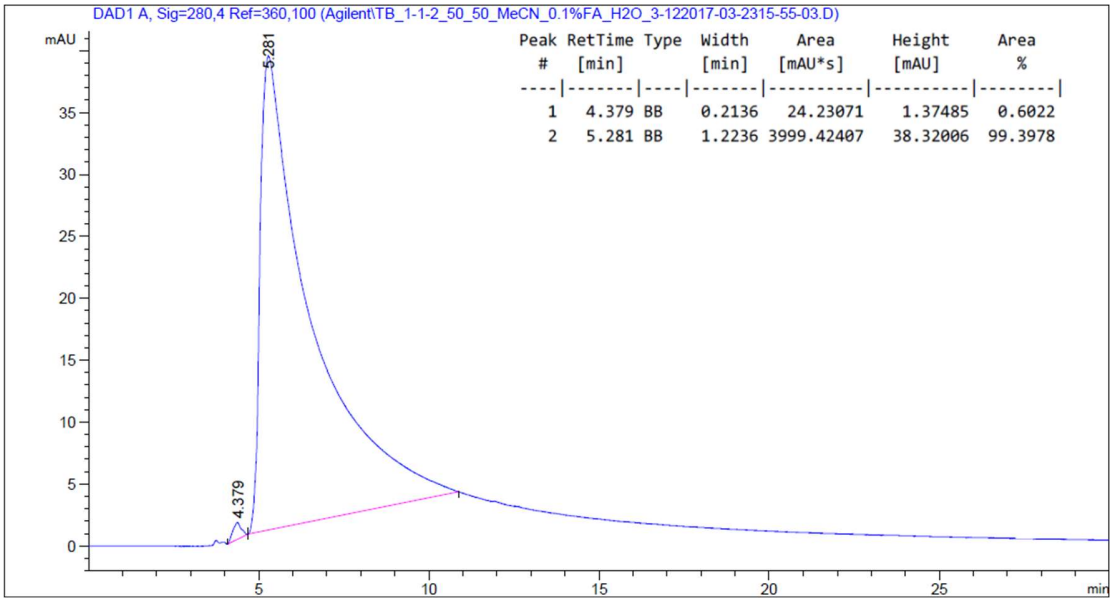


Fig 2.10. HPLC trace of crude FFA as analysed using Method 3, collected at 280 nm.

Addition of the formic acid into the mobile phase had a number of effects. The retention time of the major peak decreased from 21.16 minutes to 5.28 minutes, coelution was observed between the two visible peaks, and a substantial amount of tailing was present on the larger FFA peak. It is still unclear why this trace was of such low quality, as the sample and other method parameters were identical to the previous scans, but the problem persisted across multiple runs. It was decided to attempt the scan using a different species of acid buffer, to determine whether the presence of a buffer in general was causing the issue, or specifically formic acid.

2.3.2.4 Method 4

The same sample of impure FFA was run again, this time with a mobile phase consisting of 50:50 MeCN and an aqueous solution containing 0.1% v/v trifluoroacetic

acid (TFA) as Method 4 (Figure 2.11). TFA performs a similar role as formic acid but is less favoured amongst analytical chemists due to its tendency to suppress ionisation in liquid chromatography-mass spectrometry (LC-MS) systems, as well as due to safety concerns. However, addition of the buffer to the mobile phase produced a near identical HPLC trace to that seen with no buffer (Figure 2.7), minus the tailing. There was a minor shift in retention times, reducing the separation between two of the impurity peaks, but not to the extent that any coelution was observed.

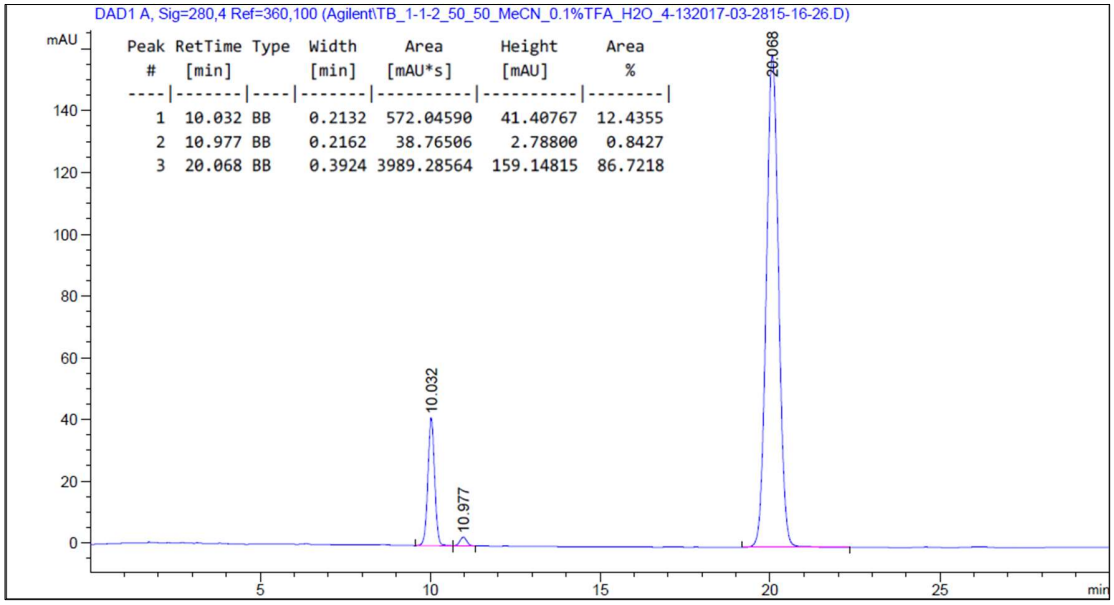


Fig 2.11. HPLC trace of crude FFA as analysed using Method 4, collected at 280 nm.

At this point it appeared that a method had been developed that could at least effectively analyse crude FFA synthesis products, providing sharp, narrow peaks and sufficient separation between analytes.

2.3.2.5 Minimising the Retention Times of Analytes

However, despite the positive attributes of this method, it was taking approximately 25 minutes for all analytes to fully elute in each scan. In addition, the retention times of the additives had not been tested at this stage and could have been higher than that of FFA, potentially making each scan even longer in duration. This is not a large problem for qualitative samples, as generally only a single scan is needed to collect the desired data, or perhaps two for reproducibility. However, as mentioned previously, in the case of quantitative data collection it is often beneficial to run analysis in triplicate and calculate an average value for the required data to minimise error and ensure accuracy. As such, a method with a long scan duration can make experiments with many samples (such as construction of calibration curves or phase diagrams, or even the creation and/or analysis of multiple doped systems at once) inefficient or even unfeasible. It was, therefore, in the interest of the project to investigate means of reducing that duration at an early stage.

To this end, the column was exchanged for an ultra-high-performance liquid chromatography (UHPLC) column, the details of which can be found in Section 2.8.1.1. UHPLC columns are much shorter than standard columns, and the stationary phase particles with which they are packed are smaller. This allows higher pressures through the column, and, thus, can significantly lower retention times. For example, for the trace displayed in Figure 2.12 (a different impure FFA synthesis product to those tested previously), the elution time for FFA was reduced from 20.07 min to 1.31 min. This allowed most scans to be run with just a 2-minute duration. A certain amount of peak broadening is experienced with this change, potentially amplified by the presence of the

amino group of FFA and related compounds, but as minimal coelution was observed this was not considered to be an issue.

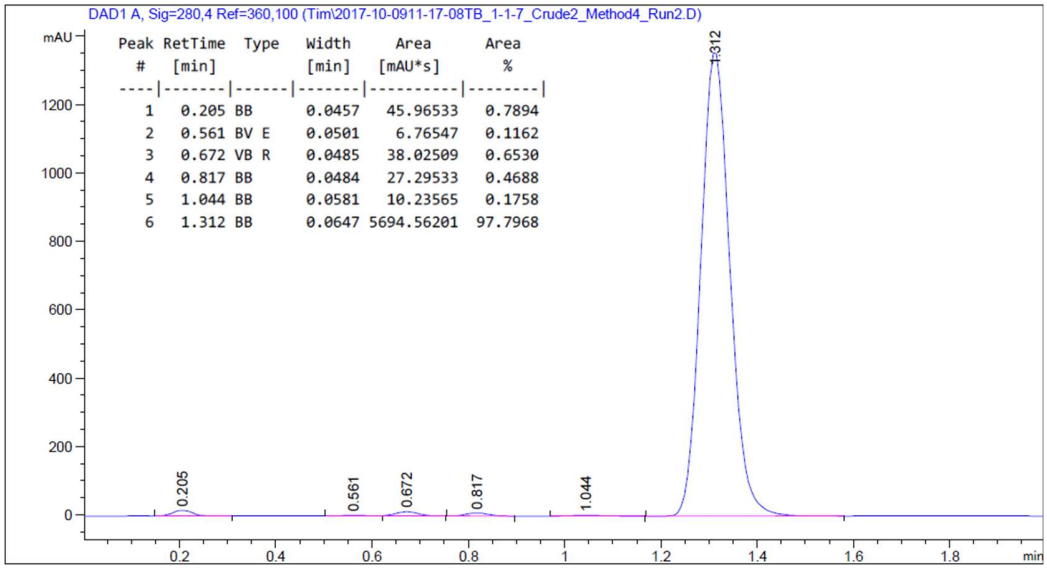


Fig 2.12. HPLC trace of crude FFA as analysed using Method 4; UHPLC Column, collected at 280 nm.

The optimal detector settings were also determined using this method, testing the same sample at a number of wavelengths (Figures 2.13 and 2.14). Of the resulting traces, the one measured at 280 nm exhibited the greatest balance of sensitivity and baseline quality. As such, the wavelength at which the detector was set remained at 280 nm. It is possible that different wavelengths may have provided better responses by HPLC for each of the additives. However, it was observed that a wavelength of 280 nm resulted in adequate resolution of all compounds tested over the course of this research. In addition, it was thought varying the wavelengths may have impacted comparability between the data collected from different systems, and, as such, it was decided to collect all HPLC data at 280 nm. Further work in this area could construct calibration curves of each

compound collected from chromatograms of a solution with multiple analytes to more closely represent the response of each material in similar systems.

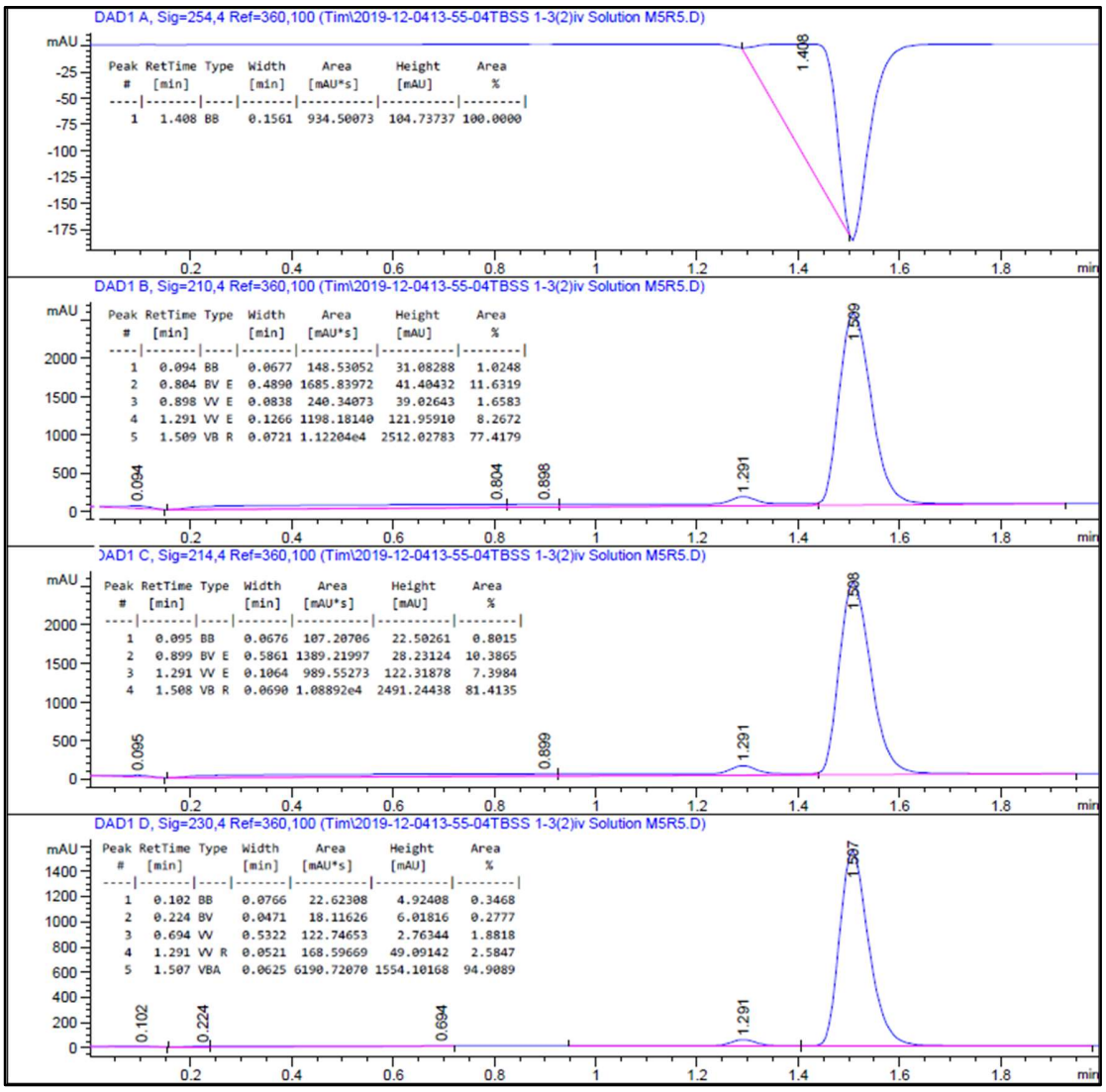


Fig 2.13. HPLC traces of the same sample of FFA **14** doped with 2 mol% Cl-FA **16** detected at (top to bottom) 254, 210, 214, and 230 nm.

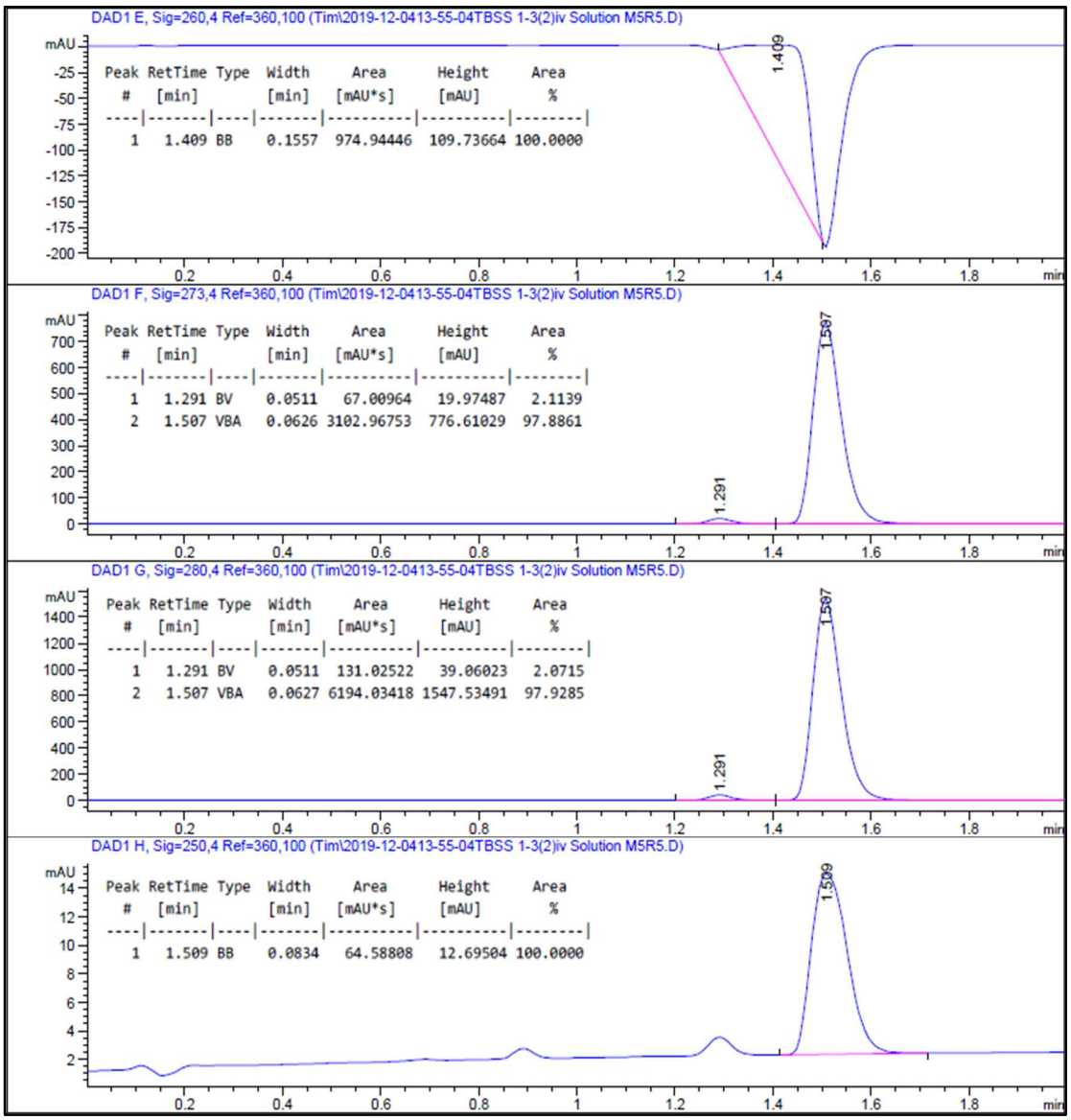


Fig 2.14. HPLC traces of the same sample of FFA **14** doped with 2 mol% Cl-FA **16** detected at (top to bottom) 260, 273, 280, and 250 nm.

2.3.3 Final HPLC Method Evaluation

This method achieved the goals of the development process. Most importantly it provided traces with good separation between the analytes of interest (see Section 2.3.4,

Figures 2.15 – 2.19), but it also was sensitive to the analytes, presenting them as sufficiently narrow and Gaussian, and with low enough retention times to be able to run scans in triplicate to ensure accurate data collection. As such, this was the basic method that would be used for the remainder of the project. Some alterations were made in the intervening time as troubleshooting methods and through learning of better practices of HPLC maintenance. For example, the addition and replacement of guard columns, adjustment of flow rate and column temperature for the regulation of maximum pressure and change to injection volume to optimise signal detection. As such, the traces collected over this course of the project can vary slightly in terms of peak shape, analyte retention times, and scan durations when viewed side-by-side. All the methods listed thus far are isocratic. As mentioned previously, gradient elution methods can improve peak width, especially for late-eluting analytes. Based on the low retention times of the analytes as part of the above method, as well as the sufficient separation between analyte peaks, it was decided that reproducibility between scans was of more value than sharper peaks, and, as such, the method was kept isocratic. The parameters of the final method can be found in the Section 2.8.8.2.

2.3.4 Chromatograms of FFA Doped with Compounds **15 - 19**

Chromatograms of samples of FFA **14** doped with 2% of each additive individually (compounds **15** – **19**) can be found below in Figures 2.15 – 2.19. Each chromatogram was collected at 280 nm and the peaks labelled with the corresponding

analyte name and structure. Chromatograms of FFA **14** doped with higher levels of each additive (5%) are presented in Appendix Section 7.2.1 for comparison. The retention times (RTs) and relative retention times (RRTs) with respect to FFA **14** of each additive (as measured using the method described above) are shown below in Table 2.2.

Table 2.2. Retention times (RTs) of Compounds **15** – **19** and their relative retention times (RRTs) compared to that of FFA **14**, as recorded by HPLC using the method described in Section 2.8.8.2.

Compound	RT (min)	RRT
Me-FA **15**	1.70	0.77
Cl-FA **16**	1.89	0.85
DF-FA **17**	1.31	0.59
MF-FA **18**	1.14	0.52
t-Bu-FA **19**	4.68	2.12

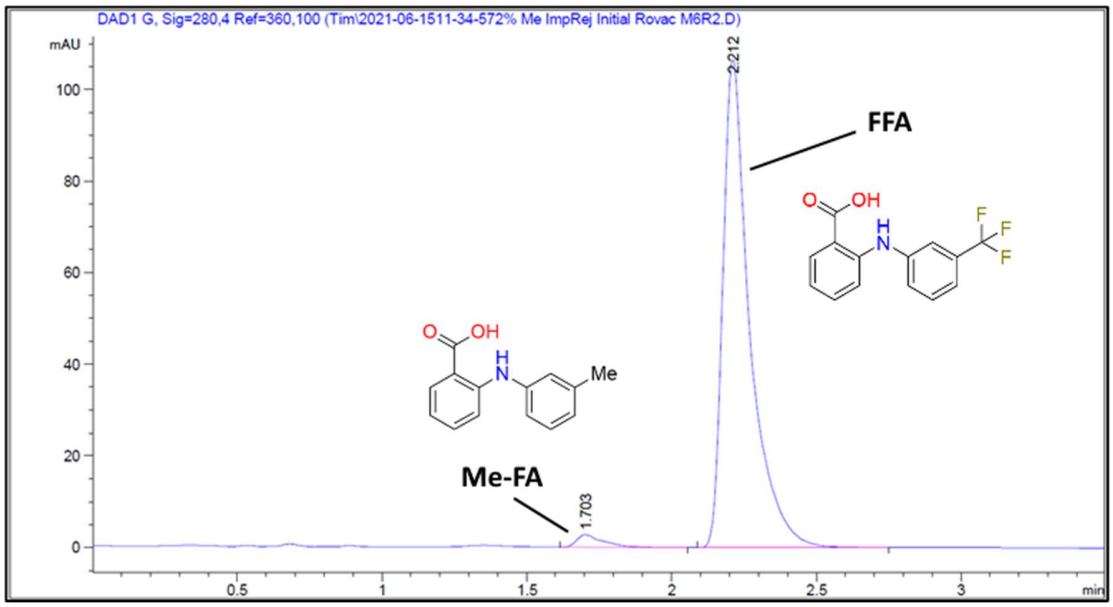


Fig 2.15. HPLC trace of FFA **14** (right, 2.212 min) doped with 2 mol% Me-FA **15** (left, 1.703 min) collected at 280 nm.

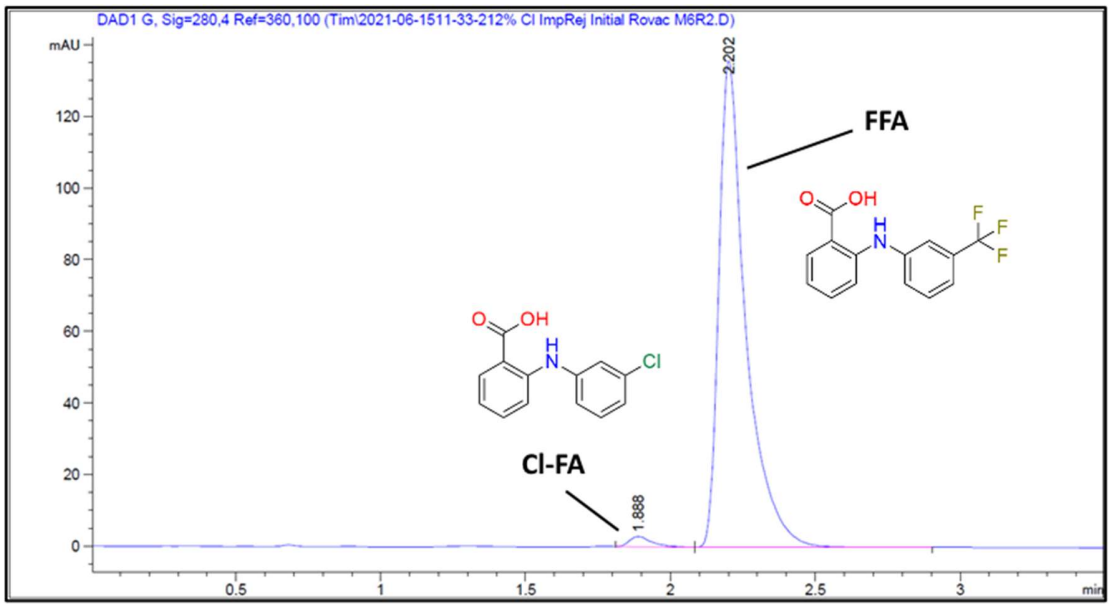


Fig 2.16. HPLC trace of FFA **14** (right, 2.202 min) doped with 2 mol% Cl-FA **16** (left, 1.888 min) collected at 280 nm.

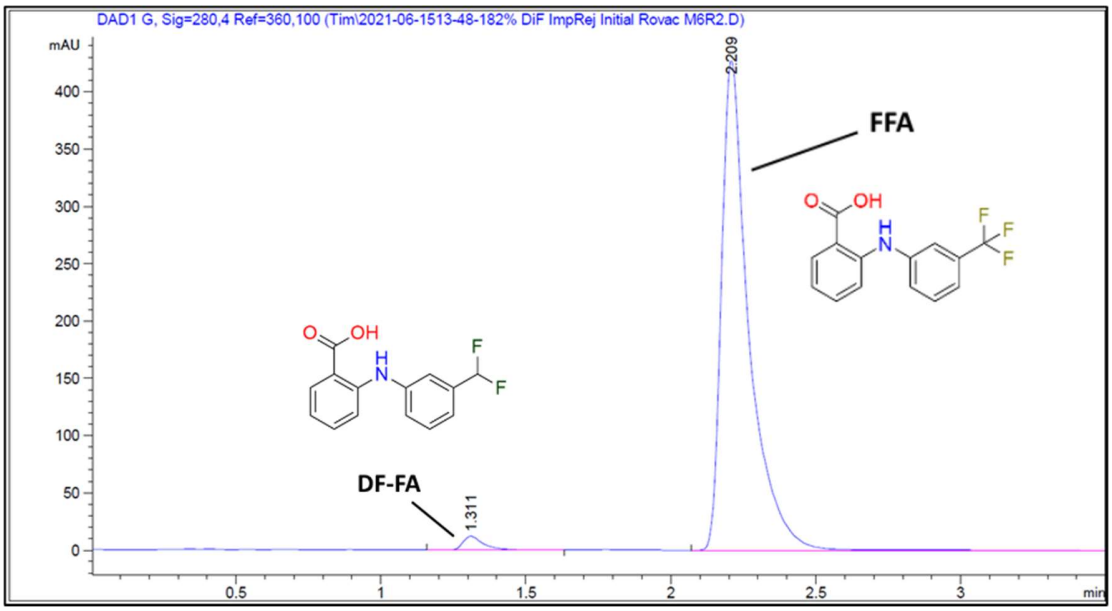


Fig 2.17. HPLC trace of FFA **14** (right, 2.209 min) doped with 2 mol% DF-FA **17** (left, 1.311 min) collected at 280 nm.

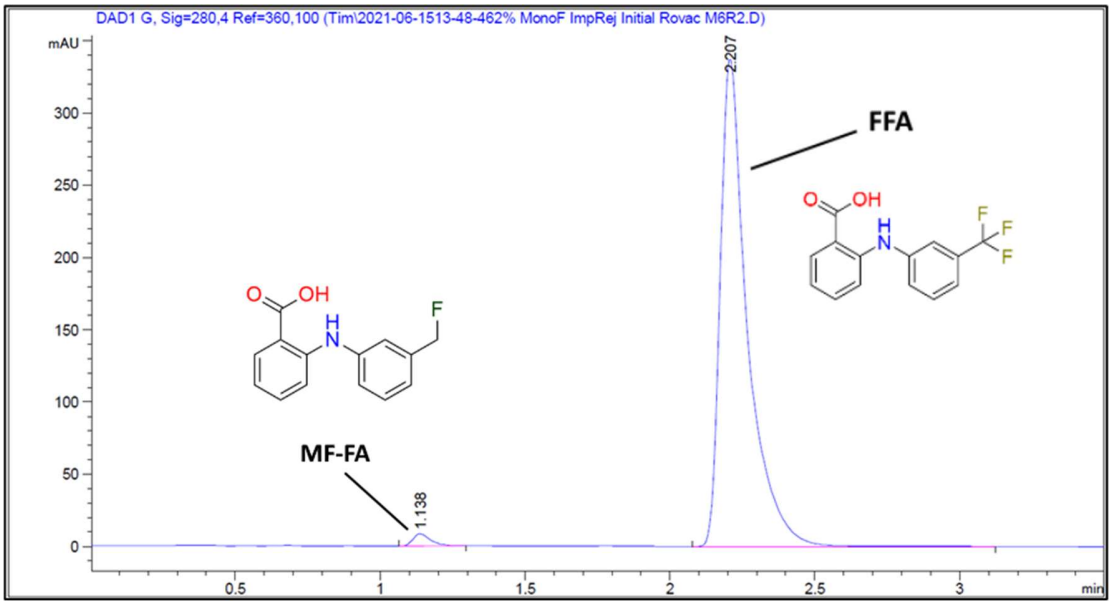


Fig 2.18. HPLC trace of FFA **14** (right, 2.207 min) doped with 2 mol% MF-FA **18** (left, 1.138 min) collected at 280 nm.

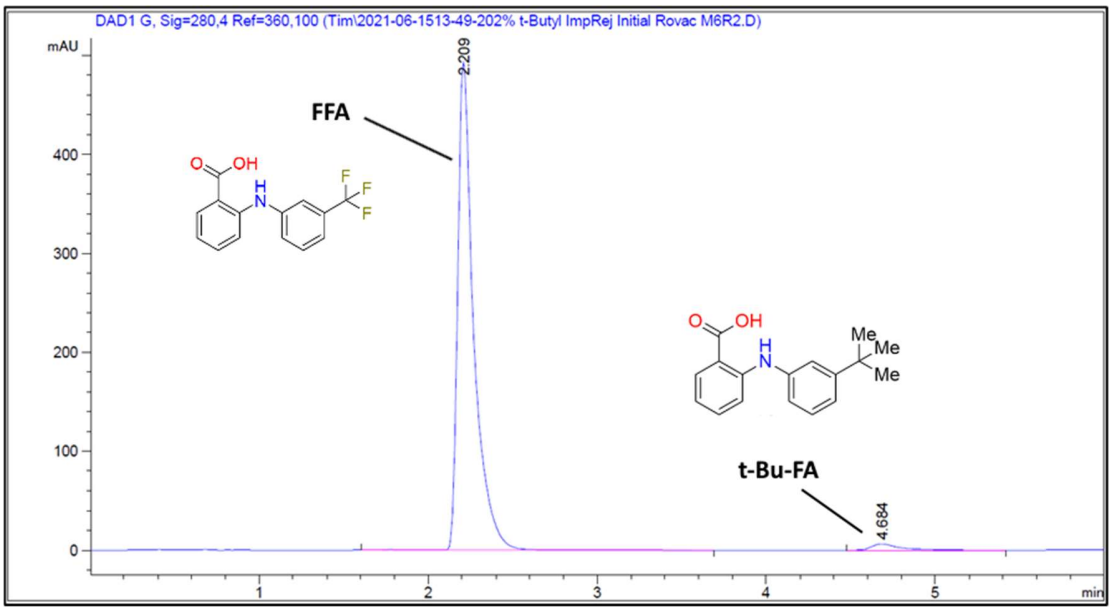


Fig 2.19. HPLC trace of FFA **14** (left, 2.209 min) doped with 2 mol% t-Bu-FA **19** (right, 4.684 min) collected at 280 nm.

2.4 Calibration Curves

Calibration curves were constructed for FFA and each of the additives. In the context of this research, calibration curves are primarily useful in the calculation of proportional additive levels in a doped sample, especially as response factors for each component can also be determined during their construction. This concept will be discussed in greater detail in Section 4.2.1.

2.4.1 Standard Solution Preparation

The process of constructing and analysing the quality of a calibration curve will be discussed in this section, using one constructed using commercial FFA as a case study. The procedure, analysis, and considerations of this process were carried out according to the Guide to Best Practice written by Prichard and Barwick.[172] In the case of this project, the standard solutions used MeCN as the solvent. Generally, standard solutions are prepared in a solvent closely matching the mobile phase of the method with which they will be tested (i.e., 50:50 MeCN / water), but in this case a purely organic solvent was opted for to aid material recovery. For most curves, up to 7 calibration standards are advised. However, if the material is more familiar and its linearity has been previously established, fewer standards are required. For example, the calibration curve for FFA being discussed in this section included 7 data points, but later iterations reduced that number to four as the linearity of the material response had been established. The additives

selected for this project were often not commercially available and, in many cases, very costly to produce, and, as such, the number of standards were limited to four.

2.4.2 Plotting Data Points and Regression Analysis

The data points for the FFA calibration curve mentioned previously are presented in Figure 2.20. The points on this plot are evenly spaced and appear linear with no obvious outliers which could bias a regression line. A linear regression curve was fit to the data points using Excel software. This regression curve and the corresponding equation are also displayed in Figure 2.20. The quality of the regression line can be assessed by regression analysis and by the plotting of the data point residuals (Figure 2.21).

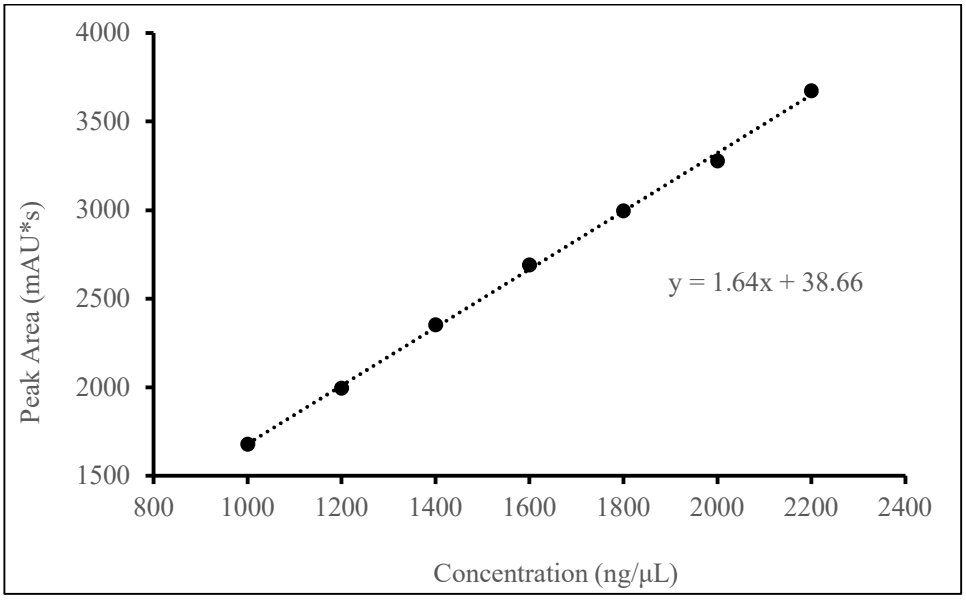


Fig 2.20. Linear regression curve fitted to the commercial FFA data points, collected at 280 nm, and the equation of that curve.

Residual analysis plots the similarity of the data points to their predicted position as calculated by the regression analysis. In this way the representation of the curve can be assessed and any patterns in the distribution of data points can be identified.

In the case of FFA (Figure 2.21), the residuals appear to be mostly randomly distributed, a desirable result as there is no trend in the spread of residuals with concentration. The distribution does appear to widen slightly with concentration, indicating a system where the standard deviation of an instrument response increases with analyte concentration. This is quite common in chemical measurement systems, and can be solved through the use of a weighted least squares regression.[173] However, in this case the increase is relatively minimal and would have little impact on the quality of the regression line, as will be demonstrated through the regression statistics.

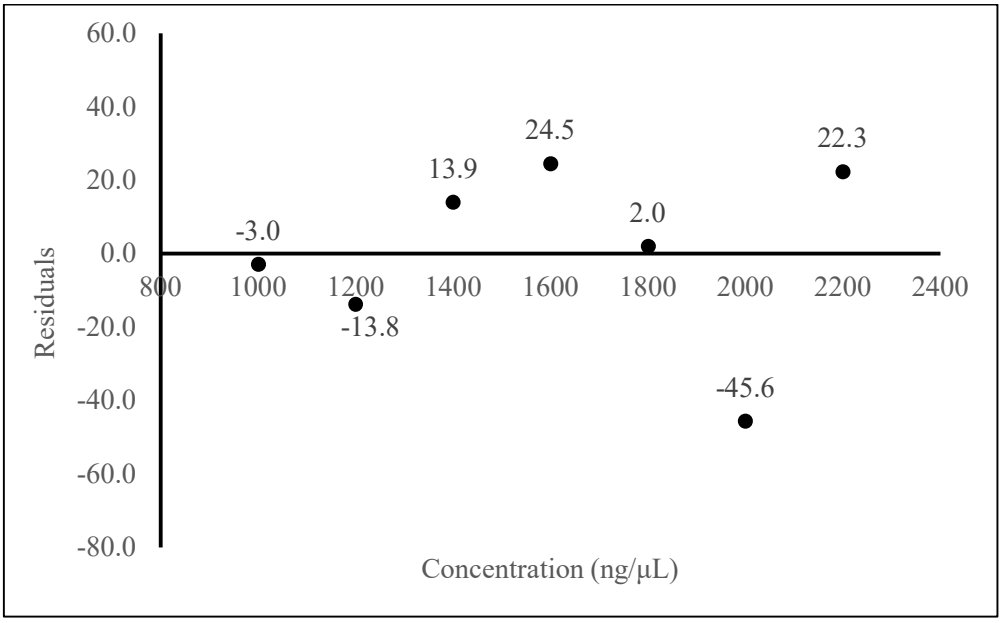


Fig 2.21. Plot of the regression residuals of the FFA commercial calibration curve.

The regression statistics for the FFA curve are presented below (Tables 2.3 – 2.5). Table 2.3 contains the three *r* values used as measures of data point correlation. Multiple R measures only the strength of the degree of correlation between the *x* and *y* values. R Square describes the fraction of the total variance in the data that is contributed by the fitted regression line. Adjusted R Square accounts for the reduction in degrees of freedom caused by additional data points. The three values are all above 0.998, indicating a very high level of correlation between the data points by each metric.

Table 2.4 lists the Analysis of Variance (ANOVA) regression statistics, further evaluating different aspects of the regression curve. The high F and low Significance F values suggest the probability of obtaining the ANOVA results by chance if there was no correlation between the concentration and response values is negligible. The final table (Table 2.5) examines the regression coefficients: the y-intercept and the slope of the regression line. The upper and lower confidence levels for the y-intercept fall either side of 0. Combined with a *p*-value > 0.05, the intercept can be said to be statistically similar to 0, a desirable attribute for a calibration curve which should ideally pass through the origin. On the other hand, the slope should have a value statistically different from 0 to represent the response of the instrument to the increasing concentration of the standards. This is achieved with a confidence range of 1.577 - 1.707, and a *p*-value < 0.05.

Judging by the high *r* values and regression analysis results within the acceptable ranges, this curve is most likely of sufficient quality for calibration.

Table 2.3. Regression statistics for the FFA commercial calibration curve, including *r* values.

Multiple R	0.999
R Square	0.999
Adjusted R Square	0.999
Standard Error	26.75
Observations	7

Table 2.4. ANOVA regression statistics for the FFA commercial calibration curve.

ANOVA	df	SS	MS	F	Significance F
Regression	1	3020160.80	3020160.80	4221.09	1.64E-08
Residual	5	3577.47	715.49		
Total	6	3023738.27			

Table 2.5. Regression coefficient statistics for the FFA commercial calibration curve.

	Coefficients	Standard Error	t Stat	P-value	Lower 95.0%	Upper 95.0%
Intercept	38.66	41.70	0.93	0.40	-68.50	145.81
Concentration (ng μL^{-1})	1.64	0.025	64.97	1.64E-08	1.58	1.71

2.4.3 Overview of Constructed Calibration Curves

As mentioned in Section 2.3.3, the HPLC method (such as flow rate and temperature) and parts (such as columns and guards) were altered over the course of the

project. As such, multiple iterations of calibration curves were constructed for FFA and some of the additives to remain applicable to samples run in the changed conditions. The equations of the linear regression curves for each plot vary between different curves of the same analyte, but the response factors remain more consistent. An example of a calibration curve and its related analyses for each of compounds **15** – **19** can be found in Appendix Section 7.3. These calibration curves were used to calculate the limit of detection (LOD) and limit of quantification (LOQ) for FFA **14** and each additive; these values are shown below in Table 2.6.

Table 2.6. Limit of detection (LOD) and limit of quantification (LOQ) values for each of compounds **14** – **19**, calculated from the calibration curves of each material presented in Section 2.4.2 for FFA **14** and Appendix Section 7.3 for compounds **15** – **19**.

Compound	**LOD (mg mL^{-1})**	**LOQ (mg mL^{-1})**
FFA **14**	0.053	0.16
Me-FA **15**	0.039	0.12
Cl-FA **16**	0.060	0.18
DF-FA **17**	0.092	0.28
MF-FA **18**	0.230	0.68
t-Bu-FA **19**	0.040	0.12

2.5 Solubility Tests

Another important attribute to determine for FFA and other materials of study is their behaviour in solution, most significantly their solubility. The solubility of materials is a key property in the pharmaceutical industry, influencing the bioavailability, dosage, and formulation of drug products. It also has a significant impact on the work done in this project. For example, Givand *et al*. demonstrated the ratio between the solubilities of an impurity and a host material in a solvent directly correlates the substitutional incorporation of the impurity into the host when the two are crystallised together in the solvent.[174] In short, the lower the solubility of the impurity or additive relative to the host, the higher the level of incorporation. This correlation has also been observed in research similar to the current work.[90] Incorporation level is dependent on a number of factors including material structure and crystal behaviour, but when the same materials are tested in an array of solvents it is clear that solubility plays an important role. Solubility measurements of FFA are especially crucial when carrying out partial dissolutions. In order to dissolve a controlled amount of mass from a crystal sample at each stage, an accurate value for the solubility of the material in the dissolution medium of choice must be determined. Partial dissolutions will be discussed in more detail in Section 5.2. Insight into solubility behaviour also has uses in this research in the areas of doped system preparation, controlled crystallisation, recrystallisation, and HPLC sample preparation.

Despite the volume of literature available surrounding FFA **14**, sources describing the solubility of the material in commonplace laboratory solvents are very scarce. Those sources that are available either do not provide sufficient detail about the material being

tested (e.g. polymorphic form) or provide values that do not align with what was observed during this research.[130,175,176] As such, it was decided to perform solubility tests on the material empirically.

2.5.1 FFA Solubility Tests

2.5.1.1 Solubility Determination of FFA at Room Temperature

Solubility tests for FFA were carried out in a wide array of solvents considered to have potential use for the research. The solvents chosen were MeCN, absolute ethanol (EtOH), ethyl acetate (EtOAc), hexane, MeOH, methyl *tert*-butyl ether (MTBE), toluene, and water. A slurry of the material was equilibrated in the solvent of interest at 25 °C. All solid-state FFA used for these tests was Form III, the most thermodynamically stable form at room temperature. To ensure measurements were representative of the correct polymorph, the form of the material should have been tested post-equilibration as well as before, but unfortunately it was not. However, FFA material crystallised from these solvents was observed to be produced in the Form III polymorph throughout the course of the research, so it is highly likely that the same form would be present here.

The results of these solubility tests are displayed in Table 2.7. Included are the solubility values in g L^{-1}, mol L^{-1} (for comparison with additive solubilities), and g kg^{-1} (used to calculate relative solubility values). The number of replicants measured (n) and the standard deviation values of the results collected (SD) are also included. It should be noted that all replicants used to determine an average solubility value in a solvent were

collected from the same solubility test, with samples removed from the solubility flask at 15 minute intervals to allow for re-equilibration.

Form III FFA exhibited the greatest solubility in MTBE by a large margin. It is also highly soluble in EtOAc, EtOH, and MeOH, moderately soluble in MeCN and toluene, and very sparingly soluble in hexane. The solubility of FFA in hexane was also measured in the same way at 19 °C, for use in partial dissolution studies (see Section 5.2.1.2) and was determined to be 1.63 g L^{-1}. FFA exhibited no solubility in water by any measurement method, the solid material appearing to be hydrophobic when suspended in the solvent.

Table 2.7. Solubility measurements of Form III FFA in different solvent systems at 25 °C, with number of replicants (n) and standard deviations (SD) for each.

Solvent	**n**	**Average Solubility (g L^{-1})**	**Average Solubility (mol L^{-1})**	**Average Solubility (g kg^{-1})**
Water	3	0.00	0.00	0.00
Hexane	3	2.40 ± 0.10	0.01 ± 0.0004	3.66 ± 0.15
MeCN	3	57.99 ± 0.18	0.21 ± 0.001	73.78 ± 0.22
Toluene	5	66.40 ± 0.64	0.24 ± 0.002	76.59 ± 0.74
MeOH	3	180.52 ± 0.56	0.64 ± 0.002	227.93 ± 0.71
EtOH	3	274.62 ± 0.77	0.98 ± 0.003	348.07 ± 0.98
EtOAc	3	377.83 ± 11.67	1.34 ± 0.042	418.88 ± 12.94
MTBE	3	758.95 ± 25.22	2.70 ± 0.090	1025.60 ± 34.09

Additionally, at an early stage of the project a mixture of the EtOAc and hexane was being considered as a means of achieving a dissolution medium with a suitable solubility strength for partial dissolution studies. As such, the solubility of FFA in

mixtures of the two solvents was tested over a range of different ratios (5 – 15% v/v EtOAc in hexane) in order to be able to estimate this solubility strength (Table 2.8). Ultimately the medium chosen for the partial dissolution studies was pure hexane, as the solubility of FFA was deemed suitable in the single solvent.

Table 2.8. Solubility measurements of Form III FFA in compositions of EtOAc and hexane at 25 °C, with number of replicants (n) and standard deviations (SD) for each.

Solvent System	n	Average Solubility (g L^{-1})	SD
5% EtOAc in Hexane	3	14.83	0.94
10% EtOAc in Hexane	3	24.50	1.08
15% EtOAc in Hexane	3	53.00	4.30

2.5.1.2 Solubility Determination of FFA at Higher Temperatures

Two of the solvents displayed in Table 2.7, MeCN and EtOH, were selected for temperature-based solubility studies as examples of moderate and good solvents respectively. The solubility of FFA in these solvents was measured at 10 °C intervals from 40 °C to 70 °C in the same manner as described in Section 2.8.3 and presented in Figure 2.22 as solubility curves against the temperature at which they were measured. As was to be expected, the solubility of the material in both solvents increased with temperature. The solubility in EtOH exhibited a gentle, more linear increase, while in MeCN the rise in solubility was much sharper, especially at higher temperatures. It is possible that there is a polymorphic transformation occurring in the FFA material at these temperatures. As will be discussed in Section 2.6.2, the previously metastable Form I becomes the thermodynamically stable form at a temperature of 42 °C. While the transformation

wasn't observed at this temperature in the solid state, at equilibrium with a solvent it may have been occurring. To ascertain this conclusively, the crystal structure of the solid FFA material isolated after the solubility tests at higher temperatures should have been tested by PXRD. Unfortunately, this was not done. However, the information gathered from these particular solubility tests was primarily used for information in the slow cooling crystallisation methods, and the presence or absence of polymorphs other than Form III would have had minimal impact on the research.

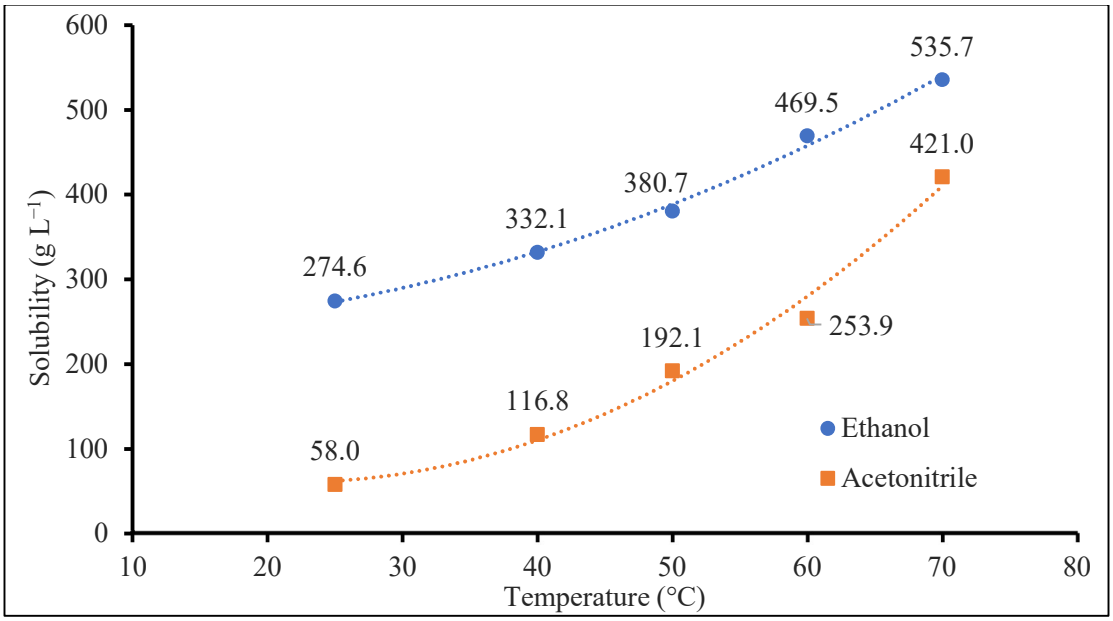


Fig 2.22. Solubility measurement curves of Form III FFA in EtOH and MeCN at increasing temperatures, from 25 - 70 °C.

Table 2.9 below shows the number of replicants measured (n) and the standard deviation values (SD) of the solubility values presented for FFA **14** at increasing temperatures above. It should be noted that all replicants used to determine an average

solubility value in a solvent were collected from the same solubility test, with samples removed from the solubility flask at 15 minute intervals to allow for re-equilibration.

Table 2.9. Number of replicants (n) and standard deviations (SD) for the solubility measurements of FFA III **14** in EtOH and MeCN at increasing temperatures from 25 °C - 70 °C.

Solvent	Value	25°C	30°C	40°C	50°C	60°C	70°C
EtOH	**n**	3	3	3	3	3	3
	SD	1.92	0.49	0.63	1.24	0.39	2.40
MeCN	**n**	3	3	3	3	3	3
	SD	1.92	0.31	0.66	0.85	1.09	1.20

2.5.2 Solubility Determination of Additives

The solubilities of the additives are of interest for many of the same reasons as FFA, for example recrystallisation and sample preparation. However, the main interest lies in comparing the solubilities of the additives to FFA. As mentioned previously, the relative solubilities of an impurity and a host has been shown to have a measurable impact on the purity of material crystallised from an impure solution; the lower the relative solubility of the impurity, the greater the extent to which it is included in the crystal. Determining the solubility of the additives under the same conditions as the FFA tests were carried out allows for a deeper understanding of the observed incorporation behaviour of each additive that will be discussed in Chapter 4.

A rigorously accurate determination of solubility requires a substantial amount of material. A sufficient volume of solvent needs to be used to facilitate the removal of

multiple aliquots of at least 1 mL saturated solution, and, as such, a sufficient amount of test material needs to be used so that an excess is present in that volume of solvent. The need to synthesise the additive places practical limits on the amounts that can be obtained, especially for DF-FA **17**, MF-FA **18**, and t-Bu-FA **19**. Even using methods of reducing the amount of material needed which run the risk of increased uncertainty, such as reducing aliquot volume or number of replicates, the available amount of these additives was not sufficient to obtain solubility data. As such, the investigations were carried out solely on Me-FA **15** and Cl-FA **16**. However, it was established that compounds **17** – **19** exhibited comparable solubility to FFA **14** and compounds **15** – **16** in all solvents used as part of the research prior to proceeding.

2.5.2.1 Determining the Solubility of Additives in Pure Solvents

The solvents in which solubilities of these two additives were determined were more limited but were chosen based on experience with FFA. Hexane was chosen as it was the dissolution medium that was to be used for partial dissolution studies. EtOH was the solvent in which the doped systems were prepared. Finally, MeCN and MeOH were the primary crystallisation solvents that were being used for the production of the majority of crystal samples in the research. The solubility of the two additives were tested at 25 °C in these solvents, using mass measurements as described in Section 2.8.3. These solubility values are displayed alongside the corresponding FFA solubilities in Figure 2.23. Unlike those in Figure 2.22, these values are presented in mol L^{-1} to allow for more representative comparison between different chemical species.

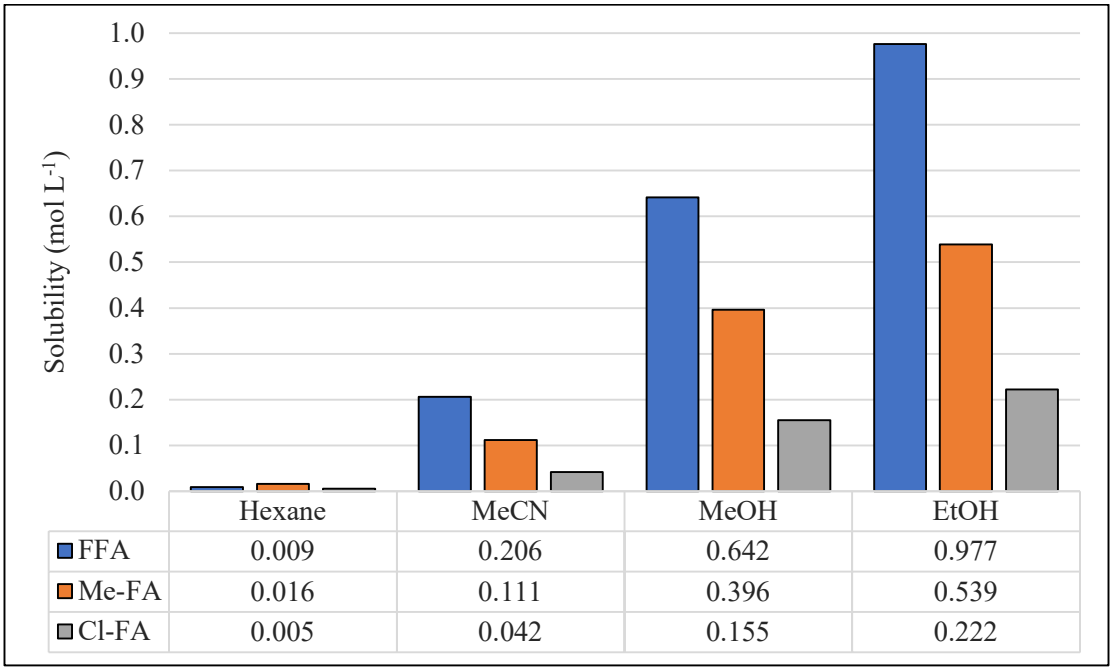


Fig 2.23. Solubility measurements of Form III FFA **14** (left), Me-FA **15** (middle) and Cl-FA **16** (right) in four solvents at 25 °C.

Table 2.10 below shows the number of replicants measured (n) and the standard deviation values (SD) of the solubility values presented for Me-FA **15** and Cl-FA **16** above. Comparable values for FFA **14** can be found in Table 2.7. It should be noted that all replicants used to determine an average solubility value in a solvent were collected from the same solubility test, with samples removed from the solubility flask at 15 minute intervals.

Table 2.10. Number of replicants (n) and standard deviations (SD) for the solubility measurements of Me-FA **15** and Cl-FA **16** in four different solvent systems at 25 °C.

Additive	Value	Hexane	MeCN	MeOH	EtOH
Me-FA 15	**n**	4	3	4	3
	SD	0.0014	0.0022	0.0025	0.0100
Cl-FA 16	**n**	4	3	3	3
	SD	0.0003	0.0018	0.0037	0.0011

The solubility of each additive follows the same pattern of Hexane < MeCN < MeOH < EtOH, matching that of FFA **14**. The relative solubility behaviour of all three materials is remarkably consistent in MeCN, MeOH, and EtOH. In each of these solvents, FFA **14** is the most soluble, followed by Me-FA **15**, and finally Cl-FA **16** is the least soluble of the three. The behaviour is slightly different in hexane, with Me-FA **15** being the most soluble of the three materials, followed by FFA **14** and Cl-FA **16**.

2.5.2.2 Pure-Component Relative Solubility (α^0)

This solubility data can be used to calculate the pure-component relative solubility (α^0) for the relationship of an additive and FFA in each solvent. α^0 is defined by Givand *et al*. as the ratio between the solubility of a pure additive/impurity $[Imp]^0$ in a solvent to the solubility of the pure host $[Host]^0$ (Formula 2.1), and is a measure of the relative solubilities of each additive in a solvent.[174] It is important to note that the values represented by the α^0 symbol are unrelated to those represented by the α_1 (selectivity coefficient value, Section 4.4) or α_2 (distribution coefficient value, Section 5.2.2.2) symbols.

Formula 2.1. $$\alpha^0 = \frac{[Imp]^0}{[Host]^0}$$

As mentioned previously, these α^0 values have been shown to have a direct correlation with the purity of crystalline material grown from that solvent. The α^0 values for each additive and solvent can be found in Table 2.11. These ratios are calculated using

g kg^{-1} solubility units to match those reported by Givand *et al*. The number of replicants and standard deviations for the data used to calculate these values can be found in Tables 2.7 and 2.10.

Table 2.11. Pure-Component Relative Solubility (α^0) values between FFA **14** and Me-FA **15** and Cl-FA **16** respectively in four solvents at 25 °C.

Solvent	**Me-FA** 15	**Cl-FA** 16
Hexane	1.45	0.53
MeCN	0.44	0.18
MeOH	0.50	0.21
EtOH	0.45	0.20

As discussed in the previous section, the behaviour of the additives in hexane differs from that in the other solvents. However, the α^0 values are remarkably consistent in the other three solvents. For both additives, the α^0 value in MeOH was slightly higher than in MeCN; in theory this could result in a slightly higher incorporation level for crystals grown in the latter solvent than the former. Indeed, a comparison of FFA **14** crystals doped with Me-FA **15** and Cl-FA **16** grown from solutions in both solvents confirmed that the lower relative solubility of the additives in MeCN is correlated with higher levels of incorporation (Section 4.3.1.6).

The difference in α^0 values between additives is much more pronounced. Considered alone, this implies that the incorporation of Cl-FA **16** should be higher than that of Me-FA **15** in both crystallisation solvents. However, when investigating incorporation behaviour between different additives, relative solubility is only one of

many factors involved. Chemical structure and lattice interactions of the additives, as well as kinetic forces, also play a major role and may overshadow the solubility effects in terms of overall incorporation. In this case, the incorporation of Me-FA **15** was higher than that of Cl-FA **16** at low additive levels (0 - 6%) but this observation was inverted at higher levels (10 - 90%). The incorporation behaviour of doped systems will be discussed in more detail in Section 4.3.

2.6 Crystallisation Method Development

Crystal samples were to be grown doped with the selected additives discussed earlier in the chapter. The properties of these doped crystals were to be assessed and compared to those of pure FFA to determine the nature of the relationships of the additives to the host material, and, as such, evaluate the effectiveness of the additives as case studies for purification-resistant impurities. As such, it was important to investigate the properties of pure FFA, specifically Form III FFA, as a precursor to the doped system studies in Chapter 4. A large amount of information on the crystalline properties of FFA is available in the literature, which simplified this area of work substantially. Using this, methods of crystal analysis were developed on the equipment available, i.e., PXRD, DSC, and TGA analysis.

2.6.1 Methods of Crystal Production

As such, developing one or multiple reliable means of producing crystal samples was a necessary step in the overall method development phase of the project. Not only was this required to produce crystalline FFA material suitable for analysis, but the same methods could also be used to produce crystal samples of FFA systems doped with the selected additives. Depending on their morphology, these doped crystalline systems would be used for a number of investigations into impure crystal behaviour and additive incorporation. Critically, they will also be the systems of studies upon which the methods of determining the distribution of additives will be based. In its Form III polymorph, FFA is reported to crystallise primarily in an acicular needle-like habit.[65] This was also observed empirically in early sample preparation processes. As such, initial development of crystallisation methods was focused on producing crystals of this habit sufficiently large in all dimensions to withstand multiple successive partial dissolution stages. The different techniques of crystal growth employed in this section are discussed in more detail in Section 1.2.2.3.

2.6.1.1 Crystallisation by Slow Evaporation

Initial crystallisation studies took the form of slow evaporation from a range of 10 solvents: acetone, chloroform, dichloromethane (DCM), EtOAc, EtOH, isopropanol (IPA), MeCN, MeOH, tetrahydrofuran (THF), and toluene. A sample of the crystal material produced by each solution in this study can be found in Figure 2.24. The evaporation of most of the solvents produced small, acicular crystals. In some samples,

namely those evaporated from acetone, IPA, and THF, the crystals produced were extremely small and almost powder-like. However, some of the samples produced more suitable crystals. EtOH and MeCN produced crystals that were small, but with more well-developed faces than the other samples. Toluene was the only solvent that produced crystals of a different habit than the others, growing in a more tabular/prismatic fashion, most likely due to the lower volatility of the solvent and, so, the slower growth rate of the crystals. The low solubility of the material in toluene most likely also played a role; the solutions in toluene may have become supersaturated less quickly, and, thus, the crystals would be able to grow at a slower rate. The crystals grown from MeOH also were slightly larger than the other samples.

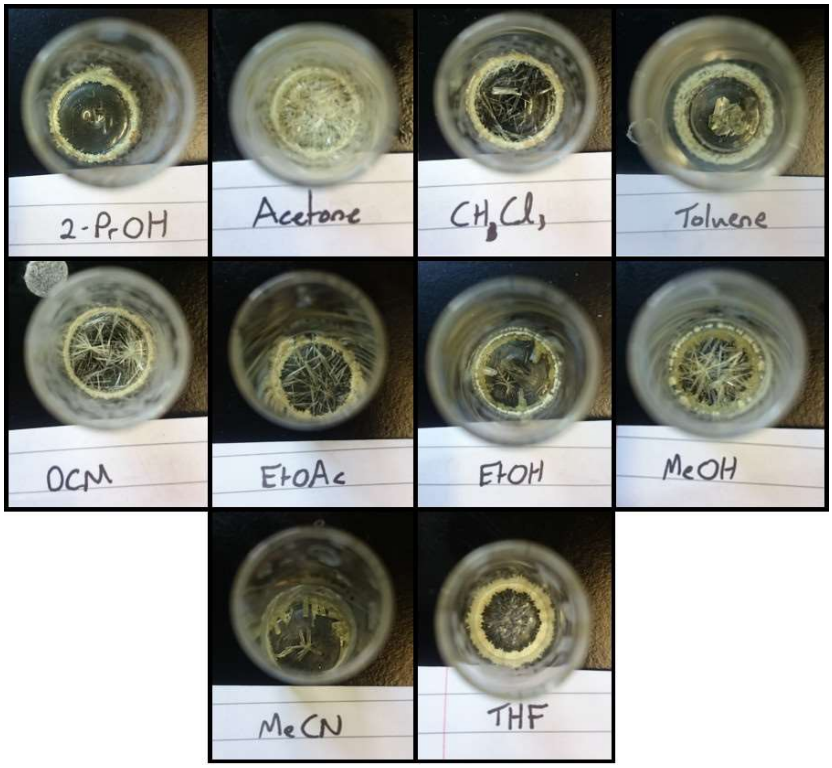


Fig 2.24. Crystal samples produced by the slow evaporation of a solution of FFA in 10 solvents: (from top left to bottom right) IPA, acetone, chloroform, toluene, DCM, EtOAc, EtOH, MeOH, MeCN, and THF.

As the solvents which produced crystals of the highest quality of the initial test, EtOH, MeCN, and toluene were chosen as the subjects of further evaporation studies. Focus was placed on toluene in particular, hoping to replicate the prismatic and/or plate-like morphology observed previously. The effect of evaporation rate on crystal quality was investigated in all three solvents. This was achieved by limiting the open area on the vial through which the solvent can evaporate to different degrees, either through the use of a perforated lid or a lid containing a needle (e.g., Figure 2.25). The perforated lid limits the rate of evaporation compared to an uncovered vial, and the needle-containing lid limits it even further.

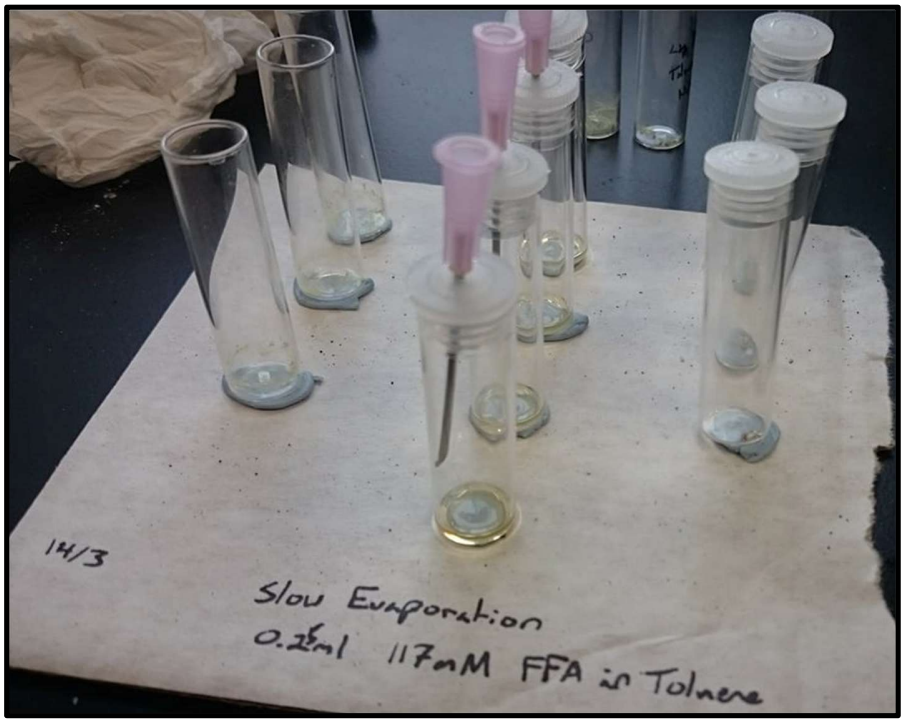


Fig 2.25. Example experimental set-up of evaporation rate crystallisation study.

After the evaporation of the toluene, the crystals produced by the uncovered vials appeared small and low-quality, crusted to the walls of the vials (Figure 2.26). The vials covered with the perforated lids on the other hand produced much more high-quality prismatic crystals in comparison (Figure 2.27). It appeared that limiting the rate of evaporation improved the quality of the crystals produced, at the cost of a substantially longer crystallisation time (up to 4 weeks). The vials stoppered with a needle-containing lid did not produce crystals; it seems the low volatility of the solvent and the limited evaporation area reduced the evaporation rate to an excess.



Fig 2.26. Crystal material produced by evaporation of a solution of FFA in toluene in uncovered vials.



Fig 2.27. Crystal material produced by evaporation of a solution of FFA in toluene in vials covered by a perforated lid.

Similar evaporation-rate tests were carried out on FFA samples dissolved in EtOH and MeCN. Reducing the rate of evaporation resulted in progressively higher quality crystals being produced from the samples dissolved in EtOH (Figure 2.28). These crystals, while somewhat large and regular in appearance, were more akin to clusters of smaller crystal fragments than individual crystal units, making them a less attractive option for future study. On the other hand, those grown from the MeCN-dissolved samples produced no quality crystals at any evaporation rate on this occasion, despite the lower volatility of the solvent and, thus, longer crystallisation period (Figure 2.29).



Fig 2.28. Crystal material produced by evaporation of a solution of FFA in EtOH in vials that were uncovered (left), covered by a perforated lid (middle), and covered by a lid containing a needle (right).

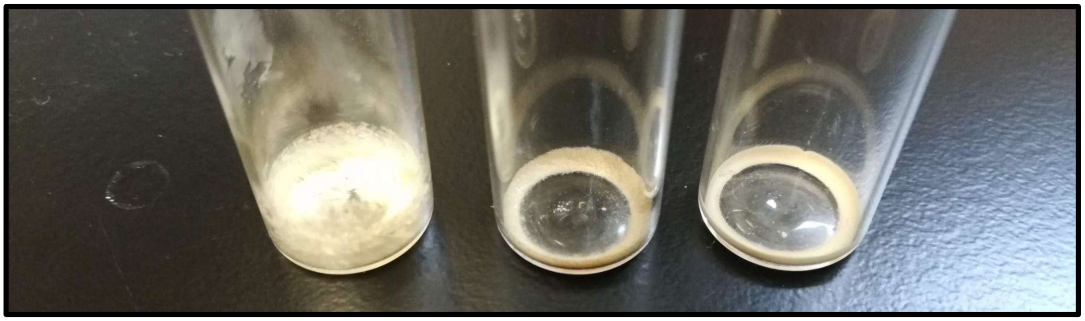


Fig 2.29. Crystal material produced by evaporation of a solution of FFA in MeCN in vials that were uncovered (left), covered by a perforated lid (middle), and covered by a lid containing a needle (right).

The prismatic crystals grown from the vials of toluene with the perforated lids proved the most promising, so further experimentation was carried out in that area. The effect of toluene solution concentration on crystal growth was investigated, with four samples containing solutions of FFA in toluene at increasing initial concentrations. The crystals produced from the evaporation of the solvent in each solution can be found in Figure 2.30. Up to and including solutions of 150 mM, individual crystals with a semblance of a prismatic morphology are produced. At higher concentrations, the crystals are much smaller, more numerous, and appear as a crust similar to the open-vial samples in Figure 2.26. This is likely a consequence of the higher levels of supersaturation caused by the evaporation of the solvent in the more concentrated solutions, resulting in a faster crystallisation time and, thus, smaller crystals.



Fig 2.30. Crystal material produced by evaporation of solutions of FFA in toluene with increasing concentrations; from left to right, 100 mM, 150 mM, 175 mM, and 200 mM.

Taking all the above slow evaporation tests into consideration, the conditions that had the most potential for the production of high-quality crystals appeared to be a slow evaporation from a low-concentration solution of toluene, with the evaporation rate limited by a perforated lid. Under these conditions, individual small but prismatic crystals were observed to grow that could be suitable for partial dissolution processes, as well as

other studies into the behaviour of doped systems. However, this technique of crystal growth has a major disadvantage in terms of crystallisation duration. As mentioned previously, the production of high-quality crystals benefits from long periods of growth; as such, crystallisation is an extremely time-consuming process. In this case, however, it was taking between 2 – 4 weeks to evaporate the volume of toluene necessary for crystal nucleation and growth to occur. Additionally, a successful crystallisation process of this nature only produces one or maybe two suitable crystals. As will be observed in Chapter 5, the development of methods for determining impurity distribution (including partial dissolution) requires many samples of crystals doped with varying additive types and levels. In turn, each of these samples is ideally composed of enough individual crystals to mitigate any variability in the results within each sample. As such, a crystallisation method would need to be able to produce enough crystals to satisfy the demands of the process. Despite the quality of the crystals, slow evaporation from toluene proved too time-consuming to be viable at that scale. Use of seeding crystals in the evaporation vials was also explored, but ultimately did not provide a significant improvement in crystal production compared to samples in which they were not included.

Using a solvent with a higher volatility could reduce evaporation times and increase the rate of crystal production, while still providing adequate time to produce high-quality crystals. EtOH was reconsidered, based on the quality of the crystals produced in the early slow evaporation tests, but the solubility of the material in the solvent was deemed too high. By the point of supersaturation, the volume of the solution would be too low, having a detrimental effect on the size of the crystals grown. As a result,

MeOH was chosen; a solvent with similar properties to EtOH, but in which FFA is significantly less soluble.

This method of crystallisation proved inconsistent, many samples produced either cakes of powder-form FFA or crystals with problematic morphologies. However, a portion of vials produced crystals that were of a size and quality appropriate for partial dissolution studies. Generally, these crystals could be described as prismatic based on the level of development on all faces, but they retain some tabular and acicular characteristics, appearing as long, thick plates (e.g., Figure 2.31). The size, morphology, and robustness of these crystals made them ideal candidates for partial dissolution; as such, crystals grown *via* this technique were used for the majority of the method development process. As each crystallisation vial could not be guaranteed to produce usable crystals, approx. 10 batches were allowed to evaporate at any given time, replacing each with fresh material and solvent as crystallisation occurred. Additionally, up to 20 crystals could be recovered from a successful crystallisation batch, offsetting the inconsistency of the process in terms of production efficiency. Use of conical flasks containing a larger amount of material and solvent increased the rate of crystal production even further. The partial dissolution method would also be adapted to make use of some of the crystal batches with problematic morphologies (Section 5.2.3).

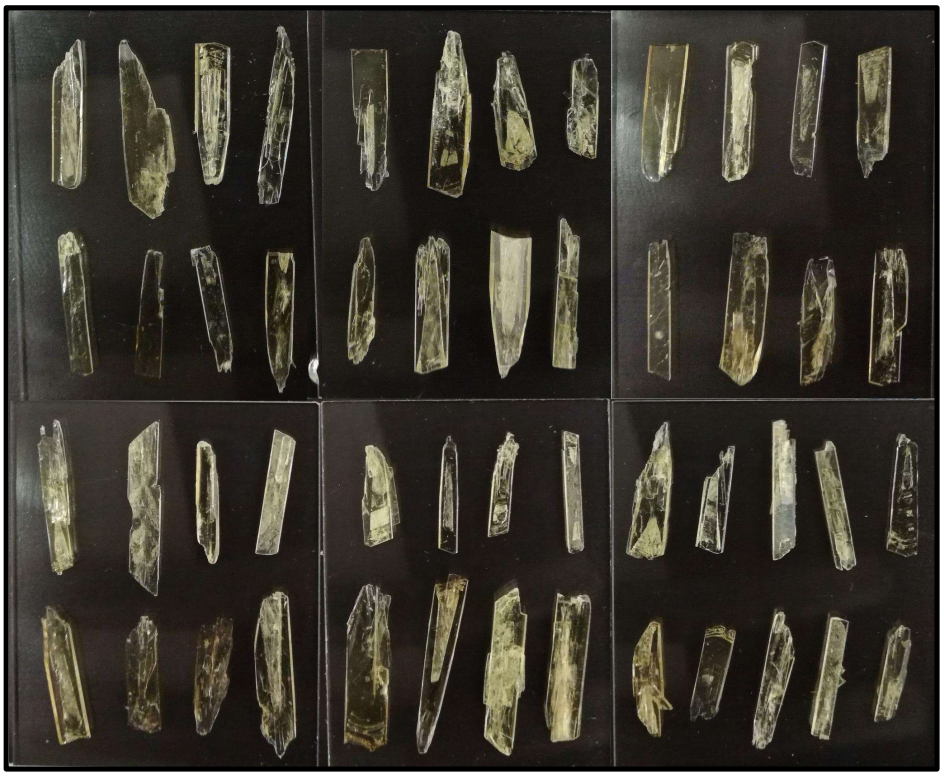


Fig 2.31. Sample of the type of crystals grown by the slow evaporation of MeOH from a solution of FFA (images in figure are the same scale).

2.6.1.2 Crystallisation by Liquid-Liquid diffusion

More efficient crystallisation options were investigated, namely liquid-liquid diffusion, seeding, and slow cooling techniques. Four liquid-liquid diffusion samples were prepared in the manner described in Section 2.8.4.2, with properties of the FFA solution differing in each. One involved a subsaturated solution of FFA in toluene, another in EtOAc. The final two were both composed of FFA in chloroform, one subsaturated, the other close to saturated, to observe the difference between the two. Based on the solubility tests discussed in Section 2.5, hexane was the only clear candidate for the anti-solvent, or precipitant. The resultant crystals, or lack thereof, from this experiment can be

found in Figure 2.32. No crystals were produced from the EtOAc vial, possibly due to a low solution concentration. The saturated chloroform solution produced a solid mass of material with little in terms of distinct crystals. The subsaturated chloroform and toluene samples did produce crystals, but they were small and low quality.

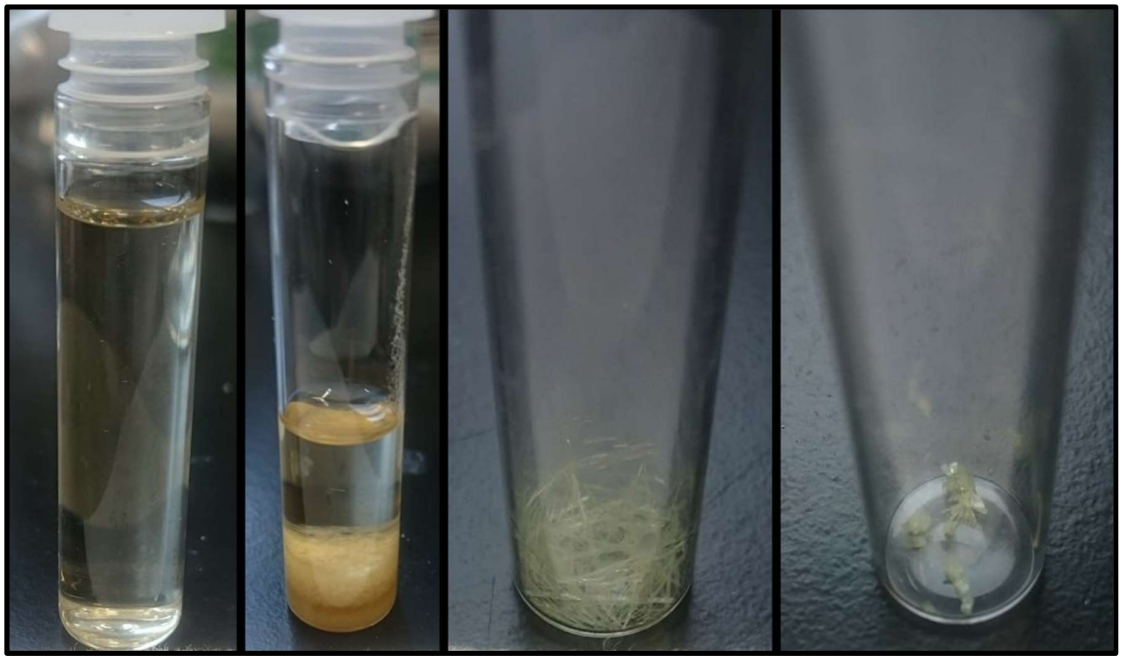


Fig 2.32. Crystal material produced by slow diffusion of a hexane precipitant into four solutions of FFA; from left to right, a subsaturated solution in EtOAc, a near-saturated solution in chloroform, a subsaturated solution in chloroform, and a subsaturated solution in toluene.

2.6.1.3 Crystallisation by Slow Cooling

The final, and most successful technique attempted at this stage of the project was crystallisation by slow cooling. Ideally this procedure is carried out in a solvent with a sufficiently high boiling point to allow for a long cooling duration. The solubility of the material in the solvent should be relatively low, so that a reasonable volume of the solvent

can be used to achieve supersaturation, and the solubility profile of the material in the solvent should be known, preferably across a wide range of temperatures. For these reasons, the slow cooling study was carried out in MeCN, a solvent that fit the above criteria.

This process produced acicular needles of FFA with high consistency (Figure 2.33). These needles were larger than any produced up to this point, and a substantial number of crystals were produced per vial. The size of the crystals, as well as the rate of production and number of individual units in each batch, meant that this method of crystallisation was deemed the most successful attempted to that point, and the crystals would be used as the basis for preliminary partial dissolution studies (Section 5.2.1.1) and some doped system behaviour investigations (Section 4.3). The pattern of growth of these needles were also of interest; they were observed to grow outwards from a single nucleation point in a rosette pattern. This allowed for the easy determination of growth direction, information that could be taken advantage of when developing the segmentation method of determining additive distributions in acicular crystals (Section 5.3).

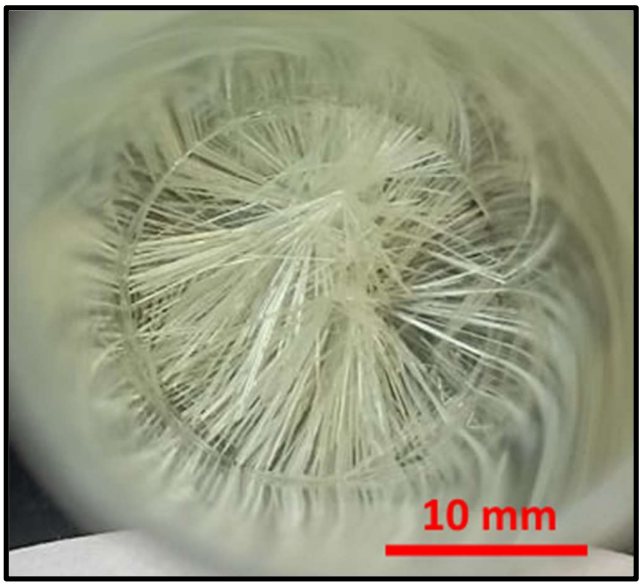


Fig 2.33. Acicular crystals produced by slow cooling of a solution of FFA in MeCN.

2.6.1.4 Alternative Methods of Crystal Production

As will be discussed in detail in Section 5.2.1.2, the crystals produced *via* the slow cooling of MeCN proved unsuitable for use in the bulk of the partial dissolution studies. Their fragility and low mass introduced issues surrounding crystal loss and required solvent volumes respectively, and, as such, it was decided a different crystal morphology was required for that area of the research. Ideally, the new crystals would be larger to allow for fewer to be used in each sample while still requiring a sufficient volume of dissolution medium, they would be more robust to prevent crystal breakage and complete dissolution over multiple successive dissolution stages, and they would be more developed across different faces to facilitate the better study of additive distributions on a surface-to-centre basis. As such, it was decided that crystals with a more prismatic habit were required.

Crystallisation by Vapour Diffusion

Vapour diffusion was studied concurrently with the later slow evaporation experiments. Experiments of this nature were carried out using a solution of FFA in MeOH and hexane as the precipitant. Initial tests produced no crystals, so the ratio of precipitant to solution was increased in an attempt to induce crystallisation more effectively. After approx. one week, a single, large, prismatic crystal was recovered from the side of the smaller vial, regular on one end and tapered towards the other, with a perpendicular growth across the surface of the liquid (Figures 2.34 and 2.35). This technique would later be used to produce similarly large crystals doped with additives for single crystal partial dissolution studies (Section 5.2.2.4).



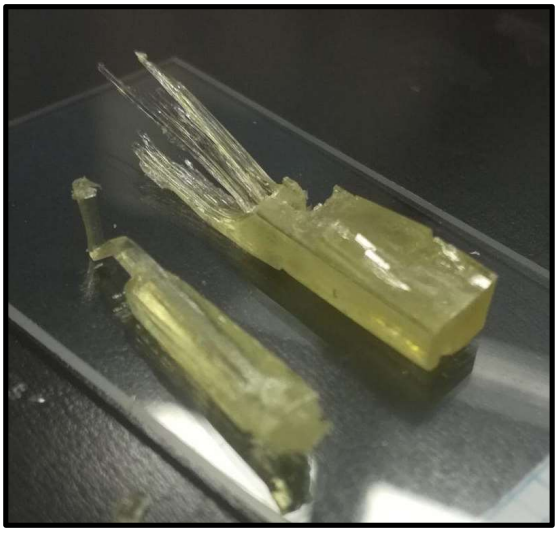


Fig 2.34, left. Sample vial containing crystal material produced by the diffusion of hexane into a solution of FFA in MeOH. **Fig 2.35, right.** The isolated crystals produced by that crystallisation process.

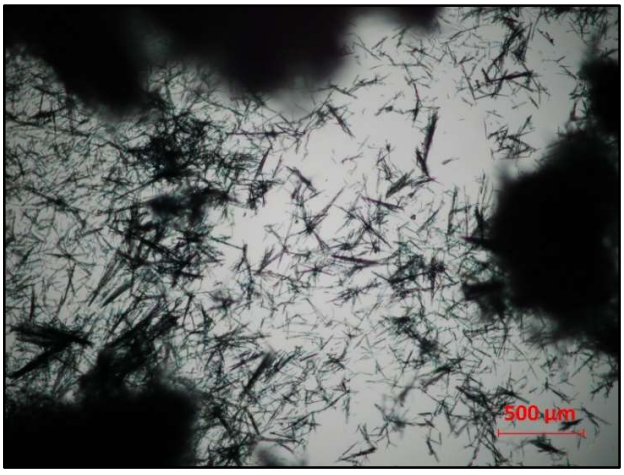
Crystallisation by Rotovap Evaporation

The final crystallisation method developed as part of this project is that of rotovap crystallisation. A combination of the evaporation and antisolvent precipitation crystallisation techniques discussed in Section 1.2.2.3, this technique involves mixing a solution of the material to be crystallised in a good solvent with a miscible antisolvent precipitant. In the case of FFA (and later the doped systems), the solvent of choice was DCM. This solvent was chosen firstly as a good solvent for FFA; while the solubility of FFA in DCM was not measured in a similar way to the other solvents in Section 2.5.1, FFA III was observed to be highly soluble in the solvent. DCM is also a solvent with a very low boiling point (39.6 °C). The boiling point of the good solvent must be lower than that of the antisolvent precipitant, to ensure it evaporated first when exposed to the vacuum. As the precipitant for this procedure is hexane, that boiling point needs to be below 69.0 °C for the crystallisation to be successful. The good solvent is then evaporated on a rotovap, reducing the solubility of the material in the mixture until it crystallises, forming a slurry in the precipitant.

Predictably, this method of crystallisation produces very poor crystals in terms of size and morphology, generally taking the form of large clusters of very small needles (Figures 2.36 and 2.37). However, the technique has an advantage in terms of crystallisation time, as the crystals can be grown in this way in a matter of minutes. As such, it has applications in situations where crystal samples are required, but the crystal habit is unimportant, such as for PXRD and DSC analysis. Additionally, unlike other crystallisation techniques described, this method crystallises nearly all material in solution, making it a very efficient form of sample preparation. As will be described in

Section 4.3, this method of crystallisation is ideal for producing doped material throughout which additives are well incorporated and evenly distributed, even at high doping levels; an attribute not guaranteed by other forms of crystallisation.





Figs 2.36 (left), 2.37 (right). Macro image (left) and microscope image (right) of crystal material produced by the evaporation by rotovap of a solution of FFA in a mixture of hexane and DCM.

2.6.1.5 Summary of Developed Methods of Crystal Production

In summary, experimentation was carried out on a wide range of different crystallisation techniques in an attempt to develop reliable methods of producing crystals suitable for use in other areas of the project. These included slow evaporation, slow cooling, seeding, liquid-liquid diffusion, vapour diffusion, and rotovap crystallisation techniques. Use of seeding crystals in evaporation studies was also explored. Based on the observations from these studies, four primary methods of crystal production were

decided on. The first, slow cooling from a supersaturated solution in MeCN, reliably produced long, acicular crystals that grew in rosette patterns from defined nucleation points. Slow evaporation of a solution in MeOH was less reliable but nevertheless proved the most efficient method of producing large prismatic crystals suitable for partial dissolution studies. Vapour diffusion was used on a handful of occasions to produce large single crystals and agglomerates for certain partial dissolution studies. Finally, crystallisation *via* rotovap proved highly efficient for the production of large amounts of crystal material for applications in which the crystal habit was inconsequential. These techniques will be used to produce crystal material for the studies described next in this chapter, as well as those discussed in Chapters 4 and 5.

2.6.2 Analysis of FFA Crystal Properties

2.6.2.1 Polymorphism of FFA

One well-documented aspect of FFA is its polymorphism. While the material has been demonstrated to be able to take at least 9 polymorphic forms,[65] most literature research focuses primarily on the most stable and commercially available Form I and Form III.[71,133,153,154] The importance of maintaining a single consistent polymorphic form across all experiments involving solid-state FFA has been discussed previously in the chapter. Different polymorphs of the same material, including FFA, can have significantly different properties including melting point and solubility.[65] As such, ignoring the potential presence of multiple different forms of FFA has the potential of introducing variability between experiments within the project. Form III is known to be the most thermodynamically stable form at typical room temperatures (18 – 25 °C). This means

that during crystallisation, Form III is the lowest energy and, thus, most energetically-favourable polymorph the material can take at this temperature. However, often crystallisation occurs according to the most kinetically favourable path, rather than producing the most thermodynamically favourable product. According to Oswald's Rule of Stages, early stages of crystallisation often form a less stable polymorph initially, as the higher-energy state more closely matches the energy of the liquid-phase.[30,177] Thus, it is possible that formation of Form III might not be the most kinetically favourable pathway of one or multiple of the crystallisation methods developed in Section 2.6.1, and, so, the material could crystallise in a different polymorph. Invariably the less stable polymorph does transition to the most stable form at the given temperature; however, this process can take an extended period of time. For example, the conversion of Form I to Form III FFA takes 12 hours at room temperature when stirred in a suspension with xylene,[178] whereas a solid-state transformation at room temperature has been reported to take over 8 days for a single crystal.[71] As such, the hypothetical kinetically-formed polymorph of FFA could exist in the less-stable form during the course of experiments using the material, before reverting to the stable Form III at a later time. Therefore, controlling the polymorphic behaviour of FFA was an important aspect of the crystallisation method development process. Monitoring of the material form is achieved through PXRD analysis.

A single polymorphic form of FFA was to be chosen for use during solid-state experiments involving the material. Form I is generally the commercially available form, and metastable at room temperature (Appendix Figure 7.25). Form IV was also considered, as this was the polymorph observed to be formed during the synthetic

production of FFA, as described in Section 3.2.4.4. However, it was decided that Form III was the best choice, as it is the most thermodynamically stable form at room temperature, with all other polymorphs transforming to become it over time. Should any other form be chosen as the focus of the project, the material would need to periodically be analysed by PXRD to ensure this transformation had not occurred. Additionally, it was observed early in the project that samples of Form I and Form IV FFA transformed into Form III after recrystallisation from most solvents (Figure 2.38). Products from the four primary crystallisation methods developed in Section 2.6.1 were tested by PXRD to ensure that Form III FFA was being produced *via* each process; confirmation that this was the case can be found in Appendix Figure 7.26.

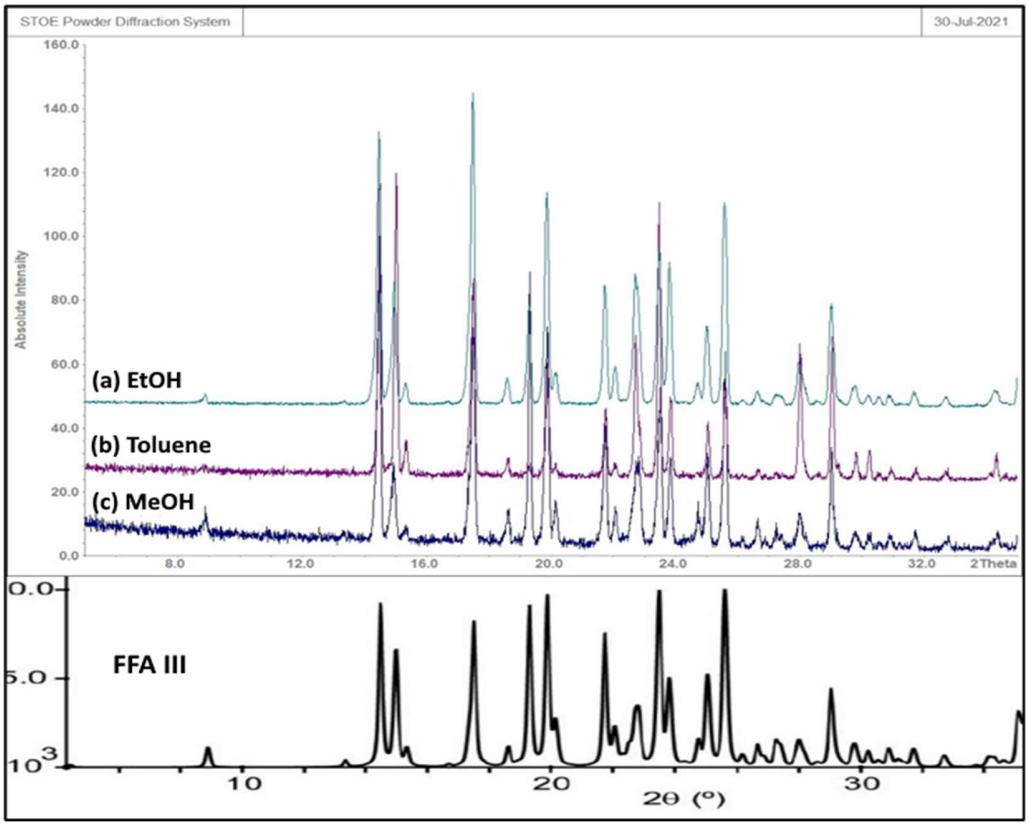


Fig 2.38. Measured PXRD pattern of other polymorphs of FFA recrystallised from (a) EtOH, (b) toluene, and (c) MeOH (top) *vs*. literature pattern for Form III FFA (bottom).[65]

López-Mejías *et al*. also report a number of solvent-based methods of forming other polymorphs of FFA, two of which are described in Section 2.8.6.[65] Form III material was subjected to these recrystallisation processes to determine the ease by which polymorphic transformation could occur. Crystallisation of the material by slow evaporation from EtOH, reported to produce Form I FFA, instead produced unchanged Form III (Appendix Figure 7.27). Likewise, evaporation of solvent from solutions in methanol and chloroform, reported to produce Form IV, also left the original form unaltered (Appendix Figure 7.28). The negative results of these transformation experiments are in fact a positive outcome in the case of this research; the difficulty in purposefully transforming Form III FFA to other polymorphs suggests that unintentional transformation during crystallisation and other processes is unlikely.

2.6.2.2 DSC Analysis of Form III FFA

As discussed in Section 1.5.1.4, Form III is only the thermodynamically stable form of FFA at lower temperatures. At a temperature of 42 °C, the previously metastable Form I becomes the stable form, and remains stable until the melting point of the material.[71] The change from Form III to Form I does not occur immediately once the threshold temperature is passed, instead requiring equilibration at a temperature of 115 °C for the transformation to occur.[178] This hysteresis effect is hypothesised to be the result of the high energy barrier required to transition from Form III to Form I, even at a temperature at which Form I is thermodynamically stable.

The relationship between Form III and Form I FFA is particularly relevant when performing DSC analysis. The transformation between the two forms was observed early

in the project, manifesting on a DSC curve of a sample of pure Form III material as in Figure 2.39. An initial melting endotherm is observed at 126 – 127 °C, corresponding with the literature melting point range of Form III FFA (125 – 127 °C), followed by a sharp exothermic peak at approx. 128 °C, and a second endotherm at 134 – 135 °C, closely matching the reported melting point of Form I (133 - 134 °C).[65] Based on this behaviour, it appears the material remains in the Form III phase from room temperature until the Form III melting point. After the material melts, it immediately resolidifies into Form I, the thermodynamically stable polymorph at that temperature and also one with a higher melting point, resulting in a crystallisation exotherm. The resolidified Form I phase then experiences a second melt at the higher melting point. The two forms are widely reported to be enantiotropically linked,[71,139,141,142] characterised by a reversible polymorphic transformation and an order of stability that changes with temperature.[179] A heat-cool-heat experiment (Appendix Figure 7.30) supported these reports. However, definitive determination of the nature of the system beyond what is observed by DSC analysis is outside the scope of this project.

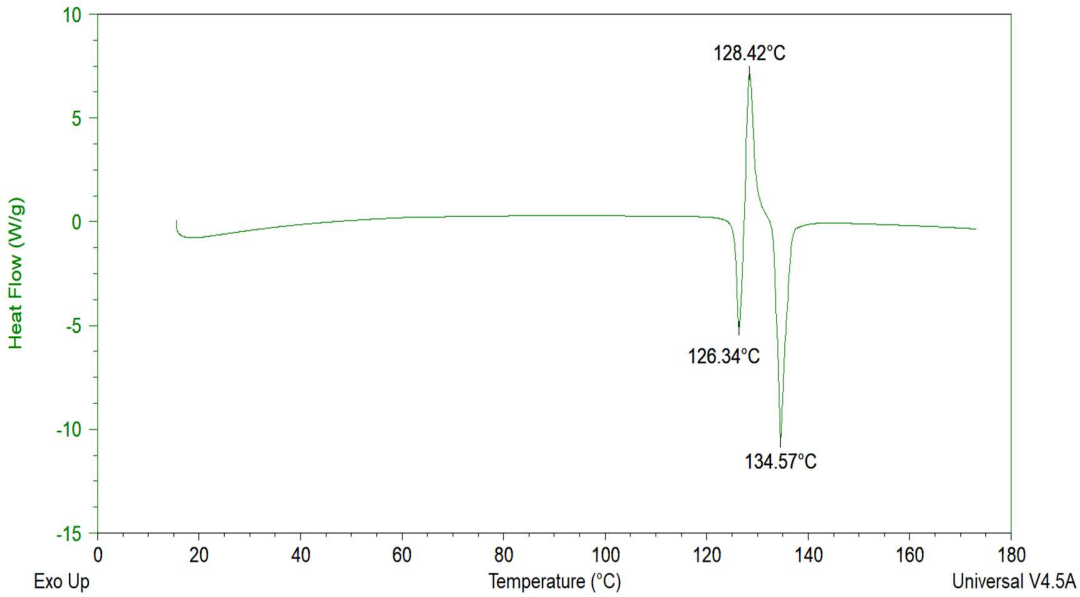


Fig 2.39. DSC curve of Form III FFA heated at a rate of 20 °C min^{-1}, exhibiting the polymorphic transition from Form III to Form I.

2.6.2.3 Controlling the Phase Behaviour of Form III FFA

The phase transformation presented a potential problem in the research when investigating the relationship between FFA and the selected additives, specifically in the construction of phase diagrams for two-component doped systems. The methods of characterising such systems by DSC often has difficulty accounting for such occurrences, as presence of multiple signals for a single analyte can disrupt the measurement of the necessary data, such as onset points and peak maximum values. As such, it was more advantageous to the research to alter the method of DSC analysis in such a way that the melting of FFA would present on a curve as a single endothermic peak. This could either be achieved by suppressing the transformation to the point that only the Form III melt is expressed or promoting it to the point that only the Form I melt is expressed.

Investigation into the Effect of Heating Rate on Phase Behaviour

It has been reported that transformation from a metastable to the stable form can be suppressed through the use of high heating rates.[180] On that basis, the effect of heating rate on the DSC output of Form III FFA was studied. Samples from the same crystal batch were scanned at increasing heating rates, from 2 – 50 °C min^{-1}, as described in Section 2.8.7.3. The results of that test can be found in Figure 2.40. A clear trend was observed throughout the samples; higher heating rates resulted in increased expression of the lower temperature Form III endotherm in comparison to the higher temperature Form I peak. This observation is consistent with a similar study by Lee *et al*.[71] While not subduing it altogether, this could certainly be interpreted as the suppression of the phase transformation as reported. Even at extremely high heating rates of 50 °C min^{-1}, the transformation was not sufficiently suppressed to allow for the sole expression of the Form III endotherm. However, it was observed that reduction of the heating rate had the inverse effect, appearing to promote the transition and the expression of the Form I endotherm relative to the Form III peak. In the sample scanned at 2 °C min^{-1}, for example, the Form III endotherm vanished into the baseline entirely, and the Form I peak was solely expressed.

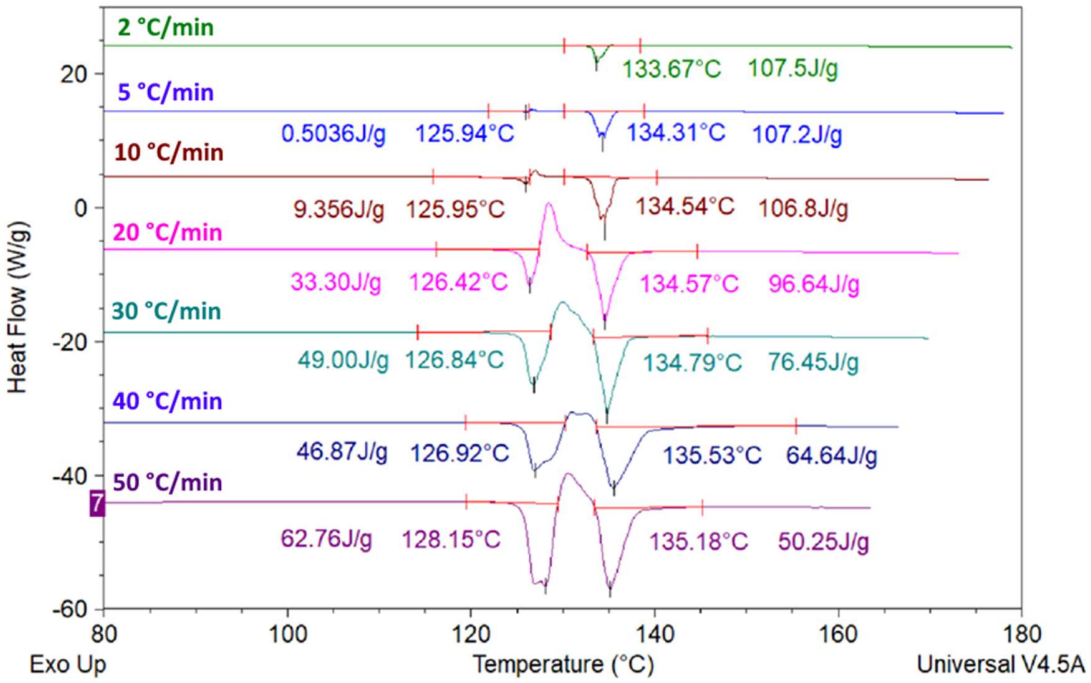


Fig 2.40. DSC curves of Form III FFA run at increasing heating rates; from top to bottom: 2, 5, 10, 20, 30, 40, and 50 °C min^{-1}.

Other trends were observed as a result of increasing the heating rates. Firstly, the intensity of the peaks appears to increase with rate, the endotherms of the higher heating rate curves being substantially larger than on the equivalent lower-rate curves, despite the sample masses being comparable. However, this increase seems to merely be visual, and the measured peak areas (calculated in J/g) remain comparable at all heating rates.

Additionally, increasing the heating rate appears to also increase the peak maximum values of the endotherm peaks. This change is gradual but significant when the curves at each extreme rate are compared. This increase was also present in the Lee *et al* research.[71]

Investigation into the Effect of Sample Grinding on Phase Behaviour

The process of sample preparation for DSC analysis includes the breaking down of larger crystal particles by grinding them in a pestle and mortar. However, grinding has been reported to induce polymorphic transformation in some materials.[181,182] As such, the effect of sample grinding was also investigated. Samples were prepared by grinding in a pestle and mortar to three extents: minimal, light, and extensive, and tested by DSC in a manner described in Section 2.8.7.4. The curves produced by the three samples can be found in Figure 2.41. Grinding of sample was observed to promote the polymorphic transformation of the material, reducing the expression of the Form III endotherm relative to that of Form I.

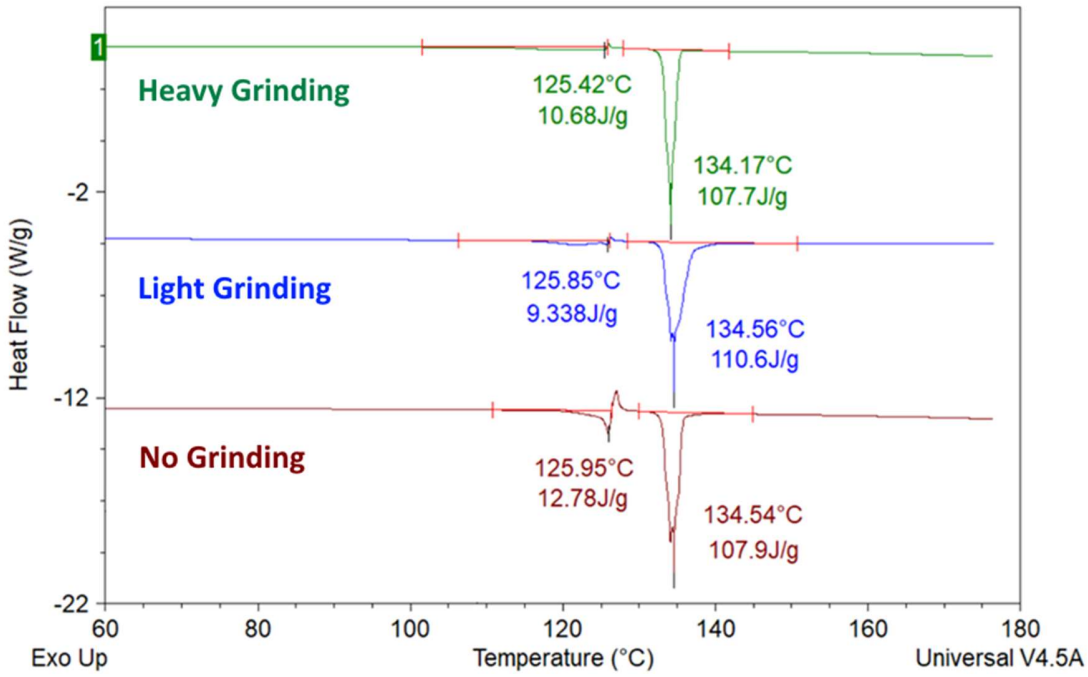


Fig 2.41. DSC curves of samples of Form III FFA with three different degrees of grinding, heated at a rate of 10 °C min^{-1}; from top to bottom: heavily ground, lightly ground, and unground.

Evaluation of Methods of Controlling Phase Behaviour

By varying the heating rate and grinding level of a DSC sample, the phase transformation of FFA can be controlled to a certain extent. As will be discussed in Section 4.6, the inclusion of the selected additives into the sample also has a pronounced effect on this transformation, even at very low doping levels. Each of these factors can be manipulated to either promote or inhibit the transformation of Form III FFA into Form I. As such, DSC curves of doped FFA can be produced in which the melting endotherm of only a single form is expressed. The decision as to whether to promote or suppress the transformation is dependent on the influence of the additive. In this manner, the collected DSC data can be used in the construction of phase diagrams to better understand the relationship between additive and host.

2.6.2.4 TGA Analysis of FFA

TGA analysis was also carried out on Form III FFA. As can be seen in Figure 2.42, FFA decomposes fully in a single step, with an extrapolated onset point of 219.7 °C and an end point of 262.8 °C. The TGA data for the five additives is discussed in Section 3.3.1. This pure component data can be used as a reference against which to compare data collected from doped systems, which can confirm or eliminate potential options when identifying the type or types of additive inclusion present.

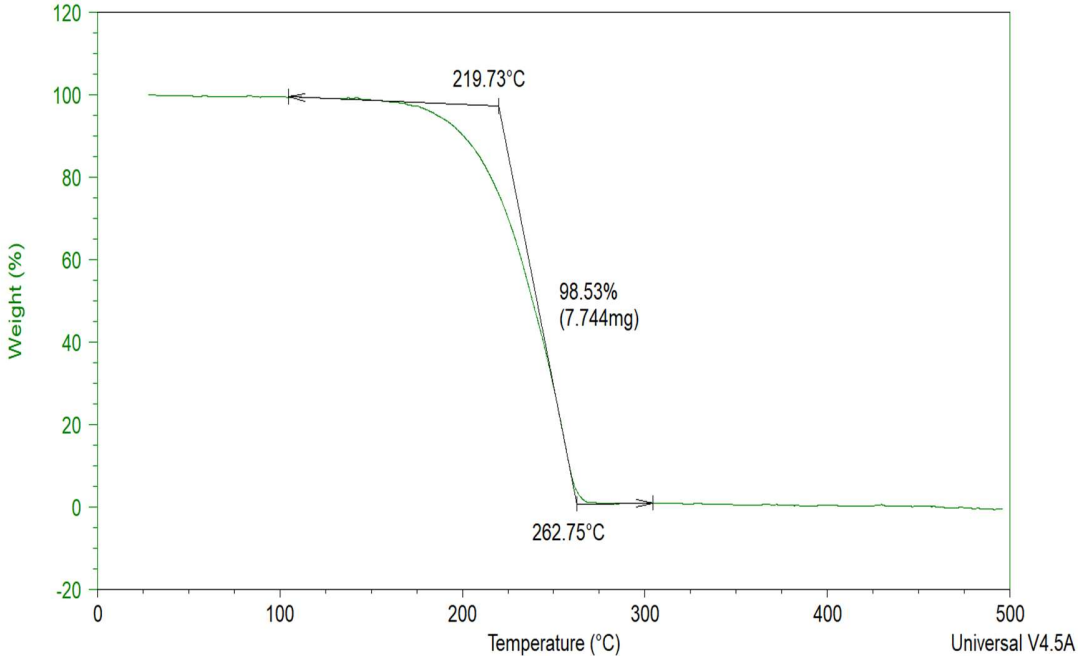


Fig 2.42. TGA curve showing the decomposition of Form III FFA.

2.7 Conclusion

This chapter describes the selection and characterisation of several materials of interest for this research, as well as the development of the analytical methods necessary to study them. The selection process of five structurally-similar analogues of flufenamic acid **14** (FFA) is described: those analogues being 2-(*m*-tolylamino)benzoic acid **15** (Me-FA), *N*-(3-chlorophenyl)anthranilic acid **16** (Cl-FA), 2-[3-(difluoromethyl)anilino]benzoic acid **17** (DF-FA), 2-[3-(fluoromethyl)anilino]benzoic acid **18** (MF-FA), and 2-((3-(*tert*-butyl)phenyl)amino)benzoic acid **19** (t-Bu-FA). These analogues are intended to act as additives resistant to purification by traditional means

when crystallised along with FFA **14**, mirroring the behaviour of the purification-resistant impurities discussed in Section 1.1.2.

The development of robust HPLC method is outlined, resulting in a reliable method that produces traces with low analyte retention times as well as good separation between the analyte peaks of all relevant materials. The criteria for high-quality calibration curves are discussed in terms of regression curves and analysis, and such curves for FFA and each of the five additives are presented. The solubility values of FFA were determined over a wide range of solvent systems and temperatures. Solubilities of two of the additives in relevant solvents are also presented. The relative pure-component solubility values were determined and used to predict the incorporation behaviour of the aforementioned additives in crystals of FFA. Various potential techniques of crystal material production were investigated, and four reliable methods are described. Each method was developed to produce crystal material with an individual habit and/or size, tailored for different aspects of research. FFA was examined by PXRD, DSC, and TGA analysis. A study into the polymorphism of FFA was carried out, focused on the thermodynamically stable Form III polymorph. Finally, the transformation between two polymorphic forms of FFA was investigated by DSC analysis, and methods of influencing said transformation were explored.

2.8 Experimental

2.8.1 HPLC

2.8.1.1 Instrument Specifications

HPLC data was obtained from an Agilent 1290 Infinity II LC System fitted with a diode array detector (DAD) and interfaced to a Dell OptiPlex 5040. Instrument control and data processing was performed using Agilent OpenLab ChemStation software. The method was developed on a reversed-phase HPLC C18 column (Agilent XDB-C18, 4.6 x 150 mm, 5 μm,). This was later exchanged for a reversed-phase UHPLC C18 column (Zorbax Eclipse Plus, 2.1 x 50 mm, 1.8 μm particle size).

2.8.1.2 Method Details

The initial method was modified from Cerretani *et al.*[168] It required a mobile phase consisting of a 77:23 v/v mixture of MeOH and water, pumped at a flow-rate of 0.8 mL min^{-1}. The injection volume was 20 μL and the detector was set at 280 nm. In the absence of a reference for temperature, the column was maintained at 20 °C.

After development, the method using the XDB-C18 HPLC column was as follows: a mobile phase consisting of 50:50 ratio of acetonitrile and a 0.1% v/v aqueous solution of trifluoroacetic acid, with a flow rate of 0.8 mL min^{-1} and a column temperature of 20 °C. Injection volume was 5 μL, and the detector was set at 280 nm. After upgrading to the Zorbax Eclipse Plus UHPLC column, the flow rate was changed to 0.5 mL min^{-1}, the injection volume lowered to 2 μL, and the column temperature raised to 30 °C. Other parameters such as mobile phase composition and detector wavelength were kept constant.

2.8.2 Calibration Curves

2.8.2.1 Standard Solution Preparation

Four to seven standard solutions were prepared for each calibration curve, based on availability of and familiarity with each material. Standard solutions were produced by weighing an appropriate mass of the material of interest to four decimal places using a using a Mettler Toledo MT5 microbalance. The material was dissolved in 100 mL MeCN in a volumetric flask with proper mixing, so that the concentrations of each standard fell between 0.25 and 2.20 mg mL^{-1}. Three aliquots were removed from each standard for analysis by HPLC.

2.8.2.2 Standard Solution Analysis

Each aliquot was scanned in triplicate by HPLC using the method parameters and equipment in use at the time. The area measurements of all the analyte peaks measured for each standard solution were averaged to determine the most representative value for the instrument response at that concentration. These values were plotted on a scatter chart to form the basis of the calibration curve. The response data (dependent variable) is plotted on the y-axis while the known concentration (independent variable) is plotted on the x-axis; this is because regression analysis focuses more on y-axis error values. Response factors (RFs) for each material were also calculated at this point, by dividing the area of the analyte peak by the sample concentration. These values remained comparable independent of concentration, so an accurate RF value for each analyte can be considered as an average of the calculated RFs across all data points from a series of standards.

2.8.3 Solubility Tests

2.8.3.1 Sample Preparation

The saturation points of each material of interest were determined by the excess solid method of solubility measurement. An appropriate volume of solvent was added to a round bottom flask containing the material, so that portions of the solution could be removed with ease for analysis, but solid material was still present in suspension after equilibration. The sample flask was immersed in an oil bath or DrySyn® heating block on an IKA RCT Basic® hot plate, which was controlled at the desired temperature using the included probe. The suspended solid was agitated in the solvent using a stirrer bar for 1 – 3 hours to ensure complete equilibration and saturation of the solution. After equilibration, 1 mL of saturated solution was removed from the flask through a 0.20 μm membrane syringe filter (Agilent 13 mm, PTFE Econofltr®) to ensure the exclusion of undissolved particulates. The aliquot of saturated solution was added to a vial with washings, and the process was repeated a number of times for a total of three or four samples per experiment, allowing for at least 15 minutes between aliquot collections for re-equilibration.

2.8.3.2 Solubility Analysis

The solvent in each sample was allowed to dry fully by evaporation. The vials were then dried further under high vacuum for at least 2 hours to ensure complete removal of the test solvent. The samples were then quantified in one of two ways. Early in the project, the solid material was redissolved in 100 mL of MeCN, a small portion of which was tested by HPLC in triplicate. The average area of the resultant peaks was used in conjunction with a previously constructed calibration curve to ascertain the concentration of the HPLC sample. The concentration of the original saturated solution could then be calculated by accounting for the MeCN dilution. Later the process was simplified by simply measuring the mass of the dry samples using a using a

Mettler Toledo MT5 microbalance and attributing that value to the concentration of 1 mL of the saturated solution (the volume removed from solution in Section 2.8.3.2).

2.8.4 Crystallisation

2.8.4.1 Preliminary Slow Evaporation Studies

Solvent Studies

For the initial slow evaporation crystallisation studies, 100 mg of pure Form III FFA were dissolved in a sufficient volume of each solvent (acetone, chloroform, DCM, EtOAc, EtOH, IPA, MeCN, MeOH, THF, and toluene) to produce a subsaturated solution of the material. Each solution was added to a clean dry vial through a syringe filter to exclude any dust or other particulates that might interfere with the nucleation or crystallisation process. The solutions were allowed to evaporate to dryness undisturbed in a fume cupboard.

Evaporation Rate Studies

To determine the effect of evaporation rate on crystal growth, solutions of FFA were made in each of the chosen solvents (toluene, EtOH, and MeCN) to a concentration of 117 mM. Each solution was divided into 0.25 mL portions across 10 clean dry vials through a syringe filter. Three of those vials were left uncovered, as per the previous experiment, three were covered by a lid that had been perforated with 4 – 6 holes using a needle, and the final four were covered by a lid pierced by a needle which remained in the lid. The solutions were allowed to evaporate to dryness undisturbed in a fume cupboard.

Solution Concentration Studies

To determine the effect of solution concentration on crystal growth, 0.25 mL solutions of FFA in toluene were produced with increasing concentrations: 100 mM, 150 mM, 175 mM, and 200 mM, and added to four clean dry vials through a syringe filter. The vials were covered by a lid that had been perforated with 4 – 6 holes using a needle and allowed to evaporate to dryness undisturbed in a fume cupboard.

2.8.4.2 Liquid-Liquid diffusion

Four solutions of FFA were produced for the liquid-liquid diffusion tests. One was 1 mL in volume, a subsaturated solution of the material in EtOAc, and the other three were 0.5 mL: a near-saturated solution in chloroform, a subsaturated solution in chloroform, and a subsaturated solution in toluene. These solutions were added to clean, dry, narrow vials through a syringe filter. An appropriate volume of hexane was layered atop the solutions so that the ratio of hexane to solution was 4:1. The layering was performed carefully using a Pasteur pipette, to ensure the interface between the solution and the precipitant was preserved. The vials were covered tightly with a lid and left undisturbed in a fume cupboard for up to a week, at which point the two liquids in each vial had fully mixed. For the vials in which crystals had grown, the excess solvent was carefully removed using a Pasteur pipette, and the crystals rinsed with cold hexane and dried in a Hirsch funnel over vacuum.

2.8.4.3 Crystal Production Procedures

Slow Cooling of MeCN Solution

In a large, uncovered vial, the desired amount of material was mixed in a suspension with a volume of MeCN so that the ratio of the two was 1.5 times the saturation point at room

temperature, as determined by the solubility tests described in Section 2.5. The suspension was heated in an oil bath to 80 °C until all material was fully dissolved. The heat was switched off, and the solution was allowed to cool slowly in the oil until it reached room temperature; a process that took 2 – 3 hours. The excess solution was removed using a Pasteur pipette, and the crystals rinsed with cold hexane. After the removal of the solution and the hexane rinse, the crystals were fully dried *via* a high-vacuum line.

Slow Evaporation of MeOH Solution

The desired amount of material was dissolved in an appropriate volume of MeOH so that the solution would be subsaturated. The solution was filtered through a syringe filter to remove any undissolved particulates and added to a large vial or flask. The vial or flask was covered with a perforated lid and allowed to rest undisturbed in a fume cupboard for about 1 week or until crystals were observed to form. The crystals were not allowed to evaporate to dryness; instead, the excess solution was carefully removed using a Pasteur pipette, and the crystals rinsed with cold hexane and dried in a Hirsch funnel over vacuum.

Vapour Diffusion of Hexane into MeOH Solution

The desired amount of material was dissolved in an appropriate volume of MeOH so that the solution would be subsaturated. The solution was filtered through a syringe filter and added to a large vial. The vial was placed in a beaker containing a volume of hexane twice that of the MeOH solution. An airtight seal was created over the mouth of the beaker with foil and parafilm, and the beaker allowed to rest undisturbed in a fume cupboard for about 1 week or until crystals were observed to form. The crystals were removed from the solution, rinsed with cold hexane, and dried in a Hirsch funnel over vacuum.

Rotovap Crystallisation from DCM / Hexane Solution

In a round-bottom flask, the desired amount of material was dissolved in an appropriate volume of DCM so that the solution would be subsaturated. An excess of hexane was added, and the solution fully mixed. The DCM is fully evaporated *via* rotovap at room temperature until only hexane remains, at which point the material precipitates out as a slurry. The crystals can then be isolated by suction filtration, rinsed with cold hexane and dried over vacuum.

2.8.5 PXRD

PXRD was performed at ambient temperature using a STOE STADI-MP diffractometer operating in transmission mode with a linear PSD detector with an anode current of 40 mA, an accelerating voltage of 40 kV and Cu $K\alpha_1$ radiation (λ = 1.5406 A) scanning in steps of 1.0 ° for 30 seconds per step from 5 to 35 ° in 2θ. Samples were held between acetate foils.

2.8.6 Polymorphic Transformation Studies

Methods for the polymorphic transformation of FFA were sourced from work by López-Mejías *et al*.[65]

2.8.6.1 Production of Form I FFA

Form I FFA is reported to be produced "by slow evaporation of an ethanol solution." To this end 10 mg of Form III FFA was dissolved in 1 mL of EtOH. The solution was added to a clean dry vial through a syringe filter to exclude any dust or other particulates that might interfere

with the nucleation or crystallisation process. The solution was allowed to evaporate to dryness undisturbed in a fume cupboard, producing crystalline FFA III.

2.8.6.2 Production of Form IV FFA

Form IV FFA is reported to be produced "by dissolving 5.8 mg of FFA in 0.3 mL of methanol or 0.5 mL chloroform followed by slow evaporation of the solvent." A sample of Form III FFA was dissolved in each solvent matching the reported specifications. The solution was added to a clean dry vial through a syringe filter and allowed to evaporate to dryness undisturbed in a fume cupboard, producing crystalline FFA III.

2.8.7 DSC

2.8.7.1 Instrument Specifications

DSC analysis was carried out on a TA Q1000 Calorimeter with an RCS 40 cooling system. Ramping was carried out from approx. 15 °C to 180 °C in aluminium pans at a heating rate appropriate to the experiment. Mass of samples fell between 2 – 5 mg.

2.8.7.2 Initial Experiments and Heat-Cool-Heat

Initial experiments were carried out at a heating rate of 10 °C min^{-1}. Heat-cool-heat scans were carried out at a heating rate of 10 °C min^{-1}, followed by a cooling rate of 5 °C min^{-1}, and finally a reheating rate of 10 °C min^{-1}. Samples were lightly ground in a pestle and mortar.

2.8.7.3 Heating Rate Study

The heating rate study consisted of seven samples of Form III FFA from the same crystal batch being heated at increasing heating rates: 2, 5, 10, 20, 30, 40, and 50 °C min^{-1}. Samples were lightly ground in a pestle and mortar.

2.8.7.4 Effect of Sample Grinding Study

For the particle size study, three samples of Form III FFA were selected from the same batch produced by rotovap crystallisation. One sample received no grinding, one was lightly ground to a coarse powder, and the final sample was heavily ground to a fine powder. All samples were heated at a rate of 10 °C min^{-1}.

2.8.8 TGA

Analysis was performed using a TA Instruments Q500 Thermogravimetric Analyzer. Pure samples of each material were crystallised by rotovap as described in Section 2.8.4.3. The crystals were heated by TGA from room temperature (15 – 20 °C) to 500 °C at a rate of 10 °C min^{-1} under isobaric conditions. The samples were heated in platinum pans.

Synthesis and Characterisation

3.1 Introduction

This chapter is primarily focused on the development of a reliable and sufficiently high-yielding synthetic method for the production of flufenamic acid **14** (FFA) and related compounds. FFA is available for purchase and relatively inexpensive, and, as such, the majority of the FFA material used in this project is acquired through commercial means. However, the five analogues of FFA described in Section 2.2.2 (compounds **15** – **19**) are unavailable to purchase through commercial channels on the scale required for this research. As a well-studied API, a large amount of literature is available pertaining to the synthesis of FFA and other pharmaceutically relevant anthranilic acid derivatives. It was thought that if FFA could be produced *via* one of the reported methods with reasonably high yields, the same synthetic route could be adapted to use different starting materials, producing the desired analogues.

This chapter describes several synthetic routes towards FFA, the development and refinement of a reliable synthetic method, the production of FFA and related analogues, and the characterisation of the synthesised material by a number of analytical techniques including HPLC, NMR, infrared (IR) spectroscopy, and mass spectrometry (MS). MS data is recorded by nominal MS (less sensitivity than HRMS but ESI+ and ESI- compatible) and high-resolution MS (HRMS). HRMS is only ESI+ compatible, but measures ionisation mass to a high degree of sensitivity and presents results to 6 decimal places. Waters i-Fit is an algorithmically-determined value of the reliability of the candidate formula calculated by the consistency between the mass shift and the isotope intensity value. This is also highly sensitive and calculated to 6 decimal places.[183] The

synthesis of each of the five analogues *via* the developed method is then described, along with full characterisation of the purified products. Finally, the identification, characterisation, and targeted synthesis of a synthetic impurity encountered during the production of FFA will be discussed.

3.2 Synthetic Routes in the Production of Flufenamic Acid

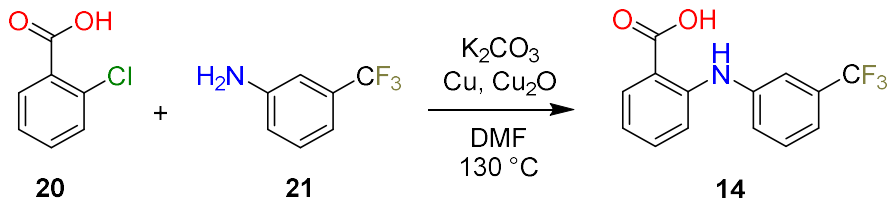
The formation of anthranilic acid derivatives like FFA is generally achieved by the coupling between an aryl halide and aryl amine. This coupling primarily proceeds *via* one of two transition metal-catalysed routes: the copper-catalysed Ullmann-Goldberg condensation reaction, or the palladium-catalysed Buchwald–Hartwig amination reaction. Two variations of each route were explored in the synthetic development stage of the project.

3.2.1 Ullmann-Goldberg Condensation

Fritz Ullmann pioneered chemistry involving the copper-mediated coupling of aryl compounds in the early 20th century, collaborating with Irma Goldberg to develop synthetic methods for the formation of biaryls, as well as aryl ethers, aryl thioethers, aryl nitriles, and aryl amines.[184–186] Despite being developed over a century ago, these synthetic routes have garnered significant interest in the last few decades as a safer and more cost-effective alternative to the palladium-mediated Buchwald-Hartwig routes.

Early procedures for the reaction required high temperatures and stoichiometric amounts of copper to achieve the desired product, but modern research has allowed for catalytic levels of the metal and milder conditions through a modified version of the original reaction.

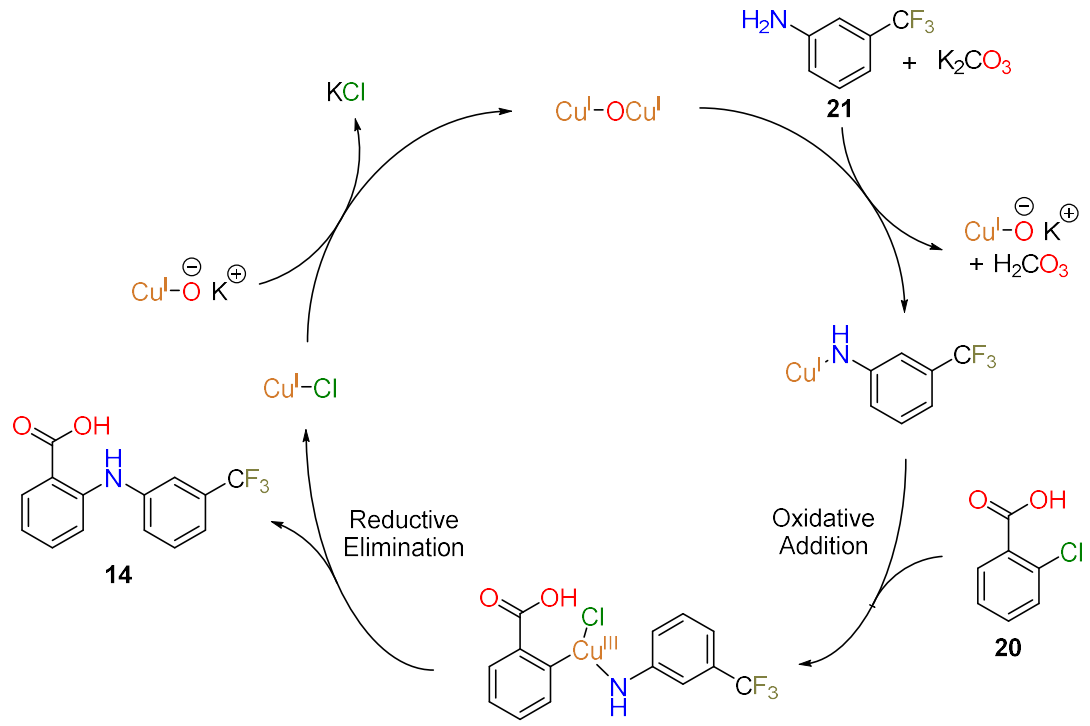
Two versions of the standard reaction were explored as part of the synthetic development of FFA and related compounds. The first, described by Mei *et al*., involves the coupling of 2-chlorobenzoic acid **20** (2-CBA) with a substituted aniline (in this case 3-trifluoromethyl aniline **21**), catalysed by metallic copper and copper(I) oxide under basic conditions.[126] The cited method states the reaction ideally takes place in diethylene glycol or 2-ethoxyethanol; these were exchanged for *N*,*N*-dimethylformamide (DMF) due to the limited availabilities of the former solvents. DMF has also been demonstrated to be an effective solvent in Ullmann-Goldberg condensations.[127] The Scheme for the initial reaction is displayed below in Scheme 3.1.



Scheme 3.1. Metallic copper / copper(I) oxide-catalysed Ullmann-Goldberg condensation towards the synthesis of FFA **14**, modified from Mei *et al*.[126]

The mechanism by which the Ullmann-Goldberg condensation and related syntheses operate is a point of contention amongst researchers. Unlike with the similar Buchwald-Hartwig coupling, there is no definitive agreed-upon route by which the

reaction proceeds.[187–190] The most popularly-adopted mechanistic route involves the oxidative addition of the aryl halide to copper(I), forming a copper(III) intermediate.[191,192] The intermediate then undergoes reductive elimination, releasing the reaction product and regenerating the copper(I) catalyst, as per Scheme 3.2.



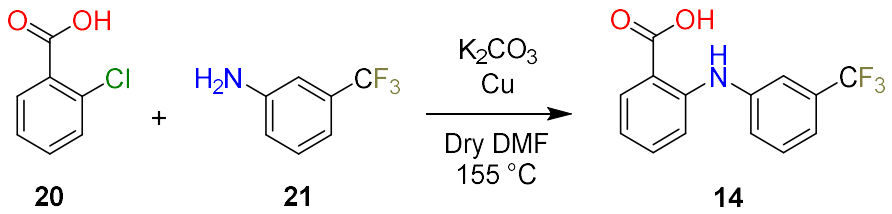
Scheme 3.2. Popularly-adopted mechanistic route by which the Ullmann-Goldberg condensation reaction proceeds, adapted to include the reagents and products from the reaction described in Scheme 3.1.

In the current work, the reaction was initially performed as described in Section 3.6.2.1. The reaction mixture began as a bright copper colour, which darkened with heating. After approx. 15 mins, the mixture was observed to turn a bright green colour. That green in turn darkened over the following two hours to a dark brown and remained that colour for the duration of the reaction. After work-up, the product was isolated as a

yellow powder. The yield of the initial reaction was poor, reaching only 13.7%. Despite the reaction being reported to be tolerant of the presence of water,[127] replacing DMF with anhydrous DMF significantly increased the yield to 29.3%. Further oxygen and water-exclusion techniques, such as flame-drying glassware prior to use, degassing the solvent, and flushing the flask with N_2, improved yields further, to a maximum of 34.7%. The crude products of these reactions were determined to generally be between 85 – 95% pure by HPLC analysis.

Even with the improvements, the yields achieved *via* the modified Mei *et al*. method were too low to be viable for use in the preparation of the chosen additives. It is possible that the use of DMF as a solvent, as opposed to those described in the literature, was interacting unfavourably with the copper(I) oxide catalyst under the employed conditions and inhibiting the reaction. As such, a different procedure was explored that was reported by Pellón *et al.* to be effective while using DMF as a solvent.[127] This procedure, detailed in Section 3.6.2.2 and visualised in Scheme 3.3 below, is very similar to the one proposed by Mei *et al*., making use of the same starting materials and potassium carbonate (K_2CO_3) base. The primary difference is that the copper catalysis of the reaction is performed entirely with metallic copper. Despite the debate around the mechanism by which the Ullmann-Goldberg condensation proceeds, all proposed routes concur that the catalytic copper species operate in the +1 oxidation state, such as copper(I) oxide in the Mei *et al*. synthesis. However, it has been observed in the literature that copper species of almost any oxidation state can be effective catalysts for the reaction.[193] It is likely that copper catalysts of an oxidation state other than +1 are oxidised or reduced to the catalytically active Cu(I) species *in situ*.[194,195] Use of this synthetic procedure resulted in

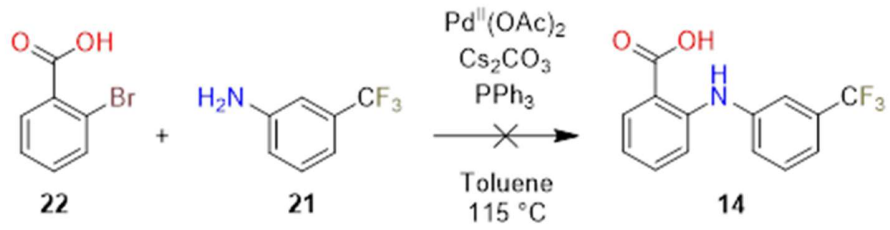
a marked improvement in yield compared to the original method, with a measured yield of 76.9% and a crude purity of 98%. In addition, with a substantially reduced reaction time and simplified work-up, the Pellón *et al*. method was a significant improvement over the modified Mei *et al*. procedure.



Scheme 3.3. Metallic copper-catalysed Ullmann-Goldberg condensation towards the synthesis of FFA, modified from Pellón *et al*.[127]

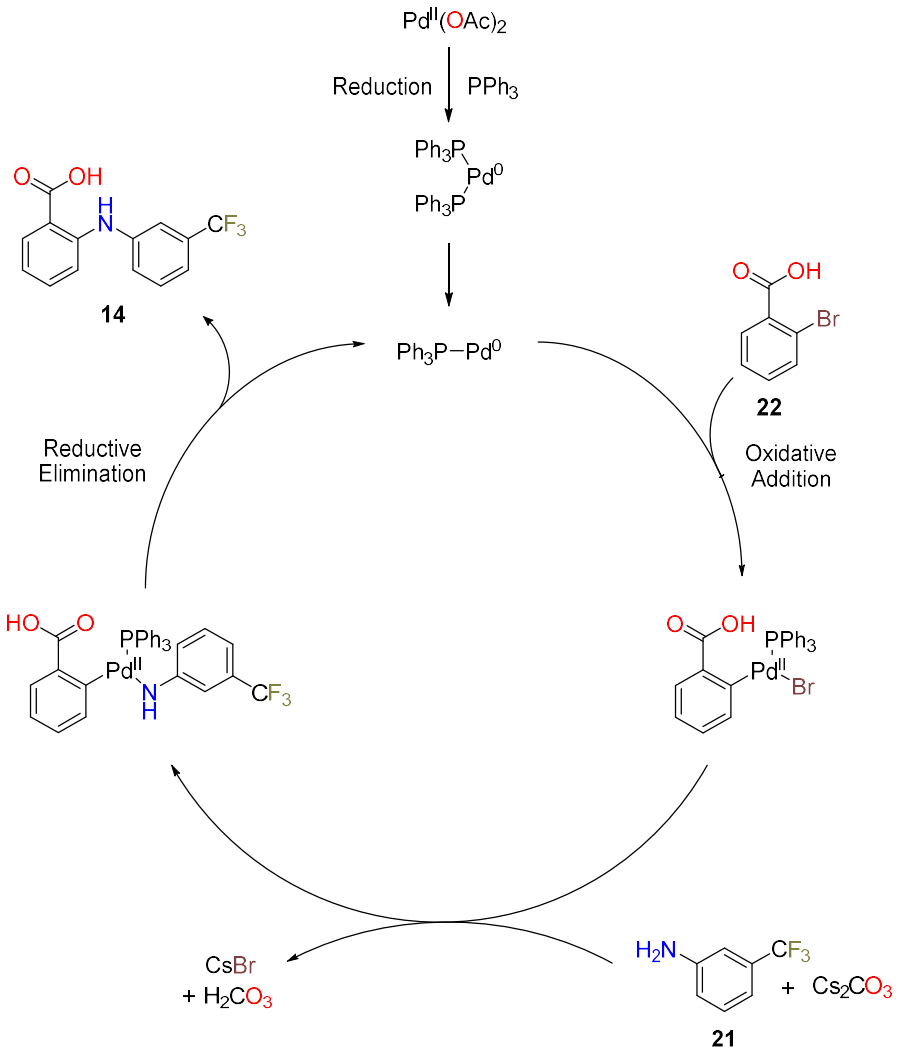
3.2.2 Buchwald-Hartwig Amination

Pd-catalysed couplings of the two reactants were also explored. The first of the two procedures attempted was described by Schuster *et al*.[128] The method describes the coupling between a substituted aryl bromide (in this case, 2-bromobenzoic acid **22**) and substituted aniline in the presence of palladium(II) acetate ($Pd^{II}(OAc)_2$), caesium carbonate (Cs_2CO_3), and racemic 2,2′-bis(diphenylphosphino)-1,1′-binaphthyl (rac-BINAP). rac-BINAP was replaced with the simpler monodentate triphenylphosphine (PPh_3) due to lack of availability of the literature ligand (Scheme 3.4).



Scheme 3.4. Palladium(II) acetate-catalysed Buchwald-Hartwig amination towards the synthesis of FFA using triphenyl phosphine, modified from Schuster *et al*.[128]

Couplings of this nature are classified as Buchwald-Hartwig aminations. Unlike the Ullmann-Goldberg condensations discussed previously, the mechanism by which these aminations proceed are well known.[196,197] The Pd(II) complex undergoes a reductive reaction with PPh_3 to generate the active catalytic Pd(0)-monophosphine species *in situ* (Scheme 3.5). The catalyst complexes with the aryl halide *via* oxidative addition. The complex undergoes nucleophilic substitution with the substituted aniline, followed by reductive elimination to produce the coupled product and regenerate the catalyst. The elimination of one of the phosphine ligands in the preparation of the catalyst is unique to monodentate species.[198] Chelated ligands (such as rac-BINAP) remain as a bisphosphine complex with palladium throughout the reaction. The presence of a 4-coordinate aryl complex is reported to influence the rate of the reductive elimination step but otherwise not affect the mechanism of reaction.

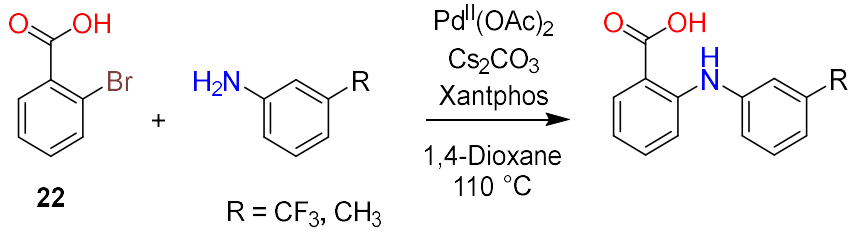


Scheme 3.5. Accepted mechanistic route by which the Buchwald-Hartwig amination reaction proceeds, adapted to include the reagents and products from the reaction described in Scheme 3.4.

Chelated bidentate phosphine compounds such as BINAP have proved to be very effective ligands in Pd(0)-catalysed reactions, in particular for asymmetric synthesis.[199] As such, it was expected that the yields produced by a reaction using first-generation monodentate PPh_3 in their stead would be lower than those reported in the Schuster *et al*.

synthesis. However, no coupling at all was observed to take place over multiple reaction attempts.

A second Buchwald-Hartwig amination procedure was attempted, described by Albaugh *et al.*[129] The procedure was very similar to that of Schuster *et al.*, also employing a $Pd^{II}(OAc)_2$ catalyst and Cs_2CO_3 as a base, but with BINAP ligand replaced with the more available Xantphos, as well as a different solvent (Scheme 3.6). Xantphos is similar to BINAP in that they both act as bidentate diphosphine ligands when coordinated to palladium. It was thought that if the lack of chelation was inhibiting the previous reaction, use of this ligand could result in a more successful coupling.



Scheme 3.6. Palladium(II) acetate-catalysed Buchwald-Hartwig amination towards the synthesis of FFA and Me-FA **15** using xantphos, modified from Albaugh *et al.*[129]

Early attempts at producing FFA with this method proved as unsuccessful as the previous method, with HPLC analysis of the reaction mixture showing no coupling had taken place. However, attempts in which the 3-(trifluoromethyl)aniline **21** was replaced with methyl-substituted *m*-toluidine resulted in a 22.5% yield of Me-FA **15**.

The low yields produced by the Pd-catalysed reactions are potentially due to the species of aryl halide. Buchwald-Hartwig reactions have been proven to be effective for aryl halides substituted with free-acids, but only in the meta and para-positions.[200]

Generally, copper-catalysed Ullmann-style reactions are the routes of choice when the use of ortho-acids are required.[126,201] The yields of the reaction could potentially have been improved through the use of a benzoate analogue of the aryl halide, followed by hydrolysis of the ester product.[202] However, as a method had already been developed which used a cheaper metallic copper catalyst and provided sufficient yields (Scheme 3.3), it was decided to focus on that route for the production of the chosen additives.

3.2.3 Methods of Purification

Purification of the crude FFA produced by the above synthetic routes was initially carried out by column chromatography, as described in Section 3.6.3. Later, this was replaced with a more efficient recrystallisation procedure. Development of this procedure involved the recrystallisation of crude FFA from three solvents, EtOAc, DCM, and toluene. The experimental details for the process can also be found in Section 3.6.3. Recrystallisation from EtOAc resulted in reasonable levels of material recovery (80+%) but an increase in purity of just 0.8% (94.5 - 95.3%). Conversely, recrystallisation from DCM provided an excellent purity of 99.3% from the same crude sample, but only a 40% material recovery. Finally, toluene proved the most suitable recrystallisation solvent, increasing the purity of the crude FFA sample from 93.8 - 99.6% with an 82% recovery. This can most likely be attributed to the high boiling point of the solvent and low room-temperature solubility of the material (see Section 2.8.3) driving the crystallisation of the pure material as the solution cooled.

3.2.4 Characterisation of FFA Products

Characterisation of the purified products of these FFA synthesis reactions was carried out by NMR (^{1}H and ^{13}C), IR, MS, PXRD and HPLC analysis. Full details of all instruments and methods of analysis are described in Section 3.6.1. The results of any analyses not discussed below will be listed in Section 3.6.4.1.

3.2.4.1 IR Analysis

Below in Figure 3.1, assignments of the primary signals visible on the IR spectrum of FFA can be seen. The presence and absence of similar peaks in the IR spectra of additives and other analysed compounds can provide information towards the identity and characterisation of those species.

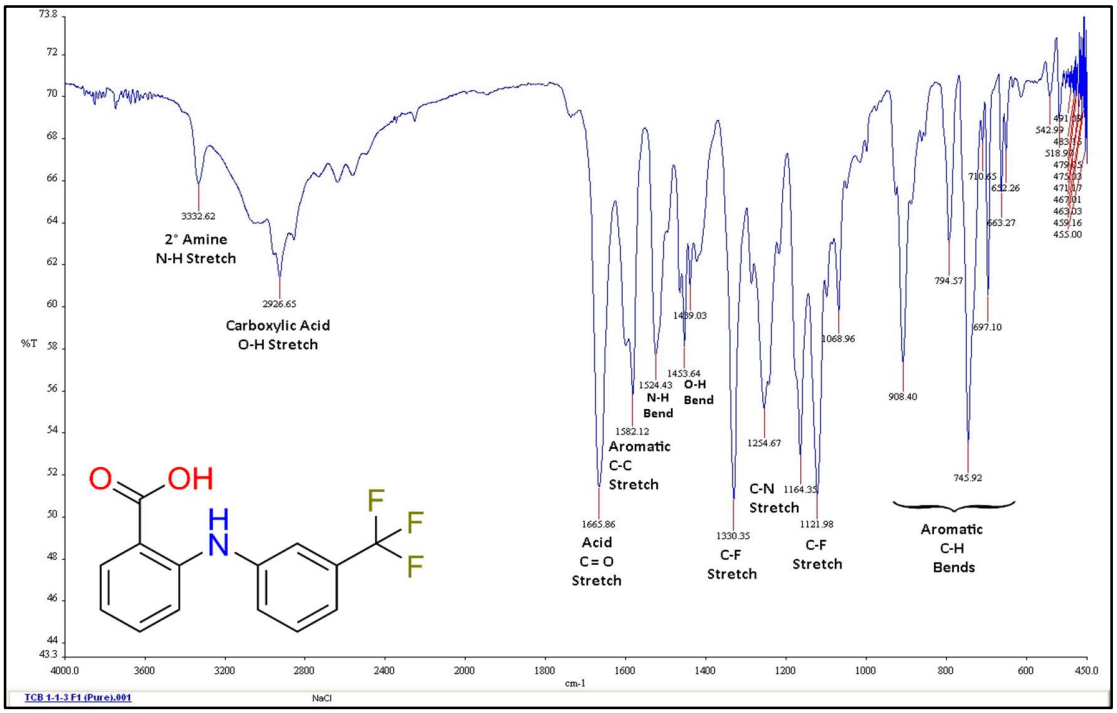


Fig 3.1. IR spectrum of FFA **14**, with labelled peaks.

3.2.4.2 Proton NMR

The ^{1}H NMR spectrum for the material is displayed in Figure 3.2 below. The labelling of atoms is consistent with that described in Section 2.2.3.1. As all relevant, observable signals correspond to protons directly bonded to aryl carbons, Figure 3.2 is focused on the aromatic region of the spectrum. Two non-aromatic protons are present on heteroatoms on the compound, the acid -O*H* and the bridging amine -N*H* (expected to appear at approx. 12.5 ppm and 3.5 ppm respectively),[203] but they are not visible on the spectrum, likely due to exchange with the deuterated solvent.

The most downfield signal is a 1H doublet of doublets of doublets centred at 8.01 ppm corresponding to C^{12}-H. This proton is highly deshielded by the acid group ortho to it, with the least amount of shielding from the meta-amino group. The splitting pattern is a result of coupling to C^{11}-H (^{3}J = 7.8 Hz), C^{10}-H (^{4}J = 1.7 Hz), and C^{9}-H (^{5}J = 0.4 Hz). The signal for the C^{11} proton is located furthest upfield at 6.83 ppm due to its position meta to the deshielding acid and para to the shielding amine. The splitting pattern for this signal is also a doublet of doublets of doublets, coupling to C^{12}-H (^{3}J = 7.8 Hz), C^{10}-H (^{3}J = 7.8 Hz), and C^{9}-H (^{4}J = 1.7 Hz). The similarity between the C^{12}-H and C^{10}-H coupling constants result in some overlap, obscuring the splitting pattern for this signal somewhat.

Between these two outliers, there is a lot of overlap in the signals of the remaining aromatic protons. The signal for C^{10}-H appears in the middle, at 7.39 ppm. This proton exhibits an identical splitting pattern to C^{11}-H but is further downfield due to the weakened deshielding effect of the meta-amine. A roofing effect can be observed between C^{10}-H and the neighbouring C^{9}-H doublet, which is overlapping with the C^{5}-H doublet centred at 7.28 ppm, indicative of the coupling between the two protons. Two of the three

major peaks of the C^4-H triplet of doublets are visible at 7.48 ppm. This proton is coupling primarily with the C^5 and C^3 protons (^3J = 7.8 Hz) but is also experiencing weaker coupling with C^6 (^5J = 0.4 Hz). The third triplet peak is lost in the combined C^3-H and the C^6-H signals, overlapping at approx. 7.45 ppm due to their shared ortho position to the deshielding -CF_3 group, and the similarity of the shielding effect of the amine in the para- and ortho-positions respectively. There is likely some heteronuclear ^4J coupling between the C^3-H and the C^6-H protons and the fluorine atoms of the -CF_3 group, but these are difficult to distinguish within the multiplet.

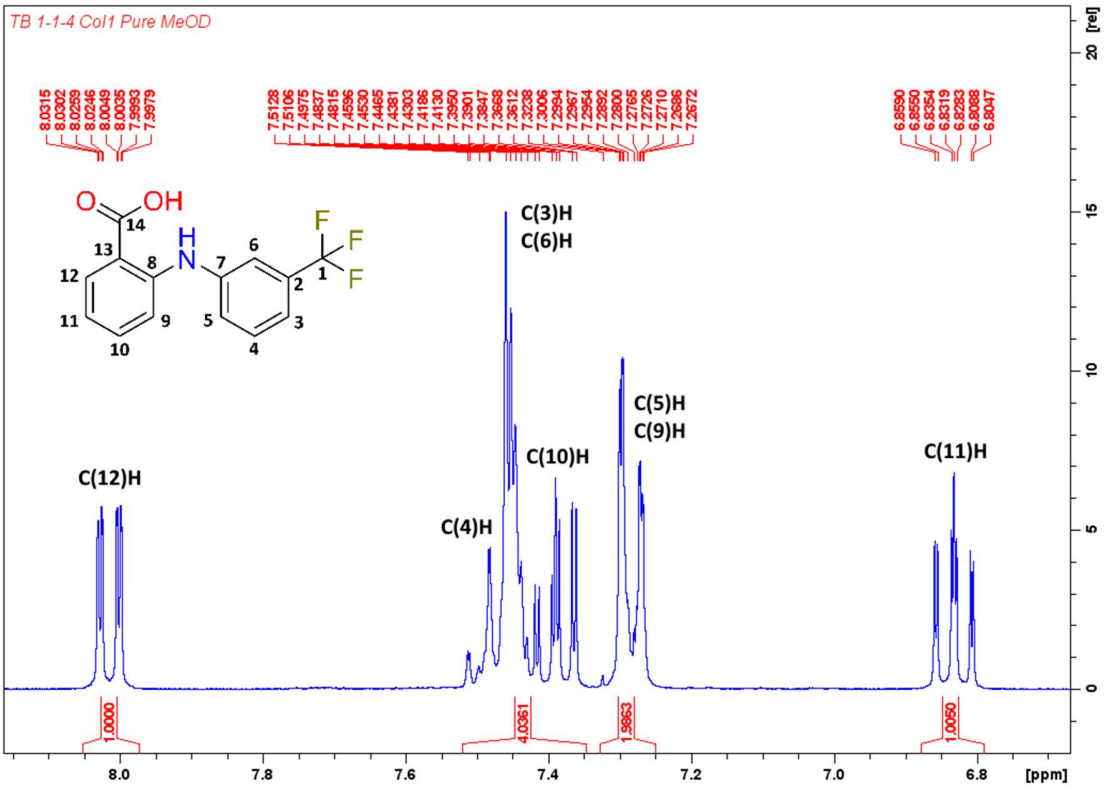


Fig 3.2. Aromatic region of the ^{1}H NMR spectrum of FFA **14**, with labelled peaks.

3.2.4.3 Carbon NMR

The ^{13}C NMR of FFA consists of 8 monoprotonated aromatic carbons, and 6 quaternary carbons, assigned to peaks in Figure 3.3. Full assignments can also be found in Section 3.6.4.1. As carbon atoms can also couple to fluorine on a ^{13}C spectrum, some peak splitting is present on the spectrum. The C-H carbons ortho to the -CF_3 group (C^3 and C^6, 120.00 and 118.04 ppm respectively) appear as quartets, coupling to the three fluorine atoms (^3J = 3.9 Hz). The quaternary carbons C^2 (132.81 ppm) and C^1 (125.51 ppm) also appear as quartets, but their low intensity means that only the two centre peaks of each are visible. The J-values of each quartet increase relative to the proximity of the carbon to the fluorine atoms (^2J = 32.1 Hz and ^1J = 271.5 Hz respectively).

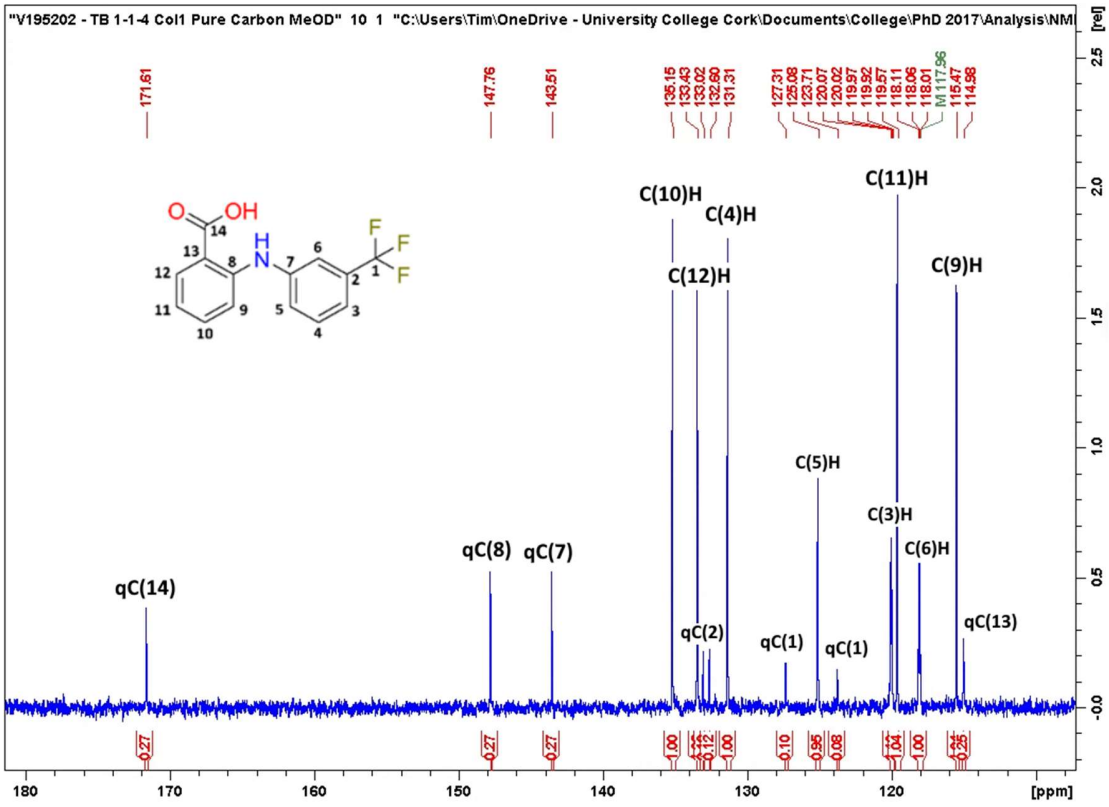


Fig 3.3. Aromatic region of the ^{13}C NMR spectrum of FFA **14**, with labelled peaks.

3.2.4.4 PXRD

When the FFA product of the metallic copper-catalysed reaction was tested by powder X-ray diffraction, it was determined that the material was produced in the polymorphic Form IV (Figure 3.4). This polymorph is distinct from both the commercially available Form I and the thermodynamically stable (up to 42 °C)[138,139] Form III. It is also the only FFA material, pure or impure, produced in the project that was identified as a polymorph other than those two forms.

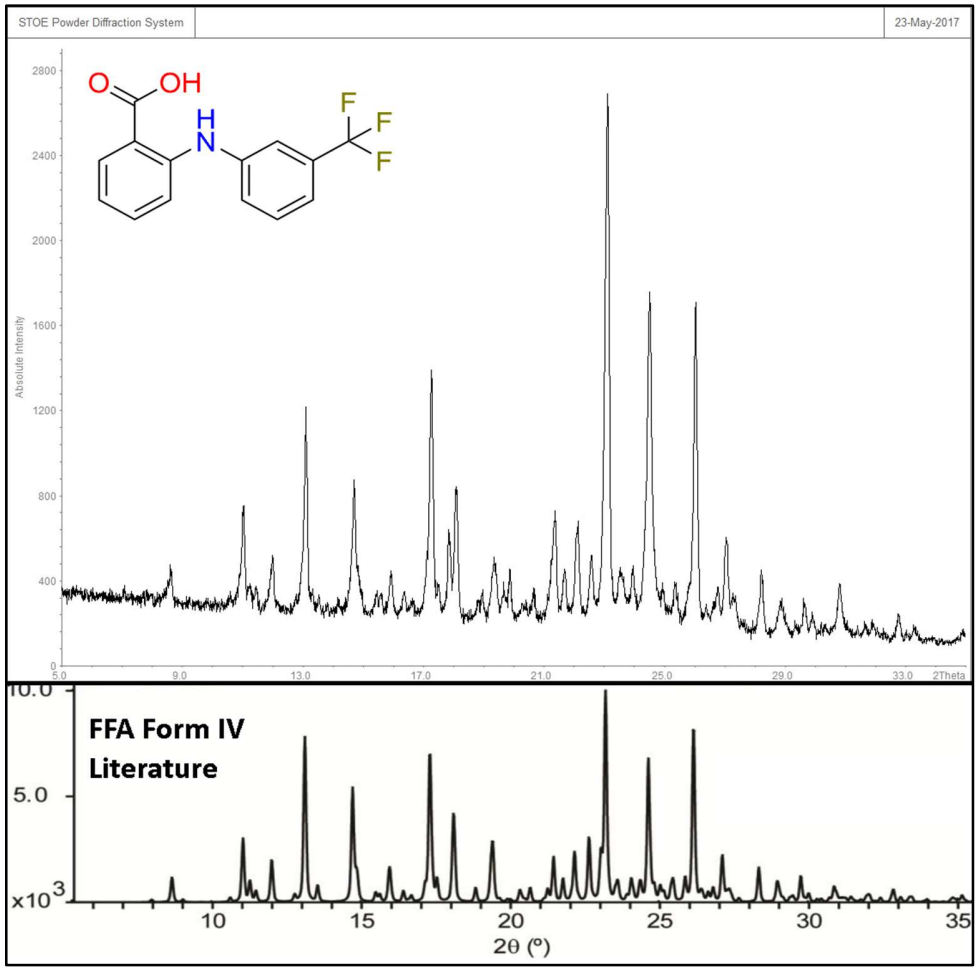
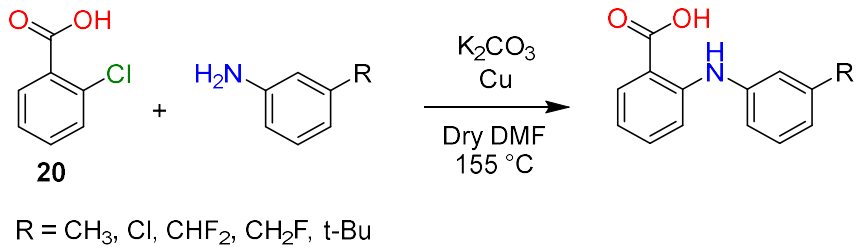


Fig 3.4. Top: Measured PXRD pattern of synthesised FFA **14**, bottom: literature pattern of polymorphic Form IV FFA.[65]

3.3 Synthetic Routes in the Production of Structurally Similar FFA Analogues

The Pellón *et al*. synthetic method was carried out using anilines meta-substituted with different groups to produce the five analogues of FFA **14** chosen in Section 2.2.4 (Scheme 3.7). The yields and crude purity achieved for each product are listed in Table 3.1.



Scheme 3.7. Metallic copper-catalysed Ullmann-Goldberg condensation towards the syntheses of compounds **15** – **19**, modified from Pellón *et al*.[127]

Table 3.1. List of substituents (R) on the aniline starting material depicted in Scheme 3.7, the product of the reaction, the pure percentage yield of the reaction, and the percentage purity of the crude product (determined by HPLC analysis).

R	Product	Yield%	Crude Purity%
CH_3	Me-FA **15**	60.7	97.8
Cl	Cl-FA **16**	70.7	98.3
CHF_2	DF-FA **17**	72.7	89.2
CH_2F	MF-FA **18**	68.5	96.2
t-Bu	t-Bu-FA **19**	72.1	95.4

3.3.1 Characterisation of FFA Analogues

The products of these reactions were characterised in the same way as FFA **14** above, by NMR, IR, MS and HPLC analysis. IR, ^{1}H NMR, and ^{13}C NMR analysis of each product is presented and described in the following section. HPLC signals of each additive are shown alongside FFA as part of doped chromatograms in Section 2.3.4 and Appendix Section 7.2.1. Any characterisation not discussed here is detailed in Section 3.6.4. PXRD, DSC, and TGA was also performed on the synthesised products, as these forms of analysis will be pertinent to the research in Chapter 4. The outputs of these analyses are presented in the Appendix, unless relevant to the discussion of the material. As DF-FA **17** and MF-FA **18** are less well reported in the literature compared to the other compounds, DEPT 90 and DEPT 135 analysis was also performed in these cases, presented in Appendix Sections 7.7.1 and 7.7.2 for each compound respectively.

3.3.1.1 Me-FA **15**

IR Analysis

The IR spectrum of Me-FA **15** (Figure 3.5) exhibits many peaks identical to that of FFA **14**. Notable changes, however, include the disappearance of the C-F stretch signals between 1350 – 1100 cm^{-1} characteristic of -CF_3,[203] as well as the emergence of certain alkyl C-H peaks in the range of 3038 – 2638 cm^{-1}.

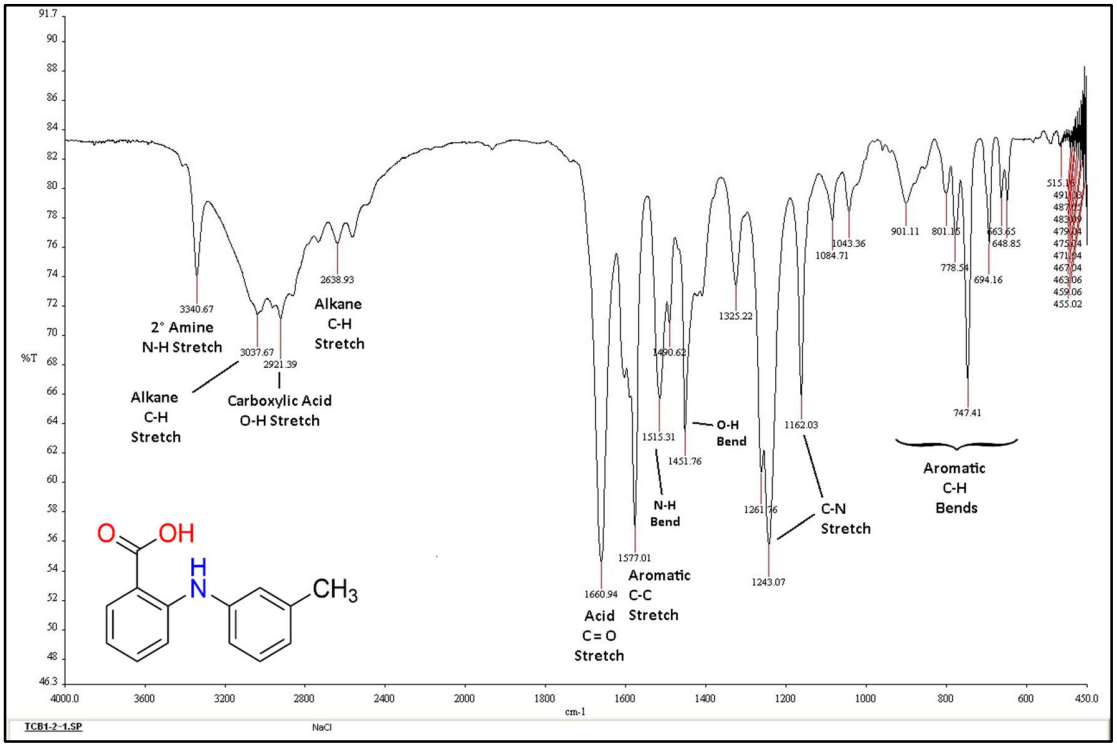


Fig 3.5. IR spectrum of Me-FA **15**, with labelled peaks.

Proton NMR

The overall ^{1}H NMR spectrum for Me-FA **15** can be found in Figure 3.6. A 3H singlet is visible at 2.34 ppm, confirming the presence of the C^{1} methyl group on the molecule. The aromatic region, shown in more detail in Figure 3.7, is similar to that of FFA **14**. The effect of the change from the deshielding -CF_3 group to the more shielding -CH_3 can be clearly observed, resulting in the upfield migration of nearly all aromatic protons on the molecule. This effect is much more pronounced for the protons on the methyl-substituted ring. The C^{5}-H doublet is no longer overlapping with the C^{9}-H doublet, appearing now at 6.88 ppm. The migration of the C^{4}-H triplet (now at 7.31 ppm) is less substantial due to its positioning meta to the new substituent. The C^{3}-H doublet and C^{6}-H singlet are still overlapping at approx. 7.01 ppm, as they were both ortho to the changed

group. The protons on C^{12} and C^{11} have moved upfield slightly to 7.96 and 6.71 ppm respectively, and the C^{10} triplet and C^{9} doublet are now overlapping at approx. 7.20 ppm, having experienced the effect of the changed group to slightly different degrees.

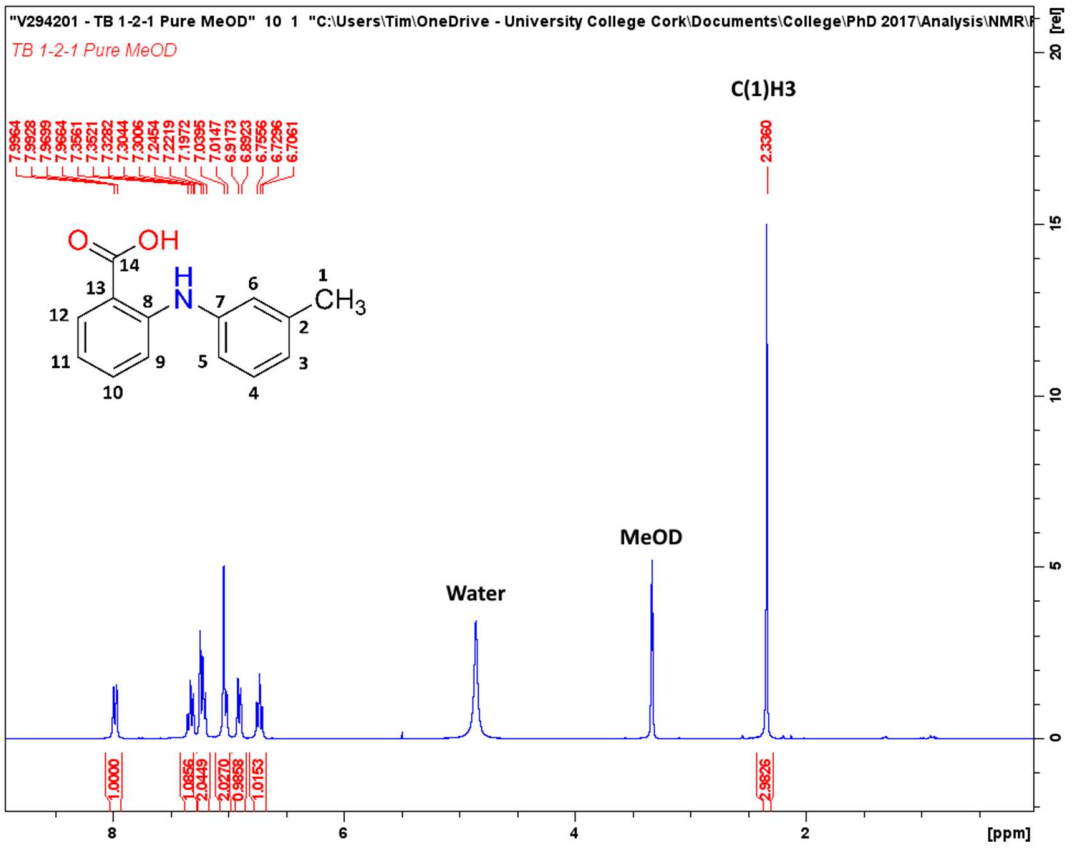


Fig 3.6. Full ^{1}H NMR spectrum of Me-FA **15**, with labelled peaks.

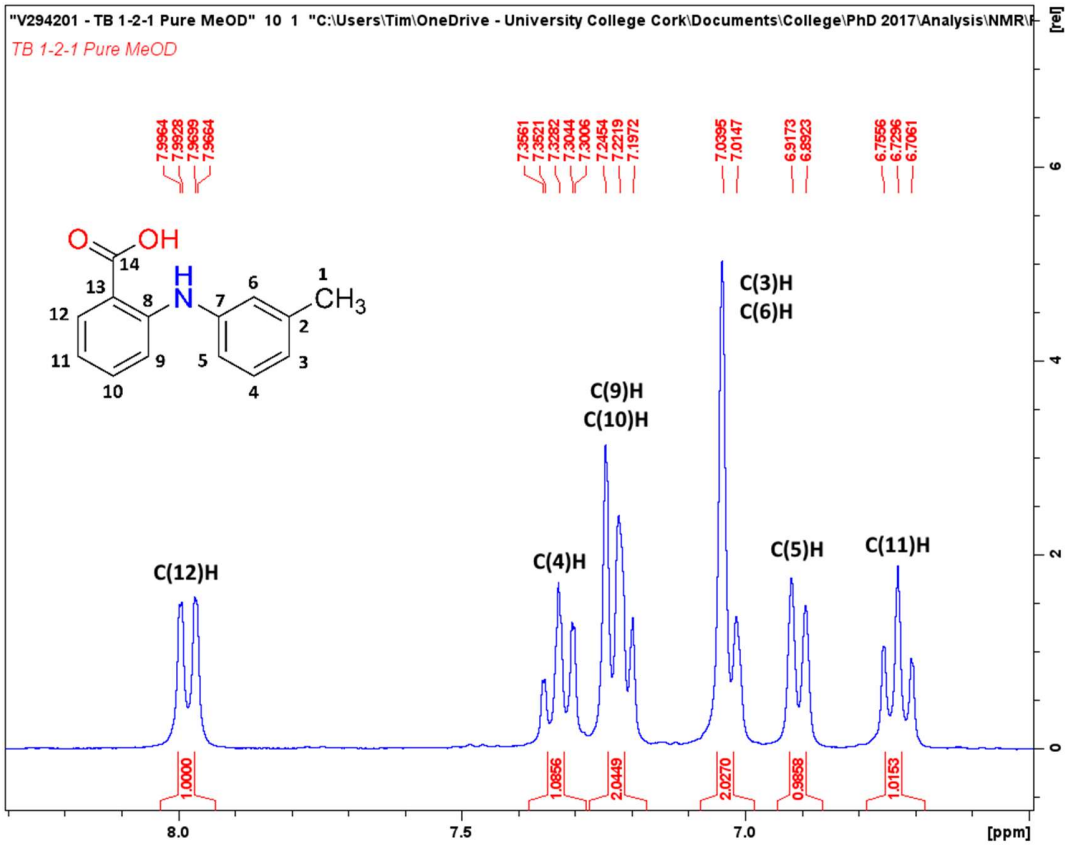


Fig 3.7. Aromatic region of the ^{1}H NMR spectrum of Me-FA **15**, with labelled peaks.

Carbon NMR

In the ^{13}C NMR spectrum of Me-FA **15** (Figures 3.8 and 3.9), a protonated signal appears at 21.51 ppm corresponding to the methyl C^{1} carbon. Likewise, the quaternary signal centred at 125.51 ppm in the FFA **14** spectrum is no longer visible. As there are no fluorine atoms present on the molecule, as there was in FFA **14**, all ^{13}C signals are visible as single peaks with no splitting. The effect of changing -CF_3 for -CH_3 is most significantly experienced by C^{2}, C^{3}, and C^{6}, which migrate downfield to 123.77, 140.47, and 125.25 ppm respectively, as well as C^{5}, which is shifted substantially upfield to 118.02 ppm.

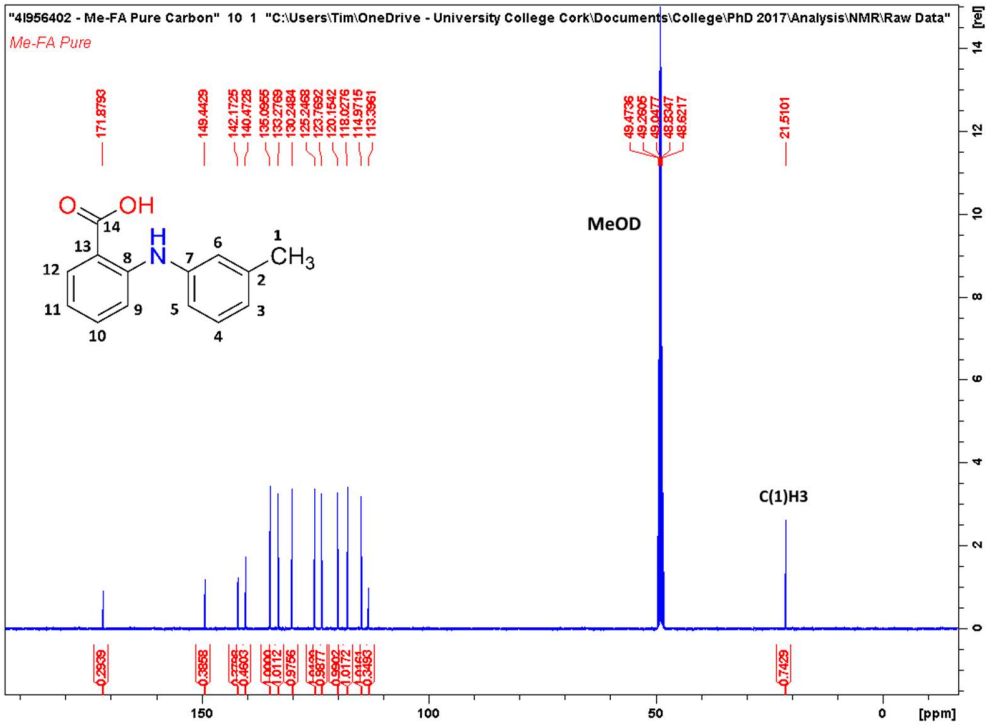


Fig 3.8. Full ^{13}C NMR spectrum of Me-FA **15**, with labelled peaks, showing the position of the C^1 methyl signal outside the aromatic region.

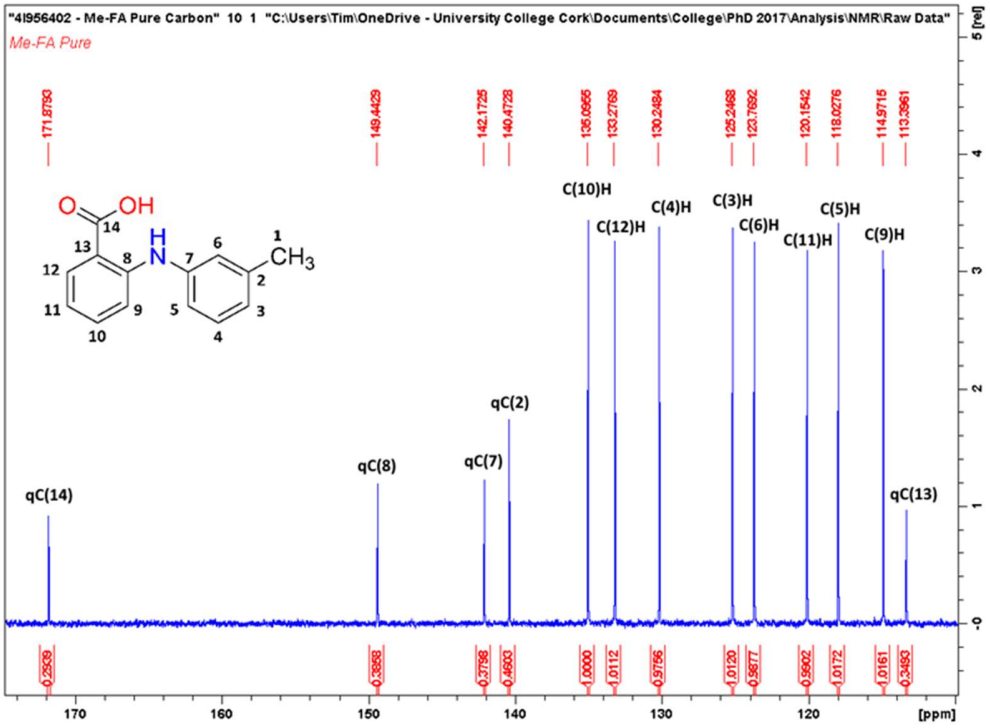


Fig 3.9. Aromatic region of the ^{13}C NMR spectrum of Me-FA **15**, with labelled peaks.

3.3.1.2 Cl-FA **16**

IR Analysis

Like with Me-FA **15**, the IR spectrum of Cl-FA **16** (Figure 3.10) is missing the C-F stretches between 1350 – 1100 cm^{-1}, instead gaining a wide signal in the region of 1155 – 1020 cm^{-1} representative of an aromatic C-Cl stretch. This is distinct from the C-Cl stretch generally observed between 830 – <600 cm^{-1}, which is not present in chloroaromatics.[203]

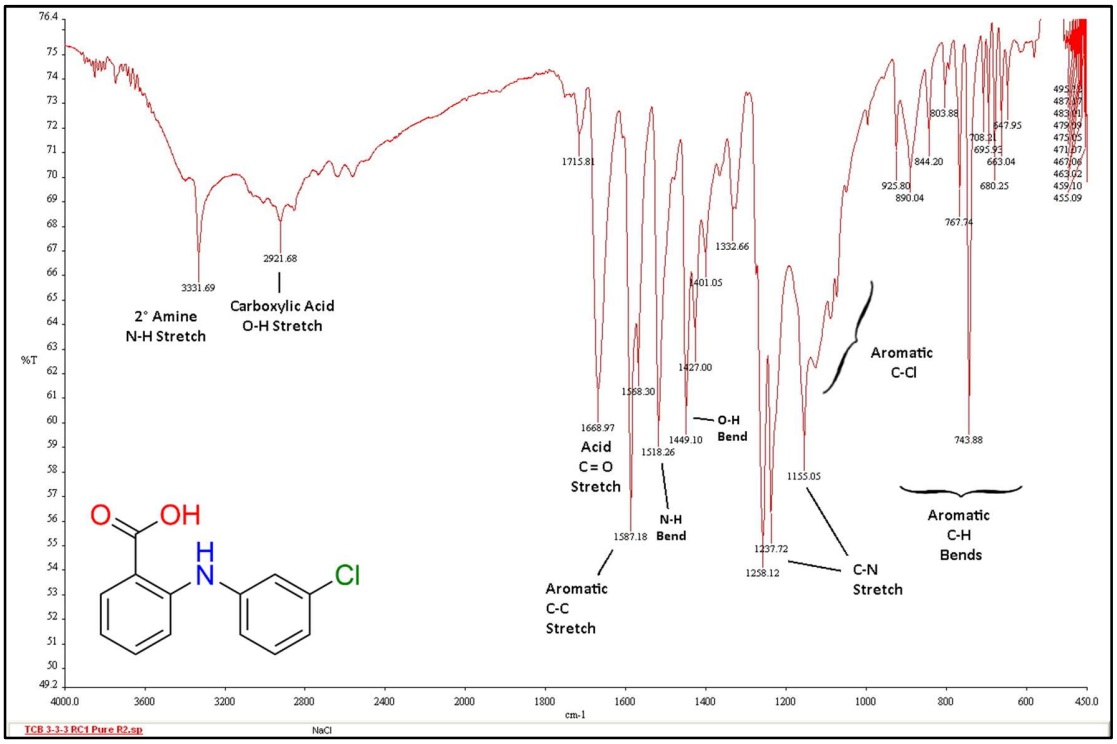


Fig 3.10. IR spectrum of Cl-FA **16**, with labelled peaks.

Proton NMR

It should be noted when comparing spectra between compounds that as there is one fewer carbon in the structure of Cl-FA **16**, the labelling of atoms in this compound differs slightly from the others described in this section.

In terms of ^{1}H NMR, the shielding effect of the -Cl group is similar to that of -CH_3, albeit weaker. This results in a slight downfield shift for most peaks on the Cl-FA **16** spectrum compared to that of Me-FA **15**, although they are still substantially upfield from those observed for FFA. The aromatic range of the ^{1}H NMR spectrum can be seen in Figure 3.11. Aside from the blanket upfield shift, the pattern of the signals on the Cl-FA **16** spectrum remains mostly unchanged from that of Me-FA **15**; the major change being that respective signals for C^{2}-H and C^{5}-H are no longer overlapping and are now visible as individual doublet and singlet peaks at 7.13 and 7.21 ppm respectively.

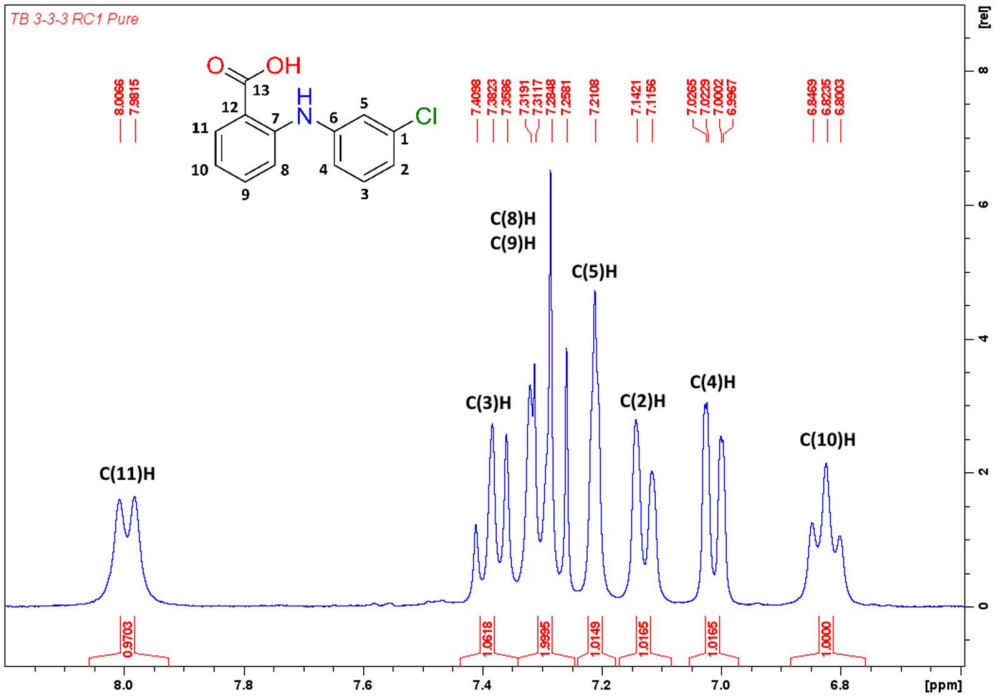


Fig 3.11. Aromatic region of the ^{1}H NMR spectrum of Cl-FA **16**, with labelled peaks.

Carbon NMR

The ^{13}C NMR spectrum collected for Cl-FA **16** (Figure 3.12) is very similar to that of Me-FA **15**; the major difference being the lack of the carbon signal at 21.51 ppm. The signals corresponding to the carbons on the substituted ring have migrated in a similar way to Me-FA **15** when compared to the equivalent FFA **14** spectrum, but to a lesser degree.

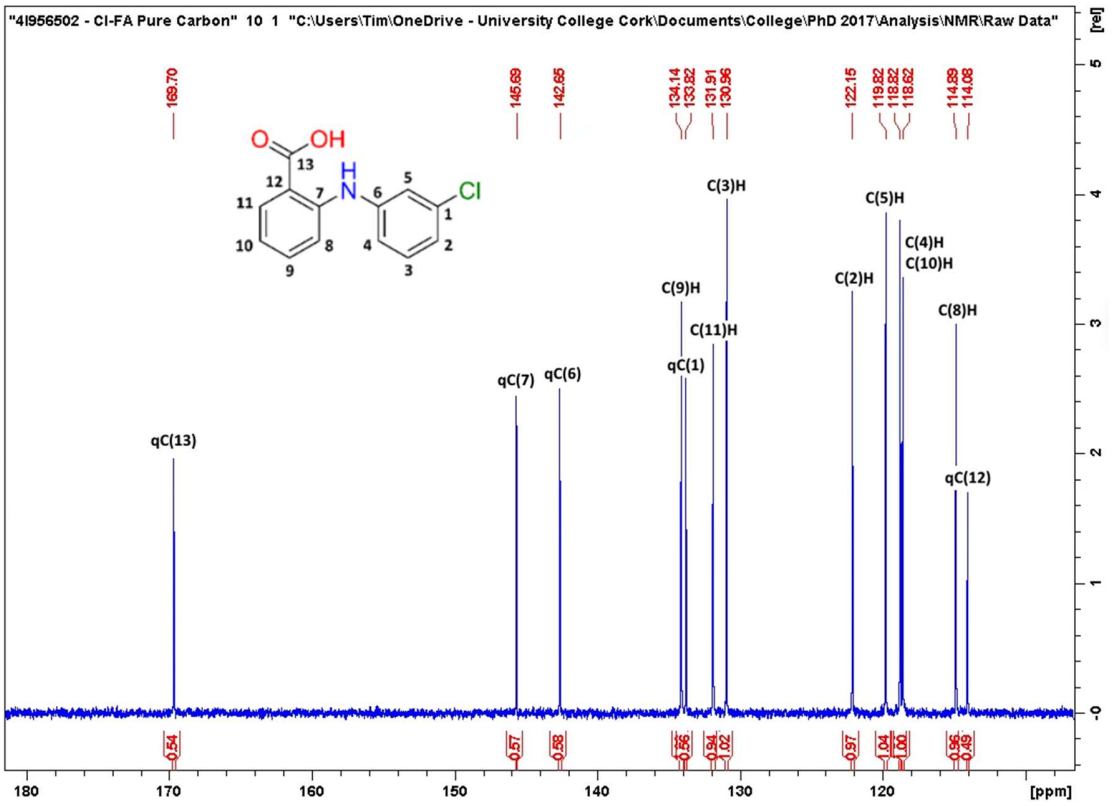


Fig 3.12. Aromatic region of the ^{13}C NMR spectrum of Cl-FA **16**, with labelled peaks.

PXRD

In addition to the other forms of analysis mentioned, Cl-FA **16** was also tested by PXRD analysis. As mentioned in Section 2.2.4.1, Cl-FA **16** is the only of the chosen additives that is known to have multiple polymorphic forms.[160] By PXRD analysis, the material produced was determined to crystallise in the Form I polymorph (Figure 3.13).

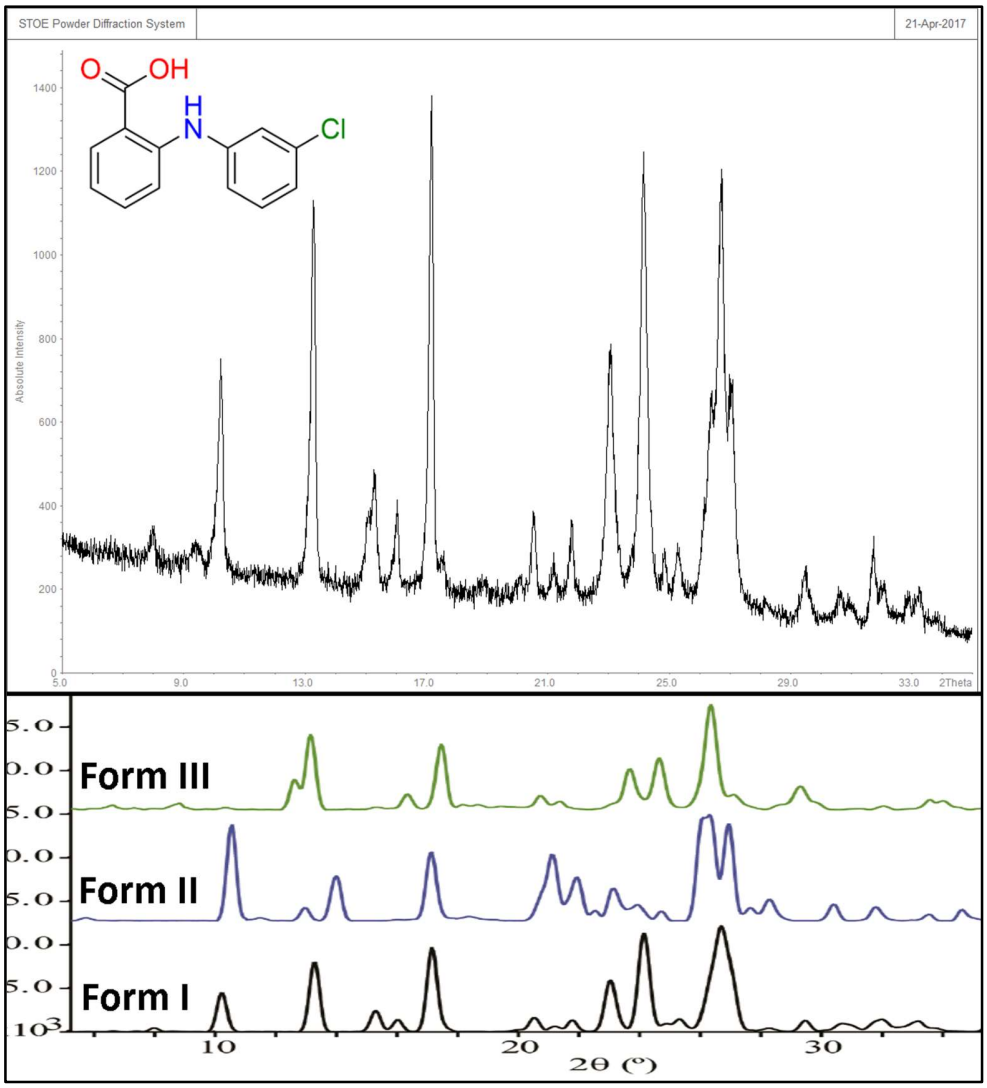


Fig 3.13. Top: Measured PXRD pattern of synthesised Cl-FA **16**, bottom: literature pattern of polymorphic Form I, Form II, and Form III Cl-FA **16**.[160]

3.3.1.3 DF-FA **17**

IR Analysis

The IR spectrum of DF-FA **17** (Figure 3.14) is difficult to distinguish from that of FFA **14**, as the nature of the bonds in the compounds are very similar. However, unlike in FFA **14**, signals are visible in the 2500 – 2000 cm^{-1} range that can be attributed to alkyl C-H stretches, albeit shifted to a lower frequency by the neighbouring aromatic and fluorine groups.

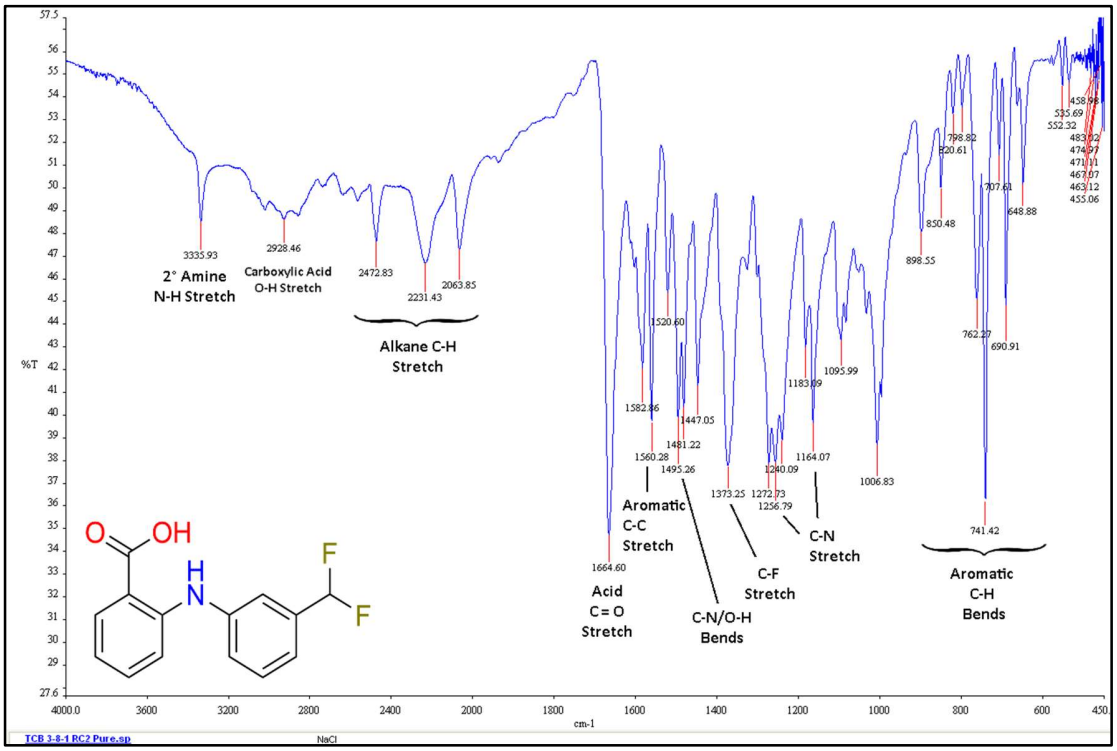


Fig 3.14. IR spectrum of DF-FA **17**, with labelled peaks.

Proton NMR

Predictably, the ^{1}H NMR spectrum for DF-FA **17** (Figure 3.15 for the aromatic region) more closely resemble that of FFA **14** than the two additives described so far. All signals on the spectrum are migrated upfield as a result of the weaker deshielding effect of -CHF_2 compared to -CF_3. Like in the Me-FA **15** spectrum, this change in shift is much more pronounced for the protons on the substituted ring (those of C^3, C^4, C^5, and C^6) due to their proximity to the changed group, while the positions of the proton peaks on the acid ring (those of C^9, C^{10}, C^{11}, and C^{12}) experience a more limited effect. The positions of the signals differ from FFA **14** in that the C^3-H and C^6-H signals are now overlapping with that of C^{10}-H rather than C^4-H, and the signals for C^5-H and C^9-H are no longer overlapping. Additionally, a very wide triplet emerges centred on 6.71 ppm (^{2}J = 56.3 Hz) representing the proton on C^1. The wide triplet pattern is the result of geminal coupling between that proton and the two C^1 fluorine atoms, the ^{2}J value observed (56.3 Hz) being characteristic of that coupling.[203]

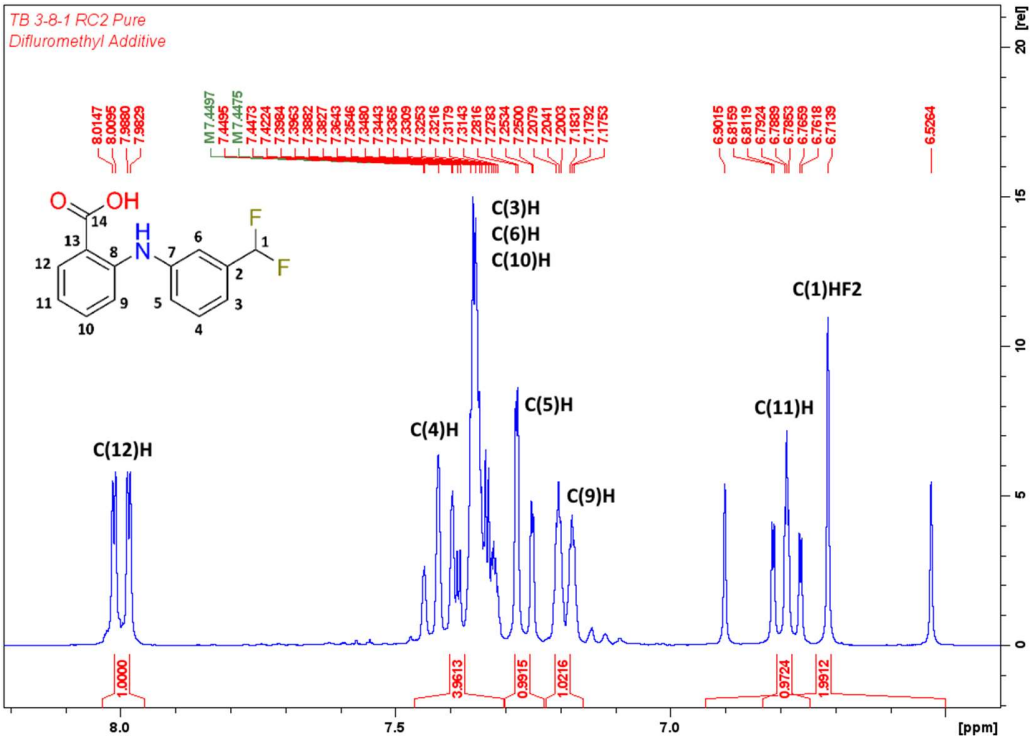


Fig 3.15. Aromatic region of the ^{1}H NMR spectrum of DF-FA **17**, with labelled peaks.

Carbon NMR

The aromatic region of the ^{13}C spectrum for DF-FA **17** is shown in Figure 3.16. The signals for the carbons on the acid ring (C^{9}, C^{10}, C^{11}, and C^{12}) remain mostly unchanged compared to those observed in FFA **14** but, like with the ^{1}H NMR spectrum, the change in substituent from -CF_3 to -CHF_2 results in peak migration for carbons on the substituted ring. C^{4} and C^{5} migrate upfield to differing degrees, as do the quaternary carbons C^{7} and C^{13}. The signals of C^{2}, C^{3}, and C^{6} on the other hand experience a substantial downfield migration. C^{1} is no longer quaternary, but now exhibits a C-H peak centred at 116.12 ppm. This peak manifests as a triplet coupled to the remaining two fluorine atoms on the carbon (^{1}J = 237.2 Hz). The large J-value and overlapping signals

obscure this triplet somewhat; a clearer image of the peak is presented in Appendix Figure 7.40. Triplet peaks are also visible corresponding to C^3 (120.88 ppm) and C^6 (119.18 ppm, overlapping) with a ^{3}J-value of 6.1 Hz, and C^2 (137.43 ppm, ^{2}J = 22.3 Hz). Coupling is also experienced to a lesser degree by C^5 (124.32 ppm, ^5J = 2.0 Hz).

DEPT 90 and DEPT 135 spectra of this compound are presented in Appendix Figures 7.41 and 7.42. As all protonated carbons on the compound are C-H, these two spectra are very similar, with 9 positive-phase signals visible in the aromatic region. The splitting of these signals is consistent with the ^{13}C spectrum described above.

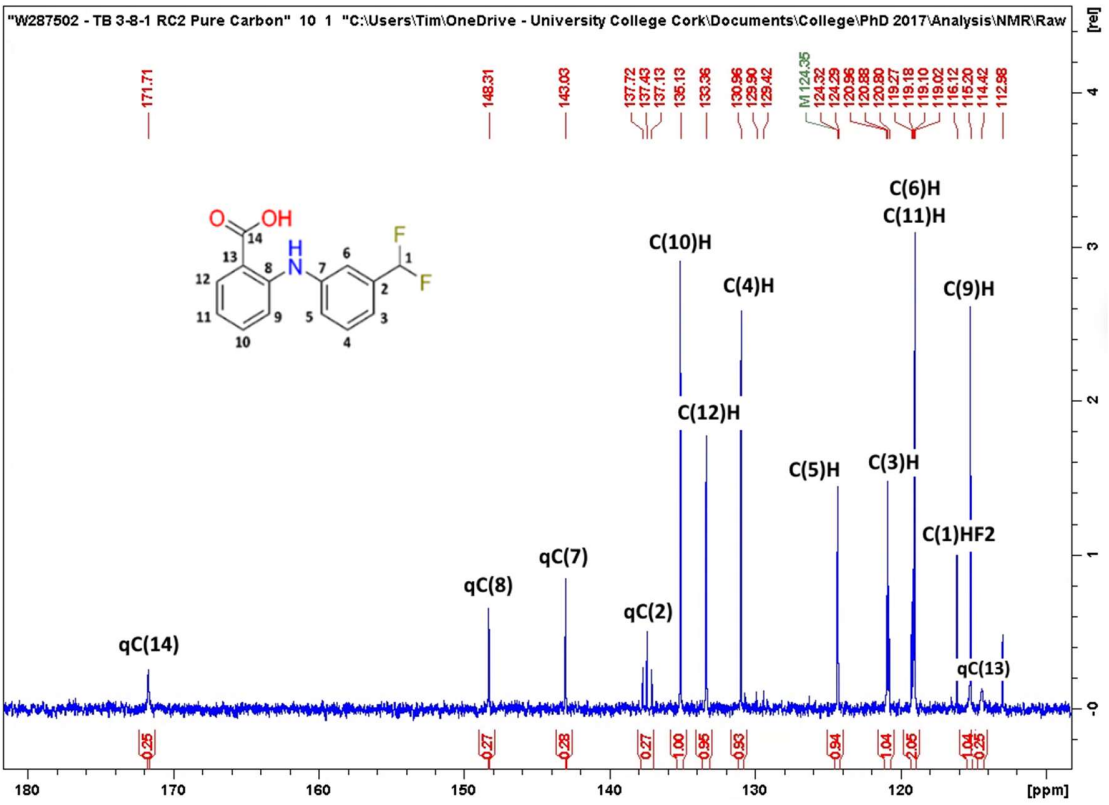


Fig 3.16. Aromatic region of the ^{13}C NMR spectrum of DF-FA **17**, with labelled peaks.

3.3.1.4 MF-FA **18**

IR Analysis

In a similar way as DF-FA **17**, the IR spectrum of MF-FA **18** (Figure 3.17) is difficult to distinguish from that of FFA **14**. However, similarly to DF-FA **17**, alkyl C-H signals can be observed at high frequencies (2700 – 2000 cm^{-1}). The C-F and C-N stretching signals are most likely overlapping between 1150 and 1250 cm^{-1}.

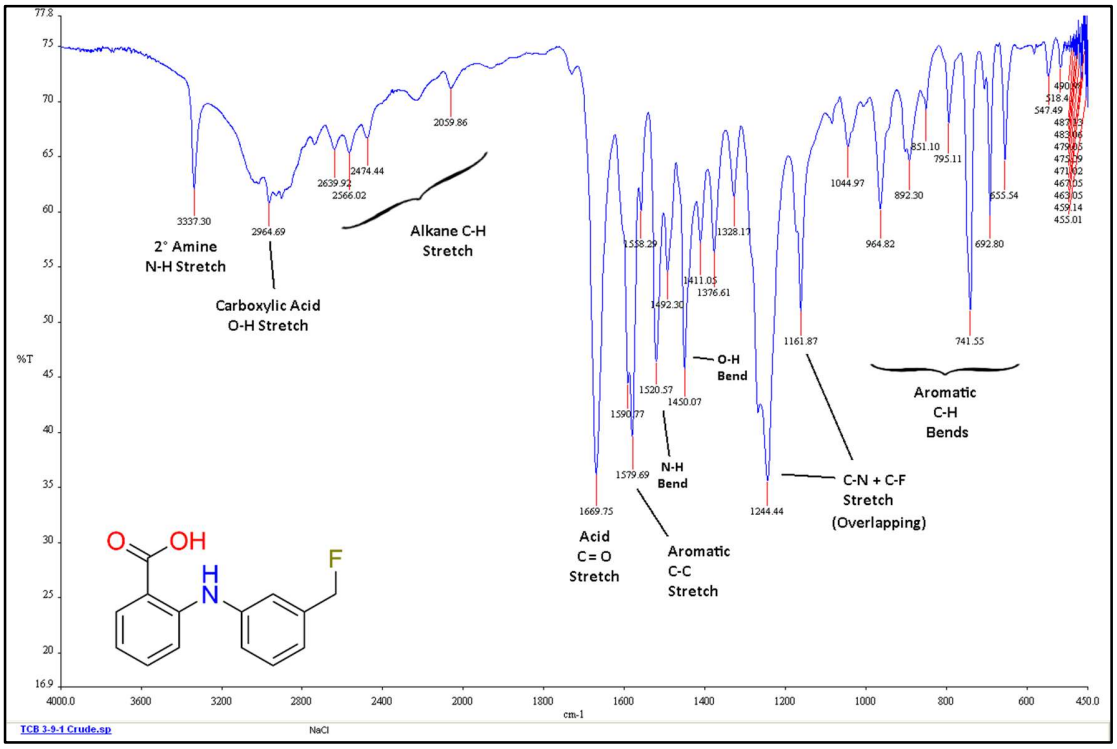


Fig 3.17. IR spectrum of MF-FA **18**, with labelled peaks.

Proton NMR

The signals on the MF-FA **18** ^{1}H NMR spectrum follow the same migration pattern as seen on the DF-FA **17** spectrum, the less deshielding -CH_2F group resulting in the aromatic proton signals moving upfield (Figure 3.19). Again, this is more pronounced for the protons on the substituted ring than those on the acid ring. The signal for C^4-H is now overlapping with that of C^{10}-H, and the C^3-H and C^6-H cluster has migrated to overlap with C^5-H. The signal for the two protons on C^1 is now represented by a 2H doublet (^{2}J = 47.8) centred on 5.33 ppm, coupling with the lone remaining fluorine atom on the carbon (Figure 3.18).

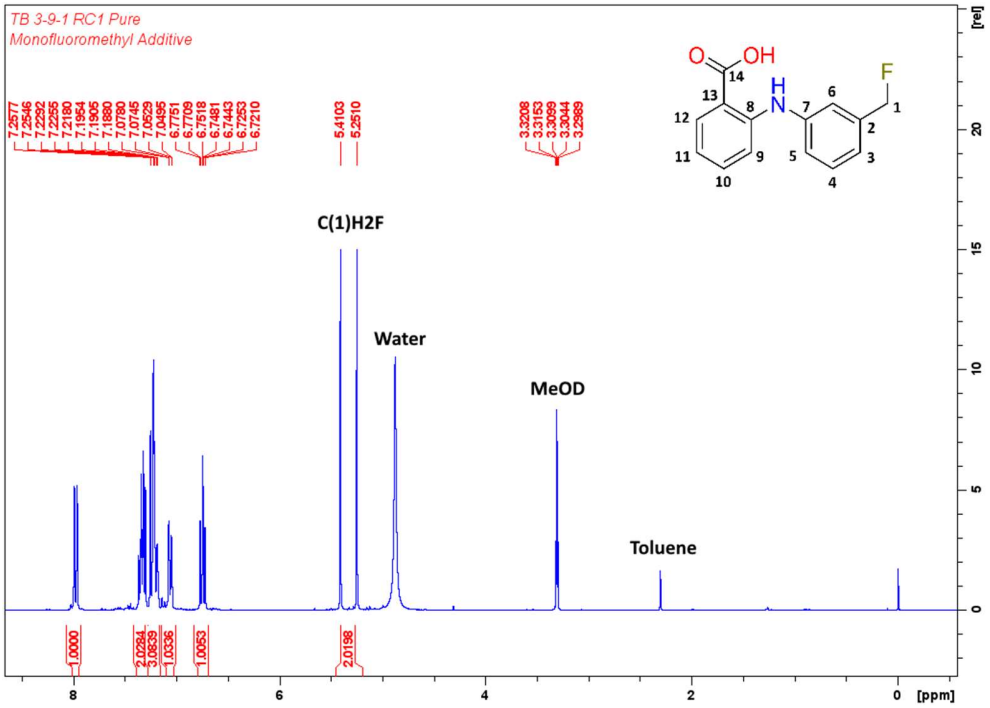


Fig 3.18. Full ^{1}H NMR spectrum of MF-FA **18**, with labelled peaks showing the position of the $C^{1}H_2F$ doublet signal outside the aromatic region.

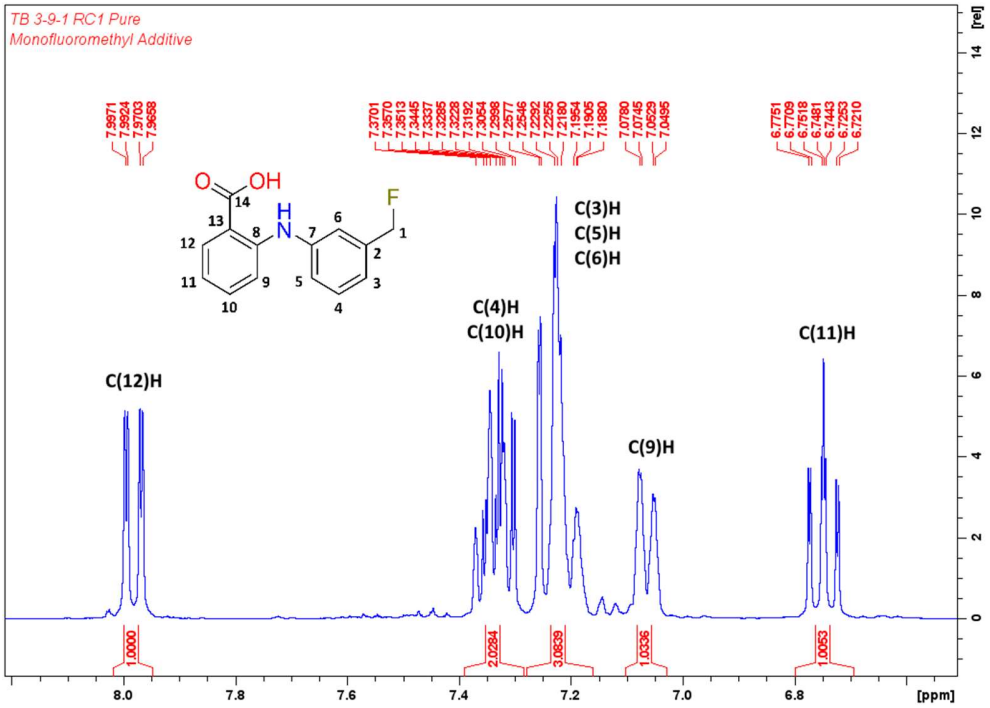


Fig 3.19. Aromatic region of the ^{1}H NMR spectrum of MF-FA **18**, with labelled peaks.

Carbon NMR

Similarly, the ^{13}C NMR spectrum for MF-FA **18** (Figures 3.20 and 3.21 for the full and aromatic region spectra respectively) continues the trend of signal migration observed between FFA **14** and DF-FA **17**, due to the weakening deshielding effect of the compound's mono-fluorinated substituent. C^{1}, coupling to the last remaining fluorine atom, is represented by a doublet at 85.24 ppm (^{1}J = 165.3 Hz), as is C^{2} (139.43 ppm, ^{2}J = 17.1 Hz) and C^{3} and C^{6} (123.08 ppm and 121.47 ppm respectively, ^{3}J = 6.1 Hz). The signal for C^{5} also appears as a narrow doublet (122.72 ppm, ^{5}J = 2.8 Hz), as does C^{4} (130.67 ppm, ^{4}J = 1.1 Hz), despite no coupling to fluorine being visible in either the FFA **14** or DF-FA **17** spectra. DEPT 90 and DEPT 135 spectra of this compound are presented in Appendix Figures 7.43 – 7.45. The DEPT 90 spectrum displays 8 C-H signals, all in

the aromatic region. The DEPT 135 spectrum displays the same, but also includes a negative-phase doublet centred at approx. 85 ppm, confirming the presence of the C^1-H_2 signal assigned in the ^{13}C spectrum. As before, the splitting pattern of all DEPT 90 and DEPT 135 signals match those observed in the ^{13}C spectrum.

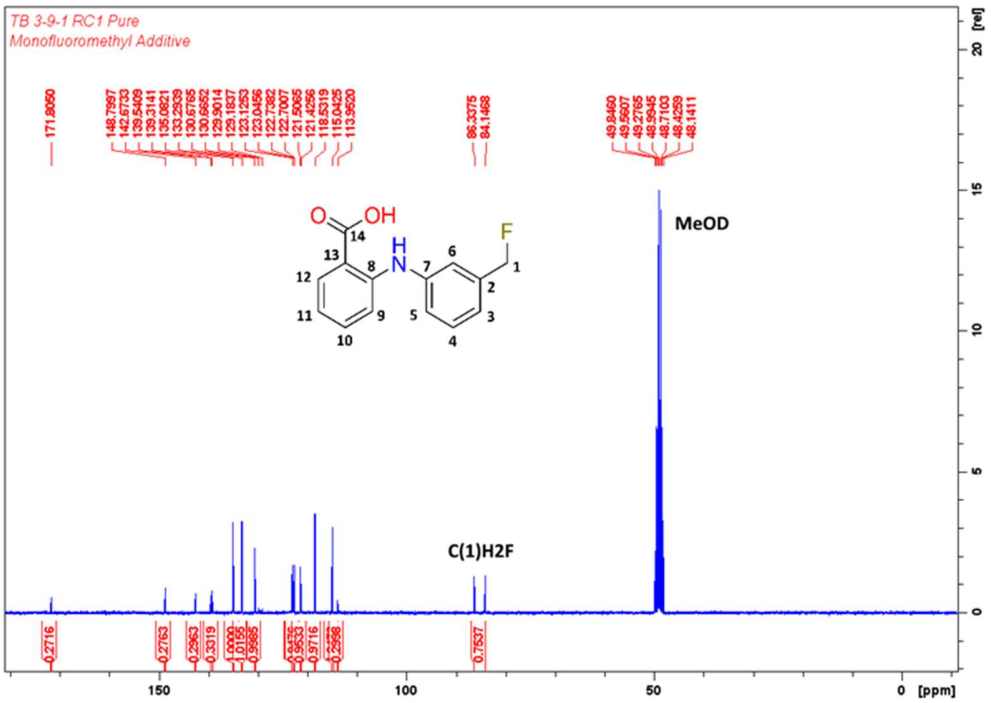


Fig 3.20. Full ^{13}C NMR spectrum of MF-FA **18**, with labelled peaks showing the position of the C^1H_2F doublet signal outside the aromatic region.

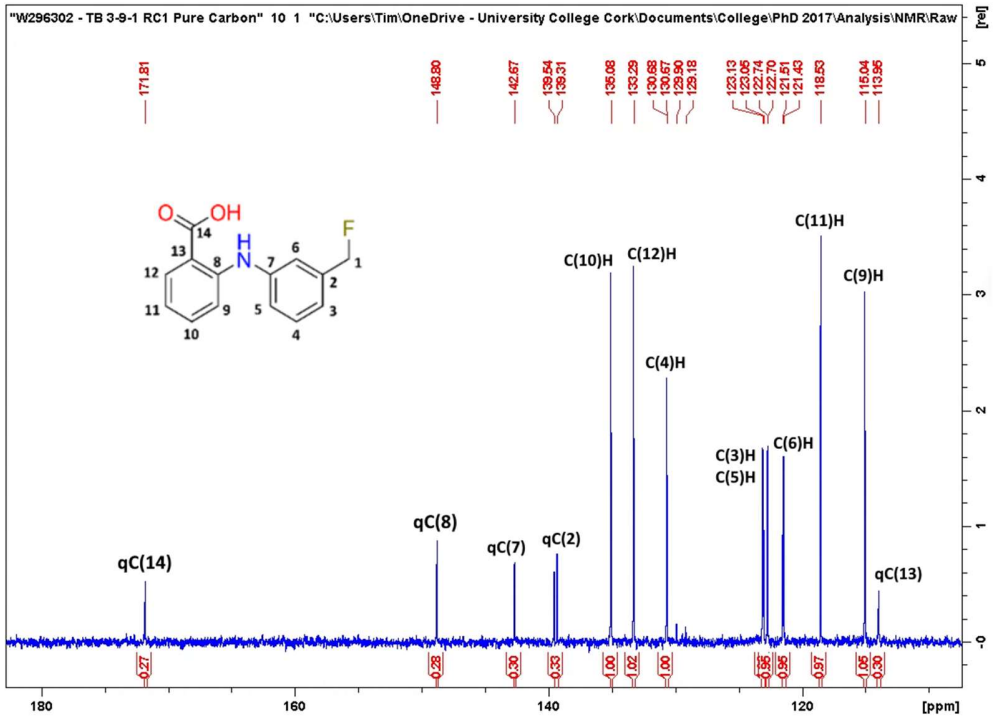


Fig 3.21. Aromatic region of the ^{13}C NMR spectrum of MF-FA **18**, with labelled peaks.

3.3.1.5 t-Bu-FA **19**

IR Analysis

The IR spectrum of t-Bu-FA **19** (Figure 3.22) is characterised by the absence of C-F peaks between 1330 and 1122 cm^{-1} (the signals at 1246 and 1162 cm^{-1} representing the amino C-N stretches) and the presence of multiple alkyl C-H stretches between 3000 and 2500 cm^{-1}.

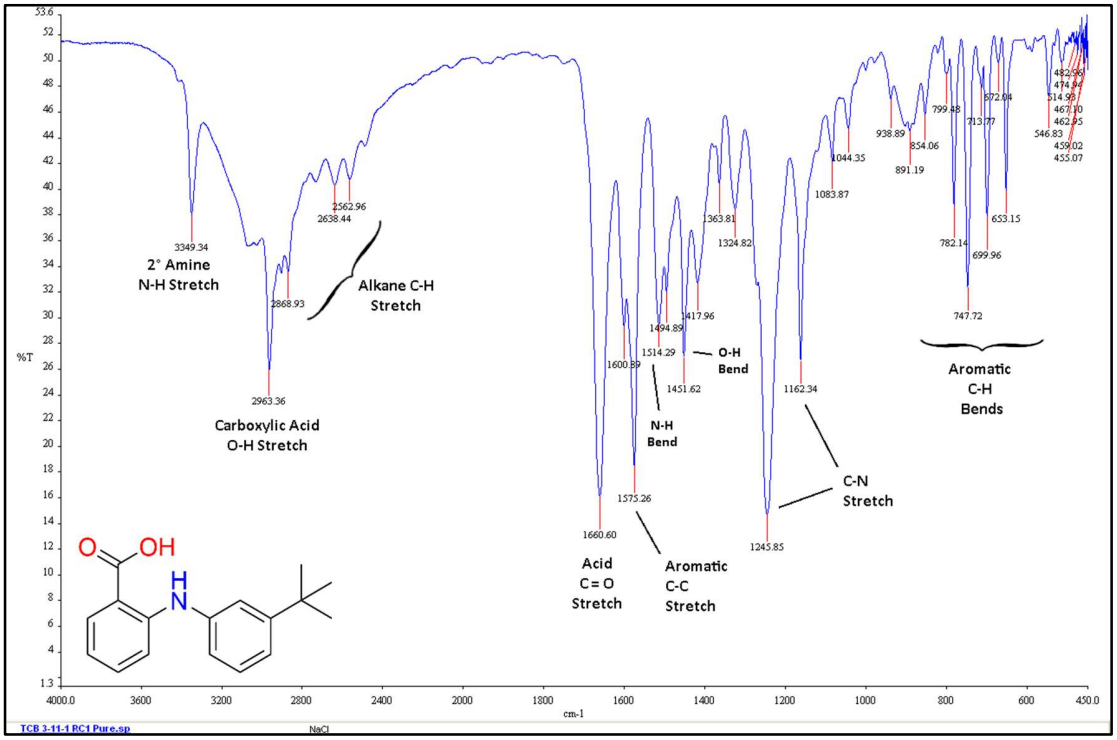


Fig 3.22. IR spectrum of t-Bu-FA **19**, with labelled peaks.

Proton NMR

The ^{1}H NMR spectrum for t-Bu-FA **19** (Figure 3.23) has a characteristic 9H singlet visible at 1.30 ppm, corresponding to the 9 equivalent protons of the *tert*-butyl group (located on C^{15}, C^{16}, and C^{17}). There is a lot of overlap in the aromatic region (Figure 3.24), but it shares a lot of similarities with that of Me-FA **15**. The C^{12}-H doublet remains furthest downfield at 7.97 ppm, and the C^{11}-H triplet furthest upfield at 6.70 ppm. The C^{3}-H and C^{5}-H doublets are also visible at 7.11 ppm and 7.03 ppm respectively. The remaining 4H multiplet encompasses the proton signals on C^{4}, C^{6}, C^{9}, and C^{10}.

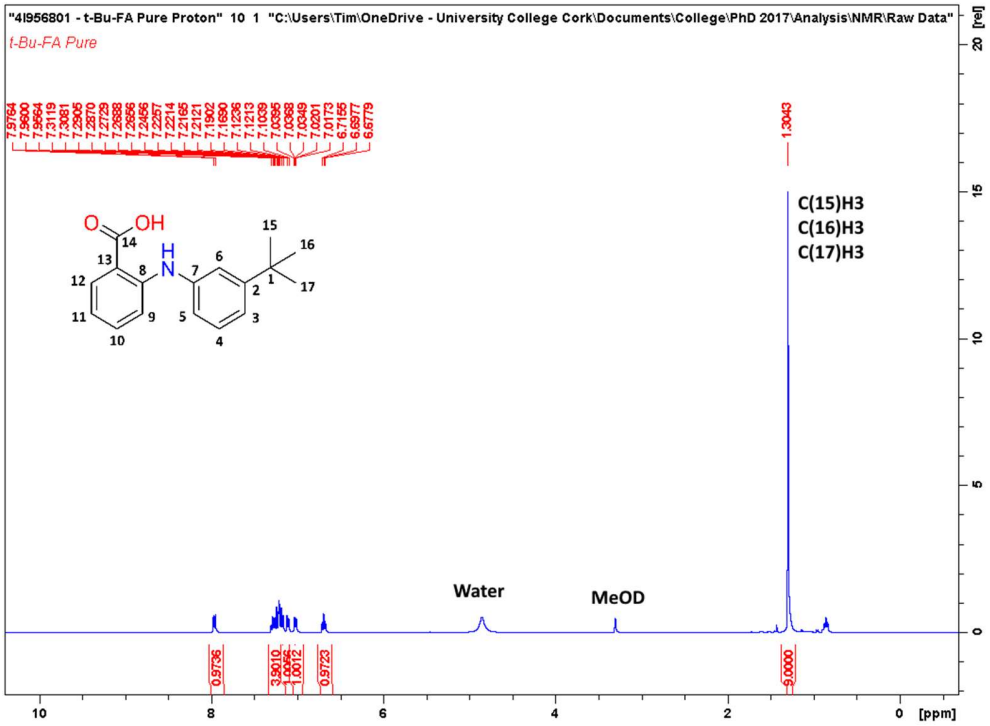


Fig 3.23. Full ^{1}H NMR spectrum of t-Bu-FA **19**, with labelled peaks showing the position of the 9H t-butyl signal outside of the aromatic region.

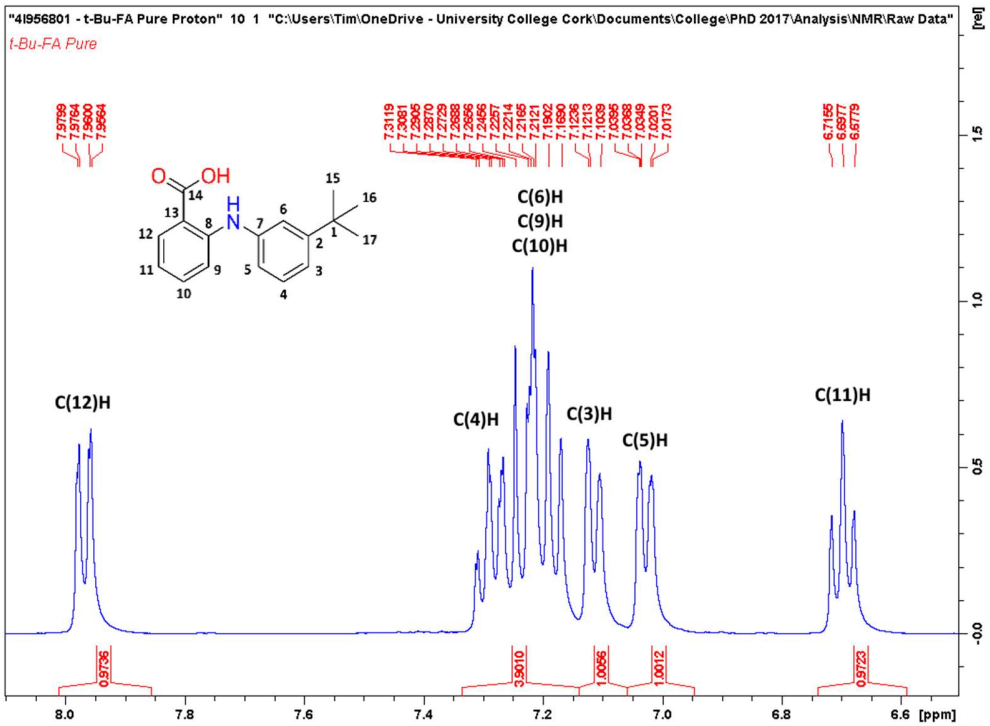


Fig 3.24. Aromatic region of the ^{1}H NMR spectrum of t-Bu-FA **19**, with labelled peaks.

Carbon NMR

Like in the ^{1}H spectrum, a characteristic upfield signal identifies t-Bu-FA **19** on the ^{13}C spectrum (Figure 3.25), this time with a 3C singlet at 31.71 ppm representing the three protonated alkyl carbons on the *tert*-butyl group (C^{15}, C^{16}, and C^{17}). The signal for the central quaternary carbon of the group (C^{1}) is visible close by at 35.49 ppm. The remainder of the signals, found in the aromatic region (Figure 3.26), resemble those seen in the spectra of the other compounds in this section.

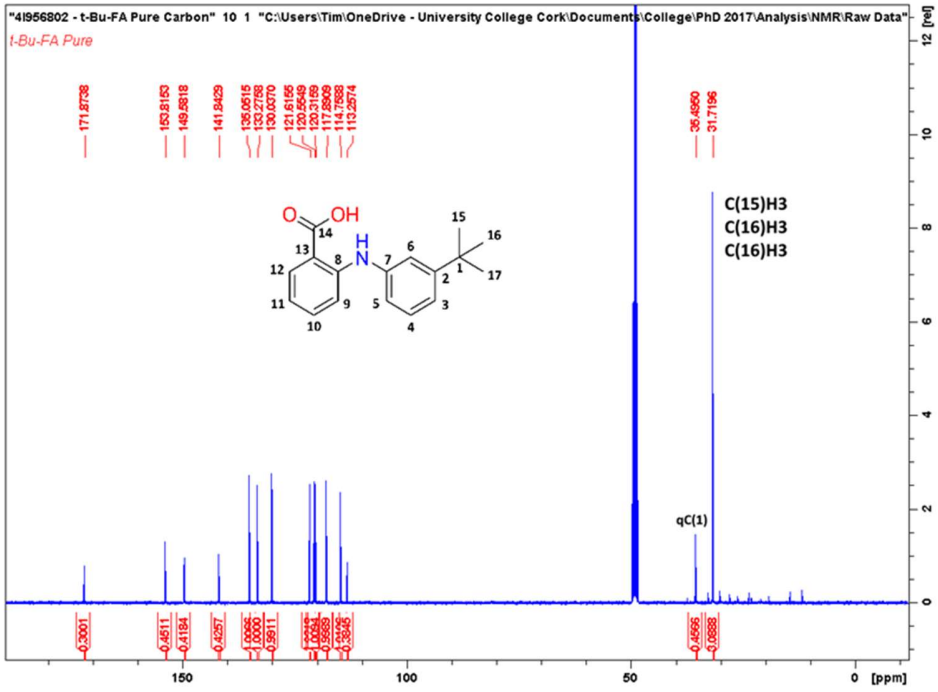


Fig 3.25. Full ^{13}C NMR spectrum of t-Bu-FA **19**, with labelled peaks showing the position of one quaternary carbon signal as well as the 3C t-butyl signal outside the aromatic region.

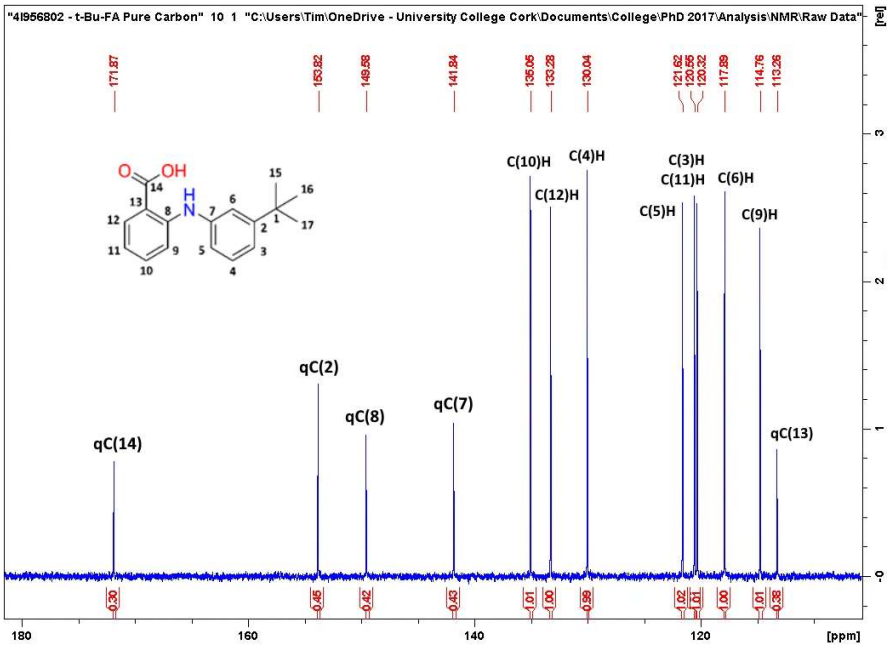


Fig 3.26. Aromatic region of the ^{13}C NMR spectrum of t-Bu-FA **19**, with labelled peaks.

Thermogravimetric Analysis

In contrast to the TGA curves of FFA **14** and the other additives (compounds **15** – **18**), which generally decompose in a single step (Figure 2.42, Appendix Figures 7.31 – 7.35), it was observed that the decomposition of pure t-Bu-FA **19** took place over two well-defined stages. Approx. 7.7% of the total mass decomposes at a temperature of 134.9 °C, followed by the remainder at 237.8 °C. The initial smaller step in the TGA curve is accompanied by a small endothermic peak appearing at a comparable temperature on the corresponding DSC curve, prior to the melting endotherm of the material at 154.0 °C. The two curves are overlaid below in Figure 3.27.

The most likely explanation for this is the formulation of the crystal material as a hydrate. The initial mass-loss step can be attributed to the melting of the hydrate crystal, followed by the evaporation of water contained within. This is represented on the DSC

curve as an endothermic peak at 127.8 °C, and the subsequent recrystallisation of the pure material by the exothermic peak at 129.0 °C. These are followed by the melting then the decomposition of the material proper at higher temperatures. An alternative explanation would be the formulation of the solid material as a hydrochloric acid (HCl) salt. This has been reported for the material,[204] and the synthetic preparation requires acidification of the reaction mixture in concentrated HCl.[127] However, no evidence of a HCl salt was observed in the IR spectrum of the material. Additionally, when calculated based on molecular weights, HCl accounts for approx. 11.9% of the HCl salt formulation of t-Bu-FA **19**. On the other hand, water would make up just 6.3% of a monohydrated product, much closer to the 7.6% mass loss measured. As such, it is more likely that the product is forming a monohydrate. Regardless of the form that pure t-Bu-FA **19** takes, it does not appear to have any bearing on the behaviour of the additive in the doped systems, as will be demonstrated in Chapter 4.

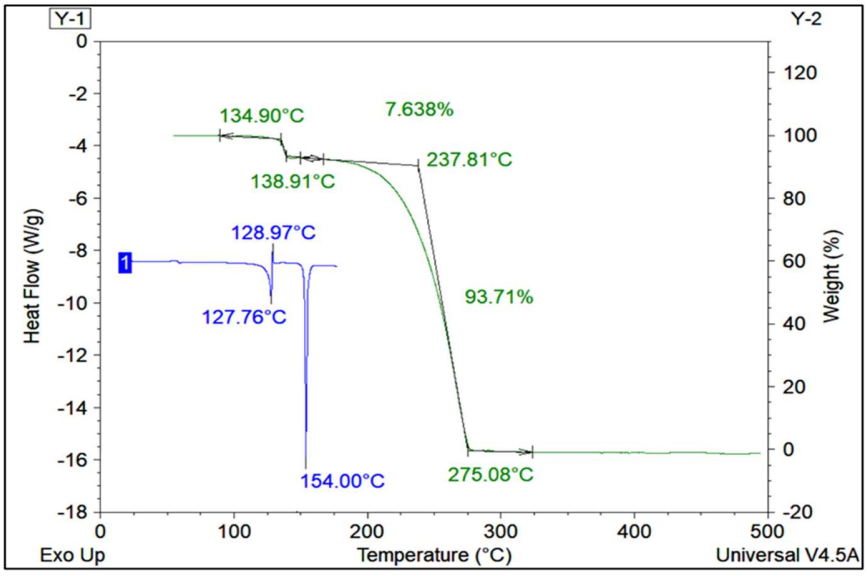


Fig 3.27. Green: measured TGA curve of purified t-Bu-FA **19** showing pre-decomposition mass loss of 7.6%, blue: measured DSC curve of purified t-Bu-FA **19** showing pre-melting endothermic peak at a similar temperature.

3.4 Investigation into Impurity Observed during Synthesis of FFA

3.4.1 Observation of Impurity Occurrence

During the early stages of synthetic development, an impurity peak was observed consistently in HPLC analysis of the crude products from multiple iterations of the Cu / Cu_2O-catalysed synthesis of FFA **14** (Scheme 3.1, Section 3.2.1). It was observed to have a relative retention time (RRT) of approx. 0.5 compared to the retention time of FFA (Figure 3.28), and to form in quantities between approx. 2 – 15% of the crude product. This peak was confirmed to be distinct from either starting material of the reaction, 2-CBA **20** or 3-(trifluoromethyl)aniline **21**, which have RRT values of 0.16 and 0.18. As the aim of the research centred around examining impure systems of FFA, it was thought that a side-product could have potential as an additive for these systems.

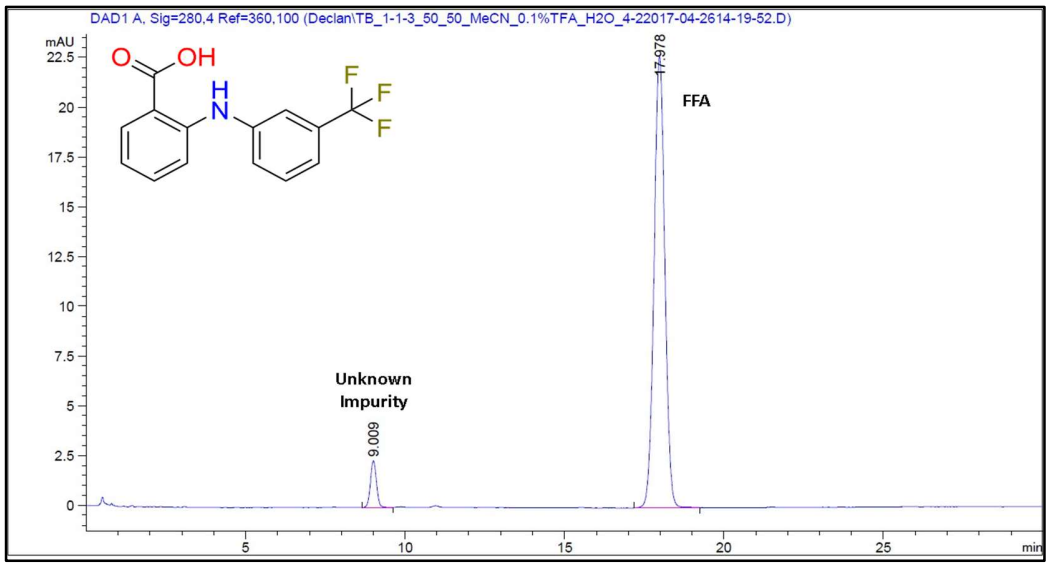


Fig 3.28. HPLC trace of crude FFA **14** product of Scheme 3.1 reaction, showing the presence of an unknown impurity, collected at 280 nm.

3.4.2 Isolation and Analysis of Impurity

The unknown impurity was isolated from the crude product of one of these reactions by column chromatography. The quantity isolated was lower than expected (43 mg, approx. 3% w/w of crude), and difficult to purify above 90%. The isolated impurity was tested by HPLC, IR, and the full array of NMR analysis available. IR, ^{1}H, and ^{13}C NMR can be found in Figures 3.30 – 3.32; the remaining spectral data is displayed in Appendix Sections 7.8.2 and 7.8.3. The choices relating to signal assignment for these spectra is explained in Section 3.4.5. The NMR analysis for this compound was performed on a 600 MHz instrument, as opposed to the 300 MHz and 400 MHz instruments used for other compounds. This provided a much higher level of resolution, but a lower level of separation in regard to peak splitting. Chemical shift and coupling constants are not affected by this change.

The spectra were analysed alongside the structures of a number of potential side-products of the synthesis of FFA **14**, predicted based on literature reactions of the starting materials performed under similar conditions to the Mei *et al.* method. These included the amide 2-chloro-*N*-[3-(trifluoromethyl)phenyl]benzamide **23**,[205] the acridones 1/3-(trifluoromethyl)acridin-9(10H)-one **24a** and **24b**,[206] and the diacid triaryl 2,2'-((3-(trifluoromethyl)phenyl)azanediyl)dibenzoic acid **25** (Figure 3.29).[207]

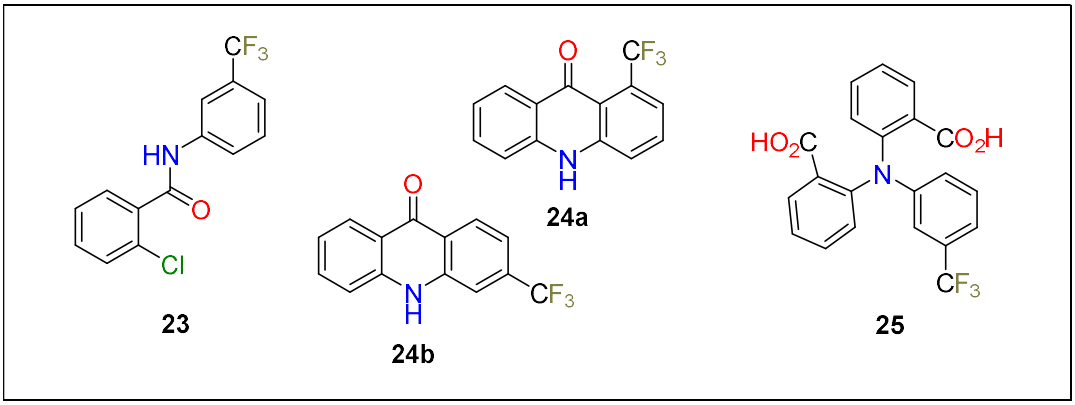


Fig 3.29. Left to right: structures of 2-chloro-*N*-[3-(trifluoromethyl)phenyl]benzamide **23**, 1/3-(trifluoromethyl)acridin-9(10H)-one **24a** and **24b**, and 2,2'-((3-(trifluoromethyl)phenyl)azanediyl)dibenzoic acid **25**, suggested identities of the unknown synthetic impurity observed in the synthesis of FFA **14**.

From the spectral analysis, a number of attributes of the species were determined. The compound was found to contain 12 aromatic protons by ^{1}H NMR, 8 of which were represented by 4 signals with integration values corresponding to 2 protons each. This suggests a compound with three disubstituted aryl rings, two of which are chemically equivalent. This suggestion was supported by ^{13}C, DEPT 90 and DEPT 135 NMR, which also exhibited a similar pattern of integration. DEPT 135q NMR confirmed the presence of quaternary carbon signals corresponding to a -CF_3 group as well as one potentially corresponding to carboxylic acid centres on the compound. From this interpretation, it was determined that the observed impurity was more likely to be the diacid triaryl **25** than the amide **23** or the acridones **24a** or **24b**. It was found that the signals from the IR and NMR spectra of the isolated impurity (Figures 3.30 – 3.32) could be reasonably assigned based on the structure of compound **25**. Additionally, mass spectrometry analysis of the isolated impurity successfully identified the ionised mass of compound **25**, although the intensity of the measured signal was quite low (Appendix Figure 7.60).

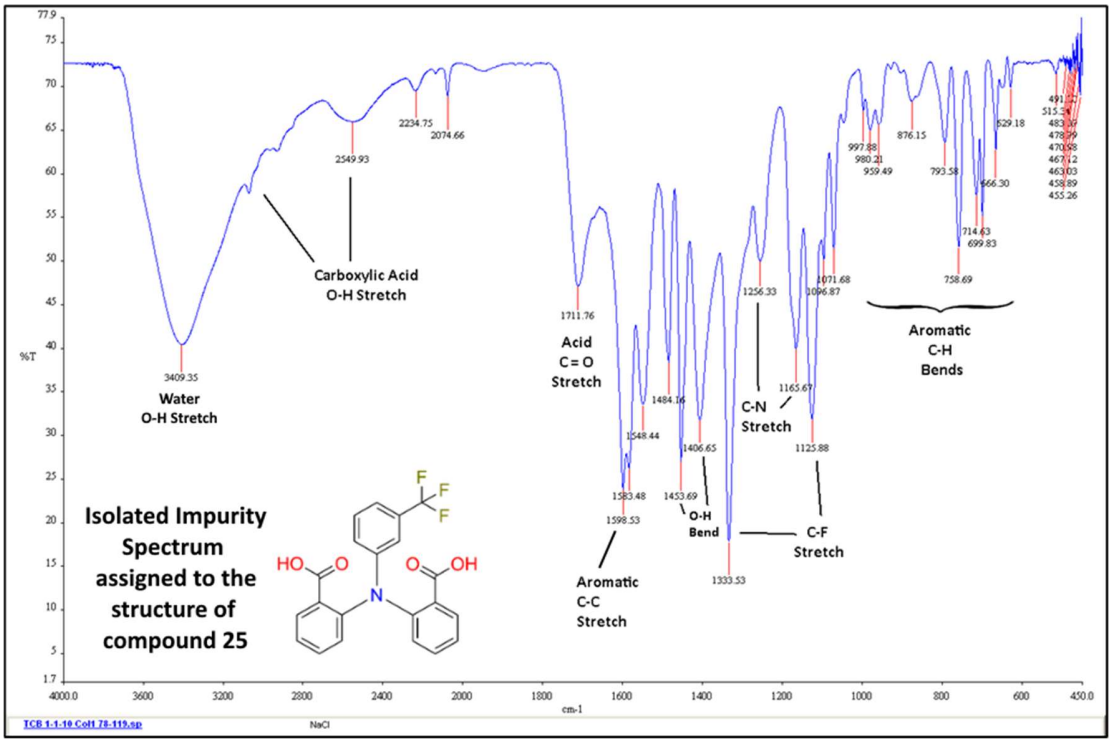


Fig 3.30. IR spectrum of isolated synthetic impurity observed in the crude product of FFA **14**, with peaks assigned based on the structure of compound **25**.

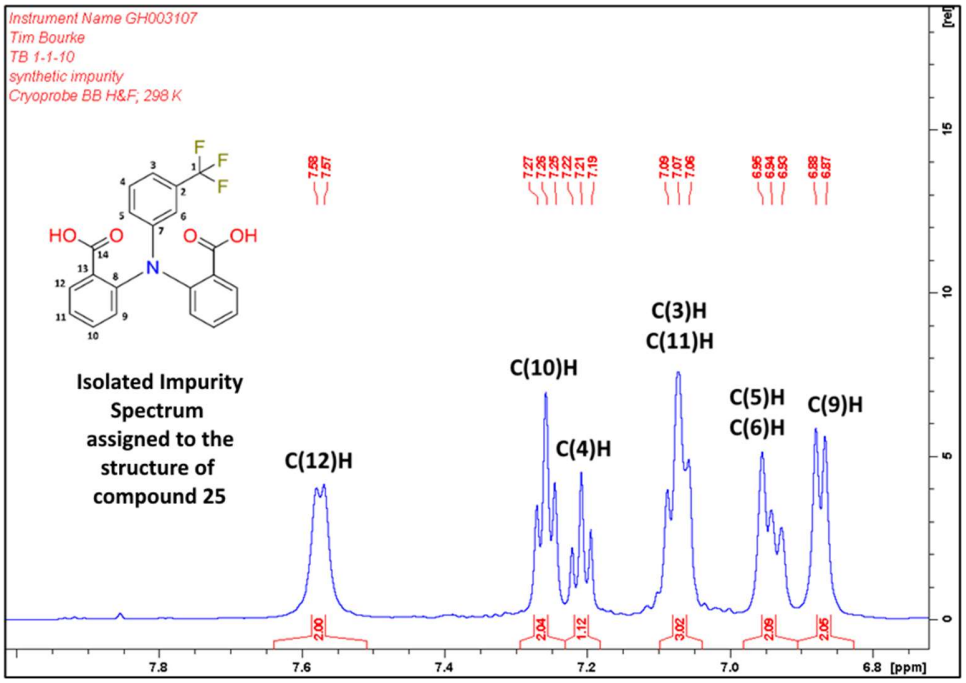


Fig 3.31. Aromatic region of the ^{1}H NMR spectrum of isolated synthetic impurity, with peaks assigned based on the structure of compound **25**.

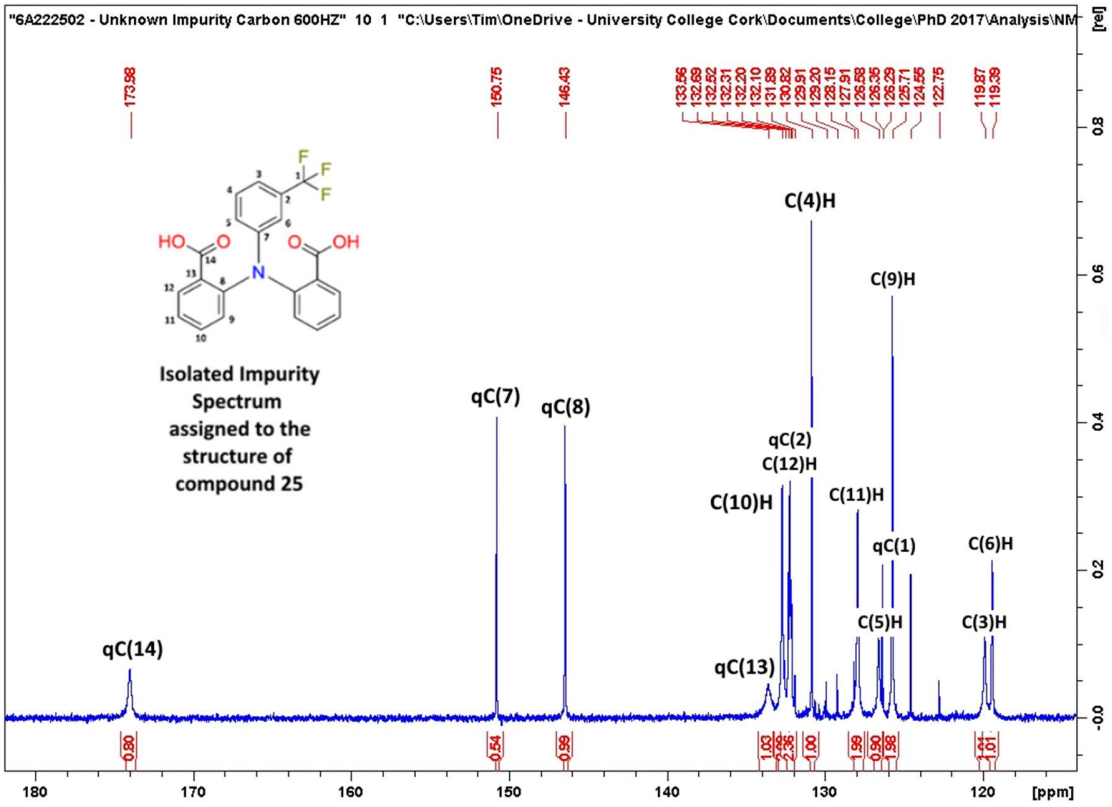
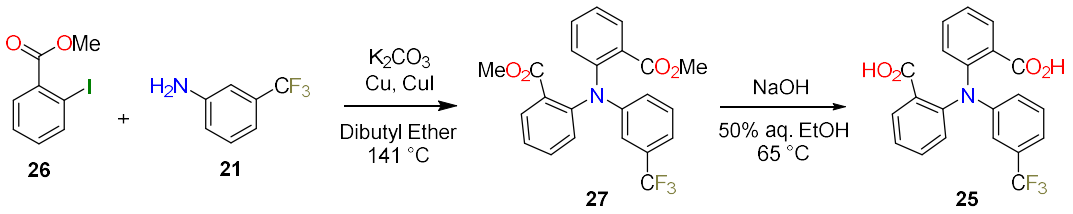


Fig 3.32. Aromatic region of the ^{13}C NMR spectrum of isolated synthetic impurity, with peaks assigned based on the structure of compound **25**.

3.4.3 Targeted Synthesis of Diacid Triaryl Compound **25**

A more targeted synthetic method (Scheme 3.8) was performed to produce compound **25**. This would generate material against which the isolated impurity could be compared to as a more definitive means of identification. The synthetic method, described by Field *et al*., is another example of an Ullmann-Goldberg condensation similar to that used previously in the synthetic development of FFA **14** (Section 3.2.1).[208] An aryl halide, this time in its ester form (methyl 2-iodobenzoate **26**), couples with 3-trifluoromethyl aniline **21** in the presence of a metallic copper / copper(I) iodide catalyst. This produces

a triaryl diester intermediate **27**, which can be cleaved to form compound **25** by a simple base-catalysed hydrolysis.



Scheme 3.8. Synthetic route towards the targeted production of compound **25**, thought to be the identity of the unknown impurity observed in the production of FFA **14**, modified from Field *et al*.[208]

The coupling stage of the reaction produced compound **27** as a white powder with a yield of 52.9%. HPLC and NMR analysis of this intermediate product were consistent with the structure of compound **27**; these spectra can be found in Appendix Section 7.7.3. The diester intermediate was subsequently hydrolysed to the free acid form compound **25**, a chalky white powder, with a yield of 97.9%, for a total reaction yield of 51.8%. Full spectral analysis of the product of this reaction can be found in Section 3.6.4.7 and Appendix Section 7.7.4.

3.4.4 Comparison of Isolated Impurity and Synthesised Compound **25**

Much of the comparative analysis of the synthesised compound **25** and the isolated impurity suggests the two materials are the same. UHPLC analysis of a 1:1 mixed sample

of the synthesised product and the isolated impurity results in a single signal with no splitting of the peak observed (Figure 3.33). This analysis, along with the assignments of the IR and NMR peaks mentioned in Section 3.4.2 and the identification of the compound **25** ionised mass *via* MS analysis of the sample, supports the idea that compound **25** is the structure of the isolated impurity.

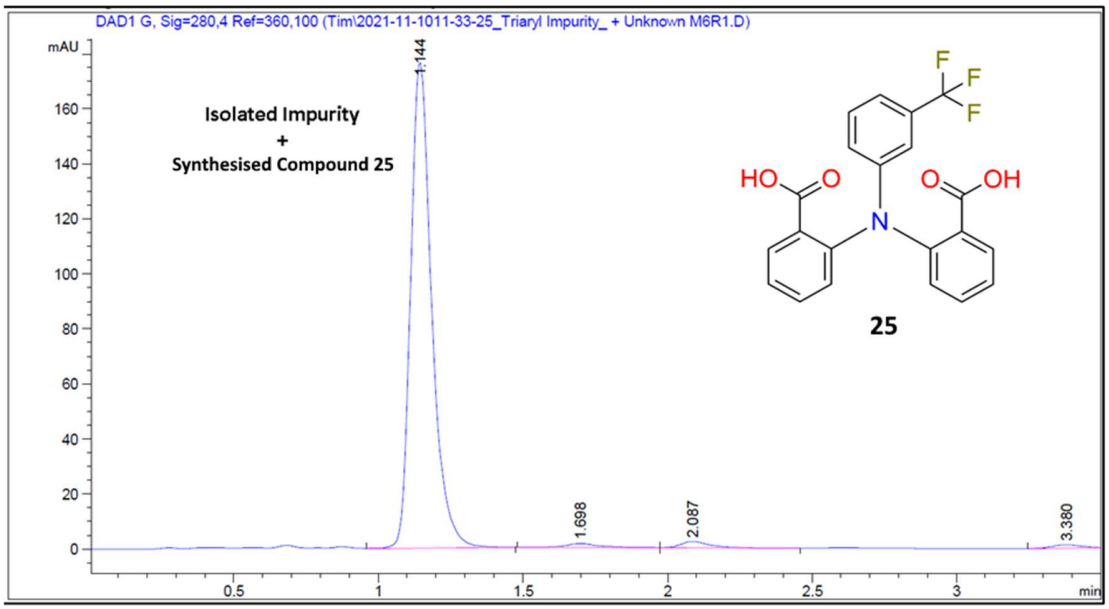


Fig 3.33. HPLC trace of a mixture of the isolated synthetic impurity observed in the production of FFA **14** and the product of a targeted synthesis of compound **25**, collected at 280 nm.

DSC analysis of both samples shows similar melting endotherms, the isolated impurity melting at approx. 235 °C and the synthesised compound **25** at approx. 229 °C (Figure 3.34). The difference in peak max temperature may stem from the lower relative purity of the isolated sample or it could indicate that the two materials are not the same.

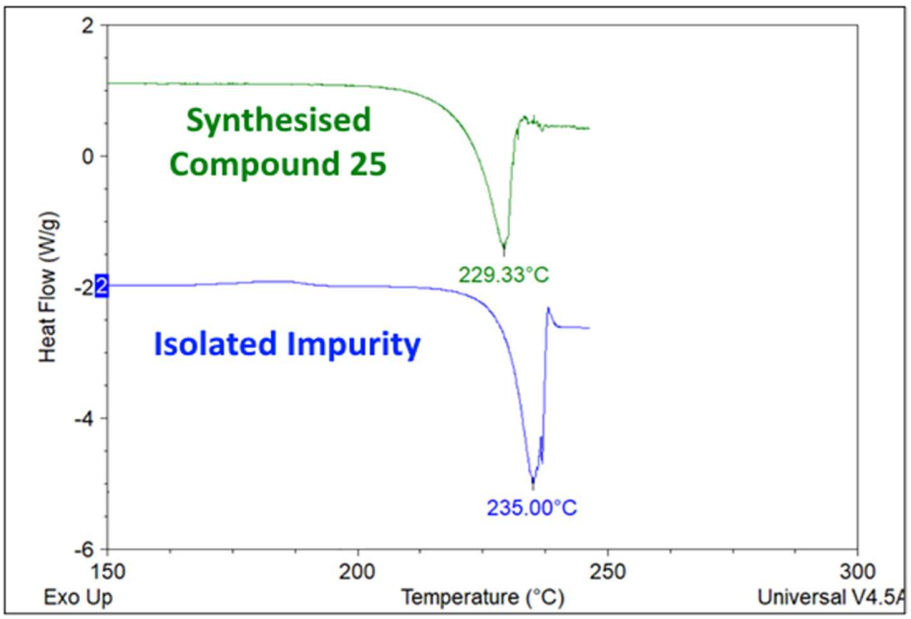


Fig 3.34. Green: measured DSC melting endotherm of the product of a targeted synthesis of compound **25**, blue: measured DSC melting endotherm of the isolated synthetic impurity observed in the production of FFA **14**.

However, significant differences between the two compounds emerge when the NMR and IR spectra are compared. Both samples have very similar peak integration and splitting patterns when measured by NMR and as discussed, the signals can be satisfactorily assigned to those expected for the structure of compound **25**. However, the chemical shifts of those peaks differ substantially between the two samples in both ^{1}H and ^{13}C NMR (Figures 3.35 and 3.36 respectively). The signals of the isolated impurity spectra in these figures are assigned based on the structure of compound **25**.

Additionally, while most of the signals on the IR spectrum of the isolated impurity can be attributed to aspects of the structure of compound **25**, the signal at 1712 cm^{-1}, in the region normally corresponding to a carbonyl C=O stretch, was observed to be quite weak in intensity. This would be unusual for a compound containing two carboxylic acid groups. Indeed, the IR spectrum of the synthesised compound **25** exhibits a much more

prominent peak in the same region (Figure 3.37). These observations do not support the idea that the isolated impurity is compound **25.**

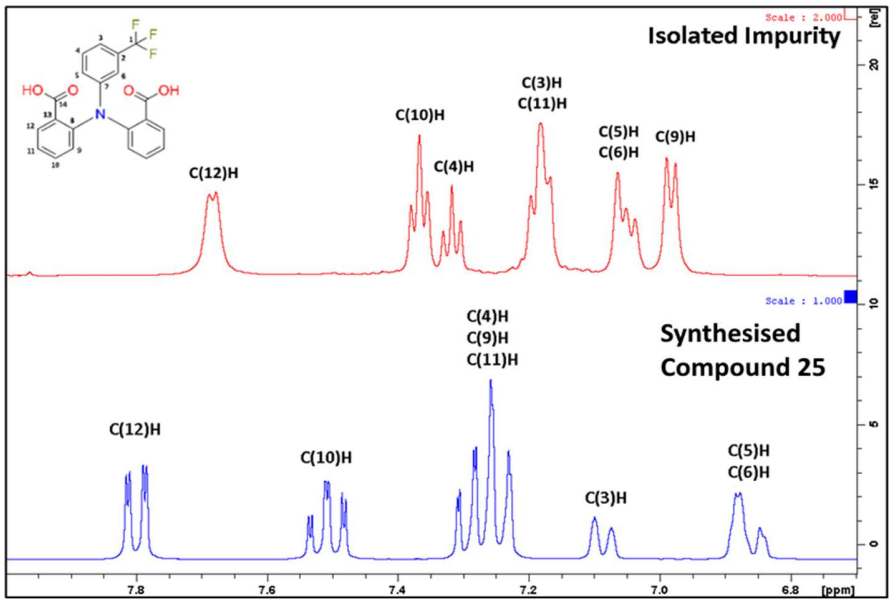


Fig 3.35. Comparison between the ^{1}H NMR aromatic regions of the isolated impurity (top) and the synthesised compound **25** (bottom).

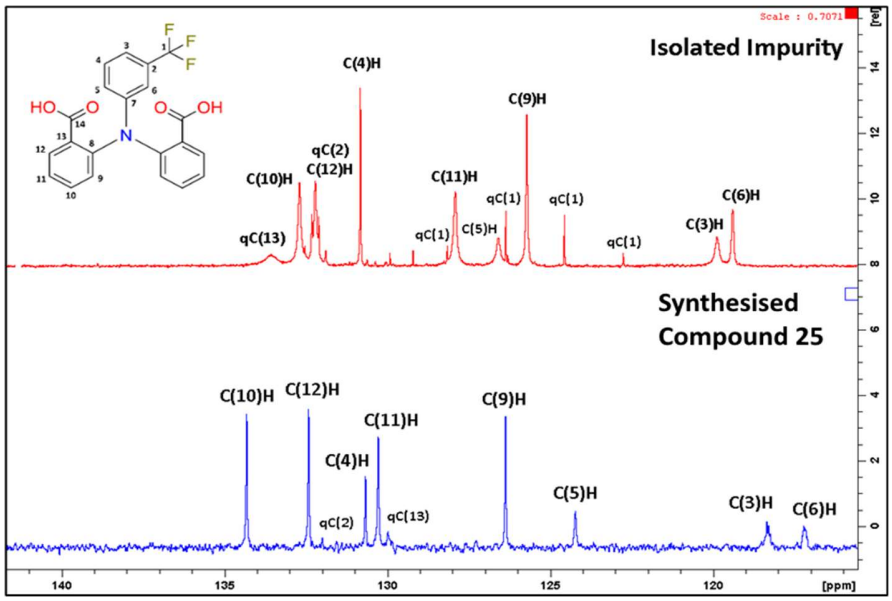


Fig 3.36. Comparison between the ^{13}C NMR aromatic regions of the isolated impurity (top) and the synthesised compound **25** (bottom).

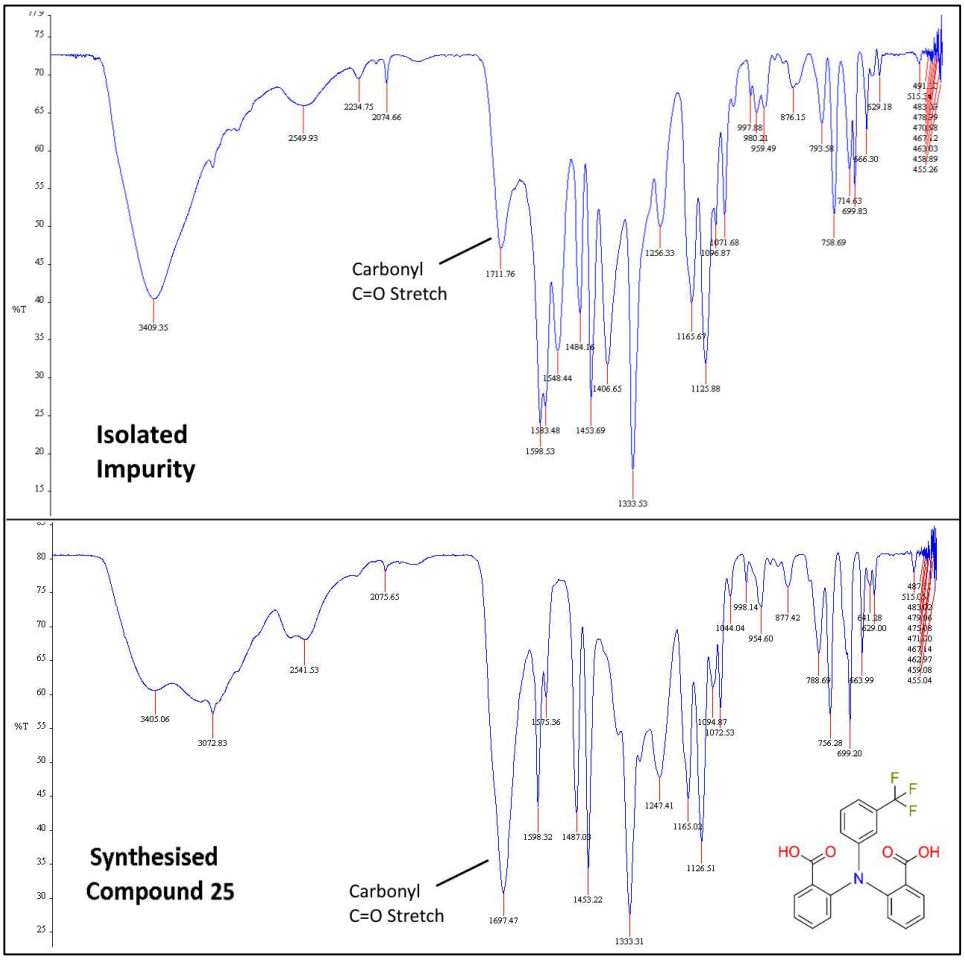


Fig 3.37. Comparison between the IR spectra of the isolated impurity (top) and the synthesised compound **25** (bottom), with a focus on the respective intensities of the carbonyl C=O stretch.

3.4.5 Possible Alternative Structure of Isolated Impurity

A possible alternative identity for the isolated impurity is the acridone triaryl by-product 10-(3-(trifluoromethyl)phenyl)acridin-9(10H)-one **28** (Figure 3.38). Such a material would appear very similar in terms of NMR analysis to compound **25**, with comparable peak intensities and splitting, but different chemical shifts. A quaternary carbon peak at a chemical shift very similar to one observed in the ^{13}C NMR analysis of

the isolated impurity (approx. 173 ppm) was reported for multiple compounds with very similar structures to compound **28**.[209] Additionally, another source reports a medium intensity IR peak for similar compounds at approx. 1638 cm^{-1} corresponding to the acridone C=O stretch, matching the unexpectedly low intensity of the signal observed in the same region of the isolated impurity spectrum.[210] A second MS scan of the isolated impurity also identified a signal corresponding to the ionised mass of compound **28**, this time with a significantly higher intensity (Appendix Figure 7.68).

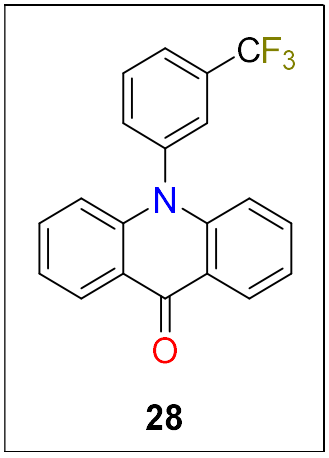


Fig 3.38. Structure of 10-(3-(trifluoromethyl)phenyl)acridin-9(10H)-one compound **28**, a suggested identity of the unknown synthetic impurity observed in the synthesis of FFA.

Although impossible to confirm without synthesising it independently for comparison, the spectral analysis suggests that the acridone triaryl compound **28** is more likely to be the identity of the isolated impurity than the diacid triaryl compound **25**. Full spectral analysis of the isolated impurity can be found in this section and in the Appendix, with assignments based on the structure of compound **25** in Figures 3.30 – 3.32 and

Appendix Section 7.8.2, and those based on the structure of compound **28** in Appendix Section 7.8.3.

However, it is also possible that the signal observed in the crude FFA product was in fact a mixture of both the diacid triaryl compound **25** and the acridone triaryl compound **28** in an unknown ratio. As the retention times between the two are so similar, being indistinguishable by UHPLC under the employed conditions, the different species would likely not appear distinct on the HPLC trace of the crude FFA product. It is possible that during isolation *via* column chromatography, only compound **28** was isolated due to the higher polarity (and, thus, higher retention factor on the silica) of the diacid compound **25**. The low level of material recovery from the chromatography process, and the trace amount of compound **25** identified by MS in the isolated impurity sample would support this explanation.

To fully characterise the isolated species and definitively determine the nature of the observed impurity, more research would need to be carried out. However, as such, information is not vital to the goals of the project, such research was considered outside the scope of the work and the investigation was not pursued further. The behaviour of the synthesised compound **25** as an additive in systems of FFA will be investigated in Section 4.3.1.5.

3.5 Conclusion

In this chapter, a number of routes towards the synthesis of FFA and related compounds were attempted. These routes either proceeded *via* the Ullmann-Goldberg condensation or Buchwald-Hartwig amination mechanisms, coupling an ortho-halogenated benzoic acid with a meta-substituted aniline in the presence of a copper or palladium catalyst respectively. After experimentation, it was determined that a metallic copper-catalysed Ullmann-Goldberg coupling described by Pellón *et al.* was the most efficient and high-yielding method tested.[127] The method was used to produce FFA material, as well as the five structurally-similar analogues chosen to act as additives in other areas of the research, compounds **15** – **19**. The products of each synthetic reaction were analysed and fully characterised by HPLC, MS, IR, DSC, PXRD, TGA, and various forms of NMR analysis. In addition, a synthetic impurity observed in the production of FFA was isolated. Characterisation data was obtained on an isolated sample of this impurity and independent synthesis of 2,2'-((3-(trifluoromethyl)phenyl)azanediyl)dibenzoic acid **25**, a candidate structure of for the impurity, was carried out. The majority of the data obtained on that material was consistent with that of the isolated impurity but differences in the observed NMR and IR data led to the proposal of an alternative structure, 10-(3-(trifluoromethyl)phenyl)acridin-9(10H)-one **28**. It is possible both compounds **25** and **28** were forming during the synthesis of FFA, but a definitive conclusion was not reached.

3.6 Experimental

3.6.1 Instrument Details and Analytical Methodologies

3.6.1.1 High-Performance Liquid Chromatography (HPLC)

The details of the HPLC instrument and column can be found in Section 2.8.1.1. Method parameters can be found in Section 2.8.1.2.

3.6.1.2 Nuclear Magnetic Resonance (NMR)

^{1}H NMR spectra were recorded at either 300 MHz on a Bruker AVANCE 300 NMR spectrometer or at 400 MHz on a Bruker AVANCE 400 NMR spectrometer unless otherwise stated. ^{13}C NMR spectra were recorded at either 75.5 MHz on a Bruker AVANCE 300 NMR spectrometer or at 100.6 MHz on a Bruker AVANCE 400 NMR spectrometer unless otherwise stated. ^{1}H (600 MHz) and ^{13}C (150.9 MHz) NMR spectra were recorded on a Bruker AVANCE 600 NMR spectrometer. Spectra were recorded in deuterated methanol (MeOD) or deuterated chloroform ($CDCl_3$) depending on the solubility profile of the analyte. Chemical shifts (δ_H and δ_C) are reported in parts per million (ppm) relative to TMS and coupling constants (J) are expressed in Hertz (Hz). Splitting patterns in spectra are labelled as s (singlet), bs (broad singlet), d (doublet), t (triplet), q (quartet), dd (doublet of doublets), ddd (doublet of doublet of doublets), and m (multiplet). NMR spectra were calibrated using the solvent signals. Two-dimensional NMR experiments (i.e., COSY) were used to aid assignments where necessary. For previously synthesised compounds, spectroscopic details agreed with reported values unless specifically stated otherwise.

3.6.1.3 Infrared (IR) Analysis

IR spectra were recorded on a Perkin Elmer Spectrum 100 FT-IR Spectrometer using a sodium chloride disc. A small amount of the solid sample was dissolved in a volatile solvent (e.g., acetone), and the solution applied to the surface of a sodium chloride disc. The solvent was evaporated under a heat lamp, depositing the sample as a thin film on the surface of the disc.

3.6.1.4 Mass Spectrometry (MS)

Nominal mass spectra were recorded on a Waters Quattro Micro Triple Quadrupole Spectrometer (QAA1202) in ESI mode using 50:50 acetonitrile / water containing 0.1% formic acid as an eluent. High resolution mass spectra (HRMS) were recorded on a Waters LCT Premier Time of Flight spectrometer (KD160) or a Waters Vion IMS Mass Spectrometer (SAA0 55K) in ESI mode using 50:50 acetonitrile / water containing 0.1% formic acid as an eluent. Mass spectrometry samples were prepared in acetonitrile.

3.6.1.5 Powder X-Ray Diffraction (PXRD)

The details of the PXRD instrument and the method parameters used can be found in Section 2.8.5.

3.6.1.6 Differential Scanning Calorimetry (DSC)

The details of the DSC instrument can be found in Section 2.8.7.1. Ramping was carried out from approx. 15 °C to 180 °C in aluminium pans at a heating rate of 10 °C min^{-1}. Mass of samples was maintained between 2 – 5 mg.

3.6.1.7 Thermogravimetric Analysis (TGA)

The details of the TGA instrument and the method parameters used can be found in Section 2.8.8.

3.6.2 Synthetic Methodologies

Synthetic reactions were carried out in a fume hood. When heating was required, the reaction flask was immersed in an oil bath or DrySyn® heating block on an IKA RCT Basic® hot plate, which was controlled at the desired temperature using the included probe.

3.6.2.1 Ullmann-Goldberg Condensation 1

The synthesis was adapted from the method described by Mei *et al.*[126] 2-Chlorobenzoic acid **20** (1.38 g, 8.83 mmol) and the desired substituted aniline (9.30 mmol) were added to a 100 mL round-bottom flask (rbf) with potassium carbonate (1.22 g, 8.83 mmol), metallic copper (49.6 mg, 0.78 mmol), copper(I) oxide (50.1 mg, 0.35 mmol) and *N*,*N*-dimethylformamide (6 mL). The solvent was later exchanged for anhydrous *N*,*N*-dimethylformamide (6 mL). The reaction mixture was heated to 130 °C under inert conditions (N_2) for 24 hours. The mixture was cooled, then poured into 30 mL deionised water. Activated charcoal (c. 1 g) was added and the mixture was filtered through Celite®. 1M hydrochloric acid was added slowly until a precipitate formed, which was then isolated by vacuum filtration. The precipitate was redissolved in 5% v/v aqueous sodium carbonate (100 mL) and filtered again through Celite®. 1M hydrochloric acid was added to lower the pH to 7 – 8, and the resulting precipitate was isolated by vacuum filtration and dried on a high vacuum line.

3.6.2.2 Ullmann-Goldberg Condensation 2

The synthesis was adapted from the method described by Pellón *et al*.[127] 2-Chlorobenzoic acid **20** (1.25 g, 8 mmol) was added to a 100 mL rbf with potassium carbonate (0.55 g, 4 mmol) and metallic copper (40 mg, 0.63 mmol). The flask was flushed with N_2 gas. The desired substituted aniline (16 mmol) and anhydrous *N*,*N*-dimethylformamide (5 mL) were added through a septum. The reaction was refluxed at 155 °C for 4 hours. The reaction mixture was cooled, then slowly added to 1:1 aqueous hydrochloric acid (20 mL with washings) and allowed to stand overnight. The precipitate was isolated *via* vacuum filtration and rinsed with dilute hydrochloric acid. The solid was redissolved in ethyl acetate, activated charcoal (*c*. 1 g) added, and the mixture filtered through Celite®. The filtrate was extracted with boiling water (3 x 30 mL) and dried over anhydrous magnesium sulfate. The solvent was removed by rotary evaporation to isolate the crude product.

3.6.2.3 Buchwald-Hartwig Amination 1

The synthesis was adapted from the method described by Schuster *et al*.[128] A solution of 2-bromobenzoic acid **22** (169.66 mg, 0.88 mmol) in toluene (5 mL) was added slowly to a solution of 3-trifluoromethyl aniline **21** (162.7 mg, 0.126 mL, 1.01 mmol), caesium carbonate (416 mg, 1.28 mmol), palladium(II) acetate (11.3 mg, 50.3 μmol), and triphenylphosphine (13.22 mg, 50.4 μmol) in toluene (15 mL) through a septum over the course of 3.5 hours at 115 °C under inert conditions (N_2). After a further 20 hours at reflux, the mixture was allowed to cool, and the solvent was removed by rotary evaporation to isolate the crude product.

3.6.2.4 Buchwald-Hartwig Amination 2

The synthesis was adapted from the method described by Albaugh *et al.*[129] 2-Bromobenzoic acid **22** (325.7 mg, 1.62 mmol) and *m*-toluidine (174.0 mg, 0.178 mL, 1.62 mmol) were added to a 100 mL rbf with caesium carbonate (0.74 g, 2.27 mmol), palladium(II) acetate (7.27 mg, 32.4 μmol), Xantphos (28.12 mg, 48.6 μmol) and anhydrous 1,4-dioxane (5 mL). The mixture was heated to 110 °C overnight under inert conditions (N_2). The reaction mixture was allowed to cool, filtered through Celite® and concentrated by rotary evaporation to isolate the crude product.

3.6.3 Purification Techniques

3.6.3.1 Recrystallisation

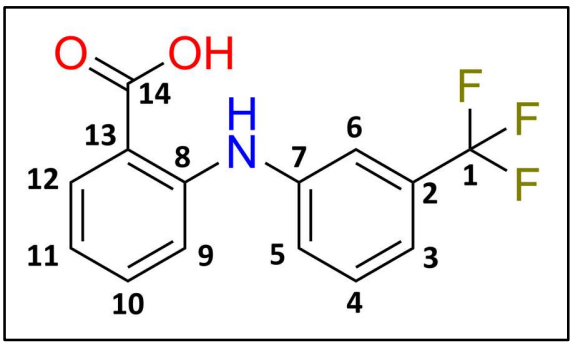
Recrystallisation of products was performed by dissolving the crude material in the minimum volume of the chosen solvent (EtOAc, DCM, or toluene) required to achieve complete dissolution at the boiling point of that solvent. The solution was removed from the heat and allowed to cool to room temperature. The resulting precipitate was isolated by vacuum filtration in a Hirsch funnel, with washings of ice-cold recrystallisation solvent, and dried further on a high-vacuum line.

3.6.3.2 Column Chromatography

Wet flash chromatography was carried out using silica gel 60 Å, 200 – 425 mesh particle size (Sigma Aldrich). The sample was prepared by dissolution in DCM and slurrying with Celite®. An eluent of 5% v/v MeOH in DCM was used initially. The concentration of MeOH was increased gradually to a maximum of 10% v/v over the course of the purification, with the addition of 1% v/v acetic acid in the later stages. Compounds were isolated from fractions by rotary evaporation.

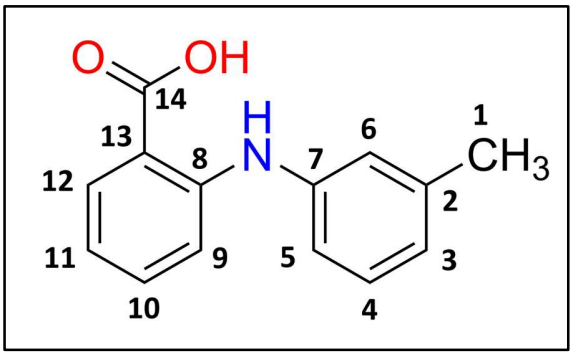
3.6.4 Compound Characterisation

3.6.4.1 Flufenamic Acid **14** (FFA)



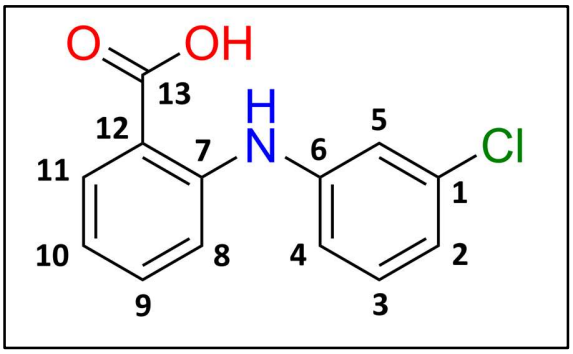
Yellow, needle-like crystals; m.p. 124.3-126.5 °C, solidifying and remelting at 133.0-134.6 °C (lit.[130] 124-125 °C, solidifying and remelting at 134.0-136 °C); IR ν_{max} (cm^{-1}) (NaCl) 3333 (amine N-H stretch), 2927 (acid O-H stretch), 1666 (acid C=O stretch), 1582 (ar. C-C stretch), 1524 (amine N-H bend), 1454 (acid O-H bend), 1330, 1122 (C-F stretches), 1255, 1164 (C-N stretches), 908, 795, 746, 697 (ar. C-H bends); ^{1}H NMR 300 MHz, δ_H (MeOD) 6.80-6.86 (1H, ddd, *J* 7.8, 7.8, 1.7 Hz, C(11)*H*), 7.27-7.30 (2H, m, C(5)*H* and C(9)*H*), 7.36-7.42 (1H, ddd, *J* 7.8, 7.8, 1.7 Hz, C(10)*H*), 7.43-7.51 (3H, m, C(3)*H* and C(4)*H* and C(6)*H*), 8.00-8.03 (1H, ddd, *J* 7.8, 1.7, 0.4 Hz, C(12)*H*), O*H* and N*H* signals not observed; ^{13}C NMR 75.5 MHz, δ_C (MeOD) 114.98 (*C*(13)), 115.47 (*C*(9)H), 117.96-118.11 (q, *J* 3.9 Hz, *C*(6)H), 119.57 (*C*(11)H), 119.92-120.07 (q, *J* 3.9 Hz, *C*(3)H), 120.12-130.91 (q, *J* 271.4 Hz, *C*(1)F_3), 125.08 (*C*(5)H), 131.31 (*C*(4)H), 132.17-133.44 (q, *J* 32.1 Hz, *C*(2)), 133.43 (*C*(12)H), 135.15 (*C*(10)H), 143.51 (*C*(7)), 147.76 (*C*(8)), 171.61 (*C*(14)); HPLC retention time 2.19 min, 1.0 relative to FFA; m/z (ESI+): 282.2, $[M+H]^+$, m/z (ESI-): 280.3 $[M-H]^-$, HRMS: $C_{14}H_{10}F_3NO_2$, Predicted m/z 282.073640, Measured m/z 282.07316 $[M+H]^+$, i-FIT Confidence (%) 99.941231.

3.6.4.2 2-(*m*-Tolylamino)benzoic acid **15** (Me-FA)



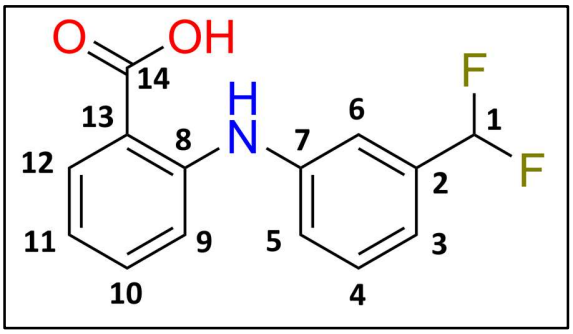
Yellow, needle-like crystals; m.p. 136.6-139.3 °C (lit.[211] 136-137 °C); IR ν_{max} (cm^{-1}) (NaCl) 3341 (amine N-H stretch), 3038, 2639 (alkyl C-H stretches), 2921 (acid O-H stretch), 1661 (acid C=O stretch), 1577 (ar. C-C stretch), 1515 (amine N-H bend), 1452 (acid O-H bend), 1243, 1162 (C-N stretches), 901, 779, 747, 694, 649 (ar. C-H bends); ^{1}H NMR 300 MHz, δ_H (MeOD) 2.34 (3H, s, C(1)*H*$_3$), 6.71-6.76 (1H, t, *J* 7.8 Hz, C(11)*H*), 6.87-6.90 (1H, d, *J* 7.8 Hz, C(5)*H*), 7.00-7.02 (2H, m, C(3)*H* and C(6)*H*), 7.20-7.25 (2H, m, C(9)*H* and C(10)*H*), 7.36-7.42 (1H, ddd, *J* 7.8, 7.8 1.2 Hz, C(4)*H*), 7.97-8.00 (1H, dd, *J* 7.8, 1.2 Hz, C(12)*H*), O*H* and N*H* signals not observed; ^{13}C NMR 100.6 MHz, δ_C (MeOD) 21.51 (*C*(1)H$_3$), 113.40 (*C*(13)), 114.97 (*C*(9)H), 118.03 (*C*(5)H), 120.15 (*C*(11)H), 123.80 (*C*(6)H), 125.25 (*C*(3)H), 130.25 (*C*(4)H), 133.28 (*C*(12)H), 135.10 (*C*(10)H), 140.47 (*C*(2)), 142.17 (*C*(7)), 149.44 (*C*(8)), 171.88 (*C*(14)); HPLC retention time 1.70 min, 0.78 relative to FFA; m/z (ESI+): 228.3 $[M+H]^+$, HRMS: $C_{14}H_{13}NO_2$, Predicted m/z 228.101905, Measured m/z 228.10167 $[M+H]^+$, i-FIT Confidence (%) 100.000000.

3.6.4.3 *N*-(3-Chlorophenyl)anthranilic acid **16** (Cl-FA)



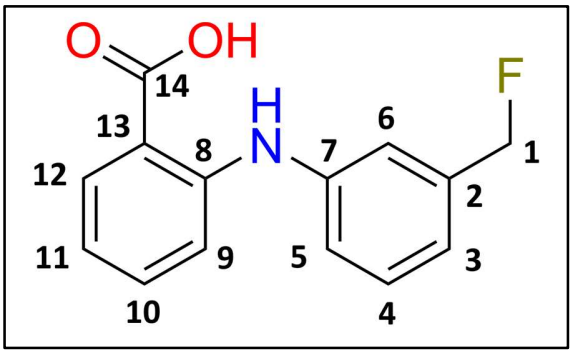
Sand-coloured powder; m.p. 169.5-169.9 °C (lit.[211] 171-173°C); IR ν_{max} (cm^{-1}) (NaCl) 3332 (amine N-H stretch), 2922 (acid O-H stretch), 1669 (acid C=O stretch), 1587 (ar. C-C stretch), 1518 (amine N-H bend), 1449 (acid O-H bend), 1258, 1238, 1155 (C-N stretches), 1150-1000 (ar. C-Cl stretches) 925, 890, 767, 744, 680 (ar. C-H bends); ^{1}H NMR 300 MHz, δ_H (MeOD) 6.80-6.85 (1H, t, *J* 7.6 Hz, C(10)*H*), 7.00-7.03 (1H, dd, *J* 8.0, 1.0 Hz, C(4)*H*), 7.12-7.14 (1H, dd, *J* 8.0, 1.0 Hz, C(2)*H*), 7.21 (1H, s, C(5)*H*), 7.26-7.32 (2H, m, C(8)*H* and C(9)*H*), 7.36-7.41 (1H, t, *J* 8.0 Hz, C(3)*H*), 7.98-8.01 (1H, d, *J* 7.6 Hz, C(11)*H*), O*H* and N*H* signals not observed; ^{13}C NMR 100.6 MHz, δ_C (MeOD) 114.08 (*C*(12)), 114.89 (*C*(8)H), 118.62, 118.82 (*C*(4)H and *C*(10)H), 119.82 (*C*(5)H), 122.15 (*C*(2)H), 130.96 (*C*(3)H), 131.91 (*C*(11)H), 133.82 (*C*(1)Cl), 134.14 (*C*(9)H), 142.65 (*C*(6)), 145.69 (*C*(7)), 169.70 (*C*(13)); HPLC retention time 1.89 min, 0.86 relative to FFA; m/z (ESI+): 248.2 $[M+H]^+$, m/z (ESI-): 246.3 $[M-H]^-$, HRMS: $C_{13}H_{10}ClNO_2$, Predicted m/z 248.047283, Measured m/z 248.04743 $[M+H]^+$, i-FIT Confidence (%) 100.000000.

3.6.4.3 2-[3-(Difluoromethyl)anilino]benzoic acid **17** (DF-FA)



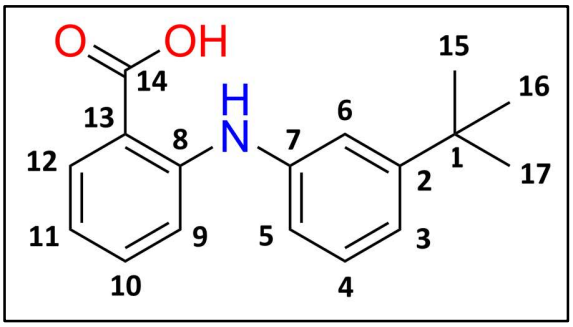
Sand-coloured or brown needles; m.p. 141.4-142.5 °C (no lit. m.p. available); IR ν_{max} (cm^{-1}) (NaCl) 3336 (amine N-H stretch), 2928 (acid O-H stretch), 2473, 2231, 2064 (alkyl C-H stretches), 1665 (acid C=O stretch), 1560 (ar. C-C stretch), 1495 (amine N-H bend), 1447 (acid O-H bend), 1373 (C-F stretch), 1257, 1164 (C-N stretches), 899, 762, 741, 690, 649 (ar. C-H bends); ^{1}H NMR 300 MHz, δ_H (MeOD) 6.53-6.90 (1H, t, *J* 56.3 Hz, C(1)*H*F_2), 6.76-6.82 (1H, ddd, *J* 7.5, 7.5, 1.2 Hz, C(11)*H*), 7.18-7.21 (1H, dd, *J* 7.5, 1.2 Hz, C(9)*H*), 7.25-7.28 (1H, dd, *J* 8.5, 1.0 Hz, C(5)*H*), 7.31-7.45 (4H, m, C(3)*H* and C(4)*H* and C(6)*H* and C(10)*H*), 7.98-8.01 (1H, dd, *J* 7.5, 1.2 Hz, C(12)*H*), O*H* and N*H* signals not observed; ^{13}C NMR 75.5 MHz, δ_C (MeOD) 112.98-119.27 (t, *J* 237.2 Hz, *C*(1)HF_2), 114.32 (*C*(13)), 115.20 (*C*(9)H), 119.02-119.27 (*C*(11)H and t, *J* 6.1 Hz, *C*(6)H), 120.80-120.96 (t, *J* 6.1 Hz, *C*(3)H), 124.29-124.65 (t, *J* 2.0 Hz, *C*(5)H), 130.96 (*C*(4)H), 133.36 (*C*(12)H), 135.13 (*C*(10)H), 137.13-137.72 (t, *J* 22.3 Hz, *C*(2)), 143.03 (*C*(7)), 148.31 (*C*(8)), 171.71 (*C*(14)); HPLC retention time 1.31 min, 0.60 relative to FFA; m/z (ESI+): 264.3 $[M+H]^+$, m/z (ESI-): 262.3 $[M-H]^-$, HRMS: $C_{14}H_{11}F_2NO_2$, Predicted m/z 264.083061, Measured m/z 264.08265 $[M+H]^+$, i-FIT Confidence (%) 100.000000.

3.6.4.5 2-[3-(Fluoromethyl)anilino]benzoic acid **18** (MF-FA)



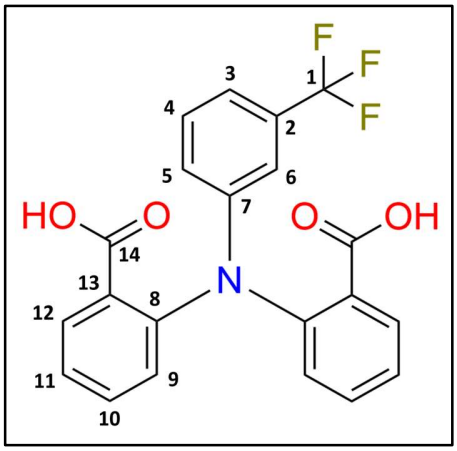
Yellow powder; m.p. 154.6-157.9 °C (no lit. m.p. available); IR ν_{max} (cm^{-1}) (NaCl) 3337 (amine N-H stretch), 2965 (acid O-H stretch), 2640, 2566, 2474 (alkyl C-H stretches), 1670 (acid C=O stretch), 1580 (ar. C-C stretch), 1521 (amine N-H bend), 1450 (acid O-H bend), (C-F stretch), 1244, 1162 (C-F and C-N stretches, overlapping), 965, 892, 742, 693, 656 (ar. C-H bends); ^{1}H NMR 300 MHz, δ_H (MeOD) 5.25-5.41 (2H, d, *J* 47.8 Hz, C(1)*H*$_2$F), 6.72-6.78 (1H, ddd, *J* 7.5, 7.5, 1.3 Hz, C(11)*H*), 7.05-7.08 (1H, dd, *J* 7.5, 1.3 Hz, C(9)*H*), 7.19-7.26 (3H, m, C(3)*H* and C(5)*H* and C(6)*H*), 7.30-7.37 (2H, m, C(4)*H* and C(10)*H*), 7.97-8.00 (1H, dd, *J* 7.5, 1.3 Hz, C(12)*H*), O*H* and N*H* signals not observed; ^{13}C NMR 75.5 MHz, δ_C (MeOD) 84.14-86.34 (d, *J* 165.3 Hz, *C*(1)H$_2$F), 113.95 (*C*(13)), 115.04 (*C*(9)H), 118.53 (*C*(11)H), 121.43-121.51 (d, *J* 6.1 Hz, *C*(6)H), 120.70-120.74 (d, *J* 2.8 Hz, *C*(5)H), 123.05-123.13 (d, *J* 6.1 Hz, *C*(3)H), 130.67-130.68 (d, *J* 1.1 Hz, *C*(4)H), 133.29 (*C*(12)H), 135.08 (*C*(10)H), 139.31-139.54 (d, *J* 17.1 Hz, *C*(2)), 142.67 (*C*(7)), 148.80 (*C*(8)), 171.81 (*C*(14)); HPLC retention time 1.14 min, 0.52 relative to FFA; m/z (ESI+): 246.3 $[M+H]^+$, m/z (ESI-): 244.3 $[M-H]^-$, HRMS: $C_{14}H_{12}FNO_2$, Predicted m/z 246.092483, Measured m/z 246.09143 $[M+H]^+$, i-FIT Confidence (%) 100.000000.

3.6.4.6 2-((3-(*tert*-Butyl)phenyl)amino)benzoic acid **19** (t-Bu-FA)



Pale yellow powder; m.p. 153.1-154.0 °C (lit.[212] 151-153 °C); IR ν_{max} (cm^{-1}) (NaCl) 3349 (amine N-H stretch), 2963 (acid O-H stretch), 2869, 2638, 2563 (alkyl C-H stretches), 1661 (acid C=O stretch), 1575 (ar. C-C stretch), 1514 (amine N-H bend), 1452 (acid O-H bend), 1246, 1162 (C-N stretches), 891, 782, 748, 700, 653 (ar. C-H bends); ^{1}H NMR 400 MHz, δ_H (MeOD) 1.30 (9H, s, C(15)*H*$_3$ and C(16)*H*$_3$ and C(17)*H*$_3$), 6.68-6.72 (1H, ddd, *J* 7.5, 7.5, 1.4 Hz, C(11)*H*), 7.02-7.04 (1H, d, *J* 7.8 Hz, C(5)*H*), 7.10-7.12 (1H, d, *J* 7.8 Hz, C(3)*H*), 7.17-7.31 (4H, m, C(4)*H* and C(6)*H* and C(9)*H* and C(10)*H*), 7.96-7.98 (1H, dd, *J* 7.5, 1.4 Hz, C(12)*H*), O*H* and N*H* signals not observed; ^{13}C NMR 100.6 MHz, δ_C (MeOD) 31.72 (*C*(15)H$_3$ and *C*(16)H$_3$ and *C*(17)H$_3$), 35.50 (*C*(1)) 113.26 (*C*(13)), 114.76 (*C*(9)H), 117.89 (*C*(6)H), 120.32-120.55 (*C*(3)H and *C*(11)H), 121.62 (*C*(5)H), 130.04 (*C*(4)H), 133.28 (*C*(12)H), 135.05 (*C*(10)H), 141.84 (*C*(7)), 149.58 (*C*(8)), 153.82 (*C*(2)), 171.87 (*C*(14)); HPLC retention time 4.68 min, 2.14 relative to FFA; HRMS: $C_{17}H_{19}NO_2$, Predicted m/z 270.148855, Measured m/z 270.14833 $[M+H]^+$, i-FIT Confidence (%) 100.000000.

3.6.4.7 2,2'-((3-(Trifluoromethyl)phenyl)azanediyl)dibenzoic acid **25**



White powder; m.p. 221.4-229.3 °C (no lit. m.p. available); IR ν_{max} (cm^{-1}) (NaCl) 3405 (amine N-H stretch), 3073, 2542 (acid O-H stretches), 1697 (acid C=O stretch), 1598 (ar. C-C stretch), 1487 (amine N-H bend), 1453 (acid O-H bend), 1333, 1127 (C-F stretches), 1247, 1165 (C-N stretches), 955, 789, 756, 699, 664 (ar. C-H bends); ^{1}H NMR 300 MHz, δ_H (MeOD) 6.85-6.88 (2H, m, C(5)*H* and C(6)*H*), 7.07-7.10 (1H, d, *J* 7.7 Hz, C(3)*H*), 7.23-7.31 (5H, m, C(4)*H* and C(9)*H* and C(11)*H*), 8.00-8.03 (2H, td, *J* 7.7, 1.6 Hz, C(10)*H*), 7.78-7.81 (2H, dd, *J* 7.7, 1.6 Hz, C(12)*H*), O*H* and N*H* signals not observed; ^{13}C NMR 75.5 MHz, δ_C (MeOD) 115.75-115.90 (q, *J* 3.8 Hz, *C*(6)H), 116.88-117.03 (q, *J* 3.8 Hz, *C*(3)H), 118.71-129.51 (q, *J* 271.5 Hz, *C*(1)F_3), 122.86 (*C*(5)H), 125.00 (*C*(9)H), 128.61 (*C*(13)), 128.91 (*C*(11)H), 129.30 (*C*(4)H), 130.18-131.47 (q, *J* 32.0 Hz, *C*(2)), 131.05 (*C*(12)H), 132.95 (*C*(10)H), 145.75 (*C*(8)), 149.34 (*C*(7)), 168.84 (*C*(14)); HPLC retention time 1.14 min, 0.52 relative to FFA; m/z (ESI+): 402.1 $[M+H]^+$, m/z (ESI-): 400.2 $[M-H]^-$, HRMS: $C_{21}H_{14}F_3NO_4$, Predicted m/z 402.094769, Measured m/z 402.09497 $[M+H]^+$, i-FIT Confidence (%) 99.886595.

Behaviour of Doped Systems

4.1 Introduction

In order to develop methods of mapping the distribution of impurities within crystals of an API, appropriate models of study must be produced, and their behaviour investigated and characterised. The models selected for this project consist of an API host, flufenamic acid **14** (FFA), doped with structurally-similar additives (compounds **15** – **19**) intended to incorporate into crystals of the host, with the potential to replace molecules of FFA within the crystal lattice. Systems doped with compounds **15** – **18** were intended to produce crystals of impure FFA **14**, the additives within which are likely to be resistant to removal by traditional purification techniques such as recrystallisation. Compound **19** (t-Bu-FA) was chosen as a less lattice-compatible additive to provide contrast.

In this chapter, the process of producing and analysing these doped systems will be discussed. The behaviour of the additives in the systems will be explored and compared, and their similarities to solid solutions assessed. The level of additive incorporation into the FFA crystal will be investigated by comparing the level of additive in a batch of crystal material to the level measured in the solution from which the crystals were grown. The level of incorporation at low doping levels and higher doping levels is compared. The resistance of the additives to rejection is evaluated through a series of purification stages by recrystallisation from toluene. The appearance and crystal structure of doped FFA systems will be compared to undoped counterparts.

The phase behaviour of systems doped with two of the additives (Me-FA **15** and Cl-FA **16**) individually will be investigated by PXRD and DSC analysis, and binary phase diagrams constructed to categorise the mixed systems. For the majority of systems studied

as part of this project, the level of additive included remained below 6%. In line with the goals of the research, this was to more closely reflect the level of impurity most commonly encountered in batches of drug products.[17] All percentage values of additive level listed can be considered molar percentages (mol%); this metric was chosen over percentage mass or other units to account for the difference in molecular mass between each additive, and between the additives and the host.

A note about the terminology used in this chapter and the text in general, specifically relating to the terms “doping level” and “level of incorporation”. “Doping level” refers to the level of additive included in the solution from which a crystal batch is grown at the moment it is created. This level is determined by HPLC analysis of a sample taken from that doped solution at its creation and is independent of any crystallisation behaviour. “Level of incorporation” or any variation of that term, is the amount of additive measured in a crystal sample. This value is measured by HPLC analysis of the dissolved crystal sample of interest and is dependent on a number of factors including additive and host structure, solvent, and method of crystallisation. The level of incorporation can be compared to the doping level of the system to make observations related to the incorporation behaviour of the additives.

4.2 Creating Doped Systems

Systems of FFA doped with additives were produced by dissolving known masses of the relevant materials in a suitable solvent, followed by the evaporation of that solvent under ambient conditions. EtOH was chosen for this process as the materials were highly

soluble in this solvent. Additionally, the solvent volatility was high enough that full evaporation of most samples could often be achieved overnight in a fume cupboard, but low enough that the concentration of the solution would not change significantly during sample preparation, which could lead to variability in doping level. Doped material would generally be produced in the form of a powder cake or small acicular crystals before being subjected to a previously developed crystallisation method. Full details of this process are described in the experimental section later in the chapter (Section 4.9.1).

4.2.1 HPLC Response Factor Correction

The level of additive in a given doped sample could be determined using HPLC analysis. A method is described in Section 2.8.1.2 that provides HPLC traces with sufficient separation between the peaks of FFA and each of the additives a solution of FFA might be doped with. A close measure of the level of additive present in a two-component sample is displayed as part of a HPLC report as the percentage area under the curve for the additive peak (e.g., Figure 4.1). HPLC is a highly sensitive method of quantitative analysis, and the peak area for a single component trace can be used to reliably determine the concentration of the corresponding material in a sample. However, complications arise when a second component is introduced to the sample. The detector responds to different materials to slightly different extents, which can be quantified as an RF unique to each material using a given HPLC configuration.[213] The software does not take the difference in RFs into account when determining the peak area percentage figure for each component.

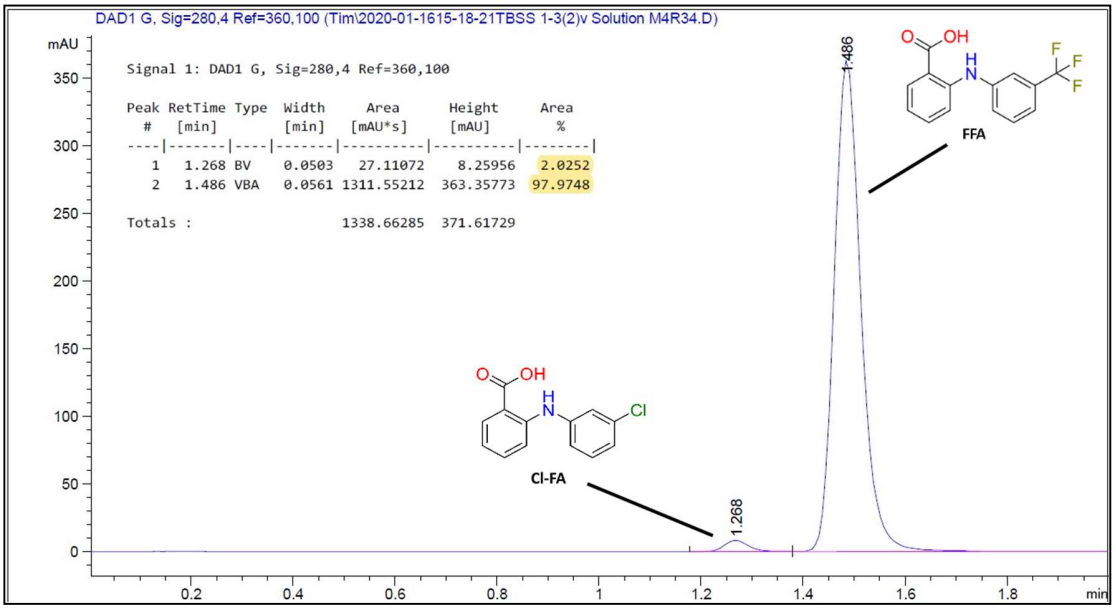


Fig 4.1. HPLC trace of FFA **14** (right peak) doped with Cl-FA **16** (left peak), with software-generated peak information, collected at 280 nm.

As the compounds being tested as part of these systems are so structurally similar, the difference in RFs and, thus, the degree by which the presented area percent value is inaccurate for one analyte is relatively low. However, it can still be corrected by use of a simple formula, noted below in Formula 4.1.[214] This formula takes into account the concentrations of the two analytes in solution, the area under each analyte peak on the HPLC trace, and the relative response factor (RRF), the division of the response factor of one analyte by the response factor of the other. A detailed description of the correction process can be found in Section 4.9.2. As an example, the sample in Figure 4.1 was determined in this manner to contain 2.10% Cl-FA **16**, as opposed to the 2.03% value calculated by the software.

Formula 4.1. $$Concentration\ A = \frac{Peak\ Area\ A}{Peak\ Area\ B} \times \frac{1}{RRF} \times Concentration\ B$$

As the interest in this project lay in the relationship between FFA **14** and each of the additives individually, FFA **14** was designated as Analyte *B* while the additive of interest would be labelled Analyte *A* to maintain consistency between systems. The concentration of an analyte in a multi-component solution is not always known but can be determined using the material's calibration curve. The actual values used for both concentrations in Formula 4.1 are immaterial for the purpose of this work; it is the concentration of one analyte relative to the other that is of interest, a value that remains constant regardless of the concentrations of individual components. Unlike peak areas and RF values, the RRF for two analytes remains constant or at least comparable despite changing conditions such as alterations to mobile phase, temperature, or column type. As such, this form of data processing is valuable in its ability to ensure HPLC outputs remain repeatable and/or comparable.

4.3 Crystal Incorporation Levels of Additives

The level of additive in a number of crystals grown from doped solutions of FFA **14** was plotted against the doping level in solution to investigate the extent to which each additive incorporates into the crystals. This comparison does not provide any information into the distribution of the additives within the crystal body, or the means of incorporation (e.g., even dispersion, surface adsorption, pockets of additive inclusion, etc); that aspect will be explored in Chapter 5. However, when viewed alongside the results from other investigations into the solid-state behaviour of these materials as detailed later in the chapter, it can provide insight into the ability of a molecule of the additive to integrate

into the host crystal. Additionally, the ideas surrounding additive inclusion discussed in Chapter 2 (i.e., effect of additive substituent size and relative solubilities) can be examined further in this section with empirical data.

Crystal samples were produced by evaporation from MeOH. These samples consisted of FFA **14** doped with varying levels of each additive individually. As discussed previously, this work is primarily focused on low doping levels with a maximum of approximately 6% additive, comparable with the levels of impurities found in pharmaceutical processes. Systems were produced containing higher levels of Me-FA **15** and Cl-FA **16** for the purposes of constructing phase diagrams; these systems were doped with 10 – 90% of each additive. Similar systems were not produced for the other additives due to limitations on the amount of accessible material. Full experimental details can be found in Section 4.9.1.

4.3.1 Results

Table 4.1 displays the average ratio of additive level in the crystal samples to doping level of the same sample. These averages are calculated from the doping levels and additive incorporation levels of all MeOH evaporation-grown crystal samples in each category on the table. A value of below 1.00 for the ratio describes a system where the incorporation level is less than that of the doping level, while a value of above 1.00 suggests that the additive is incorporated into the crystal to a greater extent than it is present in solution. The number of samples (n) and standard deviations (SDs) for the sets of ratios are also listed. For the systems containing Me-FA **15** and Cl-FA **16**, the ratios

are listed as the average for the lower (0 – 6%, 1% intervals) and higher (10 – 90%, 10% intervals) doping level sub-ranges to illustrate any changes in the trend. 0 – 6% is the range of most interest to the research at hand, as the majority of work is carried out on samples within this doping level range. The 10 – 90% range is included to explore the change in behaviour of the systems with increased additive composition.

Table 4.1. Ratio of level of additive incorporation to doping level, averaged over n samples, for crystals of FFA **14** doped with increasing levels of compounds **15** – **19**, grown by slow evaporation from MeOH.

Additive	**Doping Level Range**	**n**	**Average Incorporation Ratio In Crystal *vs.* Doping Level**	**Standard Deviation**
Me-FA **15**	0 - 6	9	1.06	0.03
	10 - 90	9	0.99	0.02
Cl-FA **16**	0 - 6	6	0.91	0.09
	10 - 90	10	1.08	0.09
DF-FA **17**	0 - 6	19	0.69	0.07
MF-FA **18**	0 - 6	16	0.71	0.07
t-Bu-FA **19**	0 - 6	4	1.24	0.12

4.3.1.1 Systems Doped with Me-FA **15**

The incorporation data for the systems containing Me-FA **15** summarised in Table 4.1 above is visualised in Figures 4.2 and 4.3 as plots of additive level in crystals *vs.* doping level. The data points are presented alongside a dotted line that represents a 1:1 ratio to highlight the deviations in the data. A dashed linear trendline is also fitted to the

data for comparison to the 1:1 ratio line, although a linear relationship is not necessarily present. Figure 4.3 includes the data points from the entire range of samples, 0 – 90% Me-FA **15**, while Figure 4.2 focuses on the 0 – 6% Me-FA **15** doping range.

At lower doping levels, it appears that Me-FA **15** is incorporated into solid-form FFA **14** to approximately the same level as it is present in the solution from which the solid material was produced. This suggests the additive is acting as expected, exhibiting high levels of incorporation into the host crystal.

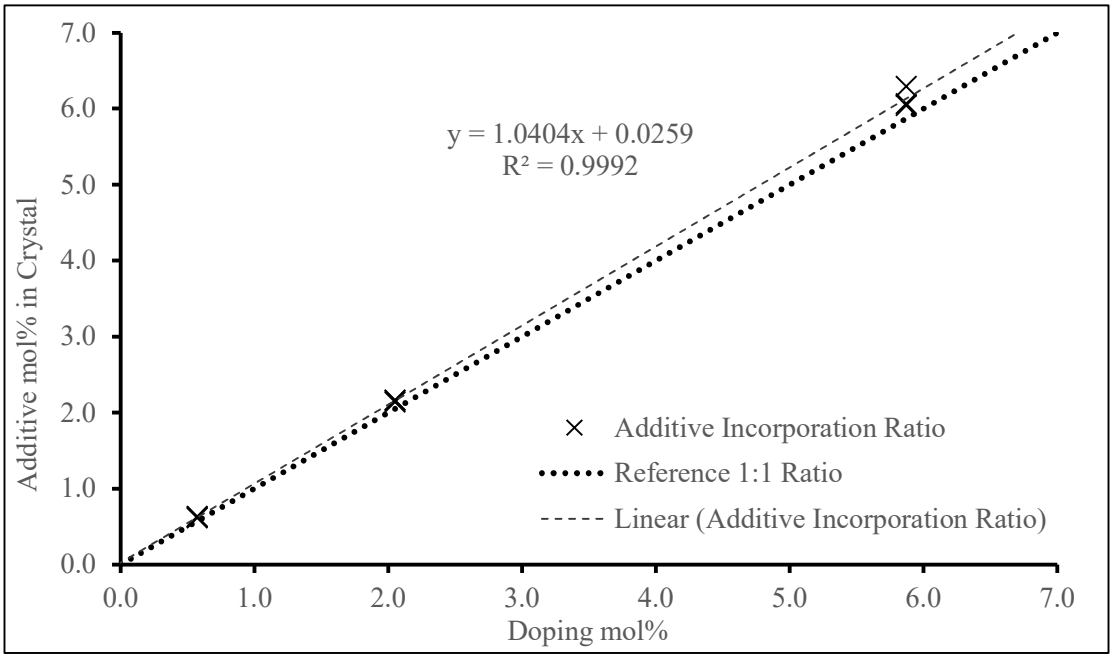


Fig 4.2. Plot of additive incorporation *vs*. doping level for crystals of FFA **14** doped with 0 - 90% Me-FA **15**, grown in MeOH.

At higher levels of doping (10 – 90%, Figure 4.3), the ratio drops slightly, but the additive levels in the crystals and solution are still comparable. Initially this phenomenon was attributed to the fact that the methyl group of the additive is smaller than the trifluoromethyl (-CF_3) group present on the host (2.00 Å *vs*. 2.15 Å respectively)[134]

facilitating the replacement of a host molecule in the crystal lattice, behaviour that was intended when choosing the additives. However, three of the four other additives (compounds **16** – **18**) also possess substituents with smaller vdW radii than a -CF_3 group and do not achieve the level of incorporation observed in systems doped with Me-FA **15**. As such, it is likely that there are other factors that influence this high level of incorporation.

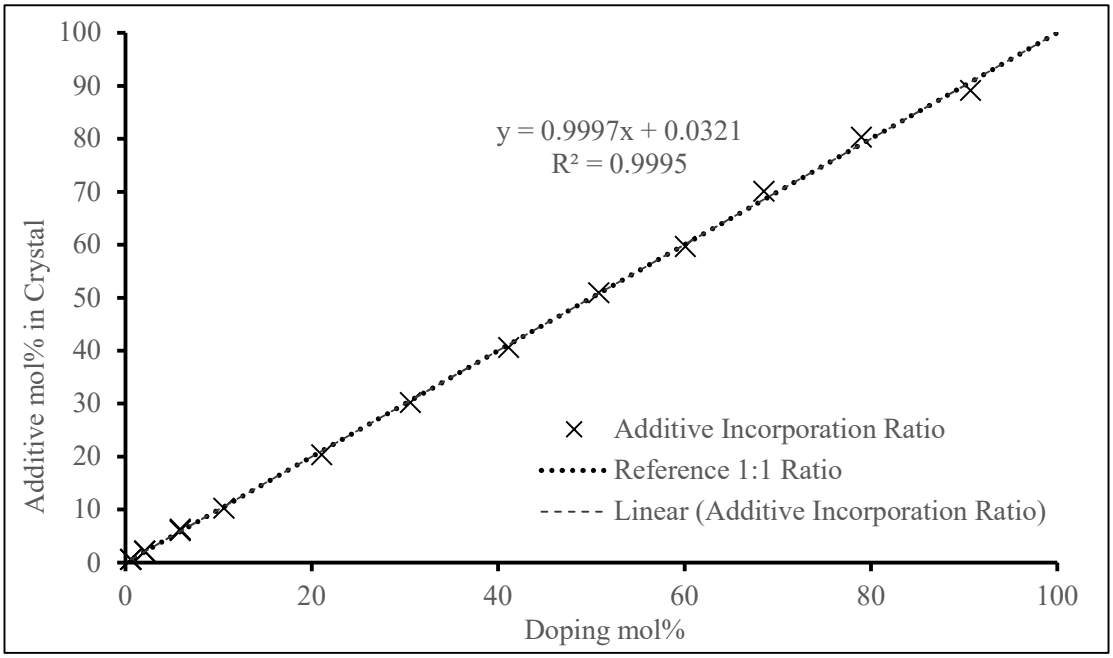


Fig 4.3. Plot of additive incorporation *vs.* doping level for crystals of FFA **14** doped with 0 – 6% Me-FA **15**, grown in MeOH.

The incorporation behaviour of crystals doped with Me-FA **15** grown by the slow evaporation of MeOH can be compared to those grown *via* slow cooling from MeCN. In Section 2.5.2.2, the pure-component relative solubility (α^0) values of Me-FA **15** and FFA **14** were calculated in both solvents. Givand *et al*. described a phenomenon whereby the lower this value was for an impure material in a solvent, the greater the extent of impurity

incorporation during crystal growth.[174] The α^0 values of the two materials was determined to be slightly lower for MeCN than MeOH, implying that the level of additive incorporation would be higher in crystals grown from the former solvent than the latter. Indeed, crystals grown from MeCN did exhibit a slightly higher incorporation ratio on average than those grown from MeOH at lower doping levels; 1.10 *vs.* 1.06 respectively. A plot for the incorporation data in the MeCN-grown crystals can be found in Figure 4.4.

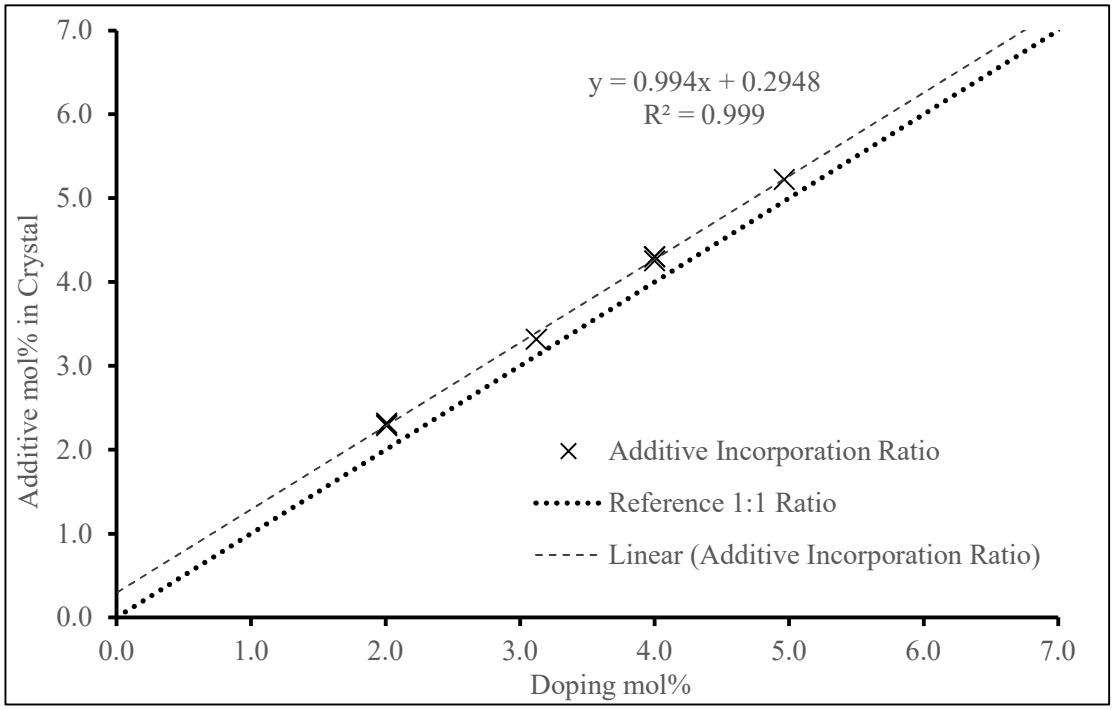


Fig 4.4. Plot of additive incorporation *vs*. doping level for crystals of FFA **14** doped with 0 – 6% Me-FA **15**, grown in MeCN.

4.3.1.2 Systems Doped with Cl-FA **16**

At low doping levels, the systems doped with Cl-FA **16** also exhibited a very similar level of additive in the solid and solution forms, with slightly more variability than samples doped with Me-FA **15** (Figure 4.5). The ratios for each data point average to 0.91,

suggesting lower but still comparable levels of additive incorporated in the crystals compared to those present in the doped solution from which those crystals were grown. In other words, at this doping level the crystallisation process of FFA **14** also displays a similar preference for incorporation of a molecule of Cl-FA **16** into its lattice as another molecule of FFA **14**, assuming lattice incorporation is occurring in the first place. This ratio persists up to an additive level of approximately 20%. At higher doping levels (10 – 90%) however, the incorporation level increases relative to the doping level resulting in a ratio of 1.08 (Figure 4.6). It appears that a change occurs in the incorporation behaviour at some level above 20% additive, after which the crystal lattice displays a higher preference for Cl-FA **16** than FFA **14**. When analysed by PXRD, a change in crystal form was also observed at approximately this composition of the two components (Section 4.5.2.4). At higher levels of additive, the pattern resembled that of pure Cl-FA **16** more closely than it did Form III FFA **14.**

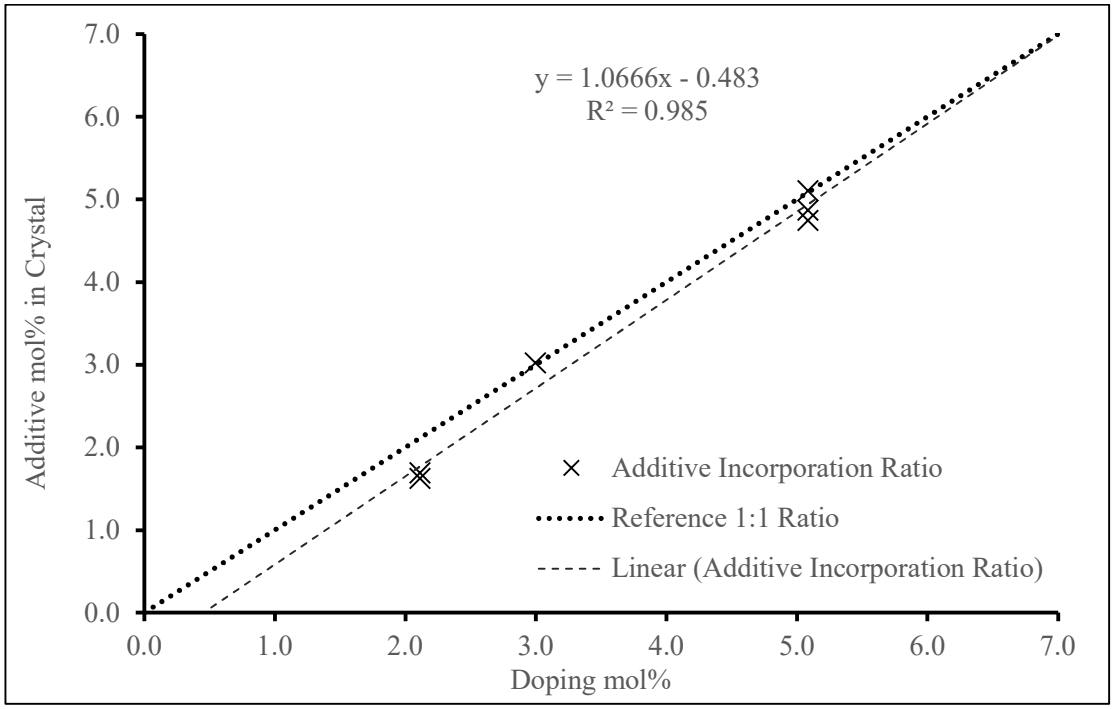


Fig 4.5. Plot of additive incorporation *vs.* doping level for crystals of FFA **14** doped with 0 – 6% Cl-FA **16**, grown in MeOH.

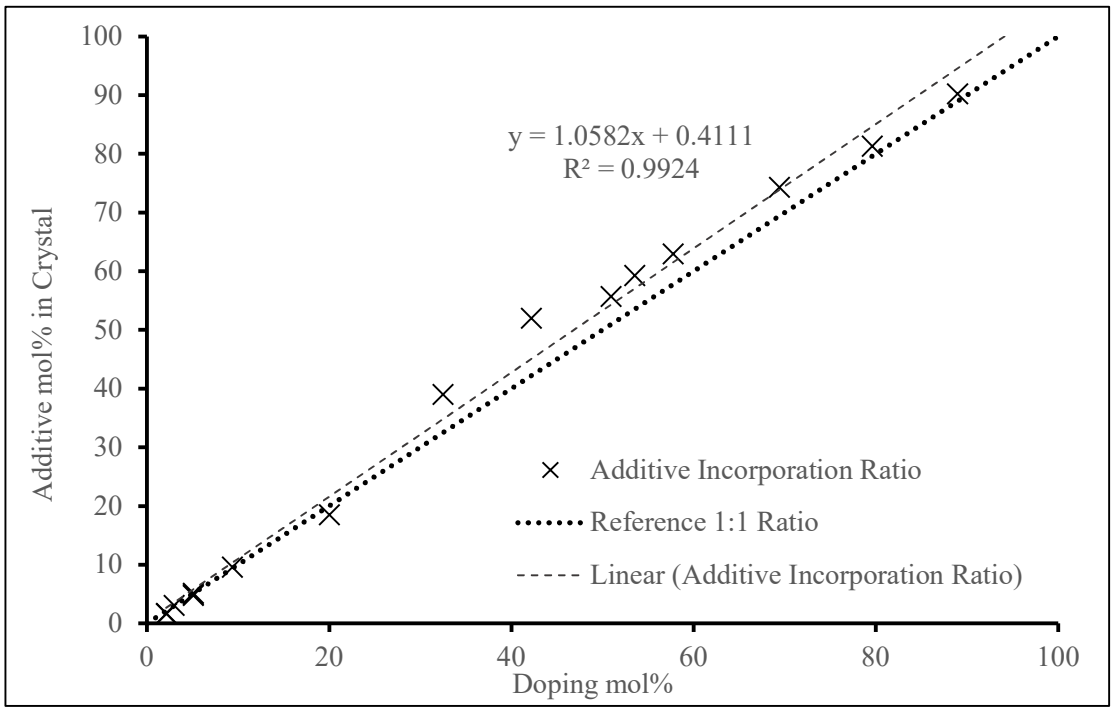


Fig 4.6. Plot of additive incorporation *vs.* doping level for crystals of FFA **14** doped with 0 – 90% Cl-FA **16**, grown in MeOH.

The pure-component relative solubilities of Cl-FA **16** and FFA **14** in MeOH and MeCN (as calculated in Section 2.5.2.2) have a similar relationship to those determined for Me-FA **15** and FFA **14** in the same solvents. The α^0 values (given in Section 2.5.2.2) were found to be lower for both additives in MeCN than MeOH, implying that crystals grown from MeCN should have a higher level of incorporation in the solvent than in MeOH. This was observed to be true for crystals doped with Me-FA **15** at low doping levels and is also observed for those doped with Cl-FA **16**, with an average incorporation ratio of 1.01 in crystals grown from MeCN *vs.* 0.91 in the crystals grown from MeOH with similar doping levels. A plot of the incorporation data for these MeCN-grown crystals can be found in Figure 4.7.

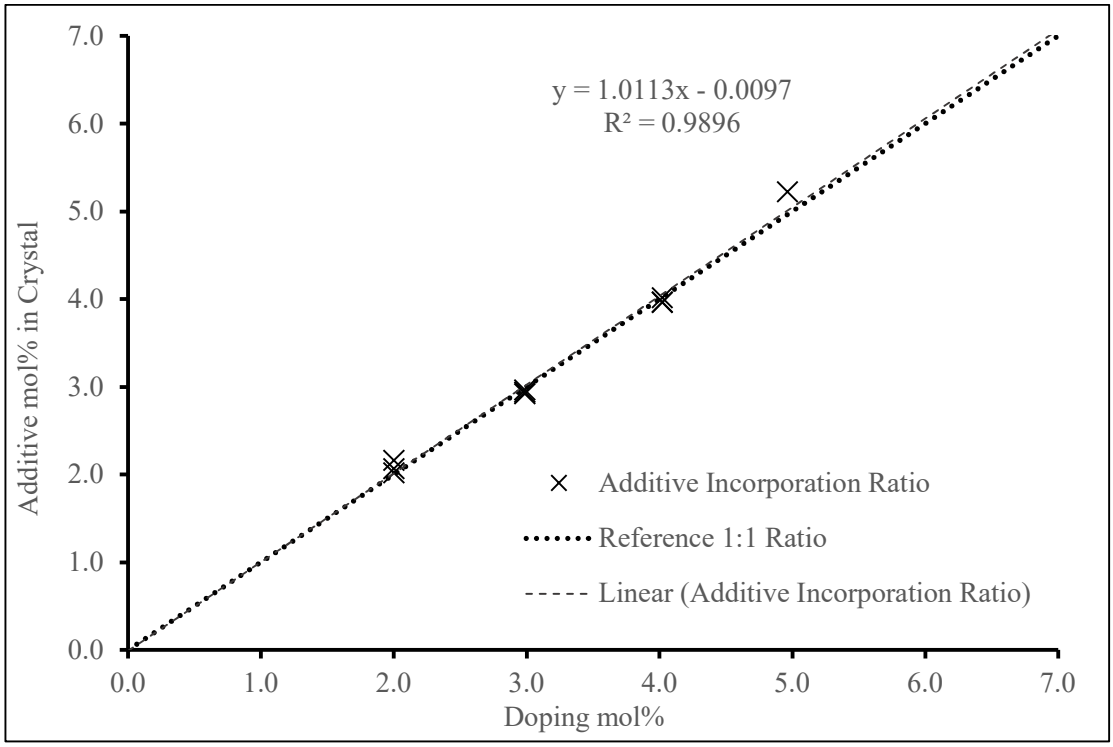


Fig 4.7. Plot of additive incorporation *vs.* doping level for crystals of FFA **14** doped with 0 – 6% Cl-FA **16**, grown in MeCN.

4.3.1.3 Systems Doped with DF-FA **17** and MF-FA **18**

In terms of incorporation into their respective crystals of FFA **14**, the behaviour of DF-FA **17** and MF-FA **18** is very similar. Both incorporate to a lesser degree than Me-FA **15** and Cl-FA **16**, to an extent that is relatively consistent across all doping levels tested, approximately 0 – 6% (Figures 4.8 and 4.9 for the systems doped with DF-FA **17** and MF-FA **18** respectively). The ratios of additive levels present in the crystal *vs*. those present in the doped solution are 0.69 and 0.70 for DF-FA **17** and MF-FA **18** respectively. Despite being lower than the previous two additives, these incorporation levels are still relatively high. Should the systems be determined to be displaying solid solution-like behaviour, it would appear that the additives were being well-incorporated into the crystal lattice.

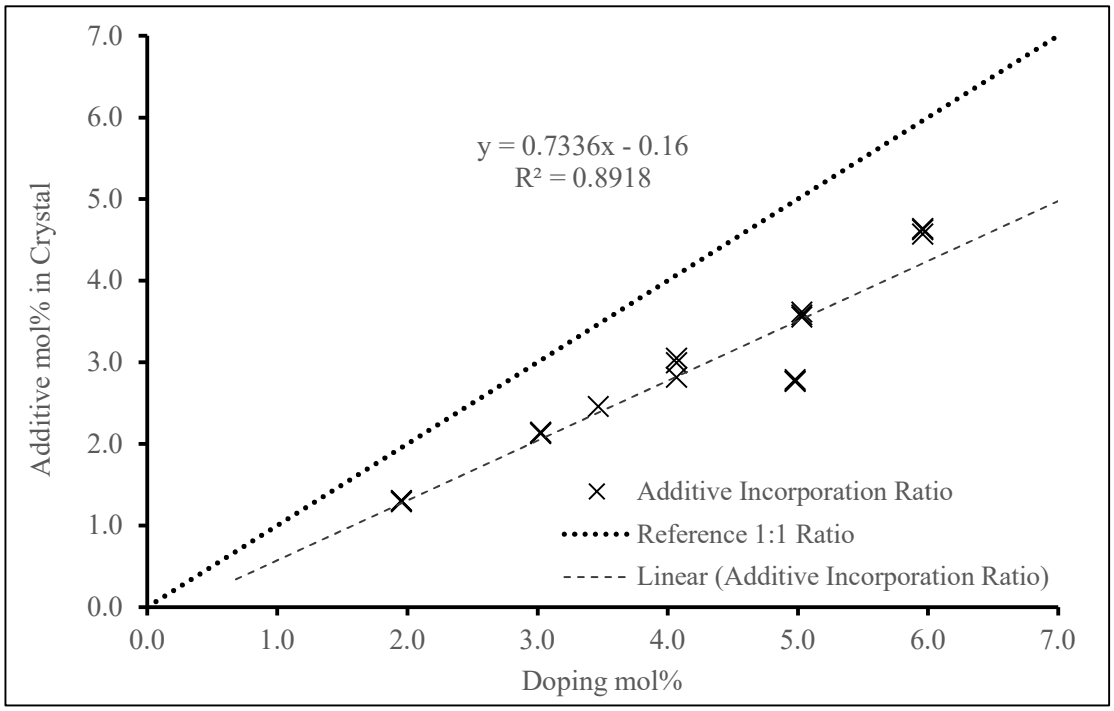


Fig 4.8. Plot of additive incorporation *vs.* doping level for crystals of FFA **14** doped with 0 – 6% DF-FA **17**, grown in MeOH.

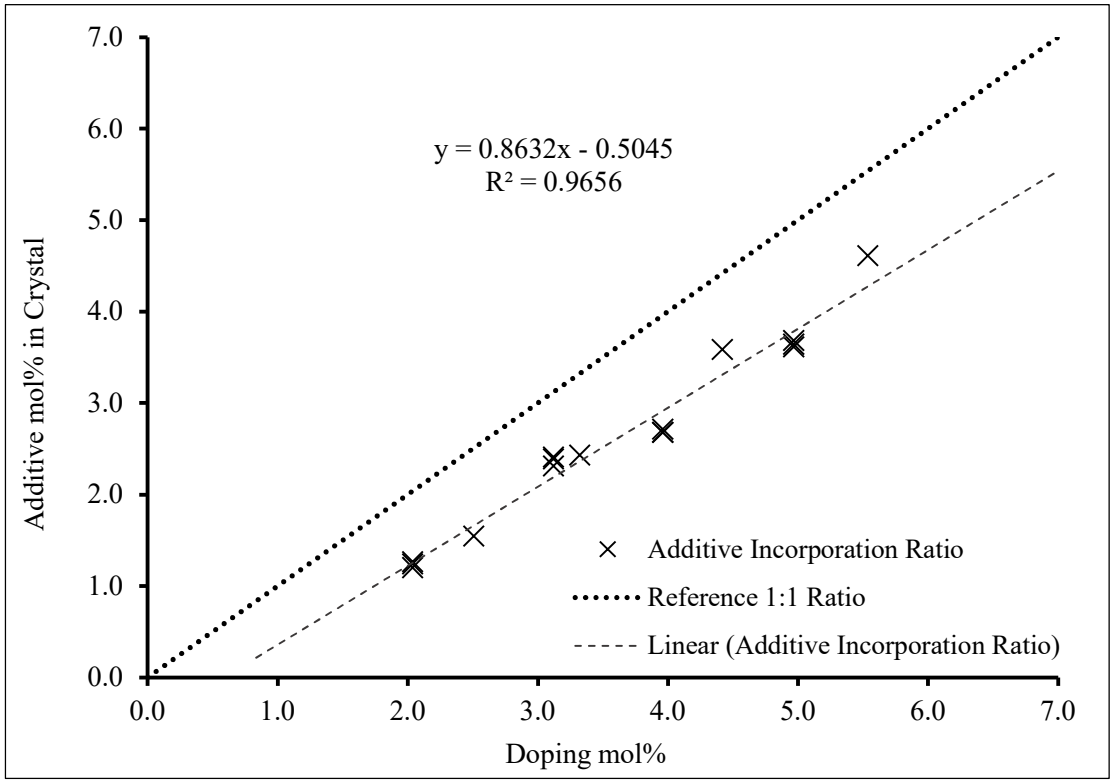


Fig 4.9. Plot of additive incorporation *vs.* doping level for crystals of FFA **14** doped with 0 – 6% MF-FA **18**, grown in MeOH.

4.3.1.4 Systems Doped with t-Bu-FA **19**

The final additive with which solutions of FFA **14** were doped was t-Bu-FA **19**. As discussed previously, this compound was intended to act as a less lattice-compatible additive for FFA **14**. It was expected that the bulky *tert*-butyl group would be too large to fit comfortably in the lattice space allowed for the -CF_3 substituent of FFA **14**, resulting in steric effects that would make the incorporation of the additive molecule unfavourable. As such, the level of t-Bu-FA **19** present in crystals of FFA **14** was expected to be low and be less likely to display solid solution-like behaviour. In this way, systems doped with t-Bu-FA **19** were intended to act as a contrasting control to the systems containing the

other additives (compounds **15** – **18**). Instead, the levels of t-Bu-FA **19** in the solid samples were observed to be higher than the corresponding doping level in all samples (Figure 4.10). The average incorporation ratio presented in Table 4.1 is correspondingly high, though the exact value may be skewed by the low number of data points. It was predicted that a certain low level of incorporation could occur, due to the structurally similarity of the additive to the host, but this high level of additive present in some of the crystal samples was unexpected.

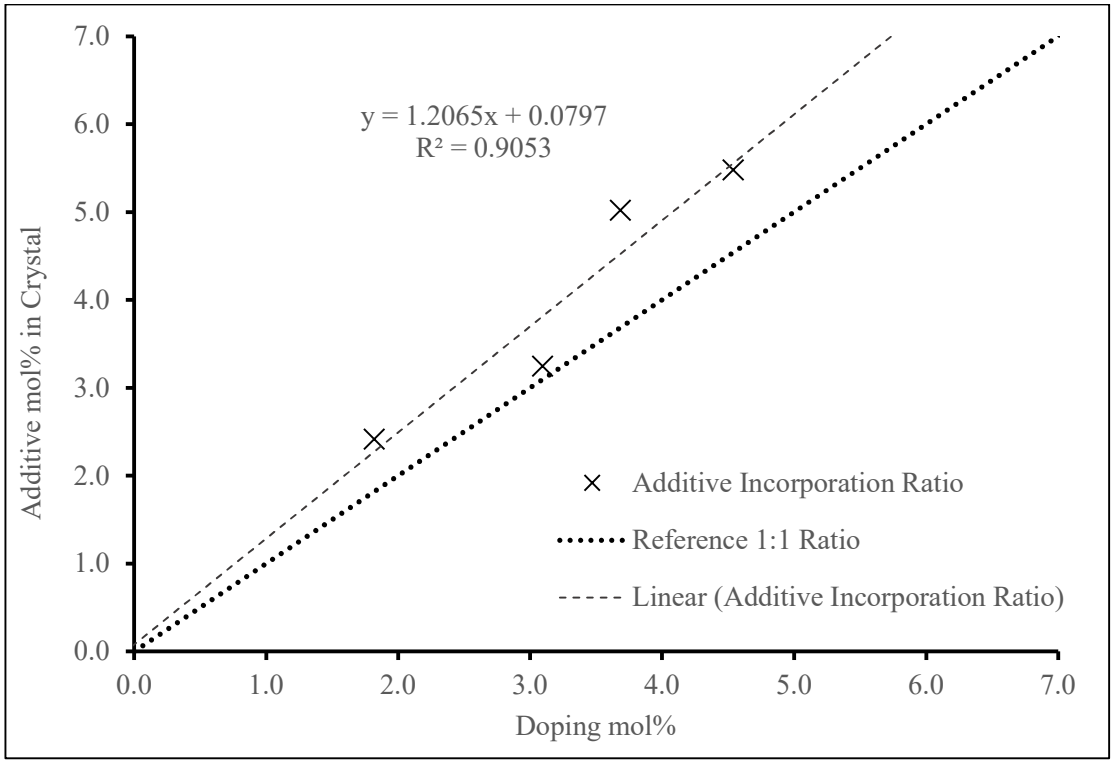


Fig 4.10. Plot of additive incorporation *vs.* doping level for crystals of FFA **14** doped with 0 – 6% t-Bu-FA **19**, grown in MeOH.

Crystals grown from MeCN exhibited an average incorporation ratio of 0.73 with a SD of 0.09, suggesting an additive percentage in the crystals consistently lower than the doping level. While much lower than the crystals grown from MeOH, the degree of t-Bu-FA **19** incorporation is still appreciable. It is possible that this difference in incorporation between crystals grown from the two solvents has to do with the relative solubilities of FFA **14** and t-Bu-FA **19** in each of these solvents, as discussed in Section 2.5.2.2. If the pure-component relative solubility (α^0) value for the materials was substantially lower for MeCN than for MeOH, it could explain the disparity in additive incorporation in crystals grown from each solvent. Unfortunately, as discussed previously, this hypothesis cannot be disproven or confirmed as the lack of material precluded the performance of solubility tests on the pure t-Bu-FA **19**.

4.3.1.5 Systems Doped with Diacid Triaryl Compound **25**

In Section 3.4, a synthetic impurity was observed to be consistently forming during the production of FFA **14**. This impurity was isolated and characterised. In the process, the structure of the impurity was identified to potentially be that of the diacid triaryl by-product 2,2'-((3-(trifluoromethyl)phenyl)azanediyl)dibenzoic acid **25**. Despite the inconclusive nature of the characterisation, it was posited that compound **25** could have potential as an additive in a doped system of FFA **14**, being a possibly naturally-forming synthetic impurity. However, due to the significant structural differences between the two compounds, it was not expected that compound **25** would be well incorporated into the crystal structure of FFA **14** in the same way as compounds **15** – **19** were.

Nevertheless, a doping experiment was attempted. Four samples of FFA **14** were

doped with increasing levels of compound **25**, from 2% to 5% in the same manner as the systems described previously. The doped system was subjected to the MeOH evaporation crystallisation method. One of the vials from that study post-evaporation can be seen in Figure 4.11. It was observed that both components crystallised separately, FFA **14** forming characteristic yellow needles and compound **25** precipitating as a white powder. One of the yellow crystals was harvested, washed to ensure no surface contamination, and tested by HPLC analysis (Figure 4.12). As expected, no analyte peak was observed at the expected retention time for compound **25**, indicating no incorporation of the compound had taken place. Similar results were observed across all samples. As such, it was decided not to proceed with compound **25** as an additive in further experiments. However, the results of this study provide an effective contrast to the more successful incorporation behaviour of systems doped with compounds **15** – **19**.



Fig 4.11. Image of the crystallisation vial after the evaporation of the MeOH solvent from a solution of FFA **14** doped with 2% compound **25**. The precipitation of yellow acicular crystals of FFA **14** and much smaller white crystals of compound **25** can be observed.

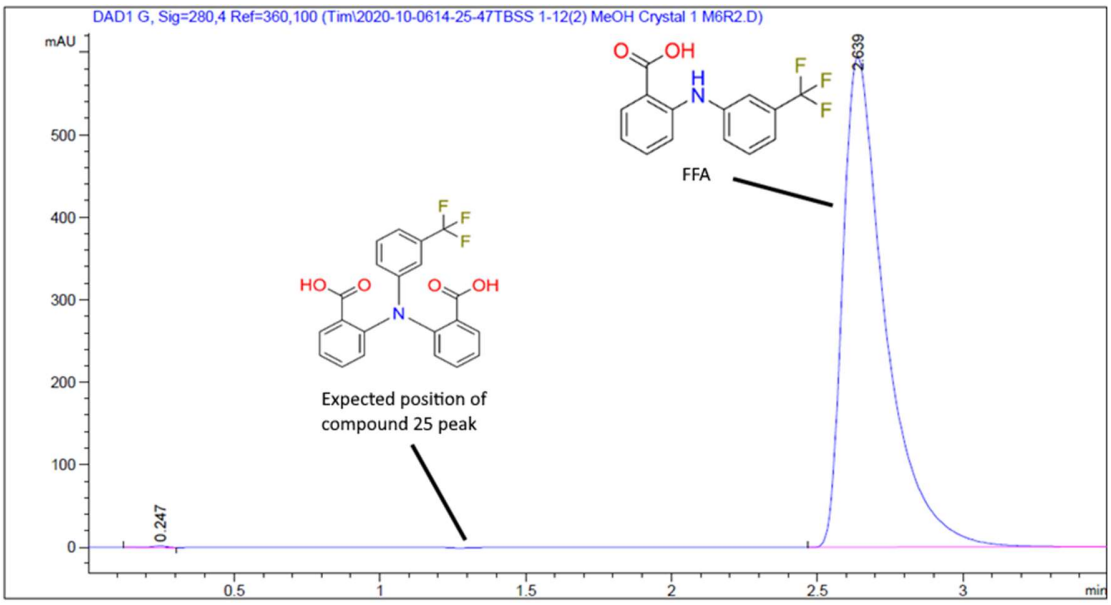


Fig 4.12. HPLC trace of a yellow acicular crystal grown from a solution of FFA **14** doped with 2% compound **25**, indicating no incorporation of the additive had taken place, collected at 280 nm.

4.3.1.6 Influence of Substituent Size and Relative Solubility on Additive Incorporation

There appears to be a loose correlation between the size of the variable substituents in the additives and the extent to which it is incorporated into crystals of FFA **14**; the smaller Me-FA **15** and Cl-FA **16**, with the smaller methyl and chloro groups, are incorporated to a significantly greater extent than the bulkier DF-FA **17** and MF-FA **18**. There is contrast between Me-FA **15** and Cl-FA **16**. Despite the chloro group of Cl-FA **16** being smaller than the methyl group of Me-FA **15** (1.8 and 2.0 Å respectively),[134] and more electronically similar to the -CF_3 group of FFA **14** (2.30 eV and 3.03 eV respectively, *vs.* 3.35 eV for -CF_3),[157] Cl-FA **16** is consistently incorporated to a lesser degree than Me-FA **15**. At higher doping levels however, Cl-FA **16** becomes incorporated

to a greater degree than Me-FA **15**, and this change is accompanied by a change in crystal structure by PXRD (Section 4.5.2.4), becoming a different phase of the system. It appears that substituent size plays an important role in the level of additive incorporation, but that level is clearly also influenced by other factors. Additionally, it could be that substituent size becomes more impactful at higher doping levels relative to those other factors, as is implied by the change in incorporation level exhibited by Me-FA **15** and Cl-FA **16**.

The influence of relative solubility of a material in the crystallisation solvent introduced in Section 2.5.2.2 appears to hold true for these systems. Both Me-FA **15** and Cl-FA **16** were determined to have a lower pure-component solubility (α^0) relative to FFA **14** in MeCN than in MeOH, which has been linked to higher levels of impurity incorporation. Consistent with this, the level of additive incorporation was observed to be higher in crystals grown from MeCN than in those grown from MeOH in both cases. Relative solubility values could also be the explanation for the difference in incorporation levels between certain crystal batches doped with t-Bu-FA **19**.

While the above tests yield important information into the extent of additive inclusion into solid FFA **14**, they provide little insight as to the nature of that inclusion. There are many methods by which additives and impurities can be present in otherwise pure crystals, of which lattice incorporation is only one. Further studies needed to be performed on the systems to gain more insight into the nature of the relationships between each additive and FFA **14**.

4.4 Additive Resistance to Purification by Recrystallisation

The doped systems were designed to mimic batches of drug products in industry that are resistant to standard purification methods, foremost among them crystallisation. It had been demonstrated previously that the additives in these systems were well incorporated into solid-form FFA **14** *via* crystallisation from additive-rich solution, but it was unknown how resistant they were to deliberate purification in the form of recrystallisation. Urwin *et al*. describe a simple method of determining the extent of impurity rejection through recrystallisation as part of their structured workflow designed to minimise impurities in industrial processes.[18] This method is also discussed in Section 1.1.3 (page 12), and the defining equation is presented below in Formula 4.2. The method uses the ratio between the impurity fraction in the solid and liquid phase post-crystallisation (K_i) and the same ratio between the host component fractions (K_A) to calculate a selectivity coefficient value (α_1) for the impure system, which determines the effectiveness of the recrystallisation process. It is important to note that the values represented by the α_1 symbol are unrelated to those represented by the α^0 (pure-component relative solubility, Section 2.5.2.2) or α_2 (distribution coefficient value, Section 5.2.2.2) symbols.

Formula 4.2. $$\alpha_1 = \frac{K_i}{K_A}$$

This α_1-value usually falls between 0 and 1. A value of close to 0 suggests good rejection of the impurity, common for systems containing foreign species that unfavourably disrupt the crystal packing of the host material. If α_1 is closer to 1, denoted by a horizontal line in Figure 4.13, the lattice of the host has near equal preference to incorporate a molecule of impurity as it does one of the host, indicative of a solid solution or co-crystal relationship. An α_1 value of greater than 1 means that the level of additive/impurity present in the solid is greater than is present in the liquid phase, suggesting the crystal material has a higher preference for the impurity than it does for the host. The threshold value allowed for α_1 in an industrial process varies significantly depending on the concentration of the impurity in the crude and the desired level of purity in the recrystallised sample, but in general the recommended maximum value is 0.05. This is worth noting for comparison to the values achieved in the systems of study in this work, and a metric by which the effectiveness of the additive incorporation can be measured.

A collection of 7 doped systems of FFA **14** were produced for this study. The first 5 were doped with approximately 2% of each additive individually to investigate the relationship between the host and the additive at low doping levels. The other two were doped with higher levels of Me-FA **15** and Cl-FA **16**, approximately 45% and 42% respectively, to ascertain how the behaviour of the additive as part of the system evolved with increased doping levels. The aim of the study was to assess the resistance of the additives to an effective purification method. In Section 3.2.3, toluene was determined to be the most effective solvent for the purification of crude FFA synthesis products, exhibiting the greatest balance of purity improvement and material recovery. As such, toluene was chosen as the crystallisation solvent. The recrystallisation process (as

described in Section 4.9.5) was performed three consecutive times on each sample, each time using the post-crystallisation "pure" solid of the last session as the pre-crystallisation "crude" of the next. This was done mostly to ensure reproducibility of results, but also to determine whether a noticeable trend in additive incorporation and/or α_1 value would emerge with successive recrystallisation stages. The procedure for calculating the α_1 value for each recrystallisation is also described in Section 4.9.5.

4.4.1 Results

4.4.1.1 Systems Doped with 2% Additive

The results for the first 5 samples, those doped with 2% of each additive, are detailed in Table 4.2 and displayed graphically in Figure 4.13. It should be noted that the percentages used as descriptors for each sample refer to the percentage additive in solution (which is controlled), not necessarily in the crystal material (which has to be determined).

Table 4.2. Selectivity coefficient values (α_1) for crystals of FFA **14** doped with 2% Me-FA **15**, Cl-FA **16**, DF-FA **17**, MF-FA **18**, and t-Bu-FA **19** across three consecutive recrystallisation stages (RC 1-3).

Sample Name	**α_1-value**			**Average**
	RC1	**RC2**	**RC3**	
2% Me-FA **15**	1.16	1.40	1.46	**1.34**
2% Cl-FA **16**	0.83	0.76	0.83	**0.81**
2% DF-FA **17**	0.76	0.59	0.57	**0.64**
2% MF-FA **18**	0.61	0.62	0.61	**0.61**
2% t-Bu-FA **19**	0.61	0.52	0.59	**0.58**

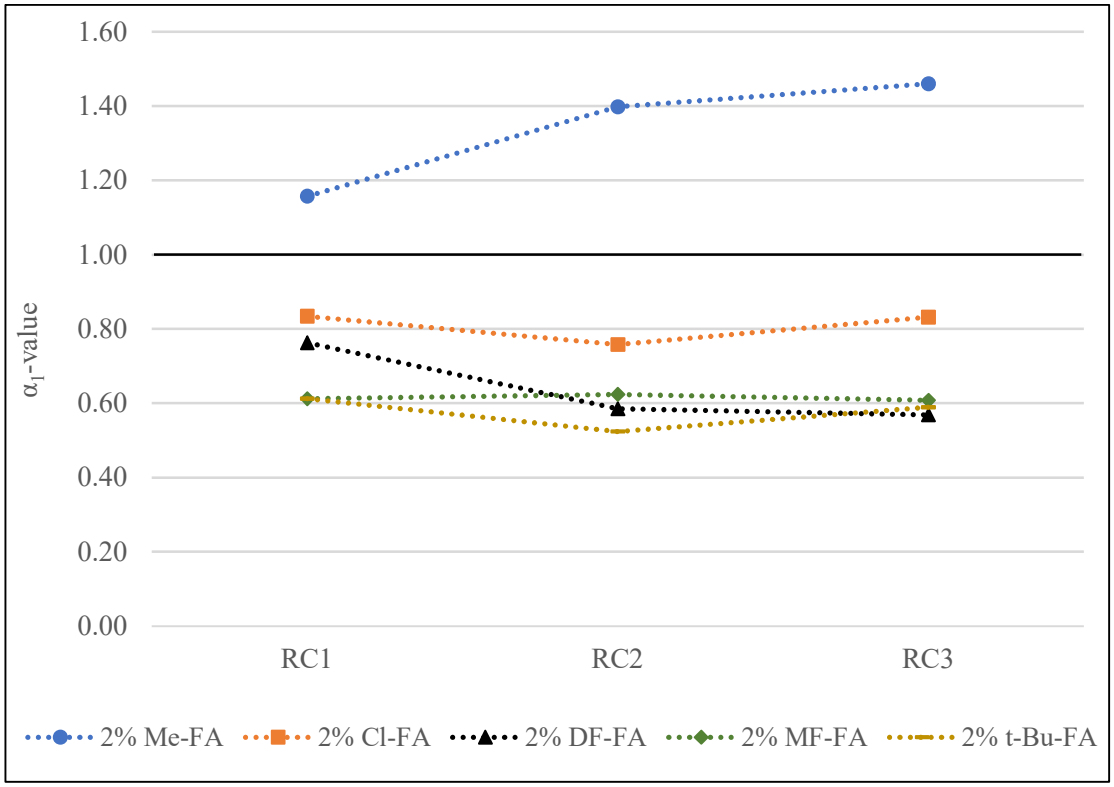


Fig 4.13. Plot of selectivity coefficient values (α_1) for crystals of FFA **14** doped with 2% Me-FA **15**, Cl-FA **16**, DF-FA **17**, MF-FA **18**, and t-Bu-FA **19** across three consecutive recrystallisation stages (RC 1-3).

Considering the maximum value of α_1 recommended to represent an effective impurity rejection is 0.05,[18] the high average values determined for each system are noteworthy, exhibiting significant resistance of the additive to purification and suggesting solid solution-like behaviour. The average selectivity for Me-FA **15** at this doping level is greater than 1; this describes a case where the level of additive present in the solid phase is greater than the level in the liquid phase post-recrystallisation. The selectivity starts at 1.16 for the first recrystallisation, then increases to a maximum of 1.46 by the third stage, representing a preference of the crystalline material for the additive almost one and a half times that of the host. The high α_1 value mirrors the high levels of Me-FA **15** found in doped crystals in comparison to the crystallisation solution.

Systems doped with Cl-FA **16** are next highest, averaging at a selectivity value of about 0.81. This implies the crystal lattice of FFA **14** has a near equal level of preference for Cl-FA **16** as the pure material and a very high resistance to purification. DF-FA **17** and MF-FA **18** are not quite as resistant to impurity rejection as the first two additives, with an average α_1 value of 0.64 and 0.61 respectively. This is unsurprising based on the observed incorporation levels of the material into FFA **14**. However, in the wider context of recrystallisation, and when presented against the extremely low values of α_1 that would constitute an effective purification, the selectivity coefficients of these materials are easily high enough to still be considered resistant to rejection. Finally, t-Bu-FA **19** exhibited an α_1 value of 0.58. While the lowest of the five additives, this selectivity value is comparable to those observed for DF-FA **17** and MF-FA **18**, and significantly exceeds the expectations for the compound. Along with the results of the incorporation test, this provides more evidence that t-Bu-FA **19** is not behaving in the manner it was expected to.

High selectivity coefficient values, such as those exhibited by all five additives, is a strong indicator of phase behaviour which can accommodate a second component, such as a solid solutions or co-crystals.[18] As co-crystals require stoichiometric amounts of each component, this implies that the additives are instead exhibiting some degree of solid solution-like behaviour at this doping level. However, these findings alone are not conclusive; the same observations could be explained by several other forms of additive incorporation, e.g., surface adsorption or solvent inclusions.

4.4.1.2 Systems Doped with 45% Me-FA **15**

The selectivity data collected from the recrystallisations of the system doped with 45% Me-FA **15** is presented in Table 4.3 alongside that of the 2% Me-FA **15** data for comparison. There is a noticeable decrease in the selectivity for the additive at the higher doping level, dropping to an average of 0.78 with a trend that decreases with consecutive recrystallisation stages. The values suggest that at higher additive concentrations the crystal structure no longer displays a preference for the additive over the host during crystallisation, as was the case with the 2% system. This stands to reason; such high levels of additive would certainly have an impact on the stability of the crystal structure of the host. That being said, even at such high doping levels the selectivity of the system for Me-FA **15** is remarkably high, nearly matching that of the 2% Cl-FA **16** sample (0.81). When the actual additive levels in the post-crystallisation solids are plotted (Figure 4.14), it is apparent that the drop in additive level is relatively minimal. While still not definitive evidence, the resistance of the 45% Me-FA **15** sample to purification strongly suggests the existence of a continuous solid solution with regards to the relationship between Me-

FA **15** and FFA **14**. Whether or not that is indeed the case can only be conclusively established through the construction of a phase diagram.

Table 4.3. Selectivity coefficient values (α_1) for crystals of FFA **14** doped with 2% and 45% Me-FA **15** across three consecutive recrystallisation stages (RC 1-3), along with an average of those values.

Sample Name	**α_1-value**			**Average**
	RC1	**RC2**	**RC3**	
2% Me-FA **15**	1.16	1.40	1.46	**1.34**
45% Me-FA **15**	0.90	0.77	0.68	**0.78**

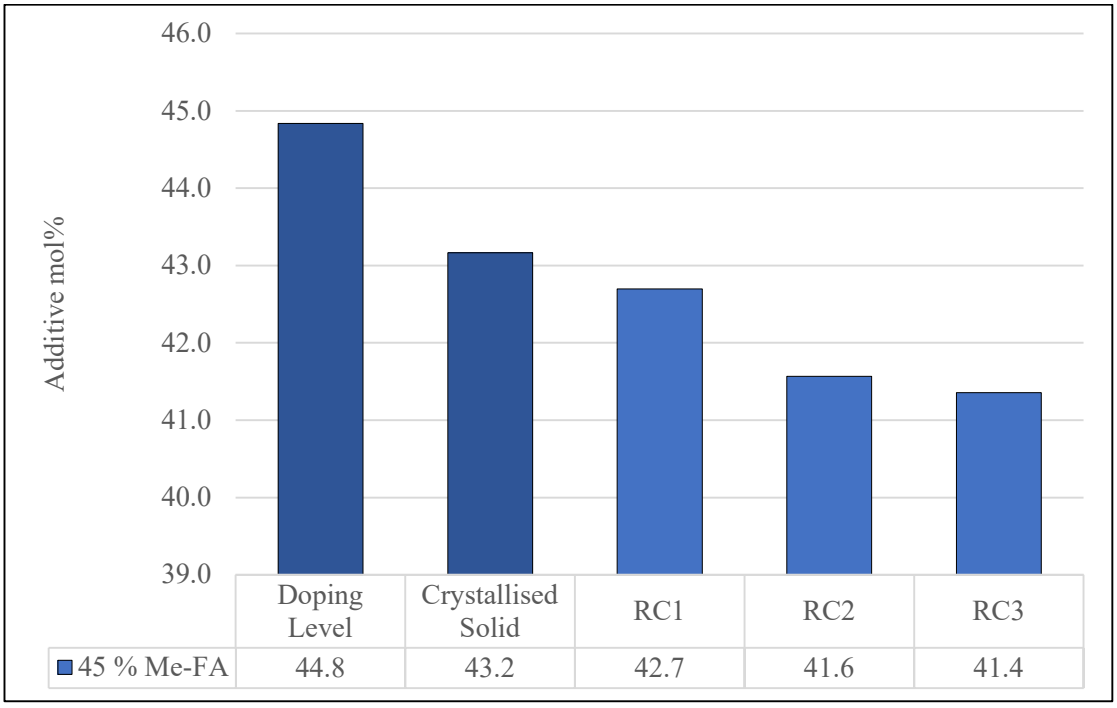


Fig 4.14. Percentage values of Me-FA **15** in a sample of FFA **14** after initial doping, after crystallisation, and after three consecutive recrystallisation stages (RC 1 – 3), demonstrating the decreasing level of additive throughout.

4.4.1.3 Systems Doped with 42% Cl-FA **16**

The systems doped with a higher level of Cl-FA **16** behaved in a notably different way to those doped with Me-FA **15**. First of all, during the sample preparation process, in which crystal samples of the material were produced by rotovap crystallisation, the additive level of the solid material increased by approximately 10% relative to the pre-crystallisation solid. This fits the pattern of incorporation behaviour observed in Section 4.3.1.2, but it should be noted that the solid samples labelled "42% Cl-FA **16**" below in reality initially contained approximately 52% additive. Like the rest of the samples in this section, the 42% Cl-FA **16** system was subjected to three consecutive recrystallisation stages. In each one of those stages the crystallising solid phase showed a consistent preference for Cl-FA **16** over FFA **14**, resulting in an average selectivity coefficient of almost 5 at this additive level (Table 4.4). This value is a clear difference from that observed at lower levels, the change between the two doping levels being several times greater than that observed in the samples doped with Me-FA **15**.

Table 4.4. Selectivity coefficient values (α_1) for crystals of FFA **14** doped with 2% and 42% Cl-FA **16** across three consecutive recrystallisation stages (RC 1-3), along with an average of those values.

Sample Name	**α_1-value**			**Average**
	RC1	**RC2**	**RC3**	
2% Cl-FA **16**	0.83	0.76	0.83	**0.81**
42% Cl-FA **16**	4.51	5.34	5.12	**4.99**

When the recrystallisation stages are plotted against the Cl-FA level of the solid phase material recovered from each, a clear increasing pattern can be observed (Figure 4.15). The PXRD patterns of the doped material (Figure 4.25, Section 4.5.2.4) imply that Cl-FA **16** becomes the dominant component in the system at incorporation levels greater than 30%, with the crystal structure of the doped material more closely resembling pure Cl-FA **16** than pure Form III FFA **14**. The observed α_1-values suggest that this change in crystal structure also results in Cl-FA **16** adopting the host role and rejecting FFA **14** from the solid phase as an unfavourable additive during the crystallisation process.

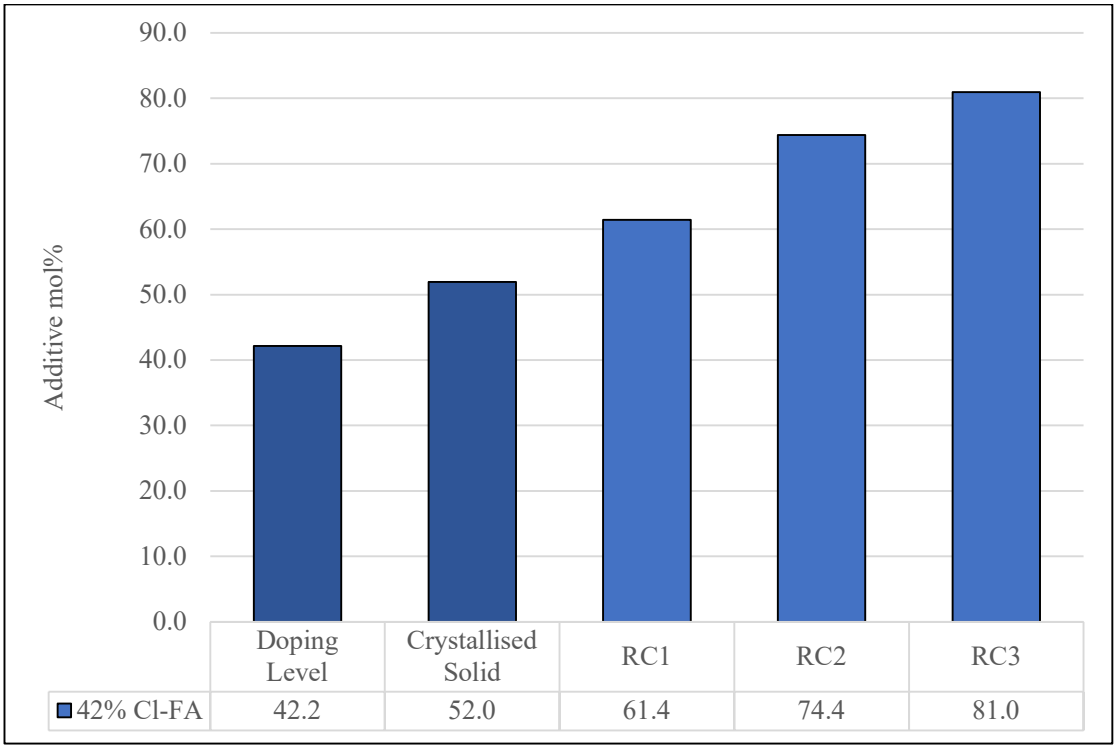


Fig 4.15. Percentage values of Cl-FA **16** in a sample of FFA **14** after initial doping, after crystallisation, and after three consecutive recrystallisation stages, demonstrating the increasing level of additive throughout.

By reversing the labelled roles of each component in the systems, the selectivity data can be presented as displayed in Table 4.5. When the data is considered in this way, with Cl-FA **16** as the host and FFA **14** as the additive, an average selectivity coefficient of 0.20 is determined. This represents a system in which the additive is rejected from the host crystal to a much higher degree than any of the additives tested thus far. As such, the purification of FFA **14** from the Cl-FA **16** system can be considered more efficient than the systems where FFA **14** is the host, albeit not enough to be considered "effective" by the aforementioned process standards, which cite a minimum α_1 value of 0.05.[18] This level of rejection is unsurprising when the relative bulk of the -CF_3 substituent of the FFA **14** "additive" is considered alongside the chloro group of the Cl-FA **16** "host".

Table 4.5. Selectivity coefficient values (α_1) for crystals of FFA **14** doped with 42% Cl-FA **16** across three consecutive recrystallisation stages (RC 1 – 3), should FFA **14** be considered the additive in the system and Cl-FA **16** the host.

Sample Name	**α_1-value**			**Average**
	RC1	**RC2**	**RC3**	
42% Cl-FA 16	0.22	0.19	0.20	0.20

4.5 Crystallisation Behaviour of Doped FFA

4.5.1 Appearance and Growth of Doped FFA Crystals

The inclusion of the chosen additives, even in very low amounts, have a noticeable impact on some aspects of the appearance and crystal growth behaviour of FFA **14**. As noted in Section 2.8.4.3, crystallising FFA using the rotovap method produced a collection of very small, pale yellow, needle-like crystals that aggregate in a fibrous mass. Inclusion of Me-FA **15** in crystals grown in the same way had little effect on the consistency of the material, but the colour becomes a notably richer yellow. The texture remained unchanged as the doping level of Me-FA **15** increased from 10 – 90% (at 10% increments), but a slight darkening of the colour could be observed to a sandier yellow/brown (closer to the colour of pure Me-FA produced in the same way). On the other hand, doping FFA **14** with Cl-FA **16** lightened the colour to an even paler yellow than pure FFA **14**. As with Me-FA **15**, this colour darkened slightly with increased additive, becoming a sandier colour at high doping levels (90%), similar again to the appearance of the pure additive. The only exception of this trend was at 30% Cl-FA **16**, at which level the colour lightened further to an off-white and the material appeared chalkier in consistency. As noted in Section 3.6.4.4, synthesised DF-FA **17** was produced in one of two forms: pale sandy yellow, or dark brown. The colour of the doped material depended on the colour of the DF-FA **17** used in the doping, pale yellow additive producing very pale-yellow doped material, slightly darker than that of material doped with Cl-FA **16**, and the dark brown producing slightly paler brown doped material, even at very low doping levels (2%). Crystal doped

with low levels of MF-FA **18** closely resembled those doped with pale yellow DF-FA **17**. Finally, crystalline FFA **14** doped with t-Bu-FA **19** produced in this way were much brighter in colour than the other doped systems, appearing as a rich yellow colour.

Slow evaporation of a solution in MeOH proved an effective way of producing large prismatic crystals of FFA **14**, as described in Section 2.6.1.4. The inclusion of additives also impacted this crystallisation method, both in terms of the appearance of the grown crystals and the effectiveness of the procedure as a whole. The method was used to successfully produce large prismatic crystals of FFA **14** doped with low levels (0.5 – 5%) of Me-FA **15**, Cl-FA **16**, and DF-FA **17**. The colour of crystals followed a similar pattern as observed with those produced by rotovap crystallisation. The crystals doped with Me-FA **15** were a richer yellow than pure FFA **14**, while those doped with Cl-FA **16** took on a much paler, almost colourless appearance. When doped with even low levels of the dark brown DF-FA **17**, a clear colour disparity can be observed in crystals of FFA **14**. Many crystals exhibited a colourless portion, transitioning to a region of dark brown. (e.g., Figure 4.16). An image of undoped FFA III **14** crystals produced in the same way is shown in Figure 4.17. All portions of the crystal exhibit uniform extinction when examined *via* polarised microscopy. Samples of FFA **14** doped with comparable levels of the pale-yellow DF-FA **17** material produced crystals with a uniform yellow colour.

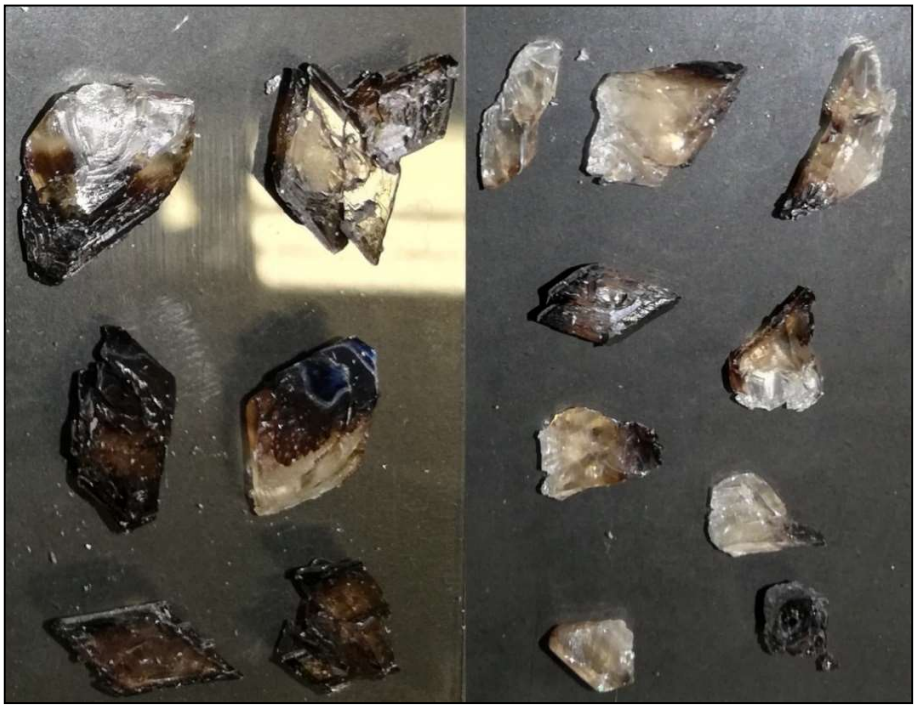


Fig 4.16. Digital image of a selection of prismatic crystals of FFA **14** doped with 2% dark brown DF-FA **17** grown *via* slow evaporation of MeOH, demonstrating the uneven colouring of the crystals.



Fig 4.17. Digital image of a selection of prismatic crystals of undoped FFA **14** grown *via* slow evaporation of MeOH.

However, inclusion of MF-FA **18** and t-Bu-FA **19** in FFA **14** at similar levels appeared to have a detrimental effect on crystal growth when the MeOH slow evaporation process was employed. In all attempted samples, the crystals produced were smaller than those of pure FFA **14**, with different crystal habits described below. Certain batches of FFA **14** doped with Me-FA **15** and DF-FA **17** also produced similar crystals.

The primary purpose of the prismatic crystals grown by this method was for partial dissolution studies the habits of these crystals, and these habits proved problematic for use with the partial dissolution technique. It was noted that the morphologies of these crystals generally fell into one of four categories, designated Types A – D (Figure 4.18).

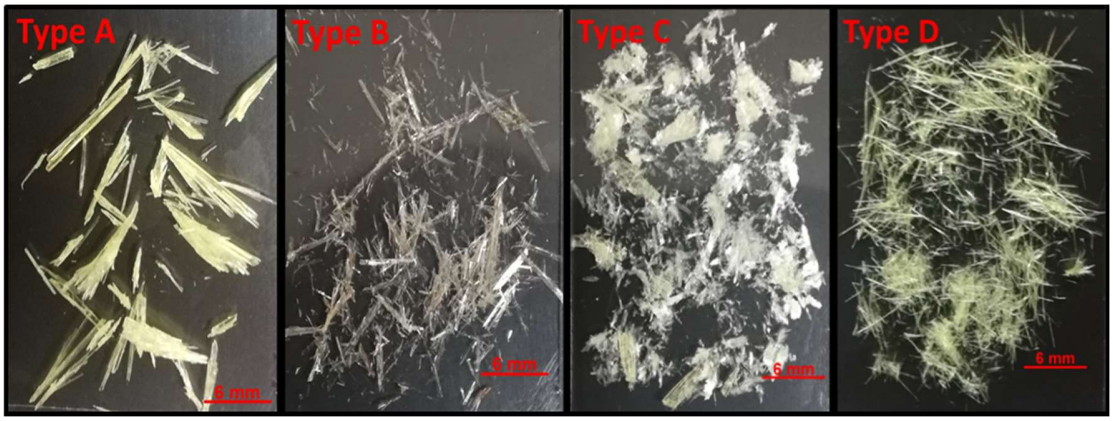


Fig 4.18. Digital images of examples of the four categories of doped FFA **14** crystals with problematic morphologies produced by the slow evaporation of MeOH. Left to right: 2% t-Bu-FA **19**, 2% DF-FA **17**, 0.5% Me-FA **15**, 5% t-Bu-FA **19**.

Type A crystals are the largest of the four, although still too small to be selected and measured individually, growing in fan-like clusters that separate easily with downward pressure. They are long and thin, appearing to be similar to the needle-like crystals produced by MeCN slow cooling, but when viewed under the microscope they

lack the tapered ends characteristic of the acicular habit. Type B crystals also share attributes with the slow cooled crystals, appearing to be acicular and growing outwards in a rosette pattern, but are much smaller in size. They are also very fragile, and fracture extremely easily when handled. As such, samples of Type B crystals consist of primarily broken crystal fragments. Type C crystals are very flat and thin, appearing to the eye as wafer-like flakes. Occasional larger prismatic crystals can also be found in batches of this crystal type. When viewed under a microscope, they have an almost fluffy appearance, and are difficult to focus on. Finally, Type D crystals are very small acicular crystals which do possess tapered ends when viewed under a microscope. On a macro level, they appear much more regular than the other types in terms of size and colour and tend to cluster into loose fibrous balls similar to cotton wool. There appeared to be a correlation between the doping level of t-Bu-FA **19** and the quality of crystal produced; systems of FFA **14** doped with 2% t-Bu-FA **19** formed larger Type A crystals, whereas systems doped with 3 – 5% t-Bu-FA **19** produced smaller Type B and D crystals. Images and size information for each of these crystal types mentioned above, as well as for the remainder of the doped crystals, can be found in Section 5.2.3.

Large acicular crystals of FFA **14** doped with low levels of compounds **15** – **18** (2 – 5%) were successfully produced by the slow cooling of a solution of the mixture in MeCN. The size and morphology of these crystals was similar to that of pure FFA **14**, but the colour was influenced by the additive as observed in the other crystallisation methods. The only systems from which large acicular crystals were not produced was those doped with t-Bu-FA **19**. Finally, very large, single prismatic crystals of FFA **14** doped with low levels of Cl-FA **16** and DF-FA **17** (2%) were successfully grown by vapour diffusion of

hexane into a solution of the material in MeOH (Figures 4.19 and 4.20). Crystals of undoped FFA grown in the same way is included for comparison to the two doped systems (Figure 4.21). The crystal doped with Cl-FA **16** exhibited somewhat even growth on all faces, while the crystal doped with DF-FA **17** was much more irregular. Attempts at growing similar crystals doped with the other additives proved unsuccessful.





Fig 4.19 (left), 4.20 (right). Digital images of the large prismatic crystals of FFA **14** doped with 2% Cl-FA **16** (left) and DF-FA **17** (right) grown *via* vapour diffusion.

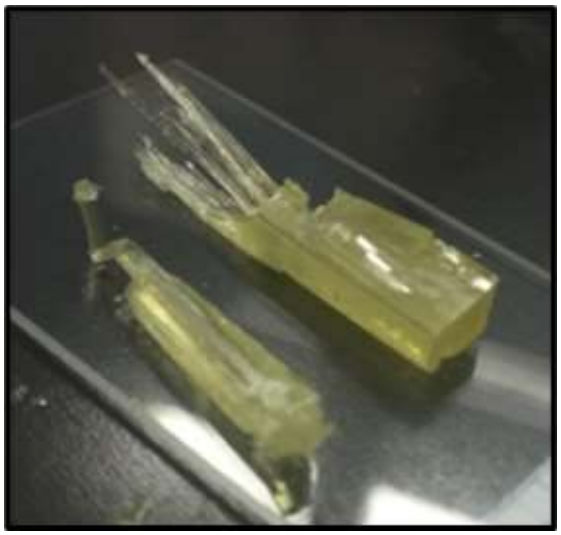


Fig 4.21. Crystals of undoped FFA III produced by the vapour diffusion crystallisation process.

4.5.2 Polymorphic Form

As discussed in Section 2.6.2, it was important that polymorphic consistency was maintained between all experiments involving solid-form FFA. Form III, the stable form at room temperature, was selected as the polymorph to preserve. The tendency of FFA to preferentially crystallise into the Form III polymorph has been established for the pure material across the four primary crystallisation procedures used in the research (Appendix Figure 7.26). Here the influence of the inclusion of additives in FFA will be explored in terms of polymorphism. This will be achieved through PXRD analysis of FFA systems doped with varying additive types and levels, as well as samples of doped crystals grown using different crystallisation methods. Analysis on samples of the crystals with problematic morphologies described previously will also be performed to determine whether the changes in crystal habit are a result of differing polymorphic forms.

4.5.2.1 Effect of Inclusion of Each Additive Type

Figure 4.22 below shows PXRD patterns of FFA **14** doped with 3% of each additive (compounds **15** – **19**) compared to the pattern of pure Form III FFA **14** (bottom). All samples were crystallised by the slow evaporation of a solution in MeOH. The pattern produced by the PXRD analysis of these doped systems closely matches that of Form III FFA **14**. Firstly, this suggests that the inclusion of any additive at this level does not result in the formation of a different polymorph of FFA **14** when crystallised in this manner. Additionally, the preservation of the Form III pattern in the PXRD scans of the doped

materials indicates that the inclusion of the additives does not disrupt the lattice structure of the pure material.

Despite being intended as a less lattice-compatible additive, the PXRD pattern for the sample doped with t-Bu-FA **19** (top) is comparable to those doped with the other additives in terms of similarity to Form III FFA **14**. This could imply that t-Bu-FA **19** is incorporated to a greater extent than might be expected. The behaviour of t-Bu-FA **19** as an additive will be explored further throughout the chapter.

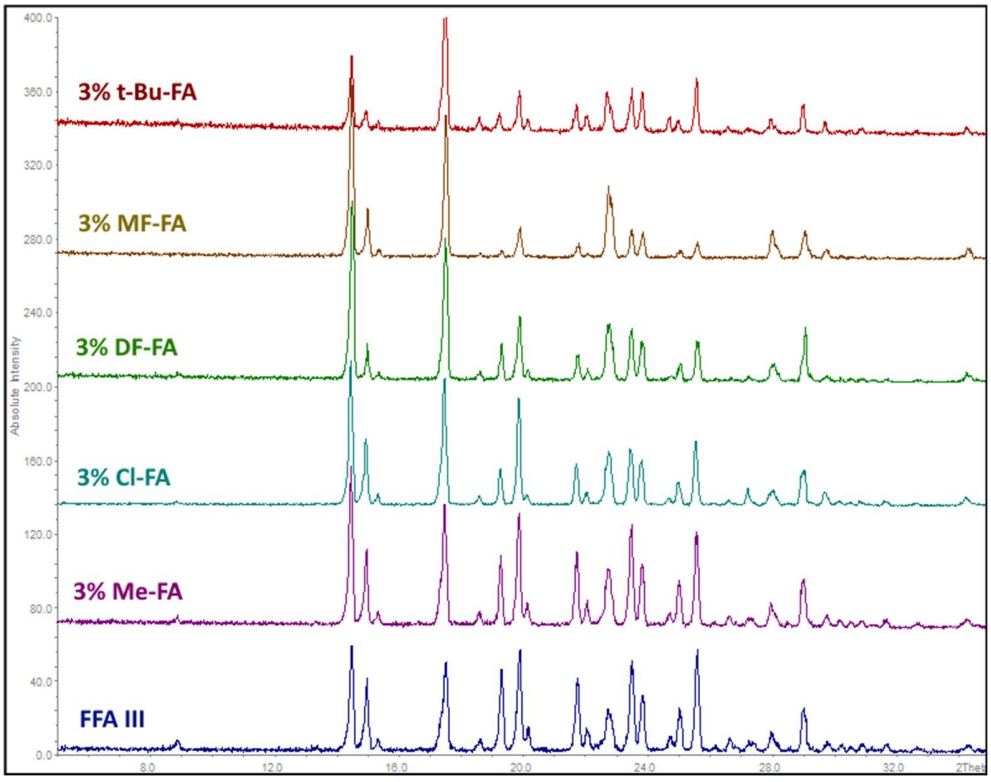


Fig 4.22. Top to bottom: PXRD patterns of FFA **14** doped with (top) 3% t-Bu-FA **19**, 3% MF-FA **18**, 3% DF-FA **17**, 3% Cl-FA **16**, and 3% Me-FA **15**, compared to that of (bottom) pure Form III FFA **14**, produced by the slow evaporation of MeOH.

4.5.2.2 Effect of Additive Inclusion on Crystallisation Methods

Figure 4.23 below displays PXRD patterns of FFA **14** doped with 4% Me-FA **15**, crystallised *via* three of the four primary crystallisation methods developed for the research: slow cooling of a solution in MeCN, slow evaporation of a solution in MeOH, and rotovap crystallisation. Patterns for doped systems crystallised *via* vapour diffusion are not included, as the material produced by this method was limited and necessary for other aspects of the work. The patterns for pure Form III FFA **14** (bottom) and Me-FA **15** (top) are also included for comparison. The doped patterns can be compared to those of pure FFA **14** crystallised *via* the same methods (Appendix Figure 7.26) to ascertain the impact of the inclusion of low levels of additive on the polymorphic form produced by each method. It appears that the Form III polymorph is preserved during each crystallisation of the doped material.

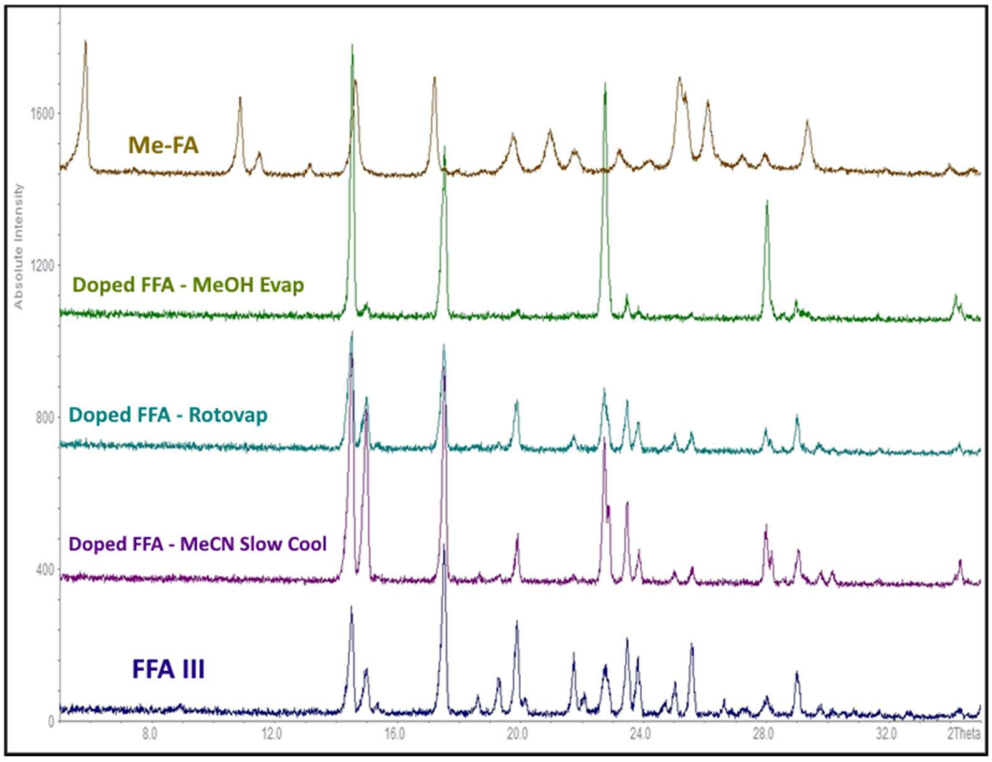


Fig 4.23. Top to bottom: PXRD patterns of pure Me-FA **15** alongside FFA **14** doped with 4% Me-FA **15**, crystallised *via* slow evaporation from MeOH, rotovap evaporation, and slow cooling of a MeCN solution, followed by the pattern of Form III FFA **14**.

4.5.2.3 Effect of Increasing Doping Levels of Me-FA **15**

Figure 4.24 illustrates the impact increasing doping levels of Me-FA **15** has on the crystal structure of the FFA **14** host. The PXRD pattern of pure Form III FFA **14** (top) is compared against those of FFA **14** doped with Me-FA **15** at levels of 10 – 90%, as well as pure Me-FA **15** (bottom). Up to a doping level of about 40%, the patterns of the doped material closely resemble that of Form III FFA **14**. In the 50% pattern, peaks start to emerge that are more representative of those seen in pure Me-FA **15**. As the doping levels increase further, these peaks are expressed more clearly, new peaks matching those in pure Me-FA **15** emerge, and some characteristic Form III FFA **14** peaks start to disappear.

The patterns imply that the FFA **14** crystal conformation is predominantly preserved up to a doping level of 40% Me-FA **15**. Even at higher doping levels, up to 90% Me-FA **15**, certain characteristic FFA **14** peaks are still visible that are not present on the pure Me-FA **15** pattern, suggesting that even at those doping levels some aspect of the Form III lattice is preserved. An alterinative explanation is that phase separation is occuring, and the diffraction patters of both pure FFA **14** and Me-FA **15** are being measured in the same sample. However, DSC analysis of the same material identifes a single phase in the sample, rather than two distinct phases corresponding to the melting points of the individual component (see Section 4.6.1).

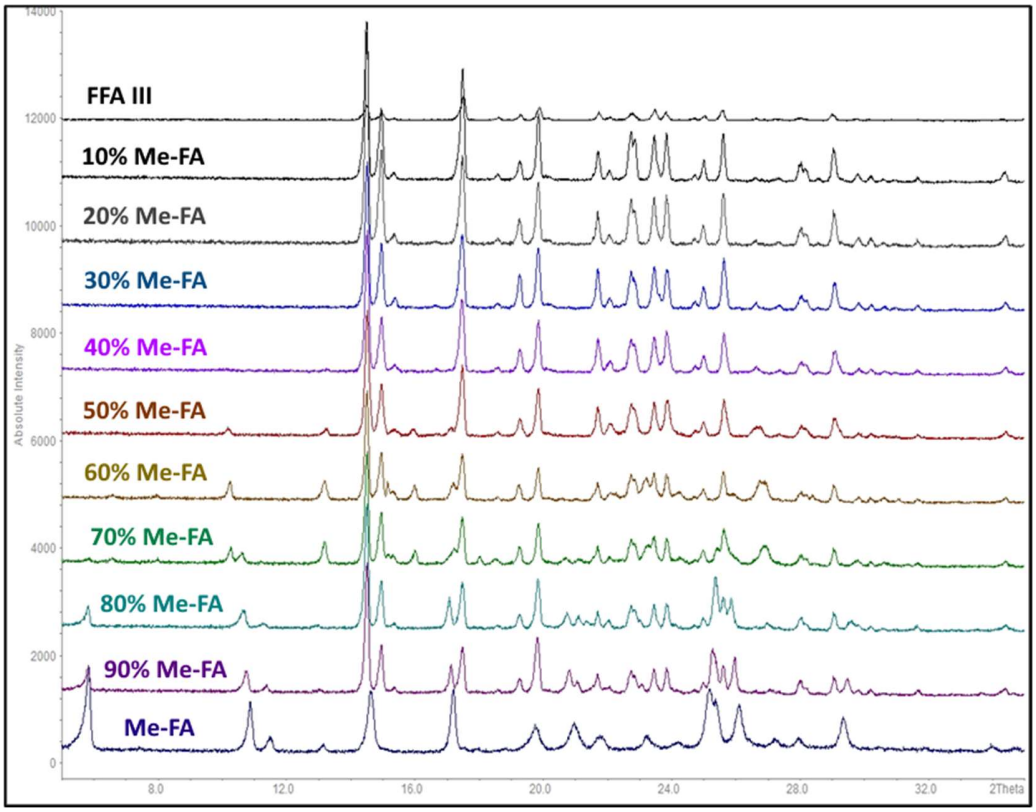


Fig 4.24. Top to bottom: PXRD patterns of pure Form III FFA **14** compared to FFA **14** doped with increasing levels of Me-FA **15** (10, 20, 30, 40, 50, 60, 70, 80, and 90%) and pure Me-FA **15**, produced by crystallisation by rotary evaporator.

4.5.2.4 Effect of Increasing Doping Levels of Cl-FA **16**

Figure 4.25 below shows a comparable series of PXRD patterns of FFA **14** systems doped with increasing levels of Cl-FA **16**, with patterns of the pure materials included. The behaviour of these systems appears to be significantly different from those doped with Me-FA **15**. The systems doped with 10 – 20% Cl-FA **16** have patterns very similar to Form III FFA **14**, implying the lattice structure of the pure material is preserved up to this level. At higher doping levels (30 – 90%) however, the patterns of the systems more closely resemble that of pure Cl-FA **16**, losing the peaks representative of FFA **14** and gaining those that bear increasingly similarity with those of Cl-FA **16**. This transition appears to originate at approx. 30% Cl-FA **16**; the pattern of the sample at this doping level clearly resembles Cl-FA **16**, but the peaks are much broader and less distinct than the patterns at other doping levels. This implies a lattice transition taking place around this composition. This observation mirrors the previously-discussed behavioural changes of material doped with a similar level of Cl-FA **16**, that is in terms of level of incorporation (Section 4.3.1.2) and resistance to purification (Section 4.4.1.3). As mentioned in Section 4.5.1, the FFA **14** material doped with 30% Cl-FA **16** was a noticeably different colour and consistency than material with other compositions of the two. This may also be linked to the ill-defined crystal structure of the material by PXRD.

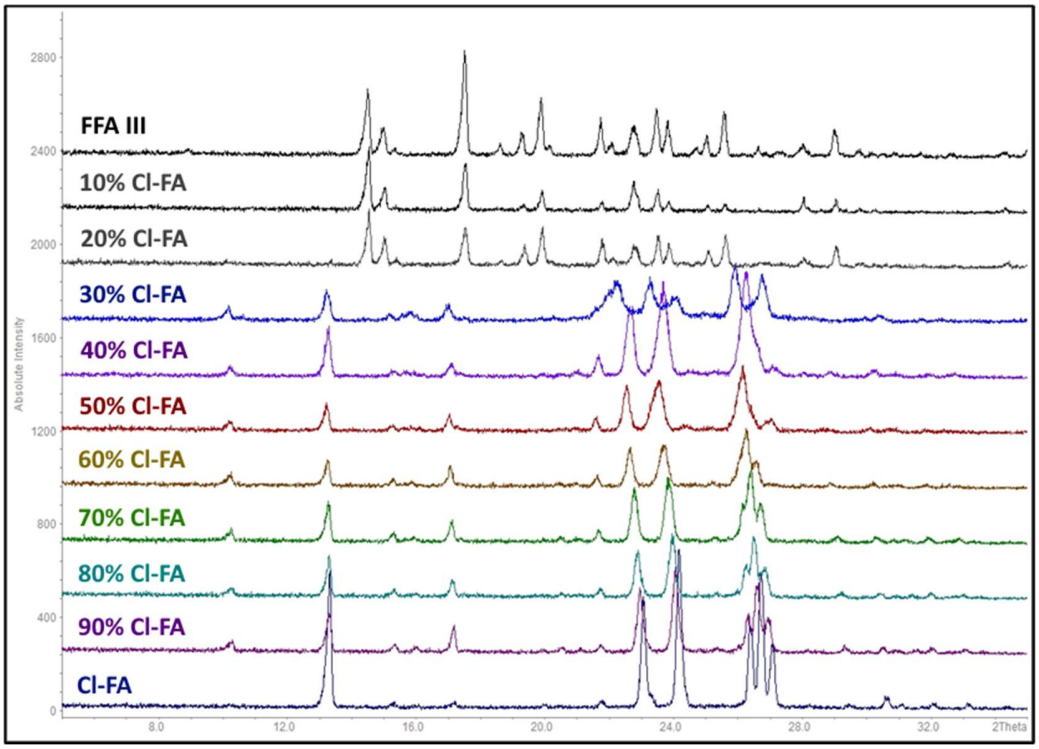


Fig 4.25. Top to bottom: PXRD patterns of Form III FFA **14** doped with increasing levels of Cl-FA **16** (0, 10, 20, 30, 40, 50, 60, 70, 80, and 90%) and pure Cl-FA **16**, produced by crystallisation by rotary evaporator.

4.5.2.5 Analysis of Crystals with Problematic Morphologies

Crystal samples of the systems with each observed type of problematic morphology (Types A – D) were analysed by PXRD to determine whether the difference in crystal habit was a result of disruption to the crystal structure of FFA and/or the presence of polymorphs other than Form III. The PXRD patterns produced by these systems can be found in Figure 4.26 alongside the pattern of pure Form III FFA for comparison. Each peak in the doped samples matched those of the pure material in terms of scattering angle. This suggests that the Form III polymorph is also preserved during the growth of these crystals, despite the difference in morphologies. The difference in

peak intensity between the five samples can be attributed to the preferred orientation effect, a reduction in the randomness of light scattering caused by certain crystal habits such as needles or plates.[215]

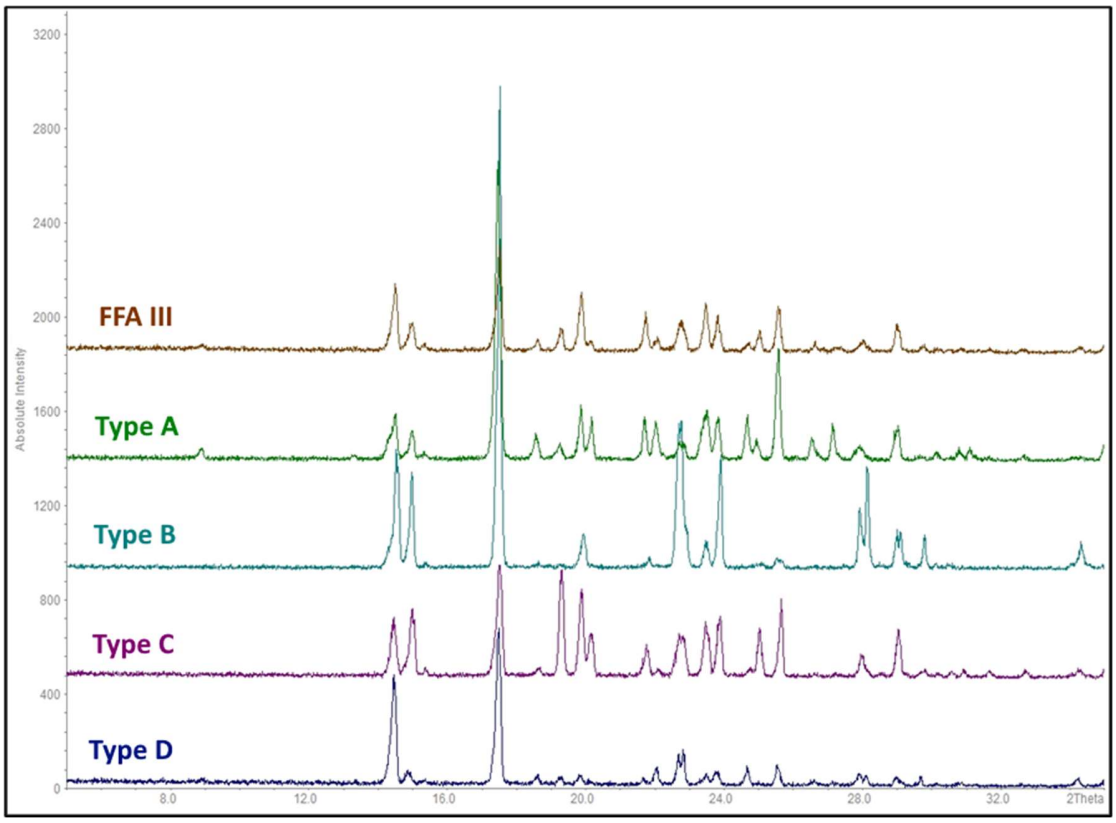


Fig 4.26. Top to bottom: Measured PXRD pattern of Form III FFA **14** alongside those of crystal samples with problematic morphologies: FFA **14** doped with 2% t-Bu-FA **19** (Type A), 2% MF-FA **18** (Type B), 2% MF-FA **18** (Type C), and 3% t-Bu-FA **19** (Type D), produced by the slow evaporation of MeOH.

4.6 Phase Behaviour of Doped Systems

The best way to characterise the effect of variation in composition on phase behaviour of a system of two components is by construction of a phase diagram. There are several different types of categories into which one of these systems can fall, depending on the nature of the constituents and how they interact in the solid phase. The subject of binary systems is discussed in more detail in Section 1.3.2, but for the purposes of this project, the discussion will mostly be limited to solid solutions, both continuous and partial/terminal, and eutectic systems.

4.6.1 FFA **14** / Me-FA **15** Systems

4.6.1.1 Polymorphic Behaviour

The relationship between the Form III and Form I polymorphs of FFA **14** has been discussed in terms of pure FFA **14** in Section 2.6.2. In short, Form III (m.p. 124 – 126 °C) is the thermodynamically stable form at room temperature, but at higher temperatures the previously metastable Form I (m.p. 132 – 134 °C) becomes more stable.[71,153] When heated as part of a DSC ramp, this manifests as an endothermic peak at the Form III melting point, followed immediately by an exotherm as the material resolidifies into Form I, which subsequently re-melts at its own melting point for a second endotherm. It was discovered that varying the heating rate and level of grinding of the sample could alter the extent to which each of these endotherms is expressed; increasing the rate resulted in a more

pronounced Form III endotherm, whereas decreasing the heating rate caused it to almost disappear entirely from the curve.

Effect of Me-FA **15** Inclusion on the Polymorphic Behaviour

It was observed that the doping of a system of Form III FFA **14** with additives altered the shape of the DSC curve. For example, inclusion of 10% Me-FA **15** into the sample caused an increase in the area of the Form III endotherm relative to that of Form I at a heating rate of 10 °C min^{-1}. Increasing the additive level to 20% additive made the effect more pronounced, this time reducing the expression of the Form I peak in a similar manner (Figure 4.27).

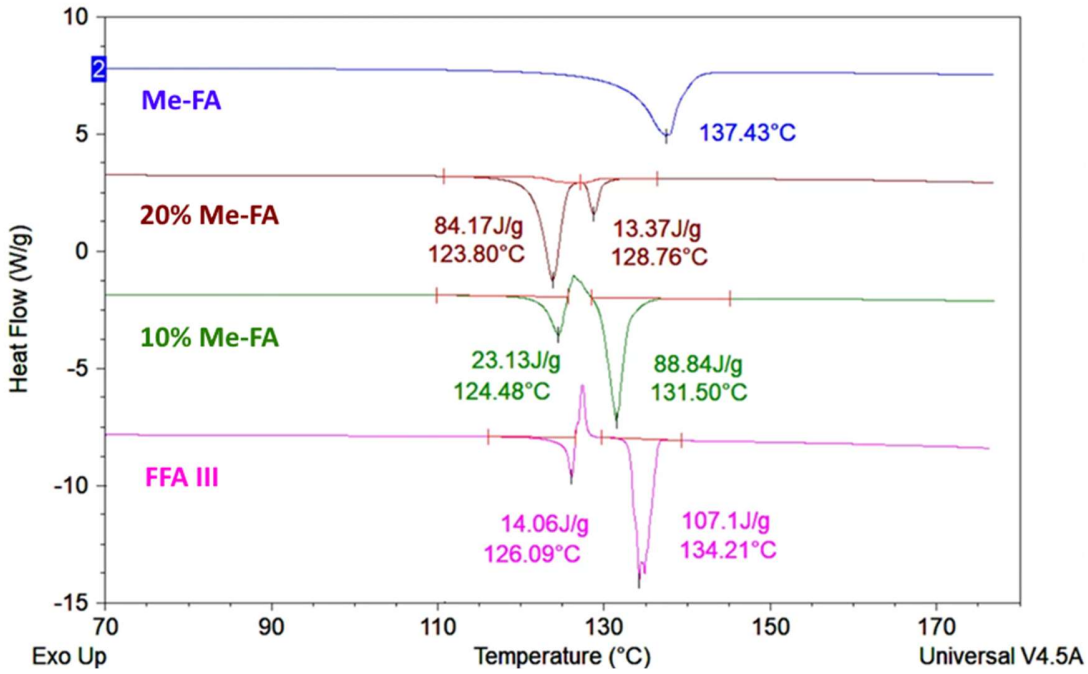


Fig 4.27. Top to bottom: DSC curves of pure Me-FA **15**, FFA **14** doped with 20% Me-FA **15**, FFA **14** doped with 10% Me-FA **15**, and pure Form III FFA **14**, labelled with peak area and peak max values. Samples were heated at 10 °C min^{-1}.

No endothermic peak is visible at a lower temperature than those of the two polymorphs in either doped sample, notable as such a peak could indicate the presence of a eutectic mixture. This suggests solid solution-like behaviour is occurring at these levels, especially since the endotherms align with that of pure FFA **14** and no melting peak appears at the melting point of the pure additive material. However, the polymorphic nature of the material makes it difficult to conclusively determine based on these curves. A final observation, and one that will be revisited later in the section, is that the melting endotherms of both polymorphic forms appear to be decreasing in temperature as the additive level is increased. This is generally characteristic behaviour of eutectic systems but has also been observed in certain non-ideal solid solutions.

Effect of Heating Rate on the Polymorphic Behaviour

As with the pure material, the expression of each endotherm in the doped samples could be altered further by varying the heating rate; higher heating rates favoured Form III while lower rates favoured Form I. The difference between the pure and doped samples lay in the degree that each peak was expressed at each heating rate. In the pure material, decreasing the heating rate to under 5 °C min^{-1} caused the Form III peak to almost disappear into the baseline entirely, while raising the rate to a very high 50 °C min^{-1} resulted in two peaks of approximately equal size (see Section 2.8.7.3). A similar decrease in heating rate also reduced the size of the Form III endotherm in the 10% Me-FA **15** sample, but to a lesser extent. On the other hand, raising the heating rate of the scan resulted in a single very large endotherm close to the Form III melting point, with no Form I peak visible (Figure 4.28). The intensity of the peaks on the curves appear to scale with

heating rate in a similar manner to previously observed in the undoped FFA **14** samples, but once again the integrations of the peaks are comparable. Sample mass was maintained at a constant 2 – 5 mg in all cases.

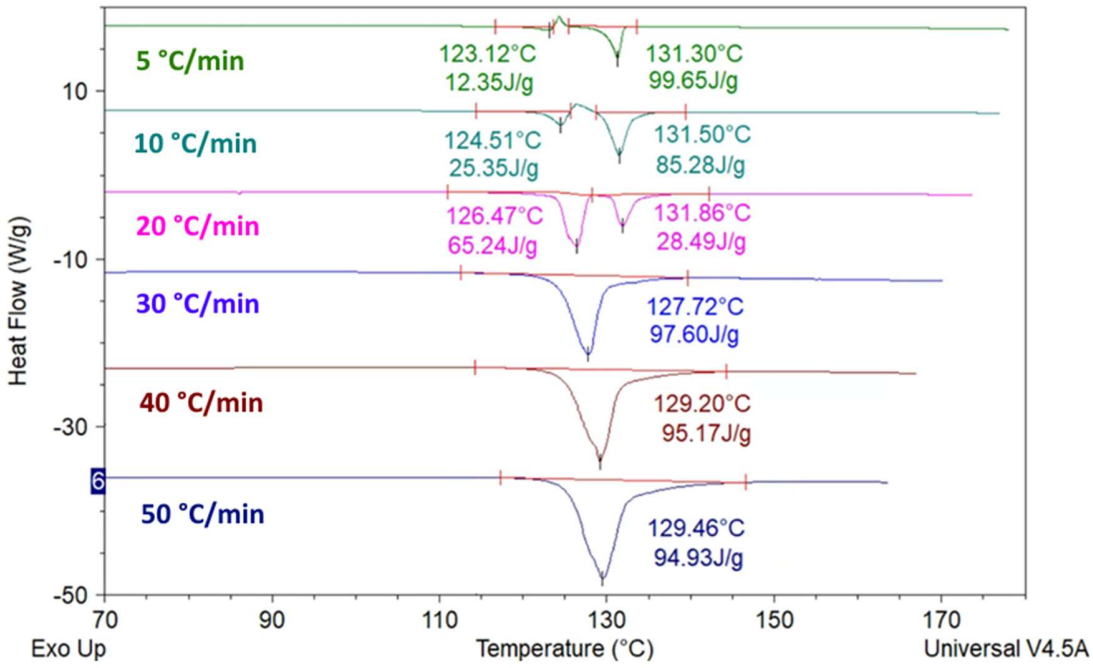


Fig 4.28. Top to bottom: DSC curves of FFA **14** doped with 10% Me-FA **15** collected at heating rates of 5, 10, 20, 30, 40, and 50 °C min^{-1}, labelled with peak area and peak max values.

Effect of Sample Grinding on the Polymorphic Behaviour

A similar test to that carried out in Section 2.8.7.4 was performed to investigate the effect of sample grinding on the phase transformation of the material. Four samples of doped FFA **14** were produced by rotovap crystallisation, two doped with approximately 10% Me-FA **15** and two with approximately 40%. One of each was ground into a fine powder using a pestle and mortar, while the other two were not subjected to any grinding.

DSC scans were performed on the four samples at a rate of 5 °C min^{-1} (Figure 4.29) and 50 °C min^{-1} (Figure 4.30). Mirroring the results observed in the case of pure FFA **14**, grinding of the material appeared to increase the expression of the Form I endotherm relative to the Form III. This remained true across all additive levels and heating rates tested.

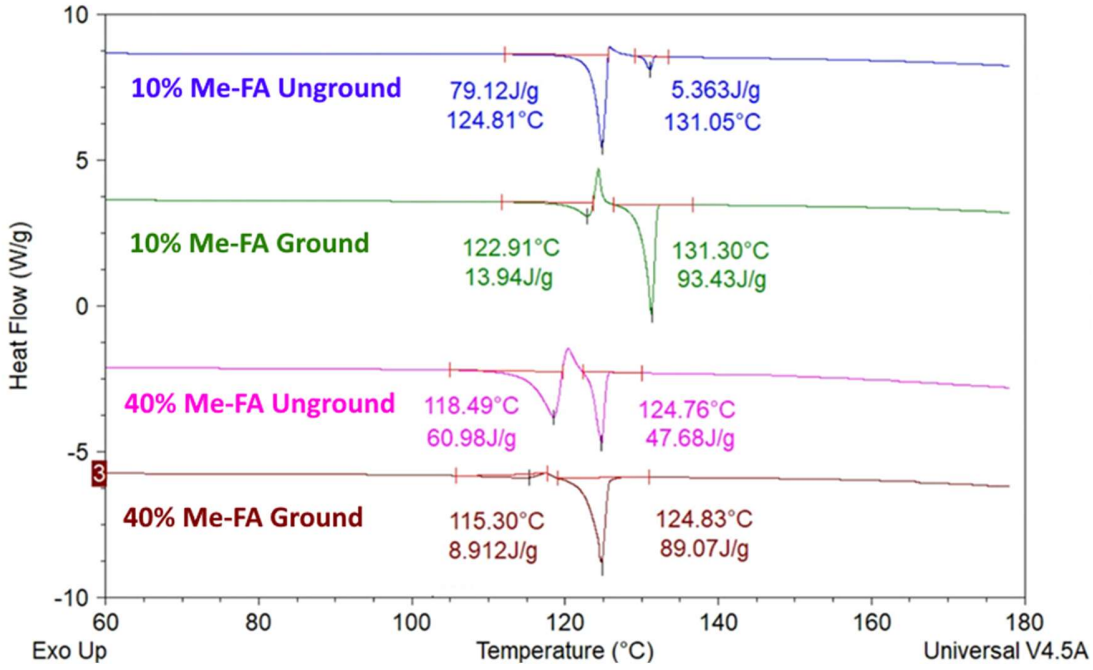


Fig 4.29. Top to bottom: DSC curves of FFA **14** doped with 10% Me-FA **15** unground and ground, and FFA **14** doped with 40% Me-FA **15** unground and ground, collected at a heating rate of 5 °C min^{-1}, labelled with peak area and peak max values.

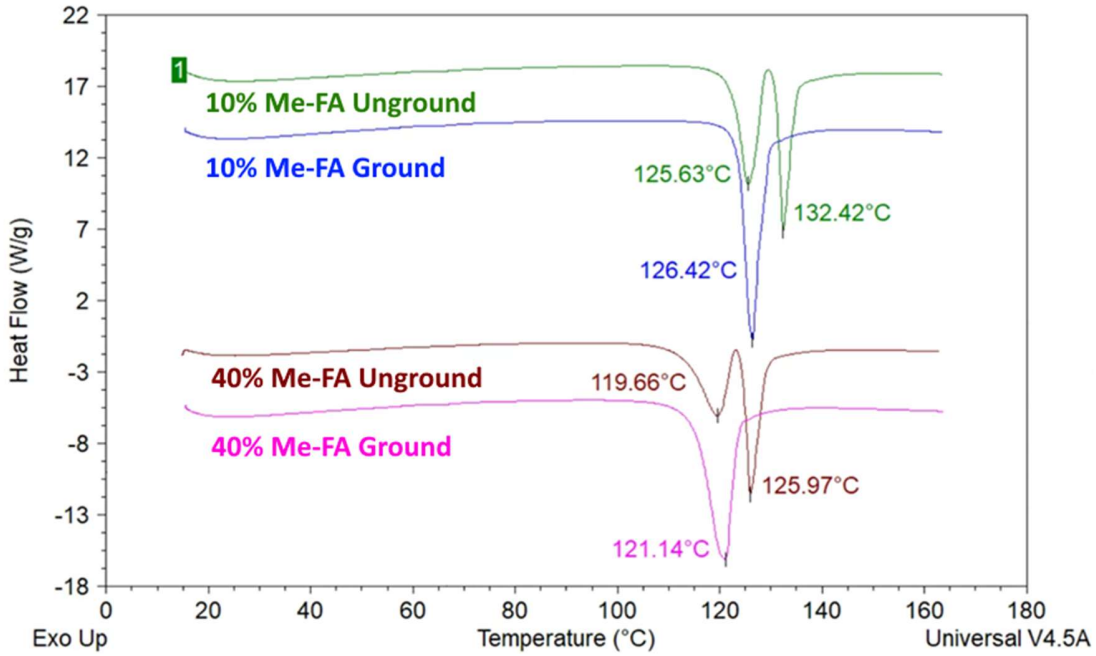


Fig 4.30. Top to bottom: DSC curves of FFA **14** doped with 10% Me-FA **15** unground and ground, and FFA **14** doped with 40% Me-FA **15** unground and ground, collected at a heating rate of 50 °C min^{-1}, labelled with peak max values.

The curves obtained as part of the grinding test also demonstrate another important observation to consider when examining DSC data of this material: the presence of the Form I endotherm appears to 'interrupt' the expression of the Form III signal, resulting in a significantly lower Form III peak maximum in scans where both are endotherms expressed compared to those where Form III is expressed alone. This decrease appears proportional to the relative expression of the Form I endotherm, yet the Form I peak does not seem affected in the same way, maintaining a similar peak maximum irrespective of peak size.

It should be noted that despite the level of control over the material granted by the variation of heating rate and grinding, expression of melting peaks as a result of phase

transitions remained subject to variability. Often, samples from the same material batch can be tested under the same conditions (heating rate, etc.) and output significantly different DSC curves. This was especially true for samples with approximately 50% Me-FA **15**. As an example, in Figure 4.31, three scans of the same material (FFA **14** doped with approximately 50% Me-FA **15**) heated at a rate of 20 °C min^{-1}. The temperature data collected from systems doped with Me-FA **15** are presented as ranges to account for this variability.

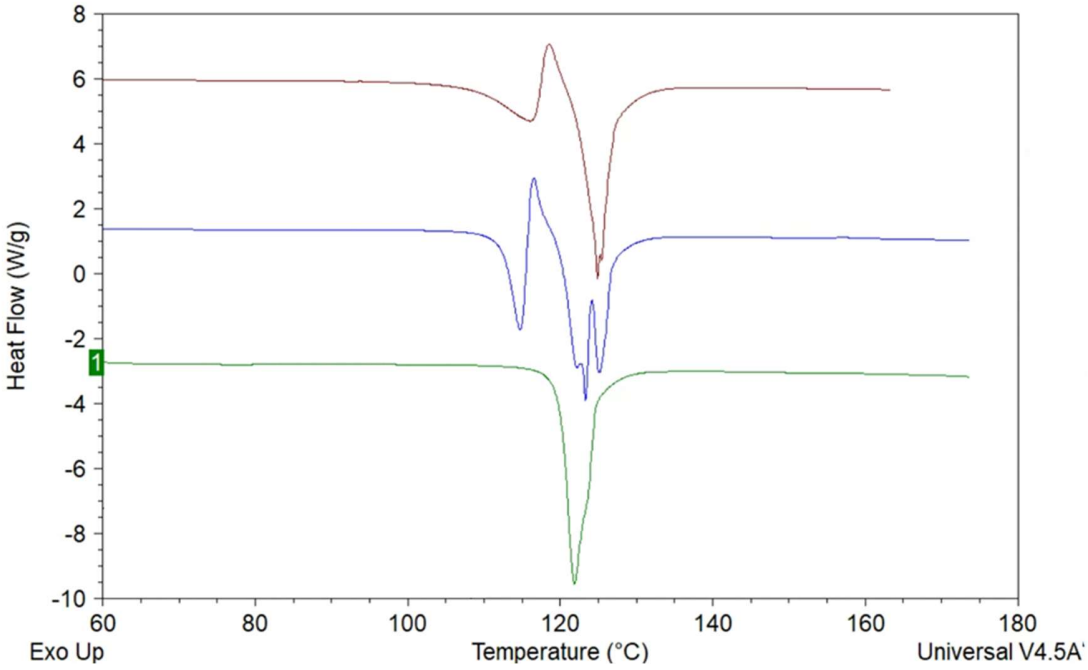


Fig 4.31. Three DSC curves of the same sample of FFA **14** doped with 50% Me-FA **15**, collected under identical conditions, to highlight the variability of data collection at higher doping levels.

4.6.1.2 Interpretation of DSC Data

The above factors contribute significant complications to the interpretation of data and make constructing a phase diagram of the doped material a more difficult process.

Due to the consistent absence of additional peaks, eutectic or otherwise, visible on DSC curves of the material at any doping level (other than those that can be attributed to FFA **14**), the presence of a continuous solid solution seems the most likely option. To construct a phase diagram for such a system, two temperature values are required, that of the onset of the melting peak of the material (T_O) and that of the peak maximum (T_P). At this point a decision needs to be made whether to obtain those values from the Form III or Form I melting peaks. The T_P value of Form I remains very consistent regardless of its intensity, but the expression of the Form III endotherm interferes with accurate measurement of T_O. On the other hand, the T_O of the Form III peak is easy to measure, but the T_P is influenced substantially by the relative size of the Form I peak. Whichever option was chosen, the elimination of the other from the curve was, therefore, desirable. By decreasing the heating rate and increasing the level of grinding, the polymorphic transformation of the material is promoted, and, thus, the expression of the Form III endotherm minimised, but not eliminated completely. The Form I endotherm on the other hand could be more easily hidden in lightly ground samples by increasing the heating rate of the scan, suppressing the transformation of Form III to Form I. For this reason, the Form III peak was chosen as the more favourable option from which to collect data for the FFA **14** / Me-FA **15** phase diagram. Initially, it was thought that the data should be collected at heating rates of 40 or 50 °C min^{-1} to ensure only the Form III endotherm would be expressed; at rates lower than that the Form I peak was often visible in the 10 and 20% doped samples. However, it was decided that the T_P at those heating rates deviated too far from the melting point of Form III FFA **14** to use as part of a phase diagram; as such, data collection was limited to curves with a maximum heating rate of 20 °C min^{-1}.

The DSC data used in the construction of the phase diagram was collected from curves of multiple repeated scans for each additive level, in the manner described in Section 4.9.6.1. The T_O and T_P values collected from these scans are presented as a range of temperature values on the plot in Figure 4.32, along with the average temperature value at each additive level. The variation in the data as a result of the previously described difficulties and inconsistencies means the collection of data from a single curve at each additive level would not be guaranteed to be an accurate reflection of the behaviour of the system at that composition. Presenting the data as a range of temperature values allows for the construction of a phase diagram more representative of the nature of the system.

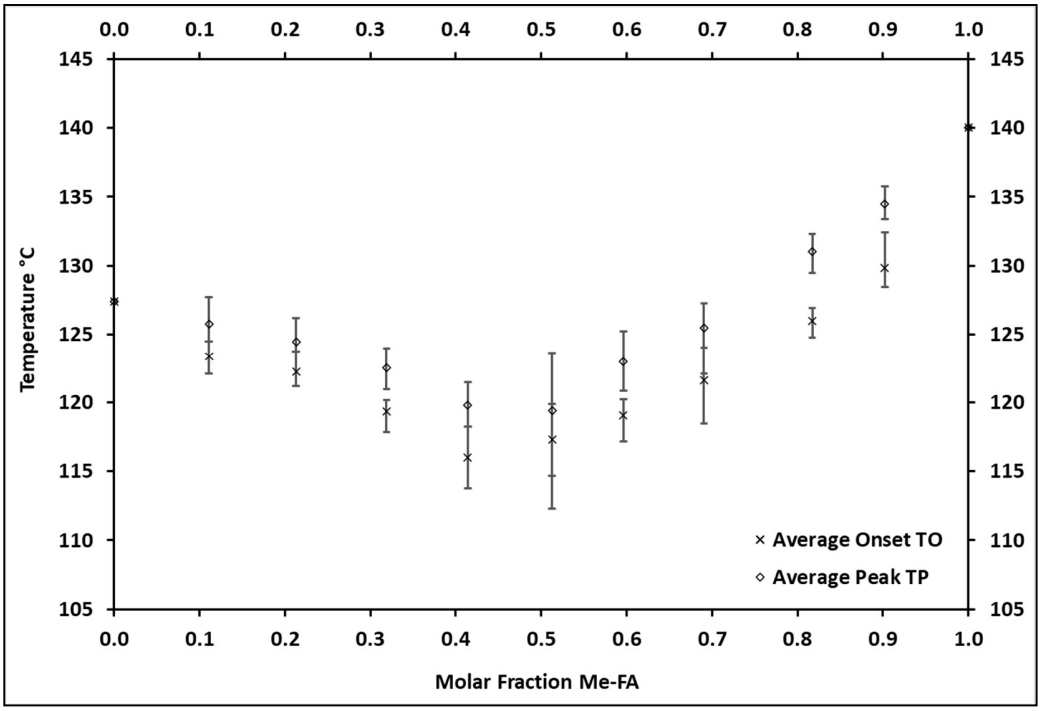


Fig 4.32. Ranges of onset (T_O) and peak (T_P) temperatures collected from multiple DSC curves of crystalline FFA **14** material doped with increasing levels of Me-FA **15**, along with the average value for each range of temperatures.

In the above system, the melting point of the material (represented by the peak onset temperature T_O and the peak max T_P) decreases with doping level from a Me-FA **15** molar fraction of 0.0 to approximately 0.4 (40%). Over this range the gap between the two measurements also widens, representing a widening of the melting endotherm on the DSC curve. At a molar fraction of 0.5, the decrease in temperature plateaus, and the gap between the average T_O and T_P values narrows substantially. A significant overlap of the T_O and T_P temperature ranges is also observable at this composition. At higher levels of Me-FA **15**, the divide widens again and the values of both T_O and T_P increase, converging at the melting point of pure Me-FA **15**. The shape of this plot closely resembles that depicted in Figure 4.33, a non-ideal continuous solid solution. These types of systems (described in Section 1.3.2.4) differ from their ideal counterparts in that the freezing and melting points of the mixed material do not necessarily fall between the melting points of the pure components, in this case occurring at a lower temperature. There appears to be a minimum point (*M*) at a composition close to 0.5, where the melting peak narrows to resemble that of the pure materials. This appears very similar to a eutectic point but differs in that the solidus and liquidus curves only ever approach each other, never meeting, despite being portrayed as overlapping on a phase diagram. The pattern of a non-ideal continuous solid solution is overlaid on the plot in Figure 4.34, and the final phase diagram for the material is displayed in Figure 4.35. The PXRD patterns of FFA doped with increasing levels of Me-FA are presented again in Figure 4.36 for comparison.

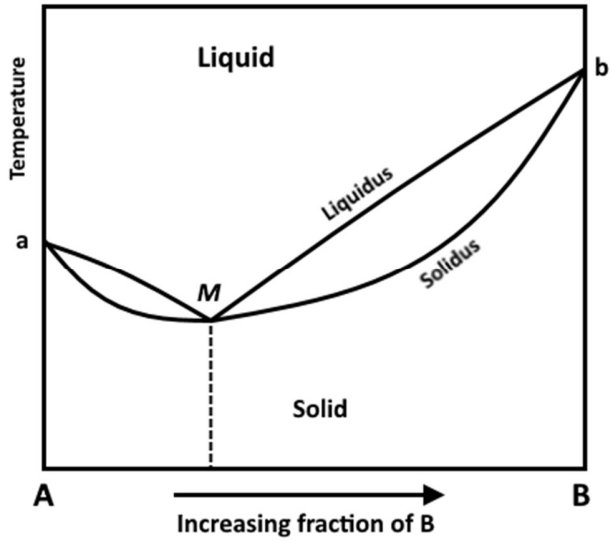


Fig 4.33. Example of continuous, non-ideal solid solution with included minimum point *M*.

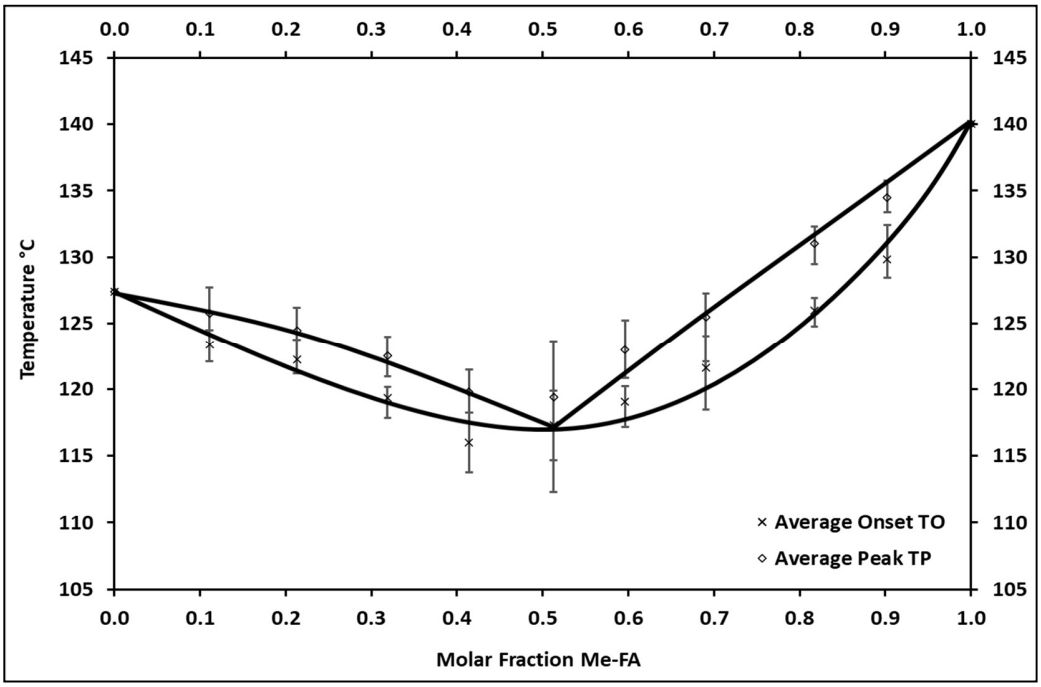


Fig 4.34. Outline of a continuous, non-ideal solid solution overlaid atop collected data from FFA **14** / Me-FA **15** system.

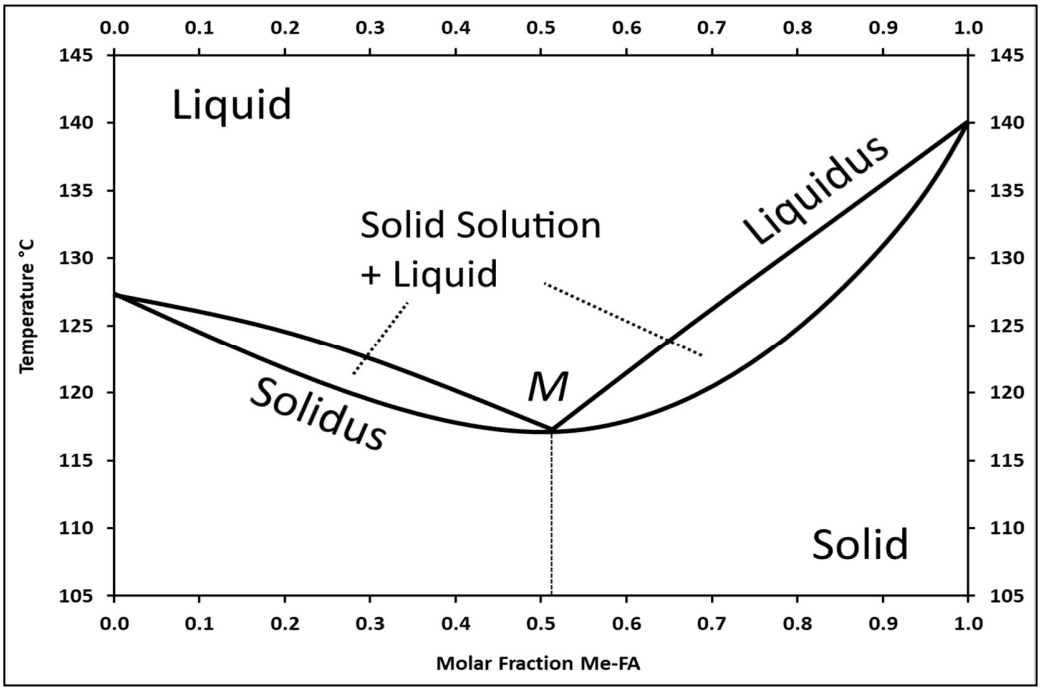


Fig 4.35. Phase diagram for the continuous, non-ideal solid solution constructed for FFA **14** / Me-FA **15** system.

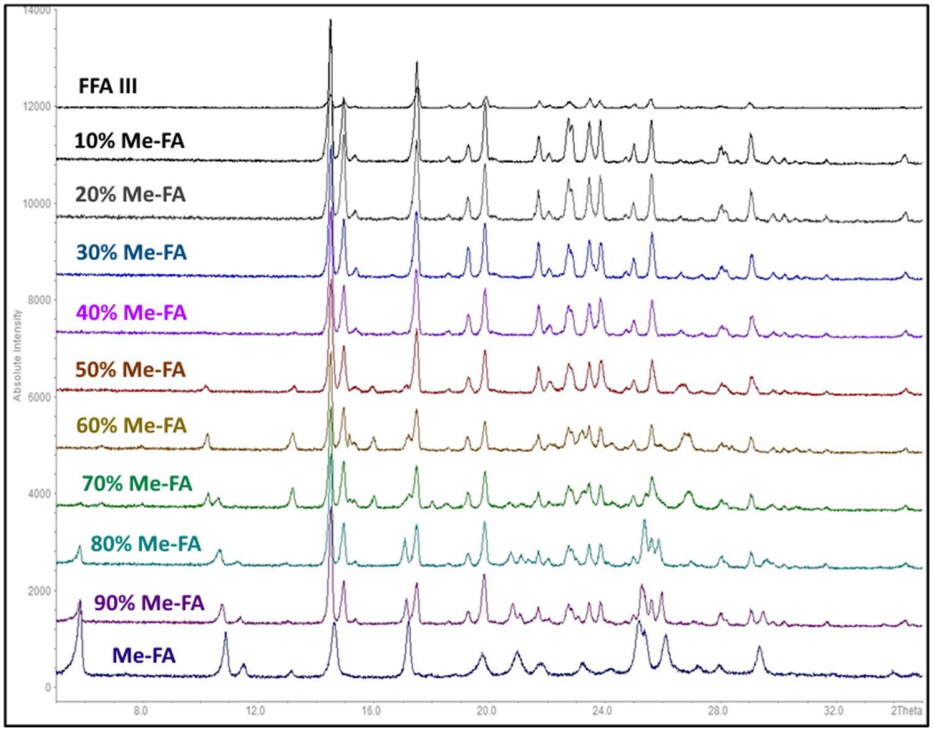


Fig 4.36. Top to bottom: PXRD patterns of pure Form III FFA **14** compared to FFA **14** doped with increasing levels of Me-FA **15** (10, 20, 30, 40, 50, 60, 70, 80, and 90%) and pure Me-FA **15**.

4.6.2 FFA **14** / Cl-FA **16** Systems

4.6.2.1 Polymorphic Behaviour

The inclusion of Cl-FA **16** also changed the polymorphic behaviour of the system relative to pure FFA **14**, but in a manner different to that of Me-FA **15**. The comparison can be seen in Figure 4.37; while at a heating rate of 10 °C min^{-1} the DSC curve of a sample of FFA **14** doped with 10% Me-FA **15** and a sample of pure Form III FFA **14** will exhibit both Form III and Form I melting endotherms, only the Form I peak is visible on the curve of a sample of FFA **14** doped with 10% Cl-FA **16**. It appears that Cl-FA **16** has the reverse effect on the polymorphic behaviour of FFA **14** to Me-FA **15**, rather than favouring the expression of the Form III endotherm it instead favours that of Form I. This observation mirrors a similar study carried out by Lee *et al.*[71] In that study, when samples of Form III FFA **14** were doped with mefenamic acid, the inclusion of the additive resulted in the shrinking of the Form III endotherm relative to the Form I peak. The study suggests the reduction in energy needed to melt and recrystallise Form III FFA as a possible explanation for this observation.

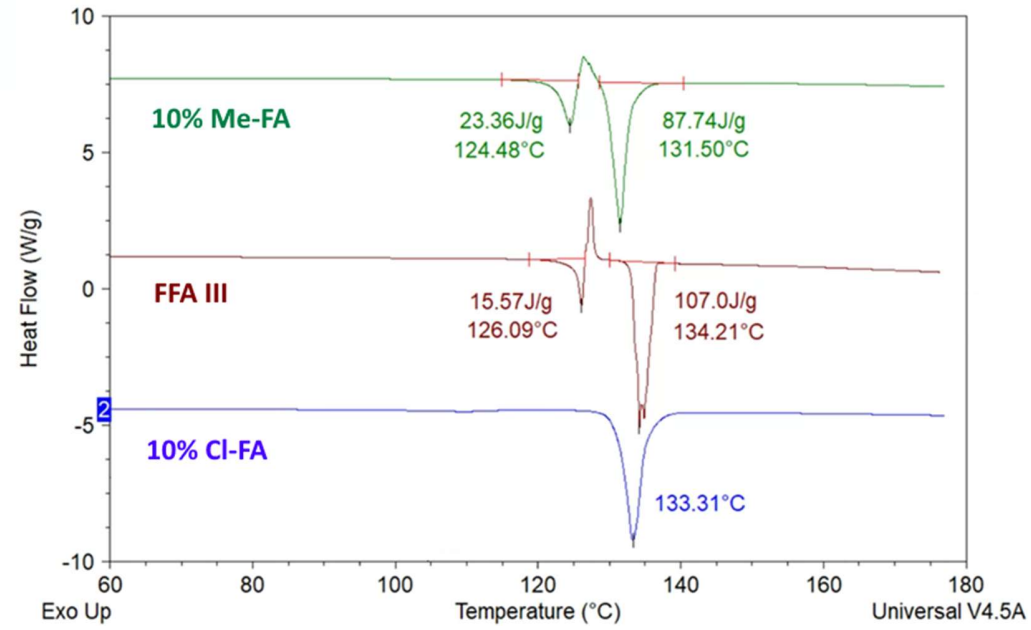


Fig 4.37. Top to bottom: DSC curves of FFA **14** doped with 10% Me-FA **15**, pure Form III FFA **14**, and FFA **14** doped with 10% Cl-FA **16**, collected at a heating rate of 10 °C min^{-1}, labelled with peak area and peak max values.

The extent of this phenomenon can be varied with heating rate, as with the previous systems. Increasing the heating rate causes the Form III endotherm to grow in size relative to Form I, but even at 50 °C min^{-1} the Form I peak is still present (Figure 4.38). At lower heating rates, e.g., 1 °C min^{-1}, the Form I peak narrows and sharpens.

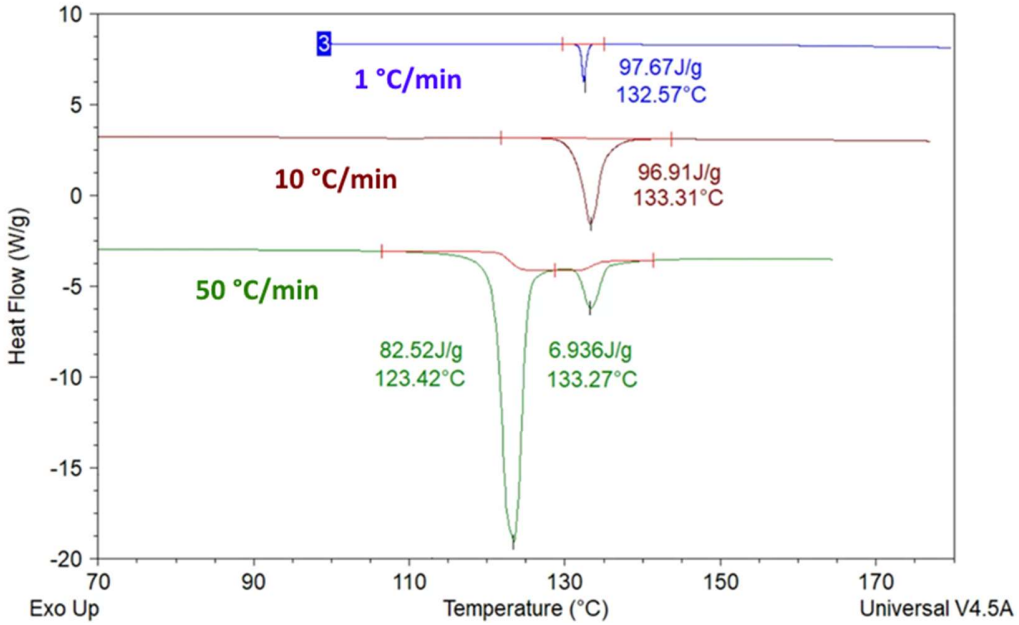


Fig 4.38. Top to bottom: DSC curves of FFA **14** doped with 10% Cl-FA **16**, collected at heating rates of 1, 10, and 50 °C min^{-1}, labelled with peak area and peak max values.

Like with the systems doped with Me-FA **15**, the expression of both Form III and Form I endotherms on the same curve would be detrimental to the collection of phase data. It was preferable to attempt to run DSC scans under conditions that would only result in one of the forms being visible on the curve. Based on the above observations, it was decided to focus on eliminating the Form III endotherm and reading data based on the Form I peak. This was achieved by analysing each sample by DSC at the low heating rate of 1 °C min^{-1}, to ensure minimisation of the Form III peak.

4.6.2.2 Observations of FFA **14** / Cl-FA **16** System Behaviour

Initial samples were created doped with Cl-FA **16** at 10% increments, from 10 – 90%. Samples were crystallised *via* rotovap and analysed by DSC. The curves of those scans are displayed in Figures 4.39 – 4.41. At an additive level of 10%, a single endotherm is visible slightly below the literature melting point of Form I FFA **14** (134.5 °C).[65] The temperature at the peak max descends gradually with increased doping level (Figure 4.39). This was also observed in systems doped with Me-FA **15** and is characteristic of, but not limited to, eutectic systems. No second lower temperature endotherm indicative of a eutectic is visible at these lower doping levels. The behaviour of the system begins to deviate from that of the Me-FA **15** doped system at higher doping levels; the temperature of the initial endotherm levels off, and a second broad endotherm emerges at a higher temperature, rapidly increasing in temperature and size as it approaches the melting point of the pure Cl-FA **16** material (169.85 °C, empirically determined). The growth of this second peak can be observed in more detail in Figure 4.40. The composition at which this second peak emerges matches the composition at which the changes in incorporation behaviour and crystal structure described earlier in the chapter were observed. Based on these collective findings, it was clear the two components form a eutectic system at higher doping levels. The composition at which the second endotherm, which represents the hyper-eutectic liquidus curve, emerges was difficult to determine at this stage, due to the broadness and low intensity of the peak and the large doping level intervals of the samples. However, it was determined to be falling at a composition between 20 and 30% Cl-FA **16** (Figure 4.41). As such, the eutectic point of the system was also expected to lie between these compositions.

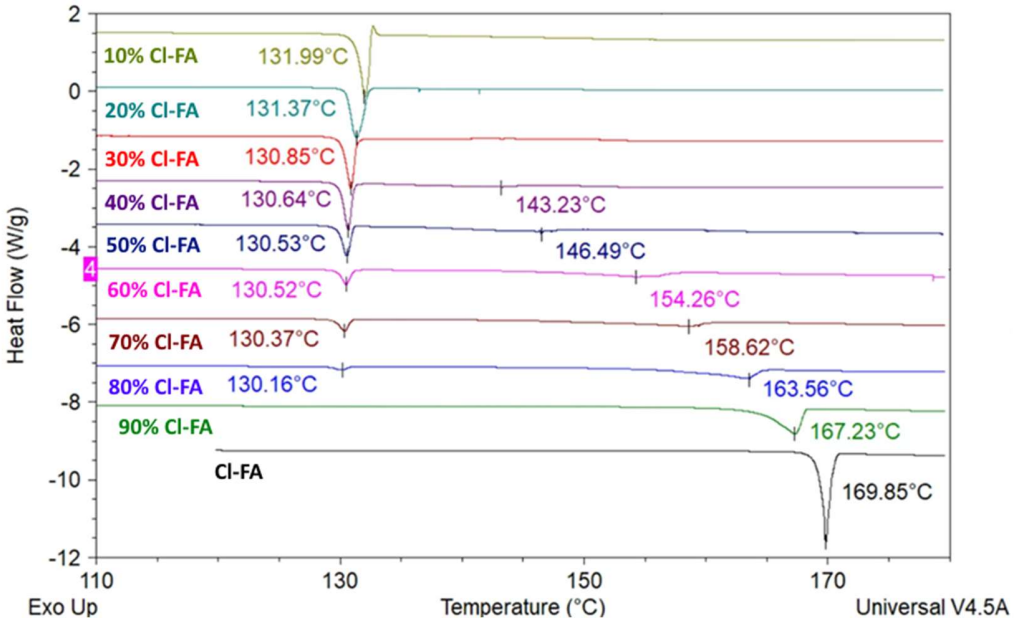


Fig 4.39. Top to bottom: DSC curves of FFA **14** doped with 10, 20, 30, 40, 50, 60, 70, 80, and 90% Cl-FA **16**, as well as pure Cl-FA **16**, collected at a heating rate of 1 °C min^{-1}, labelled with peak maximum values.

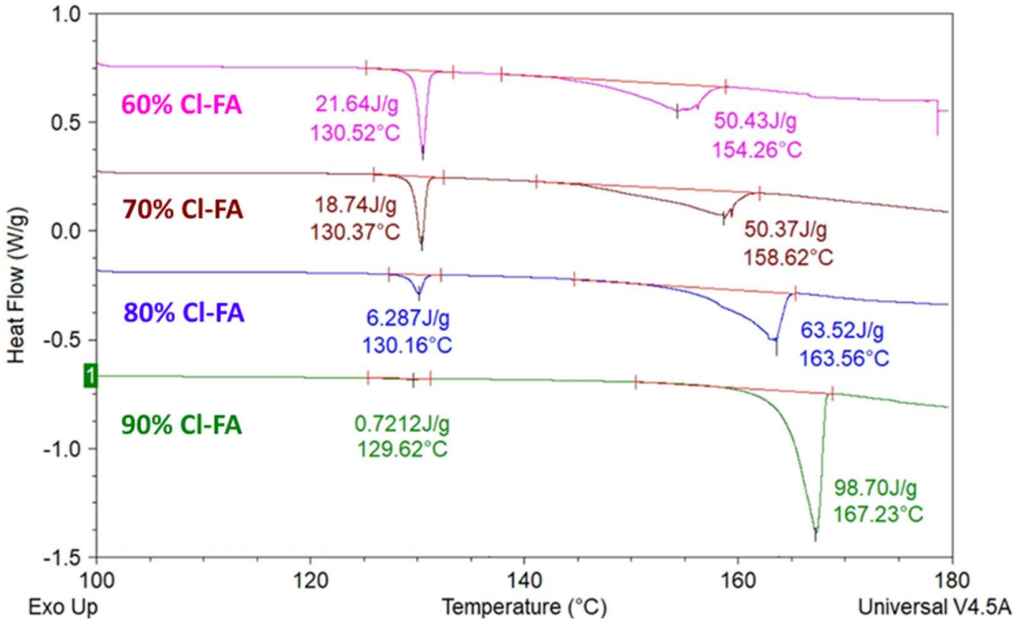


Fig 4.40. Top to bottom: DSC curves of FFA **14** doped with 60, 70, 80, and 90% Cl-FA **16**, collected at a heating rate of 1 °C min^{-1}, labelled with peak area and peak maximum values.

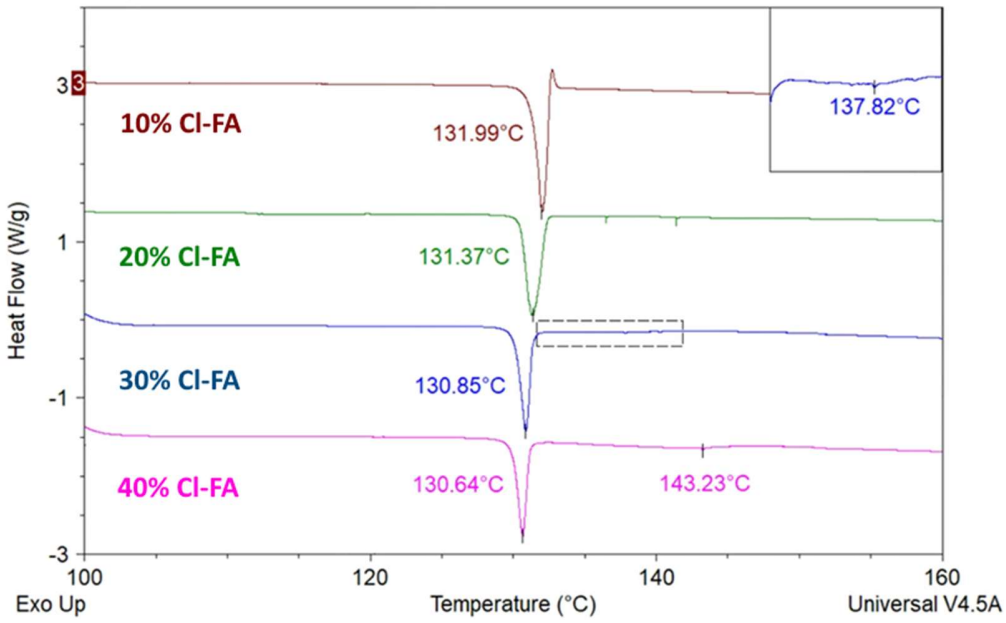
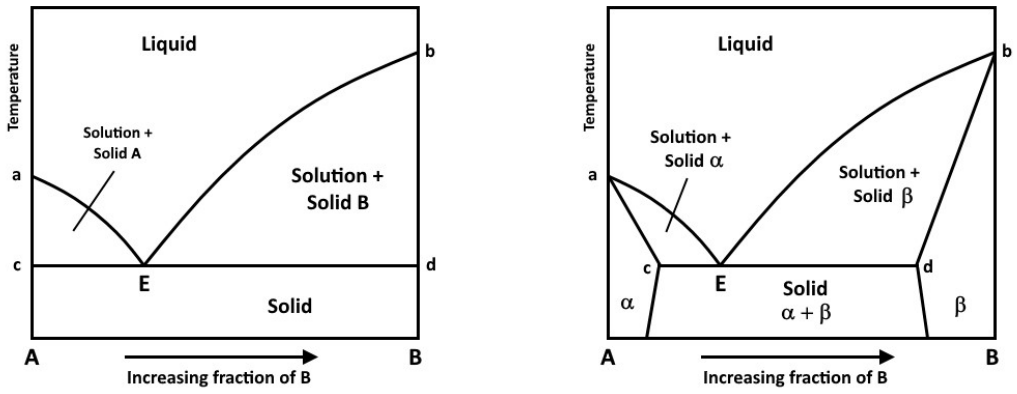


Fig 4.41. Top to bottom: DSC curves of FFA **14** doped with 10, 20, 30, and 40% Cl-FA **16**, collected at a heating rate of 1 °C min^{-1}, labelled with peak area and peak maximum values, with inset in top right showing close-up of emerging second endothermic peak.

4.6.2.3 Nature of Hypo-Eutectic Region Behaviour

Putting aside the composition of the system at the eutectic point, a question remained concerning the nature of the system at doping levels below that point. In a simple eutectic, one where no solid solution behaviour was observed, the inclusion of additive at low levels would result in an endothermic peak representing the melting of the eutectic material becoming visible on a DSC curve. This peak would appear at a temperature lower than the melting endotherm of the majority component. The temperature of this endotherm is plotted against additive fraction on the hypo-eutectic solidus curve *cE* (Figure 4.42), while the temperature of the major component endotherm

is plotted on the liquidus curve *aE.* This lower-temperature endotherm would be small at low additive levels, increasing in area relative to the higher temperature endotherm as the additive composition increases. At the eutectic point *E*, the higher temperature endotherm disappears into the baseline leaving only the lower-temperature eutectic peak visible. At compositions above that, a second higher temperature endotherm would emerge representing the melting of the new major component, the temperature of which is plotted on the hyper-eutectic liquidus curve *Eb.* This endotherm increases in temperature and area relative to the lower temperature endotherm as it approaches the pure additive melting point *b*, in a similar manner to that visible on the DSC curves in Figures 4.39 and 4.40 above. The temperature of the lower temperature endotherm remains relatively constant at all compositions. It is influenced slightly by the area of the peak, hence the slight decrease in the values observed with increasing Cl-FA **16**.



Figs 4.42 (left), 4.43 (right). Examples of a simple eutectic system (left) and a terminal solid solution (right).

If such a system were present at the hypo-eutectic compositions of the system, that lower temperature endotherm should be visible at a temperature between 129.5 - 131.0 °C in the 10 – 30% doped samples, based on the peak observed in the hyper-eutectic sample, and should increase in relative area with additive composition. This peak appears to be absent from any of the curves in Figure 4.41. This suggests solid solution behaviour characteristic of terminal or partial solid solutions. In these systems, the components are soluble in each other up to a certain composition, above which the miscibility ends, and a eutectic composition is formed in its place (Figure 4.43 above). If this were the case, no lower temperature endotherm would be observed while the components are miscible; at those compositions a single endotherm would be visible representing the solid solution α, much like was visible in the samples doped with Me-FA **15**. However, the limit of the miscibility *c* tends to be reached at compositions lower than the eutectic point *E* in these systems, at which point the endotherm representing the hypo-eutectic solidus c*E* appears as described. In this case however, no such endotherm was detected in the initial samples at any composition below the eutectic point.

New samples were created doped with between 2 – 30% Cl-FA **16** in smaller increments, firstly to pinpoint the composition of the eutectic point, and secondly to investigate whether a lower temperature endotherm representing the eutectic material would emerge at a certain composition. The DSC curves of some of these samples can be found in Figure 4.44. The drop in peak max temperature can be clearly observed, decreasing from 133.48 °C at a doping level of 2% to 130.83 °C at 30%. The inset in the bottom right is a close-up covering each sample curve within a range of approx. 128.0 °C to 130.5 °C. If an endotherm representing a hypo-eutectic solidus were to present itself at

any composition, it would almost certainly be within this region; however, no such peak is visible on any curve.

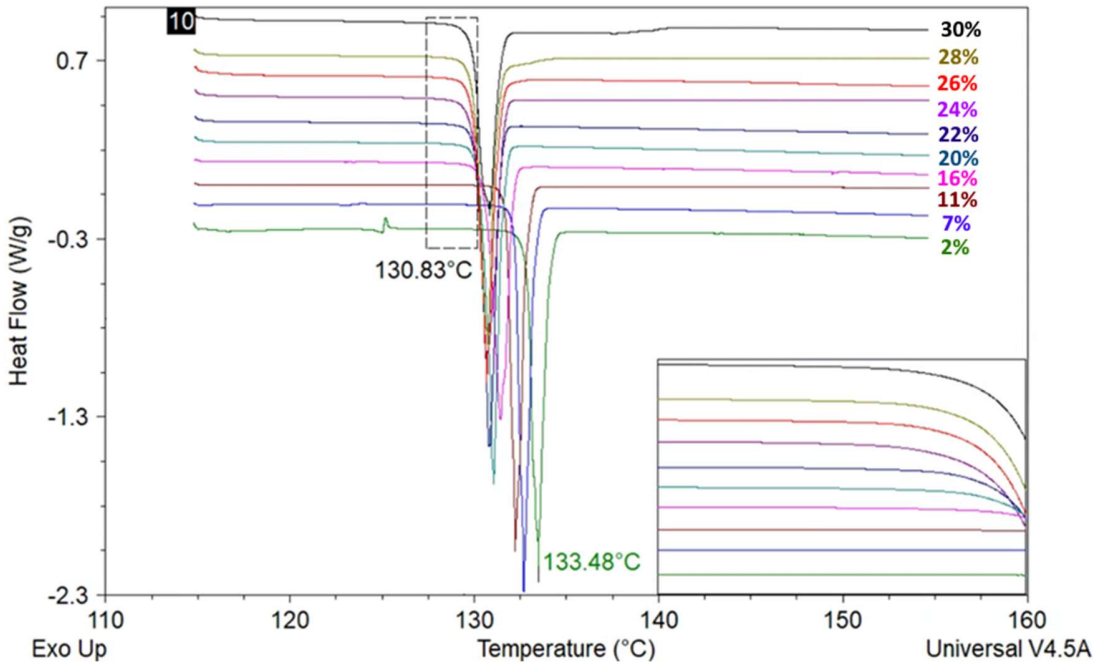


Fig 4.44. Top to bottom: DSC curves of FFA **14** doped with decreasing levels of Cl-FA **16** from 30 – 2%, collected at a heating rate of 1 °C min^{-1}, demonstrating the absence of a eutectic melting endotherm at low additive levels (inset, bottom right), as well as the change in peak maximum temperature across this range.

What is visible in Figure 4.44 is the emergence of a broad higher temperature endotherm representing the melting of the non-eutectic portion of the material. It appears to begin as a small shoulder on the tail of the primary endotherm in the 26% sample, broadening and increasing in temperature as the additive level increases to 30%. This can be seen more clearly in Figure 4.45. This puts the eutectic point of the system at approximately 24 – 26%.

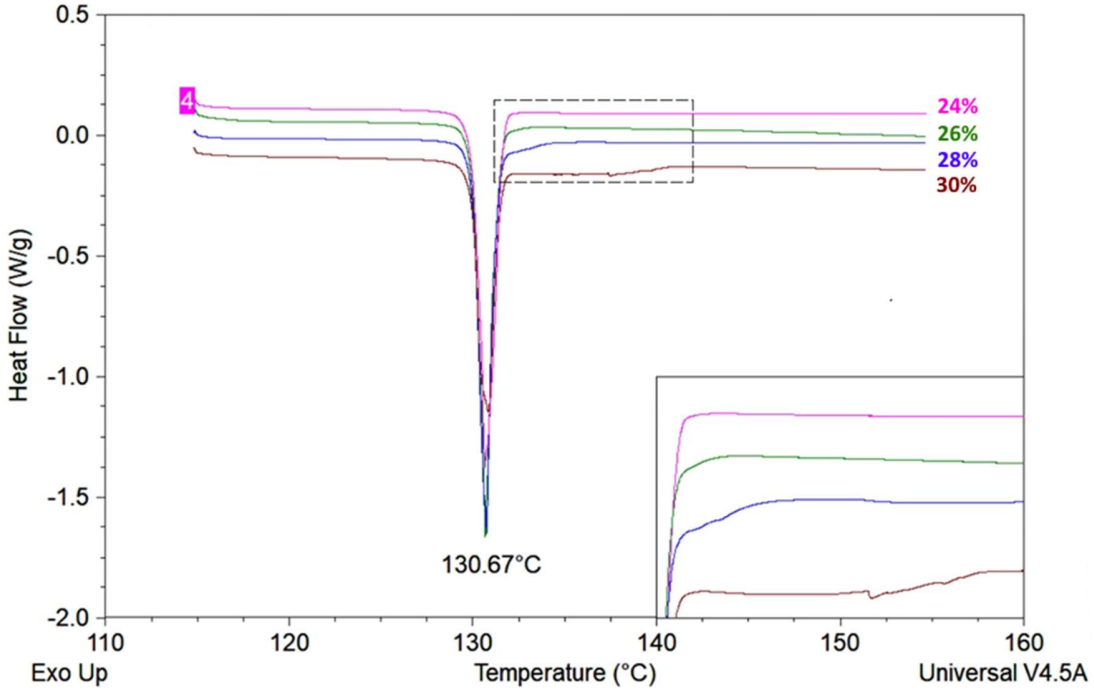


Fig 4.45. Top to bottom: DSC curves of FFA **14** doped with 24, 26, 28, and 30% Cl-FA **16**, collected at a heating rate of 1 °C min^{-1}, with inset (bottom right) showing the emergence of higher temperature non-eutectic melting peak.

4.6.2.4 Interpretation of DSC Data

It appears the system as a whole is unusual; one where the miscibility limit of the terminal solid solution (*c* in Figure 4.43) is the same as the eutectic point. Terminal solid solutions are described in Section 1.3.2.4. No eutectic system appears to be present at additive levels below that of the eutectic point; all solid material behaves as a solid solution. With this in mind, the data from the scanned samples was collected in the manner described in Section 4.9.6.2, resulting in the plot in Figure 4.46. The data collected from these curves was much more consistent than that from those doped with Me-FA **15**, with very little variation between multiple scans on the same sample. This allowed the data to

be represented by a single point for each recorded temperature without requiring the use of data ranges.

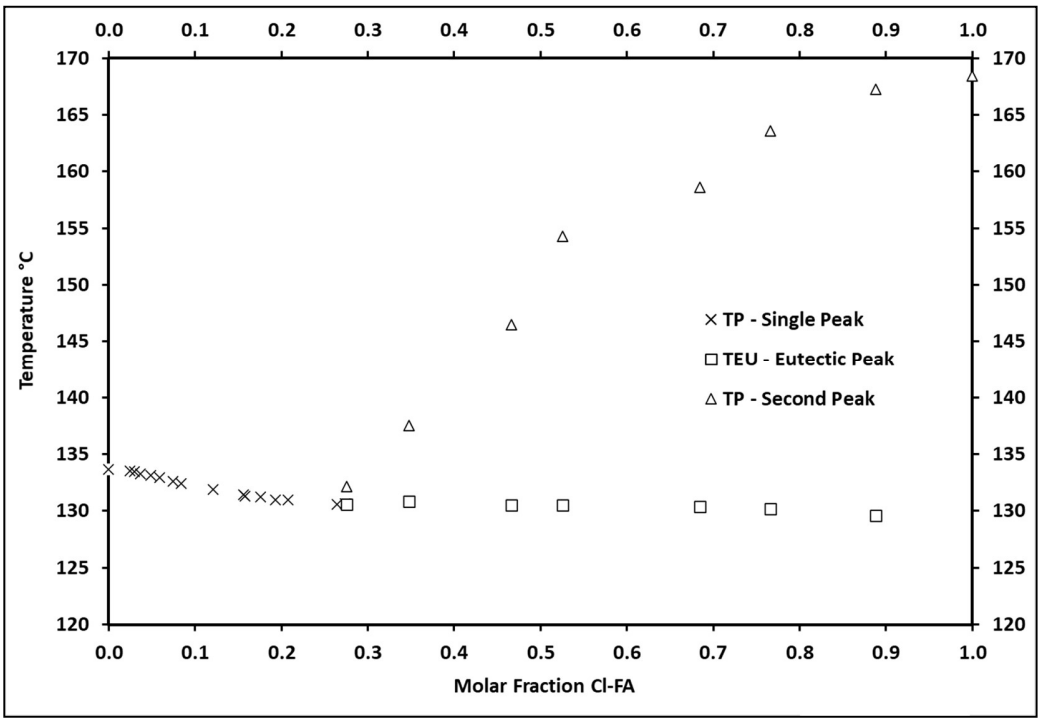


Fig 4.46. Temperature data collected from DSC curves of crystalline FFA **14** material doped with increasing levels of Cl-FA **16**, with peak max temperatures (T_P) collected up to 0.27 Cl-FA **16**, and eutectic onset (T_{EU}) and secondary peak max (T_P) temperatures being measured at higher Cl-FA **16** levels.

The pattern of a terminal solid solution as described above is overlaid in Figure 4.47, and an interpretation of the resultant phase diagram can be found in Figure 4.48. The eutectic point, as well as the transition of the system from solid solution to eutectic material, can be seen in the DSC curves and PXRD patterns of FFA doped with increasing concentrations of Cl-FA (Figures 4.49 and 4.50 respectively).

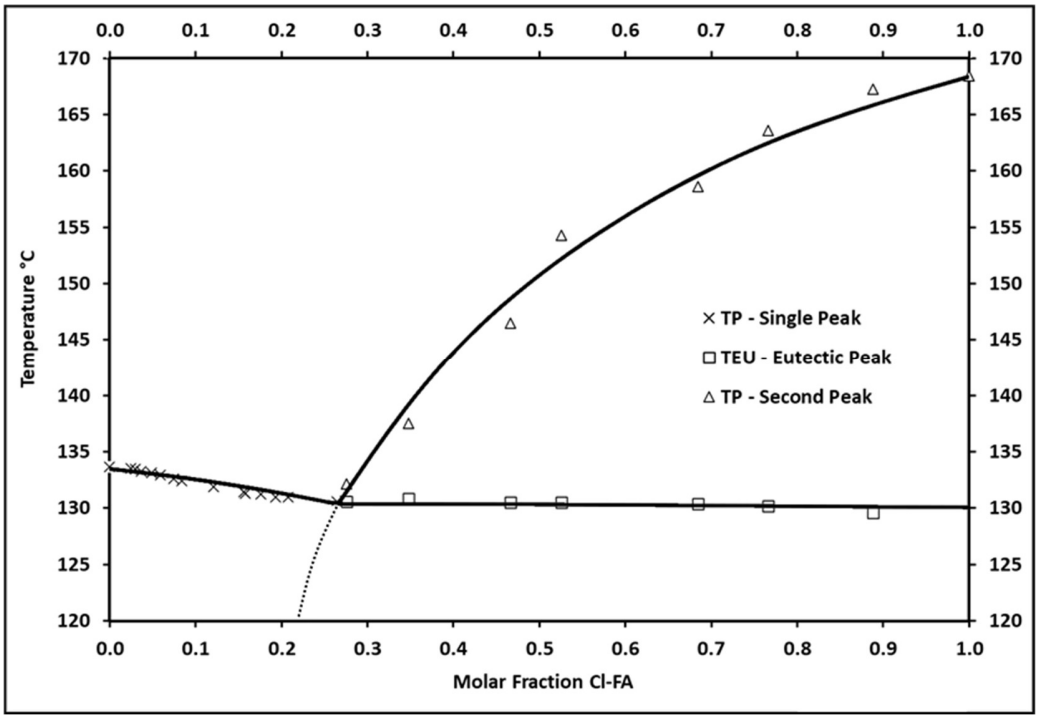


Fig 4.47. Outline of terminal solid solution overlaid atop collected data from FFA **14** / Cl-FA **16** system.

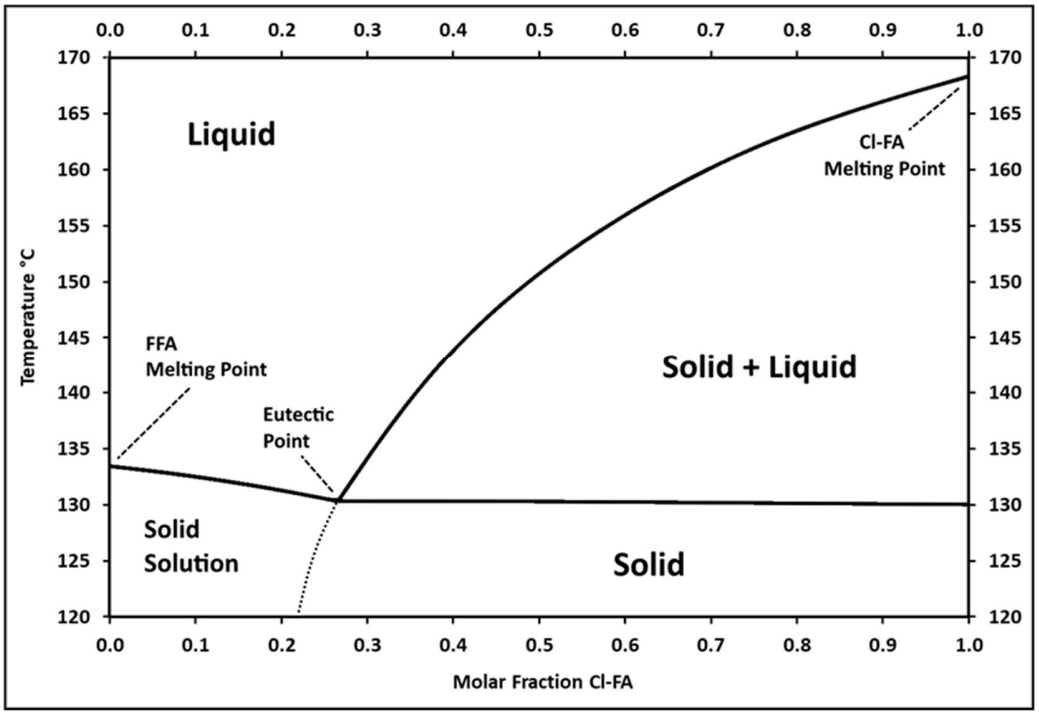


Fig 4.48. Phase diagram for terminal solid solution constructed for FFA **14** / Cl-FA **16** system.

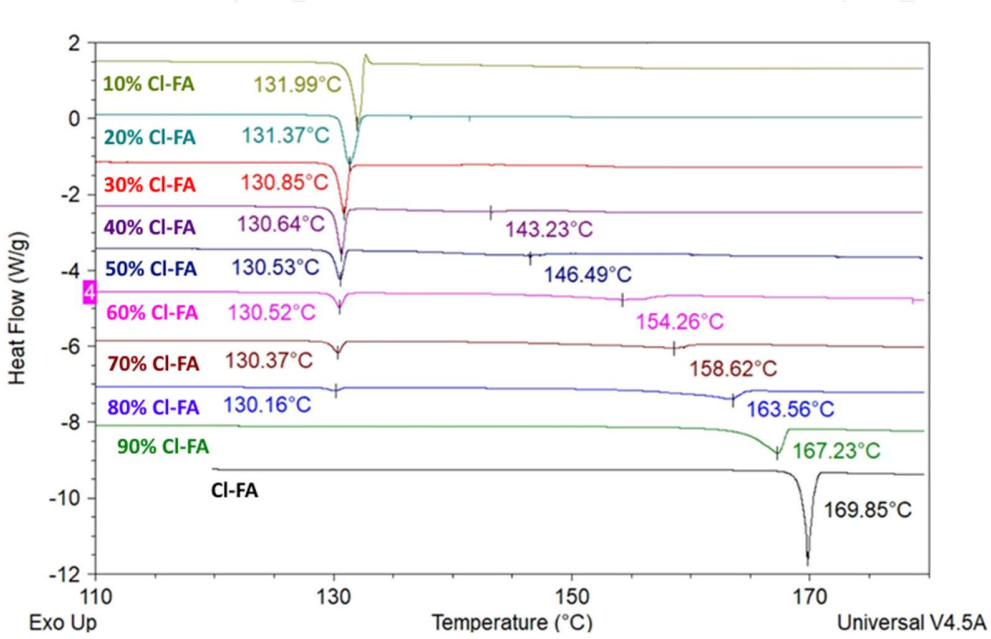


Fig 4.49. Top to bottom: DSC curves of FFA **14** doped with 10, 20, 30, 40, 50, 60, 70, 80, and 90% Cl-FA **16**, as well as pure Cl-FA **16**, collected at a heating rate of 1 °C min^{-1}, labelled with peak maximum values.

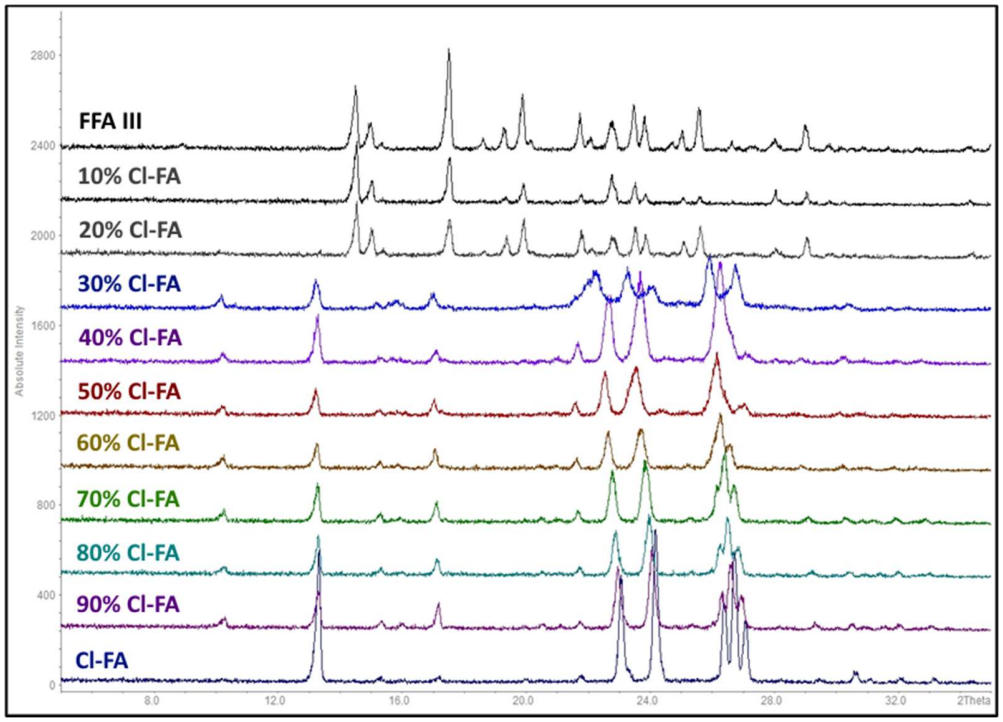


Fig 4.50. Top to bottom: PXRD patterns of Form III FFA **14** doped with increasing levels of Cl-FA **16** (0, 10, 20, 30, 40, 50, 60, 70, 80, and 90%) and pure Cl-FA **16**.

The phase diagram in Figure 4.48 is not comprehensive as it is constructed on the assumption that no solid solution behaviour is being observed on the hyper-eutectic side, at compositions that are primarily Cl-FA **16**. No such behaviour was observed in the samples tested as part of this study, the highest composition of which was approximately 89% Cl-FA **16**. Judging by the structural differences between the two molecules, in particular the size of the -CF_3 substituent of FFA **14** relative to the chloro group of Cl-FA **16**, it is likely that the miscibility limit of any potential solid solution would occur at an additive level closer to 100%. As such, it is feasible that an undetected terminal solid solution be present on that side of the diagram. However, as the focus of this research almost exclusively involves samples doped with low levels of additive, close investigation into the existence and nature of this aspect of the phase diagram is outside the scope of the project.

4.6.3 Discussion of FFA **14** / Me-FA **15** and FFA **14** / Cl-FA **16** Systems

After constructing each phase diagram, it is apparent that the inclusion of Me-FA **15** and Cl-FA **16** into crystalline Form III FFA **14** have markedly different effects on the behaviour of the system. Me-FA **15** forms a continuous, non-ideal solid solution with FFA **14** at every level of composition, with a minimum point at approximately 51% Me-FA **15**. Cl-FA **16** on the other hand forms a terminal solid solution at compositions up until the eutectic point of 24 – 26%, after which the system forms a eutectic. What both these systems have in common, however, is that they display solid solution-like behaviour at

doping levels up to 6%, the range of additive inclusion that the majority of the work in the project is focused on. This partially explains the high incorporation level and selectivity coefficients observed for the additives in FFA **14**.

4.6.4 Discussion into Other Additive Systems

Unfortunately, it was not possible to construct phase diagrams for doped systems containing DF-FA **17**, MF-FA **18**, or t-Bu-FA **19**. As mentioned before, the cost of materials required to produce samples doped with high levels of these additives would be much too high, especially in systems containing a problematically polymorphic material like FFA **14** which often require multiple DSC scans for each sample to obtain usable data. However, DSC curves of samples doped with 2 – 5% of each additive are displayed next to the corresponding pure materials in Figures 4.51 – 4.53. While not as informative as a full phase diagram in terms of system behaviour, these curves can provide some insight into the type of system present, especially when compared against systems with similar doping levels of Me-FA **15** and Cl-FA **16**.

4.6.4.1 FFA **14** / DF-FA **17** Systems

DSC curves of systems doped with 2 – 5% DF-FA **17** are presented in Figure 4.51 alongside curves of each pure component. The temperature of the endotherms on the doped sample curves appear to closely match those of pure Form III FFA **14**, and the melting peak of pure DF-FA **17** is not present. The presence of DF-FA **17** in a sample appeared to suppress the polymorphic transformation of Form III to Form I, increasing

the expression of the Form III endotherm relative to the Form I peak as the doping level increased. The behaviour of these systems is very similar to that observed for the systems containing Me-FA **15**. This similarity of melting behaviour and the lack of a visible lower-temperature endotherm indicative of a eutectic system means it is possible that the two components are forming a solid solution at these doping levels.

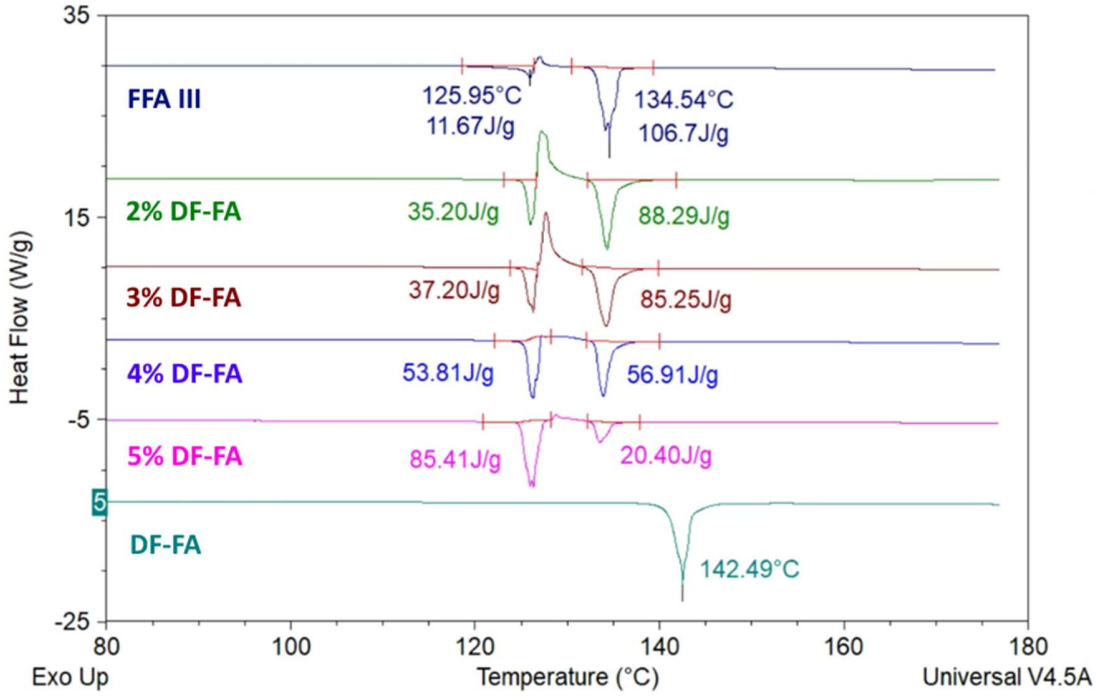


Fig 4.51. Top to bottom: DSC curves of pure Form III FFA **14**, FFA **14** doped with 2, 3, 4, and 5% DF-FA **17**, and pure DF-FA **17**, collected at a heating rate of 10 °C min^{-1}, labelled with peak area and peak max values.

4.6.4.2 FFA **14** / MF-FA **18** Systems

DSC curves of systems doped with 2 – 5% MF-FA **18** are presented in Figure 4.52 alongside curves of each pure component. Again, the temperatures of the endotherms on

the doped samples curves closely match those of pure FFA **14**, and the melting peak of pure MF-FA **18** is not visible on the curve. Similar to the samples doped with Me-FA **15** and DF-FA **17**, the inclusion of MF-FA **18** in the doped samples does appear to suppress the polymorphic transition, the Form III endotherm being consistently expressed to a higher relative degree than in pure FFA **14**. However, unlike those additives, the suppression effect is limited and does not appear to scale proportionally with increased doping level. It is possible that the two components are forming a solid solution at these doping levels for the same reasons described for the FFA **14** / DF-FA **17** system above.

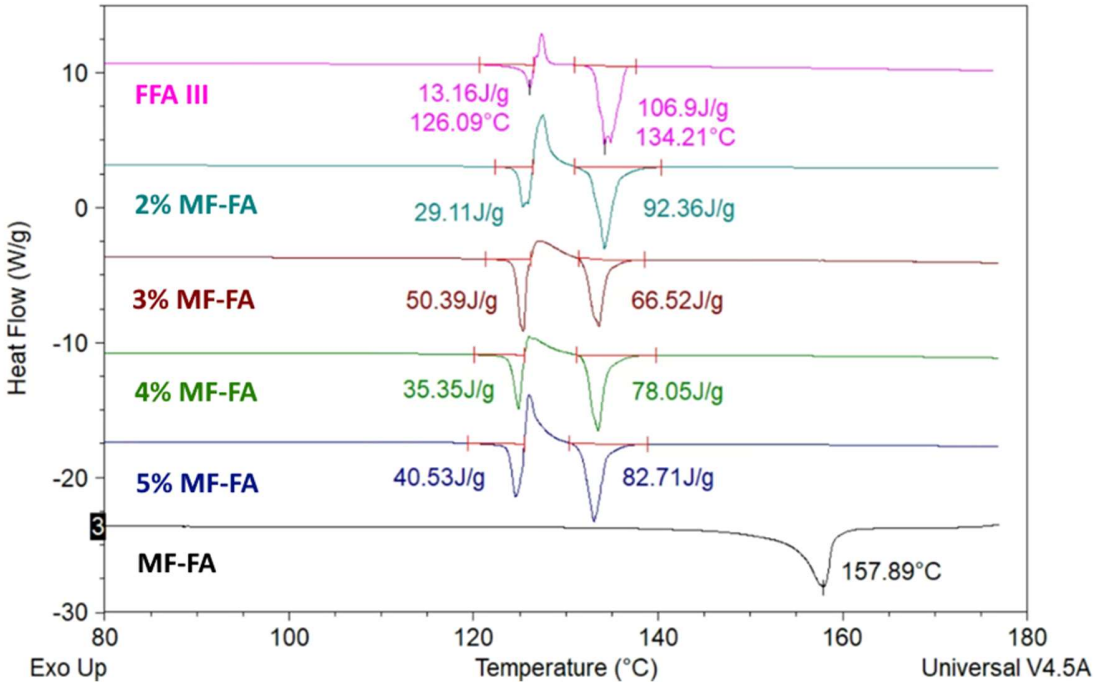


Fig 4.52. Top to bottom: DSC curves of pure Form III FFA **14**, FFA **14** doped with 2, 3, 4, and 5% MF-FA **18**, and pure MF-FA **18**, collected at a heating rate of 10 °C min^{-1}, labelled with peak area and peak max values.

4.6.4.3 FFA **14** / t-Bu-FA **19** Systems

DSC curves of systems doped with 2 – 5% t-Bu-FA **19** are presented in Figure 4.53 alongside curves of each pure component. Samples doped with t-Bu-FA **19** behave the same as those doped with other additives in that the melting endotherms match those in pure FFA **14**, and the melting peak of pure t-Bu-FA **19** is not present on any of the doped curves. The additive appears to have a similar transformation suppression effect as Me-FA **15** and DF-FA **17**, favouring the expression of the Form III endotherm and shrinking the otherwise dominant Form I peak with increasing additive inclusion. This effect is significantly more pronounced than was seen in the samples doped with Me-FA **15** or DF-FA **17**. The curves presented in Figure 4.53 were measured at a lower heating rate (3 °C min^{-1}) to demonstrate this effect more clearly. Samples doped with the aforementioned additives required much higher heating rates to achieve a comparable level of relative Form III expression. Aside from this, the behaviour of the FFA **14** / t-Bu-FA **19** system closely resembles the other systems in melting behaviour, and, as such, it is possible a solid solution is forming at these doping levels.

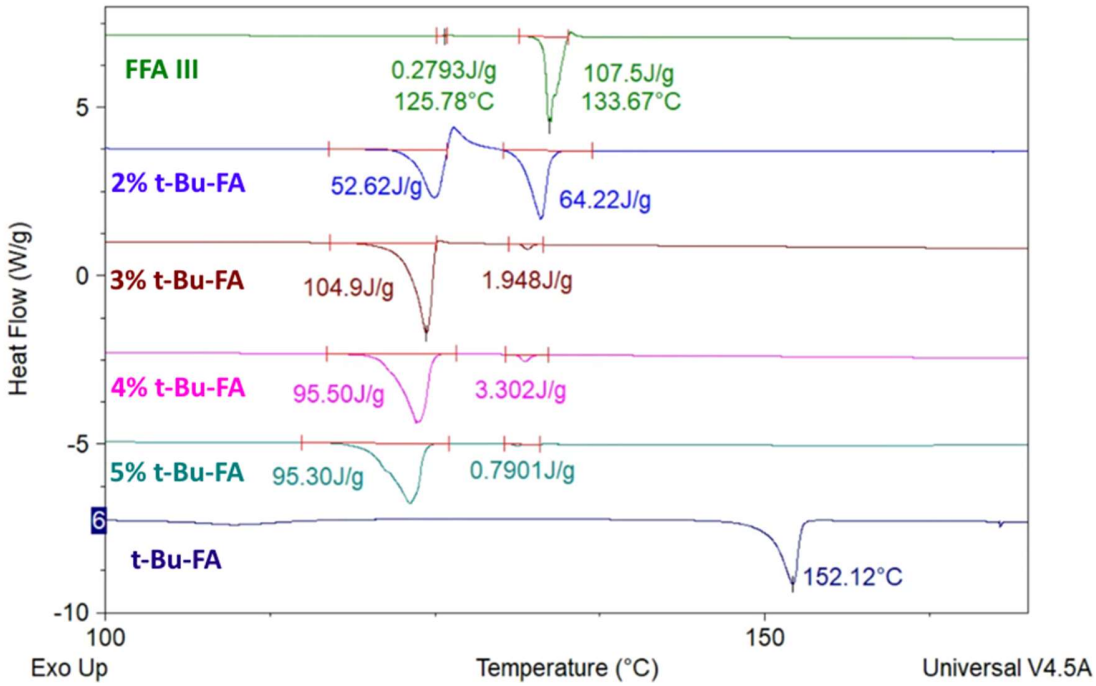


Fig 4.53. Top to bottom: DSC curves of pure Form III FFA **14**, FFA **14** doped with 2, 3, 4, and 5% t-Bu-FA **19**, and pure t-Bu-FA **19**, collected at heating rates of 3 °C min^{-1}, labelled with peak area and peak max values.

4.7 Investigation into the behaviour of t-Bu-FA **19** as an Additive

4.7.1 t-Bu-FA **19** System Observations

Now that a sufficient amount of doped system data has been presented, the case of t-Bu-FA **19** can be properly discussed. To recap, t-Bu-FA **19** was intended to exhibit less predictable inclusion into the crystal lattice. While the other four additives were intended to form substitutional solid solutions with FFA **14**, resistant to purification, the

doping of t-Bu-FA **19** was intended to produce a system that exhibits eutectic or other form of additive inclusion behaviour, and, as such, experience good rejection by purification methods. This was intended to act as a contrast to the other four additives against which their behaviour could be judged. As has been demonstrated in this chapter, this did not turn out to be the case. Instead, t-Bu-FA **19** demonstrated consistently high levels of additive incorporation, in some cases exhibiting higher levels of additive in the crystals than in the crystallisation solution. Despite producing poor crystals by MeOH evaporation compared to most other additives, PXRD scans of doped samples showed no observable disruption to the crystal structure of Form III FFA **14**. The additive exhibited high resistance to purification by recrystallisation as part of an impurity rejection study, almost matching the selectivity coefficients of two of the other four additives. Finally, DSC curves of the doped systems behave similarly to a confirmed solid solution (FFA **14** / Me-FA **15**).

4.7.2 Ruling out Types of Additive Inclusion

There are several categories of system into which the relationship between an impurity/additive and a crystal host can fall, a selection of which are discussed in Section 1.3.1. It is important to use the data collected to eliminate some of these possibilities before theorising about the nature of the FFA **14** / t-Bu-FA **19** system. In general, additives and impurities are present in samples in the form of physical mixtures, solvent agglomerations or inclusions, surface-level depositions or adsorptions, co-crystals, eutectic mixtures, or solid solutions.

4.7.2.1 Physical Mixtures, Solvent Agglomerations, and Inclusions

A physical mixture of components, aside from most likely being identified by the appearance of the material, would produce a discrete endothermic peak at the melting point of the pure additive material, which was not observed. An agglomeration, where additive-rich mother liquor is trapped between aggregated crystals, can be ruled out as no such aggregation was observed. The inclusion of mother liquor within crystal particles, however, is more of a possibility. Such inclusion can occur after rapid growth rates, or potentially as a result of interactions between the crystallisation solvent and the surface of the crystal.[18,92] Some of the crystals in which the high additive levels were observed were grown *via* the slow evaporation of MeOH, so it is unlikely that rapid growth rates would be occurring, but it was possible some unknown interaction between MeOH and FFA **14** was resulting in macroscale additive inclusion.

Solvent inclusions can sometimes be observed in the body of the crystal, especially if the crystal is at least partially transparent, but no such inclusions were visible in crystals of FFA **14** doped with t-Bu-FA **19**. Digital microscope and macro images of such crystals can be found in Section 5.2.3. Lack of visually observable inclusions does not prove they are not present, however. There are a number of ways to definitively test for the presence of inclusions: PXRD analysis could detect an irregularity in the crystal structure, TGA would quickly identify the presence of solvent in a crystal sample, and DSC analysis could display additional peaks for samples with different phases from the solid material.

Looking at the PXRD data reported previously in the chapter (Section 4.5.2.1), it is clear by the fact that the peaks in both patterns match very closely that there is no major disruption to the crystal structure of FFA **14** as a result of the additive. At such low

additive levels this is not an exceedingly meaningful observation on its own; it is possible that a small amount of a second crystal structure was overshadowed by the more abundant Form III, or alternatively that a solvent inclusion was present that did not interfere with the host structure to an observable extent. The PXRD data suggests that t-Bu-FA **19** is being incorporated into crystals of FFA **14** without altering the crystal structure of the host.

A TGA curve of a sample of FFA **14** doped with 2% t-Bu-FA **19** is displayed in Figure 4.54. The decomposition of the material takes place entirely over the course of a single step, with an extrapolated onset point of 213.4 °C and an end point of 260.9 °C; slightly lower than the equivalent values in pure FFA **14**. Should additive-rich mother liquor be entrapped within crystals of FFA **14**, this would be represented by stepwise decreases in sample mass during decomposition; a phenomenon not observed in this case. The behaviour of the material can also be viewed alongside TGA curves of each component individually (Appendix Figure 7.31 – 7.35). Should multiple discrete crystal phases be present in the sample, they would be represented by individual decomposition temperatures when tested by DSC. The fact that the material decomposes entirely in a single step suggests the presence of a solid solution or eutectic system in this regard. The behaviour of the 2% t-Bu-FA **19** system matches that of systems doped with comparable levels of Me-FA **15**, Cl-FA **16**, DF-FA **17**, and MF-FA **18** (Appendix Figures 7.36 – 7.39 respectively). It should also be noted that the two-step decomposition observed in the TGA curve of pure t-Bu-FA **19** (see Section 3.3.1.5) is not observed in the doped sample. This implies that the suspected hydrate form of t-Bu-FA **19** does not affect the doped material to any appreciable extent.

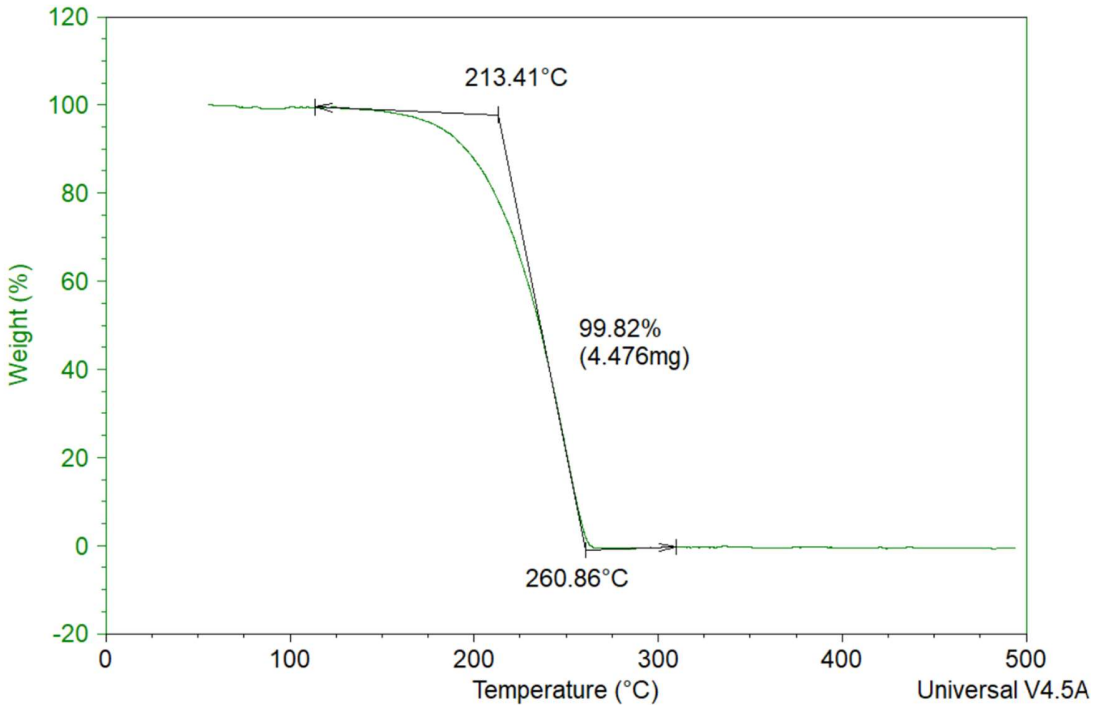


Fig 4.54. TGA curve showing the single-stage decomposition of a sample of FFA **14** doped with 2% t-Bu-FA **19**.

In DSC analysis, the evaporation of volatile components manifests as a broad low-temperature endotherm on the curve,[216] a detail that would be visible should pockets of additive-rich mother liquor still be present within the crystals. However, it is unlikely that these pockets would be present after the sample preparation process, i.e., grinding. In their place would likely be additive-rich solid material that would appear on the curve as a second endotherm distinct from that of pure FFA **14**, likely closer to the pure additive melting point of ~152 °C, assuming no lattice incorporation was occurring. No such endotherm is visible at any level of additive examined; only the existing FFA **14** endotherms are present on the curves in Figure 4.53.

4.7.2.2 Surface Deposition or Adsorption

No tests carried out in the course of this chapter provide information into the location of the additives within the host crystals. It was possible, therefore, that a large amount of surface deposition and/or surface adsorption of additive was occurring during crystallisation. This could result in a high level of additive being present in or on the outer layers of the crystal with little to no incorporation throughout the rest of the solid bulk, a distinction that would not be highlighted by additive level tests or even necessarily impurity rejection tests. To determine whether this was the case, a simple series of partial dissolutions were carried out on a sample of FFA **14** crystal doped with 2.36% t-Bu-FA **19**. Partial dissolution (PD), a technique that will be covered in detail in Section 5.2, is a process by which the outer layers of a crystal are sequentially stripped away by means of controlled dissolution by a solvent in order to map the distribution of additives or impurities on a surface-to-centre basis. Two dissolution stages were carried out on the crystals, each dissolving 20 – 30% of the crystals by mass in a manner described in Section 4.9.7.2. The additive level found in the first dissolution (PD1) was 2.57%, higher than the value for the crystal as a whole, while the level observed in the second dissolution (PD2) was 2.09%, lower than that of the complete crystal. These results imply that the level of additive is highest on the surface and/or outer layer of the crystal and decreases closer to the centre. The relatively high PD1 value could be the result of deposition of additive material on the surface of the crystals, or evidence of a pattern of increasing additive incorporation with crystal growth. While this short study did not provide enough data to produce a detailed map of the distribution of the additive throughout a crystal of FFA **14**, it did confirm that the additive is present throughout the crystal, not solely on the surface.

This ruled out surface deposition or adsorption as the sole contributing factor for the high additive levels being detected.

4.7.2.3 Eutectic or Solid Solution

Process of elimination suggests that, at this level, the additive is indeed incorporated into the crystal structure of FFA **14**, either as a solid solution or a eutectic. The gradual decrease in melting point of both the Form III and Form I with increasing additive level as measured by DSC (Section 4.6.4.3) is characteristic of a eutectic system, but a eutectic endothermic peak is absent; one would expect to see it at a lower temperature than the pure material representing the solidus on the diagram. It is possible that the eutectic endotherm is being lost in the fronting of the Form III peak. On the other hand, the broadening of the Form III peak with increasing additive level is indicative of the presence of a solid solution, as was observed with systems doped with Me-FA **15**. It is possible that the additive is behaving like Cl-FA **16**, and a terminal solid solution is forming at these low doping levels.

With such a limited range of additive levels, and the presence of phase transitions complicating the DSC curve, it is difficult to definitively classify the nature of the solid-state relationship between FFA **14** and t-Bu-FA **19**. However, it is safe to infer that some form of incorporation of the additive into the crystal structure of FFA **14** is occurring, whether it be solid solution, eutectic, or some combination of the two. This bore further investigation, as t-Bu-FA **19** was chosen to exhibit less effective incorporation into the lattice of FFA **14**.

4.7.3 Discussion of Possible Lattice Interactions of FFA **14** Doped with t-Bu-FA **19**

The crystal structure of Form III FFA **14** unit cell was examined on a molecular level when choosing the additives (Section 2.2.3). One aspect of the crystal packing of Form III FFA **14** is that the molecules are orientated in the unit cell in such a way that the trifluoromethyl (-CF_3) groups of two molecules are facing each other, at a distance of 4.156 Å (C···C) or 3.038 Å (F···F). This orientation is illustrated using Mercury software in Figure 4.5. The separation is such that neither attractive nor repulsive forces are experienced to any significant degree between the -CF_3 groups of two molecules of FFA **14**.[133] However, if one of those FFA **14** molecules were to be replaced with a molecule of t-Bu-FA **19** within the crystal lattice, retaining the same crystal structure, one of the -CF_3 groups would instead be a *tert*-butyl group. In that case, it is likely that there would be hydrogen bonding interactions between the protons on the *tert*-butyl group and the electronegative fluorine atoms of FFA **14**, contributing to stabilisation of the crystal structure. The precise distance between H···F in that situation is unknown, but due to the size of the *tert*-butyl group in comparison to -CF_3, it can be assumed that it would be shorter than the F···F distance measured in pure Form III FFA **14** (3.038 Å), close enough for hydrogen bonding to potentially occur.[217] Naturally, these interactions would not be as strong as the O–H···O acid dimer hydrogen bonds due to the comparative unavailability of the alkyl protons, but they would doubtless contribute some degree of stabilisation to the crystal structure. This could provide a plausible explanation as to why t-Bu-FA **19** was so well incorporated into the crystal structure despite the steric implications of its structure.

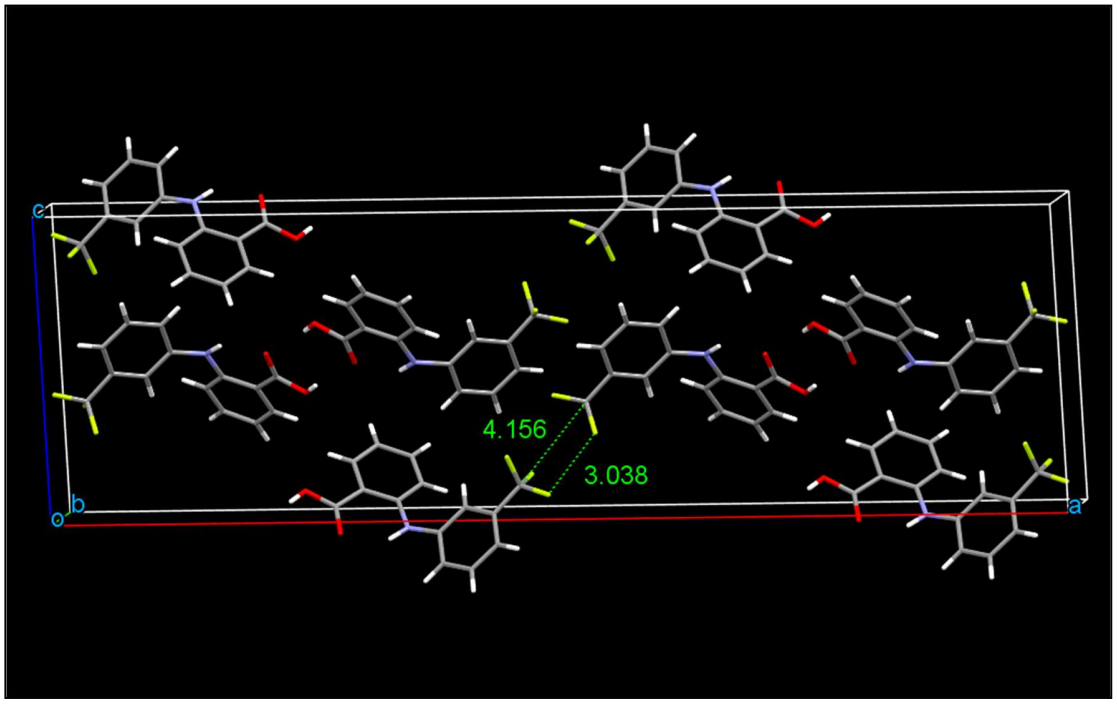


Fig 4.55. Packing structure of Form III FFA **14** crystal lattice, demonstrating the orientation of the -CF_3 groups relative to each other, as well as the distance between the groups.

When analysed by DSC, inclusion of t-Bu-FA **19** significantly increased expression of the Form III endotherm over the Form I relative to pure FFA **14** (Figure 4.53, Section 4.6.4.3). When considered with the above rationalisation, it is possible that the H-bonding interactions present in those doped systems contribute to the stability of the Form III polymorph relative to the Form I at higher temperatures, increasing the energy required to melt and recrystallise the material, and, thus, suppressing the polymorphic transformation for Form I FFA.

4.7.4 Discussion of Possible Lattice Interactions of FFA **14** Doped with Other Additives

4.7.4.1 FFA **14** / Me-FA **15** Interactions

This idea can also be extended to systems containing the other additives to potentially explain their behaviour in terms of solid-state incorporation and resistance to purification. If the same logic discussed above is applied to systems containing Me-FA **15** for example, it could be posited that a similar hydrogen bonding effect was present between the methyl group of the additive and the -CF_3 group of FFA **14**. A crystal structure with this type of interaction would experience similar stabilisation effects as systems in which t-Bu-FA **19** is incorporated but without the unfavourable steric effects. This could potentially provide an explanation for the inclusion of a molecule of Me-FA **15** into the crystal lattice being even more favourable than incorporating a molecule of FFA **14** in the same position at low levels, i.e., the incorporation of Me-FA **15** in the solid phase being consistently comparable to or higher than the corresponding doping level (Section 4.3.1.1), and the measured selectivity (α_1-value*)* of the FFA **14** crystal lattice for Me-FA **15** consistently exceeding that of molecules of the pure material (Section 4.4.1.1).

The inclusion of Me-FA **15** had a similar effect on the polymorphic transformation of Form III FFA **14** as that of t-Bu-FA **19** when tested by DSC analysis (Section 4.6.1). This supports the idea of hydrogen bonds between molecules of FFA **14** and additives in the crystal lattice stabilising the structure of Form III FFA **14**, suppressing its transformation into Form I during the heating process.

4.7.4.2 FFA **14** / Cl-FA **16** Interactions

A sample doped with Cl-FA **16** would not experience any H-bonding interactions between the chloro and -CF_3 group, but the small size of the chloro and its relatively similar electronegativity to -CF_3 (3.03 eV and 3.35 eV respectively)[157] could explain the near equal preference for the additive in the solid phase and solution as seen in the incorporation tests, and the high levels of resistance of the additive to purification by recrystallisation. However, a crystal structure incorporating Cl-FA **16** would not experience the C_4–H···F stabilisation of the pure material, which in theory could decrease the affinity of the lattice for this additive at higher doping levels. This could be manifesting in the pattern change observed by PXRD (Section 4.5.2.4), where the system began resembling the crystal structure of pure Cl-FA **16** rather than pure FFA **14** at doping levels above 20%. The high levels of additive incorporations observed at higher doping levels (Section 4.3.1.2) is most likely due to preferential interactions between molecules of Cl-FA **16**, rather than additive-host interactions. This preference was demonstrated clearly in Section 4.4.1.3 during the impurity rejection tests, where Cl-FA **16** was repeatedly observed to reject FFA **14** during the recrystallisation of high additive level samples.

When heated, samples doped with Cl-FA **16** behave in a manner opposite to those doped with the other additives, facilitating the polymorphic transformation of Form III FFA **14** to Form I rather than suppressing it (Section 4.6.2). This phenomenon may also be linked to the above factors. The lack of both the hydrogen bonding capabilities of the other additives and the C_4–H···F interactions of the pure FFA **14** material could contribute to a decrease in stabilisation of the Form III crystal lattice with the inclusion of Cl-FA **16**.

In turn, this could reduce the energy needed for melting and recrystallisation of the material, facilitating the transformation into the Form I polymorph, and resulting in the high relative expression of the Form I melting endotherm in DSC curves of the doped material.

4.7.4.3 FFA **14** / DF-FA **17** and FFA **14** / MF-FA **18** Interactions

The relevant substituents on both DF-FA **17** and MF-FA **18** are larger than either those of Me-FA **15** or Cl-FA **16** (Bondi volumes of 18.8, 16.0, 13.7, and 12.0 cm^3 mol^{-1} respectively).[163] It is possible that the mixture of H and F atoms on the substituent weakens both the C–H···F interactions that stabilises systems containing Me-FA **15** or t-Bu-FA **19** and the C_4–H···F interactions already present in pure Form III FFA **14**, resulting in systems doped with these additives being less stable than their CH_3- and Cl-substituted counterparts. This could provide an explanation for why these additives are incorporated to a lesser degree than Me-FA **15** and Cl-FA **16** (Section 4.3.1.3), as well as why they are less resistant to purification by recrystallisation (Section 4.4.1.1), in spite of the fact that DF-FA **17** and MF-FA **18** should be the most similar to FFA **14**.

In terms of their effect on the polymorphic behaviour of Form III FFA **14**, both additives appeared to suppress the transformation from Form III to Form I, but to a lesser extent than was observed in samples doped with t-Bu-FA **19** or Me-FA **15** (Section 4.6.4). This suggests that the effect of hydrogen bonding posited for samples doped with those two additives could also be occurring here. However, as mentioned above, the presence of fluorine atoms on the substituent would no doubt lessen the strength of those stabilising bonds, contributing to the weaker suppression observed for these samples.

4.8 Conclusion

In this chapter, the behaviour of FFA **14** systems doped with the various additives described in Section 2.2.4 (compounds **15** – **19**) was explored. It was established that inclusion of any of the additives at low levels (≤ 6%) did not have a significant impact on the crystal structure of the host material when measured by PXRD, crystallising in the same polymorph as pure FFA **14** in all observed instances. It was observed that aspects of the Form III pattern were observed in systems doped with up to 90% Me-FA **15**, while systems doped with Cl-FA **16** adopted a pattern closer to that of the pure additive at doping levels higher than 20%. High levels of all additives were found to be incorporating into crystals of FFA **14** when compared to their corresponding doping level. The additives were also observed to be highly resistant to purification by recrystallisation at low doping levels, a strong indicator of solid solution-like behaviour. This resistance was also observed at higher levels of Me-FA **15** doping, but at similar levels the lattice showed a greater preference for Cl-FA **16** than FFA **14**.

The impact of the additives on the polymorphic transformation between Form III and Form I FFA **14**, as observed through DSC heating, was evaluated and the expression of the respective endotherms controlled. The nature of the systems doped with Me-FA **15** and Cl-FA **16** was determined by the construction of phase diagrams; the former was found to be forming a continuous non-ideal solid solution with a minimum point at an approx. molar fraction of 0.51, while the latter was observed to be forming a terminal solid solution up to the eutectic point of approx. 0.27, after which it exhibited hyper-eutectic behaviour. The nature of the relationships between FFA **14** and DF-FA **17** / MF-FA **18** has not been investigated to the same degree as those between FFA **14** and Me-FA

15, Cl-FA **16**, and t-Bu-FA **19**. However, judging by the similarity of their behaviour to that of those other additives, it can be asserted with some confidence that they most likely form similar solid solution-like systems. Finally, an investigation was carried out into the unexpected behaviour of t-Bu-FA **19**, the additive chosen as a contrast and intended to exhibit less predictable inclusion into the FFA **14** lattice. It was determined that systems doped with the additive were displaying solid solution or eutectic-type behaviour similar to the other additives, and possible explanations for this on a molecular level were explored.

Establishing that crystalline systems of FFA **14** doped with the additives display solid solution-like attributes was an important aspect of the project. Appreciable incorporation into a host crystal and resistance to purification by crystallisation are key characteristics of the types of impurity discussed in Section 1.1.2. While not the only systems that act in this manner, this behaviour is particularly typical of solid solutions. By producing doped crystalline systems of an API that also exhibit these characteristics, they can be established as systems that satisfactorily mimic batches of product containing those impurities. Now the additives have been shown to be appropriate models for purification-resistant impurities, methods of determining their distribution within crystals of FFA **14** can be developed.

4.9 Experimental

4.9.1 Preparation of Doped Systems

Doped systems were prepared *via* the mixing of component solutions. The amount of each material needed was calculated (in moles) based on the desired mass of the system and the molar ratio of the two components in the system. Each molar value was converted into a mass value, and that mass of material weighed out using a Mettler Toledo MT5 microbalance set to 4 decimal places. The material was dissolved completely in EtOH to form a homogenous solution of known concentration, and an appropriate volume of that solution was measured into a clean, dry vessel. The two component solutions were thoroughly mixed, then transferred to a second clean, dry vessel through a HPLC-grade filter to exclude any solid particulates such as dust or dirt. Samples were evaporated to dryness, then redissolved based on the desired crystallisation method described in Section 2.8.4.3 (e.g. methanol evaporation). After redissolution, a sample would be taken for HPLC analysis to determine an accurate doping level. The details of the HPLC instrument and column can be found in Section 2.8.1.1. Method parameters can be found in Section 2.8.1.2.

4.9.2 Response Factor Correction

The RFs for the individual analytes are calculated by dividing the recorded area under the peaks for HPLC traces of each pure analyte material in mAU*s by the corresponding concentration of the sample in mol L^{-1} (Formula 4.3). The details of the HPLC instrument and column can be found in Section 2.8.1.1. Method parameters can be found in Section 2.8.1.2. This step was carried out during the construction of calibration curves for each compound as outlined in Section 2.4, the RF being calculated for each measured data point and then averaged to produce

a representative value for each material. The RRF for any two analytes can be found by dividing the RF of one by the RF of the other (Formula 4.4). Formula 4.1, first presented in Section 4.2.1, can then be used to estimate the concentration of one of the analytes based on the known concentration of the other analyte (as determined using the calibration curve of that analyte), the RRF, and the peak area values of the two materials as measured from a HPLC trace of the doped system. Finally, the value estimated in Formula 4.1 as the concentration of analyte A, the additive, can be presented as a percentage of the sum of the concentration values estimated for analytes A and B to calculate the corrected molar percentage of additive in the sample.

Formula 4.3. $$Response\ Factor\ (RF) = \frac{Peak\ Area}{Concentration}$$

Formula 4.4. $$Relative\ Response\ Factor\ (RRF) = \frac{Response\ Factor\ A}{Response\ Factor\ B}$$

Formula 4.1. $$Concentration\ A = \frac{Peak\ Area\ A}{Peak\ Area\ B} \times \frac{1}{RRF} \times Concentration\ B$$

4.9.3 Crystallisation Behaviour

The crystallisation behaviour of pure and doped systems was monitored by PXRD analysis. The details of the PXRD instrument and the method parameters used can be found in Section 2.8.5. Analysis of crystals under polarised light was achieved using a Nikon Eclipse 50i polarising microscope with a Nikon Digital Sight DS-Fi1 digital camera. Macro digital images were captured using an Honor 7x dual 16 MP camera with High Dynamic Range and Phase Detection Auto Focus.

4.9.4 Incorporation Tests

Samples of FFA **14** doped with each additive individually were prepared according to the method described in Section 4.9.1. Prior to evaporation of the EtOH solution, the additive level in the doped system was determined by HPLC. The details of the HPLC instrument and column can be found in Section 2.8.1.1. Method parameters can be found in Section 2.8.1.2. Subsequently, the material was crystallised according to the appropriate method described in Section 2.8.4.3. A sample of the crystals produced by this process were also tested by HPLC to determine the additive level. For systems containing each additive, the additive level in the solution (doping level) was plotted against the additive level in the crystals produced by each crystallisation method. The incorporation ratio was calculated by dividing the additive level in a crystal sample by the corresponding doping level. These values could be averaged to determine representative values over a desired range of doping levels, and standard deviations calculated.

4.9.5 Impurity Rejection Tests

Seven doped samples of FFA **14** were produced for this experiment. Five contained 2% of each additive individually; Me-FA **15**, Cl-FA **16**, DF-FA **17**, MF-FA **18**, and t-Bu-FA **19**. The other two contained 45% of Me-FA **15** and 42% Cl-FA **16** respectively. The doped systems were prepared in the manner described in Section 4.9.1 and crystallised by rotovap as described in Section 2.8.4.3. Recrystallisation was carried out by dissolving each sample in the minimum volume of acetonitrile at a temperature of 80 °C, followed by the cooling of the sample at room temperature to allow for the precipitation of solid material. The resulting solid and liquid phases were separated by suction filtration. This process was performed three consecutive times on each sample, each time using the post-crystallisation “pure” solid of the last session as the pre-

crystallisation "crude" of the next. Samples were taken at each stage in the proceedings for HPLC analysis, so that values for the additive levels of each sample were obtained for the post-recrystallisation solid phase and liquid phase for each of the three stages, as well as for the doping solution and the post-rotovap crystal samples.

The selectivity coefficient value (α_1) for each impure system was determined by first calculating the experimental distribution coefficient of a component (K_c). This was achieved by dividing the mole fraction of the component in the post-crystallisation solid phase (X_s^c) by the mole fraction of the component in the post-crystallisation liquid phase (X_l^c) (Formula 4.5). This calculation is carried out twice to determine the experimental distribution coefficient of the additive or impurity (K_i) as well as the experimental distribution coefficient of the API host (K_A) present in the material after recrystallisation. The selectivity coefficient for the recrystallisation (α_1) is defined as the ratio between K_i and K_A (Formula 4.2), first introduced in Section 4.4.

Formula 4.5. $$K_c = \frac{X_s^c}{X_l^c}$$

Formula 4.2. $$\alpha_1 = \frac{K_i}{K_A}$$

4.9.6 Phase Behaviour

All phase diagrams were composed using two-component systems (host and additive) over two phases (solid and liquid). Data was collected by DSC analysis; the details of the DSC instrument can be found in Section 2.8.7.1. The conditions were isobaric, all analysis being carried out at atmospheric pressure, and the temperature and composition of the samples were varied to

record the data. All doped systems in this section were prepared in the manner described in Section 4.9.1 and crystallised by rotovap as described in Section 2.8.4.3.

4.9.6.1 FFA **14** / Me-FA **15** System

Initial Scans

Samples of FFA **14** doped with 10% and 20% Me-FA **15** were tested by DSC at a heating rate of 10 °C min^{-1}. The samples were heated from room temperature (15 – 20 °C) to 180 °C at the chosen rate. No sample grinding took place in the preparation of these samples.

Heating Rate Test

FFA **14** samples doped with 10% Me-FA **15** were tested by DSC at 6 different heating rates: 5, 10, 20, 30, 40, and 50 °C min^{-1}. The samples were heated from room temperature (15 – 20 °C) to 180 °C at the chosen rate. No sample grinding took place in the preparation of these samples.

Grinding Test

Two FFA **14** samples doped with 10% Me-FA **15** and two doped with 40% were produced. One sample at each additive level was subjected to rigorous grinding in a pestle and mortar, the other was left unground. All four samples were tested by DSC at a heating rate of 5 °C min^{-1} and 50 °C min^{-1}. The samples were heated from room temperature (15 – 20 °C) to 180 °C at each rate.

Phase Diagram Data Collection

Nine crystal samples of FFA **14** were produced doped with increasing levels of Me-FA **15**: 10, 20, 30, 40, 50, 60, 70, 80, and 90% Me-FA **15**. Pure Me-FA **15** was also crystallised in the same manner as the doped samples. The samples were tested by DSC over a range of heating rates between 5 and 20 °C min^{-1}. The samples were heated from room temperature (15 – 20 °C) to 180 °C at each rate. No sample grinding took place in the preparation of these samples. The data used in the construction of the continuous solid solution phase diagram was collected by determining the extrapolated peak onset temperature (T_O) and the peak maximum temperature (T_P) of the Form III endothermic melting peaks of between 5 and 19 repeated scans at each composition using the TA Universal Analysis software. Outliers were excluded based on box chart analysis, and the remaining temperature values for T_O and T_P were plotted against the corresponding additive level of the sample as a range. The mean T_O and T_P values were plotted in a similar manner. The literature melting temperature value was used for pure Form III FFA **14**.[65] The solidus and liquidus curves of the phase diagram were overlaid atop the data points manually.

4.9.6.2 FFA **14** / Cl-FA **16** System

Initial

Samples of FFA **14** doped with 10% Cl-FA **16** were tested by DSC at a heating rate of 10 °C min^{-1}. The samples were heated from room temperature (15 - 20 °C) to 180 °C at the chosen rate. No sample grinding took place in the preparation of these samples.

Heating Rate Test

FFA **14** samples doped with 10% Cl-FA **16** were tested by DSC at 3 different heating rates: 1, 10 and 50 °C min^{-1}. The samples were heated from room temperature (15 - 20 °C) to 180 °C at the chosen rate. No sample grinding took place in the preparation of these samples.

10-90%

Nine crystal samples of FFA **14** were produced doped with increasing levels of Cl-FA **16**: 10, 20, 30, 40, 50, 60, 70, 80, and 90% Cl-FA **16**. Pure Cl-FA **16** was also crystallised in the same manner as the doped samples. The samples were all tested by DSC at a heating rate of 1 °C min^{-1}. The samples were heated from 100 °C to 180 °C at this rate. No sample grinding took place in the preparation of these samples.

2-30%

Ten crystal samples of FFA **14** were produced doped with increasing levels of Cl-FA **16**: 2, 7, 11, 16, 20, 22, 24, 26, 28, and 30% Cl-FA **16**. The samples were all tested by DSC at a heating rate of 1 °C min^{-1}. The samples were heated from 115 °C to 155 °C at this rate. No sample grinding took place in the preparation of these samples.

Phase Diagram

The data used in the construction of the terminal solid solution phase diagram was collected differently depending on composition. From a molar fraction of 0.00 to 0.26 Cl-FA **16**, the max temperature of the single melting endotherm was recorded (labelled as "T_P – Single Peak" in Section 4.6.2.4, Figure 4.46). After the emergence of the eutectic point, molar fraction of 0.28 – 0.89, the data was collected as per a eutectic system, by determining the onset temperature of

the eutectic peak ("T_{EU} – Eutectic Peak") and the peak maximum temperature of the higher-temperature peak ("T_P – Second Peak") using the TA Universal Analysis software. The temperature values were plotted against the corresponding additive level of the sample. The solidus and liquidus curves of the phase diagram were overlaid atop the data points manually.

4.9.6.3 FFA **14** / DF-FA **17** System

4 crystal samples of FFA **14** were produced doped with increasing levels of DF-FA **17**: 2, 3, 4, and 5% DF-FA **17**. Pure DF-FA **17** was also crystallised in the same manner as the doped samples. The samples were tested by DSC at a heating rate of 10 °C min^{-1}. The samples were heated from room temperature (15 - 20 °C) to 180 °C at the chosen rate. No sample grinding took place in the preparation of these samples.

4.9.6.4 FFA **14** / MF-FA **18** System

4 crystal samples of FFA **14** were produced doped with increasing levels of MF-FA **18**: 2, 3, 4, and 5% MF-FA **18**. Pure MF-FA **18** was also crystallised in the same manner as the doped samples. The samples were tested by DSC at a heating rate of 10 °C min^{-1}. The samples were heated from room temperature (15 - 20 °C) to 180 °C at the chosen rate. No sample grinding took place in the preparation of these samples.

4.9.6.5 FFA **14** / t-Bu-FA **19** System

4 crystal samples of FFA **14** were produced doped with increasing levels of t-Bu-FA **19**: 2, 3, 4, and 5% t-Bu-FA **19**. Pure t-Bu-FA **19** was also crystallised in the same manner as the doped samples. The samples were tested by DSC at a heating rate of 3 °C min^{-1}. The samples

were heated from room temperature (15 - 20 °C) to 180 °C at the chosen rate. No sample grinding took place in the preparation of these samples.

4.9.7 t-Bu-FA **19** Inclusion Studies

4.9.7.1 TGA

Crystals of FFA **14** doped with 2% t-Bu-FA **19** were prepared in the manner described in Section 4.9.1 and crystallised by rotovap as described in Section 2.8.4.3. The crystals were heated by TGA from room temperature (15 - 20 °C) to 500 °C at a rate of 10 °C min^{-1}. The details of the TGA instrument can be found in Section 2.8.8. The samples were heated in platinum pans. No sample grinding took place in the preparation of these samples.

4.9.7.2 Partial Dissolutions

Crystals of FFA **14** doped with 2.36% t-Bu-FA **19** were prepared in the manner described in Section 4.9.1 and crystallised by slow cooling from MeCN as described in Section 2.8.4.3. A sample of 10 such crystals were suspended in a volume of hexane appropriate to dissolve 20 – 30% of the total sample mass, as calculated by the solubility of FFA **14** in the solvent at room temperature. The suspension was agitated at 300 rpm at room temperature for a duration of 90 minutes, after which solvent was removed using a Pasteur pipette and set aside, and the crystals rinsed with fresh cold hexane and dried in a Hirsch funnel over vacuum. The process was repeated one more time for a total of two dissolution stages. The additive level of the material isolated from each solution post-dissolution was determined by HPLC analysis. The details of the HPLC instrument and column can be found in Section 2.8.1.1. Method parameters can be found in Section 2.8.1.2.

Methods of Determining the Distribution of Impurities

5.1 Introduction

As a result of the work carried out in Chapters 2 – 4, systems of crystalline FFA **14** doped with five different additives (compounds **15** – **19**) were successfully produced. The behaviour of these doped systems was investigated, and they were shown to exhibit high relative levels of incorporation and resistance to purification by recrystallisation, while preserving the crystal structure of the pure API host at low doping levels. These attributes are often indicative of solid solution-like behaviour. They are also characteristic of many impurities encountered in other API processes that cause problems during the purification of impure products and intermediates.[14,17,107] As such, the doped systems of study produced as part of this project can be considered to satisfactorily mimic those impure systems encountered in the pharmaceutical industry.

The primary goal of the research is the development of techniques for determining the pattern of distribution of purification-resistant additives and impurities within crystal batches of API products. Some means of determining such distributions exist but have significant limitations. A useful method is Raman spectroscopy, which would allow for the identification of the different vibrational modes of host and impurity material.[218] However, the technique could only distinguish between an impurity and host if they were contained in separate phases. Should an impurity exist in the same phase as the host, as would be the case in solid solution-like systems, the analysis would be ineffective.

Now that suitable systems of study have been produced, that process can take place. The focus of this development is on two techniques: partial dissolutions and segmentation analysis. This chapter describes the development of both techniques,

modifying and refining the procedures to improve both the additive distribution and crystal sizing data collected. The robustness of the methods will be challenged through their application to FFA systems doped with various types and levels of additive, as well as different crystal morphologies. The goal of this research is to develop methods of determining impurity distribution that are applicable to a wide range of crystalline API systems, and, thus, have potential for use in a process chemistry setting as a tool towards informing more effective purification methods.

5.2 Partial Dissolutions

Sometimes referred to as stepwise or sequential dissolution, partial dissolution (PD) is a process by which the outer layer/layers of a crystal or batch of crystals is stripped away by means of controlled dissolution in a solvent, often one in which the material is poorly soluble. Ideally, this operation can be repeated multiple times, removing as many layers as desired or is feasible in regard to the crystal size and morphology. Analysing the impurity content in the solution resultant from each dissolution stage can provide insight into the distribution of those impurities within the crystals on a surface-to-centre level. By extension, the change in additive incorporation level as it relates to crystal growth for a given crystal batch can be better understood. Partial dissolutions have the potential to be a practical technique in an industrial setting, providing a researcher with information into the distribution and behaviour of impurities that cannot be satisfactorily rejected *via* traditional purification methods. While there have been reports in the literature of

preliminary studies using this approach,[90,91,119,121] to this point a bench-top procedure suitable for application to API systems has not been reported.

The distribution of impurities throughout a crystal body can be plotted in a number of ways, two of which are used in this research. The first is the simplest, where the additive molar percentage value is plotted against a metric known as the dissolution midpoint, a way of representing the position within a crystal from which the additive data was collected. Each dissolution stage is assigned as a percentage of the original sample mass. As such, the level of dissolution can be presented as a size-independent metric allowing for more meaningful comparison between plots from different samples. It also allows the presentation of additive distributions as a continuous series, as opposed to restraining it to discrete categories like dissolution stages, providing more insight into the additive levels at different points in a crystal. In some cases, the level of additive can be presented in the form of a distribution coefficient (α_2) values rather than a percentage. For a homogeneous solid solution (or a system that behaves like a homogeneous solid solution), the α_2-value denotes the relationship between the mole fraction of an additive within a solid solution crystal and the mole fraction of the additive in the solution from which that crystal was grown. Therefore, it can act as a measure of additive incorporation independent of doping level, by which the incorporation level in systems of differing additives and doping levels can be compared.[219,220]

It is important to note that the values represented by the α_2 symbol are unrelated to those represented by α^0 (pure-component relative solubility value, Section 2.5.2.2) or α_1 (selectivity coefficient value, Section 4.4). The dissolution midpoint and distribution coefficient are discussed in more detail in Sections 5.2.1.2 and 5.2.2.2 respectively.

Table 5.1 is presented below with information on the PD samples and studies discussed in this chapter, describing sample codes, the composition of the crystals in that sample, and the section name and number where that study is discussed. A separate table (Table 5.8) will be included in Section 5.2.3 describing the samples used in that section.

Table 5.1: A list of names of the crystal samples studied in Sections 5.2.1 and 5.2.2, alongside their composition and the section of the chapter in which they are discussed.

Section Name/Number	FFA Crystals Doped With	Sample Name
Primary Method Development 5.2.1.1	-	Primary-1
	-	Primary-2
Secondary Method Development 5.2.1.2	2% Cl-FA	Secondary-1
	2% Cl-FA	Secondary-2
	2% Cl-FA	Secondary-3
Effect of Increased Sample Size 5.2.2.1	2% Cl-FA	ISS-1
Effect of Different Additive Types and Levels 5.2.2.1	0.5% Me-FA	DATL-1
	5% Me-FA	DATL-2
Effect of Crystal Size and Morphology 5.2.2.3	2% DF-FA	CSM-1
	2% DF-FA	CSM-2
	2% DF-FA	CSM-3
Studies on Single Prismatic Crystals 5.2.2.4	2% Cl-FA	SPC-1
	2% DF-FA	SPC-2

5.2.1 PD Method Development

5.2.1.1 Primary Development

The first partial dissolution tests were intended to be a process of familiarisation with the procedure, highlighting any potential difficulties of the technique or its application on the systems of study. As such, the method was based on similar work reported within the group.[90,119] To simplify the process and preserve additive material in these early stages, crystal samples of pure FFA were used initially. The crystals were grown *via* slow cooling of a solution in MeCN (described in more detail in Section 2.8.4.3). This method produces long, narrow acicular crystals of FFA (e.g., Figure 5.1).

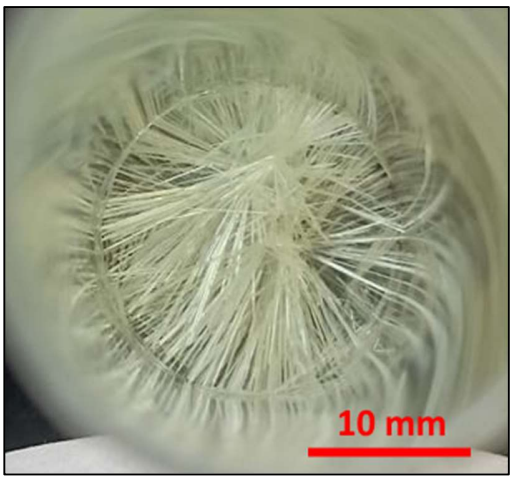


Fig 5.1. Vial of acicular FFA crystals grown *via* the slow cooling of a supersaturated solution in MeCN.

For the primary PD study, a sample of 50 crystals of FFA (Primary-1) were selected from the same batch. Images of these crystals were analysed by image analysis software to determine the length and total surface area of each crystal. To achieve this,

images of the individual crystal particles were captured using a polarising microscope equipped with a digital camera. Surface areas were measured by defining a perimeter around the crystals by threshold analysis and measuring the area within. As the crystals were generally flat, the total surface area of the particles is estimated by doubling the surface area of the measured face. Lengths were collected by selecting points at either end of the crystal in the longest dimension by eye and measuring the distance between the two points. Surface area and length measurements, while not necessary to the process, provide a useful metric for monitoring the progression of a PD study by tracking the changing size distribution of crystals across each dissolution stage.

The mass of the sample was also measured. This metric is more important to the process as it dictates the volume of solvent that will be used as the dissolution medium. An amount of solvent is chosen that is sufficient to dissolve the desired mass of crystal material, based on the solubility or an experimentally-determined dissolution target value. Hexane was selected as the dissolution medium for the initial study. FFA only exhibits a low level of solubility in hexane (2.40 mg ml^{-1} at 25 °C) due to the non-polar, aprotic nature of the solvent, and its high volatility and low boiling point facilitates sample preparation. A series of three dissolution stages were carried out on the sample. The crystals were suspended in enough hexane to dissolve 10% of the pre-dissolution crystal mass based on their mass and solubility value above. The suspension was agitated for 90 minutes at ambient temperature (20 – 25 °C) before the hexane was filtered off, and the recovered crystals rinsed with cold hexane, dried under vacuum, and resized. Full details of the sample sizing and dissolution process used in this study are described in Section 5.5.1.1.

The sizes of the crystals in a sample can be tracked over multiple consecutive dissolution stages using a size distribution plot. A distribution plot tracking the surface areas across the Primary-1 series of dissolutions is shown below in Figure 5.2, while a similar plot of crystal lengths can be found in Appendix Figure 7.78. The crystals are sorted by size according to the chosen metric and numbered from smallest to largest. The crystal number is plotted alongside the corresponding size measurement to produce a size distribution for the sample. The size distribution of the fresh undissolved crystals is labelled "pre-dissolution". The distribution of the crystals after each dissolution stage are named after that stage, i.e., the crystals measured after the first dissolution stage are labelled "PD1", after the second "PD2", etc.

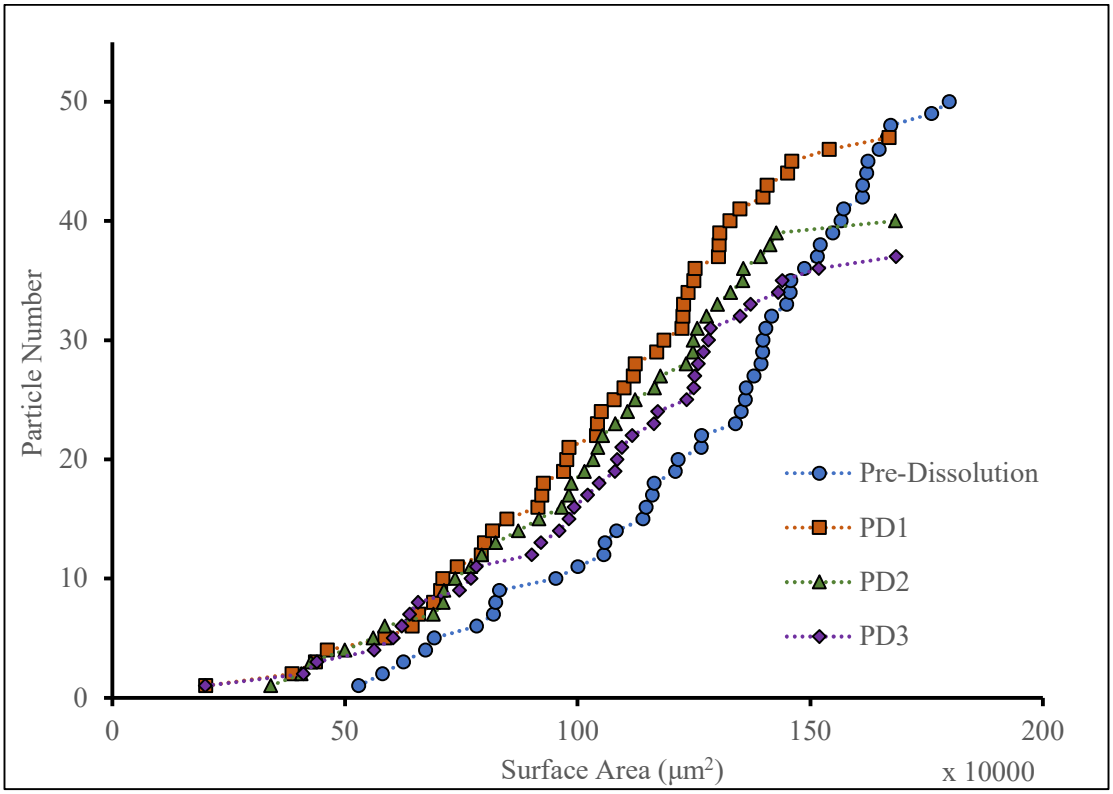


Fig 5.2. Surface area distribution plot of the Primary-1 crystals over the first three dissolution stages in the primary partial dissolution method development.

Even at these early stages of method development, the effectiveness of the technique was clear. An overall decrease in crystal surface areas and lengths was observed over the course of the dissolution series, as can be seen in the respective size distribution plots. However, a number of potential issues were noticed that could be improved upon to refine the technique and create a more robust method. The first was related to the dissolution medium. As described in Section 5.5.1.1, the volume of hexane used as the dissolution medium was chosen for its ability to dissolve the outer layer of the crystals in a controlled manner, based on the total mass of the sample and the solubility of the material in the solvent. For example, the volume of hexane added in the study described above was sufficient to dissolve 10% of the total crystal mass based on these factors. However, as the mass of the acicular crystals used in the Primary-1 sample was so low, this in turn necessitated a low volume of solvent to be used as the dissolution medium. This volume of medium was insufficient to fully suspend the crystals, which resulted in cases where the levels of dissolution were lower than intended and uneven.

Additionally, a portion of the crystals in the sample was damaged or lost during the PD process. These crystals were generally fractured during the agitation of the sample or lost during manipulation between stages. This a common problem with acicular crystals due to their narrow morphology, and one that is exacerbated with successive dissolution stages, as the crystals grow smaller and more fragile. Fractured crystals must be removed from the sample for future dissolution stages, as they can skew additive distribution data. This in turn can also skew mass and surface area comparisons between dissolution stages, having a detrimental effect on dissolution tracking. The effect of this on the plotting of

size distribution data can be seen in Figure 5.2 above, the drop in crystal count on the y-axis results in overlap and less comparable distribution plots for each stage.

Two further single-stage dissolution studies (Primary-2 and Primary-3) were carried out under similar conditions with comparable results; the surface area distribution plots for these can be found in Appendix Figures 7.79 and 7.80.

Changes in Method

Both of the major issues encountered were directly related to the morphology of the crystals used in the samples; the low mass of the crystals necessitated low volumes of solvent, and the fragility of the crystals led to frequent breakages. As such, it was decided to continue the development of the PD technique using crystals produced by a different crystallisation process. As described in Section 2.6.1.4, the crystallisation of FFA by slow evaporation of a solution in MeOH produced large prismatic crystals. These crystals were much better suited for the PD process than the acicular crystals used previously. The larger size of the prismatic crystals increased the mass of each particle, allowing for a higher volume of solvent to be used in a dissolution study while maintaining a manageable sample size. Additionally, the prismatic morphology of the crystals made them much less susceptible to fracture and loss in most cases, even after multiple successive dissolution stages.

The change in crystal type necessitated a change in the measurement of surface area. Originally, the acicular crystals were smaller and could be sized from microscope images, as described in Section 5.5.1.1. However, the prismatic crystals proved too large to be sized in this manner. As such, macro digital photography was required to capture

images of the crystals at each dissolution stage. When properly scaled, these images can be used in conjunction with image analysis software to accurately determine the surface areas of the particles in the image. In the case of this research, ImageJ was the image analysis software chosen to track the crystal sizes.[221,222] Surface area measurements were determined by binary analysis amongst other image processing techniques (Figure 5.3), the full details of which are described in Section 5.5.1.2.



Fig 5.3. Sample of FFA crystals grown by slow evaporation from MeOH (left) and image analysis of those crystals during sizing process (right).

5.2.1.2 Secondary Development

A series of further method development studies were carried out to assess the effect of the changes to crystal sample morphology and image analysis on the PD process.

The primary objective was to carry out a series of partial dissolution stages that would reliably dissolve a predetermined level of crystal bulk with reasonable control, in this case 10% by mass. These studies were carried out on crystals of FFA **14** doped with 2% Cl-FA **16**. This allowed for the process of determining additive distribution within the samples to be developed at the same time as the dissolution process.

Additionally, the necessity and impact of the inclusion of an anti-flocculating agent in the dissolution medium was assessed. The aggregation of crystals in suspension has the potential to interfere with the dissolution process by inhibiting access of the solvent to the faces of the crystal particles, resulting in low and uneven levels of dissolution of a sample. Some reported research involving partial dissolution makes use of anti-flocculating agents in the dissolution medium to counter such effects.[90,121] One such agent is 2-(2-ethylhexyloxy)ethanol (EHE). With a low molecular weight, it shares the basic structural features of a non-ionic surfactant, a polar protic primary alcohol head and a long branched non-polar hydrocarbon tail.[223] EHE has been shown to inhibit flocculation of crystals during dissolution when added to hexane.[90] As such, it was selected for experimentation in this work.

Two samples of 10 similarly-sized crystals were selected from the same batch by eye, labelled Secondary-1 and Secondary-2. Initially, two PD stages were performed on each sample. The dissolution medium used for the Secondary-1 dissolutions was pure hexane as used previously, but the Secondary-2 medium contained a low amount of EHE. The level of EHE included is chosen based on the measured surface area of the crystals to ensure effective prevention of particle aggregation; detailed descriptions of this can be found in Section 5.5.1.3. The crystals were suspended in enough of each respective

solvent to dissolve 10% of the pre-dissolution crystal mass based on their mass and solubility value. The suspensions were agitated for 90 minutes at ambient temperature (20 – 25 °C) before the hexane was filtered off, and the recovered crystals rinsed with cold hexane, dried under vacuum, and resized.

The surface area distribution plots for Secondary-1 and Secondary-2 in this study can be found in Figures 5.4 and 5.5 respectively. The levels of dissolution by mass observed for each sample are listed in Table 5.2.

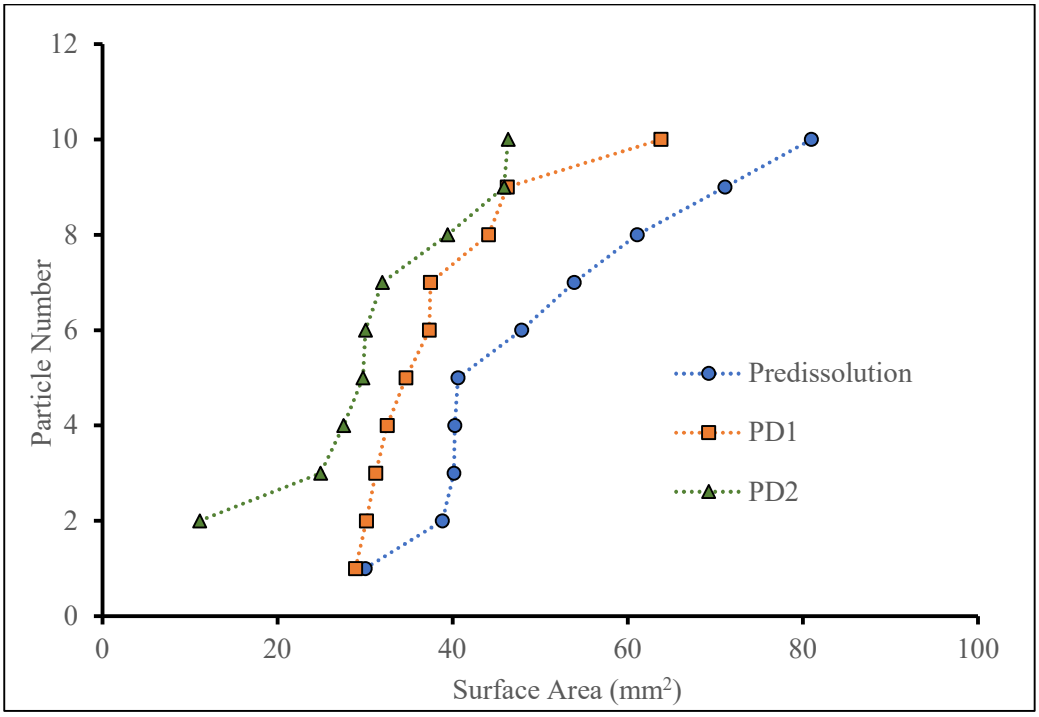


Fig 5.4. Surface area distribution plot of the Secondary-1 crystals over two dissolution stages at the start of the secondary partial dissolution method development.

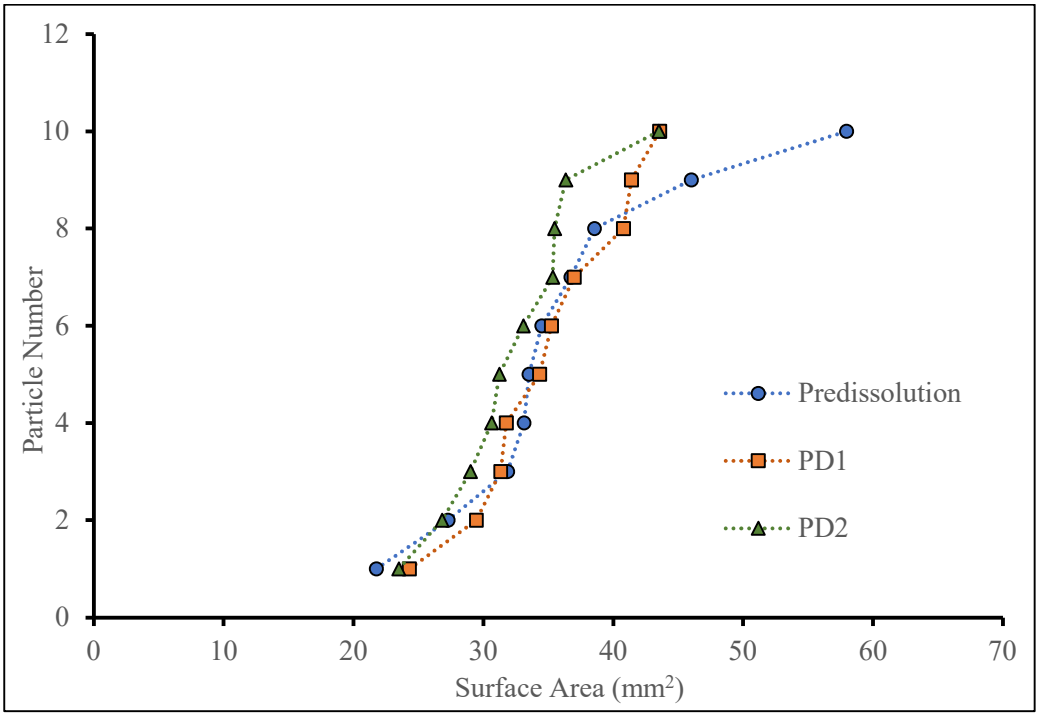


Fig 5.5. Surface area distribution plot of the Secondary-1 crystals over two dissolution stages at the start of the secondary partial dissolution method development.

Table 5.2. Percentage of original crystal mass dissolved over two dissolution stages of Secondary-1 and Secondary-2 at the start of the secondary method development.

	PD1	**PD2**
% Secondary-1 Mass Dissolved	10.9%	4.7%
% Secondary-2 Mass Dissolved	14.0%	8.0%

During agitation, very little difference was observed between the samples in terms of their behaviour in suspension; the crystals moved freely in the dissolution media in both samples and no aggregation of particles was observed in either vial. It appears that the inclusion of EHE in the dissolution medium had little effect on the agglomeration

behaviour of the crystal samples. Additionally, the crystals were observed to be more soluble in a dissolution medium containing EHE than one that was pure hexane, as can be seen from the higher levels of dissolution achieved for Secondary-2 than Secondary-1. Based on this, it was decided that the inclusion of an anti-flocculating agent was unnecessary for the dissolution of prismatic crystals of FFA, exhibiting no clear benefit to the dissolution process and impacting dissolution level control. As such, EHE was omitted from future dissolution studies on this crystal type.

In both samples there also appears to be a significant drop in dissolution level in PD2 relative to PD1. A similar change in dissolution level was observed in multiple other studies described later in the chapter. As this higher dissolution level consistently correlates to a higher measured level of additive in this and the other studies it is most likely that the level of additive in a crystal portion is directly related to the solubility and/or dissolution rate of the material. This distribution and effect of additive levels within these crystals is discussed in more detail at the end of this section.

In all, the levels of dissolution observed in the study were reasonably close to the intended dissolution level of 10%. This implies, along with surface area distribution plots that present a clear decrease in particle size and a significant decrease in crystal breakage, that the changes to the PD technique have resulted in visible improvements to the data collected. However, there was still room for refinement of the method to better control the dissolution process and the means by which it can be measured. The decrease in surface area on the size distribution plots for both samples (Figures 5.4 and 5.5 above) varied significantly between crystals, and some overlap was observed between the pre-dissolution and PD1 distributions on the Secondary-2 plot. While not essential to the

successful application of the partial dissolution process, these were noted as potential areas of improvement for the method.

Changes in Method

The subsequent improvements primarily took the form of changes to the image capture and analysis process. Care was taken to improve the quality of the images captured of the crystal samples before and after each stage in the dissolution process, with changes in lighting, crystal positioning, and the use of a camera mount. Through these efforts, negative aspects of the original images (such as blur and glare) that could have affected the sizing of the crystals were significantly reduced. Changes were also made to the image scaling process to improve consistency between different images.

The dissolution target value used to determine the volume of hexane used as the dissolution medium was also altered. Aside from the higher-than-normal PD1 dissolution levels discussed previously, the level of dissolution observed in PD2 and a number of subsequent test dissolutions consistently fell short of the intended levels. It appeared that volume of hexane chosen based on the previous target value, the measured solubility of FFA in hexane (2.4 mg mL^{-1}, Section 2.5.1.1), was insufficient to dissolve the expected amount of crystal mass. This is most likely due to the limited run-time of each dissolution stage not allowing for full equilibration of the mixture. The differences in the temperature at which the solubility tests and dissolutions were run likely also had an impact. This was not necessarily a significant problem for the application of the PD process, as it is generally preferable to dissolve a lower amount of crystal mass than a higher one. Nonetheless, it was decided that altering this dissolution target value would be beneficial

to the control of each dissolution stage. The updated value, 0.99 mg mL^{-1}, was selected based on the volumes of solvent used and the levels of dissolution observed in PD2 and the subsequent dissolution stages. The intended level of dissolution was also increased from 10% to 15% to limit the overlap of size distribution plots.

The changes to the method were evaluated through two final dissolution stages, performed on seven crystals used previously as part of Secondary-1 (sample named Secondary-3 here for distinction). The crystals were suspended in enough hexane to dissolve 15% of the pre-dissolution crystal mass based on their mass and the target dissolution value (0.99 mg mL^{-1}). The suspensions were agitated for 90 minutes at ambient temperature (20 – 25 °C) before the hexane was filtered off, and the recovered crystals rinsed with cold hexane, dried under vacuum, and resized. Full details of the adjusted PD procedure used in this and future dissolution studies are detailed in Section 5.5.1.2. The surface area distribution plot for these stages can be found in Figure 5.6, and the dissolution levels observed are listed in Table 5.3. When compared to the dissolution levels and distribution plots in the previous stages of method development, the improvements are clear. The levels of dissolution, especially in PD2, are much closer to the intended level of 15%, and the data points on the size distribution plot for the series are evenly spaced, with good separation and no overlap.

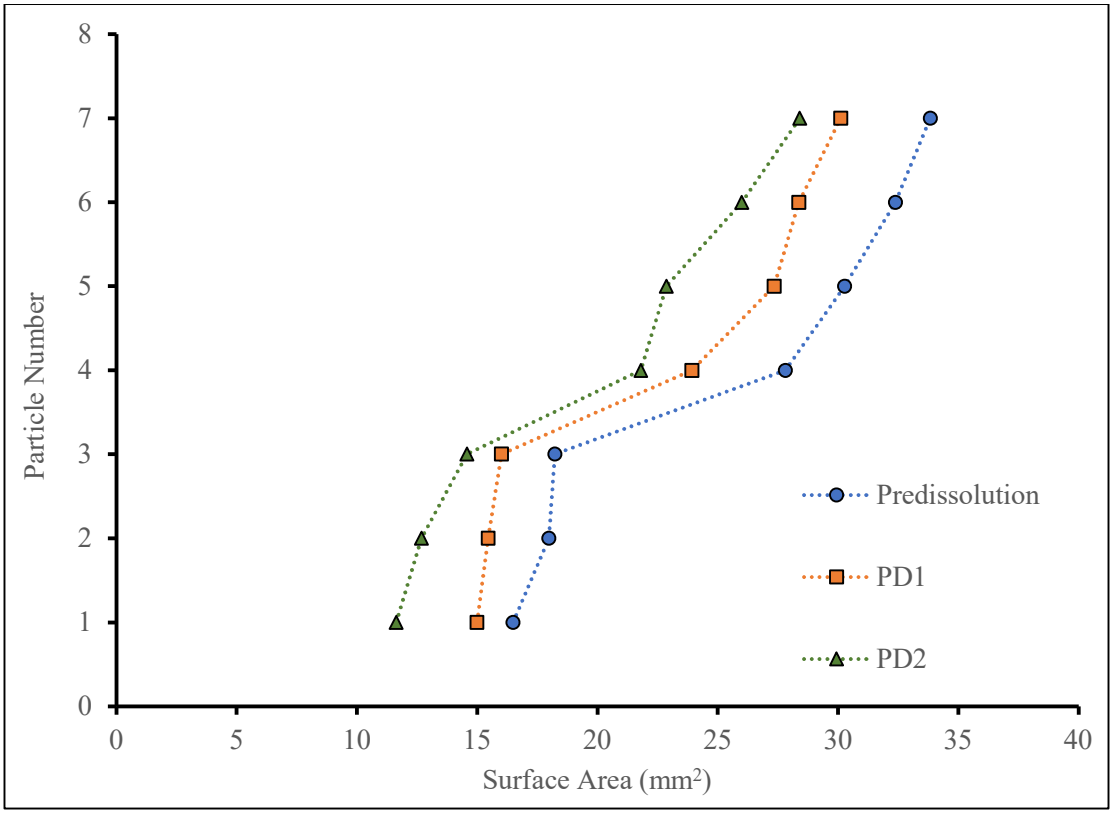


Fig 5.6. Surface area distribution plot of the Secondary-3 crystals over two dissolution stages at the end of secondary partial dissolution method development.

Table 5.3. Percentage of original crystal mass dissolved over two dissolution stages of Secondary-3 at the end of the secondary method development.

	PD1	**PD2**
% Secondary-3 Mass Dissolved	11.2%	15.9%

Distribution of Additive Levels throughout Method Development

Throughout the secondary method development process described in this section, a total of 12 dissolution stages were performed on the crystals in the Secondary-1 sample. The final dissolution stage (dubbed PD12) involved full dissolution of the remaining crystal particles. By comparing the percentage Cl-FA **16** level in the solutions collected from each stage (determined by HPLC), a pattern of the additive distribution within the Secondary-1 crystals can be plotted from a surface-to-centre basis (Figure 5.7). The additive level collected from the first dissolution stage is significantly higher than the doping level of the system (2.11%), then drops sharply over the next few stages before plateauing at a level of approx. 1.49%. This pattern implies that Cl-FA **16** is present throughout the crystal, and the level of additive is highest at the surface and lower towards the crystal centre. In other words, the incorporation of additive increases with crystal growth. This could be related to the difference in doping and incorporation levels during crystallisation. At the start of its growth, the crystal incorporates additive to an extent lesser than the doping level. This causes an increase in Cl-FA **16** levels in the crystallisation solution, which in turn could drive up the incorporation level in the later stages of crystal growth. A similar plot of additive distribution was constructed for the Secondary-2 PD stages (Appendix Figure 7.69).

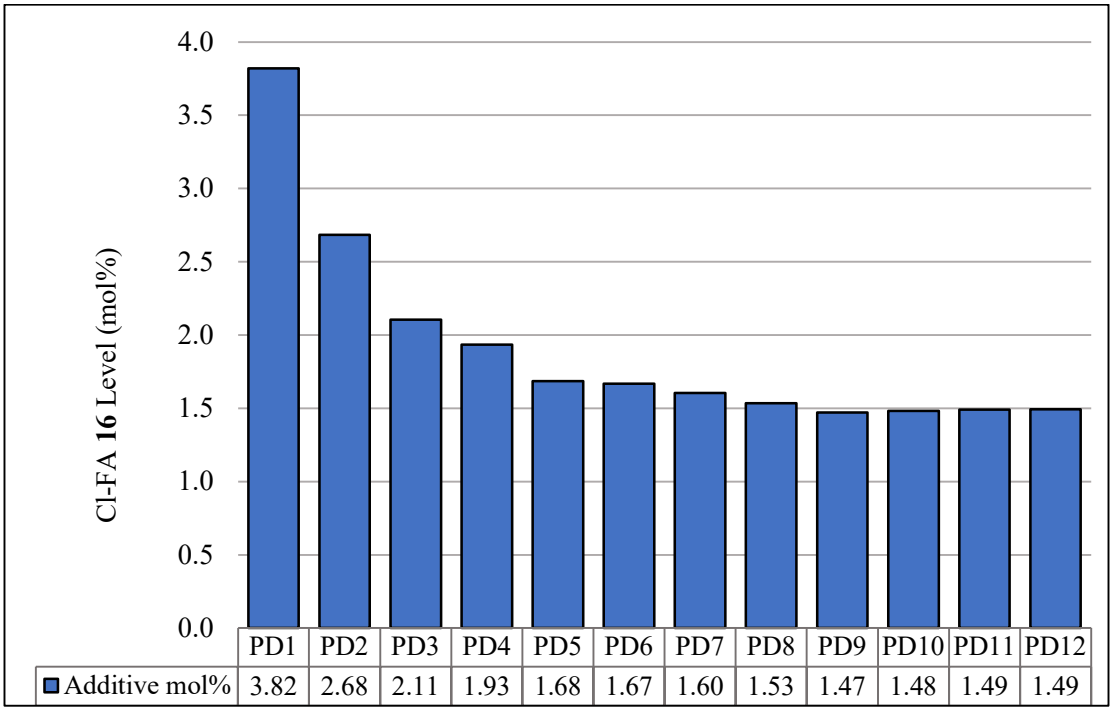


Fig 5.7. Level of Cl-FA **16** measured in each dissolution stage of Secondary-1 crystals, illustrating the pattern of additive incorporation from crystal surface to centre.

The non-homogeneity of components within solid solution crystals is a well-known phenomenon.[99] This is sometimes illustrated through the use of a ternary phase diagram, like the one in Figure 5.8. Such diagrams were discussed briefly in Section 1.3.2.5. A solid solution consisting of components *A* and *B* can be represented on such a diagram, with the inclusion of the solvent from which a crystal of the solid solution is grown as the third component *S*. Points *a* and *b* on the *AS* and *BS* axes respectively represent the solubility of each pure component in the solvent, and *ab* plots the solubilities of the solid solutions at each composition between the pure components. Experimentally-determined tie lines can be drawn connecting points along the *ab* curve to the *AB* axis. Using such a plot, the change in composition as a function of crystal growth through solvent evaporation can be tracked. For example, if a solution at point *X* is evaporated

under isothermal conditions until the composition reaches point *Y*, a solid solution of *A* and *B* will crystallise. The overall composition of these crystals will match that of *C* at this point, and the surrounding solution will match that of *L* on the *ab* curve; the compositions of *C* and *L* are based on the experimentally determined tie-lines mentioned previously. As the solvent evaporates further, the crystal grows, the system moves from point *Y* towards point *Z*, and points *C* and *L* move with it based on position of the tie-line at each point along *YZ*. In this way, the composition of the solid solution changes with solvent evaporation and consequently crystal growth. In the case of Figure 5.8, a solid solution crystal would be produced that decreases in relative *B* incorporation from centre to surface. Construction of representative ternary phase diagrams for the systems of interest would require substantial collection of empirical data and is outside of the scope of this project, but the concept serves to illustrate the theory behind the changing additive levels throughout the majority of crystals tested in this chapter.

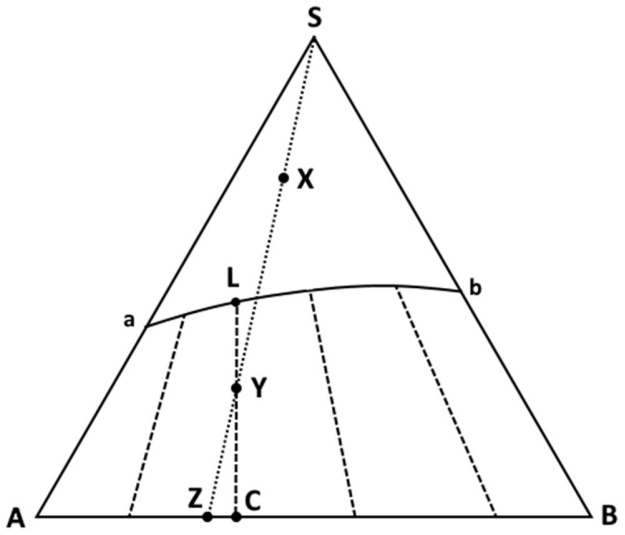


Fig 5.8. Illustration of a ternary phase diagram of solid solution *A/B*, including crystallisation solvent *S*.

The level of additive observed in the solution collected from PD1 is notably disproportionate compared to the rest of the Secondary-1 system. A similar observation has been reported in some literature studies.[17,90] One explanation is that a small amount of crystallisation solution present on the crystals after their isolation from the mother liquor could be evaporating, depositing additive-rich material on the surface of the crystals, and resulting in the disproportionately high levels of additive being recorded during those dissolutions. The high level of additive may be linked to the high dissolution levels observed in the early PD stages, as noted previously.

The additive distribution data can also be presented as a function of dissolution mid-point (Figure 5.9). Each dissolution stage is assigned as a percentage of the original sample mass. As such, the level of dissolution can be presented as a size-independent metric allowing for more meaningful comparison between plots from different samples. It also allows the presentation of additive distributions as a continuous series, as opposed to restraining it to discrete categories like dissolution stages, providing more insight into the additive levels at different points in a crystal. This distinction can be especially meaningful in situations where the level of dissolution varies significantly between stages, as well as the final dissolution stage wherein the remaining body of the crystal is entirely dissolved, and often involves a higher level of crystal dissolution than the other stages in a series. A full description of the determination of dissolution midpoints can be found in Section 5.5.1.5.

A dotted line is also included in Figure 5.9 that represents the doping level of the system when it was first created. This is a close representation of the level of additive in solution at the start of crystallisation (dissolution midpoint = 0%). It becomes less

representative as the level of additive in solution changes over the course of crystal growth, but it still provides a useful way of comparing the additive incorporation to the initial additive content of the system.

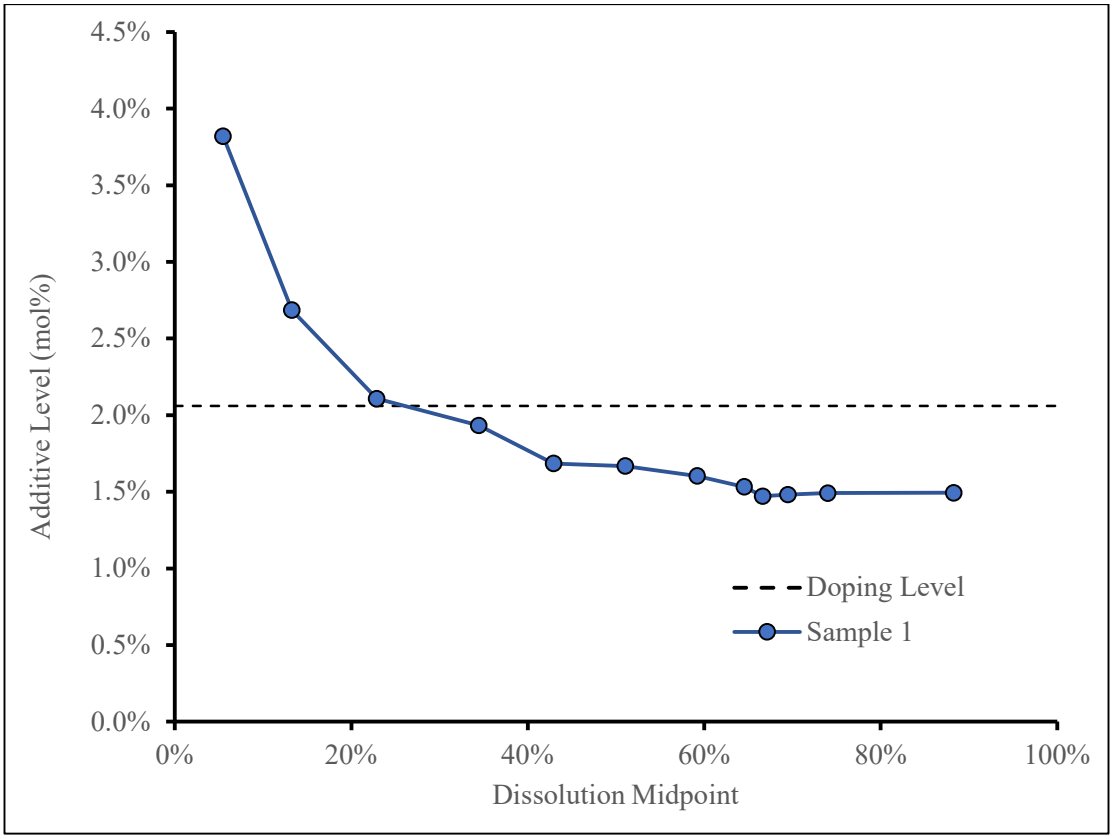


Fig 5.9. Plot of additive level *vs.* dissolution midpoint of Secondary-1 crystals, illustrating the pattern of additive incorporation from crystal surface to centre.

5.2.2 Application of Partial Dissolution Method to Different Systems

Now that a satisfactory partial dissolution method had been developed for use on the systems of interest, the technique could be applied to a wider array of crystalline systems of doped FFA. This section describes the application of the developed method on FFA systems doped with different additive types and levels to assess the effect of these factors on the PD process and distributions of those additives. The effect of sample size and crystal morphology was also investigated.

5.2.2.1 Effect of Increased Sample Size

A study was performed to investigate the applicability of the developed procedure to systems with a larger sample size. As the studies in the secondary method development stage were carried out on samples consisting of low particle numbers (7 − 10 crystals per study), it is possible that performing a study on a larger scale could introduce unforeseen complications to the process. These methods were being developed for use in the pharmaceutical industry which traditionally deals with much larger batches of product than has been tested as part of this project. As such, performing a study on a larger scale is important for ensuring the process is applicable to systems with a higher number of particles.

However, there are limitations to the size of a sample that can be studied. Without access to the appropriate laser diffraction equipment for particle counting and sizing, those measurements must be carried out manually. This limits the number of crystals that can

realistically be managed as part of a multi-stage dissolution study. Limitations also arise from the number of similarly-sized crystals available for use, as well as the level of solvent required for a scaled-up dissolution. As such, a sample of 49 crystals was selected from the same batch of FFA **14** doped with 2% Cl-FA **16** as used in previous studies (named ISS-1). This represented a significant increase in sample size when compared to other partial dissolution studies in this project, while being small enough to still be manageable in terms of particle sizing, required crystal growth, and corresponding solvent volume. An image of the ISS-1 crystals prior to dissolution can be seen below (Figure 5.10).

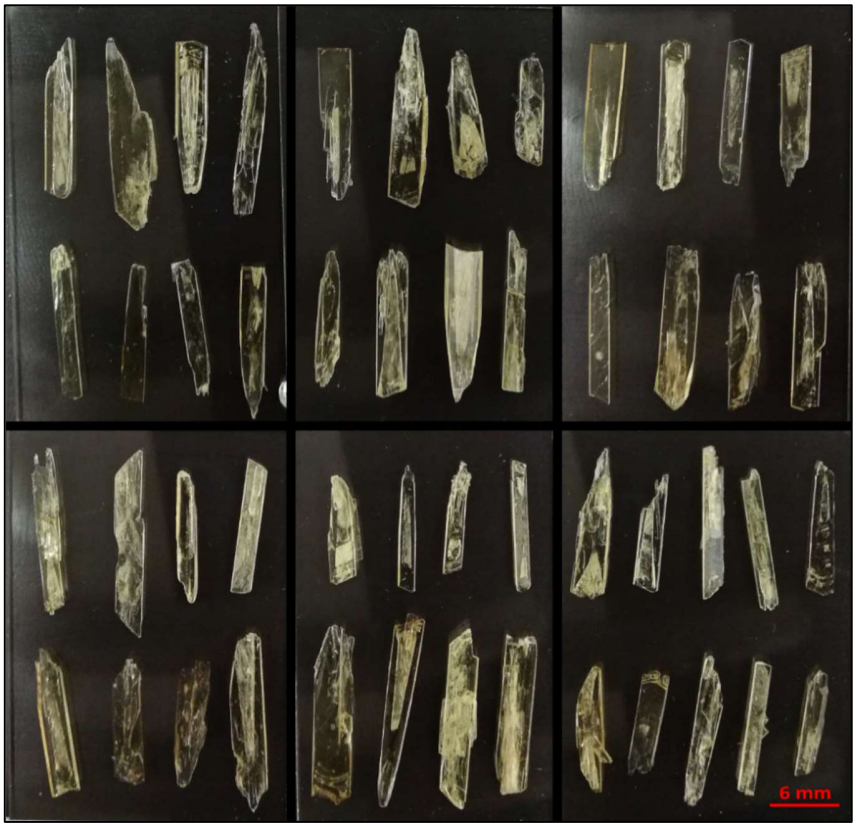


Fig 5.10. ISS-1, 49 prismatic FFA **14** crystals doped with 2% Cl-FA **16** grown *via* slow evaporation from MeOH selected as sample to investigate effect of sample size on PD process.

Box plot analysis was used to ensure similarly sized crystals were chosen for each sample, including ISS-1 (Figure 5.11). Box plots are a statistical tool that provides information on the spread and normality of a data sample, as well as identifying any mild or extreme outliers in the sample. Unless exceptional, the normality of the data distribution is not of huge significance to the study; box plot analysis is primarily carried out to identify size outliers in the sample. Outliers on either extreme of the size distribution can cause similar issues. An exceptionally small crystal relative to the rest of the sample will likely be dissolved to a disproportionately high extent. Likewise, an exceptionally large crystal would likely experience dissolution to a lesser extent than the other crystals. In both situations, an uneven level of dissolution would be occurring across the sample, potentially impacting additive distribution data collected from the study. The sizes at which these disparities start causing issues with the PD process are not known, but the crystals in a sample were all kept relatively similar in size to avoid the possibility of introducing these problems. Box plot analysis for each of the samples described in the remainder of the chapter (for which surface area values were measured) can be found in Appendix Section 7.9.4.

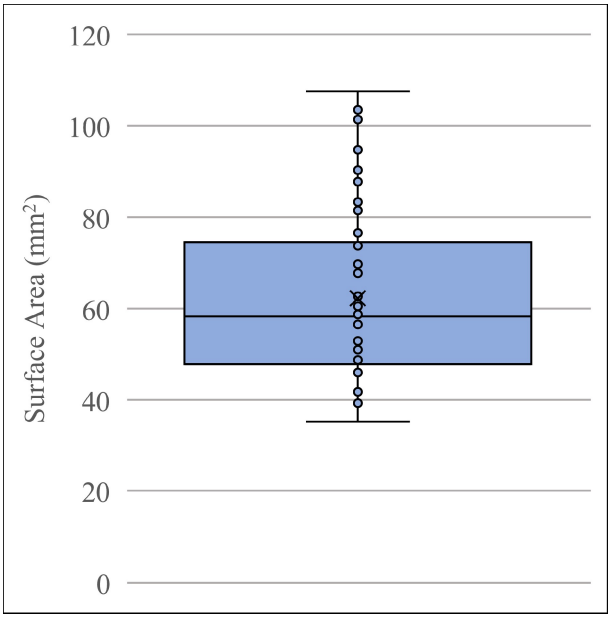


Fig 5.11. Box plot of crystal surface areas distribution of ISS-1 prior to dissolution.

Crystal Dissolution Levels

The crystals were suspended in enough hexane to dissolve 15% of the pre-dissolution crystal mass based on their mass and the target dissolution value (0.99 mg mL^{-1}). The suspensions were agitated for 90 minutes at ambient temperature (see Table 5.4) before the hexane was filtered off, and the recovered crystals rinsed with cold hexane, dried under vacuum, and resized.

The levels of crystal dissolution achieved in each stage were relatively close to the intended level of 15% (Table 5.4). As observed previously, the dissolution level of the first stage was higher than intended, possibly due to the high additive level observed in PD1. The dissolution level of the second stage in this case was also high, perhaps partly for the same reason as the first, but also potentially due to the higher ambient temperature experienced during that stage. The dissolution levels achieved in PD3 and PD4 were much

more even and close to the intended level. The surface area distribution plot for this study can be found in Figure 5.12.

Table 5.4. Percentage of original crystal mass dissolved over four dissolution stages of ISS-1.

	PD1	**PD2**	**PD3**	**PD4**
Temperature (°C)	20	22	20	21
% Mass Dissolved	16.9%	17.9%	14.3%	14.3%

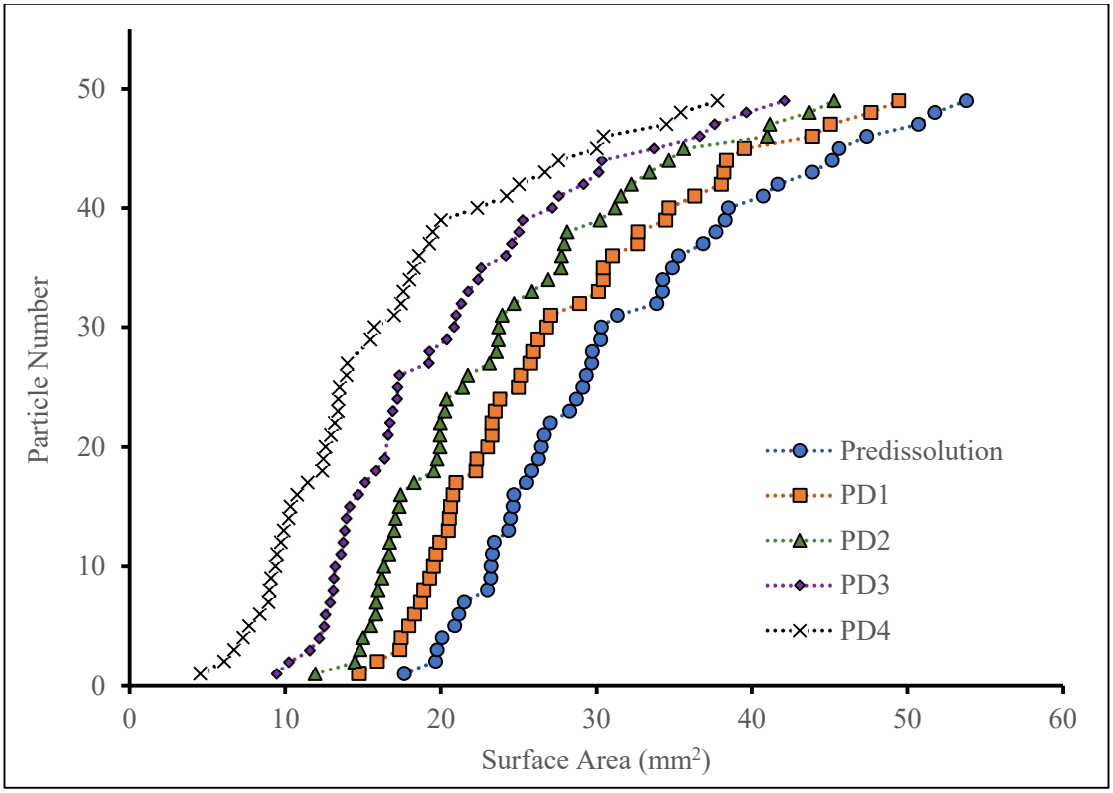


Fig 5.12. Surface area distribution plot of ISS-1over four dissolution stages.

Additive Incorporation Levels

The pattern of additive incorporation observed for ISS-1 can be directly compared to those in Section 5.2.1.2 (Secondary 1 and Secondary 2), as the crystals were selected

from the same batch; the plots of additive incorporation *vs*. dissolution mid-point for all three are presented in Figure 5.13. The dissolution mid-point is explained in detail in Section 5.2.1.2. Like the previous samples, there is a disproportionately high level of additive present in the first dissolution stage, most likely due to the deposition of additive-rich mother liquor on the crystal surface *via* evaporation, followed by a stark drop in subsequent stages before the values plateau at a percentage value lower than that of the doping level (2.06%).

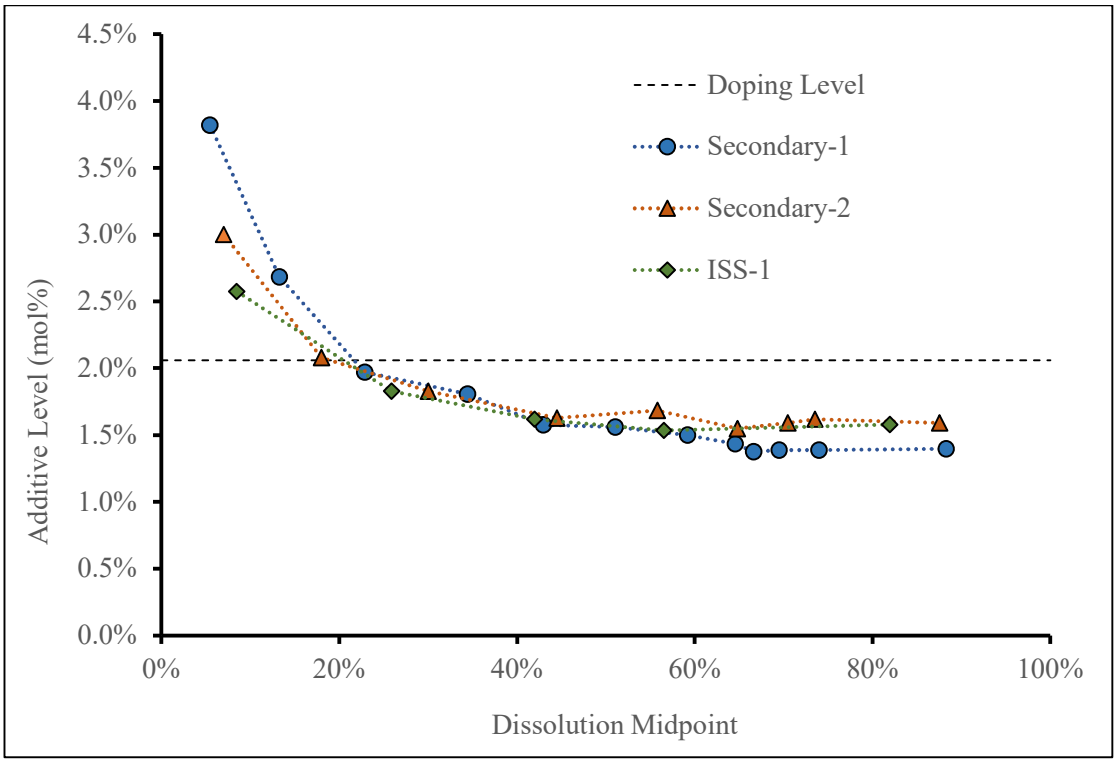


Fig 5.13. Plot of additive level *vs.* dissolution midpoint of ISS-1, compared to similar plots from Secondary-1 and Secondary-2 determined during secondary method development (all doped with 2% Cl-FA **16**).

In all, few complications appear to arise from applying the developed partial dissolution method to samples with a higher crystal count. Higher volumes of solvent are required due to the increased sample mass, which could become unfeasible with some equipment set-ups. However, should this become an issue the method can be altered to increase the solubility of the sample in the dissolution medium, either by increasing the temperature at which the experiment is carried out, or replacing/supplementing the medium with a more potent solvent system. The probability of crystal loss also increases with larger samples, but the impact it has on the resulting data also decreases. It remains to be seen if these observations hold true at even higher particle counts, as would be experienced by those handling batches of pharmaceutical products in a process setting.

5.2.2.2 Effect of Different Additive Types and Levels

Up to this point, all partial dissolution studies had been performed on crystals selected from the same batch; one doped with approximately 2 mol% Cl-FA **16**. As such, it was necessary to apply the developed method to crystal samples doped with different levels and types of additive. Both these factors can affect the properties and behaviour of a crystal system. In Sections 4.6.1 and 4.6.2, the inclusion of even very low levels of Me-FA **15** and Cl-FA **16** respectively were shown to have notably different effects on the polymorphic behaviour of FFA **14** when analysed by DSC. These effects were also demonstrated to change with doping level. As such, comparison of partial dissolution studies on crystals doped with varying levels of Me-FA **15** with the studies already performed on systems doped with Cl-FA **16** would allow for any differences arising from the variation in additive type and level to be highlighted and accounted for in the PD

method. Additionally, any differences between the distribution behaviour of the two additives could also be observed. To this end, two batches of FFA **14** crystals were studied: one doped with 0.5% Me-FA **15** (DATL-1) and another doped with 5% Me-FA **15** (DATL-2). Images of these crystal samples can be seen in Figures 5.14 and 5.15 respectively.



Fig 5.14. DATL-1, prismatic FFA **14** crystals doped with 0.5% Me-FA **15** grown *via* slow evaporation from MeOH and selected as sample to investigate effect of additive type and level.



Fig 5.15. DATL-1, prismatic FFA **14** crystals doped with 5% Me-FA **15** grown *via* slow evaporation from MeOH and selected to investigate effect of additive type and level.

Crystal Dissolution Levels

The crystals were suspended in enough hexane to dissolve 15% of the pre-dissolution crystal mass based on their mass and the target dissolution value (0.99 mg mL^{-1}). The suspensions were agitated for 90 minutes at ambient temperature (see Table 5.5) before the hexane was filtered off, and the recovered crystals rinsed with cold hexane, dried under vacuum, and resized.

The levels of dissolution achieved at each stage for the DATL-1 and DATL-2 crystals can be seen in Table 5.5, and the surface area distribution plots can be found in Appendix Figures 7.81 and 7.82 respectively. Aside from a slightly lower level for DATL-1 PD1, the dissolution level achieved for all stages across both studies was very even, falling within 1% of the intended value.

Table 5.5. Percentage of original crystal mass dissolved over four dissolution stages of DATL-1 and DATL-2 during investigation into the effect of additive type and level.

	PD1	**PD2**	**PD3**	**PD4**
Temperature (°C)	19 - 22	19 - 20	19 - 20	19 - 20
% DATL-1 Mass Dissolved	12.6%	14.7%	15.4%	14.9%
% DATL-2 Mass Dissolved	14.8%	14.5%	15.1%	14.1%

Additive Incorporation Levels

A noticeable difference was observed compared to the Cl-FA **16** samples when measuring the additive levels of the solutions recovered from the above dissolution studies. When presented as a function of dissolution midpoint (Figures 5.16 and 5.17 respectively), an increasing trend is observed across successive dissolution stages. In DATL-1, the additive level measured close to the surface of the crystal is lower than the doping level of 0.57% Me-FA **15**, then increases in a near-linear fashion further towards the centre of the crystal, exceeding the doping level. DATL-2 follows a very similar pattern, but the doping level of 5.87% is not exceeded. These patterns imply that the crystal incorporates a higher level of additive at the start of crystallisation, and a progressively lower amount as the crystal grows larger; the reverse of that seen in the systems doped with Cl-FA **16**. When the pattern of incorporation is compared to the level of crystal mass loss observed at each dissolution stage, it appears that the correlation between the level of additive in a portion of crystal and the solubility and/or dissolution rate of that portion previously noted in the systems doped with Cl-FA **16** is also observed here. Many factors affect the dissolution process, but it does appear that the level of additive has some impact on the level of dissolution achieved.

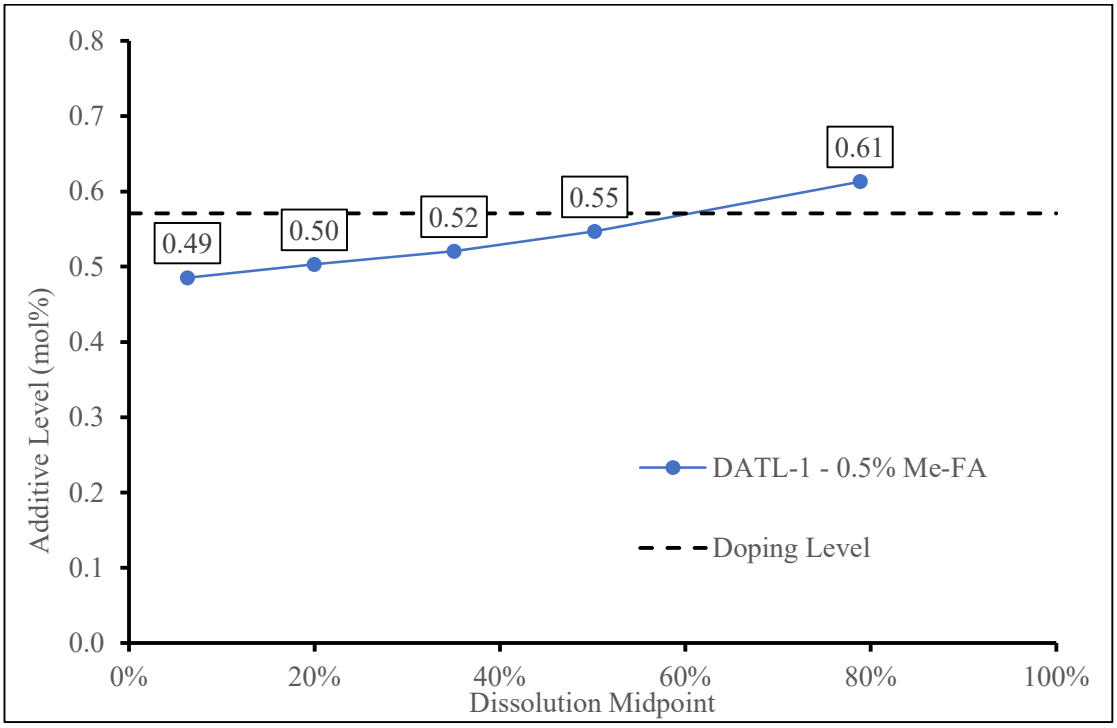


Fig 5.16. Plot of additive level *vs.* dissolution midpoint of DATL-1 crystals (doped with 0.5% Me-FA **15**) compared to doping level.

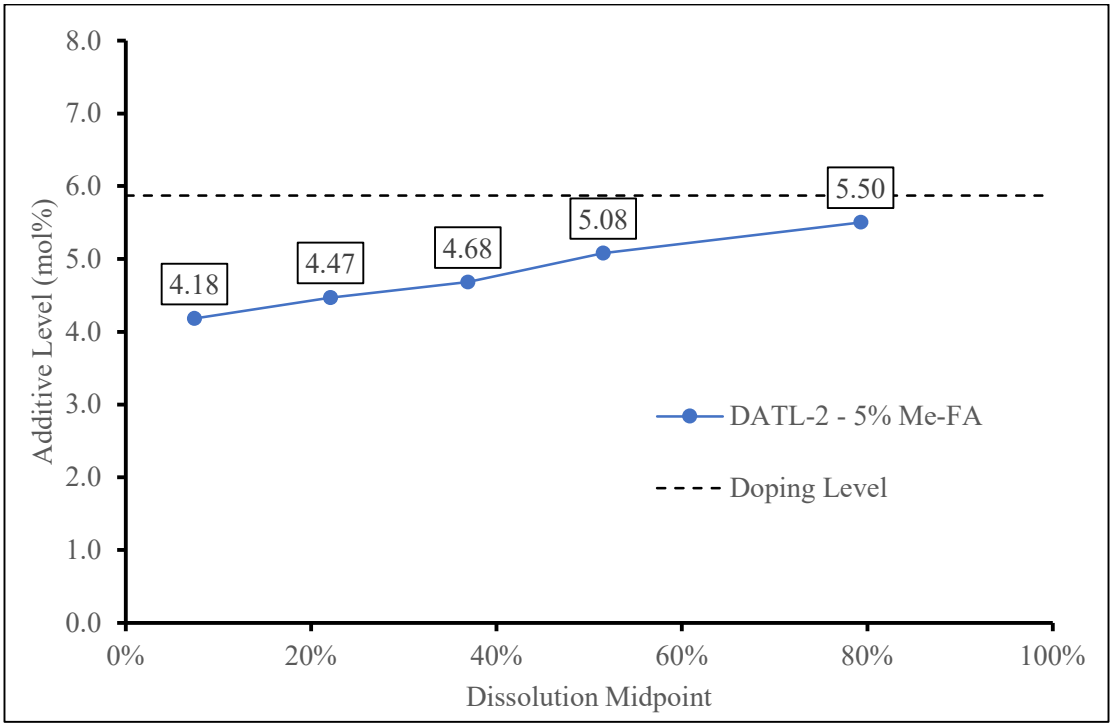


Fig 5.17. Plot of additive level *vs.* dissolution midpoint of DATL-2 crystals (doped with 5% Me-FA **15**) compared to doping level.

The additive distributions of studies on samples with different doping levels can be more easily compared by plotting their distribution coefficient (α_2) values rather than their additive levels. For a homogeneous solid solution (or a system that behaves like a homogeneous solid solution), the α_2-value denotes the relationship between the mole fraction of an additive within a solid solution crystal and the mole fraction of the additive in the solution from which that crystal was grown. Therefore, it can act as a measure of additive incorporation independent of doping level, by which the incorporation level in systems of differing additives and doping levels can be compared.[219,220] This results in a Figure for α_2 that represents the level of additive in a crystal layer as a ratio of the doping level of the crystallisation solution. An α_2-value of less than 1 denotes a crystal layer in which the level of additive incorporation exceeds the level of additive in the solution that crystal is being grown from. On the other hand, an α_2-value of greater than 1 implies the incorporation level of additive in that layer is lower than that of the surrounding solution. α_2-values can be used graphically as an alternative to additive percentage on the y-axis, generally plotted against dissolution stage or dissolution midpoint.

It is worth noting that by using distribution coefficient in the place of additive percentage, it reverses the slope of a series of data. For example, for a partial dissolution study that exhibits increasing levels of additive through successive dissolution stages, transforming the additive level data from percentage additive to distribution coefficients will result in a trend of decreasing α_2-values. A more correct way of calculating the α_2 is to use the level of additive in the liquid phase at the time the level of additive in the solid phase was measured, rather than using the doping level measured at the creation of the system. However, as these solution levels were not measured, the doping level provides a

close approximation that still makes the patterns of additive incorporation clear. The process by which α_2 is calculated is described in Section 5.5.1.5. It is important to note that the values represented by the α_2 symbol are unrelated to those represented by α^0 (pure-component relative solubility value, Section 2.5.2.2) or α_1 (selectivity coefficient value, Section 4.4).

A comparison of the two systems doped with Me-FA **15** is presented in Figure 5.18, alongside the one of the distributions measured in the studies of the 2% Cl-FA **16** crystals (ISS-1). Not only are the pattern of the Me-FA **15** incorporation reversed relative to that of ISS-1, they also are much more linear and lack the plateau that is observed closer to the centre of the Cl-FA **16** crystals. Despite both the Me-FA **15** and Cl-FA **16** exhibiting similar solid solution-like behaviour at lower doping levels (only diverging at higher levels of additive incorporation, see Section 4.6), it appears that the nature of the additive has a significant impact on its distribution within prismatic crystals of FFA **14**. A more minor difference can be observed between the samples doped with different levels of the Me-FA **15** additive. The pattern of additive incorporation between the two is comparable, but the sample doped with 0.5% Me-FA **15** (DATL-1) appears to have a consistently higher level of incorporation at each dissolution stage, even when corrected for doping level. This may be attributed to the slightly smaller average crystal size of DATL-1 compared to DATL-2 (31.8 mm^2 *vs.* 35.5 mm^2 prior to dissolution), or it could be that relative incorporation decreases with doping level.

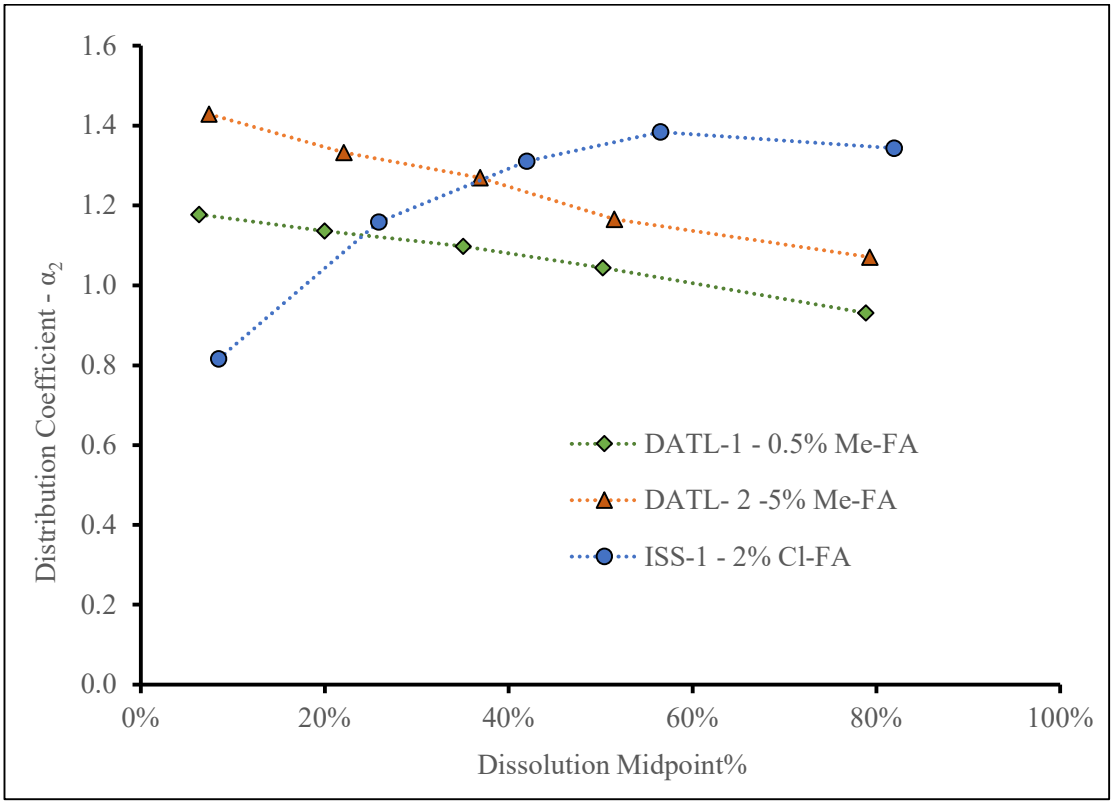


Fig 5.18. Plot of α_2-value *vs.* dissolution midpoint of DATL-1 and DATL-2 crystals (doped with Me-FA **15**), compared to similar plot for ISS-1 (doped with Cl-FA **16**).

Despite the difference in incorporation pattern between the samples doped with Cl-FA **16** and Me-FA **15**, little impact was observed on the application of the partial dissolution method. It would appear that adjustment of the method is not necessary when it is applied to samples containing different additives and/or impurities. The pattern of additive incorporation within the sample crystals also seems to have little impact, save for the minor effect of additive level on the solubility and/or dissolution rate of the material in the solvent.

5.2.2.3 Effect of Crystal Size and Morphology

Unlike with some additive types, FFA **14** solutions doped with DF-FA **17** produced a relatively large batch of crystals suitable for partial dissolutions. Most of these crystals were a similar morphology to those doped with Me-FA **15** and Cl-FA **16**; prismatic in nature but exhibiting tabular qualities in terms of depth and a generally larger length than width. Enough crystals with this morphology were produced to segregate them into two samples based on their surface area (Figures 5.19 and 5.20). A number more crystals were also produced, these ones with a slightly different morphology, exhibiting much more circularity than the previous crystals (Figure 5.21). The production of these crystals allowed not only for a study into the effect of DF-FA **17** on the PD method, but also for one into the effect of crystal habit on the procedure. At this point, additive type and level had been varied to test the robustness of the method, but these studies had only been carried out on a single type of crystal. To provide further evidence that the method is applicable to systems beyond those directly studied as part of this project, it should be tested on crystals with different morphological characteristics. To that end, dissolution studies were carried out on the three 2% DF-FA **17** crystal samples described above: the sample of smaller prismatic crystals with the more tabular habit (Figure 5.19) were designated CSM-1, the larger prismatic/tabular crystals (Figure 5.20) were designated CSM-2, and the prismatic crystals with higher circularity (Figure 5.21) were designated CSM-3.



Fig 5.19. Smaller prismatic FFA **14** crystals doped with 2% DF-FA **17** grown *via* slow evaporation from MeOH and selected as CSM-1 to investigate effect of crystal size and morphology.



Fig 5.20. Larger prismatic FFA **14** crystals doped with 2% DF-FA **17** grown *via* slow evaporation from MeOH and selected as CSM-2 to investigate effect of crystal size and morphology.

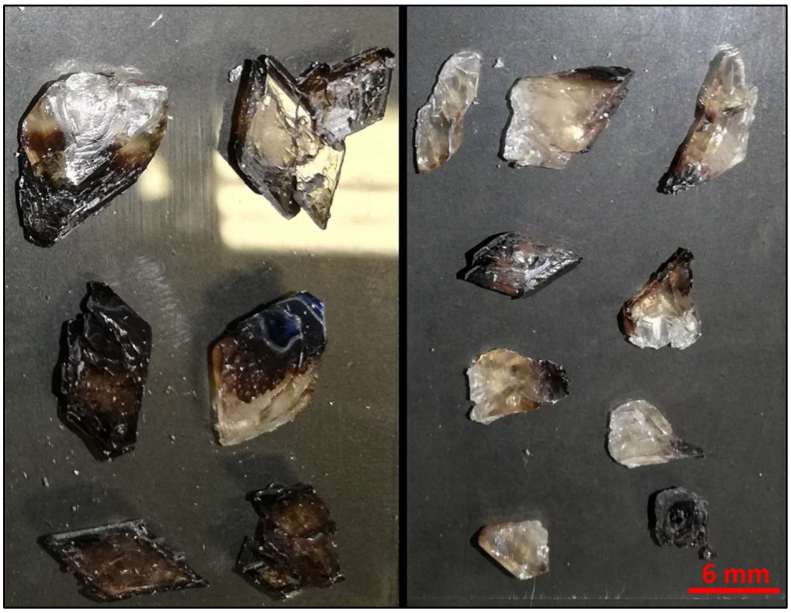


Fig 5.21. Prismatic FFA **14** crystals doped with 2% DF-FA **17** with a higher level of circularity grown *via* slow evaporation from MeOH and selected as CSM-3 to investigate effect of crystal size and morphology.

Crystal Dissolution Levels

The crystals were suspended in enough hexane to dissolve 15% of the pre-dissolution crystal mass based on their mass and the target dissolution value (0.99 mg mL^{-1}). The suspensions were agitated for 90 minutes at ambient temperature (see Table 5.6) before the hexane was filtered off, and the recovered crystals rinsed with cold hexane, dried under vacuum, and resized.

The percentage levels of dissolution observed for each stage of the dissolution of the three samples are listed in Table 5.6. The level of dissolution for the PD1 stage of all three samples was high, possibly due to a combination of the increased additive level of the outer crystal layers, as observed previously, and a higher experimental temperature.

For the most part the levels for PD2 – PD4 were closer to the intended levels. Surface area distribution plots for CSM-1 – CSM-3 can be found in Appendix Figures 7.83 – 7.85 respectively. The plot for CSM-3 differs from those of CSM-1 and CSM-2 in that the surface area measurements for CSM-3 are slightly less representative of the true surface areas due to the more circular morphology of the crystals. In spite of this, the measured surface values remain an adequate metric by which to track the dissolution of the crystals.

Table 5.6. Percentage of original crystal mass dissolved over four dissolution stages of CSM-1 – CSM-3 during investigation into the effect of crystal size and morphology.

	PD1	**PD2**	**PD3**	**PD4**
Temperature (°C)	22-24	19-20	19-20	19-20
% CSM-1 Mass Dissolved	18.5%	15.7%	15.3%	17.7%
% CSM-2 Mass Dissolved	21.0%	14.8%	16.6%	14.5%
% CSM-3 Mass Dissolved	18.2%	18.4%	15.6%	14.7%

Additive Incorporation Levels

In terms of additive distribution, the trends observed within all three samples are very similar. The level at the surface of the crystals exceeds the doping level (1.95%), then drops below as more layers are stripped away before levelling off towards the centres of the crystals. While the values for CSM-1 and CSM-2 were comparable, the additive levels of the prismatic CSM-3 samples were consistently higher than those of the other two across all stages. As the three samples differed only by crystal morphology, this implies that this may indeed have an effect on the level of additive incorporation, though

in this case not the pattern of that incorporation within the crystal. The additive values for the three samples are overlaid in Figure 5.22.

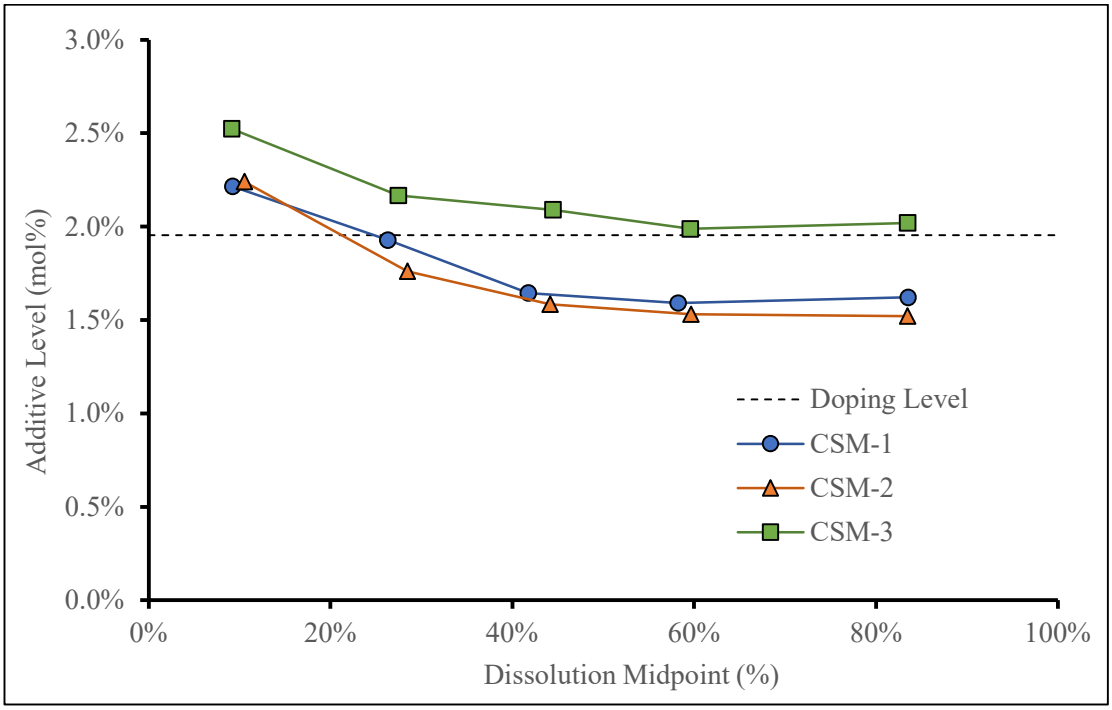


Fig 5.22. Plot of additive level *vs.* dissolution midpoint of CSM-1 – CSM-3 crystals (doped with 2% DF-FA **17**), compared to doping level.

The pattern is also notably similar to that observed in the 2% Cl-FA **16** studies. The distributions of CSM-1 – CSM-3 can be compared to that of ISS-1 (doped with Cl-FA **16**) from Section 5.2.2.2 in terms of their distribution coefficient (α_2) to facilitate comparison (Figure 5.23). The crystals in the ISS-1 had a very similar morphology to those of CSM-1 and CSM-2, and likewise the patterns of incorporation of those three samples are most comparable. The data suggests that crystal morphology may have an

impact on the incorporation of additives, at least in the system of study. As equilibrium was not reached in the dissolution (see Section 5.4.2 for discussion), the difference may stem from the slower dissolution of the larger CSM-3 particles.

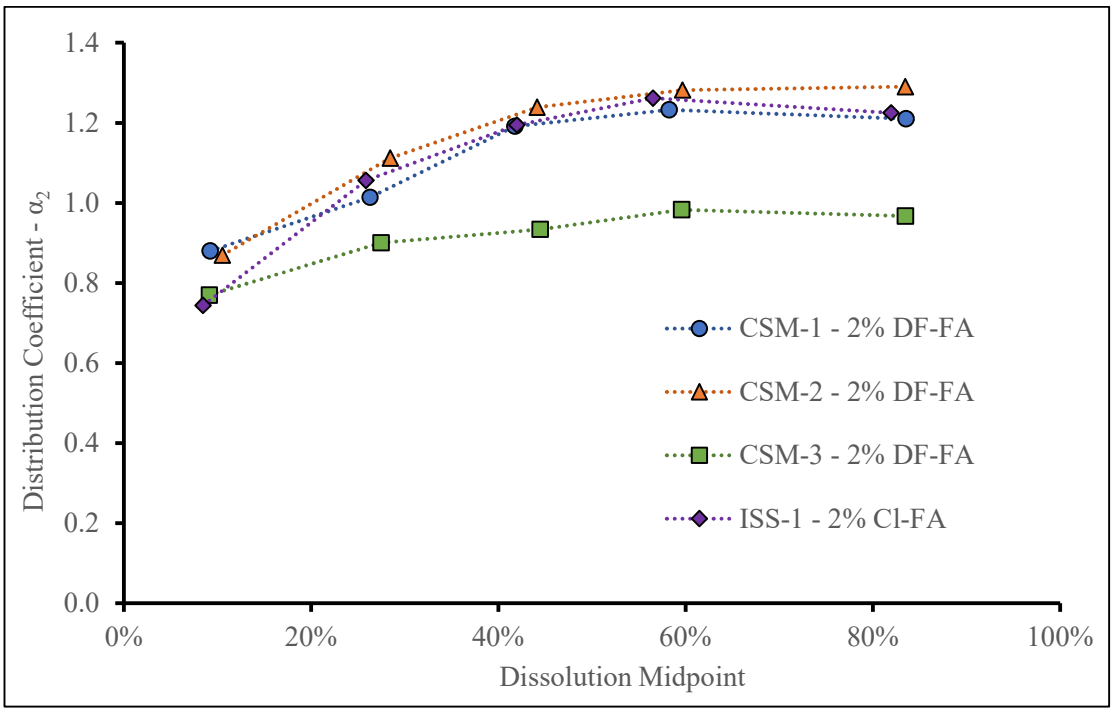


Fig 5.23. Plot of α_2-value *vs.* dissolution midpoint of CSM-1 – CSM-3 crystals (doped with DF-FA **17**), compared to similar plot for ISS-1 (doped with Cl-FA **16**).

5.2.2.4 Studies on Single Prismatic Crystals

Partial dissolution experiments were carried out on two large crystals of FFA **14**, doped with approximately 2 mol% Cl-FA **16** (SPC-1) and DF-FA **17** (SPC-2) individually. These crystals were grown *via* slow vapour diffusion, as described in Section

2.6.1.4. Production of these crystals allowed for investigation into the distribution of additives within a single crystal, rather than a batch. Some previous research of stepwise dissolution from which the current method is adapted focused on the dissolution of single crystals, for example those of phenacetin and L-asparagine monohydrate.[90,91,119] Performing a similar investigation on the systems of study is valuable as a way of identifying differences between single and multi-crystal samples in terms of procedure and/or results. It was discovered later than SPC-2 may have in fact been an agglomeration of multiple crystals rather than a single unit. However, it was still of value to perform the experiment on the agglomerate for comparison to SPC-1 and similar multi-particulate samples.

The intention during these studies was to run a higher number of dissolution stages on these large crystals, potentially 8−10, each with a lower level of dissolution, to produce a more detailed map of the distribution of additives within each crystal. Unfortunately, the dissolution process progressively weakened the structural integrity of the crystals, exposing flaws and resulting in the fracturing of both crystals after just four dissolution stages. This was less surprising for SPC-2 than for SPC-1, due to its agglomerated nature. Images of the crystals throughout the dissolution process can be seen in Figures 5.24 and 5.25 for SPC-1 and SPC-2 respectively. After disintegration, the remaining fragments were fully dissolved and the additive level measurements labelled as PD5.

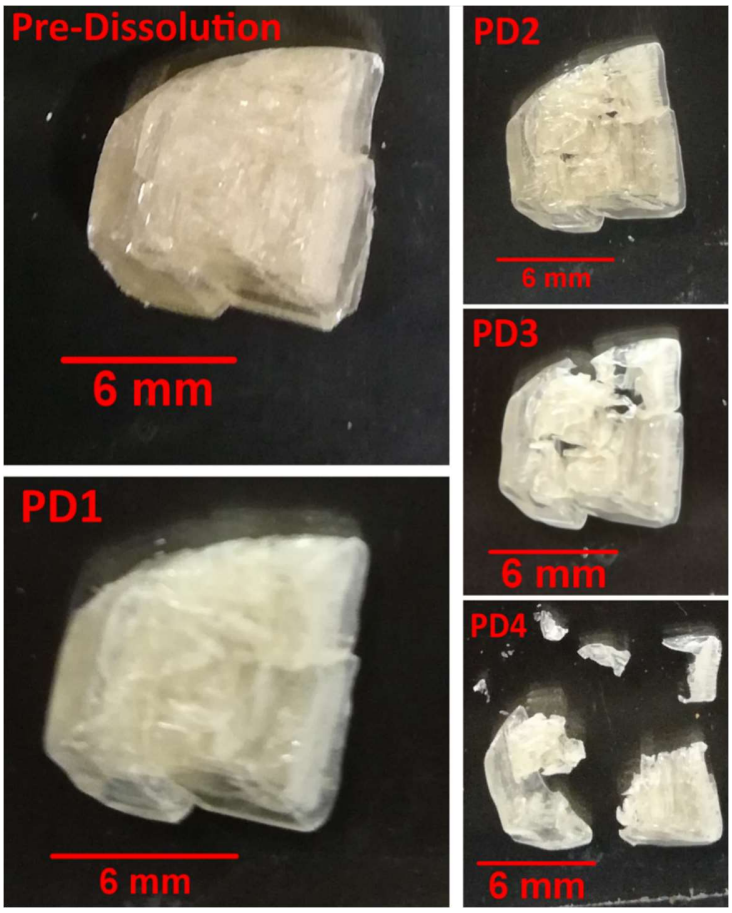


Fig 5.24. Large single prismatic SPC-1, grown *via* slow evaporation from MeOH, over the course of four dissolution stages.

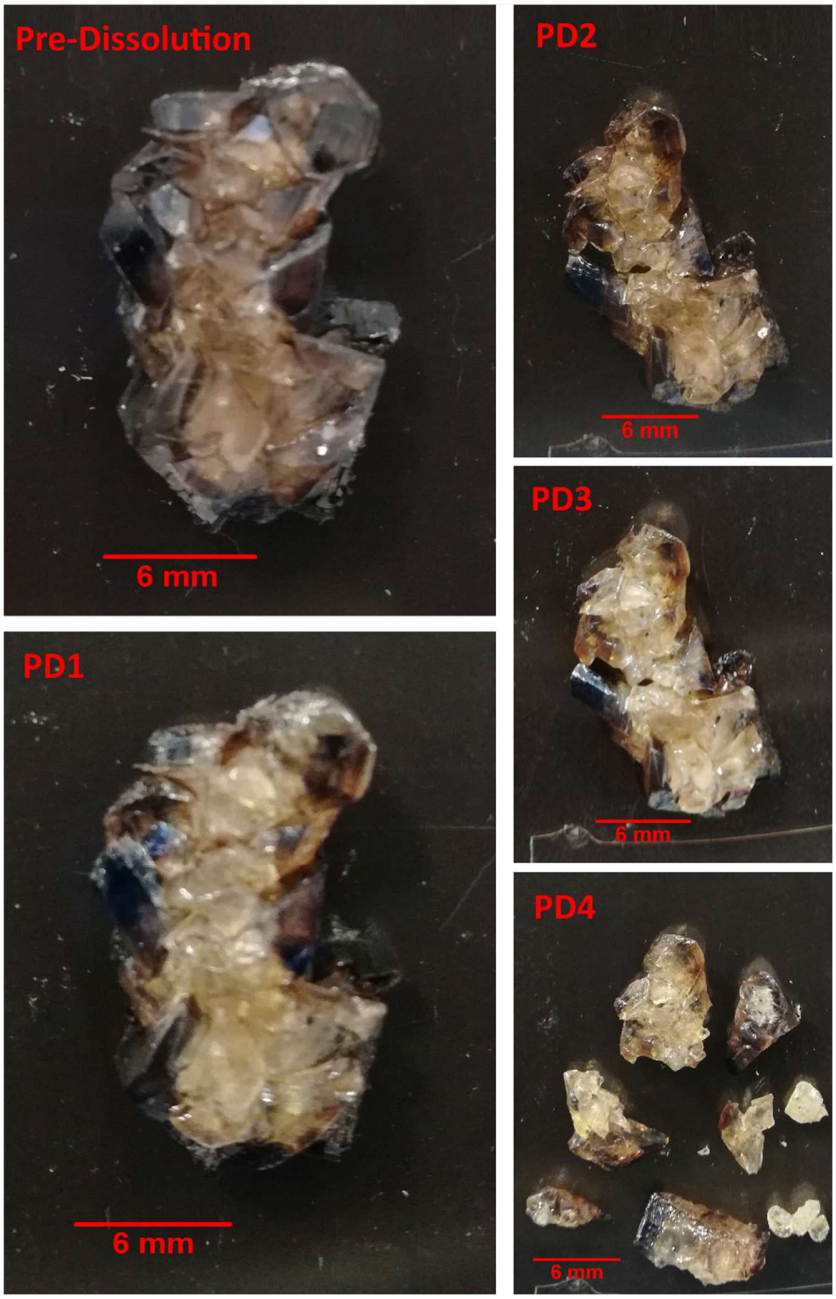


Fig 5.25. Agglomerate of crystals (SPC-2), grown *via* slow evaporation from MeOH, over the course of four dissolution stages.

Crystal Dissolution Levels

The crystals were suspended in enough hexane to dissolve 15% of the pre-dissolution crystal mass based on their mass and the target dissolution value (0.99 mg mL^{-1}). The suspensions were agitated for 90 minutes at ambient temperature (see Table 5.7) before the hexane was filtered off, and the recovered crystals rinsed with cold hexane, dried under vacuum, and resized.

The levels of dissolution observed in these studies can be found in Table 5.7. While the dissolution levels achieved SPC-2 match the expected values (lower than 15%) based on the decreased surface area of the sample, those of SPC-1 are higher than expected. This is partly a result of the lower mass-to-surface-area ratio of the smaller SPC-1 crystal when compared to that of SPC-2. Additionally, as can be seen in Figure 5.24 above, it is likely that small fragments of the crystal were becoming dislodged during the dissolution process, giving the appearance of higher dissolution levels.

As will be discussed in more detail in Section 5.2.4, full equilibration was not achieved during the partial dissolution studies described in this work. Instead, a defined experimental duration of 90 minutes was maintained for all studies. While this afforded more consistency within and between studies, it also introduced significant variability by introducing dissolution rate and kinetics as experimental factors.

Table 5.7. Percentage of original crystal mass dissolved over four dissolution stages of large crystals SPC-1 and SPC-2.

	PD1	PD2	PD3	PD4
Temperature (°C)	19 - 23	19	19	20 - 21
% SPC-1 Mass Dissolved	17.6%	17.8%	16.2%	15.9%
% SPC-2 Mass Dissolved	12.2%	7.0%	9.5%	12.3%

Additive Incorporation Levels of SPC-1

The additive distribution within SPC-1 is shown in Figure 5.26. The level of additive seems to decrease from the surface of the crystal inwards but rises for the final dissolution.

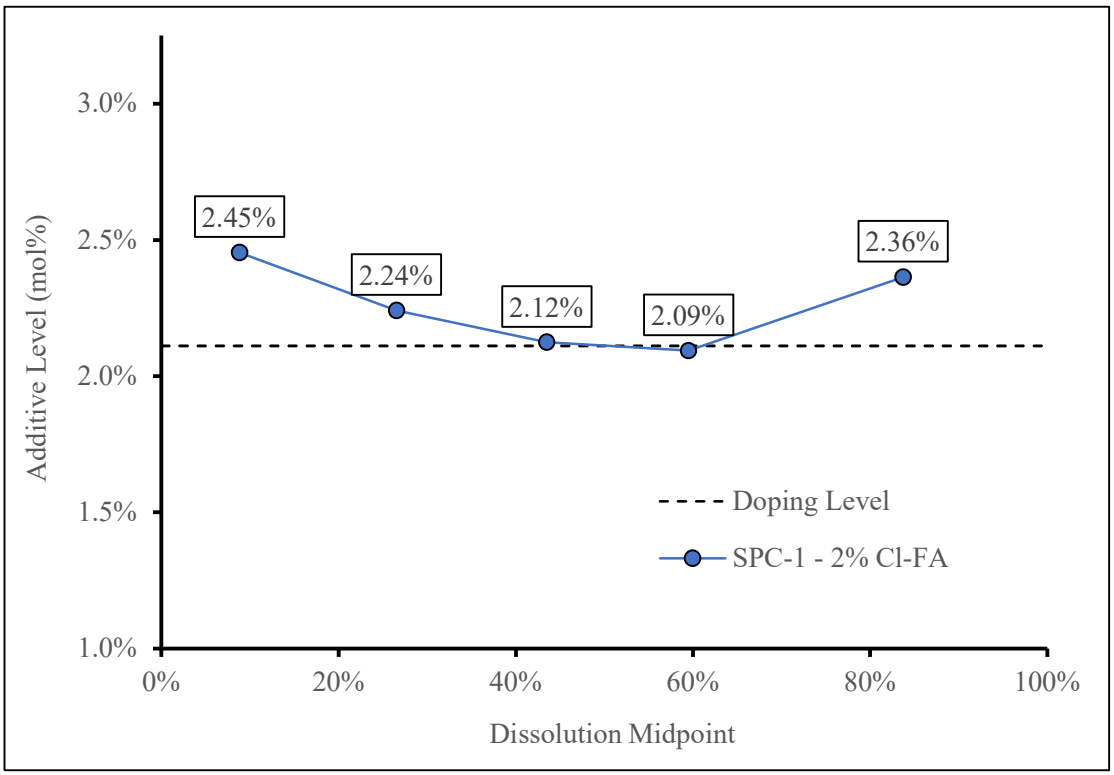


Fig 5.26. Plot of additive level *vs.* dissolution midpoint of large single crystal doped with 2% Cl-FA **16** (SPC-1) compared to the doping level.

When compared to the multi-particulate samples doped with Cl-FA **16** studied previously in terms of distribution coefficient α_2 (Figure 5.27), the patterns follow a similar trend; the differences being the more pronounced increase in additive level in the final dissolution stage of the single crystal, and the overall significantly higher incorporation level of the single crystal in comparison to the batch. The latter observation mirrors that of the study on the effect of crystal morphology on additive incorporation (Section 5.2.2.3); larger, more prismatic crystals appear to incorporate additive to a greater extent that those that are smaller and more tabular.

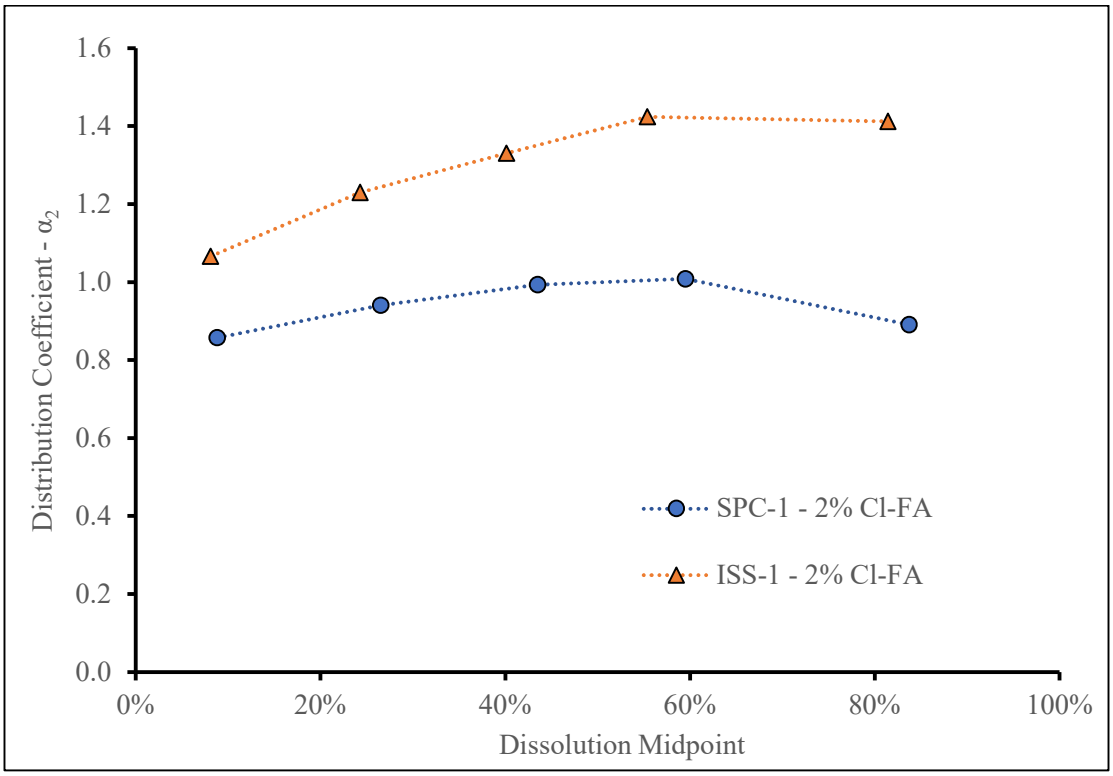


Fig 5.27. Plot of α_2-value *vs.* dissolution midpoint of SPC-1 compared to similar plot for ISS-1 (also doped with 2% Cl-FA **16**).

Additive Incorporation Levels of SPC-2

The additive distribution within the agglomerate SPC-2 is plotted in Figure 5.28. The pattern is similar to the other samples doped with DF-FA **17**, higher near the crystal surface, then dropping with successive dissolutions and plateauing towards the centre.

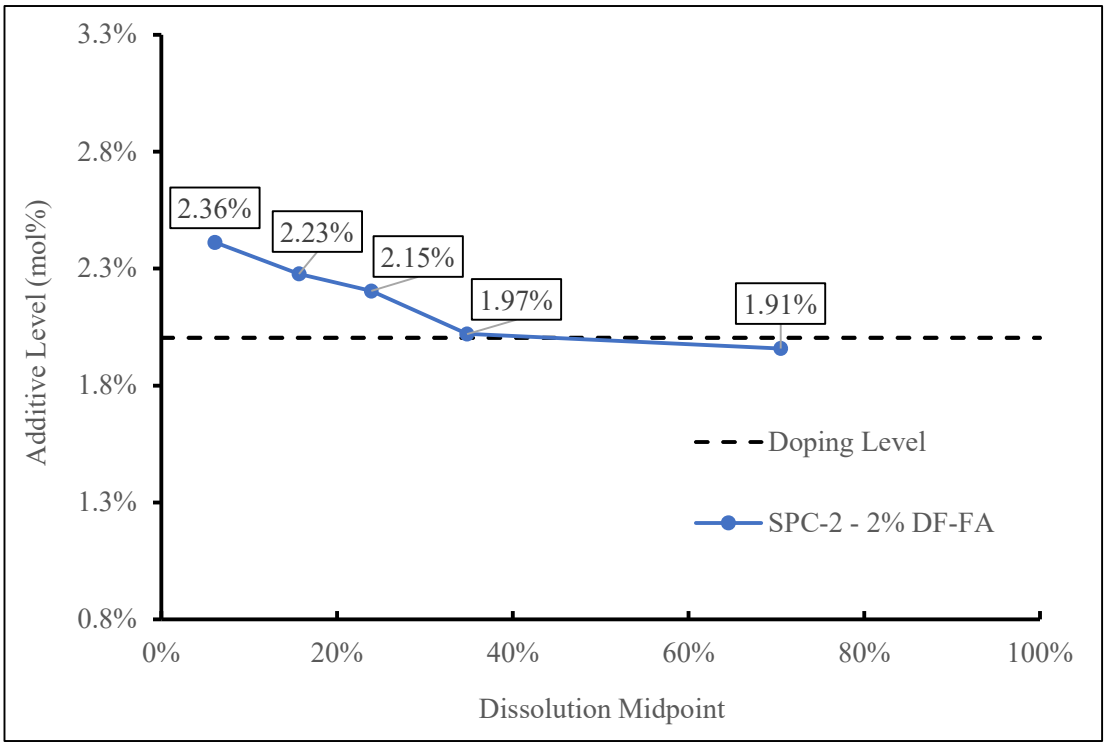


Fig 5.28. Plot of additive level *vs*. dissolution midpoint of SPC-2 compared to the doping level.

A comparison of the distribution coefficient (α_2) values of all samples doped with DF-FA **17** discussed to this point can be found in Figure 5.29. Based on this plot, it seems the additive pattern for the agglomerate is much more comparable to that of CSM-3 from the Section 5.2.2.3 study. There also seems to be a clear divide between the distributions found in the more prismatic *vs.* the more tabular crystals; further indication that the level of additive incorporation may be correlated to crystal morphology in these systems,

although not directly to crystal size, as the CSM-3 crystals incorporated additive to a slightly higher degree than SPC-2 despite their smaller size.

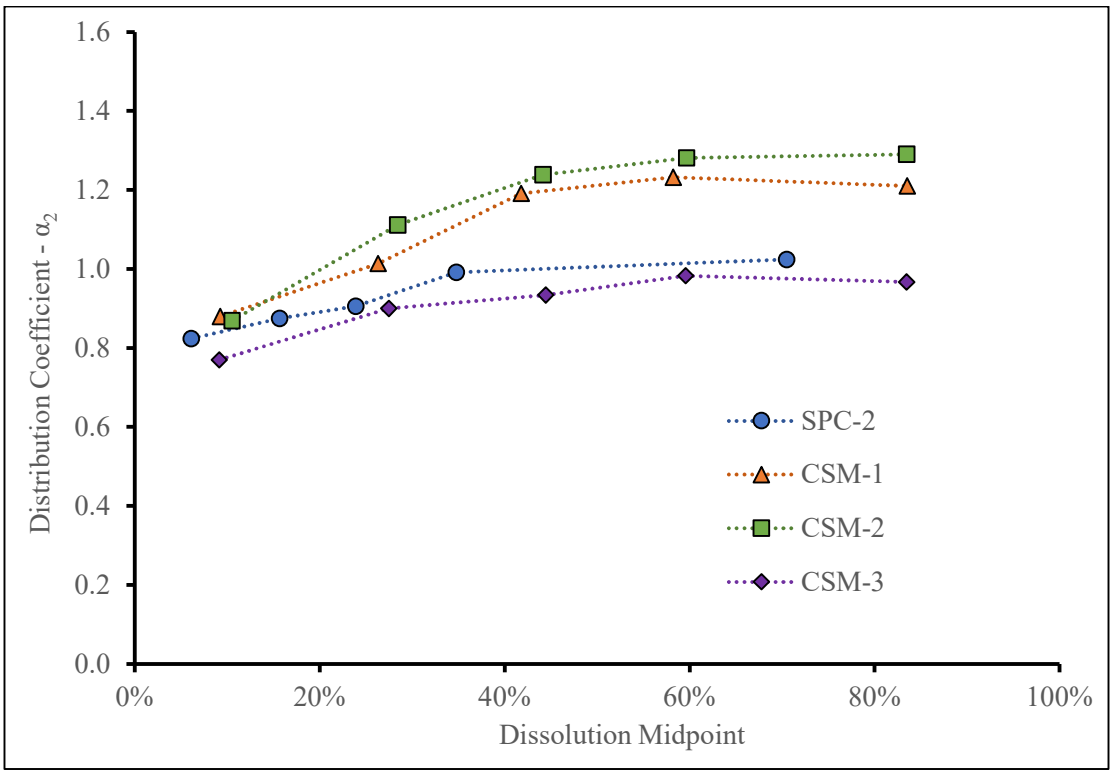


Fig 5.29. Plot of α_2-value *vs.* dissolution midpoint for SPC-2, compared to similar plots for CSM-1 – CSM-3 (also doped with 2% DF-FA **17**).

It appears that the partial dissolution method is equally applicable to both single crystal/agglomerate samples and multi-crystal batches, producing comparable results for each. Were this area of research to be expanded, more time would be dedicated to development of more robust single crystals that could withstand a higher number of dissolution steps without fracturing, as this was the major issue encountered in the single crystal/agglomerate studies. Additionally, a dissolution target value would be determined

that would take the reduced surface area of a larger crystal into account, in order to better control the level of dissolution in each stage.

5.2.3 Crystal Systems with Problematic Morphologies

The partial dissolution studies described in the previous sections were performed on crystals grown by slow evaporation and vapour diffusion. The crystals used in those studies were selected from larger batches based on their morphology, size, and robustness, attributes that made them well suited to the developed PD method. However, crystallisation is an unpredictable process, and many attempts to produce material resulted in crystals that were less suitable for use with the technique. In particular, no crystals doped with MF-FA **18** and t-Bu-FA **19** were produced that were considered fit for use in the PD method as developed to this point. These kinds of crystals were classified into four categories based on their habit, Types A – D; detailed descriptions can be found in Section 4.5.1 and example images are shown again in Figure 5.30. All crystals described in this section were produced by the slow evaporation of MeOH from a solution of doped material.

Part of the reason that these crystals are considered "problematic" is that they are often significantly smaller and more fragile than those studied previously in the chapter. The issues introduced by small, fragile crystals have been discussed in Section 5.2.1.1; however, performing partial dissolution studies on crystal samples with these problematic morphologies would afford a number of advantages to the current work. It would allow for a larger number of studies to be carried out on crystals containing a much wider range

of additive types and levels, as well as a selection of different crystal morphologies, investigating the application of the PD method on a more diverse range of samples. Furthermore, if this method were to be applied to an industrial setting, the types of crystal samples being investigated would likely be more comparable to these crystal types than the large prismatic crystals being discussed earlier in the chapter.

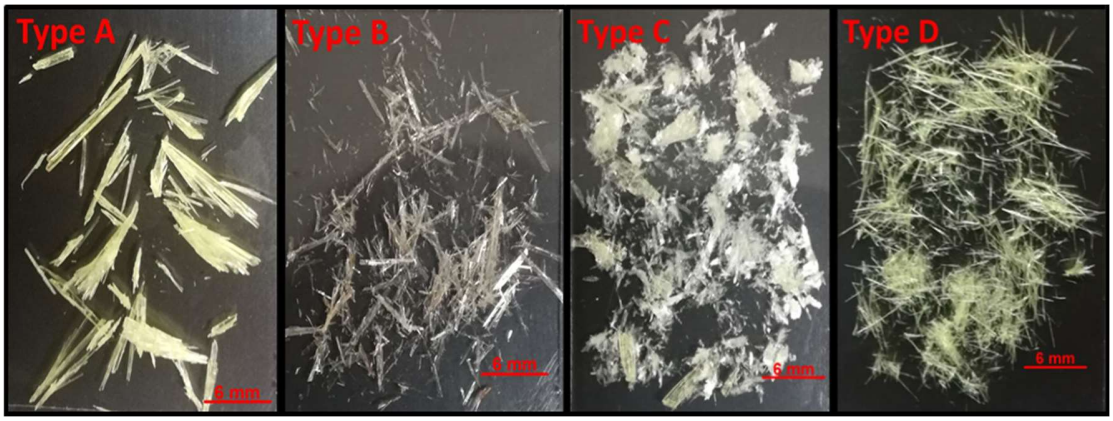


Fig 5.30. Digital images of examples of the four categories of doped FFA **14** crystals with problematic morphologies produced by the slow evaporation of MeOH. Left to right: PM-A1, PM-B3, PM-C1, PM-D2.

The advantage of developing the PD method using larger crystals was to be able to track the progress of the dissolution by both mass and surface area, to ensure a controllable level of dissolution was being achieved in each stage. However, the process can be performed without the need for the same level of tracking. The batches of crystals with problematic morphologies mostly consist of large amounts of small crystals. The primary issue that would be encountered should these batches be studied using the original method is that of surface area measurement. In an industrial setting this problem could be solved by use of a particle sizer, allowing for the size distribution determination of large

samples of crystals. In the case of this project however, mass measurements alone are sufficient to track the progress of dissolutions in the studies.

The partial dissolution process as described in Section 5.5.1.2, minus surface area measurements, was performed on a selection of crystal samples from each category doped with different additive types and levels. The dissolution target value used to determine the appropriate volume of solvent for these tests was the one determined based on solubility tests of powder-form FFA (1.63 mg ml^{-1} at 19 °C) rather than the target value used in the previous studies (0.99 mg ml^{-1} at 19 °C). As the size of these crystals was much lower, and, as such, the surface-area-to-mass ratio much higher, this was done in an attempt to better control the level of dissolution in each stage. Once again, the need for an anti-flocculant in the dissolution medium was assessed on a sample of Type C crystals and a sample of Type D crystals, which due to their size and morphologies were considered most likely to exhibit agglomeration. This was performed as described in Section 5.5.1.4. As before, little agglomeration was observed in any sample, and the dissolution behaviour of neither batch was aided by the inclusion of EHE. A table is presented below with all the sample names used in this section and the crystal types and batches they represent for ease of reading (Table 5.8).

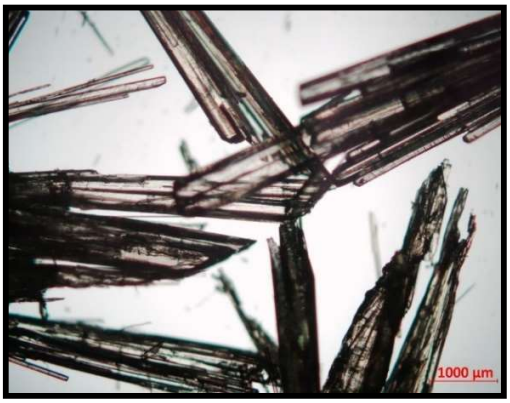
Table 5.8. A list of names of the crystal samples studied in this section, alongside their composition and the crystal Type category (A – D) they have been assigned to.

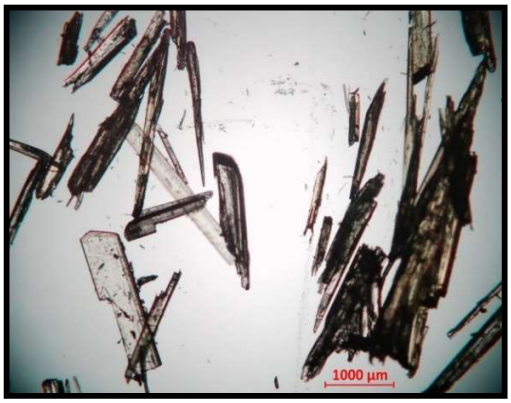
Problematic Crystal Type	FFA Crystals Doped With	Sample Name
A	2% t-Bu-FA	PM-A1
	2% t-Bu-FA	PM-A2
	2% t-Bu-FA	PM-A3
	5% Me-FA	PM-A4
B	0.5% Me-FA	PM-B1
	5% Me-FA	PM-B2
	2% DF-FA	PM-B3
	2% MF-FA	PM-B4
	4% t-Bu-FA	PM-B5
C	0.5% Me-FA	PM-C1
	5% Me-FA	PM-C2
	2% MF-FA	PM-C3
D	3% t-Bu-FA	PM-D1
	5% t-Bu-FA	PM-D2

5.2.3.1 Type A

The crystals designated as Type A are the largest of the four kinds, but much smaller and more irregular than other crystals grown by MeOH evaporation. Most of the crystals that fall into this category originated from a batch doped with 2% t-Bu-FA **19**. This batch produced a substantial number of Type A crystals, meaning that several samples from the same batch could be run and compared. The crystals in the batch were divided into three samples: first separating the largest crystals from the smallest by eye and then subdividing those large crystals into two smaller groups. The large crystals groups were designated as PM-A1 and PM-A2, while the small crystals were labelled

PM-A3. Microscope images for the three samples pre-dissolution can be found below in Figures 5.31 and 5.32, and images of the crystals at each stage in the dissolution process can be found in Appendix Figures 7.91 – 7.93 respectively. Crystals were also collected from a batch doped with 5 mol% Me-FA **15** that fell into the Type A category; these were designated as PM-A4. These crystals were slightly smaller than those in PM-A1 and PM-A2, but otherwise comparable in morphology. Microscope images of crystals from this sample pre-dissolution can be found below in Figure 5.33, and images of the crystals over the course of their dissolution can be found in Appendix Figure 7.94.





Figs 5.31 (left) and 5.32 (right). Microscope images (x40 magnification) of PM-A1 and PM-A2 (2% t-Bu-FA **19**, left) and PM-A3 crystals (2% t-Bu-FA **19**, right) prior to dissolution.



Fig 5.33. Microscope image (x40 magnification) of PM-A4 crystals (5% Me-FA 15) prior to dissolution.

Crystal Dissolution Levels

The crystals were suspended in enough hexane to dissolve 15% of the pre-dissolution crystal mass based on their mass and the target dissolution value (1.63 mg mL^{-1}). The suspensions were agitated for 90 minutes at ambient temperature (see Table 5.9) before the hexane was filtered off, and the recovered crystals rinsed with cold hexane, dried under vacuum, and reweighed.

The dissolution levels observed for each stage in the dissolution of the four Type A samples are listed in Table 5.9 below. Aside from a higher-than-normal value for PM-A1 PD1 (most likely the result of fine crystallites present alongside the larger crystals), the dissolution levels achieved across the four samples were close to the expected figures. It was anticipated that the level of dissolution would fall short of the 15% value observed in previous studies given the powder-form solubility value used to determine the solvent volume. On average the levels of PM-A3 and PM-A4 were higher than those of PM-A1 and PM-A2 owing to the higher relative surface area of the smaller crystals.

Table 5.9. Percentage of original crystal mass dissolved over four dissolution stages of PM-A1 - PM-A4 of the Type A problematic crystal morphology.

Type A	**PD1**	**PD2**	**PD3**	**PD4**
Temperature (°C)	20-22	19	19	19
% PM-A1 Mass Dissolved	23.1%	9.5%	8.6%	9.7%
% PM-A2 Mass Dissolved	13.5%	10.3%	10.6%	9.2%
% PM-A3 Mass Dissolved	12.9%	13.8%	10.6%	12.5%
% PM-A4 Mass Dissolved	13.3%	12.0%	16.6%	9.8%

Additive Incorporation Levels

The additive distributions of Samples PM-A1 to PM-A3, those doped with 2% t-Bu-FA **19**, can be found in Figure 5.34 as a function of the dissolution midpoint of each sample. The three samples exhibit very similar patterns of additive incorporation: a gradual increase with successive dissolution stages, suggesting a decrease in incorporation as the crystal grows. This behaviour is similar to that observed for crystals doped with Me-FA **15** described in Section 5.2.2.2. PM-A1 and PM-A3 exhibit a slightly higher additive level near the surface of the crystal, most likely another example of the same surface deposition observed in previous studies.

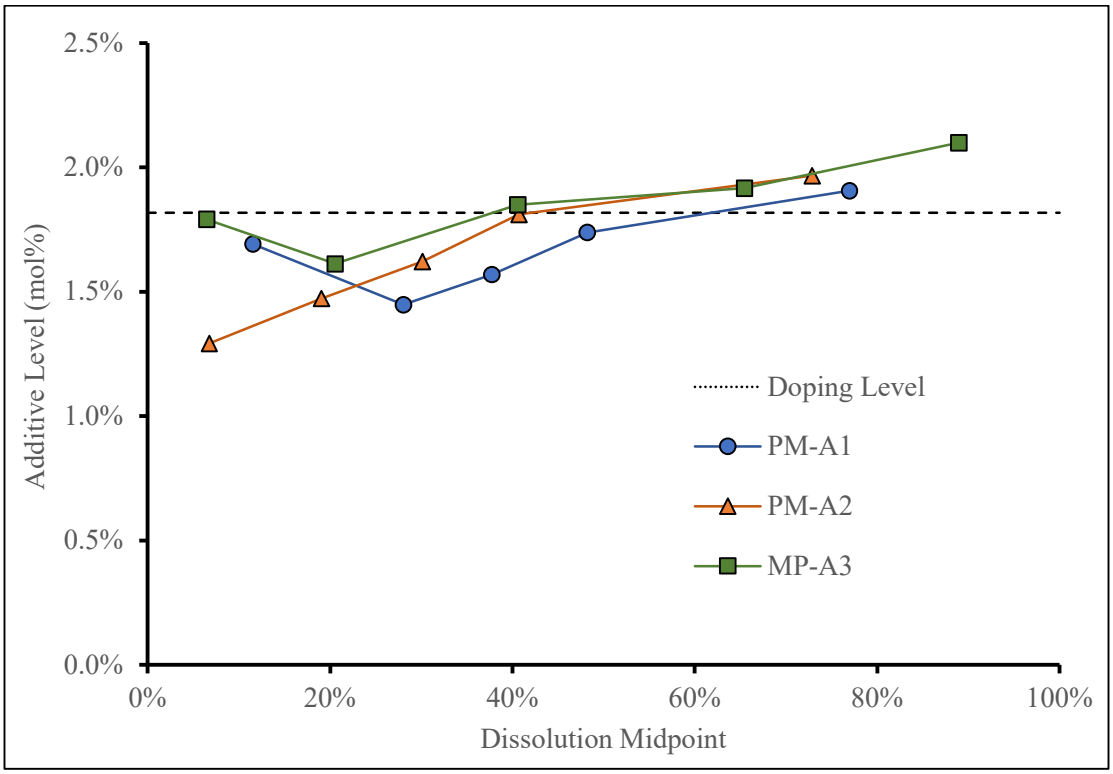


Fig 5.34. Plot of additive level *vs.* dissolution midpoint of PM-A1 – PM-A3 (each doped with 2% t-Bu-FA **19**) compared to the doping level.

The pattern of additive distribution in PM-A4 appeared close to even, or decreasing very slightly. This is the first sample studied thus far that has not displayed a clear trend of increasing or decreasing additive level from the surface to the centre of the crystal. The surface layer (PD1) value is slightly higher, likely another case of the deposition effect, but the rest of the data points could be considered close to equivalent in value. This pattern of incorporation can be plotted against that of DATL-2, a sample also doped with 5% Me-FA **15** studied previously (Figure 5.35). In this plot the difference between the two samples can be observed.

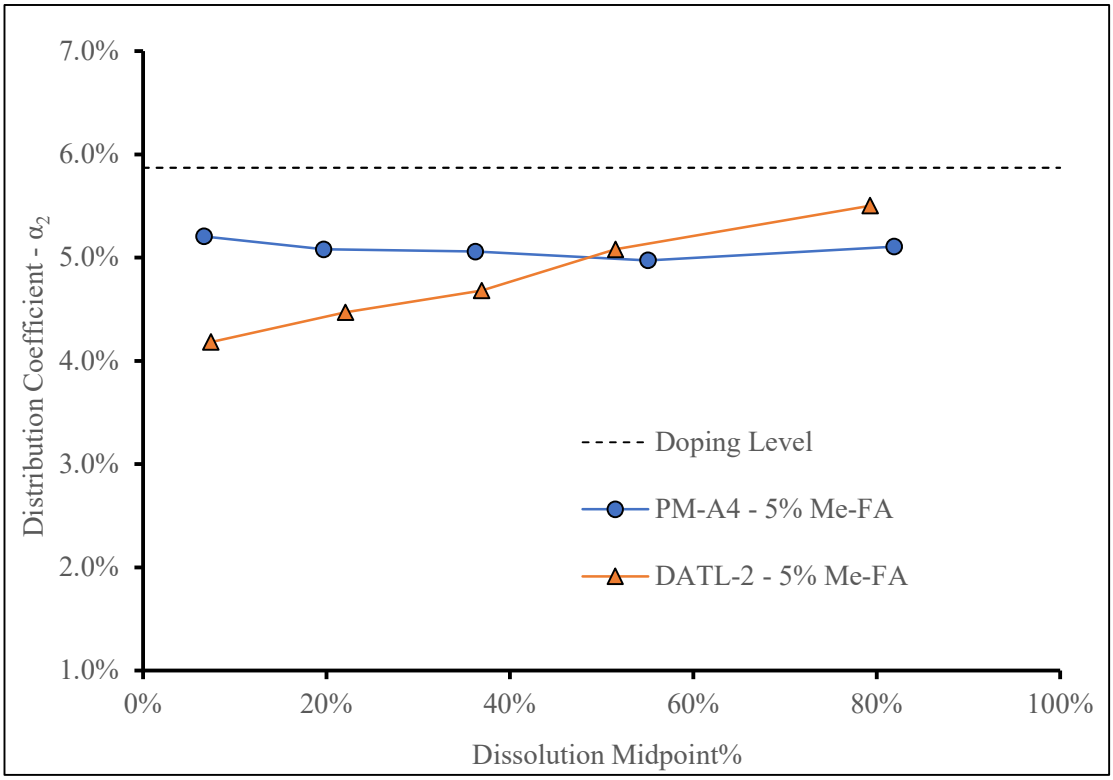
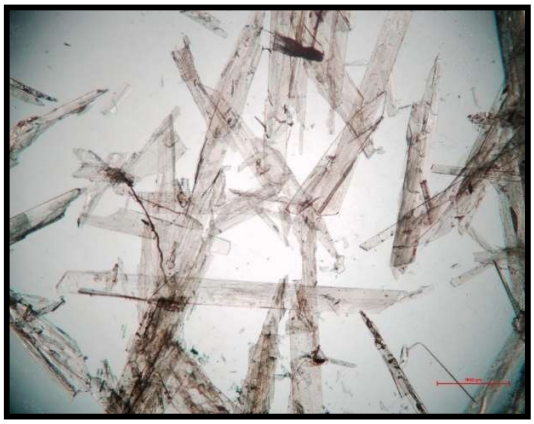


Fig 5.35. Plot of α_2-value *vs.* dissolution midpoint of PM-A4 (doped with 5% Me-FA **15**), compared to similar plot for DATL-2 from the investigation into different additive types and levels (also doped with 5% Me-FA **15**) and the doping level for both.

5.2.3.2 Type B

Type B crystals are much smaller than those of Type A, and much more fragile. They share similarities to those grown by MeCN slow cooling; needle-like particles growing outwards from a few defined nucleation points in rosette patterns. When they are removed from the vial however they fragment extremely easily. This behaviour makes sense when the crystals are viewed under a microscope; instead of the acicular morphology they appear to have to the naked eye these crystals are long and more tabular, and this lack of third-dimensional depth is what contributes to their fragility. Type B crystals are also the problematic crystal habit most commonly encountered during this research, encompassing five individual samples across systems doped with four different additive types: those doped with 0.5% Me-FA **15**, 5% Me-FA **15**, 2% DF-FA **17**, 2% MF-FA **18**, and 4% t-Bu-FA **19**.

A sample of each of these batches (designated PM-B1 – PM-B5 respectively) was subjected to the partial dissolution process, the dissolution levels of each can be found in Table 5.10. Additionally, microscope images of the PM-B1 – PM-B5 pre-dissolution can be found below in Figures 5.36 – 5.40 respectively, and images of the crystals at each stage of the dissolution process can be found in Appendix Figures 7.95 – 7.99 respectively.

Figs 5.36 (left) and 5.37 (right). Microscope images (x40 magnification) of PM-B1 crystals (0.5% Me-FA **15**, left) and PM-B2 crystals (5% Me-FA **15**, right) prior to dissolution.




Figs 5.38 (left) and 5.39 (right). Microscope images (x40 magnification) of PM-B3 crystals (2% DF-FA **17**, left) and PM-B4 crystals (2% MF-FA **18**, right) prior to dissolution.

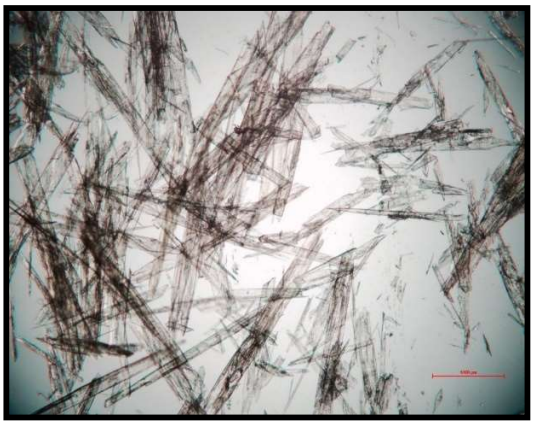


Fig 5.40. Microscope image (x40 magnification) of PM-B5 crystals (4% t-Bu-FA **19**) prior to dissolution.

Crystal Dissolution Levels

The crystals were suspended in enough hexane to dissolve 15% of the pre-dissolution crystal mass based on their mass and the target dissolution value (1.63 mg mL^{-1}). The suspensions were agitated for 90 minutes at ambient temperature (see Table 5.10) before the hexane was filtered off, and the recovered crystals rinsed with cold hexane, dried under vacuum, and reweighed.

The dissolution levels achieved for all stages of PM-B1 – PM-B3 were consistent, remaining slightly lower than the "intended" dissolution level of 15%. The PM-B4 and PM-B5 crystals were particularly fragile, possibly due to the detrimental effect of the additive on crystallisation. As such, the sample contained a high proportion of smaller crystal fragments. This resulted in a higher level of dissolution at each stage.

Table 5.10. Percentage of original crystal mass dissolved over four dissolution stages of PM-B1 – PM-B5 of the Type B problematic crystal morphology.

Type B	**PD1**	**PD2**	**PD3**	**PD4**
Temperature (°C)	19-22	19-23	20-23	20-24
% PM-B1 Mass Dissolved	11.0%	11.4%	10.6%	8.2%
% PM-B2 Mass Dissolved	12.1%	13.3%	15.4%	13.9%
% PM-B3 Mass Dissolved	11.0%	10.1%	10.7%	10.5%
% PM-B4 Mass Dissolved	14.6%	19.3%	15.5%	14.2%
% PM-B5 Mass Dissolved	14.9%	14.4%	13.4%	12.6%

Additive Incorporation Levels

The fragile nature and subsequent fragmentation of the crystals was expected to interfere with the measured pattern of additive incorporation. However, the trends instead appeared relatively comparable to similar studies. The additive levels for PM-B1 and PM-B2 are displayed in Appendix Figures 7.70 and 7.71 respectively. The patterns for both exhibit a slight increase across successive dissolution stages, suggesting a decrease in additive incorporation with crystal growth. This is a similar albeit less pronounced trend as observed with DATL-1 and DATL-2, crystals also doped with 0.5% and 5% Me-FA **15** respectively, discussed in Section 5.2.2.2. A comparison of the α_2-values of each sample can be viewed in Figure 5.41. The steeper trend of main series crystals is logical; the larger size of the crystals accompanies a longer period of growth, and, as such, a more substantial difference between the additive levels and the surface and core of the crystals compared to the smaller Type B samples.

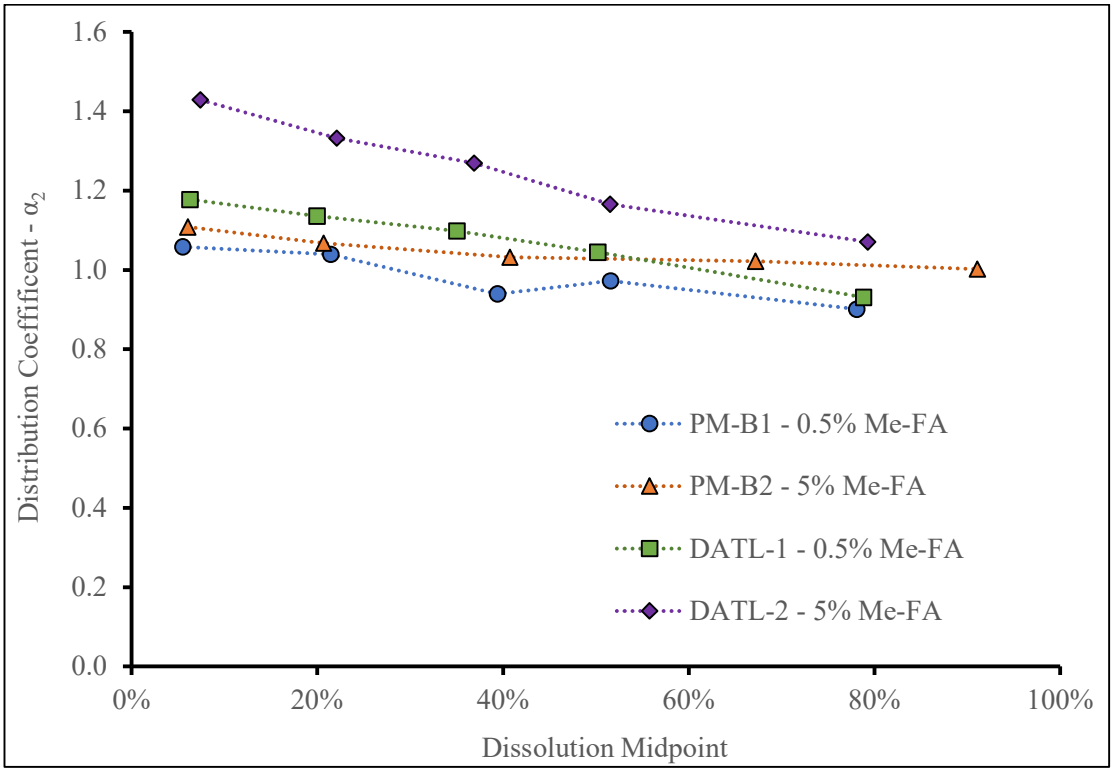


Fig 5.41. Plot of α_2-value *vs.* dissolution midpoint of PM-B1 and PM-B2 crystals (doped with 0.5% and 5% Me-FA **15** respectively), compared to similar plots for samples doped with the same additive type and levels (DATL-1 and DATL-2).

The additive pattern of the PM-B3 crystals is similar to the other samples doped with 2% DF-FA **17** in Section 5.2.2.3 (CSM-1 – CSM-3) and Section 5.2.2.4 (SPC-2), higher near the surface then decreasing and plateauing near the crystal centre (Figure 5.42). Interestingly, when compared to those samples by distribution coefficient (α_2), it appears the incorporation most closely matches that of the larger prismatic crystals than the more tabular crystals, despite their own smaller, tabular morphology.

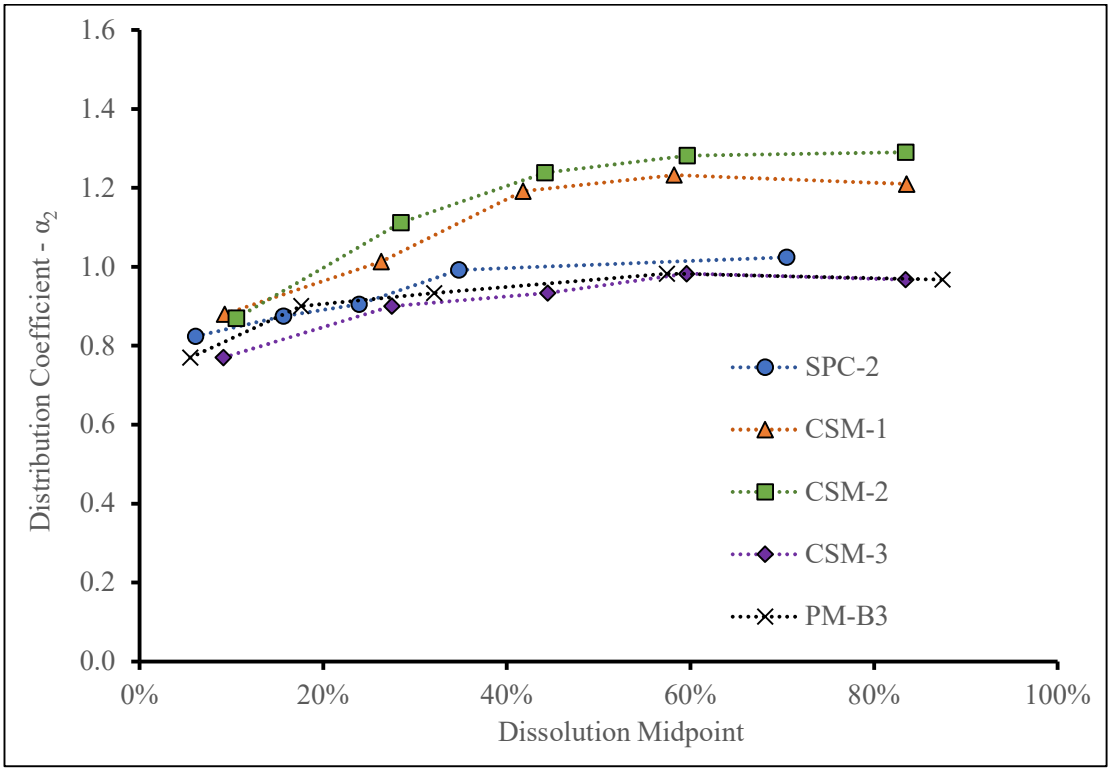


Fig 5.42. Plot of α_2-value *vs.* dissolution midpoint of PM-B3 crystals (doped with 2% DF-FA **17**), compared to similar plots for other samples doped with DF-FA **17** (CSM-1 – CSM-3 and SPC-2).

PM-B4 is the first sample tested from a crystal batch doped with MF-FA **18**. The pattern of additive incorporation was similar to that of the samples doped with DF-FA **17**, in that the measured values also decreased over successive dissolution stages (Figure 5.43). Unlike those samples however, the pattern did not appear to plateau towards the crystal centre, instead decreasing in a near-linear manner from PD2 – PD5. The PD1 value was disproportionately high, most likely due to the deposition of additive-rich mother liquor on the crystal surface.

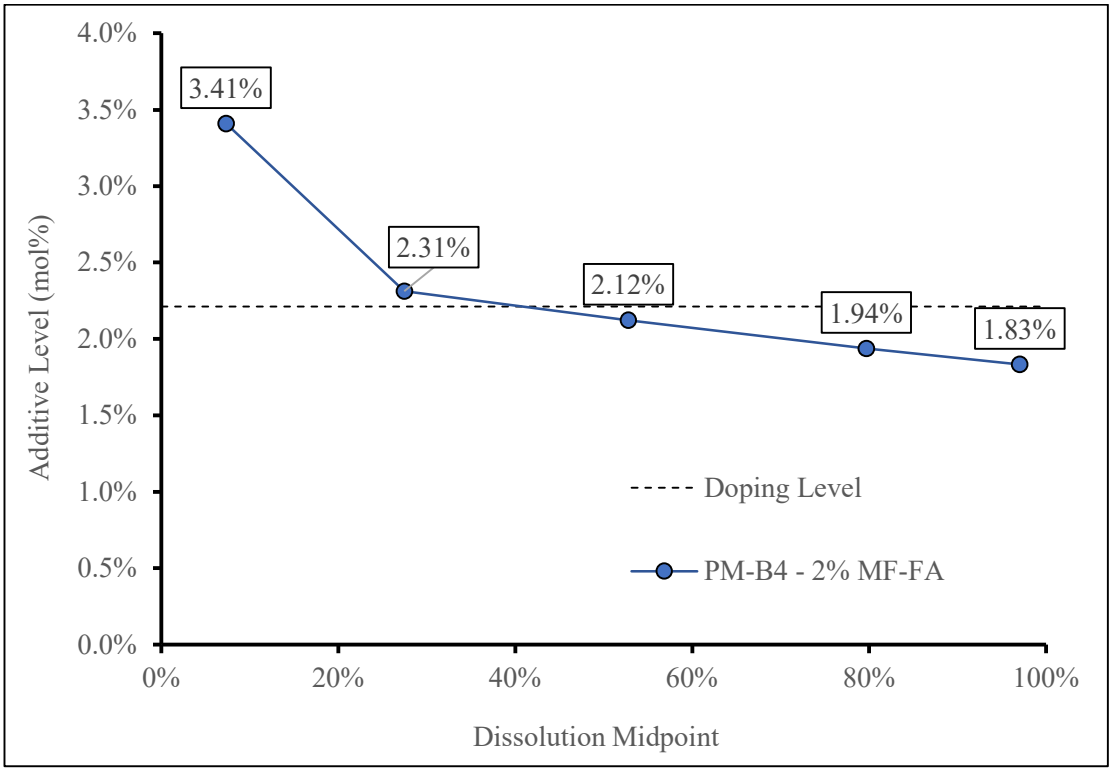


Fig 5.43. Plot of additive level *vs.* dissolution midpoint of PM-B4 crystals doped with 2% MF-FA **18** compared to the doping level.

PM-B5, doped with 4% t-Bu-FA **19**, exhibits a decreasing additive level from the surfaces of the crystals in the batch to their centres (Appendix Figure 7.72). This result is interesting, as it runs counter to the pattern observed in the Type A crystals doped with 2% t-Bu-FA **19** (PM-A1 – PM-A3), the additive level of which increases across the stages. A comparison plot is displayed in Figure 5.44. The distribution coefficient (α_2) plots of the Type A crystals exhibit a negative slope, which translates into an increasing trend of additive incorporation over a PD series, whereas the Type B sample has a positive slope. One explanation is that, at least in this case, the morphology of the crystal sample affects the pattern of additive incorporation within; a phenomenon that had not been observed so distinctly before this point. Another possibility is that the pattern changes with higher

levels of doping and incorporation, similar to how these higher levels affect the crystal growth process. As only a limited number of discrete batches have been studied, there is always the possibility that the pattern of incorporation is dictated by some other unidentified factor which can vary between batches. Alternatively, the fragmented nature of the Type B sample may be resulting in data that is not representative of the system.

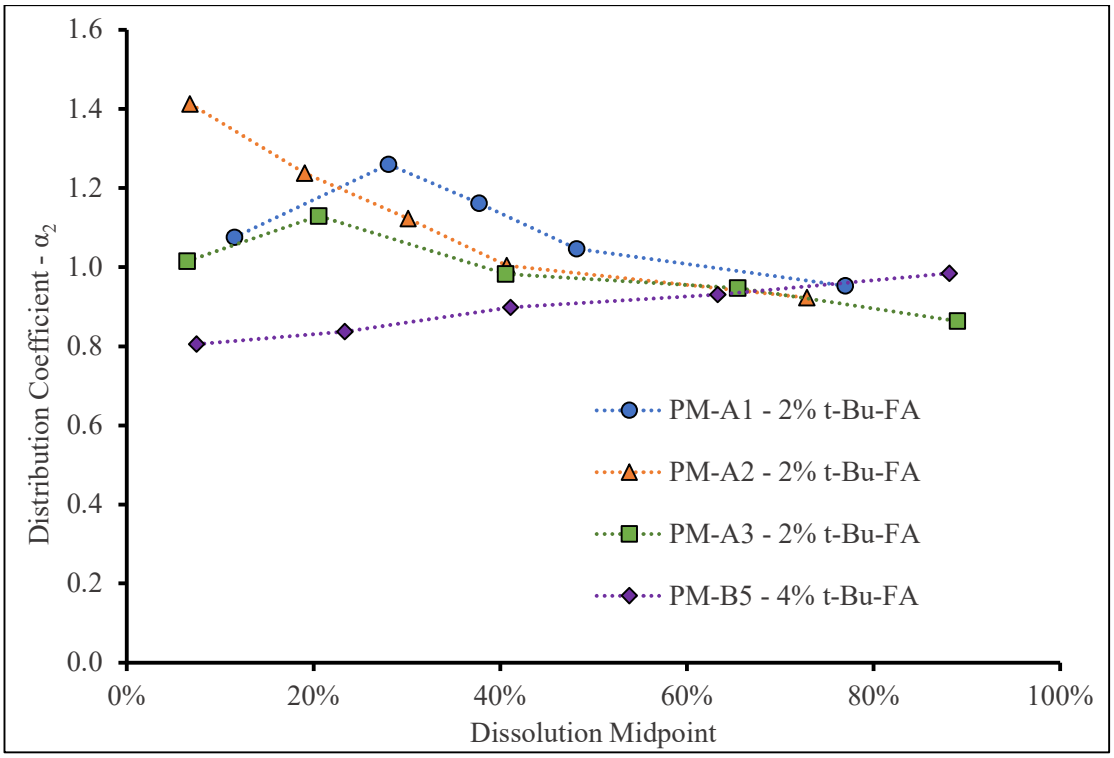


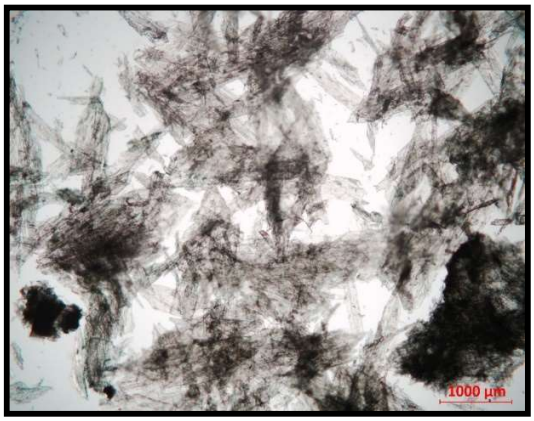
Fig 5.44. Plot of α_2-value *vs.* dissolution midpoint of PM-B5 crystals (doped with 4% t-Bu-FA **19**), compared to similar plots for PM-A1 – PM-A3 (doped with 2% t-Bu-FA **19**).

5.2.3.3 Type C

Type C crystals appear to the naked eye as very thin, wafer-like flakes, indistinct particles which clump together. When viewed under a microscope, the pre-dissolution samples seem to be composed of larger particles surrounded by smaller ones that resemble

fluff, making it difficult to focus on the image as a whole. The partial dissolution process changes the appearance of the samples, fully dissolving the smaller particles first to reveal the larger more prismatic crystals underneath. Crystals from three batches were observed to fall into the Type C category: those doped with 0.5% Me-FA **15**, 5% Me-FA **15**, and 2% MF-FA **18**. Crystals from these batches were labelled PM-C1 – PM-C3 respectively. Microscope images of PM-C1 – PM-C3 pre-dissolution can be found below in Figures 5.45 – 5.47 respectively, and images of the crystals at each stage of the dissolution process can be found in Appendix Figures 7.100 – 7.102 respectively.





Figs 5.45 (left) and 5.46 (right). Microscope images (x40 magnification) of PM-C1 crystals (0.5% Me-FA **15**, left) and PM-C2 crystals (5% Me-FA **15**, right) prior to dissolution.

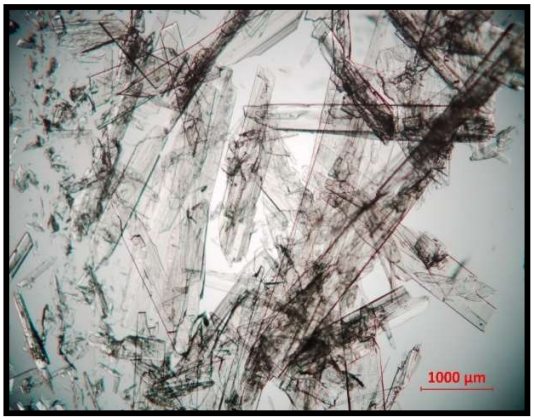


Fig 5.47. Microscope image (x40 magnification) of PM-C3 crystals (2% MF-FA **18**) prior to dissolution.

Crystal Dissolution Levels

The crystals were suspended in enough hexane to dissolve 15% of the pre-dissolution crystal mass based on their mass and the target dissolution value (1.63 mg mL^{-1}). The suspensions were agitated for 90 minutes at ambient temperature (see Table 5.11) before the hexane was filtered off, and the recovered crystals rinsed with cold hexane, dried under vacuum, and reweighed.

The samples were subjected to the partial dissolution process, and the dissolution levels of each can be found in Table 5.11. The dissolution of the smaller particles results in generally higher dissolution levels being observed in the PD1 and PD2 stages, and lower levels in PD3 and PD4 as the larger particles are dissolved.

Table 5.11. Percentage of original crystal mass dissolved over four dissolution stages of PM-C1 – PM-C3 of the Type C problematic crystal morphology.

Type C	**PD1**	**PD2**	**PD3**	**PD4**
Temperature (°C)	19-22	19-23	20-23	20-24
% PM-C1 Mass Dissolved	13.7%	15.6%	14.3%	11.1%
% PM-C2 Mass Dissolved	14.9%	10.4%	11.0%	10.1%
% PM-C3 Mass Dissolved	17.4%	18.2%	12.6%	7.4%

Additive Incorporation Levels

The level of Me-FA **15** incorporation in PM-C1 varies between 0.56% and 0.62% with no clear increasing or decreasing trend visible across the successive dissolution stages (Figure 5.48). This could be due to the sample being composed of a mixture of

smaller and larger particles (Figure 5.45, Appendix Figure 7.100). It is likely that the smaller particles are being dissolved in their entirety early in the process leaving the larger particles intact, presumably with only their outer layers being subjected to dissolution. As a result, the measured pattern is less representative of the additive distribution in the crystals on a surface-to-centre basis than in other crystal samples. While the collected data is less meaningful for this particular study, it highlights the importance of limiting a sample to particles of a similar size.

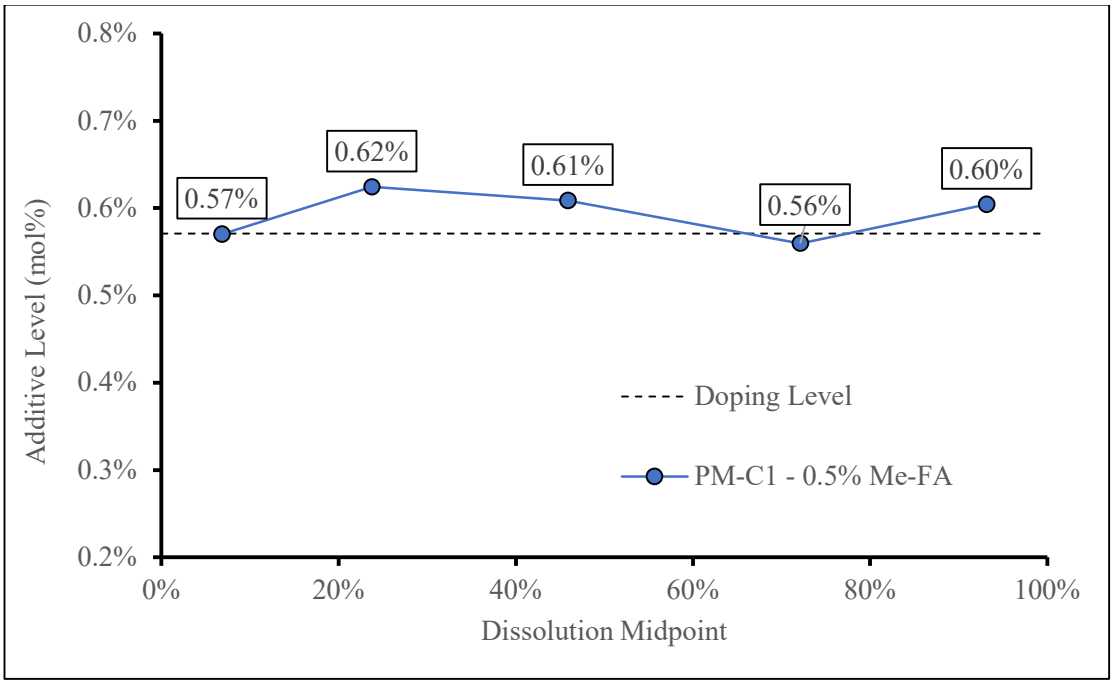


Fig 5.48. Plot of additive level *vs.* dissolution midpoint of PM-C1 crystals doped with 0.5% Me-FA **15** compared to the doping level.

PM-C2 and PM-C3 had a very similar appearance to PM-C1 both to the naked eye and under a microscope pre-dissolution. However, after the first dissolution stage the smaller particles appeared to have been dissolved completely or were lost due to static

electricity during transfer. As can be seen in Appendix Figures 7.101 and 7.102 respectively, the post-dissolution crystals for PDs 1 – 4 within PM-C2 and PM-C3 appear relatively comparable, suggesting the bulk of the dissolution was stripping layers of the larger crystals rather than fully dissolving smaller ones. For contrast, there were still smaller crystals visible in the post-PD3 images of PM-C1 in Appendix Figure 7.100. The patterns of additive incorporation for PM-C2 and PM-C3 appear much more representative of their respective systems than PM-C1, closely matching the patterns of similar Type B samples (Figures 5.49 and 5.50 for PM-C2 and PM-C3 respectively).

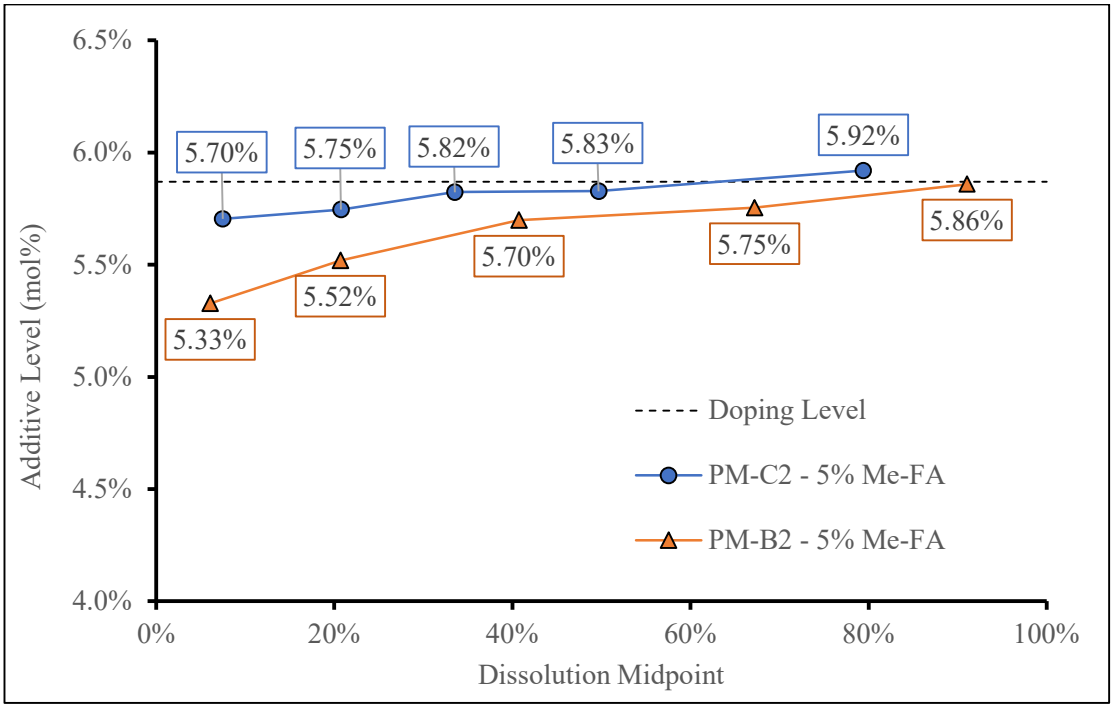


Fig 5.49. Plot of additive level *vs.* dissolution midpoint of PM-C2 crystals compared to similar plot for PM-B2 (both doped with 5% Me-FA **15**) and the doping level for both.

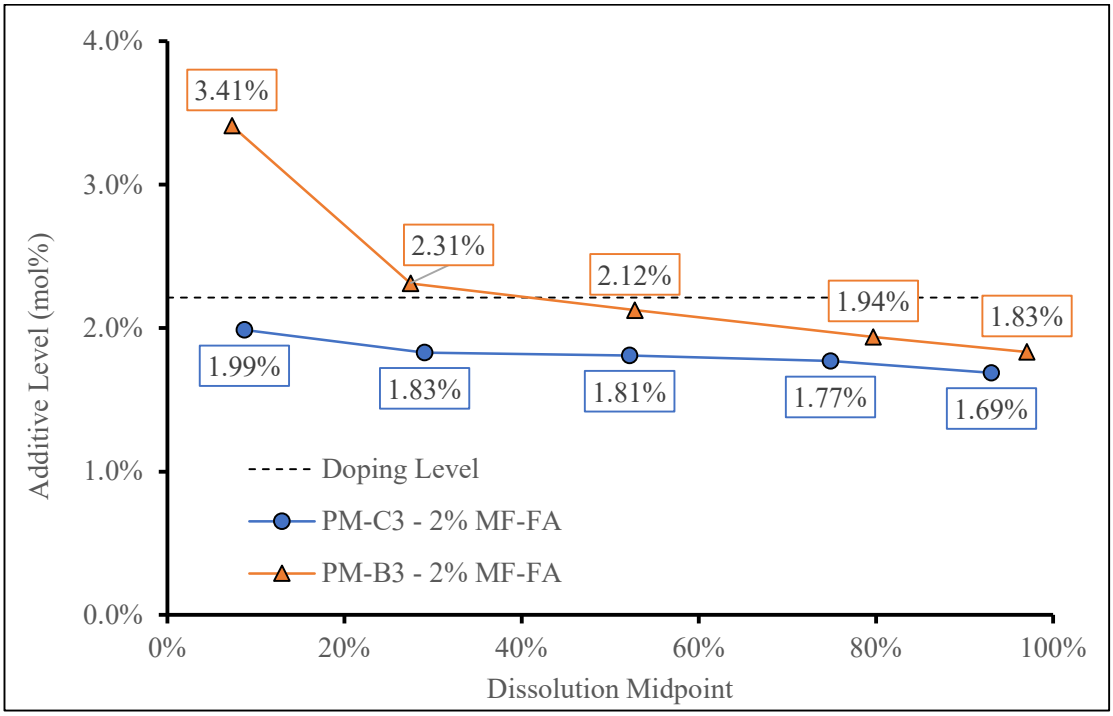


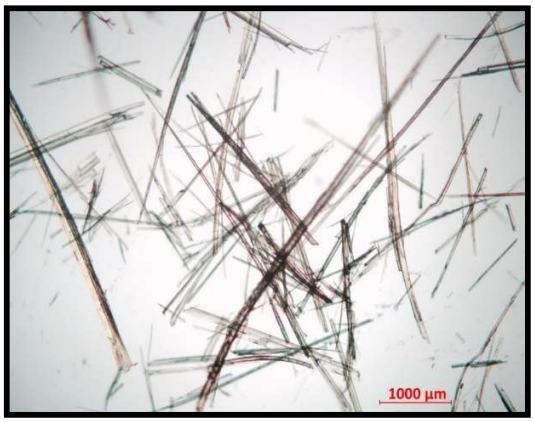
Fig 5.50. Plot of additive level *vs.* dissolution midpoint of PM-C3 crystals compared to similar plot for PM-B3 (both doped with 2% MF-FA **18**) and the doping level for both.

5.2.3.4 Type D

The final problematic crystal category observed was designated as Type D. These batches consisted of very small, very narrow acicular needles that appeared regular in size and shape to the naked eye. Microscope images revealed some size disparity between individual particles, but they remained the crystal type most consistent with each other in this regard. Type D crystals have a tendency to aggregate in a coarse ball shape in a dry vial, reminiscent of tumbleweed, but dispersed and moved freely when suspended in a liquid medium. Only two batches of crystals were categorised as Type D, doped with 3% and 5% t-Bu-FA **19** (PM-D1 and PM-D2 respectively). Microscope images of these two samples pre-dissolution can be found below in Figures 5.51 and 5.52 respectively, and

images of the crystals at each stage of the dissolution process can be found in Appendix Figures 7.103 and 7.104 respectively.





Figs 5.51 (left) and 5.52 (right). Microscope images (x40 magnification) of PM-D1 crystals (3% t-Bu-FA **19**, left) and PM-D2 crystals (5% t-Bu-FA **19**, right) prior to dissolution.

Crystal Dissolution Levels

The crystals were suspended in enough hexane to dissolve 15% of the pre-dissolution crystal mass based on their mass and the target dissolution value (1.63 mg mL^{-1}). The suspensions were agitated for 90 minutes at ambient temperature (see Table 5.12) before the hexane was filtered off, and the recovered crystals rinsed with cold hexane, dried under vacuum, and reweighed.

These samples were subjected to four dissolution stages under the similar conditions to the other crystal types in this series of studies. The dissolution levels can be found in Table 5.12. The levels of dissolution were similar as those observed for the Type C crystals, higher initially as smaller crystallites dissolved, then generally lower for later stages.

Table 5.12. Percentage of original crystal mass dissolved over four dissolution stages of Samples 1 and 2 of the Type D problematic crystal morphology.

Type D	**PD1**	**PD2**	**PD3**	**PD4**
Temperature (°C)	20-22	19-23	20-23	20-23
% PM-D1 Mass Dissolved	19.7%	11.2%	14.1%	10.6%
% PM-D2 Mass Dissolved	14.2%	11.4%	9.8%	7.7%

Additive Incorporation Levels

These samples both share a similar pattern of additive incorporation; higher close to the surface of the crystals and descending in a near linear manner towards the centre with no apparent plateau (Figure 5.53). This result closely mirrors that of the PM-B5, doped with 4% t-Bu-FA **19**, the three of them standing counter to the three samples from the Type A batch doped with 2% t-Bu-FA **19** (PM-A1 - PM-A3). The difference between these two groups of samples could stem from the level of additive, from the morphology and/or size of the Type A crystals compared to the Type B and D, or another factor or factors entirely.

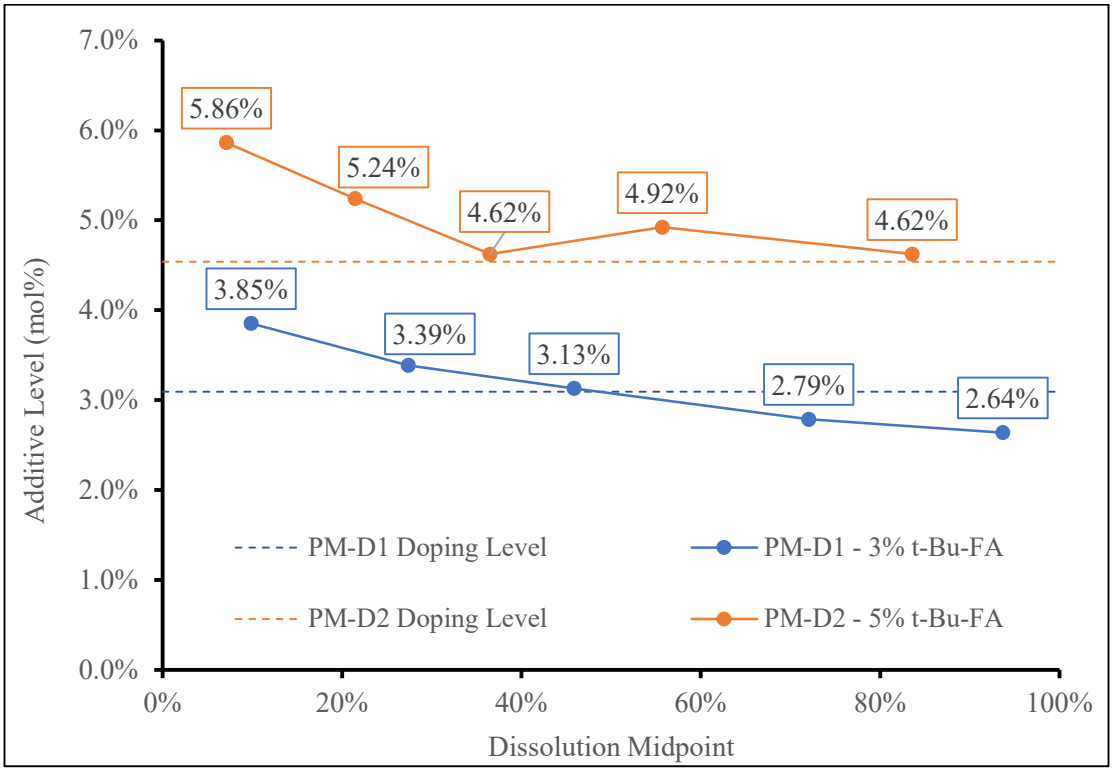


Fig 5.53. Plot of additive level *vs.* dissolution midpoint of PM-D1 and PM-D2 crystals and the doping level for each.

5.2.3.5 Discussion of Studies on Crystal Systems with Problematic Morphologies

The above studies show that although the partial dissolution method was developed using samples consisting of a few large, prismatic crystals, it can be adjusted and applied to samples composed of higher crystal counts and different crystal morphologies. This includes those previously considered unsuitable for the process due to their size and irregularity. The studies on problematic crystal types also reinforces the idea that surface area measurements, while a valuable tool for tracking the dissolution progress, are not a requirement for the method, and mass measurements alone are

sufficient to perform studies where obtaining surface area measurements is not possible. That being said, use of a particle size analyser would improve the data by allowing for the determination of area distributions at each dissolution stage. Another area for potential improvement would be through the sieving of samples prior to testing. This would provide two benefits to the process: firstly, the removal of crystals and crystal fragments below a certain size threshold would minimise the amount of sample lost due to static electricity while handling, and secondly segregating batches in respect to particle size would allow for more regular levels of dissolutions within the subdivided samples, avoiding misrepresentative additive incorporation distribution data such as was observed in Section 5.2.3.3.

5.2.4 Discussion of Partial Dissolution Technique

A partial dissolution method was developed that allowed for the controllable dissolution of a single crystal or batch of crystal particles across multiple dissolution stages in order to map the distribution of one or more additives/impurities within the crystal(s) on a surface-to-centre basis.

As has been demonstrated over the course of this chapter, there are a number of components that must be considered when developing a robust and effective partial dissolution method. Firstly, the crystal particles in the sample must be of a similar size and morphology. Should too large a size disparity exists within the sample, the level of dissolution achieved could be uneven, having a potentially detrimental effect on the additive distribution data collected. The mass of the sample should be sufficient to

necessitate a volume of dissolution medium that allows for the full suspension of the sample during the dissolution process. Crystal morphology appears to have little impact on the effectiveness of the PD technique. However, larger prismatic crystals have been shown to be best suited to the procedure due to their higher mass and resistance to damage over successive dissolution stages. This is especially true should the dissolution process require tracking by manual measurement of crystal lengths or surface areas; other crystal morphologies such as acicular crystals have proved less suitable in this regard.

The dissolution medium should be one in which the material of interest is known to display an appreciable but low level of solubility. This allows for better control over the degree of dissolution achieved and ensures the sample can be suspended in a sufficient volume of medium. An anti-flocculating agent can be used if particle aggregation in the dissolution medium is observed, but it will most likely affect the solubility of the sample material in the medium and could reduce dissolution control. During dissolution, the suspension should be sufficiently agitated to allow for even dissolution, but gently enough to avoid excessive damage to the crystal particles. The temperature at which the dissolution stages are performed should be maintained at a constant level if possible.

The progress of the dissolution can be tracked by sample mass to determine the volume of dissolution medium needed to dissolve the intended amount of material, and to measure the percentage material dissolved during each stage. Other metrics can also be used to track the dissolution progress, such as crystal length and surface area. To obtain such measurements, high quality images of the particles could be captured before and after each dissolution stage, either under a microscope or using macro digital photography. These images can be scaled using an internal rule and measured using image

analysis software. Alternatively, particle sizing instrumentation can be used to determine a distribution of the size of the crystals in a sample.

Additive levels for the PD stage are determined by measuring the proportional additive content relative to the host in the medium remaining after a dissolution stage, using HPLC analysis. This is repeated for each dissolution stage, as well as for a final dissolution in which the remaining crystal is fully dissolved and the additive content of the resulting solution measured. The additive distribution data can be displayed by discrete stages, but it is preferable to present it as a function of the dissolution midpoint, which assigns a value for the position within the crystal from which the additive measurement was taken based on measured masses. Additive level data can also be processed into distribution coefficients (α_2), which facilitates comparison between batches with different additive types and levels.

There are a number of limitations to the partial technique as it is described in this text. The foremost among them is the lack of full equilibration achieved during the dissolution. It was decided early in the project to maintain a set duration of 90 minutes for each dissolution stage; this was intended to reduce variability between experiments, and to present a clear experimental method for application to other systems. However, this meant that full equilibration of the crystals and dissolution solvent was likely not reached. This may have impacted the results of the experiment in several ways. Firstly, the kinetics and rate of dissolution become factors, affecting the behaviour and extent of the dissolution based on crystal surface area and additive concentration, among others. Should sufficient equilibration time have been allowed in each stage, these factors would not need to be accounted for. The relative solubilities of FFA and the additives in hexane

would affect the dissolution behaviour, increasing or decreasing the level of dissolution observed for the additive and host depending on the composition of the crystal. This would in turn affect the amount of additive observed in solution for each stage. It is clear in hindsight that the problems introduced by the limited dissolution time most likely outweigh the advantages it affords. Given more time, a detailed investigation into the behaviour of the systems at equilibrium would be carried out and the impact it has on the data produced by the dissolution studies would be assessed.

There are also limitations to the results presented here in terms of statistical robustness. Ideally, each experiment should have been reproduced a minimum of three times, and the mean results presented alongside standard deviations to account for any variability in the process. In reality however, we were limited by sample availability; in each case a series of dissolutions used the entirety of the produced batch of crystals. As subsequent samples could not be guaranteed to possess the same level of incorporation, even with identical doping levels, multiple replications of the same experiment were not possible. With that being said, the focus of the research was on the development of the methods rather than on the meaningfulness of the results, so the impact of statistical rigor is somewhat lessened by that fact.

This process has potential for application in the pharmaceutical industry. As discussed in Section 1.12, impurities are often encountered in batches of crystalline drug product that are not easily removed by traditional purification methods such as washing, slurrying, or crystallisation. Running a partial dissolution analysis on a sample of crystals from one of these batches would allow a researcher to gain insight into the distribution of

these impurities within the crystals in the batch, and, as such, inform a strategy for purification.

5.3 Segmentation Analysis

5.3.1 Background and Technique Description

As demonstrated in Section 5.2.3.1, acicular or needle-like crystals are less well-suited for use with the partial dissolution procedure as developed than those with a more prismatic morphology. Their narrow and fragile nature makes them prone to breaking during agitation, especially after multiple successive dissolution stages. This can introduce inaccuracies in the determination of additive levels by prematurely exposing the core of one or more crystal particles in a sample. Additionally, if the progress of the dissolution is being tracked by manual crystal length or surface area measurements, as they were in this research, the low sample mass can potentially lead to result in inadequate circulation of the dissolution medium and uneven dissolutions. Common particle sizing techniques such as laser diffraction and focused beam reflectance measurement (FBRM) also have difficulty accurately measuring particles with lower sphericity, such as needles.[224,225]

Acicular crystals are defined by their growth occurring primarily on a single face. They also tend to grow in a single direction from a defined nucleation point. As such, their growth progression can be tracked along the length of the needle from the nucleation point to the tip, contrary to more prismatic morphologies that require tracking outward from the

crystal core to its surface. Because of this, even without the methodological limitations, the most effective way to map additive levels within acicular crystals is most likely not partial dissolution, a technique that determines the pattern of additive inclusion on a surface-to-centre basis.

Detailed in this section is a simple alternative technique of determining the rough distribution of additives within acicular crystals as a function of their growth, providing much the same type of information as a partial dissolution study. This straightforward procedure can be carried out on a bench, with no specialised equipment necessary save for an HPLC or other means of determining additive level relative to a host. This method was developed using doped acicular crystals of FFA **14** grown by the slow cooling of a supersaturated solution of the material in MeCN. The solution from which the crystals were grown had been doped with low levels (2 – 6 mol%) of compounds **15** – **18**. No crystals doped with t-Bu-FA **19** were tested, as the inclusion of the additive inhibited the growth of crystals by this method. An example of a batch of these crystals in the crystallisation vessel can be seen in Section 5.2.1.1 earlier in the chapter (Figure 5.1). As can be observed in the image, crystals were observed to form large clusters, each crystal in the cluster growing outward from a single nucleation point, in a 'rosette' pattern. This motif allowed for the easy determination of the direction of growth for each crystal.

For each sample, 30 intact crystals were selected from a batch and divided lengthwise into three segments, taking particular care to orientate them so that the direction of their growth was preserved. In this way, three subsamples (labelled *a*, *b*, and *c* as illustrated in Figure 5.54) were created within each sample that consisted of fragments of the crystals at three consecutive stages of crystal growth. The additive levels of these

subsamples can be determined by HPLC, the results of which can be plotted in respect to their position in the crystal to provide a basic map of the pattern of additive incorporation over its growth. Similar to the partial dissolution studies, material restrictions precluded multiple repetitions of the same segmentation analysis experiments being performed. As such, standard deviations could not be measured for these experiments, something that should be considered when viewing the results presented in Section 5.3.2. Full details of the experimental method are described in Section 5.5.2.

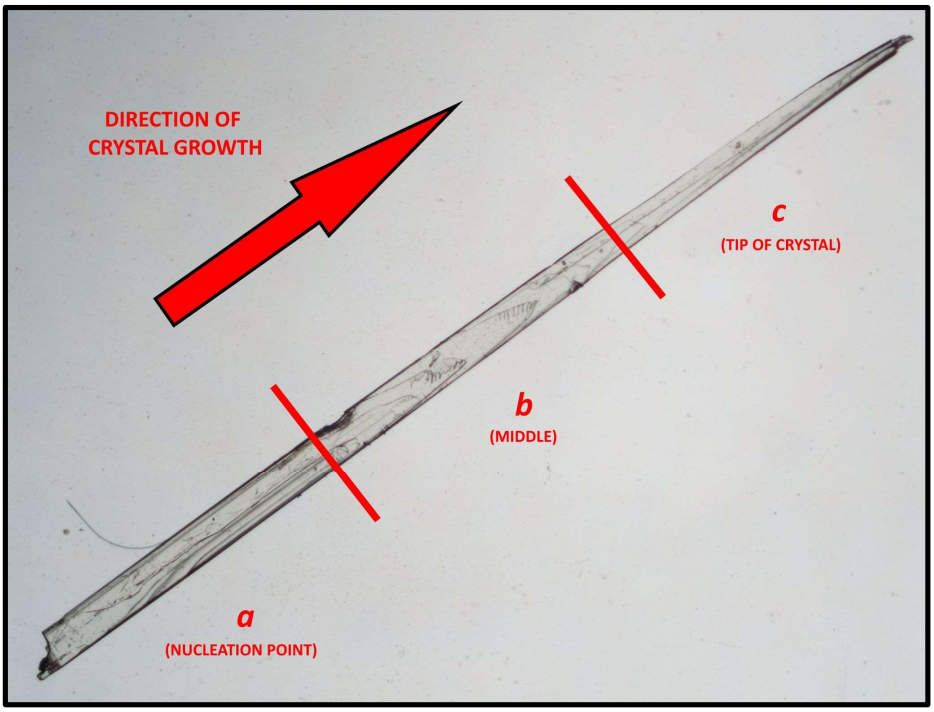


Fig 5.54. Diagram of segmentation process on an acicular crystal of FFA, illustrating the direction of crystal growth and labelling of segments *a*, *b*, and *c*.

5.3.2 Segmentation Analysis Study Results

In all, 8 samples of acicular crystals of doped FFA **14** were tested in this way: those doped with between 2 and 6% Me-FA **15**, Cl-FA **16**, DF-FA **17**, and MF-FA **18** individually. The level of additive measured in segments *a* – *c* of each sample is listed in Table 5.13 alongside the doping level and of the corresponding batch. The pattern of incorporation for each sample is visualised as a function of the distribution coefficient (α_2) values determined for each measured additive level in Figure 5.55. When plotted in this way, the α_2-values allow for the direct comparison of additive incorporation patterns between samples with different doping levels in the same way as they did in the partial dissolution studies. A description of α_2-values and what they represent can be found in Section 5.2.2.2.

Table 5.13. Percentage additive recorded in segments *a* – *c* from each sample of acicular crystals, alongside the corresponding additive type and doping level.

Additive Type	**Doping Level%**	**mol% Additive in Segments of Crystals**		
		a	***b***	***c***
Me-FA **15**	2.01	2.09	2.16	2.25
	3.12	3.17	3.24	3.38
Cl-FA **16**	4.02	3.44	3.66	3.80
	5.08	4.35	4.69	4.83
DF-FA **17**	3.46	2.43	2.46	2.52
	5.96	3.93	3.99	4.10
MF-FA **18**	2.51	1.49	1.54	1.59
	3.32	2.36	2.43	2.51

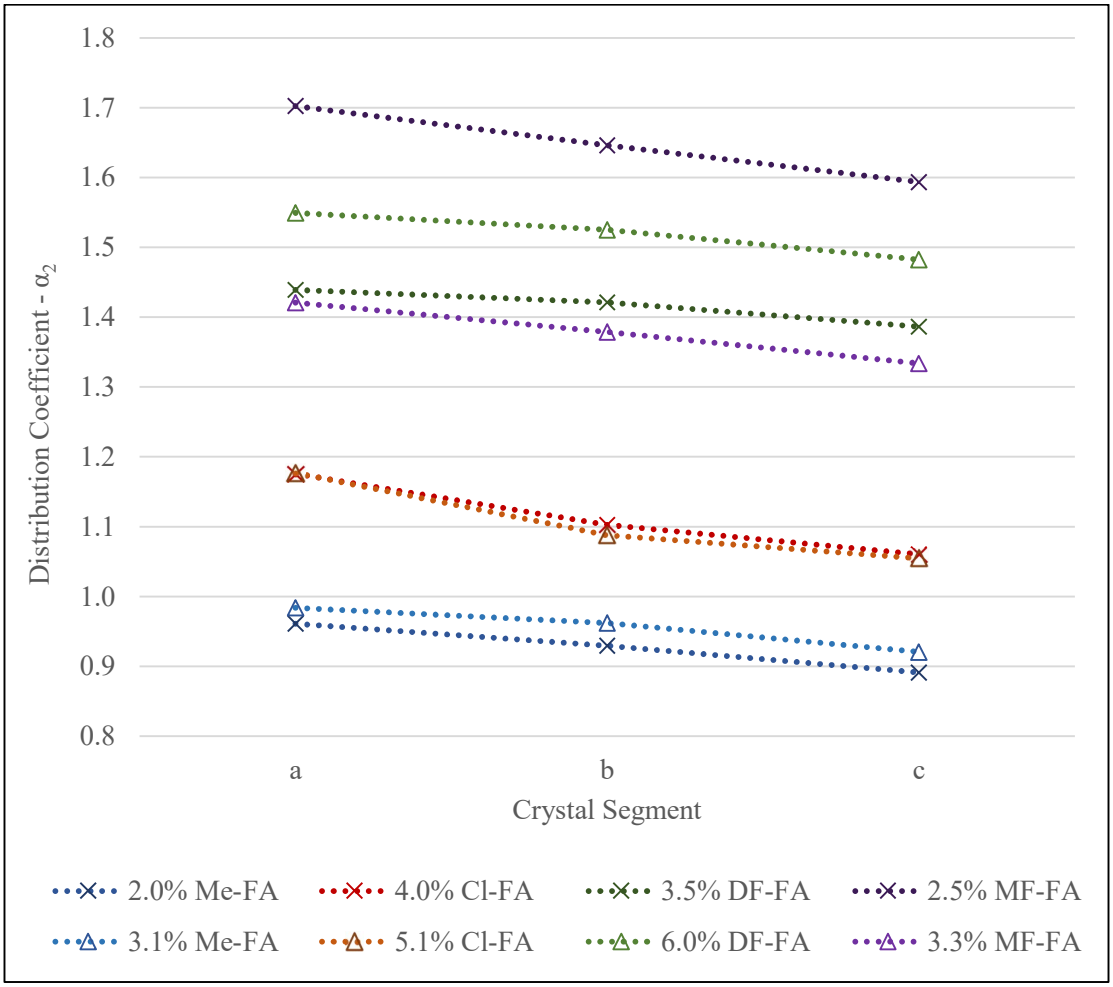


Fig 5.55. Plot of α_2-value *vs.* segment *a* – *c* of acicular crystals in each sample.

In terms of the extent of additive incorporation into the crystals of FFA **14**, the doped systems behave in a similar way as was observed in Section 4.3. Me-FA **15** is incorporated to the greatest extent, with the additive levels in the crystals exceeding the doping levels in in both samples studied (denoted by an α_2-value less than 1). Next highest is Cl-FA **16**, with the incorporation falling only slightly below the doping level. While the measured incorporation levels of DF-FA **17** and MF-FA **18** into FFA **14** were very similar when tested previously, on average the incorporation of DF-FA **17** appears to be higher than MF-FA **18** in the systems studied here, although they still exhibit the lowest values

of the additives tested. In particular, the crystals doped with 2.51% MF-FA **18** exhibited much lower levels of incorporation than the other systems. There appears to be little correlation between doping level and α_2-value across the 8 systems studied.

The pattern of incorporation is constant across all additives and doping levels tested as part of this study, increasing in a near-linear manner from segments *a* to *c*. An increasing trend in measured additive level results in one that decreases when the results are converted to α_2-values. This suggests that in all systems tested, the amount of additive incorporated into the acicular crystals increased as the crystals grew. Similar patterns of incorporation were observed in the PD studies in Section 5.2 for systems doped with Cl-FA **16**, DF-FA **17**, MF-FA **18**, and Type A crystals doped with t-Bu-FA **19**. However, the opposite trends were observed in those studies for all systems doped with Me-FA **15** and Type B and Type D crystals doped with t-Bu-FA **19**. As crystals doped with t-Bu-FA **19** suitable for this procedure were not successfully grown, the pattern of incorporation within acicular crystals of this kind is not known. However, the incorporation of Me-FA **15** into acicular crystals can be directly compared to those tested previously, and the reversal of the trend is notable.

5.3.3 Discussion of Segmentation Analysis Technique

This process is a useful way of quickly gaining a basic insight into the distribution of impurities within acicular crystals. The number of segments can be varied based on the size of the crystal, means of crystal fragmentation, and level of incorporation detail required. The technique is a simple and effective substitute for (or accompaniment to)

partial dissolution tailored for acicular crystals that both accounts for the differences in crystallisation behaviour between needle-like and prismatic crystals and overcomes the limitations of the PD technique in terms of sizing and crystal fragility, issues commonly encountered with acicular crystals.

There are limitations to the procedure as it was performed in this project. The division of the crystals is carried out using a metal spatula into fragments of approximately equal size as determined by eye. This is a laborious process, especially for large samples, and may introduce subjective variability between samples as well as between crystals within the same sample. Additionally, dividing the crystals in a sample into just three segments limits the depth of information that can be obtained from the study compared to that which is obtained from partial dissolutions. For example, with just three data points it is difficult to determine whether the pattern of additive inclusion relative to crystal growth is a near-linear increase, similar to the some of the systems described in Section 5.2.3.2, or whether the rate of additive change varies throughout the crystal, as in the Section 5.2.2.1 system. However, further development of the method could work towards correcting for these limitations, perhaps through automated control of the segmentation process or the use of a higher number of divisions per crystal.

5.4 Discussion of Patterns of Additive Incorporation

During the process of developing the partial dissolution and segmentation analysis methods described in this chapter, a large amount of data was gathered pertaining to the incorporation behaviour of compounds **15** – **19** within crystals of FFA **14**. It was generally observed, at least during the partial dissolution studies, that crystals doped with the same additive exhibited similar patterns of incorporation. This is indicative of the effect the additive has on the crystallisation process, and the differences in the mechanisms through which the incorporation of each additive occurs. The consistency of these patterns is also a testament to the robustness and reproducibility of the developed methods. The results of the PD studies of all systems doped with each additive are overlaid and presented as a function of dissolution midpoint and distribution coefficient (α_2) values in Appendix Section 7.9.2.

The majority of the development of the PD process carried out in this project was performed on FFA **14** crystals doped with Cl-FA **16**. This was primarily due to the fact that these systems produced a large amount of suitable prismatic crystals *via* the evaporation of MeOH. Most of the Cl-FA **16** doped systems studied followed a very similar pattern; a constant level of additive incorporation lower than the doping level for the centre 40 – 50% of the crystal bulk, followed by a notable increase in additive level as the crystal grows larger, with a disproportionately high level recorded near the crystal surfaces. The latter observation may be a representation of the distribution of additives within the crystals or could be the result of the deposition of additive-rich mother liquor on the surfaces of the crystals, as discussed in Section 5.2.1.2. The pattern of Cl-FA **16**

incorporation within the single doped crystal (SPC-1) studied in Section 5.2.2.4 deviated somewhat from those of the multi-particulate batches, with a shallower increase and higher overall incorporation level, although the basic pattern is comparable. The difference could be a result of the change in sample size, but it more likely stems from the alternative crystallisation method by which the single crystal sample was produced. The pattern of Cl-FA **16** incorporation measured within acicular FFA **14** crystals by segmentation analysis is similar to those described above, i.e., additive increase with crystal growth, but the data collected from that technique is not detailed enough to compare directly.

The pattern of Me-FA **15** incorporation is notably different to that of Cl-FA **16**, as discussed briefly in Section 5.2.2.2. The incorporation level is initially high, often matching or exceeding the doping level. A near-linear decrease in additive level is then consistently observed from the crystal centre to its surface, ending with a recorded value lower than the doping level in all cases. The slope of the decrease varies between samples. Samples doped with Me-FA **15** do not exhibit the disproportionately high additive level near the crystal surfaces; this is likely due to the lower additive level present in the crystallisation solution caused by high incorporations levels early in the crystallisation process. There is no clear impact of doping level on the level of incorporation; of the two additive levels tested, Me-FA **15** is incorporated to a higher relative degree on average in systems those doped with 0.5% additive than those doped with 5% additive, but the difference is slight and inconsistent. The pattern of incorporation observed in acicular crystals of FFA **14** doped with Me-FA **15** run counter to those observed in these studies, instead exhibiting similar increases to the other additives. It can be speculated that this is

the result of the difference in crystallisation behaviour of crystals grown by slow evaporation and slow cooling, and the mechanisms of additive incorporation that accompany the two.

DF-FA **17** incorporates into crystals of FFA **14** in a very similar manner to Cl-FA **16**, with constant additive levels observed at the start of crystal growth followed by an increase above doping level towards the surface of the crystals. Larger prismatic crystals with a higher degree of circularity, such as CSM-3 (Section 5.2.2.3) and that of SPC-2 (Section 5.2.2.4) exhibited a higher degree of DF-FA **17** incorporation than the more tabular prismatic crystals in CSM-1 and CSM-2 (Section 5.2.2.3). This could be attributed to crystal size; however, it is more likely to be related to crystal morphology, as the finer Type B crystallites (PM-B3, Section 5.2.3.2) displayed comparably high levels of incorporation to CSM-3. MF-FA **18** appears to share a similar pattern of incorporation as DF-FA **17** and Cl-FA **16**; however, as the inclusion of the additive detrimentally affected the growth of suitable crystal samples, the data collected on the additive is limited in this regard. Both additives have patterns of inclusion in acicular crystals that match those observed in the PD studies.

Finally, the incorporation behaviour of t-Bu-FA **19** into crystals of FFA **14** is somewhat less consistent than that of the other additives. First of all, similarly to MF-FA **18**, t-Bu-FA **19** inhibited the crystallisation of FFA **14** by slow evaporation, meaning all the samples doped with this additive that were studied belonged in one of the categories of crystal with problematic morphologies dubbed Types A – D. The three samples tested from those in the Type A category (PB-A1 – PB-A3) exhibited a predominantly decreasing pattern of additive incorporation from crystal centre to surface, similar to that

observed with the samples doped with Me-FA **15**. On the other hand, those from the Type B (PM-B5) and D (PM-D1 and PM-D2) categories were observed to have a near-linear increase in additive level as the crystals grew. This could be related to crystal size, as Type A crystals are notably larger than the other crystal types, or morphology; Type A crystals have a more prismatic habit than the fragile needles of Types B and D. Alternatively, it could be related to doping level, as the Types B and D crystals ranged from 3 – 5% additive while the Type A crystals were doped with just 2%. When the similarities between the behaviour of systems doped with t-Bu-FA **19** and Me-FA **15** at the 2% doping level (as explored in Chapter 4) are considered alongside the similar patterns of incorporation at this level, it can be speculated that the latter factor has the most significant influence on both crystallisation and incorporation behaviour.

5.5 Experimental

5.5.1 Partial Dissolutions

5.5.1.1 Primary Development

Sample Sizing Procedure

The mass of a crystal sample was measured before and after a dissolution stage using a Mettler Toledo MT5 microbalance. Images of the individual crystal particles were captured using a Nikon Eclipse 50i polarising microscope with a Nikon Digital Sight DS-Fi1 digital camera. NIS-Elements software version BR 3.1 was used to analyse the images. Surface areas were measured by defining a perimeter around the crystals by threshold analysis and measuring the area within.

The total surface area of the particles is estimated by doubling the surface area of the measured face. Lengths were collected by selecting points at either end of the crystal in the longest dimension by eye and measuring the distance between the two points. Those measurements could be displayed in μm and μm^2 units by the software for length and surface area respectively, taking into account the magnification of the objective used when capturing the images.

PD Method Details

After measurement, the sample crystals were suspended in hexane in a glass vial. The volume of hexane was appropriate to dissolve 10% of the sample, based on the total pre-dissolution mass of the sample and the solubility of the material in the solvent (2.40 mg ml^{-1} at 25 °C). The same volume of hexane was used for each dissolution stage in a series. The suspension was agitated at a rate of 300 rpm for 90 minutes using Fisherbrand ZX3 Vortexer. The temperature of the dissolution was not controlled, taking place at room temperature (18 – 20 °C). After the allotted time, the dissolution medium was removed using a Pasteur pipette and set aside. The crystals were rinsed with cold hexane and dried in a Hirsch funnel. The mass and size of the crystals were measured, and the process repeated for the desired number of dissolution stages.

5.5.1.2 Secondary Development

Sample Sizing Procedure

An Honor 7x dual 16 MP camera with High Dynamic Range and Phase Detection Auto Focus was used to capture digital macro photographs of the larger prismatic crystals. The camera was mounted on a stable retort stand. The crystals were photographed on a glass slide set atop a matte black surface at in a manner that minimised glare and maximised contrast between the crystals and the background. A scale, such as a ruler or slip of graphing paper was included in

each image. The images were analysed using ImageJ image analysis software. The images were scaled using the included rule. The image was converted to 8-bit greyscale, and the "find edges" and "binary analysis" features used to outline the particles. Any gaps in the outline were filled manually using the "paint" tool. The area within these outlines can be measured using the tracing and measuring tools, and the measured areas presented as mm^2 values. The total surface area of the particles is estimated by doubling the surface area of the measured face. Mass values were measured before and after a dissolution stage using a Mettler Toledo MT5 microbalance set to 4 decimal places.

PD Method Details

The sample crystals were suspended in hexane in a glass vial. The volume of hexane was appropriate to dissolve 15% of the sample, based on the total pre-dissolution mass of the sample and an experimentally determined dissolution target value of the crystals in the solvent (0.99 mg ml^{-1} at 18 – 20 °C). The same volume of hexane was used for each dissolution stage in a series. The suspension was agitated at a rate of 300 – 500 rpm (depending on the size of the particles) for 90 minutes using Fisherbrand ZX3 Vortexer. The temperature of the dissolution was not controlled, taking place at room temperature (18 – 20 °C). Later the agitator was changed to a VWR Incubating Orbital Mini Shaker, which afforded incubation and a certain degree of temperature control. Studies in which this instrument were used can be identified through the inclusion of experimental temperatures in the table of percentage dissolution levels. After the allotted time, the dissolution medium was removed using a Pasteur pipette and set aside. The crystals were rinsed with cold hexane and dried in a Hirsch funnel. The mass and size of the crystals were measured, and the process repeated for the desired number of dissolution stages. The additive level of the solution collected after each dissolution stage was determined by HPLC analysis. The details of the HPLC instrument and column can be found in Section 2.8.1.1. Method

parameters can be found in Section 2.8.1.2. Scans of each solution were performed in triplicate, the average peak areas of which were corrected using the formulae described in Section 4.9.2 to determine a percentage of additive within the sample.

5.5.1.3 Test of Anti-Flocculating Agent for Prismatic Crystals

Two samples of 10 similarly-sized prismatic crystals of FFA **14** doped with 2% Cl-FA **16** (Secondary-1 and Secondary-2) were selected from the same batch by eye. The crystals were weighed and sized as described in Section 5.5.1.2. Secondary-1 was suspended in a volume of hexane appropriate to dissolve 10% of the sample, based on the total pre-dissolution mass of the sample and the solubility of the material in the solvent (2.40 mg ml^{-1} at 25 °C). Secondary-2 was suspended in a solution of 2-(2-ethylhexyloxy)ethanol (EHE) in hexane, the volume of which was measured in the same way. The amount of EHE included was chosen based on the surface area measurements for the crystal particles in Secondary-2 pre-dissolution, at a level of 1 μmol per 6 mm^2 of crystal surface area. Both samples were subjected to two dissolution stages. Unless otherwise specified here, these dissolutions took place under the conditions described in Section 5.5.1.2.

5.5.1.4 Test of Anti-Flocculating Agent for Crystals with Problematic Morphologies

Two samples of similar mass were selected from a batch of Type C FFA **14** crystals doped with 5% Me-FA **15** (PM-B2), and another two selected from a batch of Type D FFA **14** crystals doped with 5% t-Bu-FA **19** (PM-D2). The crystals were weighed and sized as described in Section 5.5.1.2. One sample from each batch was suspended in a volume of hexane appropriate to dissolve 15% of the sample, based on the total pre-dissolution mass of the sample and the solubility of the

material in the solvent (1.93 mg ml^{-1} at 19 °C). The other sample from each batch was suspended in a solution of EHE in hexane, the volume of which was measured in the same way. No surface area data was measured for these samples, so EHE was included in the dissolution medium at a concentration of 2% v/v. The crystals were agitated at a rate of 250 rpm. Unless otherwise specified here, these dissolutions took place under the conditions described in Section 5.5.1.2.

5.5.1.5 Data Processing Methods

Dissolution Midpoint

The dissolution mid-point for a PD stage was calculated using mass measurements of the sample. The measurements before and after the dissolution stage are expressed as a percentage based on the level of the original crystal dissolved, i.e., pre-dissolution the level would be 0%, if no crystal remained the level would be 100%. With the measurements defined this way, the dissolution midpoint is equal to the percentage dissolution before the PD stage plus half of the difference between the levels before and after the stage. As such, it is equivalent to the middle point of the defined region. Dissolution midpoints in the context of a partial dissolution study would be presented along the x-axis of a scatter chart from 0% to 100% left to right, plotted against the corresponding measured level of additive or distribution coefficient (α_2) value in that portion of the crystal.

Distribution Coefficient

The distribution coefficient of an additive is calculated as in Formula 5.1, where α_2 refers to the distribution coefficient, X^S_{imp} refers to the molar fraction of additive in the solid phase (i.e., the dissolved crystal layer), and X^L_{imp} refers to the molar fraction of additive in the liquid phase (i.e., the solution from which the crystal was grown, a.k.a. the doping level). This results in a

figure for α_2 that represents the level of additive in a crystal layer as a ratio of the doping level of the crystallisation solution. α_2 can be used graphically on plots of additive distribution as a replacement for additive percentage on the Y-axis, generally plotted against dissolution stage or dissolution midpoint.

Formula 5.1. $$\alpha_2 = \frac{X_{imp}^{L}\,(1-X_{imp}^{S})}{X_{imp}^{S}\,(1-X_{imp}^{L})}$$

5.5.2 Segmentation Analysis

Samples of approximately 30 intact crystals was selected from several batches doped with differing additive types and levels. These samples were arranged on glass slides, taking particular care to orientate them so that the direction of their growth was preserved. At this stage, each crystal was divided lengthwise by eye into three segments of approximately equal length. Within each sample, the segments were collected into subsamples which were labelled in respect to their position in the whole crystal; segment *a* was the fragment closest to the nucleation point, segment *b* was the middle section, and segment *c* was the crystal tip, the latest portion in terms of crystal growth. In this way, three subsamples were created within each sample that consisted of fragments of the crystals at three consecutive stages of crystal growth. The subsamples were dissolved in MeCN, and the additive levels determined by HPLC analysis. Scans of each subsample were performed in triplicate, the average peak areas of which were corrected using the formulae described in Section 4.9.2 to determine a percentage of additive within the sample.

Conclusion

The goal of this research was to develop methods of determining the distribution of purification-resistant impurities within samples of crystalline API products. As the management and removal of impurities is an important aspect of pharmaceutical drug production, such methods would be valuable in the design of targeted strategies for the purification of systems for which crystallisation has proved ineffective.

The first goal was to select a system of study upon which to develop these methods, consisting of host and additive materials. Flufenamic acid **14** (FFA) was selected as the host, being a well-studied crystalline API. The five additives selected were 2-(*m*-tolylamino)benzoic acid **15** (Me-FA), *N*-(3-chlorophenyl)anthranilic acid **16** (Cl-FA), 2-[3-(difluoromethyl)anilino]benzoic acid **17** (DF-FA) and 2-[3-(fluoromethyl)anilino]benzoic acid **18** (MF-FA), and 2-((3-(*tert*-butyl)phenyl)amino)benzoic acid **19** (t-Bu-FA). These additives retained much of the structure of FFA **14** but possessed different aryl-ring substituents in the place of the $-CF_3$ group. In the case of compounds **15** – **18**, these substituents were smaller in size than $-CF_3$; in this manner they were expected to form solid solution-like systems when doped into samples of FFA **14**. The purification-resistant impurities encountered in industrial processes have consistently been observed to share properties with solid solutions, specifically in terms of incorporation level and resistance to rejection by crystallisation.[17] As such, it was decided that doped systems exhibiting similar solid solution-like properties would be effective systems of study upon which to develop the methods of interest. Compound **19** was the exception to this idea. Substituted with a bulkier *tert*-butyl group in the place of the $-CF_3$, it was not expected to incorporate as well as the other

additives or exhibit the same solid solution-like attributes. In this way it was intended to act as a contrast against which the behaviour of the other additives could be measured.

Key methods of analysis were developed by which the pure components and impure systems could be qualified and quantified. A reliable and selective HPLC method was developed, as were effective parameters for PXRD and DSC analysis. Different crystallisation techniques were explored, and four central means of crystal production were chosen and refined, each producing crystal material with a different morphology and/or size. Solubility tests were carried out on FFA **14**, Me-FA **15**, and Cl-FA **16** in a range of different solvents and at different temperatures. Finally, a reliable synthetic method for producing compounds **14** – **19** was developed, and the products of each synthesis fully characterised. In the synthetic development process, an impurity was noticed to be consistently present in the impure products of FFA **14** synthetic reactions. The impurity was isolated and characterised by a wide range of analysis types. The identity of the impurity was narrowed down to two similar possibilities, the diacid triaryl compound **25**, and the acridone triaryl compound **28**, but no definitive conclusion could be drawn.

Impure systems were produced by doping samples of FFA **14** with each of compounds **15** – **19** individually. Studies on these impure systems showed that at low doping levels, all of the additives were well incorporated into crystal samples of FFA and showed significant resistance to purification by recrystallisation. Me-FA **15** and Cl-FA **16** showed particularly high levels of both these metrics, with the crystal lattice showing near equal preference for molecules of each additive as it did for molecules of the host. At higher doping levels, the incorporation of Me-FA **15** remained relatively consistent with

that observed at lower levels. The behaviour of Cl-FA **16** however was notably different, with the additive appearing to assume the host role in the system at compositions above 24% Cl-FA **16**. The behaviour of these systems was explored further through the construction of phase diagrams, the data of which was collected from DSC analysis. This involved overcoming an issue involving the polymorphic transformation of FFA **14** at higher temperatures. By the construction of these diagrams, it was discovered that Me-FA **15** formed a continuous non-ideal solid solution with FFA **14** with a minimum point at a composition just above 50% Me-FA **15**. The FFA **14** / Cl-FA **16** system, on the other hand, was more unusual, forming a terminal solid solution up to a Cl-FA **16** level of approx. 24%, a composition that intersected with the eutectic point. The system behaved as a eutectic at higher compositions of Cl-FA **16**. Construction of these diagrams confirmed the formation of solid solutions between FFA **14** and Me-FA **15** and Cl-FA **16** respectively at doping levels similar to those commonly found in impure pharmaceutical products (0 – 6%).[17]

By comparing the behaviour of systems doped with compounds **17** – **19** to that of these systems (in terms of additive incorporation, purification resistance, and DSC / PXRD analysis), it can be inferred that those systems likely also exhibit solid solution-like properties, and, as such, are appropriate models for the types of purification-resistant impure systems discussed previously. This result was somewhat unexpected for those systems doped with t-Bu-FA **19**. While the additive was expected to demonstrate poor inclusion into crystals of FFA **14**, it instead behaved in a similar manner to compounds **15** – **18**, even exhibiting the highest levels of incorporation of all additives tested in some instances. An array of tests were performed to determine the nature of this incorporation,

which concluded that the system was most likely forming a solid solution or eutectic. Based on similarities to systems doped with the other additives, it is most likely the former, but this has not been definitively concluded. Possible explanations for this unexpected behaviour are presented in the text, but similarly further experimentation would need to be performed to verify or disprove them.

Finally, methods of measuring the distribution of the additives throughout the doped systems were developed. This work focused primarily on the development of partial or stepwise dissolutions, the process of sequentially stripping the outer layers from a crystal or batch of crystals and measuring the impurity content of each layer to map the distribution of the impurities on a surface-to-centre basis. The development of this technique involved iterative refinements to crystallisation method, solvent volume selection, anti-flocculant use, particle sizing techniques, agitation rate, and temperature control. Once a reliable method had been developed, it was applied to a variety of systems of FFA doped with compounds **15** – **19**. In this manner, the robustness of the method was explored with regard to sample size, additive type, additive level, crystal morphology, and crystal size. It was found that the technique was applicable to all samples tested with minimal adjustments needed. A modified version of the technique was also successfully applied to large samples of crystals with four different types of morphology that made them problematic for particle sizing.

During the development of the partial dissolution method, it was discovered that acicular crystals were not well suited for use by this technique. As such, a separate method was developed to determine the distribution of impurities within these crystals. By segmenting a sample of impure acicular crystals along their length, the change in impurity

incorporation could be measured as a function of continuous crystal growth, providing much the same information as a partial dissolution would.

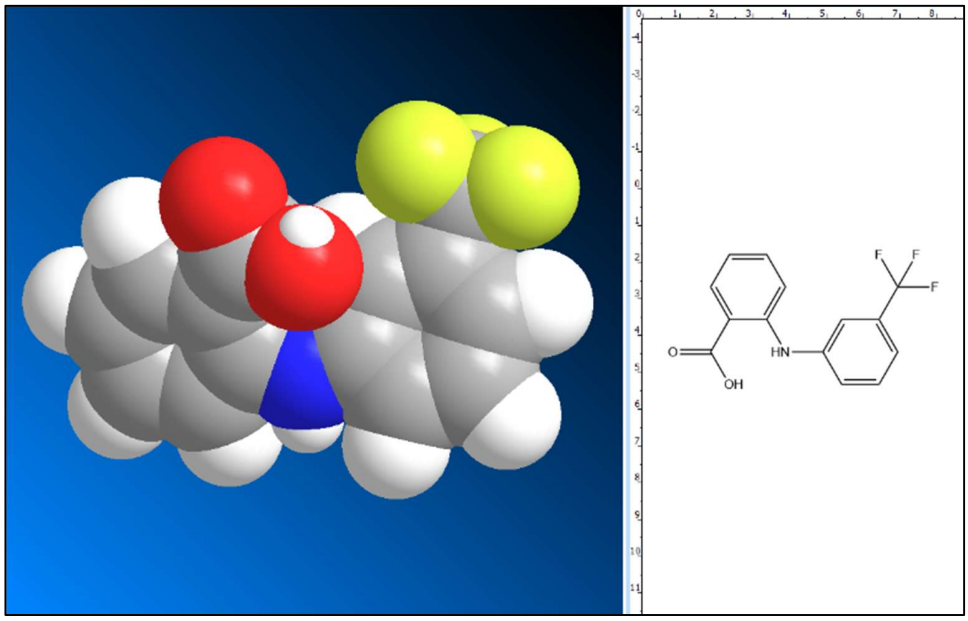
In cases where an impurity or multiple impurities in a batch of industry drug product prove difficult to reject by standard crystallisation, alternative purification techniques may be necessary. These techniques can range from simple washing to more complex phase transformations or changes to methodology. In these cases, information into the nature of the impurity and its distribution within the host crystal is vital in informing an effective, targeted purification strategy.

The techniques presented in this work can be compared to other approaches to mapping impurity distributions in crystalline samples, such as Raman spectroscopy or TOF-SIMS (time-of-flight secondary ion mass spectrometry). The methods described here have some advantages over those approaches. For one, they can be performed on a bench without the need for specialised or costly equipment. In addition, if combined with dedicated particle sizing instrumentation, the partial dissolution approach has the potential to process large samples of material in a relatively non-labour-intensive manner. Raman spectroscopy is limited in its capacity to distinguish between an impurity and an API only if they were contained in separate phases.[218] TOF-SIMS is a very sophisticated means of mapping impurities on the surface of crystals; however, it lacks the ability to measure impurity levels elsewhere in the crystal body.[226] That limitation can be overcome through use in conjunction with ion beam milling; however, this is not a widely available technique. The partial dissolution approach allows for direct sampling of crystal regions from the surface of a crystal sample to its centre.

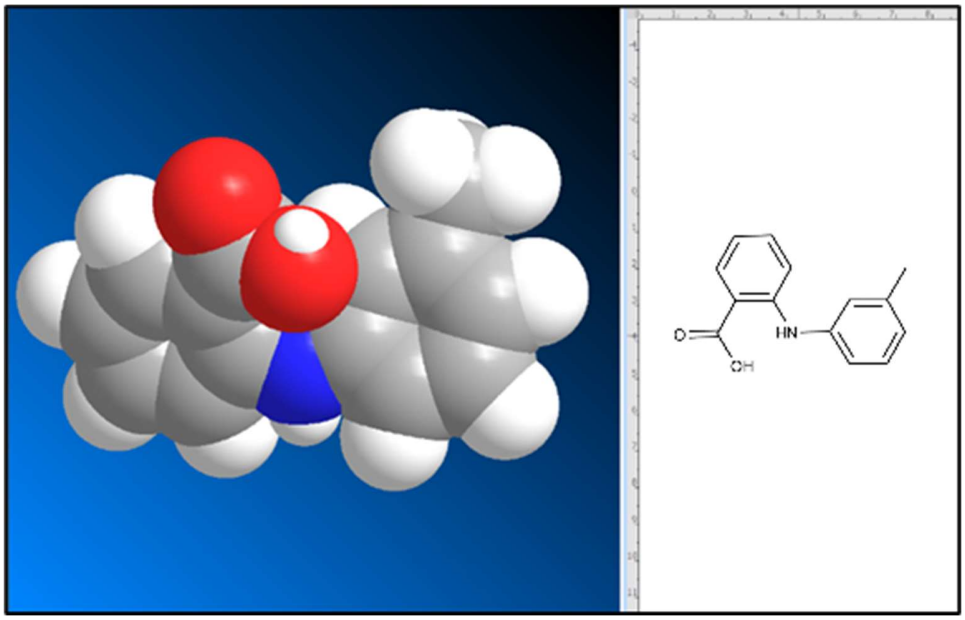
There are limitations to the approaches we have developed, however. Firstly, the dissolution process is inherently imprecise which impacts the reproducibility of the data. A variety of measures designed to mitigate this imprecision are described in Section 5.2.1, including the use of an experimentally determined dissolution target value for selecting solvent volume and the strict control of agitation rate and temperature during dissolution. With further research, there is potential for the methodology to offer reasonably well-controlled dissolution for large samples of particles. The techniques as described are also quite labour intensive, mainly due to the manual particle sizing by digital image analysis. However, as mentioned above this could be made easier by use of a particle sizing instrument, with the added benefit of measuring larger samples and smaller particles, which could be further improved by automation. Finally, the slurrying of crystal particles in suspension may not be inert and has the potential for changes to crystal form. However, this is unlikely in most cases given the short processing times, and easily detectable by XRD analysis.

Appendix

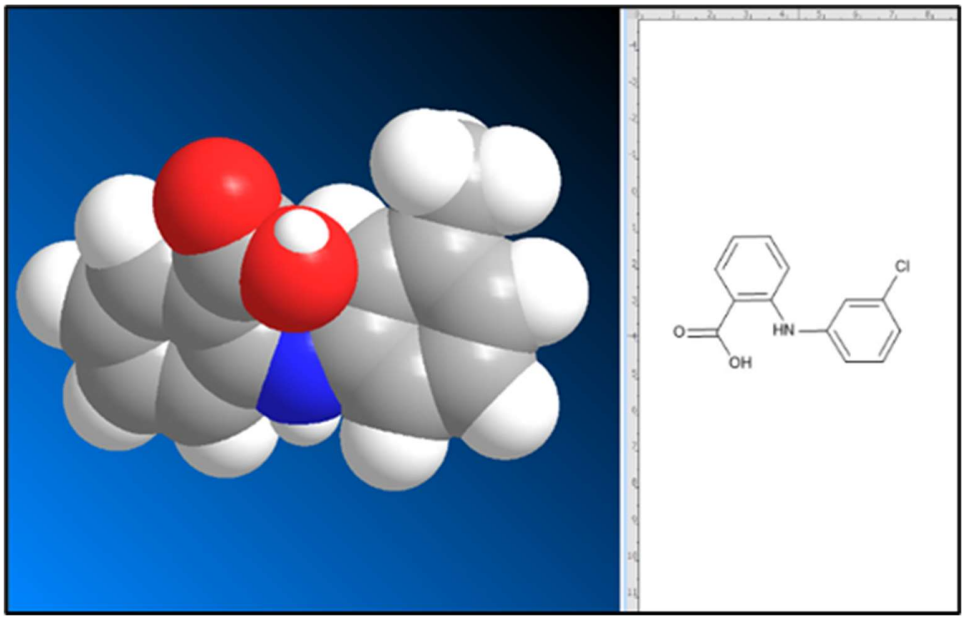
7.1 Space-Fill Diagrams of Compounds **14** – **19**



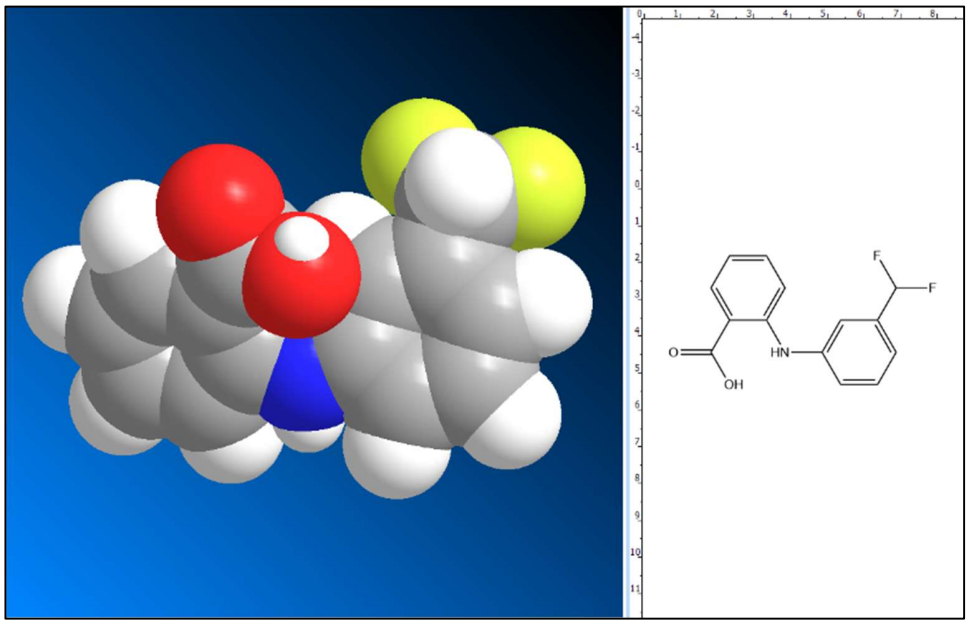
Appendix Fig 7.1. Space-fill diagram of FFA **14**, showing minimum energy conformation and relative size of variable substituent.



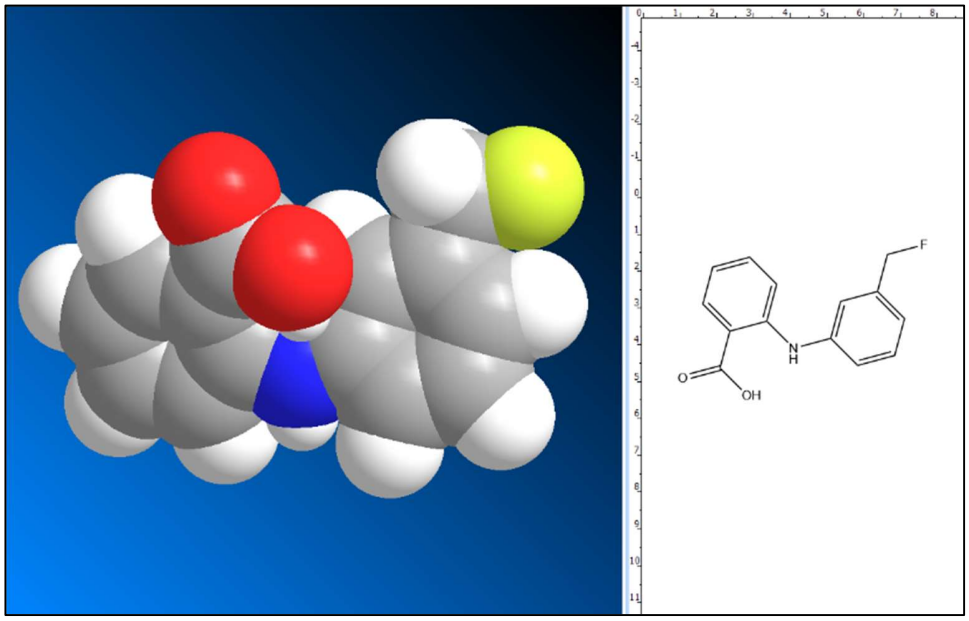
Appendix Fig 7.2. Space-fill diagram of Me-FA **15**, showing minimum energy conformation and relative size of variable substituent.



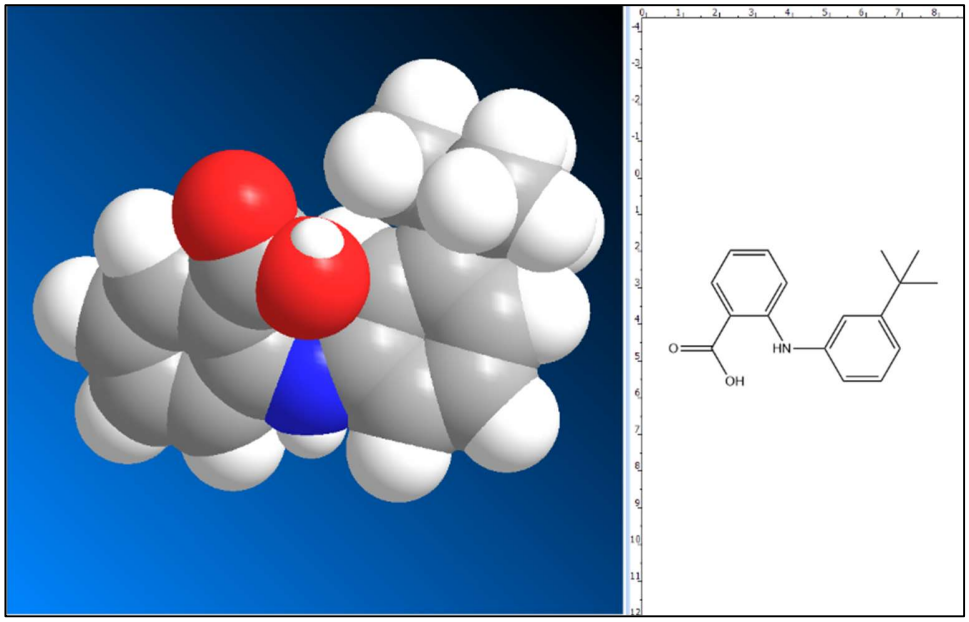
Appendix Fig 7.3. Space-fill diagram of Cl-FA **16**, showing minimum energy conformation and relative size of variable substituent.



Appendix Fig 7.4. Space-fill diagram of DF-FA **17**, showing minimum energy conformation and relative size of variable substituent.



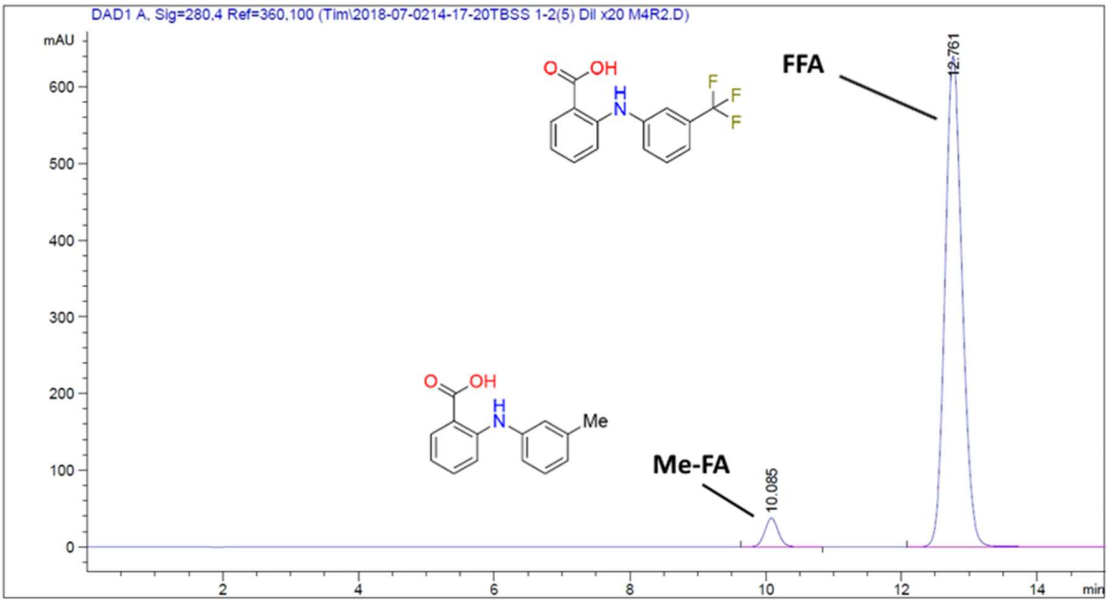
Appendix Fig 7.5. Space-fill diagram of MF-FA **18**, showing minimum energy conformation and relative size of variable substituent.



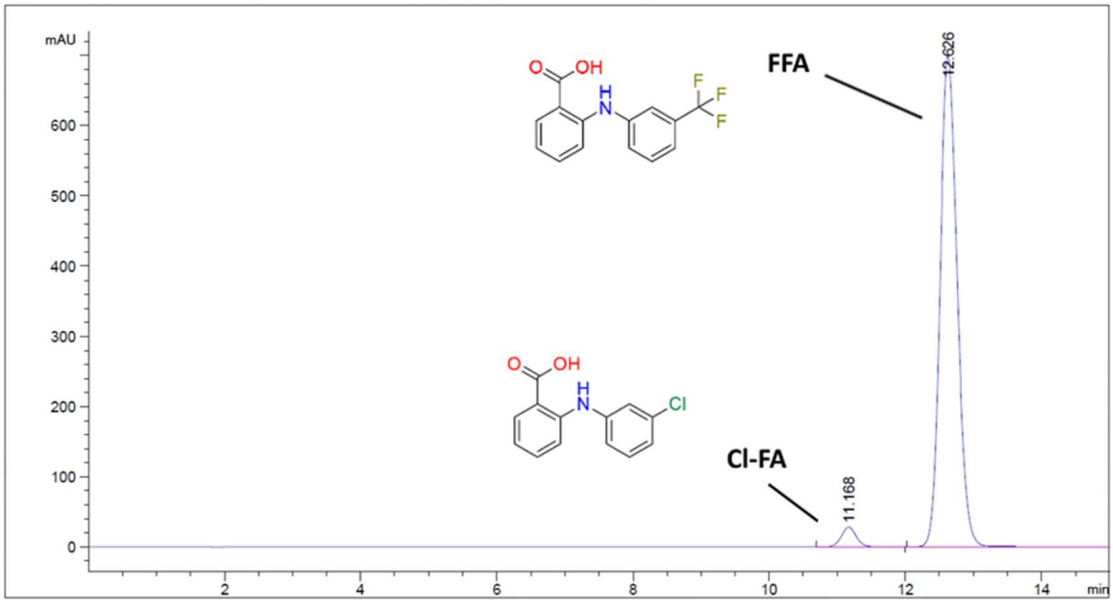
Appendix Fig 7.6. Space-fill diagram of t-Bu-FA **19**, showing minimum energy conformation and relative size of variable substituent.

7.2 HPLC Analysis

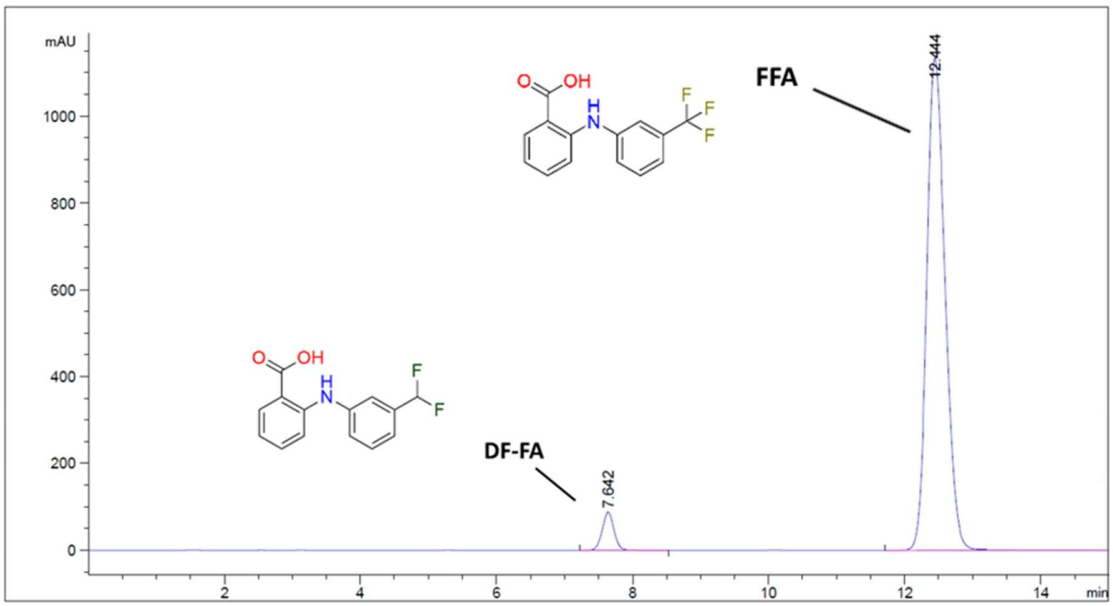
7.2.1 FFA **14** doped with different levels of Compounds **15** – **19**



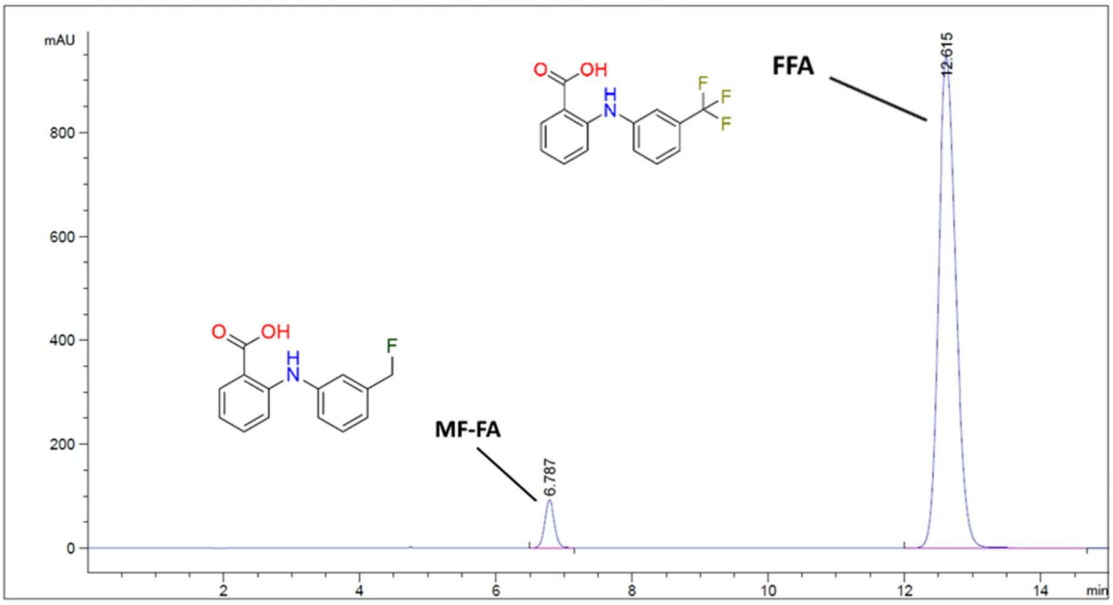
Appendix Fig 7.7. HPLC trace of FFA **14** (right, 12.76 min) doped with 5 mol% Me-FA **15** (left, 10.06 min) collected at 280 nm.



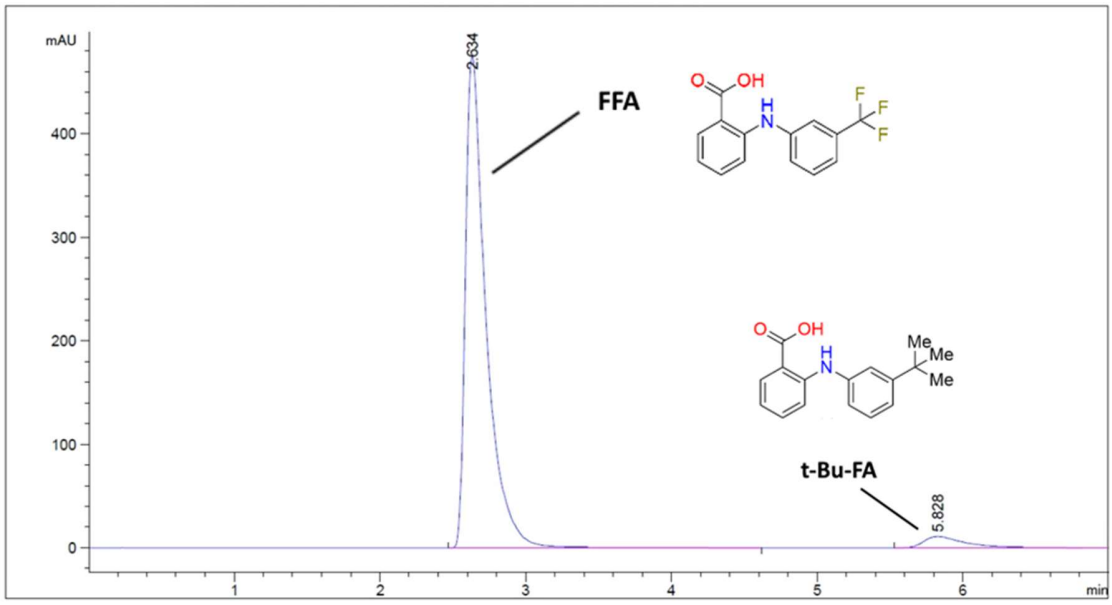
Appendix Fig 7.8. HPLC trace of FFA **14** (right, 12.63 min) doped with 5 mol% Cl-FA **16** (left, 11.17 min) collected at 280 nm.



Appendix Fig 7.9. HPLC trace of FFA **14** (right, 12.44 min) doped with 5 mol% DF-FA **17** (left, 7.64 min) collected at 280 nm.

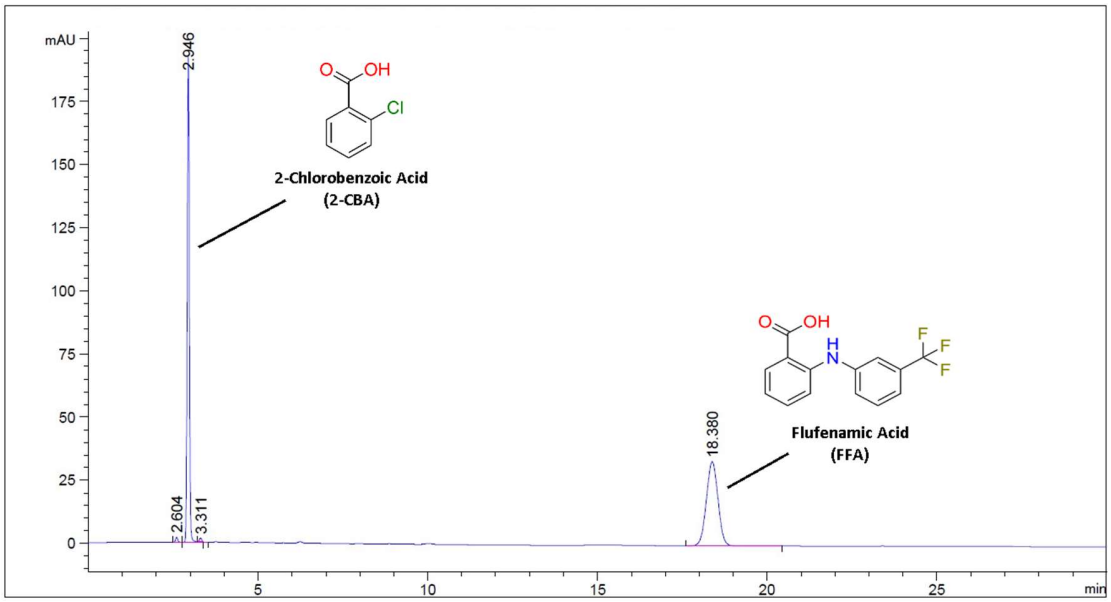


Appendix Fig 7.10. HPLC trace of FFA **14** (right, 12.62 min) doped with 5 mol% MF-FA **18** (left, 6.79 min) collected at 280 nm.

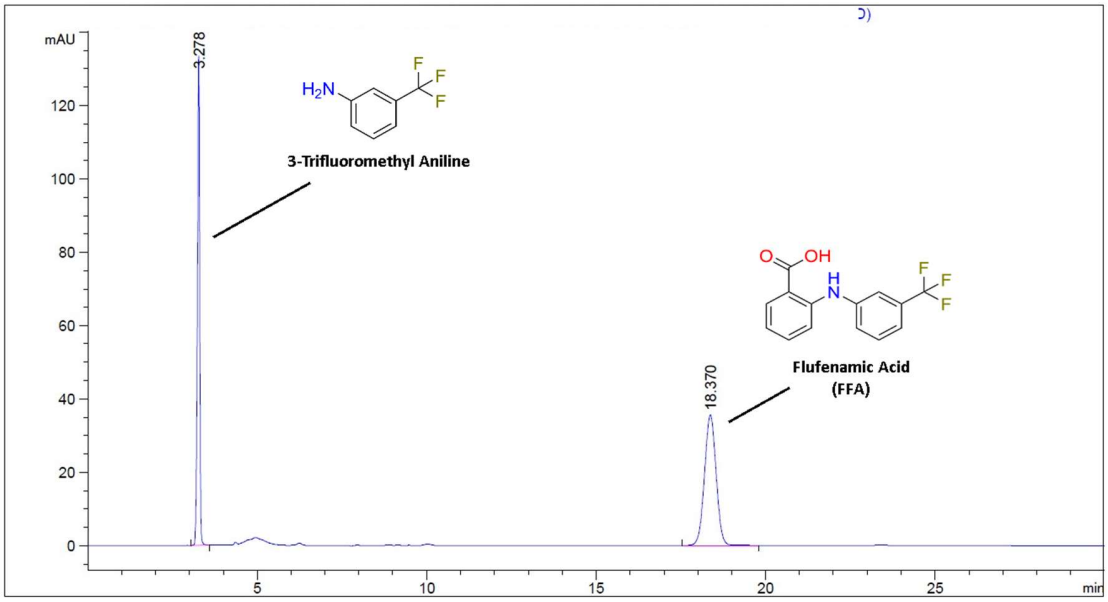


Appendix Fig 7.11. HPLC trace of FFA **14** (left, 2.63 min) doped with 5 mol% t-Bu-FA **19** (right, 5.83 min) collected at 280 nm.

7.2.2 FFA **14** *vs.* Synthetic Starting Materials



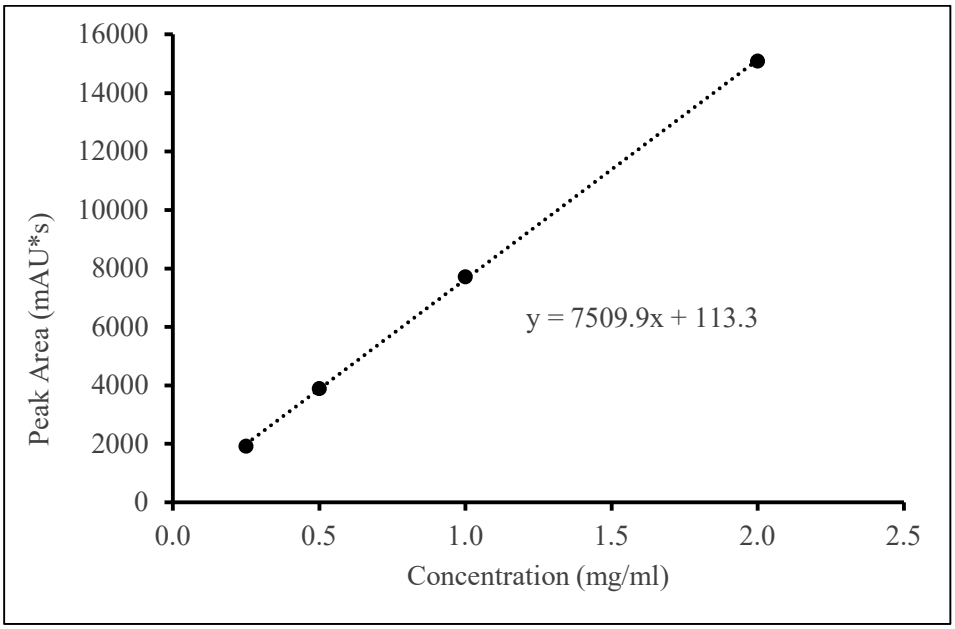
Appendix Fig 7.12. HPLC trace of FFA **14** spiked with the synthetic starting material 2-chlorobenzoic acid **20**, collected at 280 nm.



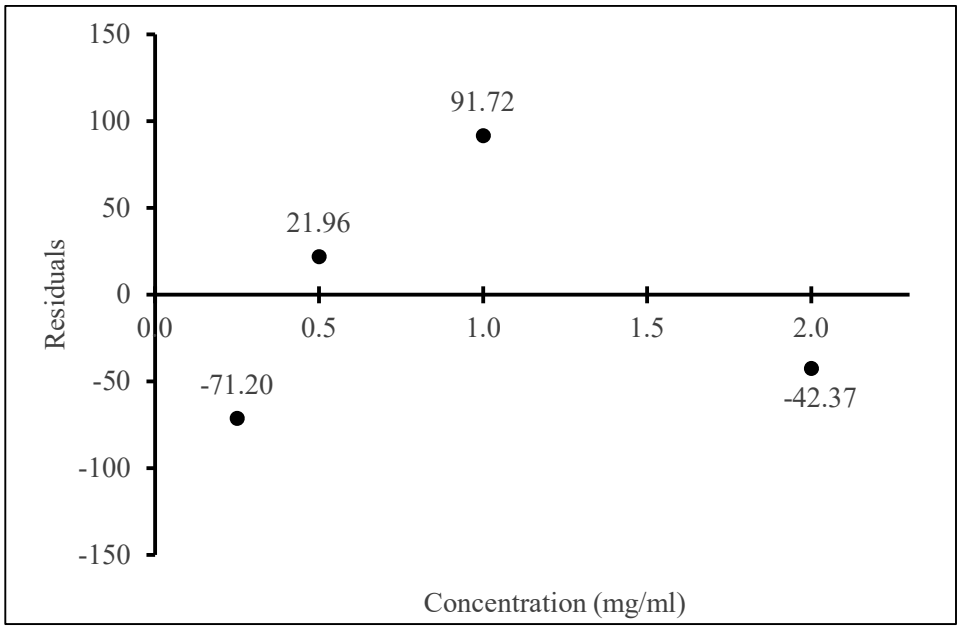
Appendix Fig 7.13. HPLC trace of FFA **14** spiked with the synthetic starting material 23-trifluoromethyl aniline **21**, collected at 280 nm.

7.3 Calibration Curves

7.3.1 Me-FA **15** Calibration Curve



Appendix Fig 7.14. Calibration curve for Me-FA **15** with linear regression curve equation, collected at 280 nm.



Appendix Fig 7.15. Plot of Residual Values for Me-FA **15** Calibration Curve.

Appendix Table 7.1. Residual Statistics for Me-FA **15** Calibration Curve.

Multiple R	1.000
R Square	1.000
Adjusted R Square	1.000
Standard Error	88.77
Observations	4

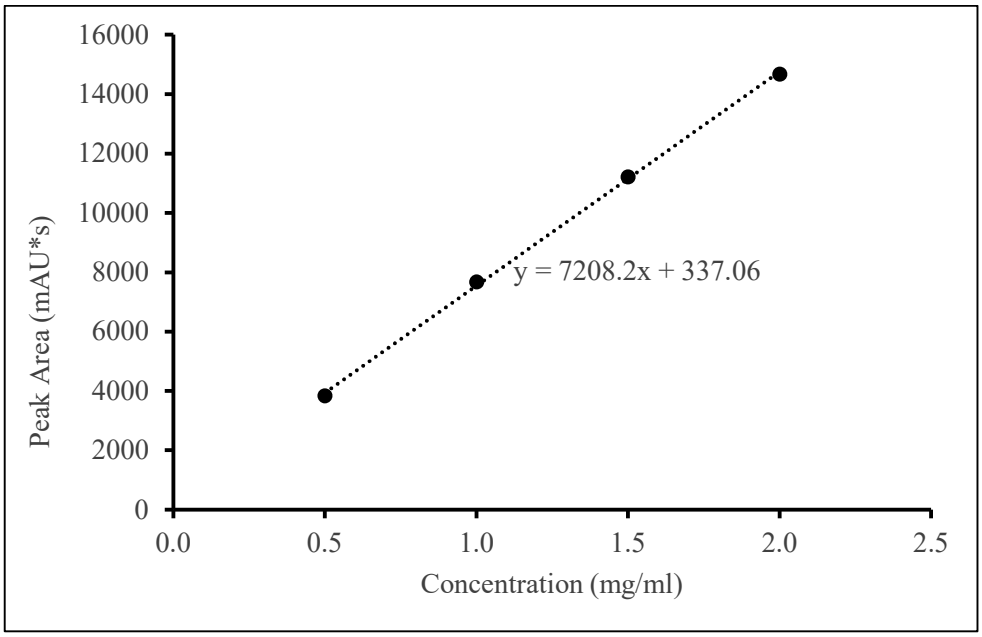
Appendix Table 7.2. ANOVA Statistics for Me-FA **15** Calibration Curve.

ANOVA	df	SS	MS	F	Significance F
Regression	1	101342056.14	101342056.14	12861.84	7.774E-05
Residual	2	15758.56	7879.28		
Total	3	101357814.70			

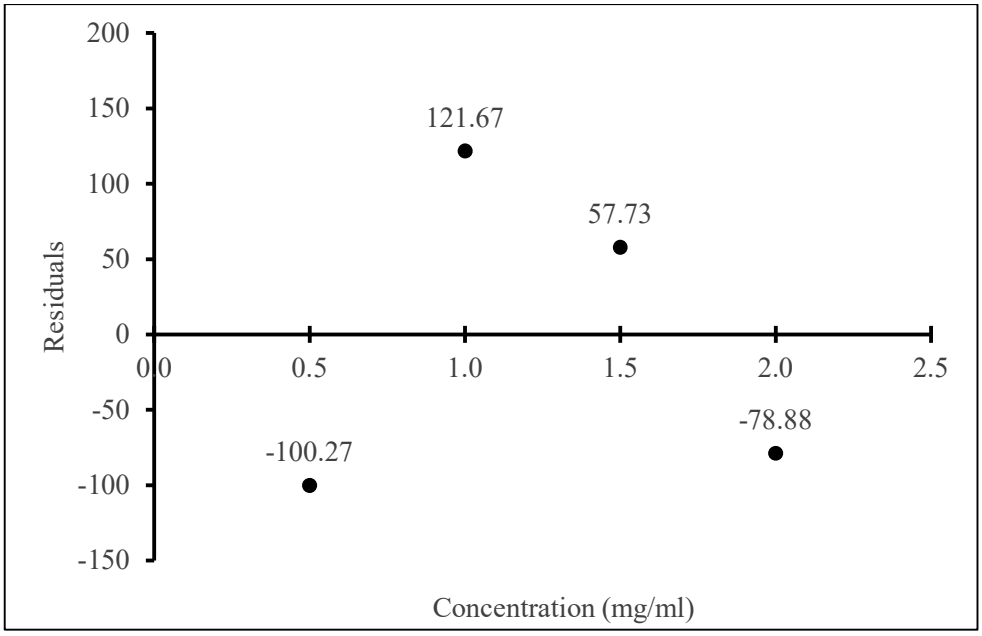
Appendix Table 7.3. Residual Coefficients Statistics for Me-FA **15** Calibration Curve.

	Coefficients	Standard Error	t Stat	P-value	Lower 95.0%	Upper 95.0%
Intercept	113.30	76.31	1.49	0.28	-215.05	441.65
Concentration (mg/mL)	7509.93	66.22	113.41	7.774E-05	7225.01	7794.85

7.3.2 Cl-FA **16** Calibration Curve



Appendix Fig 7.16. Calibration Curve for Cl-FA **16** with linear regression curve equation, collected at 280 nm.



Appendix Fig 7.17. Plot of Residual Values for Cl-FA **16** Calibration Curve, collected at 280 nm.

Appendix Table 7.4. Residual Statistics for Cl-FA **16** Calibration Curve.

Multiple R	1.000
R Square	0.999
Adjusted R Square	0.999
Standard Error	131.17
Observations	4

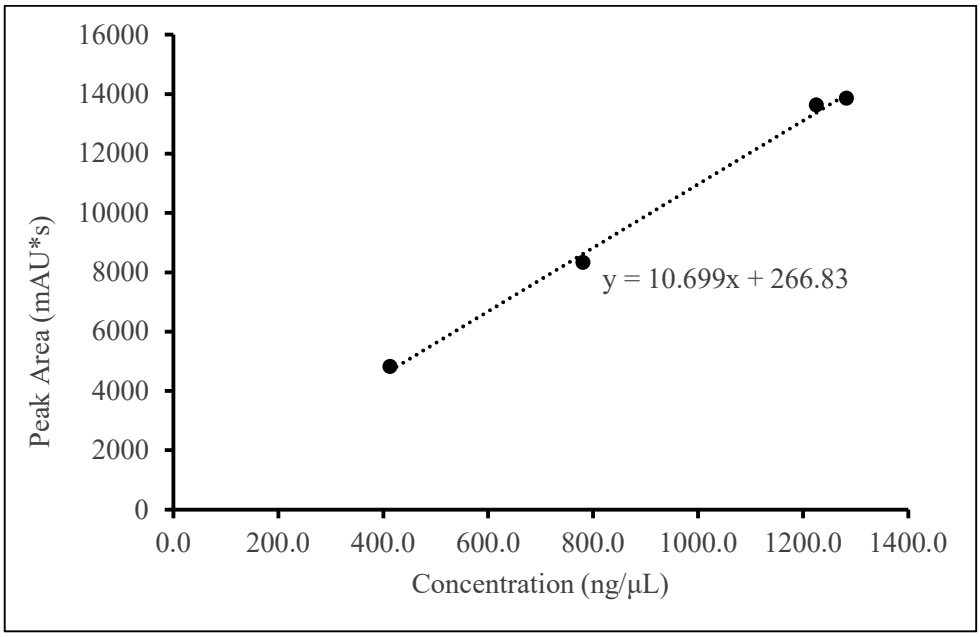
Appendix Table 7.5. ANOVA Statistics for Cl-FA **16** Calibration Curve.

ANOVA	df	SS	MS	F	Significance F
Regression	1	64948491.35	64948491.35	3774.81	2.648E-04
Residual	2	34411.54	17205.77		
Total	3	64982902.89			

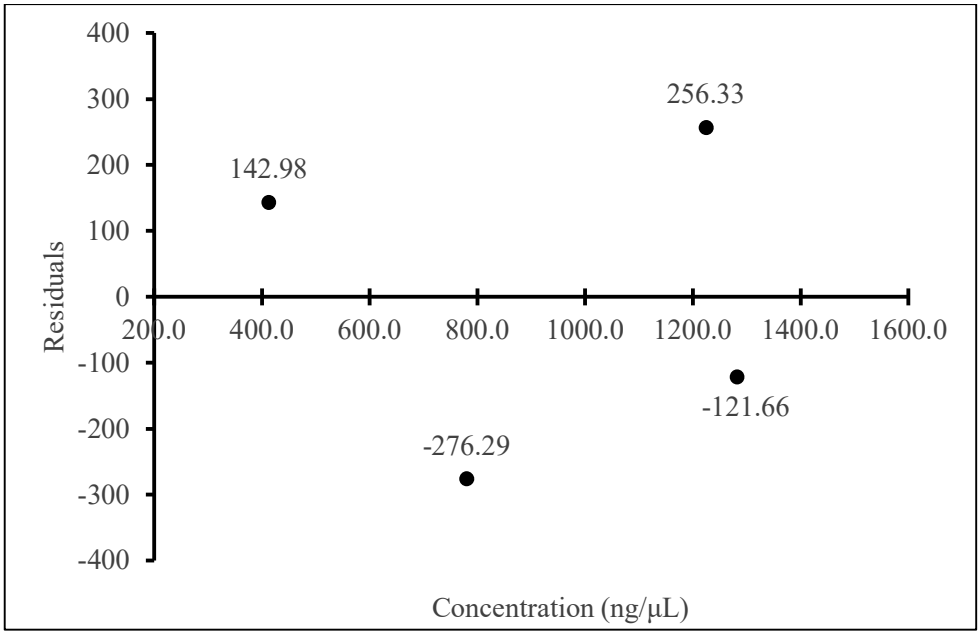
Appendix Table 7.6. Residual Coefficients Statistics for Cl-FA **16** Calibration Curve.

	Coefficients	Standard Error	t Stat	P-value	Lower 95.0%	Upper 95.0%
Intercept	337.07	160.65	2.10	0.17	-354.16	1028.29
Concentration (mg/mL)	7208.25	117.32	61.44	2.648E-04	6703.45	7713.04

7.3.3 DF-FA **17** Calibration Curve



Appendix Fig 7.18. Calibration Curve for DF-FA **17** with linear regression curve equation, collected at 280 nm.



Appendix Fig 7.19. Plot of Residual Values for DF-FA **17** Calibration Curve.

Appendix Table 7.7. Residual Statistics for DF-FA **17** Calibration Curve.

Multiple R	0.998
R Square	0.997
Adjusted R Square	0.995
Standard Error	297.73
Observations	4

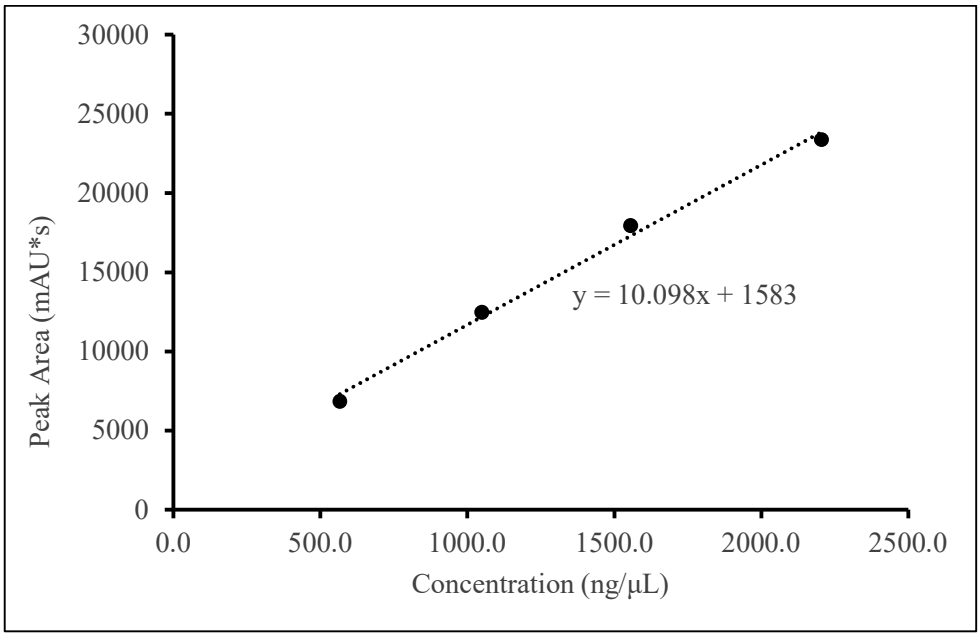
Appendix Table 7.8. ANOVA Statistics for DF-FA **17** Calibration Curve.

ANOVA	df	SS	MS	F	Significance F
Regression	1	57408548.74	57408548.74	647.64	0.002
Residual	2	177286.45	88643.23		
Total	3	57585835.19			

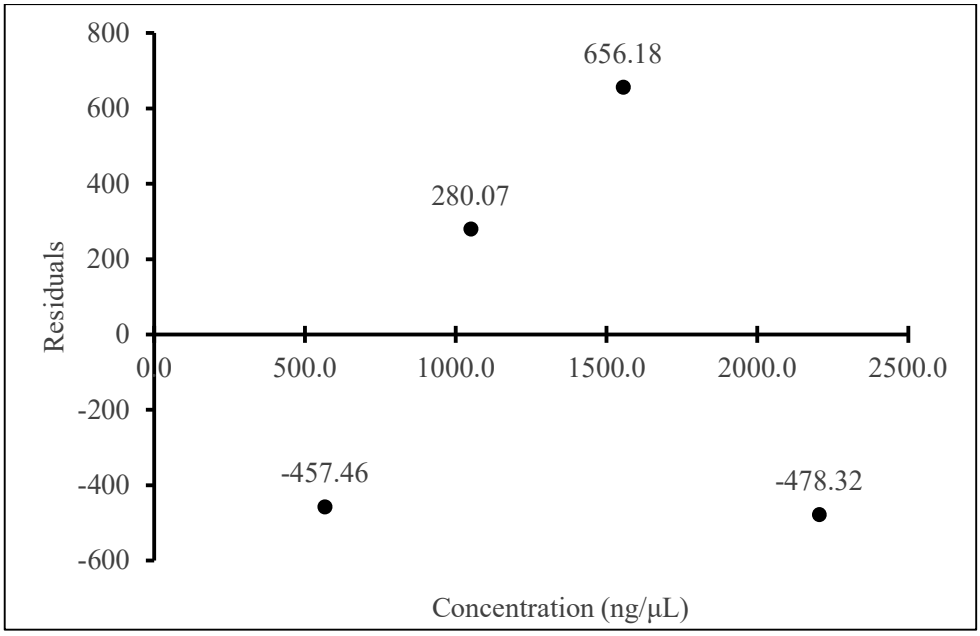
Appendix Table 7.9. Residual Coefficients Statistics for DF-FA **17** Calibration Curve.

	Coefficients	Standard Error	t Stat	P-value	Lower 95.0%	Upper 95.0%
Intercept	266.83	416.42	0.64	0.59	-1524.86	2058.52
Concentration (ng/µL)	10.70	0.42	25.45	0.002	8.89	12.51

7.3.4 MF-FA **18** Calibration Curve



Appendix Fig 7.20. Calibration Curve for MF-FA **18** with linear regression curve equation, collected at 280 nm.



Appendix Fig 7.21. Plot of Residual Values for MF-FA **18** Calibration Curve.

Appendix Table 7.10. Residual Statistics for MF-FA **18** Calibration Curve.

Multiple R	0.997
R Square	0.994
Adjusted R Square	0.991
Standard Error	688.14
Observations	4

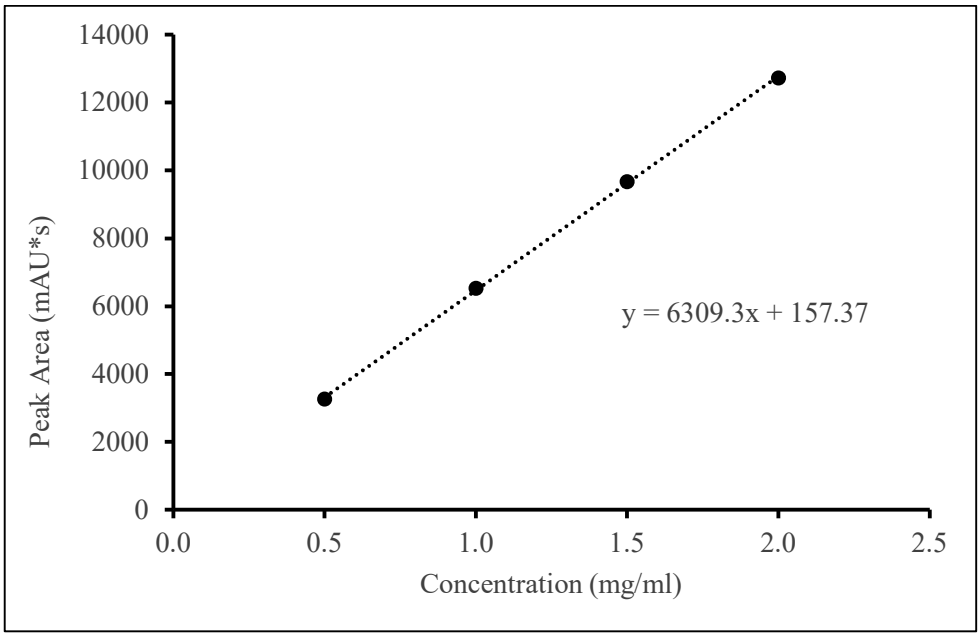
Appendix Table 7.11. ANOVA Statistics for MF-FA **18** Calibration Curve.

ANOVA	df	SS	MS	F	Significance F
Regression	1	150669999.66	150669999.66	318.13	0.003
Residual	2	947063.80	473531.90		
Total	3	151617063.45			

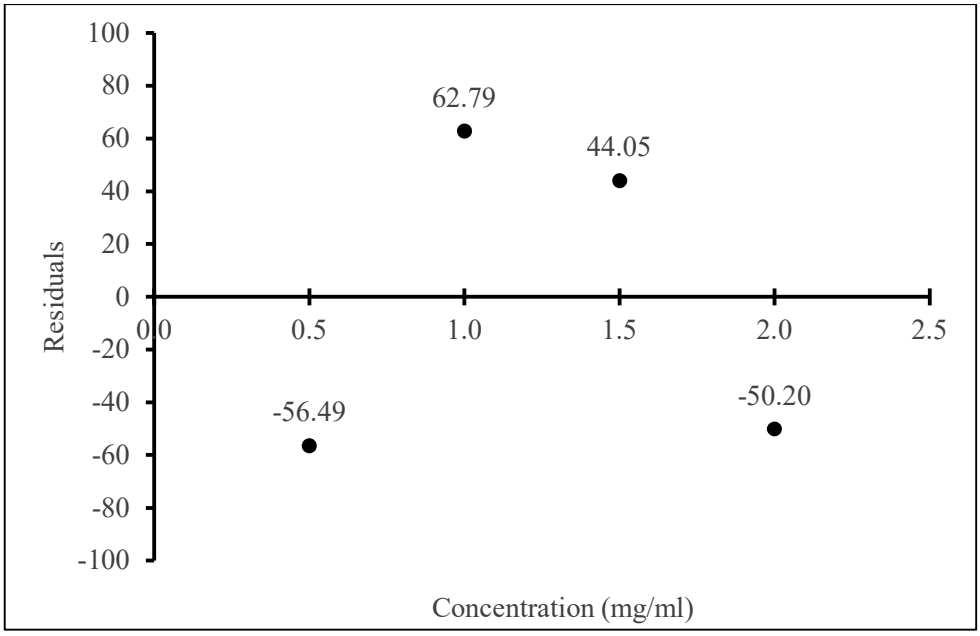
Appendix Table 7.12. Residual Coefficients Statistics for MF-FA **18** Calibration Curve.

	Coefficients	Standard Error	t Stat	P-value	Lower 95.0%	Upper 95.0%
Intercept	1582.96	835.04	1.90	0.198	-2009.90	5175.81
Concentration (ng/µL)	10.10	0.57	17.84	0.003	7.66	12.53

7.3.5 t-Bu-FA **19** Calibration Curve



Appendix Fig 7.22. Calibration Curve for t-Bu-FA **19** with linear regression curve equation, collected at 280 nm.



Appendix Fig 7.23. Plot of Residual Values for t-Bu-FA **19** Calibration Curve.

Appendix Table 7.13. Residual Statistics for t-Bu-FA **19** Calibration Curve.

Multiple R	1.000
R Square	1.000
Adjusted R Square	1.000
Standard Error	76.14
Observations	4

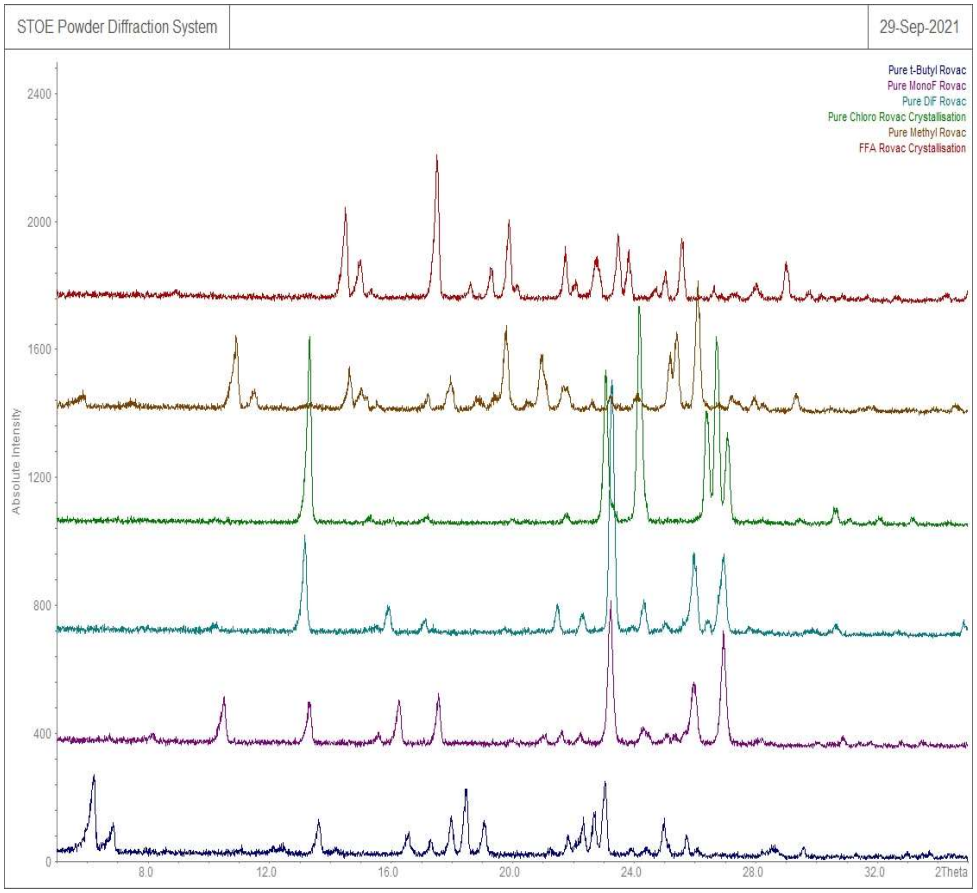
Appendix Table 7.14. ANOVA Statistics for t-Bu-FA **19** Calibration Curve.

ANOVA	df	SS	MS	F	Significance F
Regression	1	49759483.80	49759483.80	8582.87	1.165E-04
Residual	2	11595.07	5797.53		
Total	3	49771078.86			

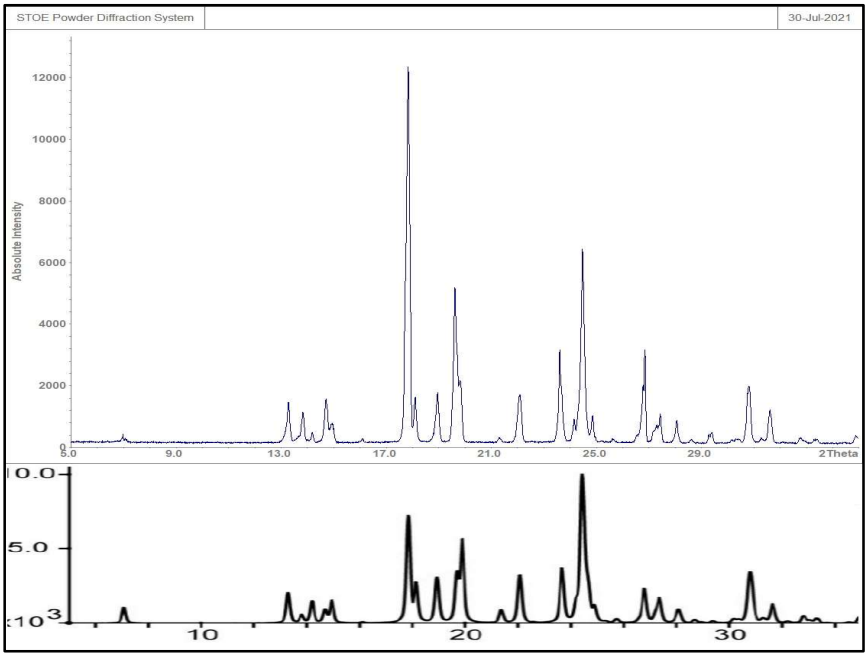
Appendix Table 7.15. Residual Coefficients Statistics for t-Bu-FA **19** Calibration Curve.

	Coefficients	Standard Error	t Stat	P-value	Lower 95.0%	Upper 95.0%
Intercept	157.37	93.25	1.69	0.234	-243.87	558.61
Concentration (mg/mL)	6309.33	68.10	92.64	1.165E-04	6016.30	6602.35

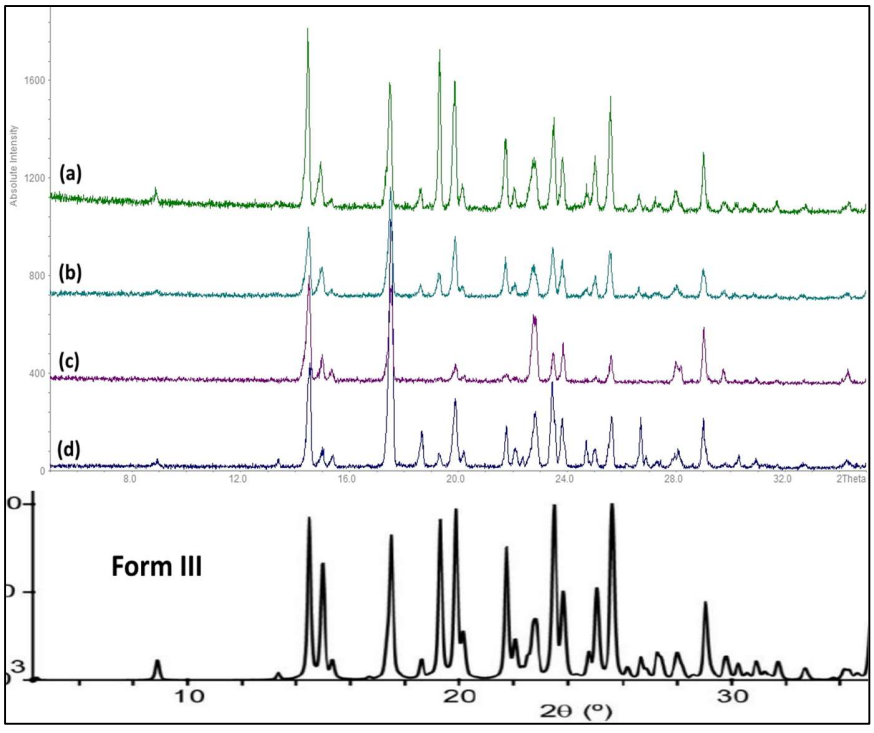
7.4 PXRD Analysis



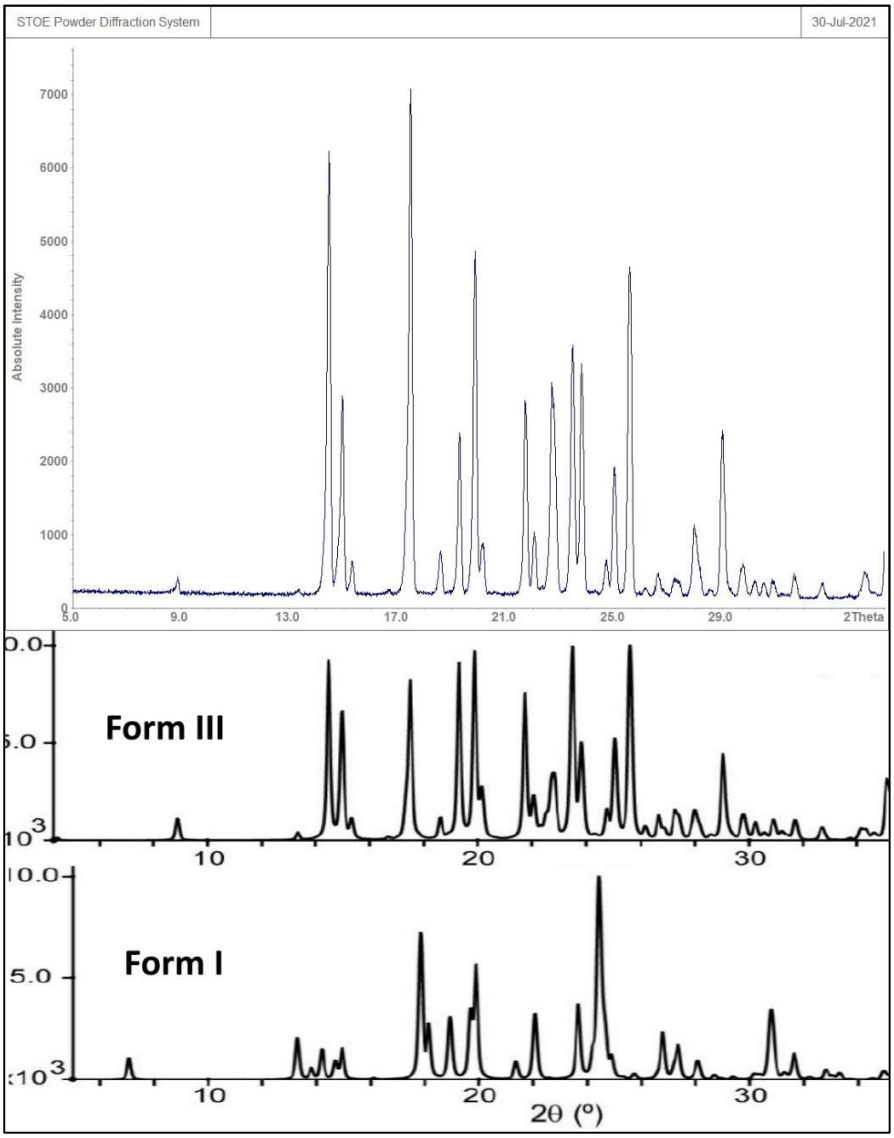
Appendix Fig 7.24. Top to bottom: PXRD patterns of purified and synthesised FFA **14**, Me-FA **15**, Cl-FA **16**, DF-FA **17**, MF-FA **18**, and t-Bu-FA **19**.



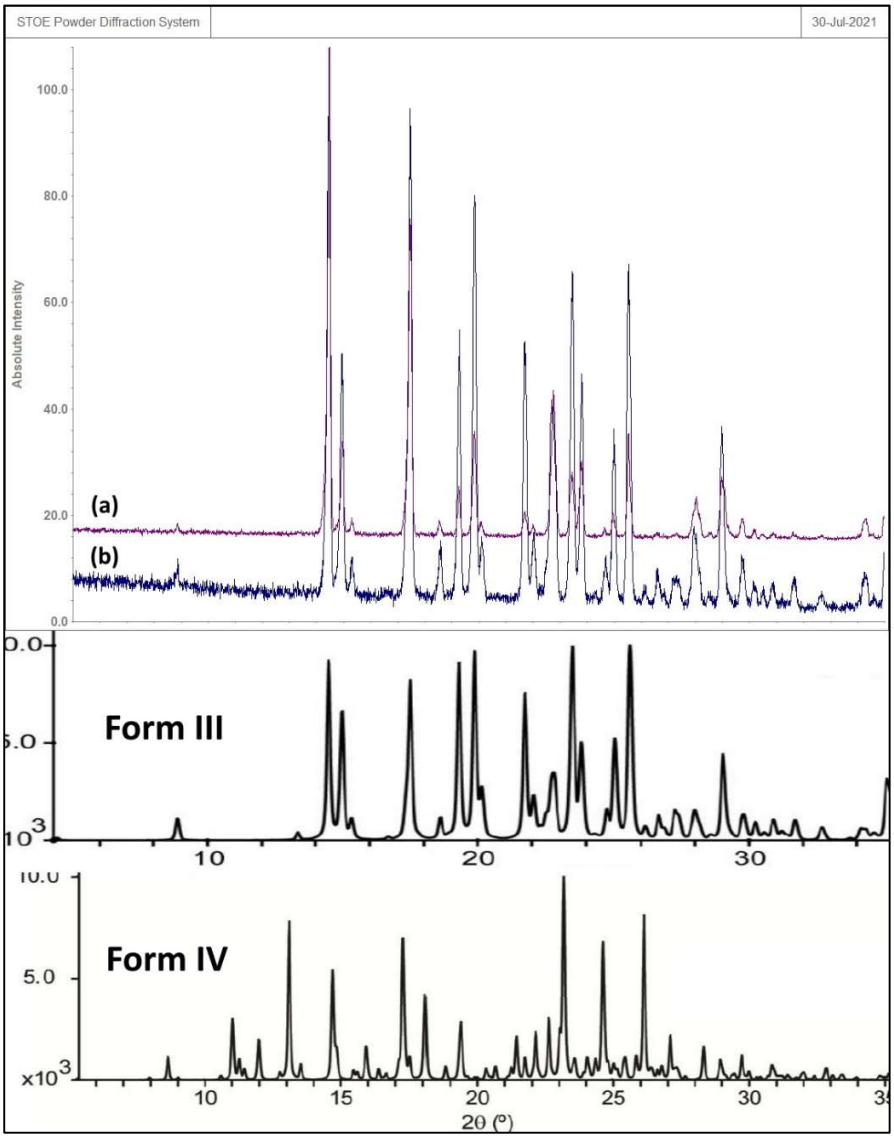
Appendix Fig 7.25. Measured PXRD pattern of commercial FFA **14** (top) *vs.* literature pattern for Form I FFA **14** (bottom).[65]



Appendix Fig 7.26. Measured PXRD patterns of FFA **14** crystallised *via* (a) slow evaporation from MeOH, (b) rotovap evaporation, (c) slow cooling of a MeCN solution, and (d) vapour diffusion (top) *vs*. literature pattern for Form III FFA **14** (bottom).[65]

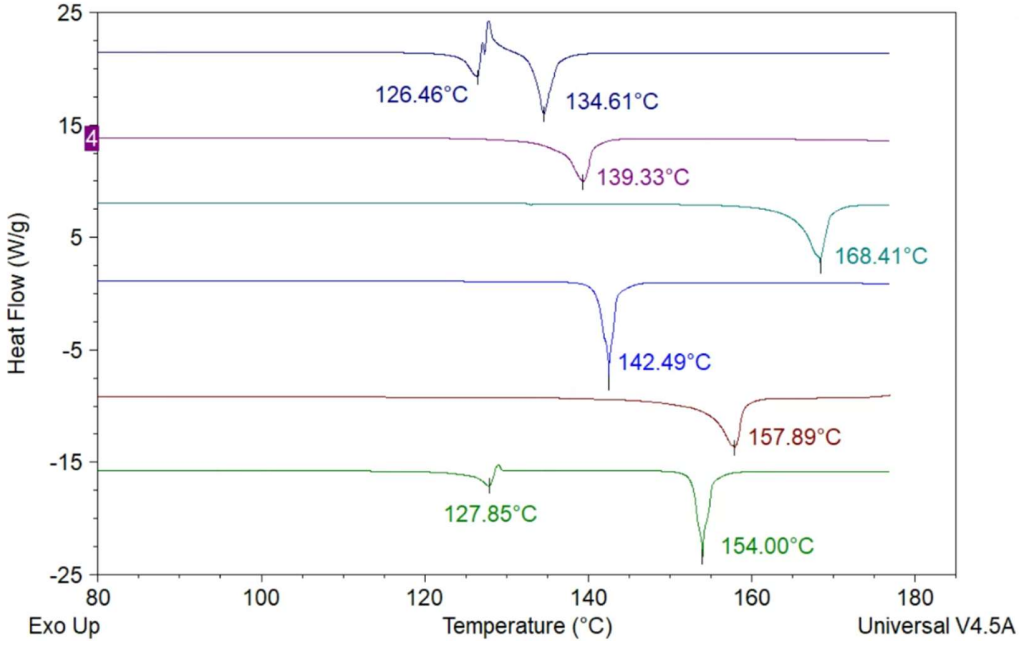


Appendix Fig 7.27. Measured PXRD pattern of FFA **14** recrystallised from EtOH (top) *vs.* literature patterns for Form III and Form I FFA **14** (bottom).[65]

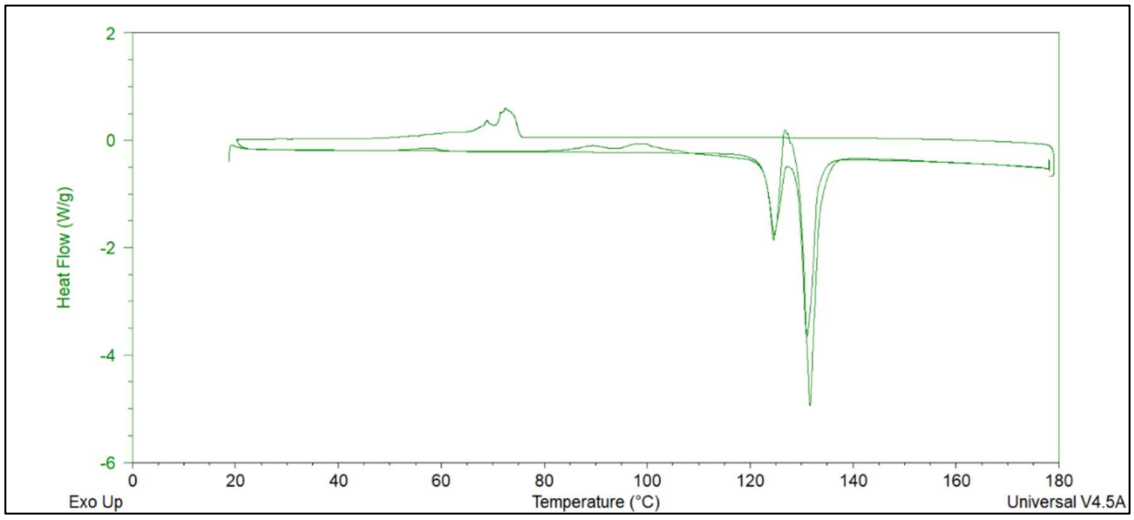


Appendix Fig 7.28. Measured PXRD patterns of FFA **14** recrystallised from (a) MeOH, and (b) chloroform (top) *vs*. literature patterns for Form III and Form IV FFA **14** (bottom).[65]

7.5 DSC Analysis



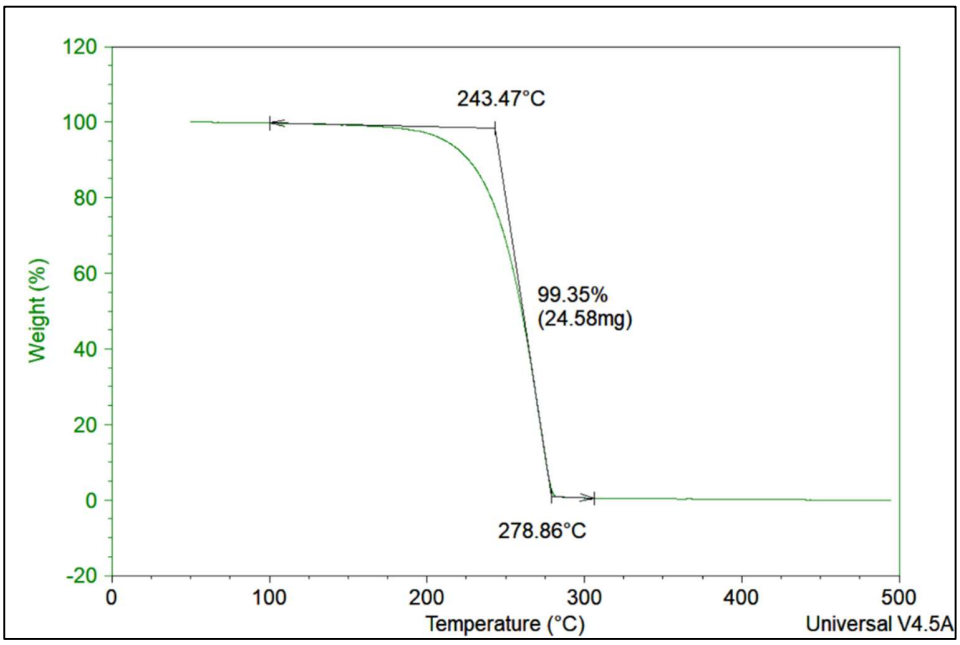
Appendix Fig 7.29. Top to bottom: DSC curves of purified and synthesised FFA **14**, Me-FA **15**, Cl-FA **16**, DF-FA **17**, MF-FA **18**, and t-Bu-FA **19**.



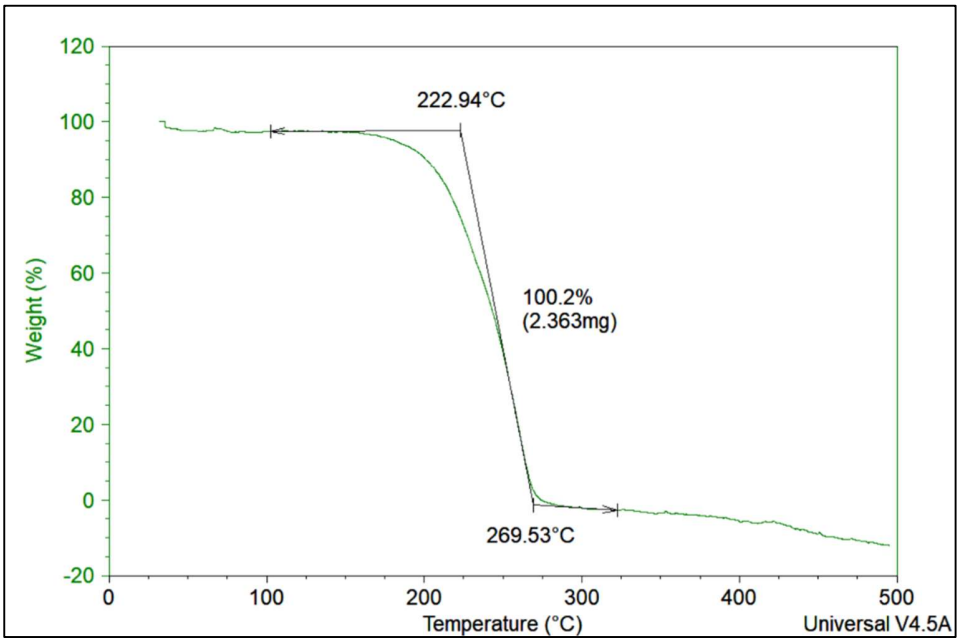
Appendix Fig 7.30. DSC curve of Form III FFA **14** heated to melting, cooled, and subsequently reheated, exhibiting the reversible transformation from Form III to Form I which was observed to be occurring during both heating stages. Such a reversible transformation is indicative, but not definitive evidence, of an enantiotropic system.

7.6 TGA Analysis

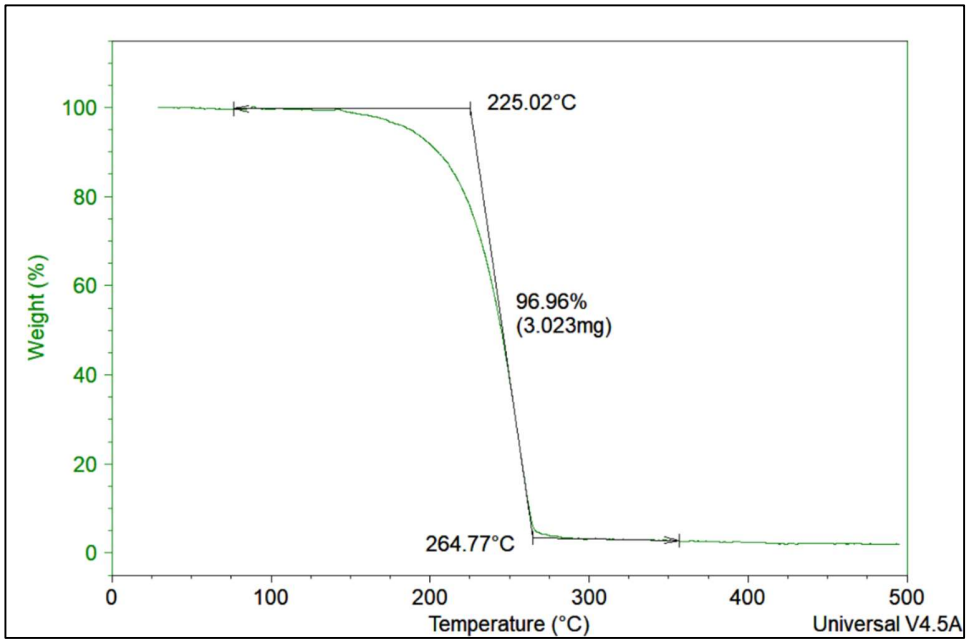
7.6.1 TGA Curves of Pure Materials



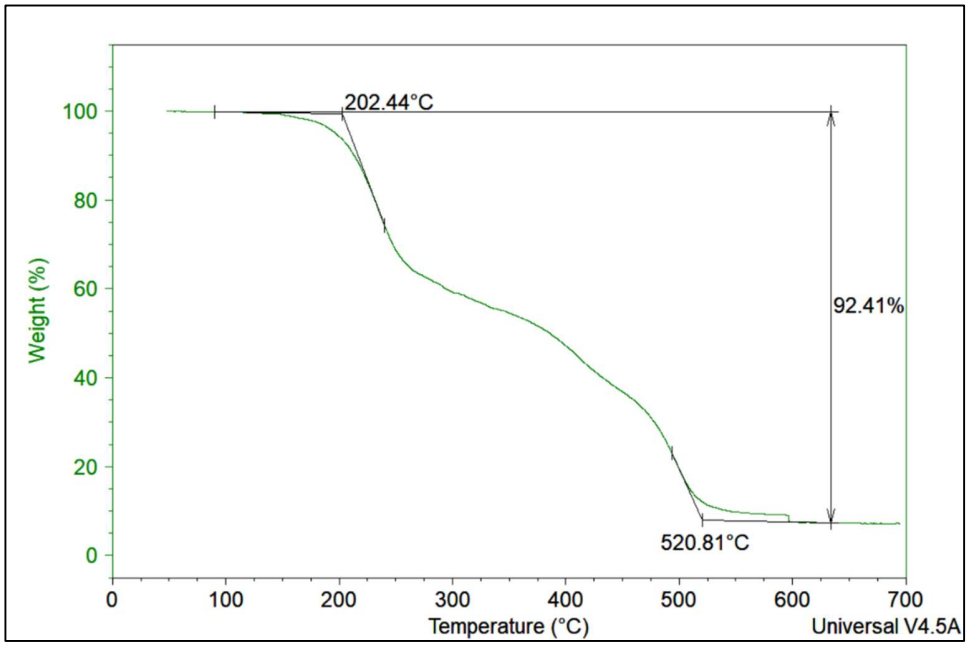
Appendix Fig 7.31. TGA curve of pure Me-FA **15**.



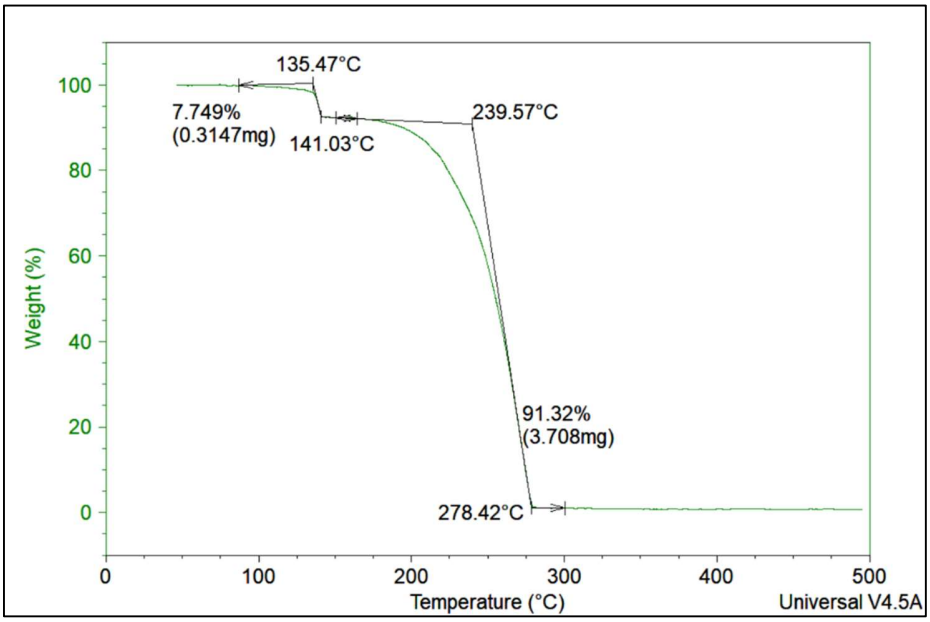
Appendix Fig 7.32. TGA curve of pure Cl-FA **16**.



Appendix Fig 7.33. TGA curve of pure DF-FA **17**.

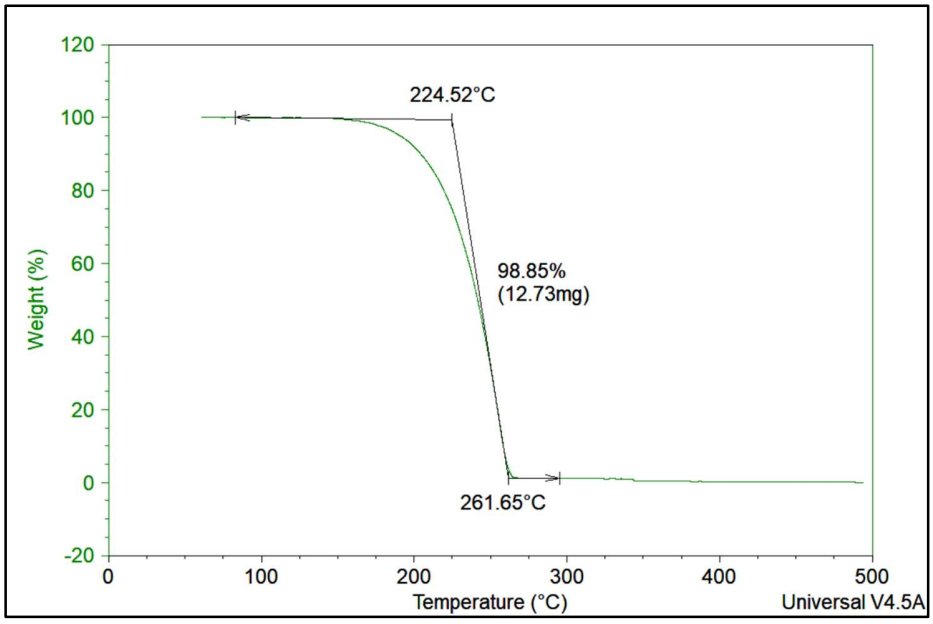


Appendix Fig 7.34. TGA curve of pure MF-FA **18**.

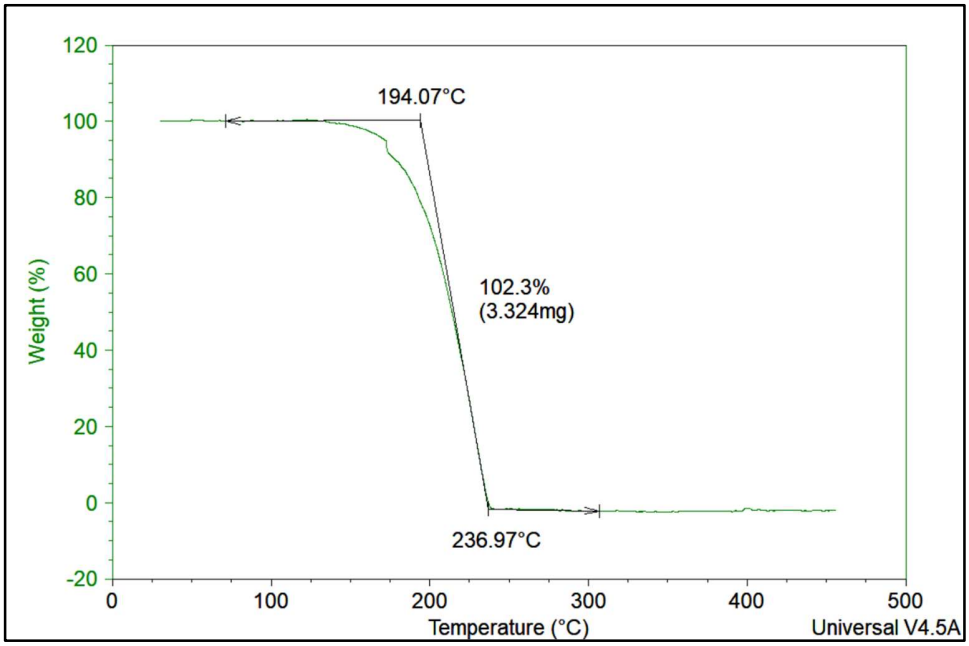


Appendix Fig 7.35. TGA curve of pure t-Bu-FA **19**.

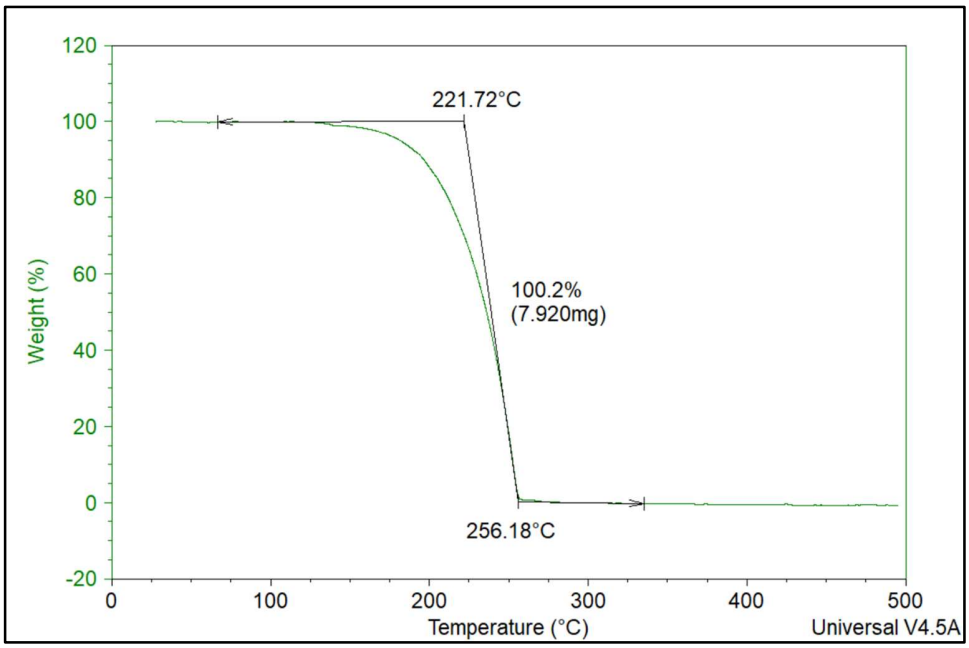
7.6.2 TGA Curves of Doped Materials



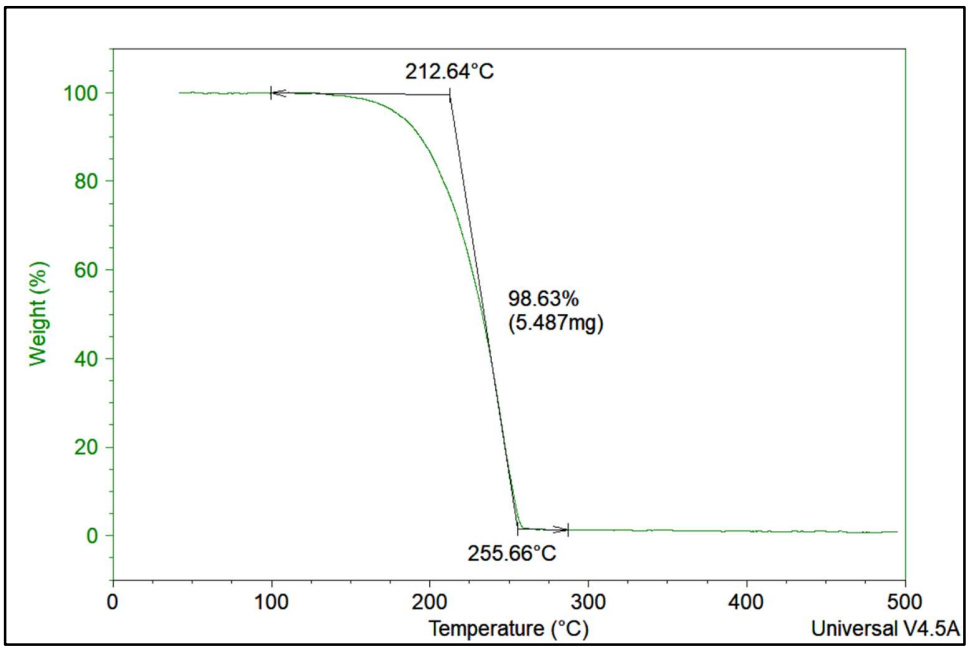
Appendix Fig 7.36. TGA curve of FFA **14** doped with 2 mol% Me-FA **15**.



Appendix Fig 7.37. TGA curve of FFA **14** doped with 3 mol% Cl-FA **16**.



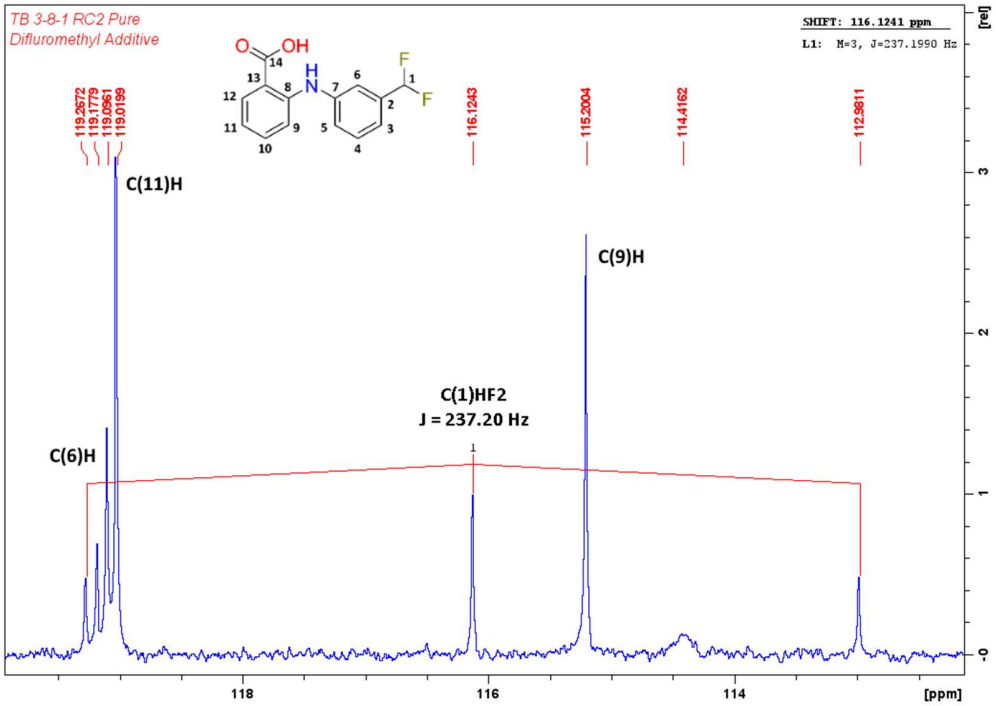
Appendix Fig 7.38. TGA curve of FFA **14** doped with 2 mol% DF-FA **17**.



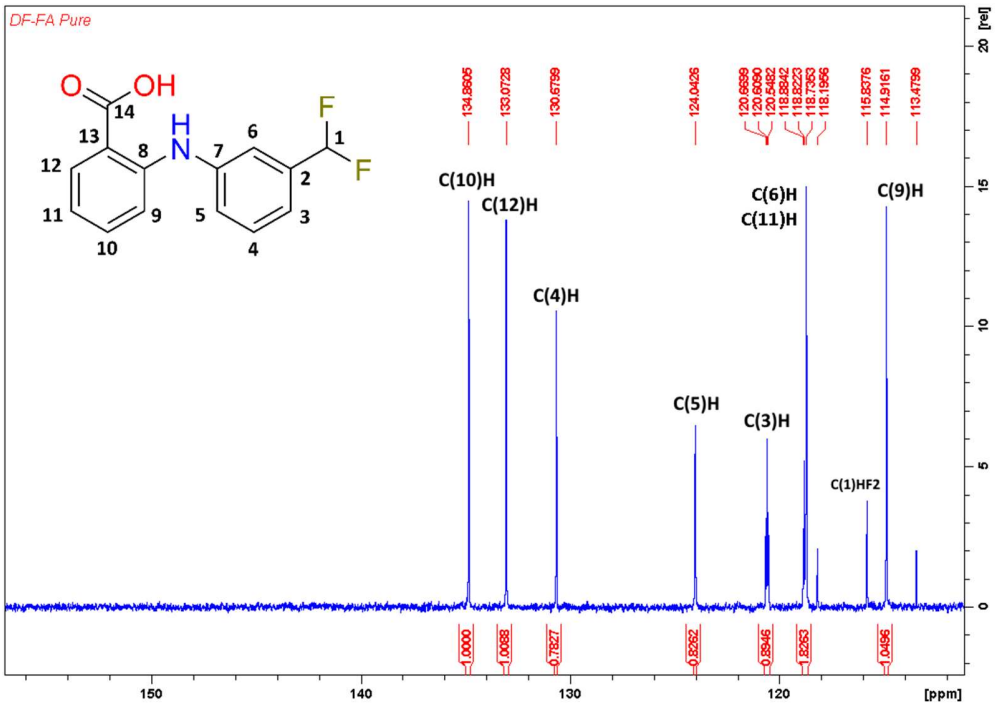
Appendix Fig 7.39. TGA curve of FFA **14** doped with 2 mol% MF-FA **18**.

7.7 Synthetic Method Development

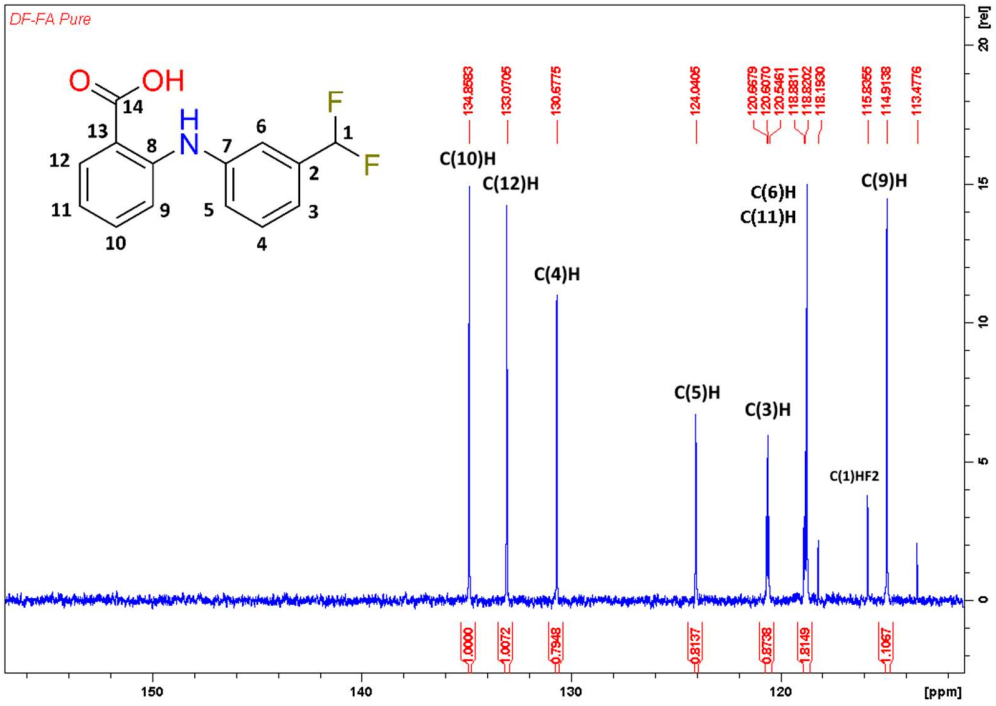
7.7.1 DF-FA **17** Additional NMR Analysis



Appendix Fig 7.40. A portion of the aromatic region of the ^{13}C NMR spectrum of DF-FA **17**, illustrating the large splitting of the C^1 carbon peak due to coupling with two geminal fluorine atoms.

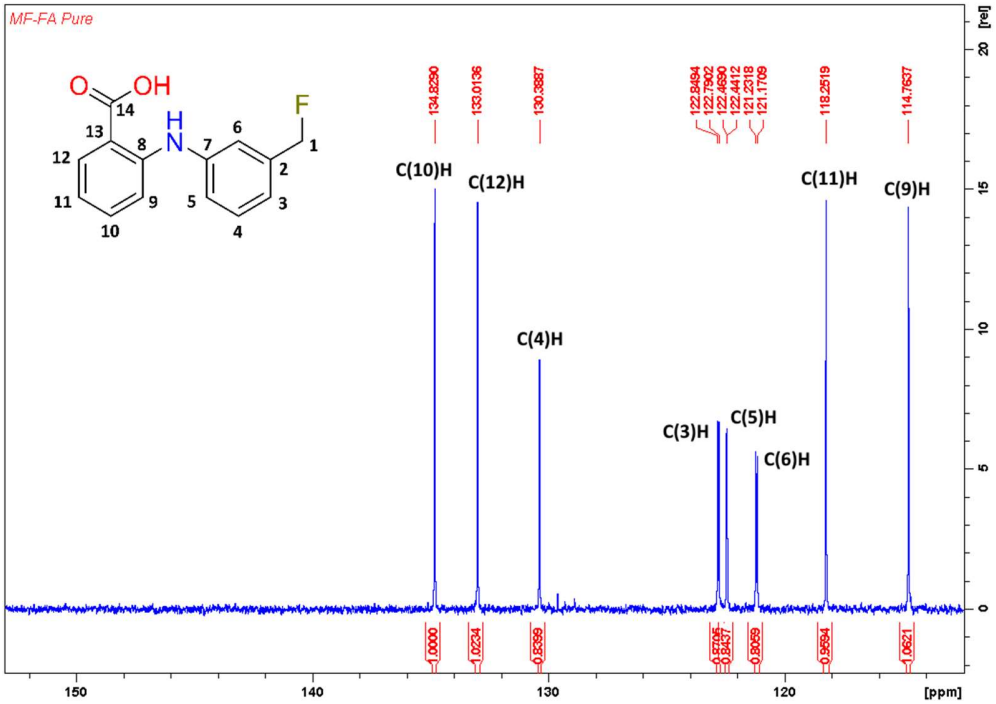


Appendix Fig 7.41. Aromatic region of the DEPT 90 NMR spectrum of DF-FA **17**, with labelled peaks.

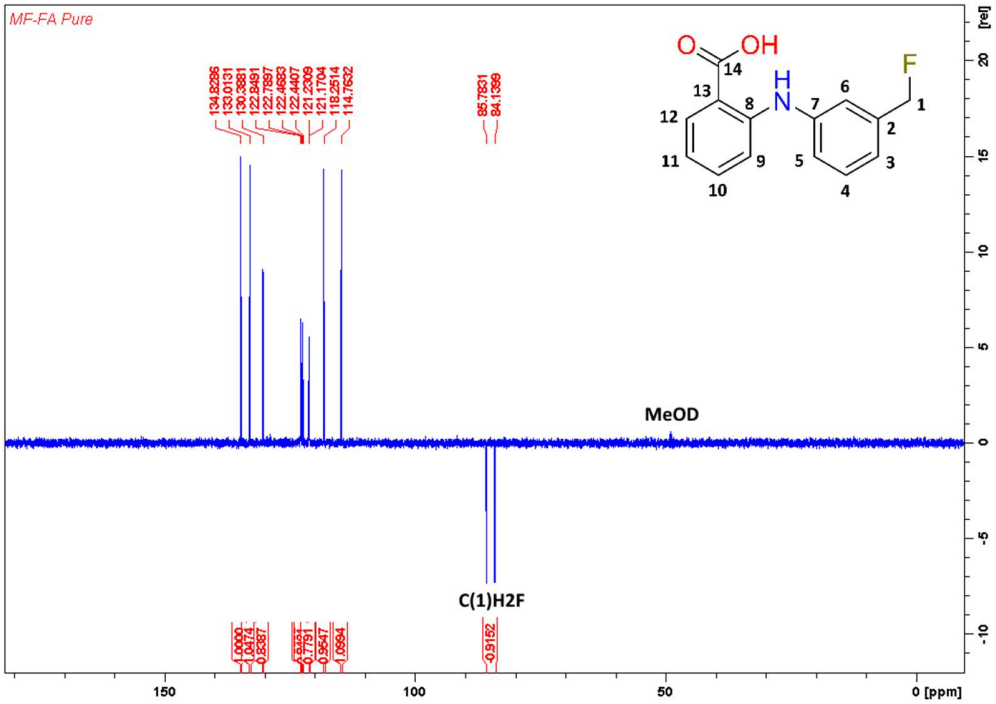


Appendix Fig 7.42. Aromatic region of the DEPT 135 NMR spectrum of DF-FA **17**, with labelled peaks.

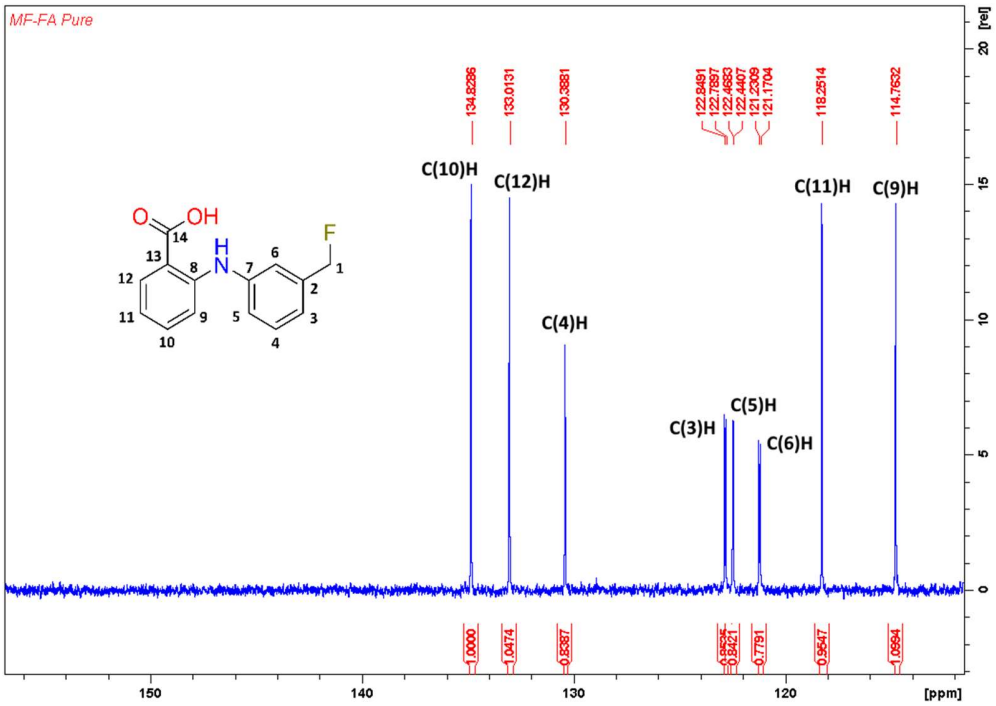
7.7.2 MF-FA **18** Additional NMR Analysis



Appendix Fig 7.43. Aromatic region of the DEPT 90 NMR spectrum of MF-FA **18**, with labelled peaks.

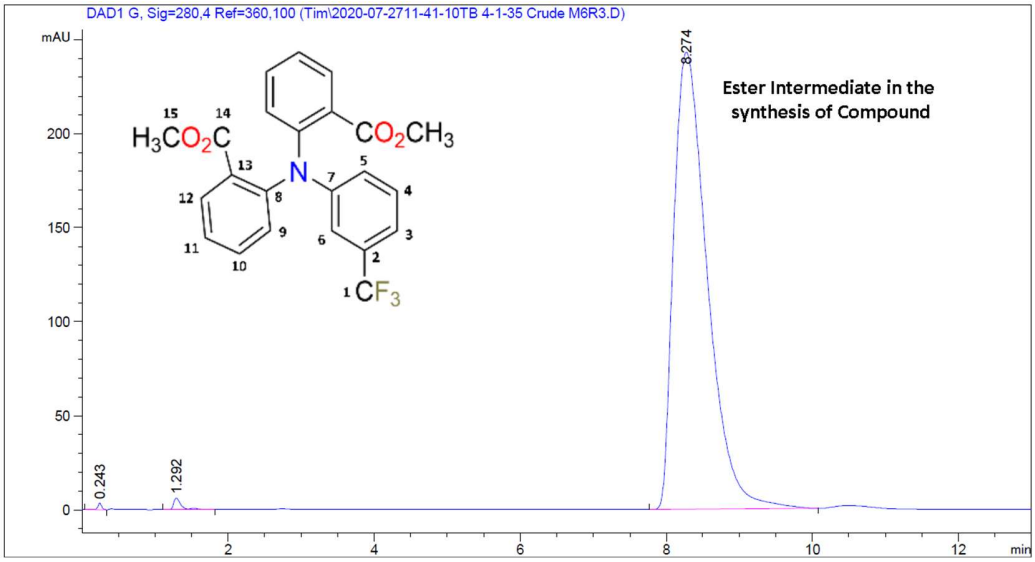


Appendix Fig 7.44. Full DEPT 135 NMR spectrum of MF-FA **18**, with labelled peaks.

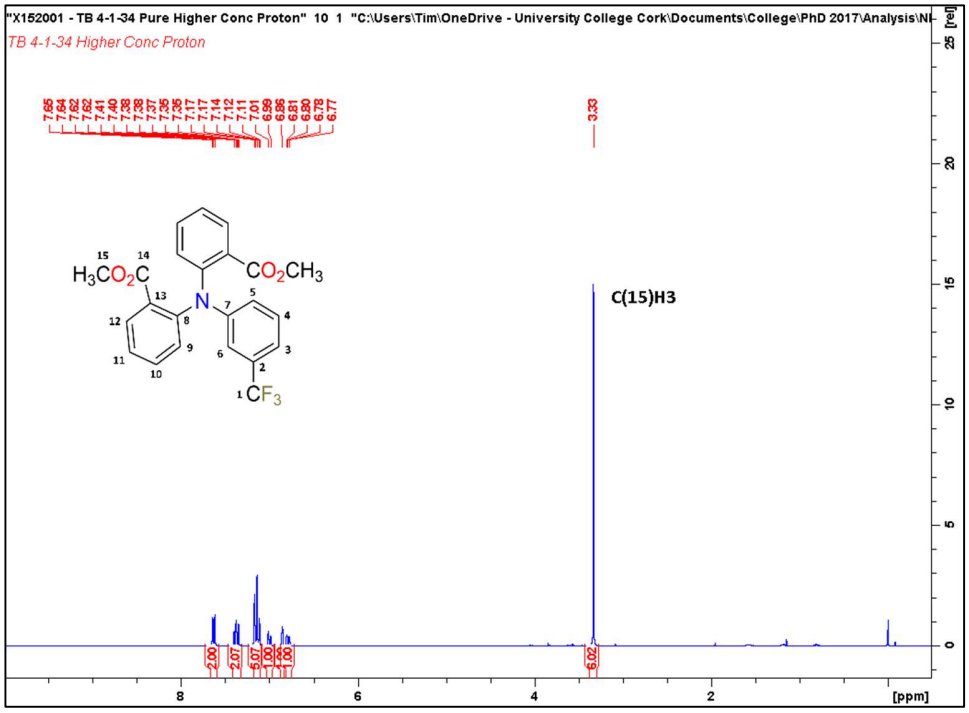


Appendix Fig 7.45. Aromatic region of the DEPT 135 NMR spectrum of MF-FA **18**, with labelled peaks.

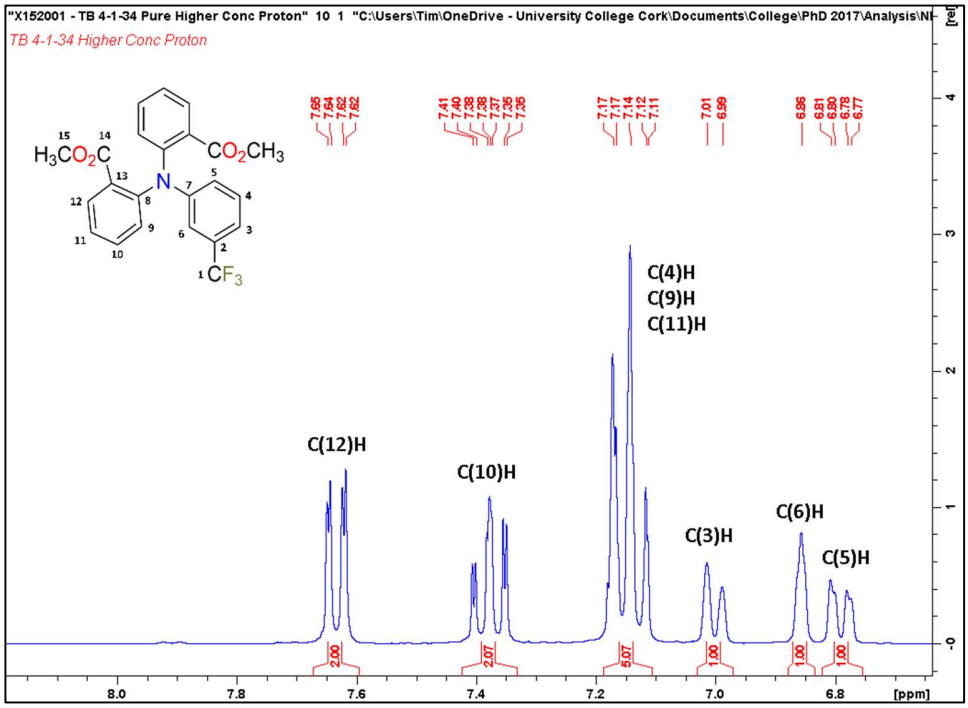
7.7.3 Compound **27** (Diacid Triaryl Synthesis Ester Intermediate) Analysis



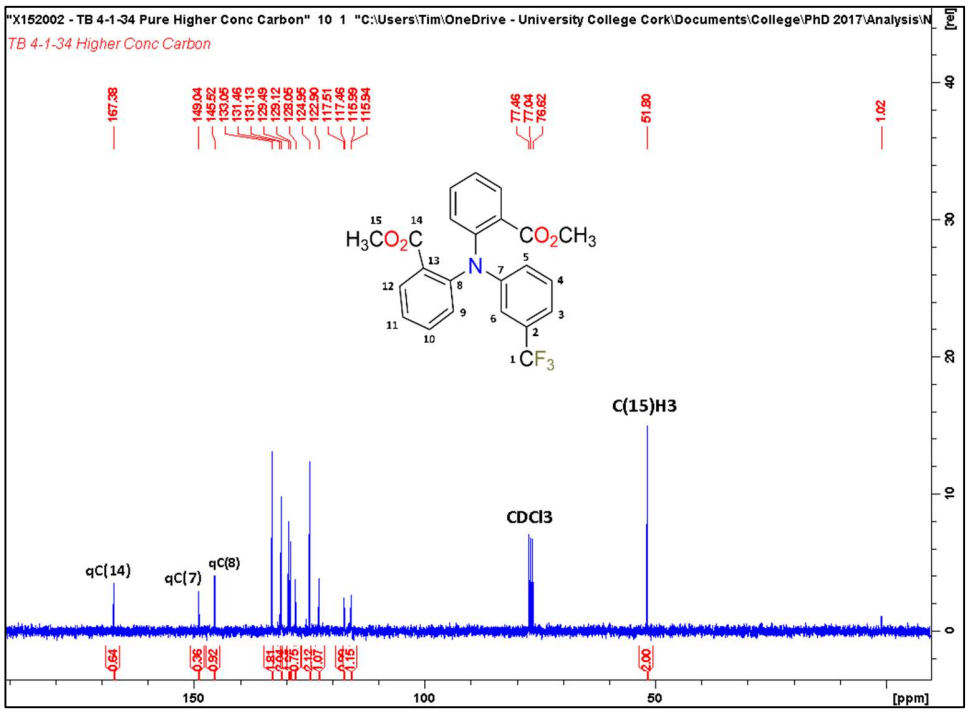
Appendix Fig 7.46. HPLC trace of compound **27**, the triaryl ester intermediate in the synthetic route to compound **25**.



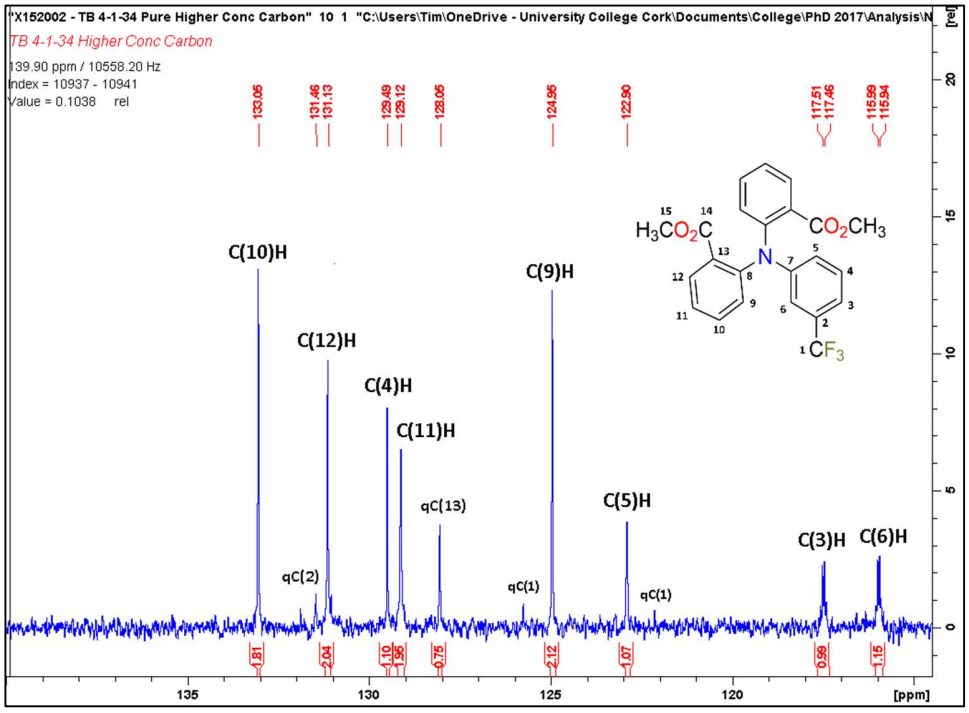
Appendix Fig 7.47. Full ^{1}H NMR spectrum of compound **27**, the triaryl ester intermediate in the synthetic route to compound **25**.



Appendix Fig 7.48. Aromatic region of the ^{1}H NMR spectrum of compound **27**, the triaryl ester intermediate in the synthetic route to compound **25**.

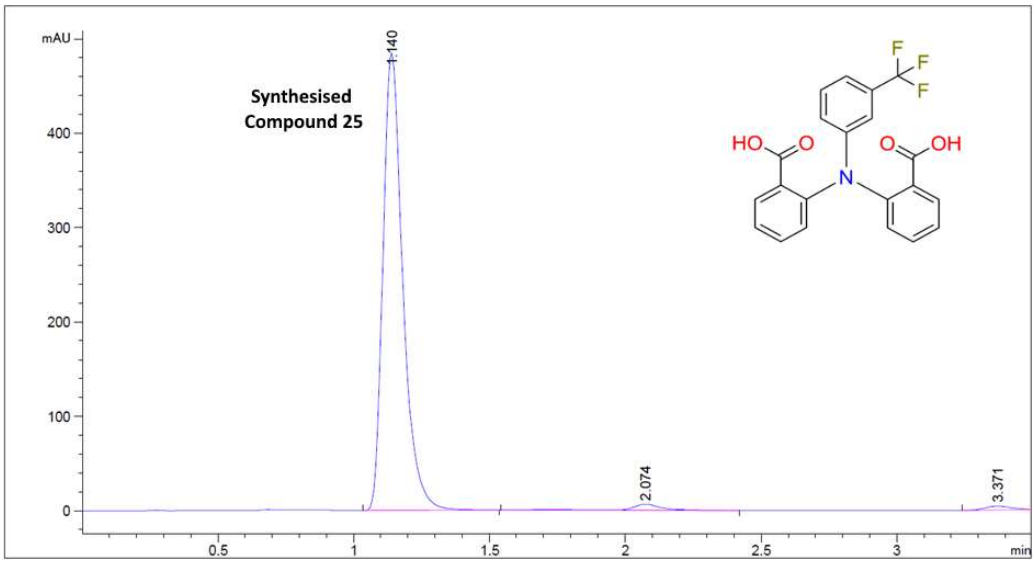


Appendix Fig 7.49. Full ^{13}C NMR spectrum of compound **27**, the triaryl ester intermediate in the synthetic route to compound **25**.

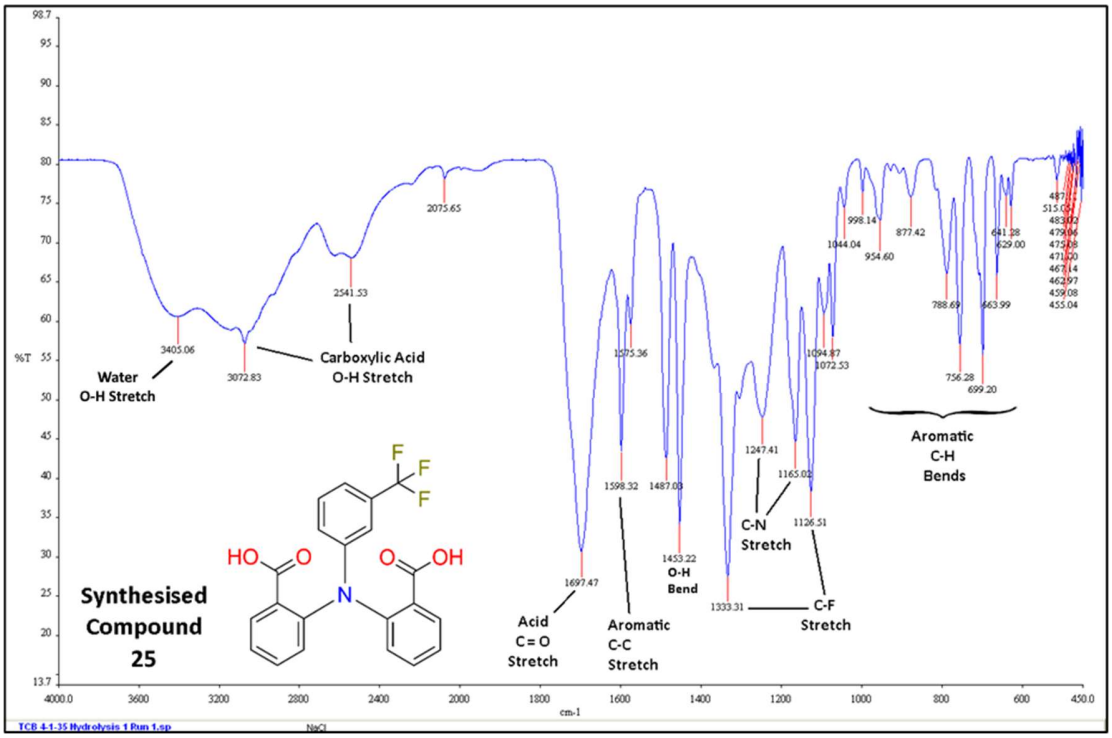


Appendix Fig 7.50. Aromatic region of the ^{13}C NMR spectrum of compound **27**, the triaryl ester intermediate in the synthetic route to compound **25**.

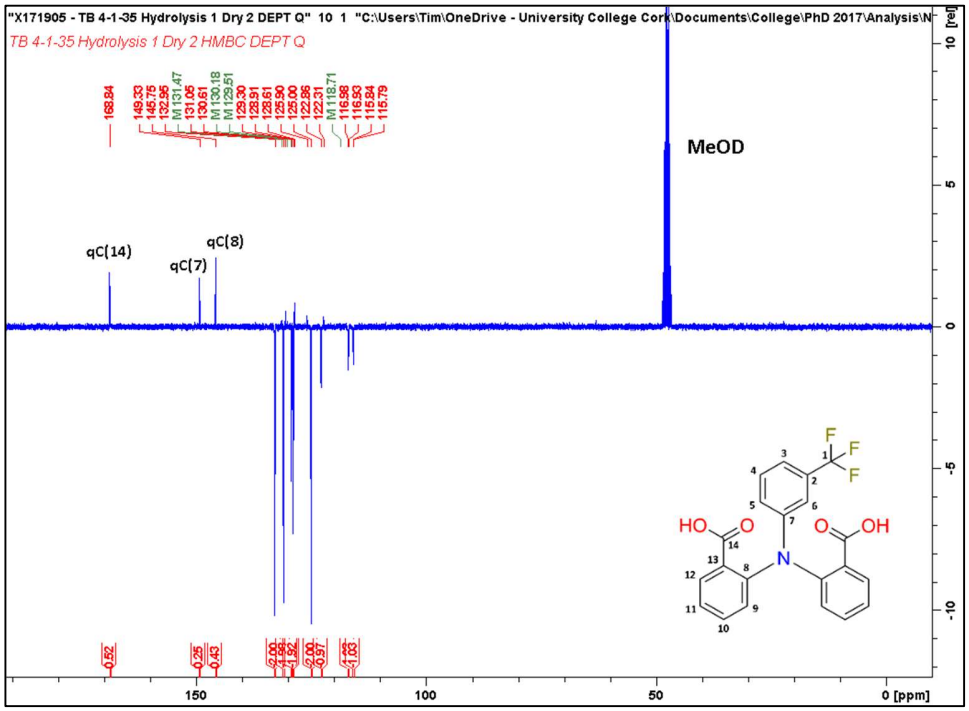
7.7.4 Diacid Triaryl Compound **25** Synthetic Product Analysis



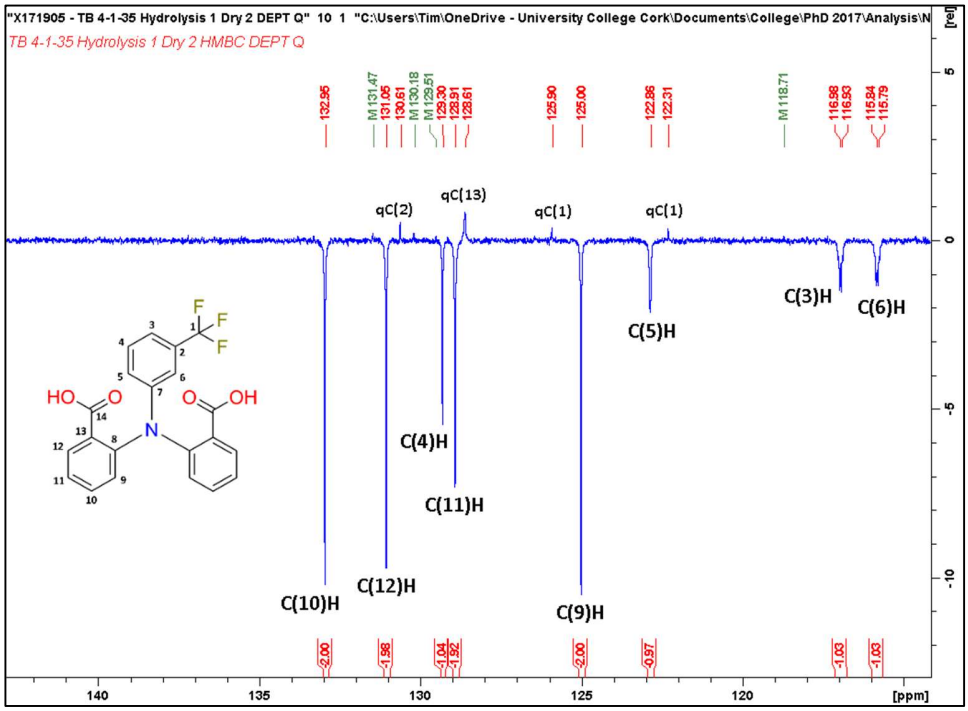
Appendix Fig 7.51. HPLC trace of the product of the triaryl compound **25** synthesis.



Appendix Fig 7.52. IR spectrum of the product of the triaryl compound **25** synthesis.



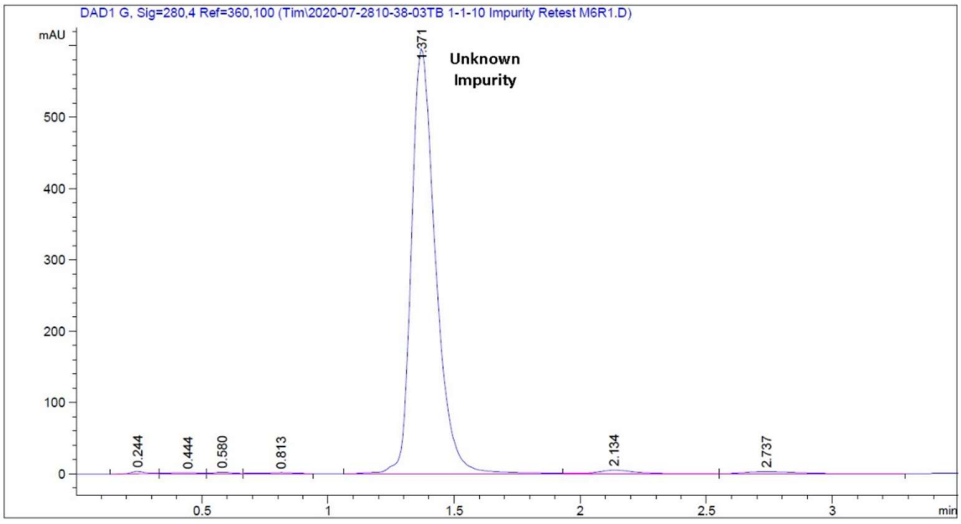
Appendix Fig 7.53. Full DEPT 135q NMR spectrum of the product of the triaryl compound **25** synthesis, with labelled peaks.



Appendix Fig 7.54. Aromatic region of the DEPT 135q NMR spectrum of the product of the triaryl compound **25** synthesis, with labelled peaks.

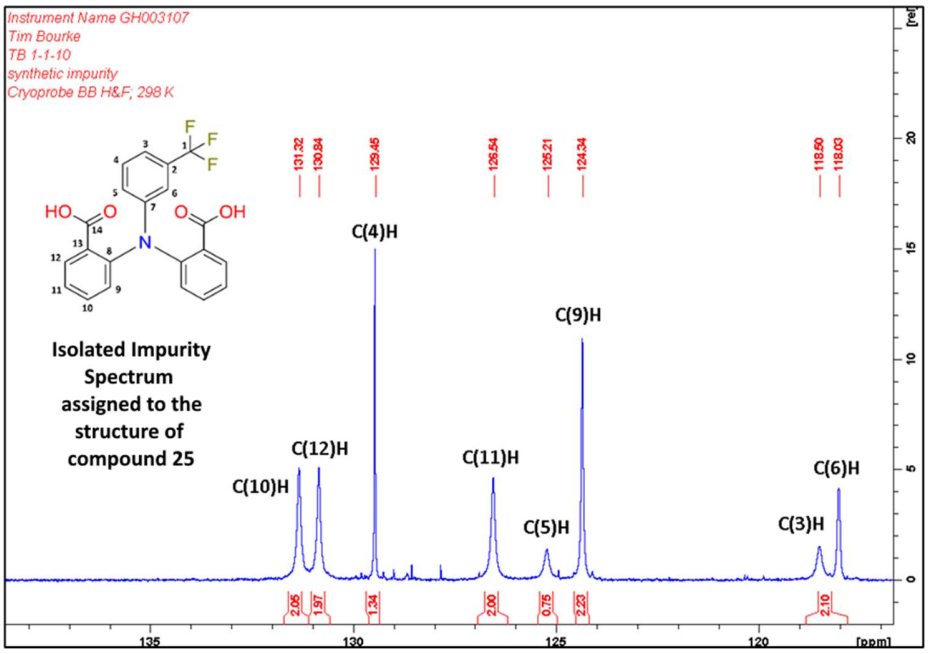
7.8 Isolated Synthetic Impurity Analysis

7.8.1 HPLC Trace of Isolated Impurity

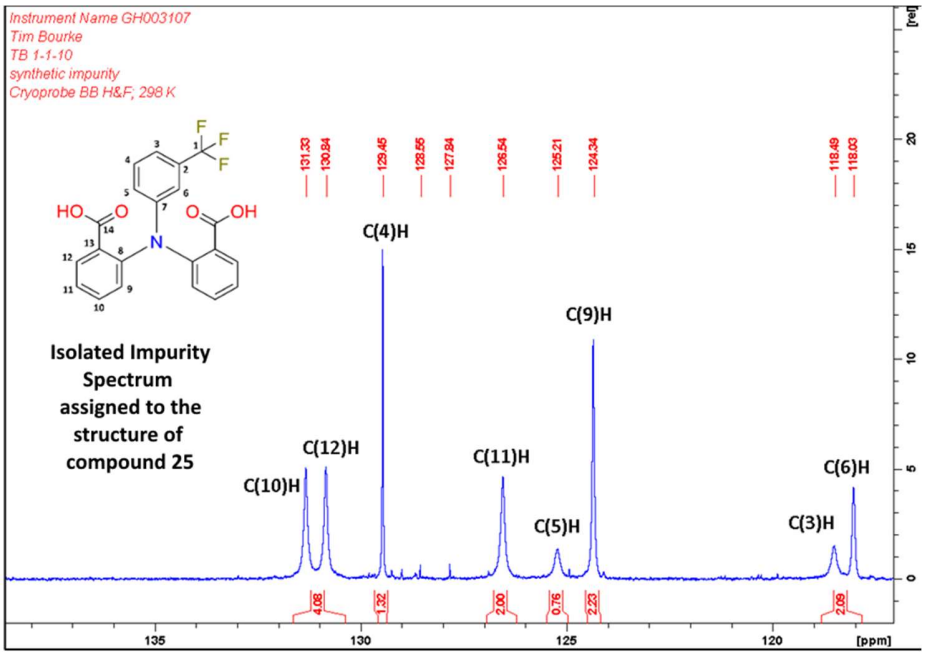


Appendix Fig 7.55. HPLC trace of isolated synthetic impurity observed in the crude product of FFA **14**.

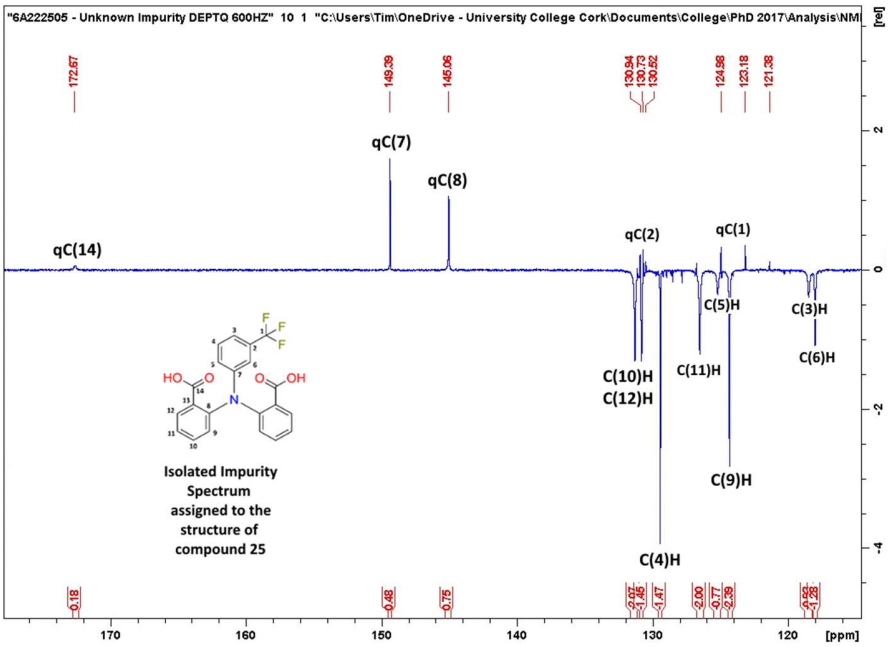
7.8.2 Spectra Assigned to Structure of Compound **25**



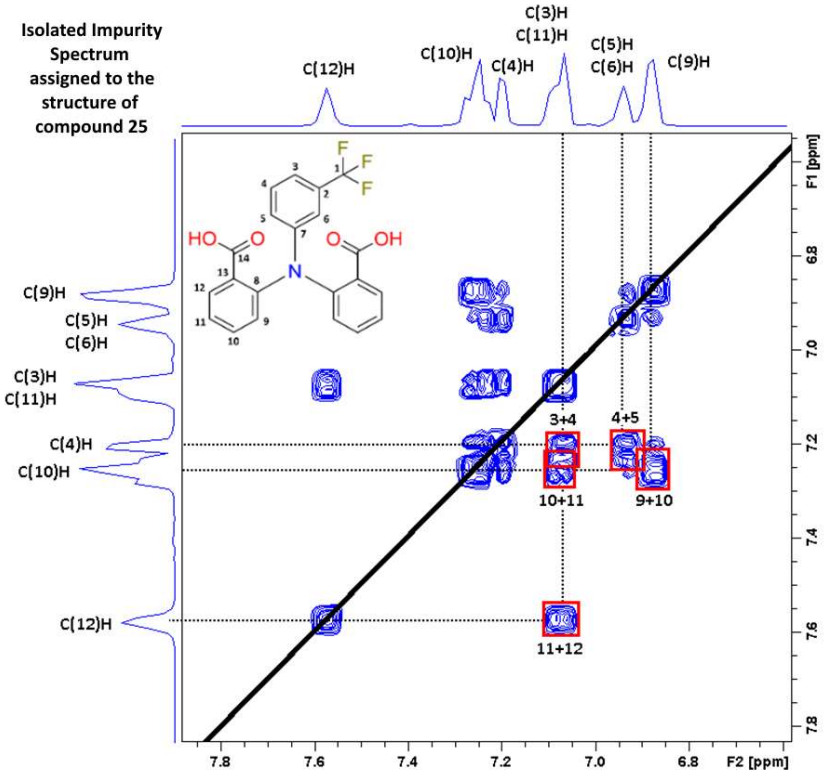
Appendix Fig 7.56. Aromatic region of the DEPT 90 NMR spectrum of isolated synthetic impurity, with peaks assigned based on the structure of compound **25**.



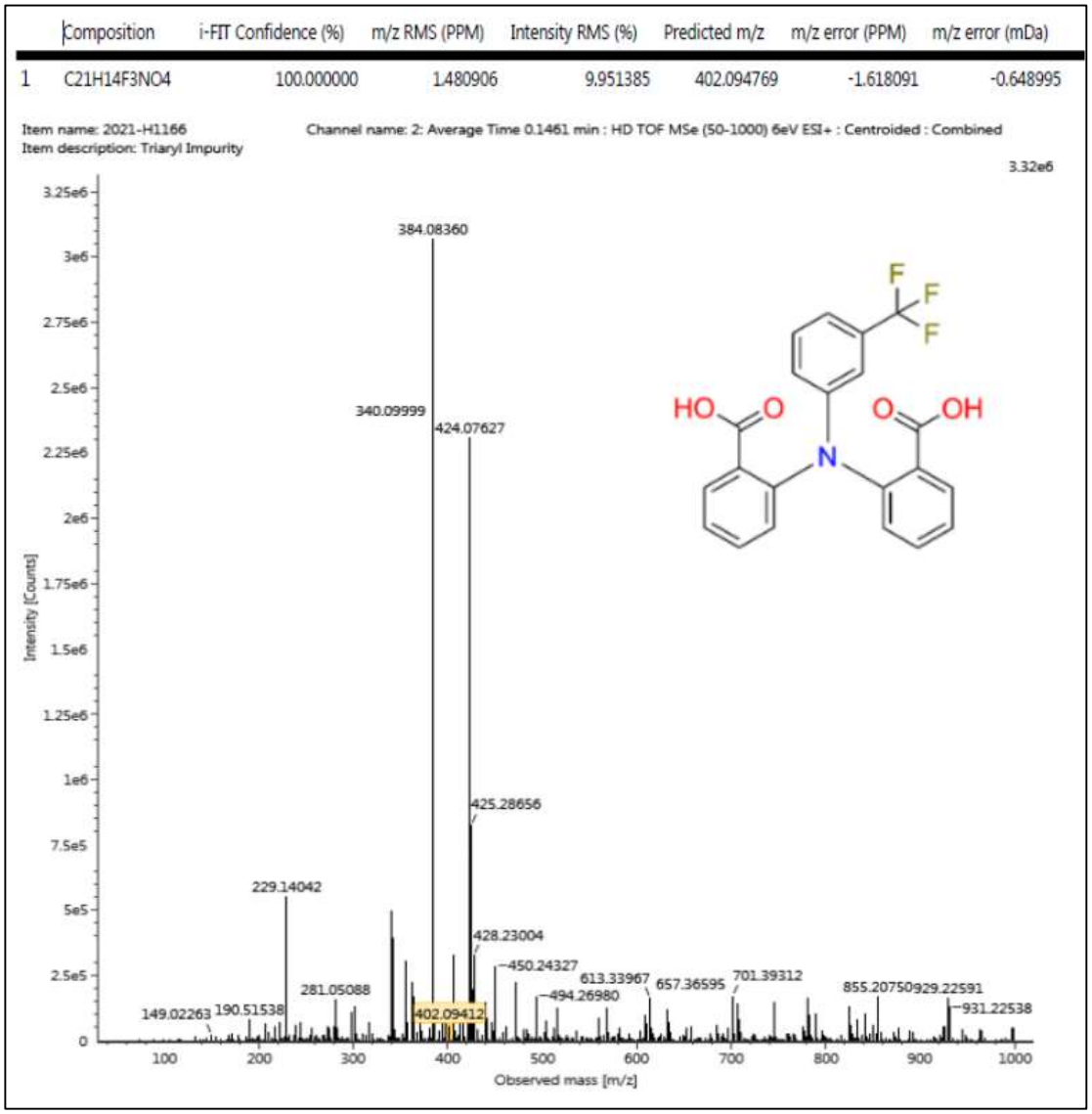
Appendix Fig 7.57. Aromatic region of the DEPT 135 NMR spectrum of isolated synthetic impurity, with peaks assigned based on the structure of compound **25**.



Appendix Fig 7.58. Aromatic region of the DEPT 135q NMR spectrum of isolated synthetic impurity, with peaks assigned based on the structure of compound **25**.

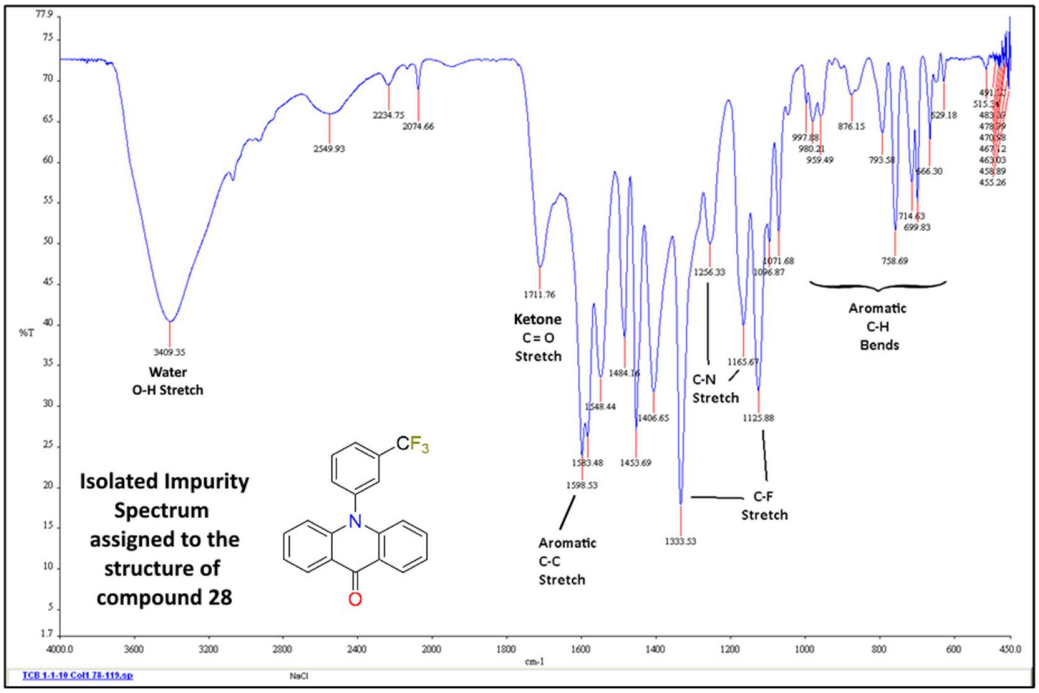


Appendix Fig 7.59. Aromatic region of the COSY NMR spectrum of isolated synthetic impurity with peaks and coupling assigned based on the structure of compound **25**.

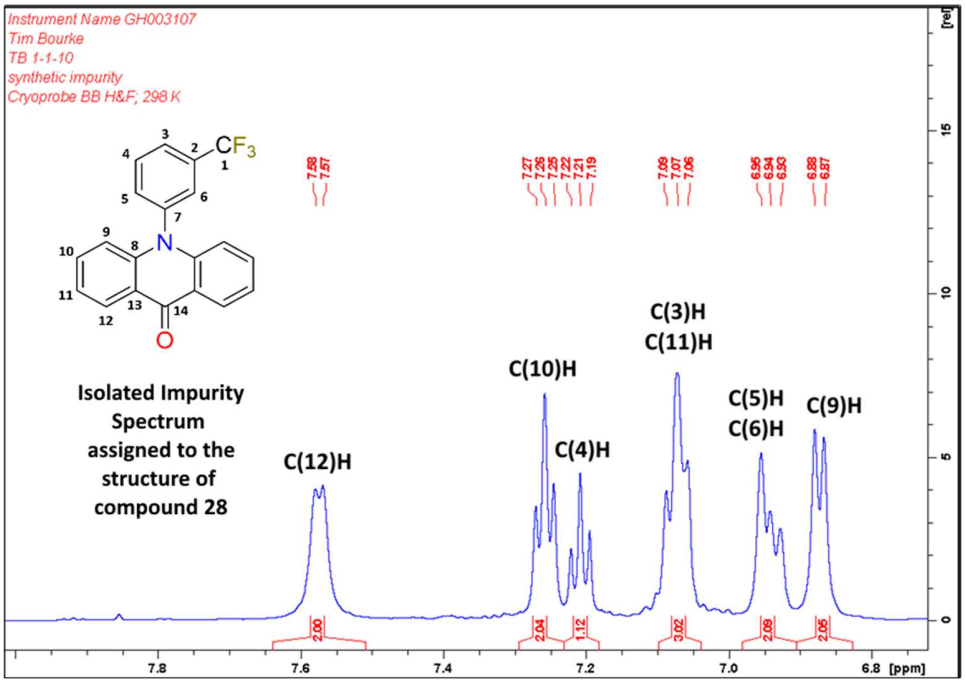


Appendix Fig 7.60. Mass spectrometry analysis of isolated impurity, identifying the ionised molecular mass of compound **25** with 100% i-FIT confidence.

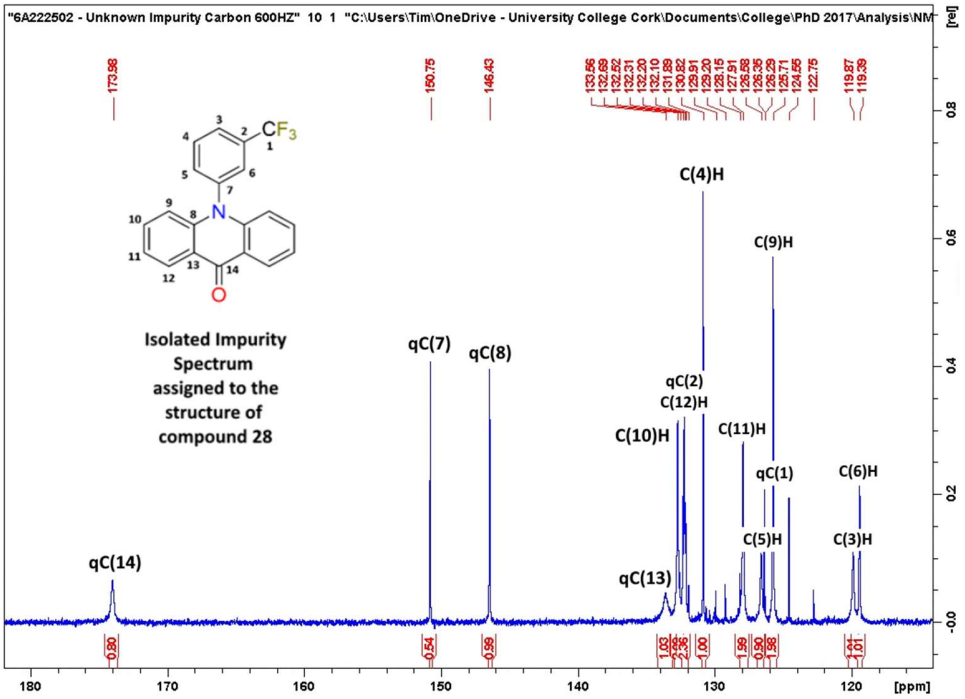
7.8.3 Spectra Assigned to Structure of Compound **28**



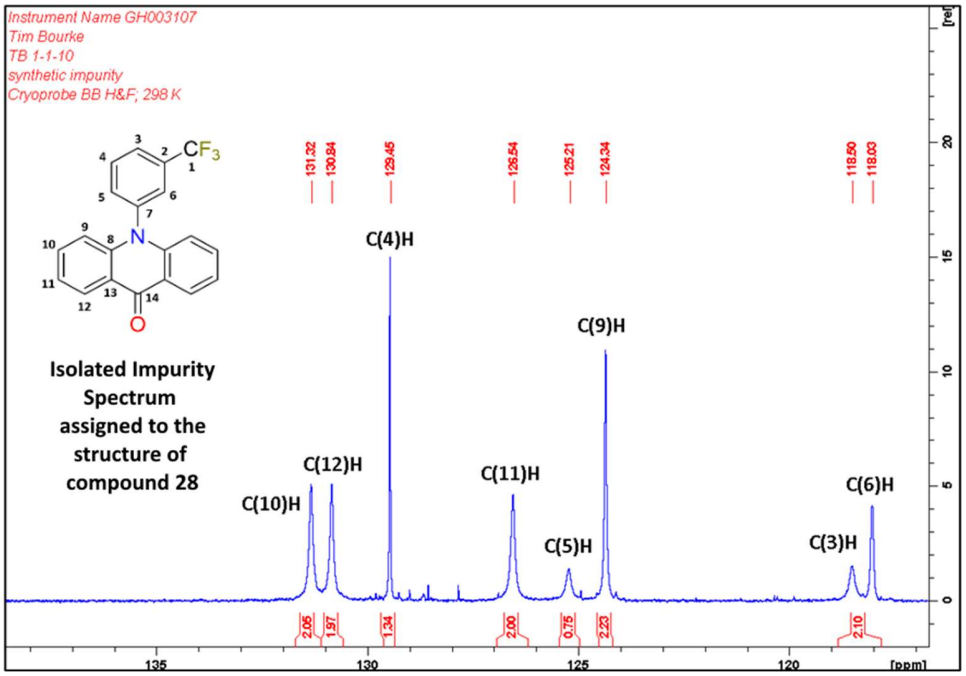
Appendix Fig 7.61. IR spectrum of isolated synthetic impurity observed in the crude product of FFA **14**.



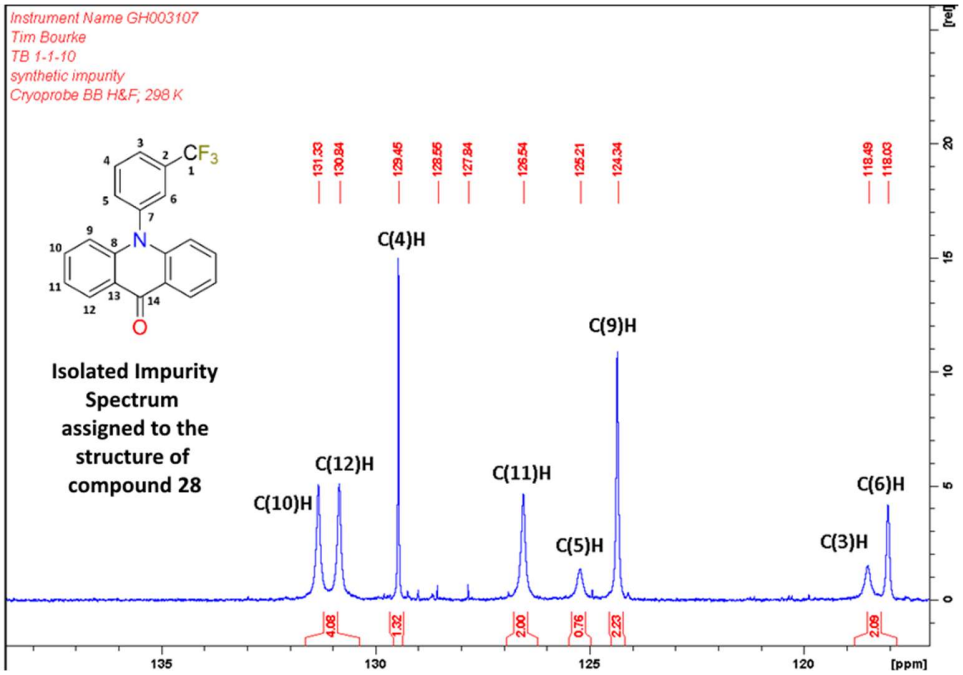
Appendix Fig 7.62. Aromatic region of the ^{1}H NMR spectrum of isolated synthetic impurity, with peaks assigned based on the structure of compound **28**.



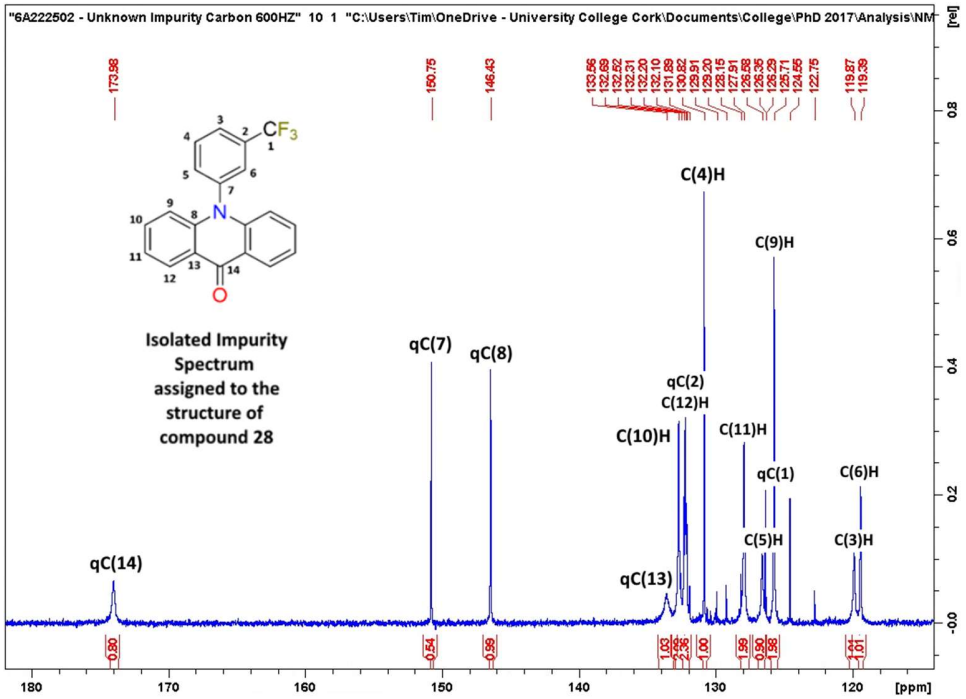
Appendix Fig 7.63. Aromatic region of the ^{13}C NMR spectrum of isolated synthetic impurity with peaks assigned based on the structure of compound **28**.



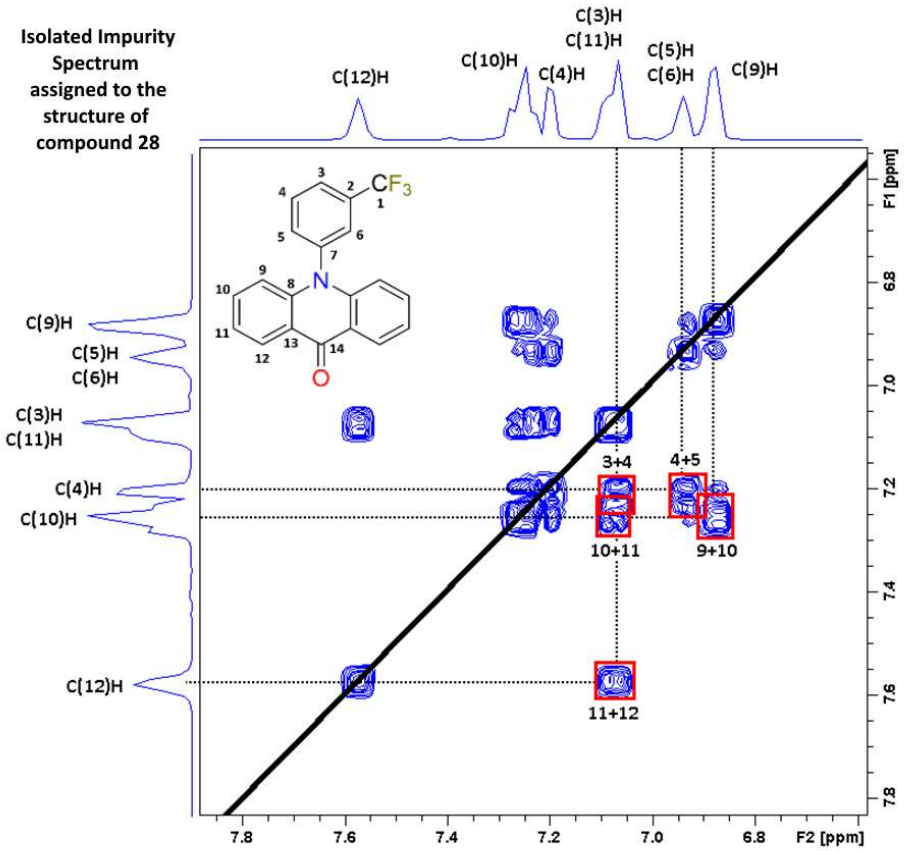
Appendix Fig 7.64. Aromatic region of the DEPT 90 NMR spectrum of isolated synthetic impurity, with peaks assigned based on the structure of compound **28**.



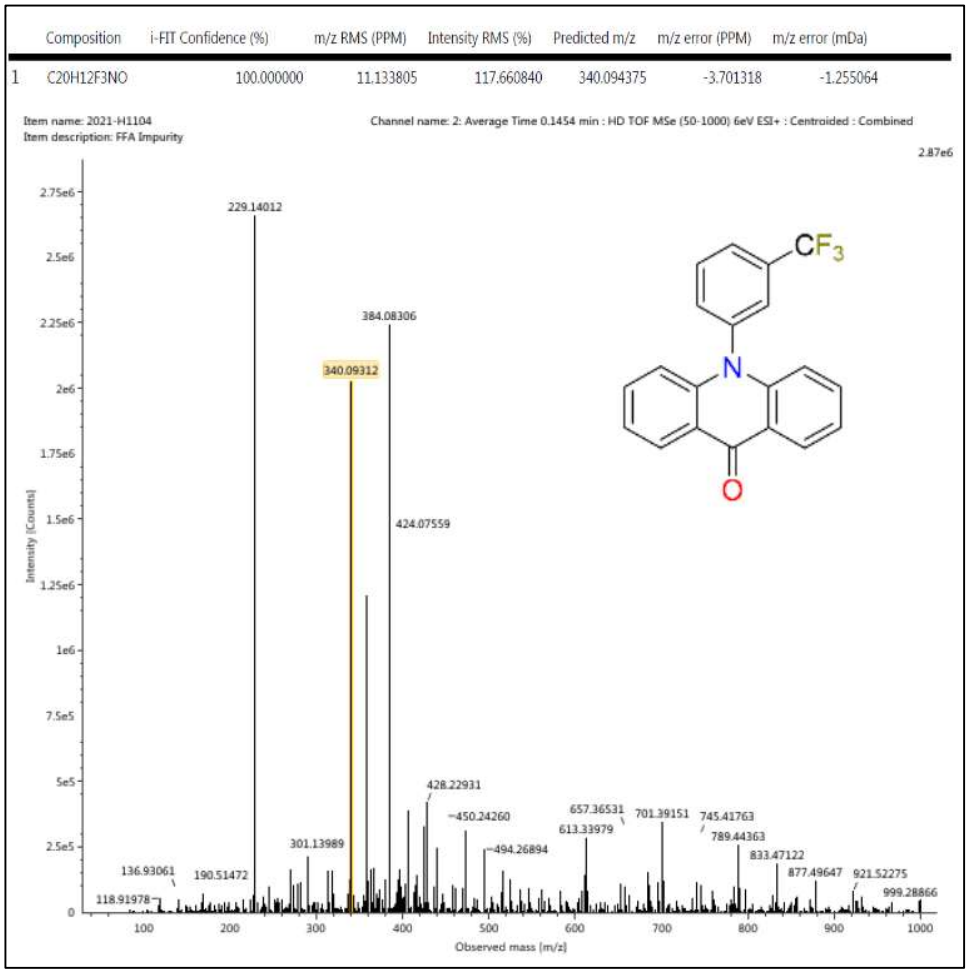
Appendix Fig 7.65. Aromatic region of the DEPT 135 NMR spectrum of isolated synthetic impurity, with peaks assigned based on the structure of compound **28**.



Appendix Fig 7.66. Aromatic region of the DEPT 135q NMR spectrum of isolated synthetic impurity, with peaks assigned based on the structure of compound **28**.



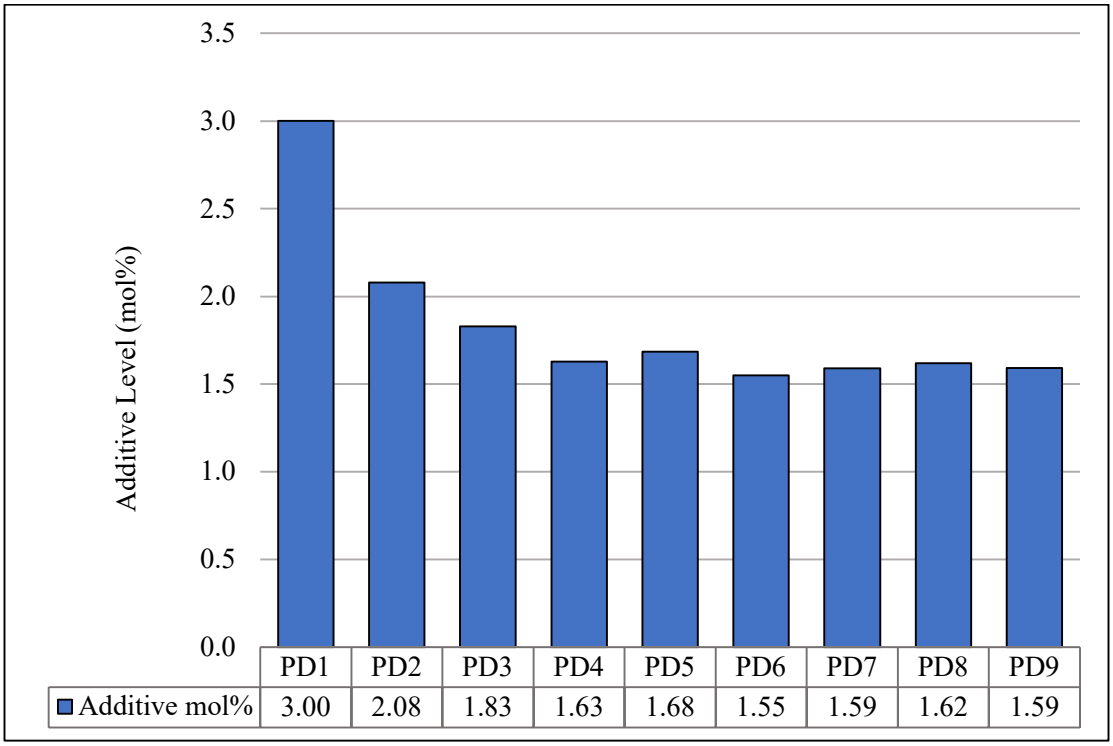
Appendix Fig 7.67. Aromatic region of the COSY NMR spectrum of isolated synthetic impurity, with peaks and coupling assigned based on the structure of compound **28**.



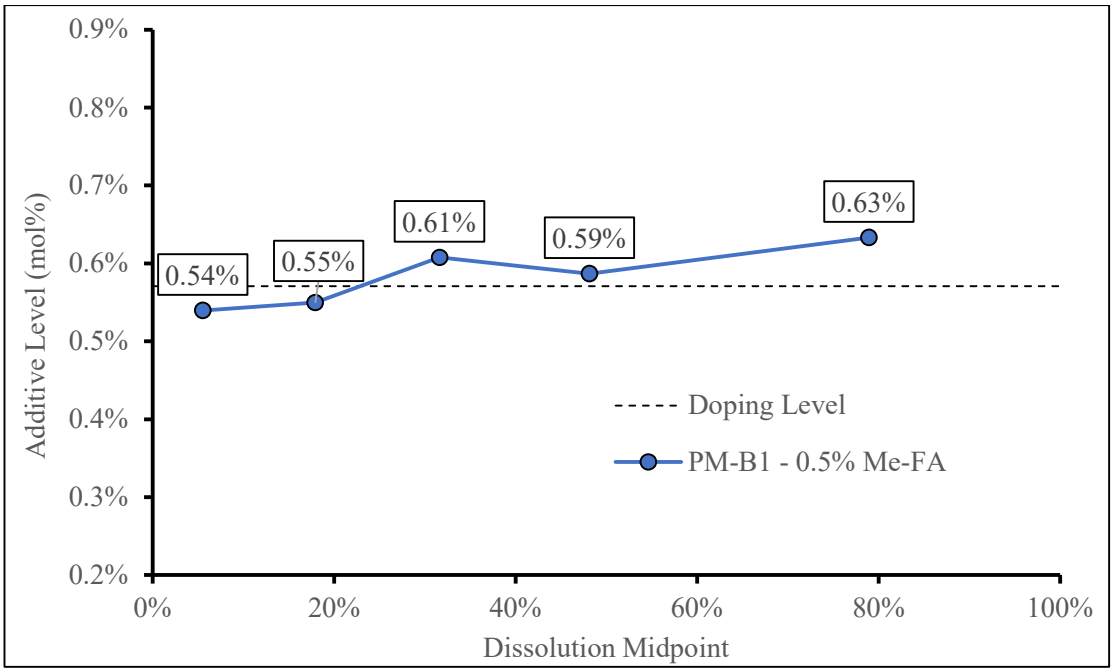
Appendix Fig 7.68. Mass spectrometry analysis of isolated impurity, identifying the ionised molecular mass of compound **28** with 100% i-FIT confidence.

7.9 Partial Dissolution Plots

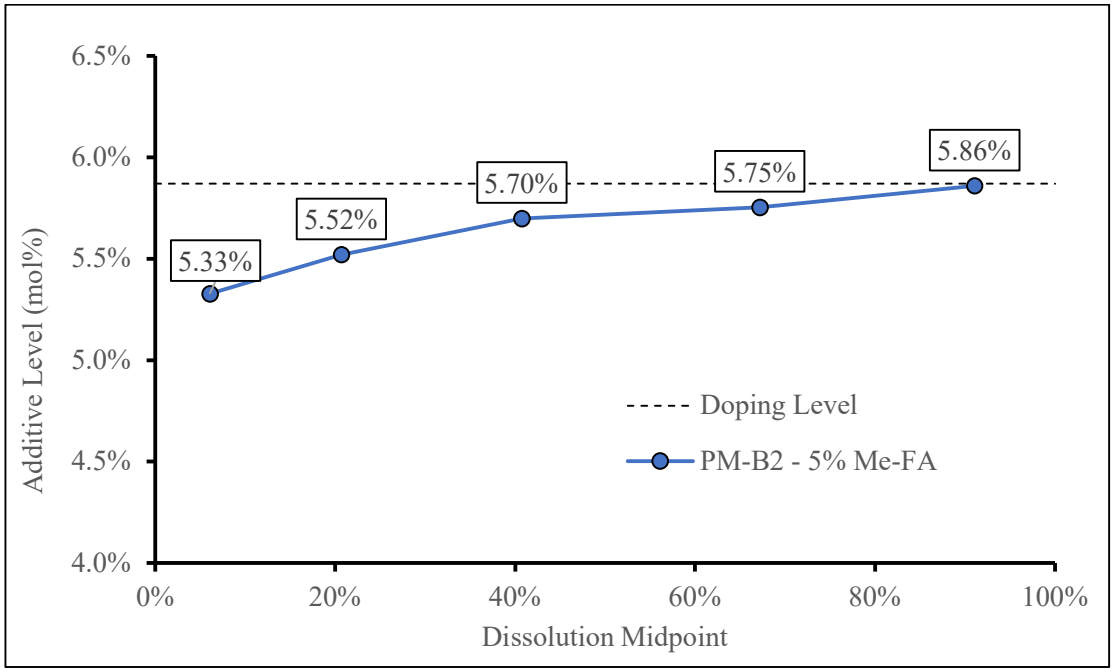
7.9.1 Additional Additive Distribution Plots



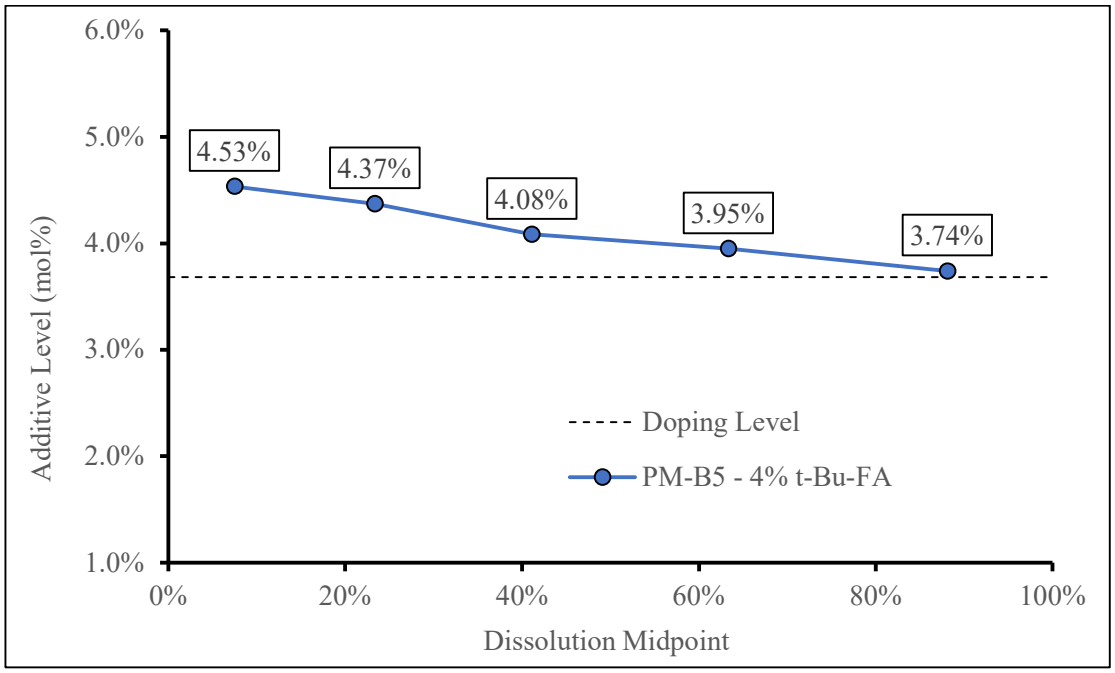
Appendix Fig 7.69. Level of additive measured in each dissolution stage of Secondary-2 crystals during secondary method development process.



Appendix Fig 7.70. Plot of additive level *vs.* dissolution midpoint of PM-B1 crystals compared to the doping level.

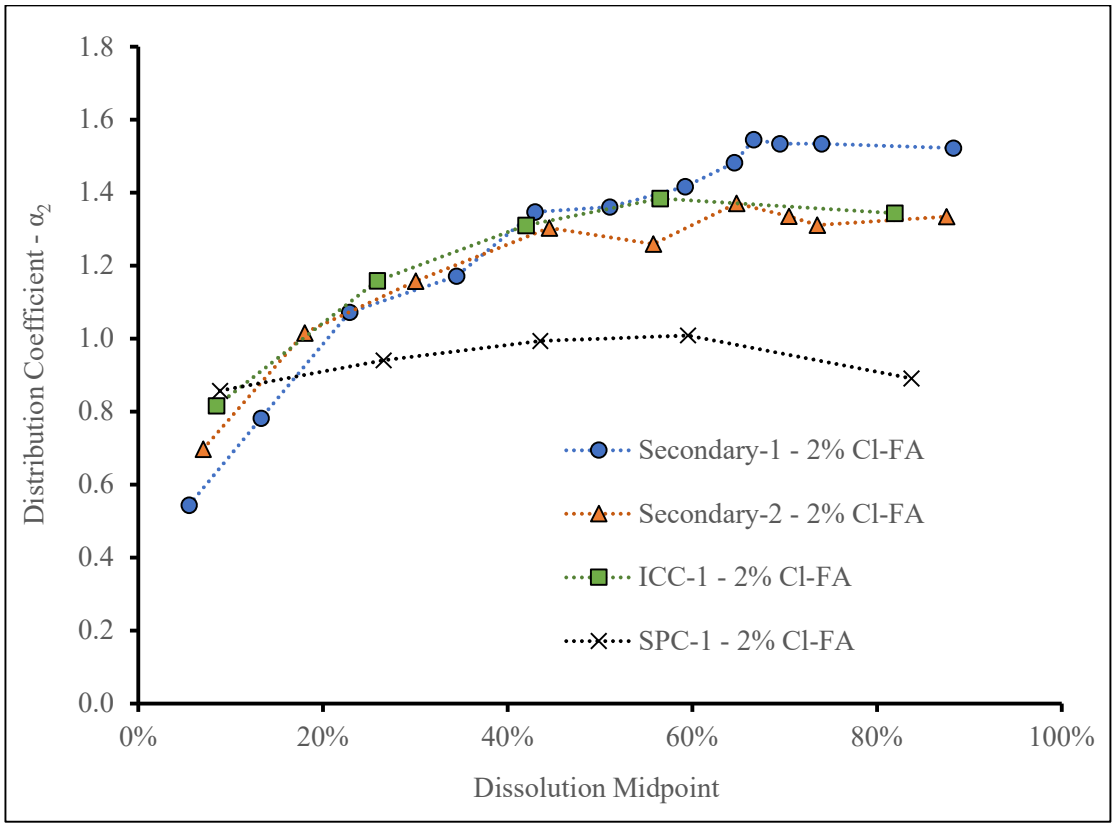


Appendix Fig 7.71. Plot of additive level *vs.* dissolution midpoint of PM-B2 crystals compared to the doping level.

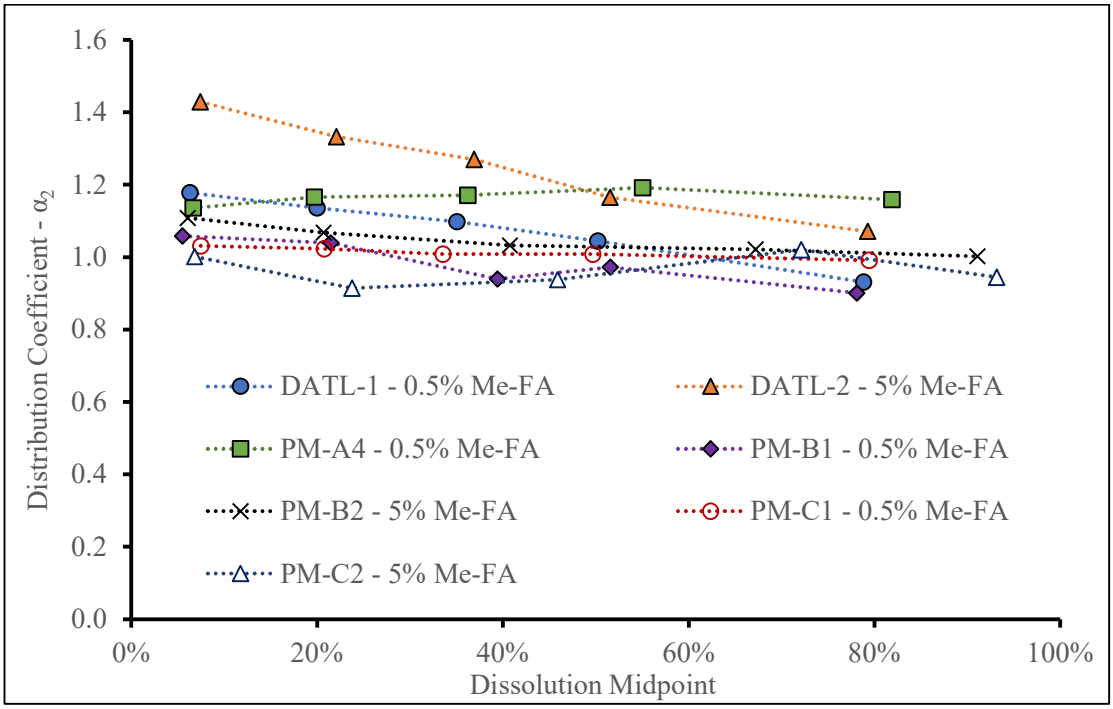


Appendix Fig 7.72. Plot of additive level *vs.* dissolution midpoint of PM-B5 crystals compared to the doping level.

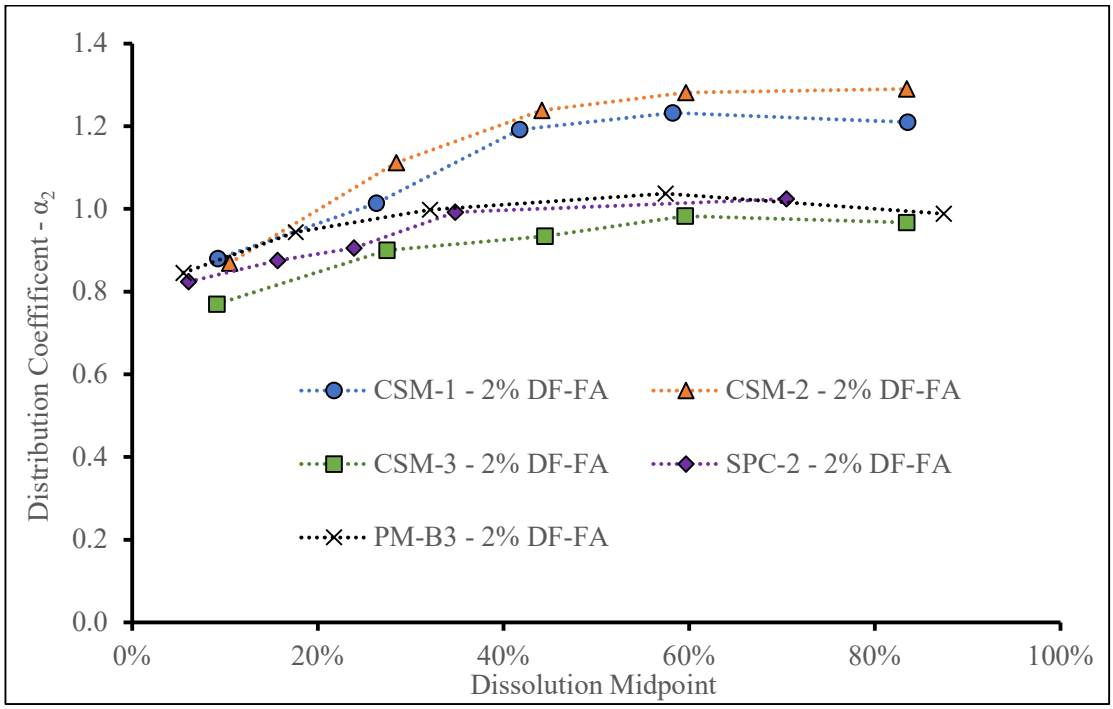
7.9.2 Distribution Coefficient Plots Collected by Additive



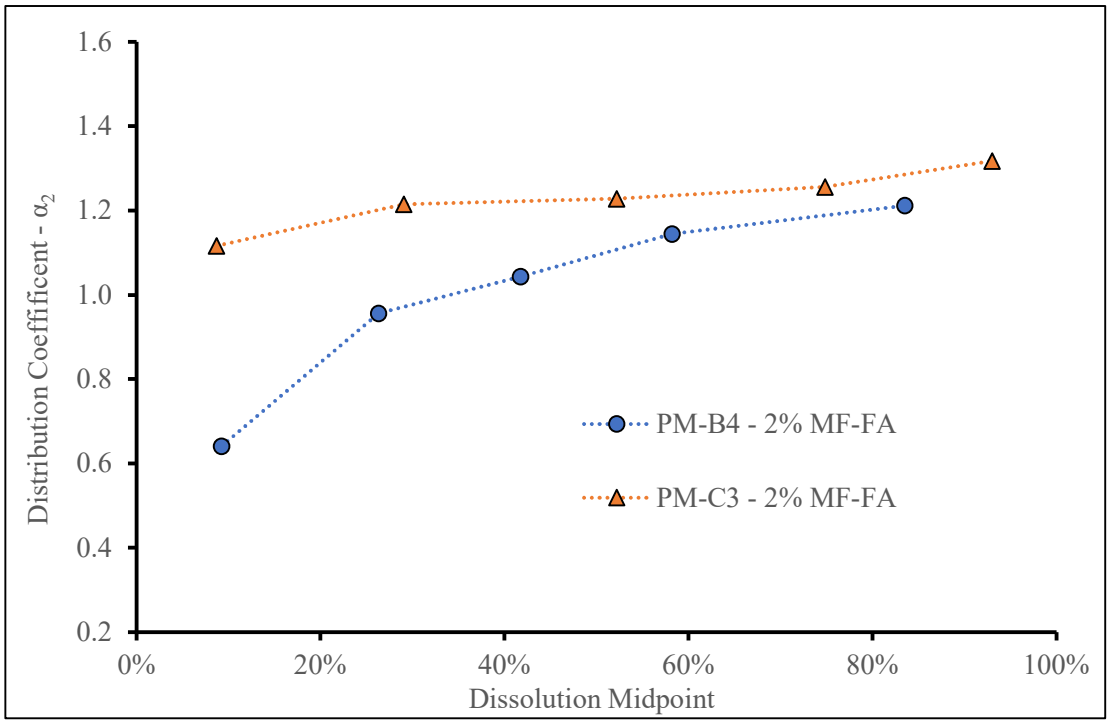
Appendix Fig 7.73. Plot of α_2-value *vs.* dissolution midpoint for all studies performed on crystal samples doped with Cl-FA **16**.



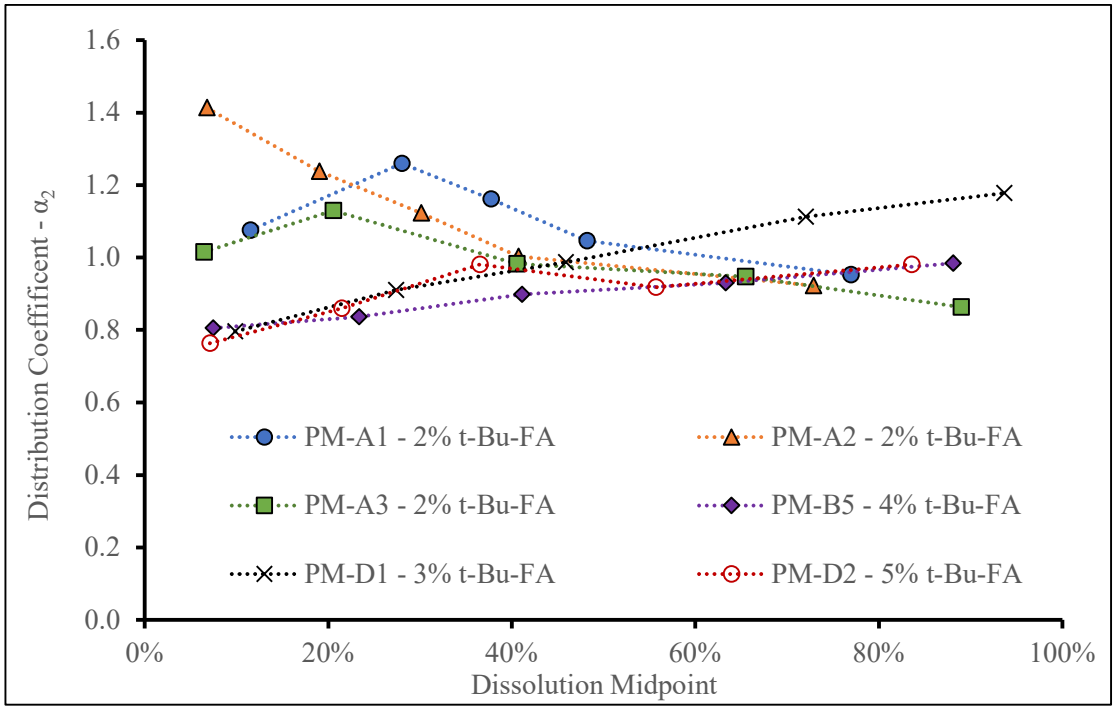
Appendix Fig 7.74. Plot of α_2-value *vs.* dissolution midpoint for all studies performed on crystal samples doped with Me-FA **15**.



Appendix Fig 7.75. Plot of α_2-value *vs.* dissolution midpoint for all studies performed on crystal samples doped with DF-FA **17**.

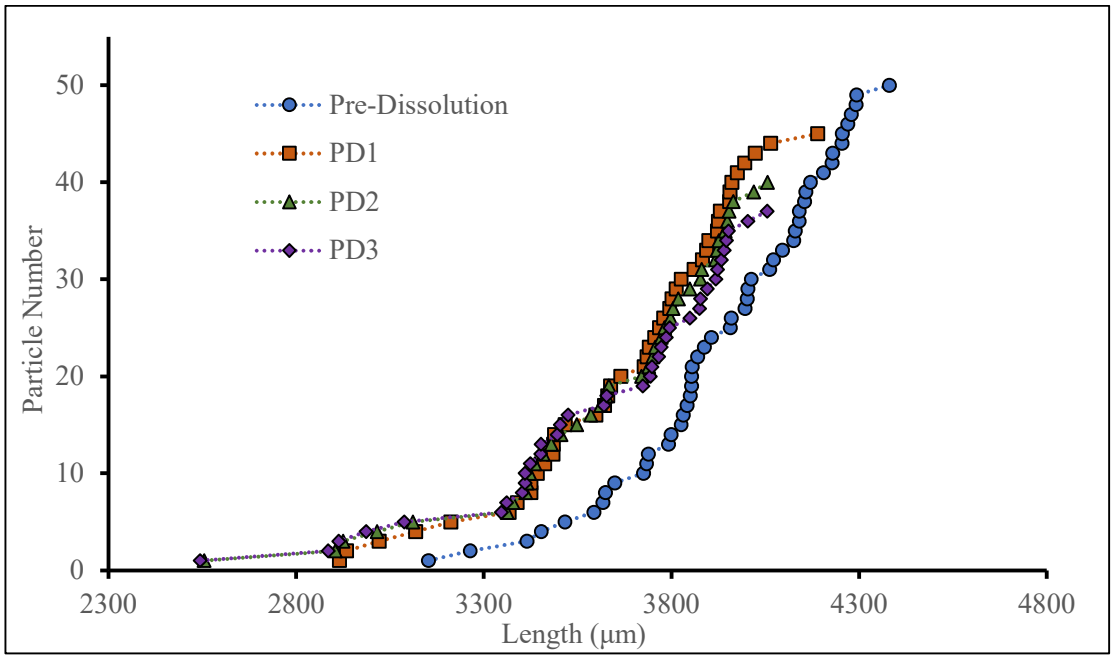


Appendix Fig 7.76. Plot of α_2-value *vs.* dissolution midpoint for all studies performed on crystal samples doped with MF-FA **18**.

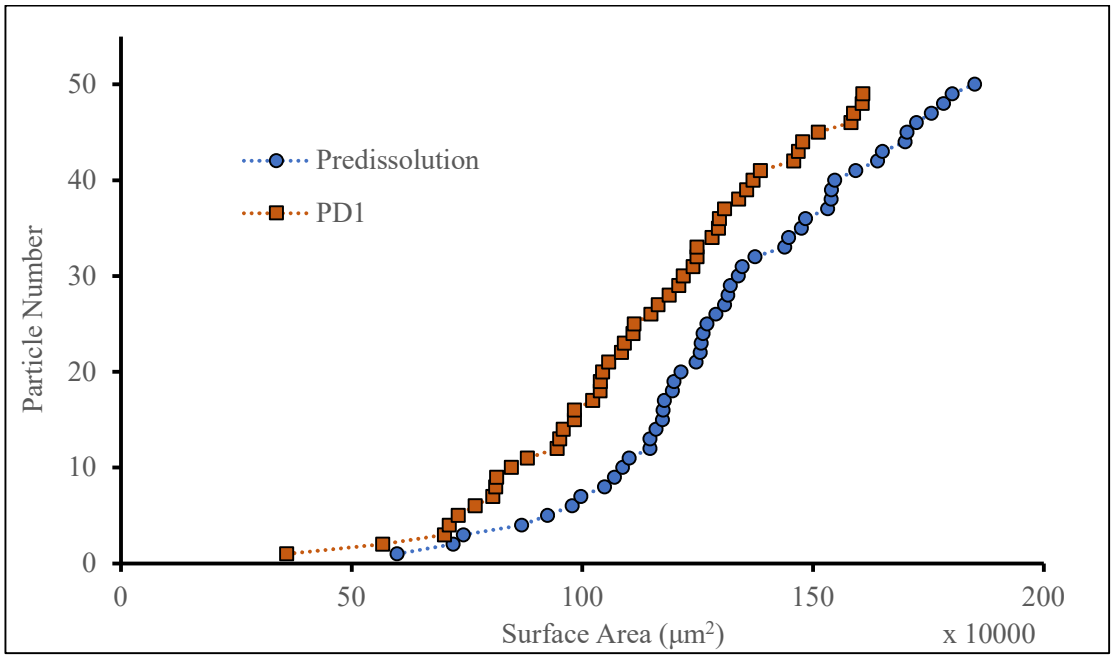


Appendix Fig 7.77. Plot of α_2-value *vs.* dissolution midpoint for all studies performed on crystal samples doped with t-Bu-FA **19**.

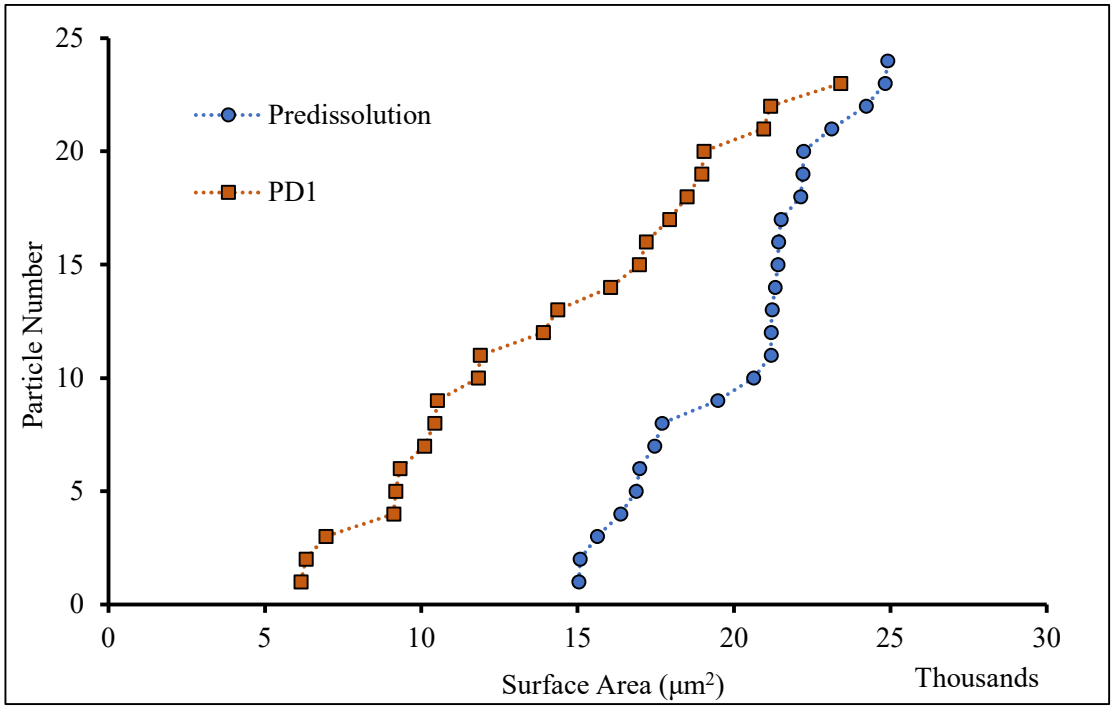
7.9.3 Size Distribution Plots of PD Studies



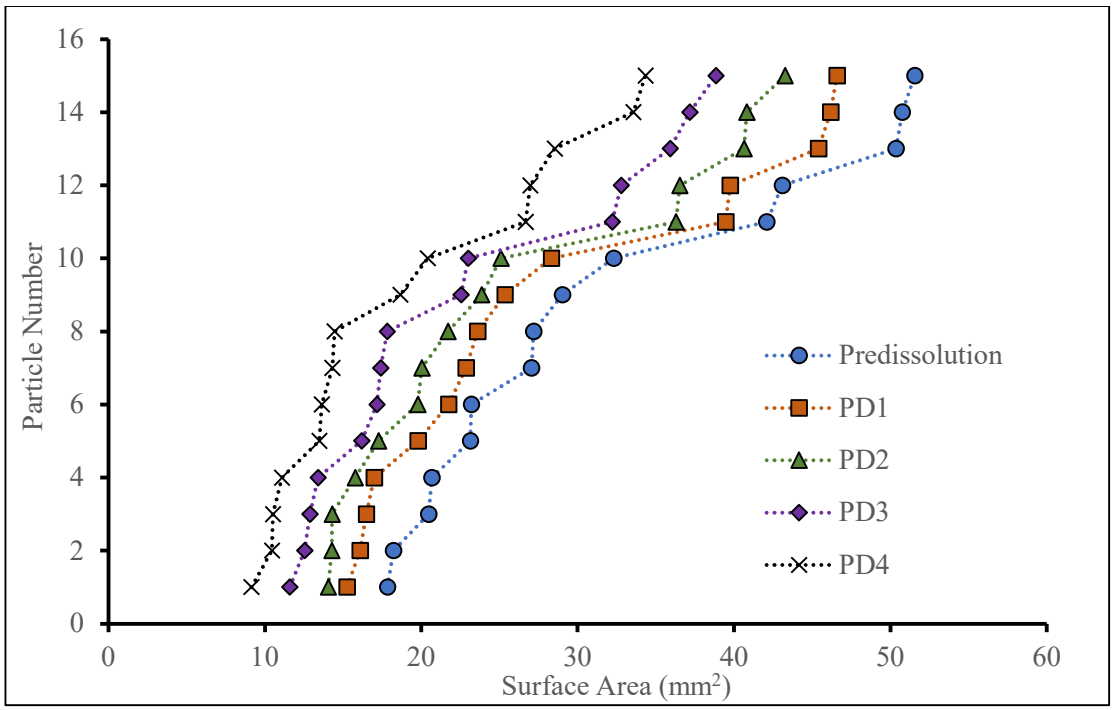
Appendix Fig 7.78. Length distribution plot of the sample crystals over the first three dissolution stages of Primary-1 in the primary partial dissolution method development.



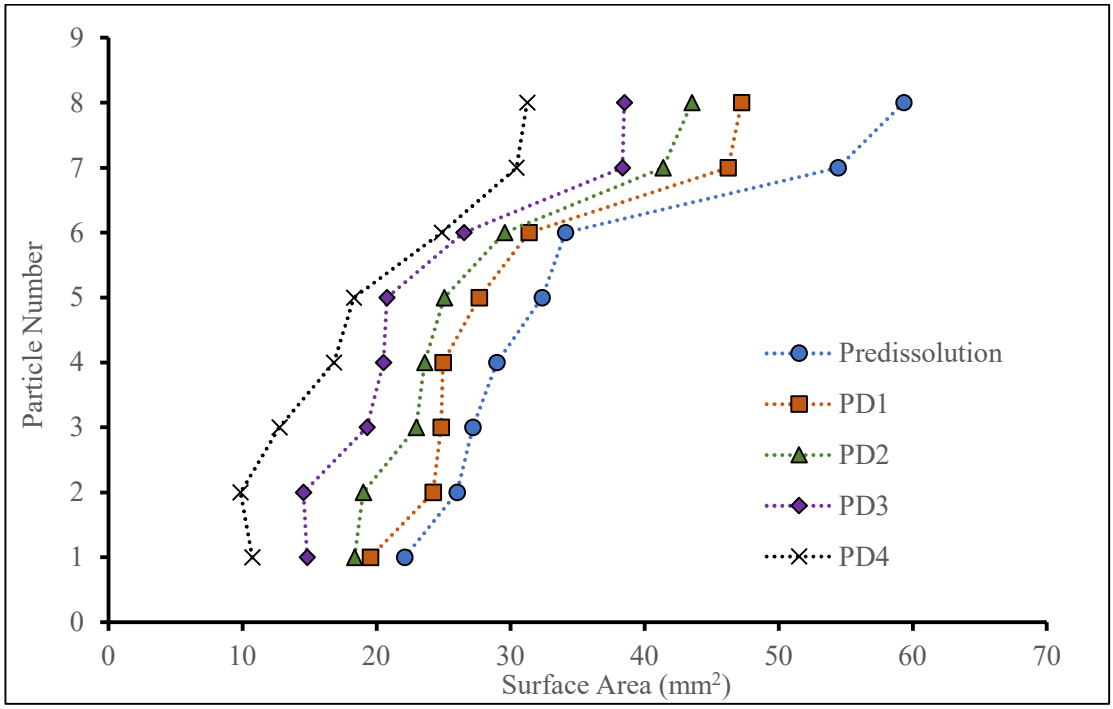
Appendix Fig 7.79. Surface area distribution plot of the Primary-2 study in the primary partial dissolution method development.



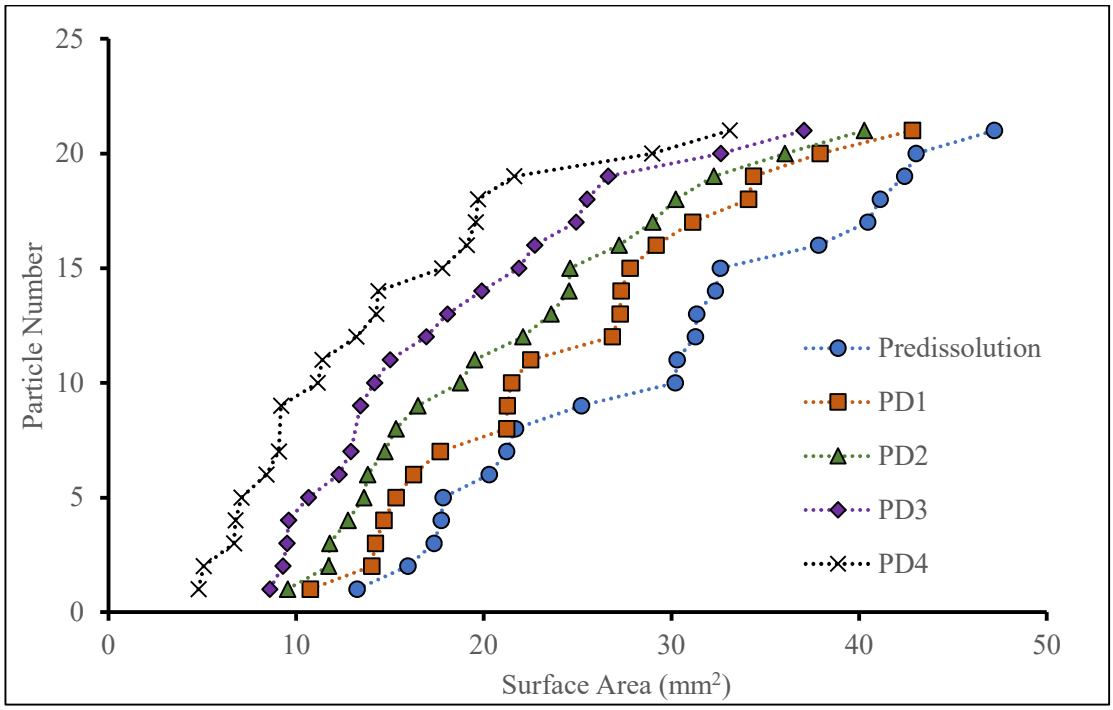
Appendix Fig 7.80. Surface area distribution plot of the Primary-3 study in the primary partial dissolution method development.



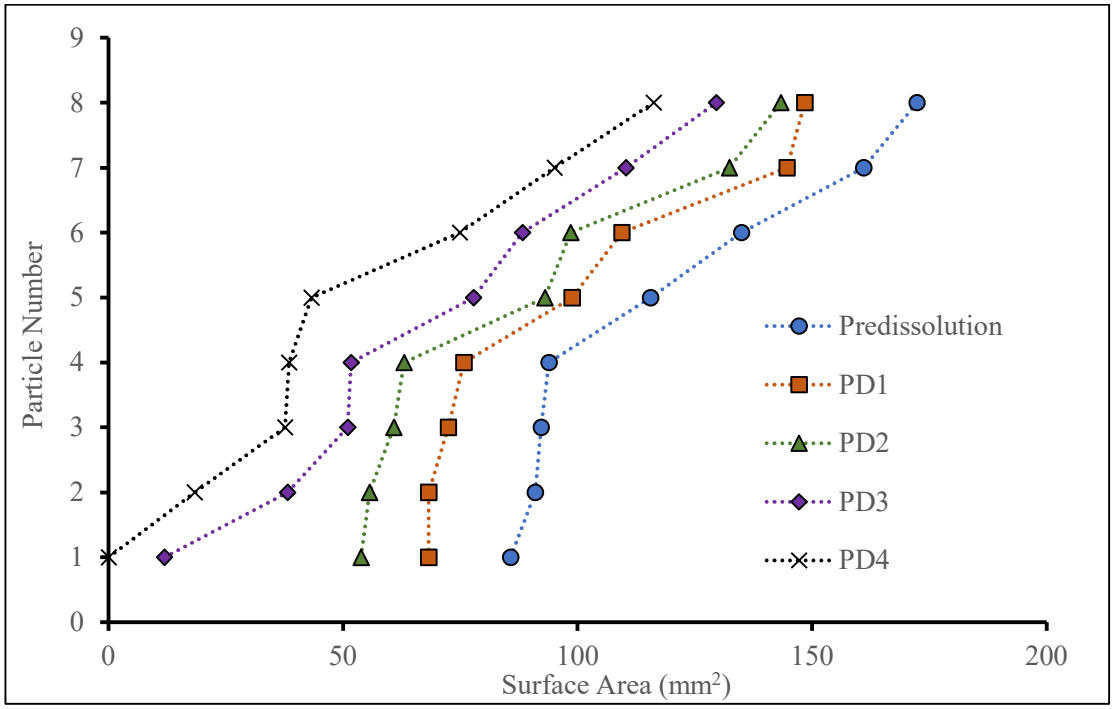
Appendix Fig 7.81. Surface area distribution plot of DATL-1 (0.5% Me-FA **15**) crystals as part of a study on the effect of different additive types and levels.



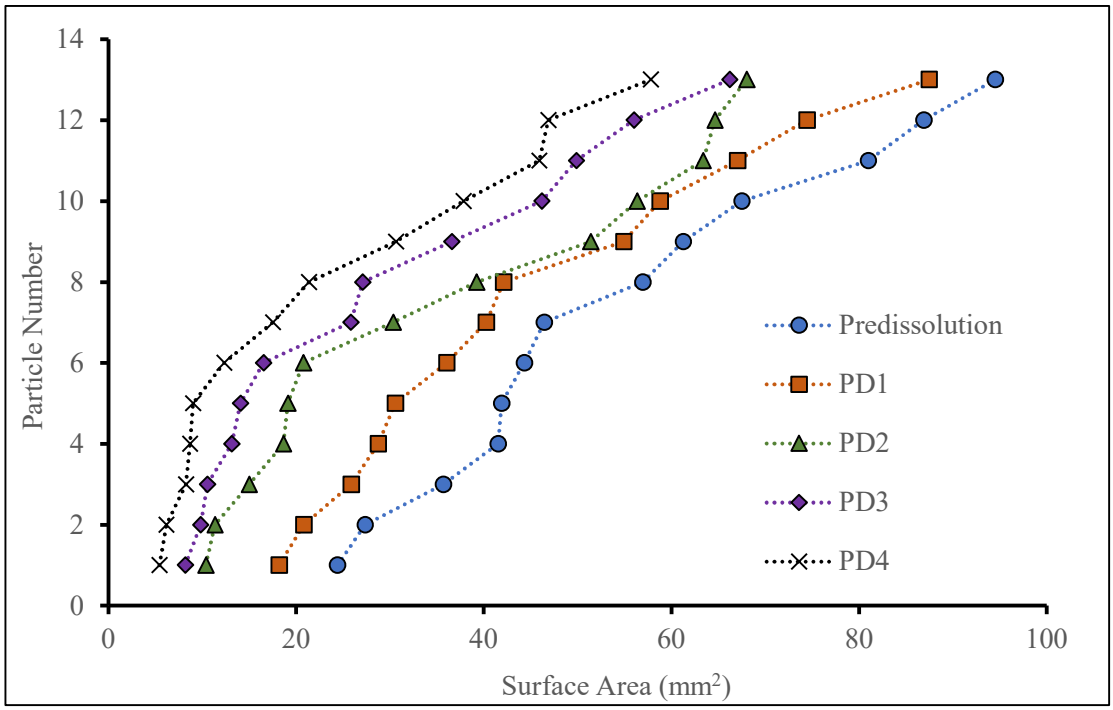
Appendix Fig 7.82. Surface area distribution plot of DATL-2 (5% Me-FA **15**) crystals as part of a study on the effect of different additive types and levels.



Appendix Fig 7.83. Surface area distribution plot of CSM-1 (2% DF-FA **17**) crystals as part of a study on the effect of different crystal sizes and morphologies.

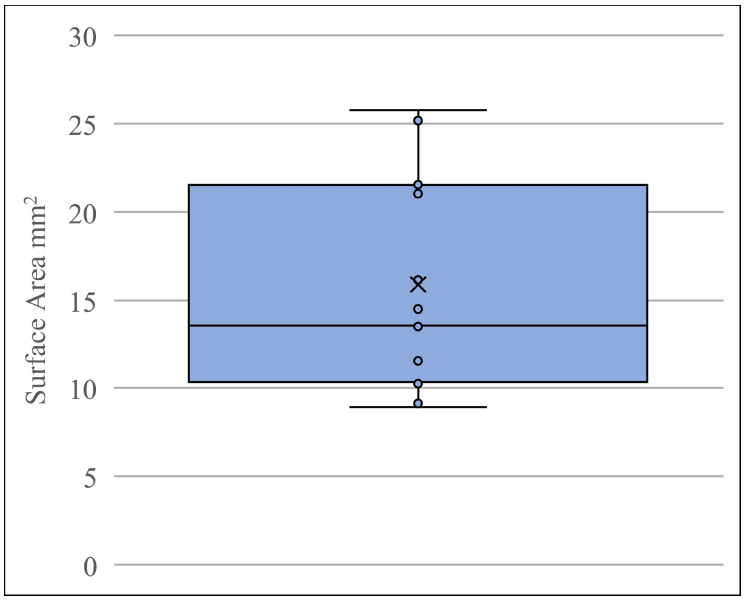


Appendix Fig 7.84. Surface area distribution plot of CSM-2 (2% DF-FA **17**) crystals as part of a study on the effect of different crystal sizes and morphologies.

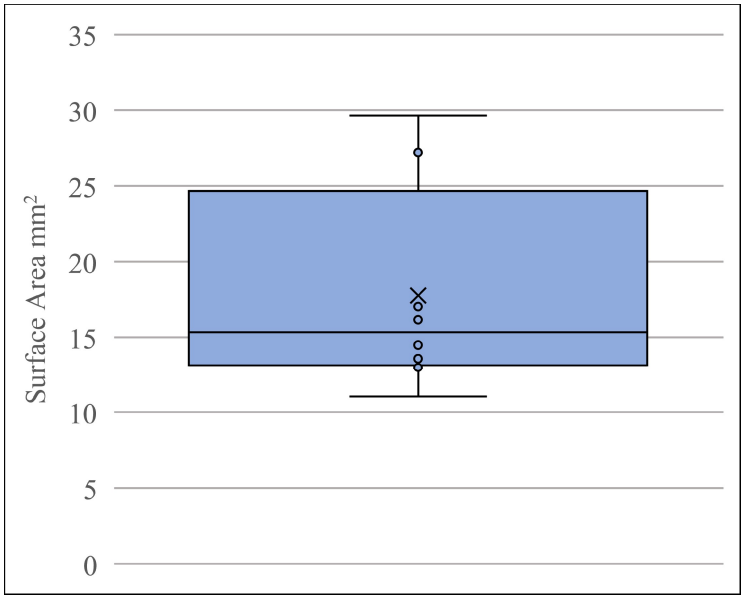


Appendix Fig 7.85. Surface area distribution plot of CSM-3 (2% DF-FA **17**) crystals as part of a study on the effect of different crystal sizes and morphologies.

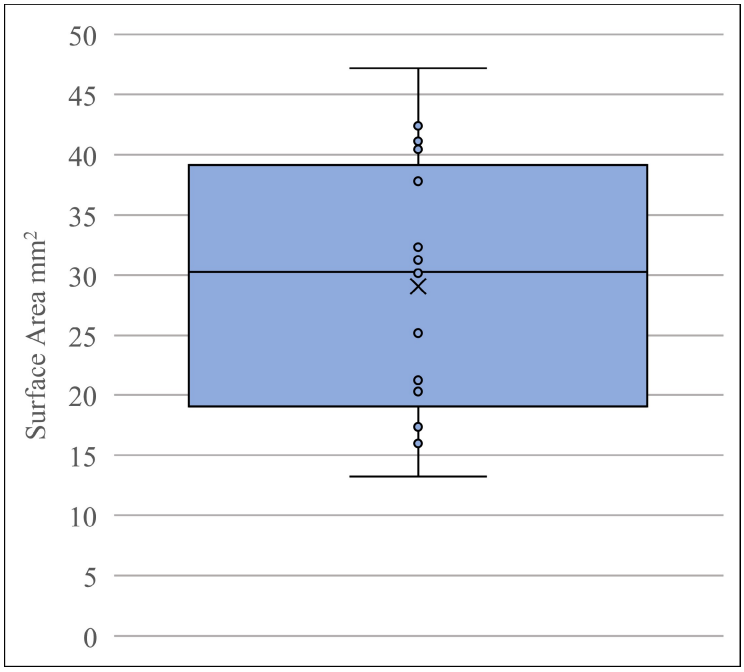
7.9.4 Box Plots of Crystal Sample Surface Areas



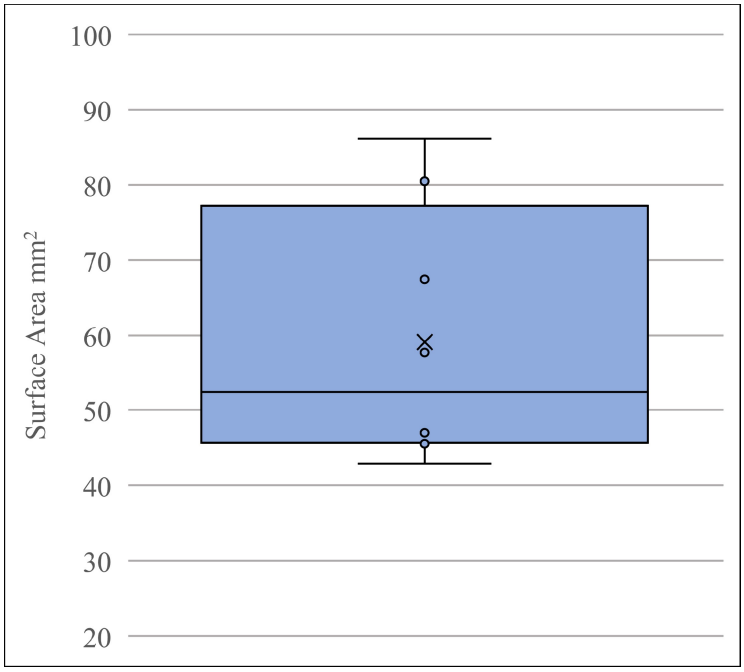
Appendix Fig 7.86. Box plot of crystal surface areas distribution of DATL-1 (0.5% Me-FA **15**) crystals as part of a study on the effect of different additive types and levels.



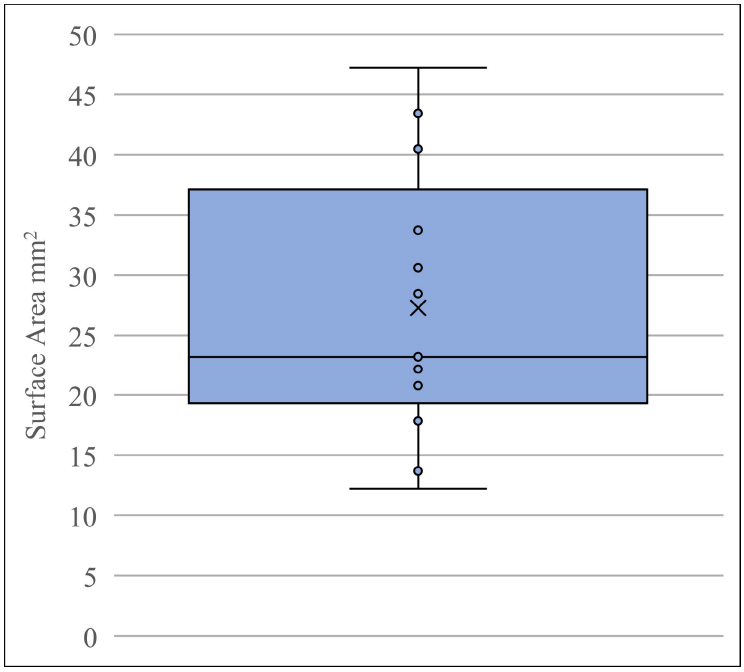
Appendix Fig 7.87. Box plot of crystal surface areas distribution of DATL-2 (5% Me-FA **15**) crystals as part of a study on the effect of different additive types and levels.



Appendix Fig 7.88. Box plot of crystal surface areas distribution of CSM-1 (2% DF-FA **17**) crystals as part of a study on the effect of different crystal sizes and morphologies.



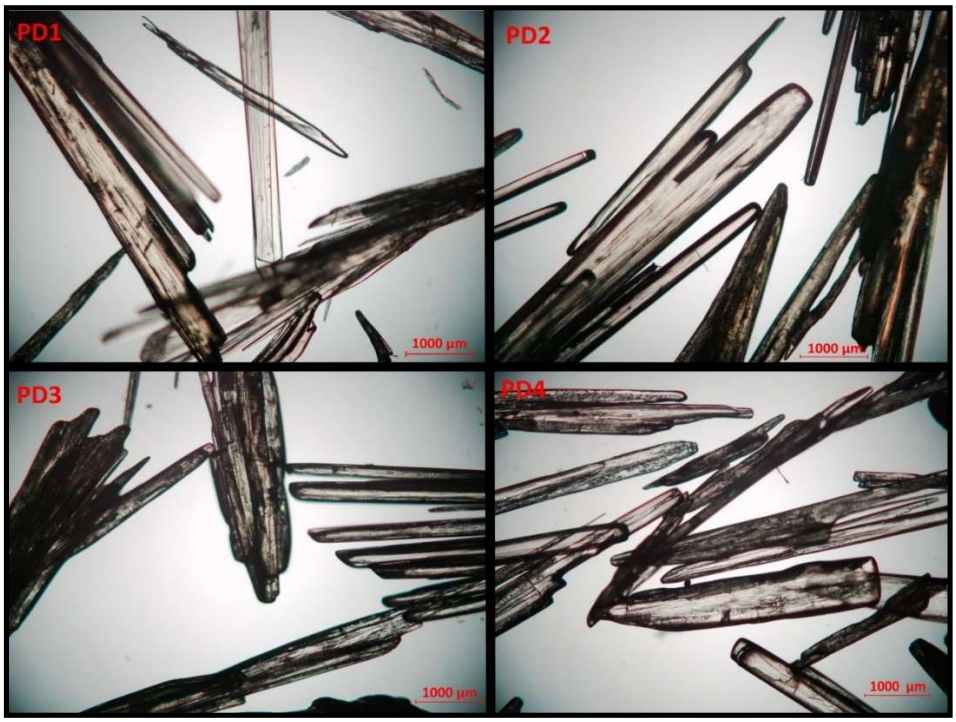
Appendix Fig 7.89. Box plot of crystal surface areas distribution of CSM-2 (2% DF-FA **17**) crystals as part of a study on the effect of different crystal sizes and morphologies.



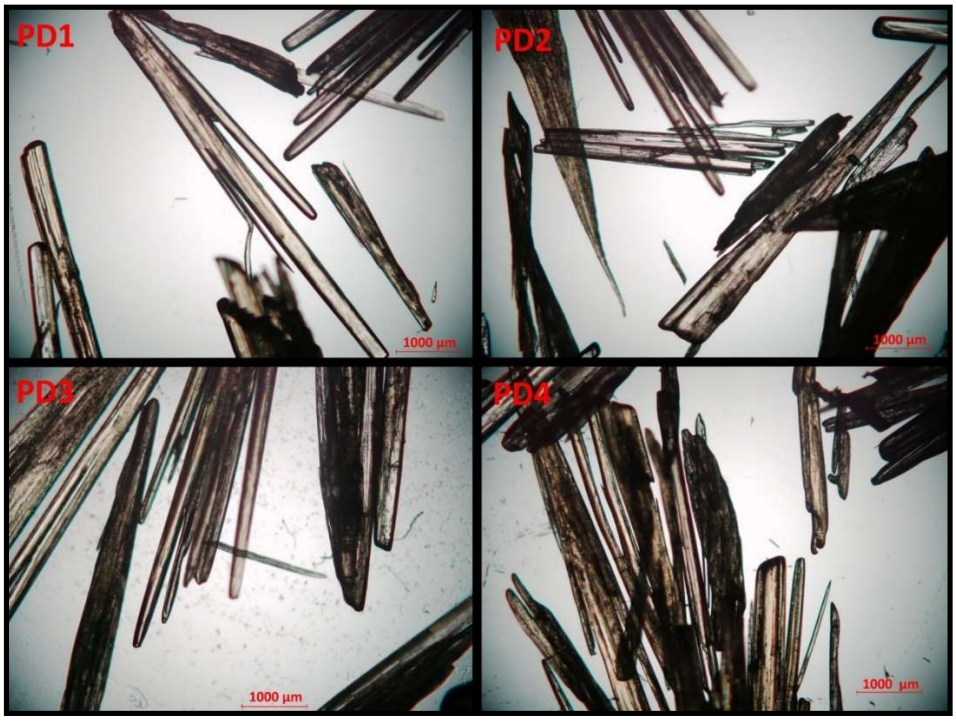
Appendix Fig 7.90. Box plot of crystal surface areas distribution of CSM-3 (2% DF-FA **17**) crystals as part of a study on the effect of different crystal sizes and morphologies.

7.9.5 Microscope images of Crystals with Problematic Morphologies

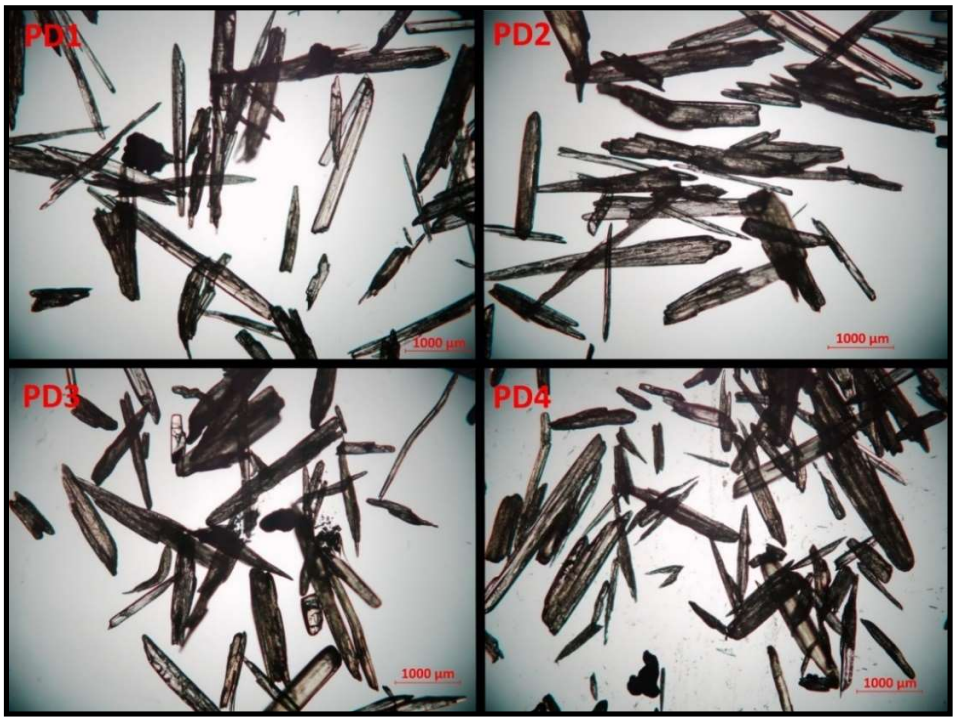
7.9.5.1 Type A Systems



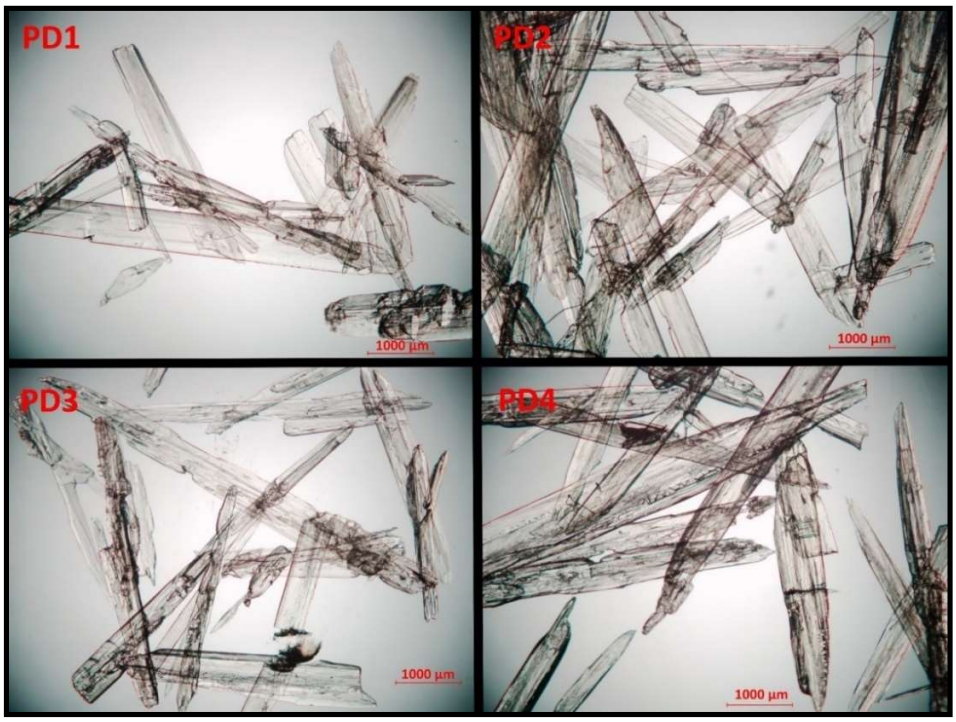
Appendix Fig 7.91. Microscope images (x40) of PM-A1 crystals (2% t-Bu-FA **19**) after each dissolution stage.



Appendix Fig 7.92. Microscope images (x40) of PM-A2 crystals (2% t-Bu-FA **19**) after each dissolution stage.

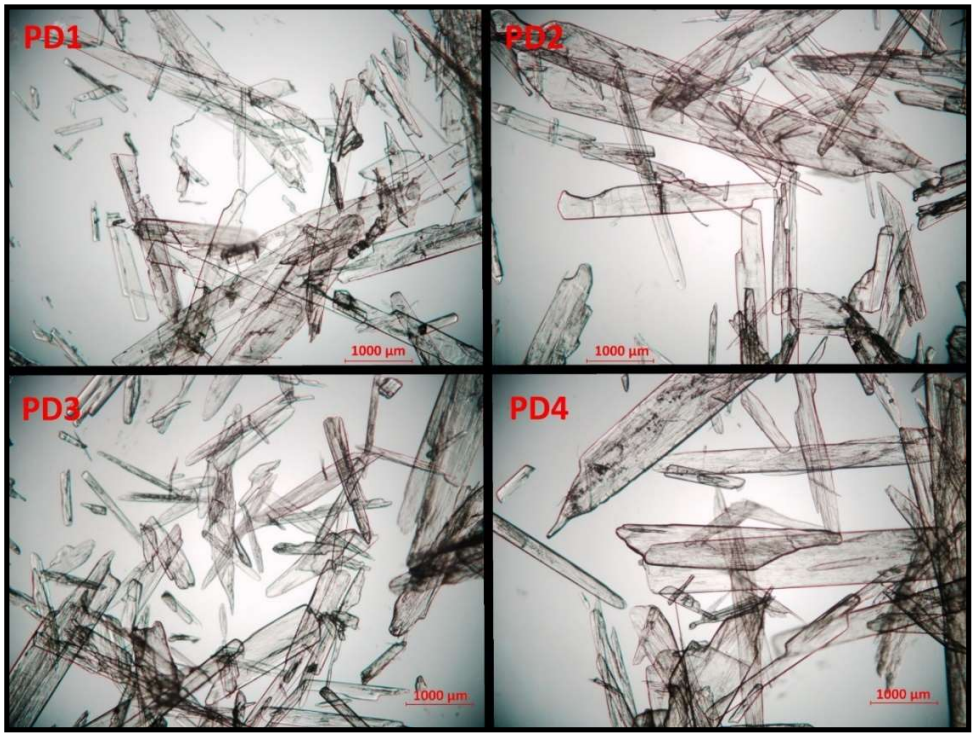


Appendix Fig 7.93. Microscope images (x40) of PM-A3 crystals (2% t-Bu-FA **19**) after each dissolution stage.

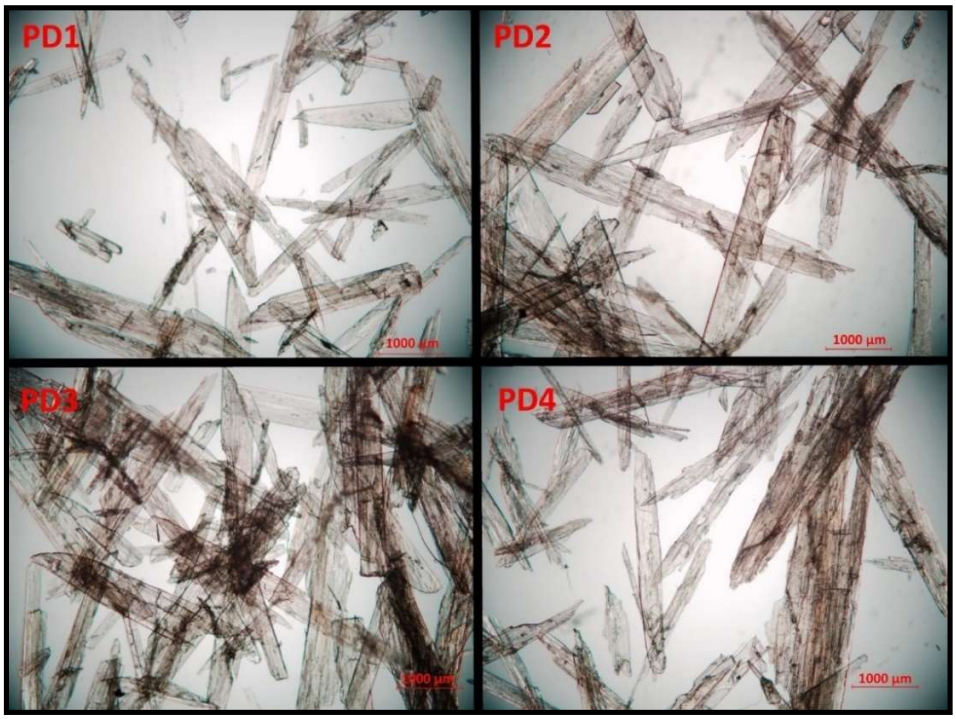


Appendix Fig 7.94. Microscope images (x40) of PM-A4 crystals (5% Me-FA **15**) after each dissolution stage.

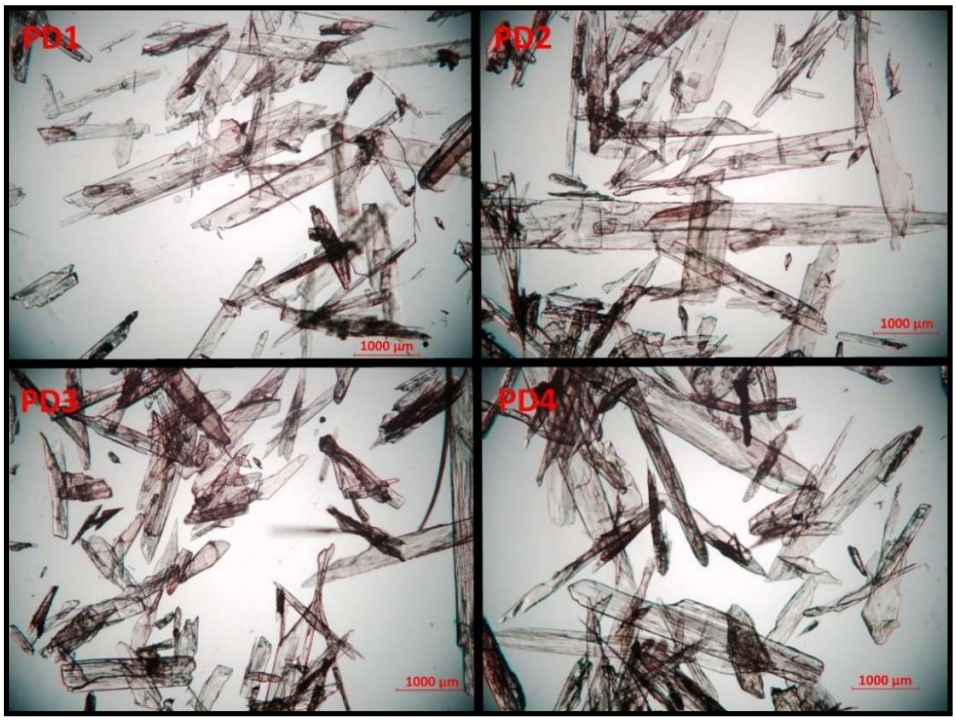
7.9.5.2 Type B Systems



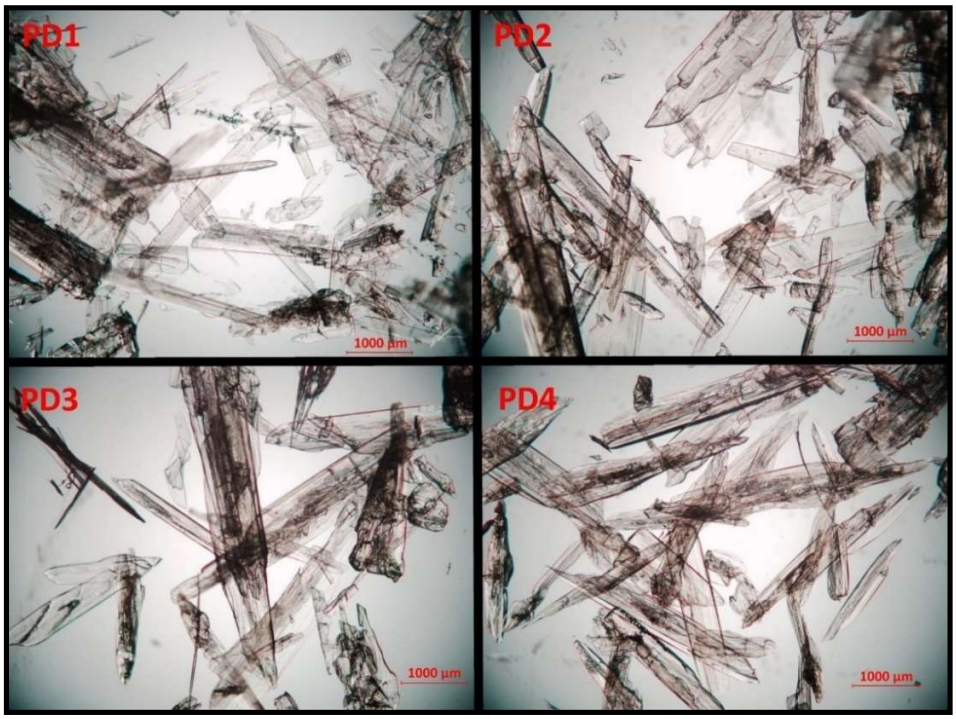
Appendix Fig 7.95. Microscope images (x40) of PM-B1 crystals (0.5% Me-FA **15**) after each dissolution stage.



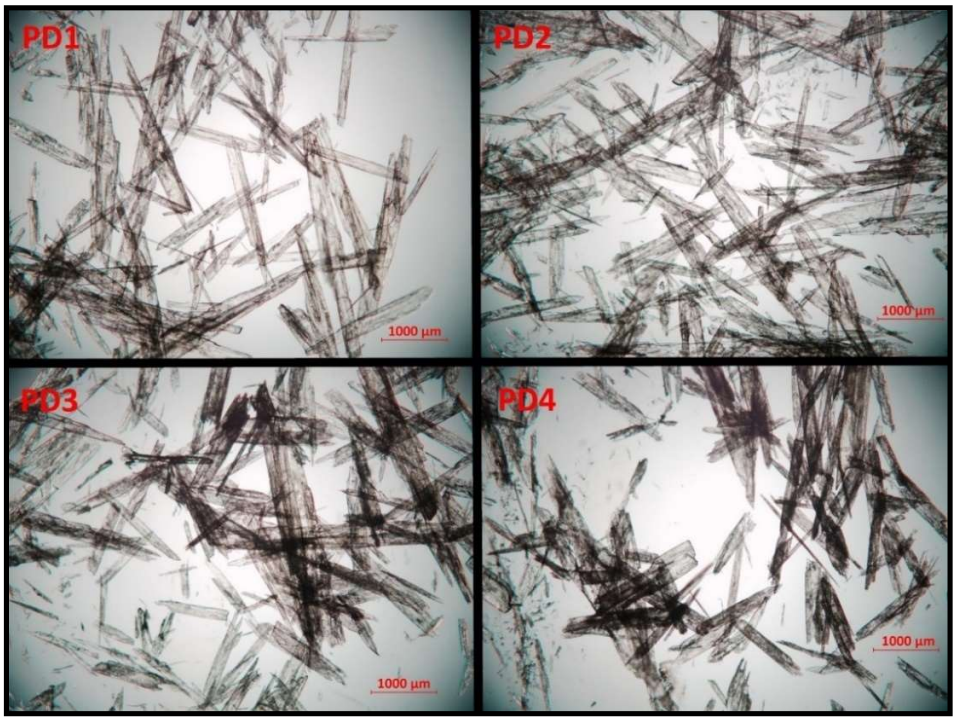
Appendix Fig 7.96. Microscope images (x40) of PM-B2 crystals (5% Me-FA **15**) after each dissolution stage.



Appendix Fig 7.97. Microscope images (x40) of PM-B3 crystals (2% DF-FA **17**) after each dissolution stage.

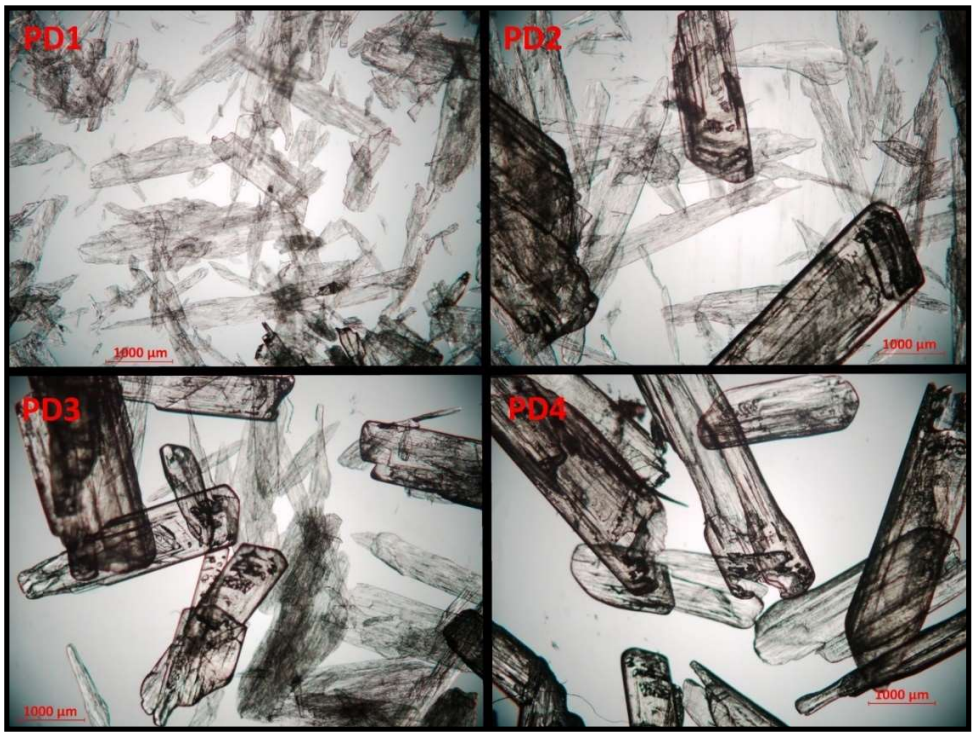


Appendix Fig 7.98. Microscope images (x40) of PM-B4 crystals (2% MF-FA **18**) after each dissolution stage.



Appendix Fig 7.99. Microscope images (x40) of PM-B5 crystals (4% t-Bu-FA **19**) after each dissolution stage.

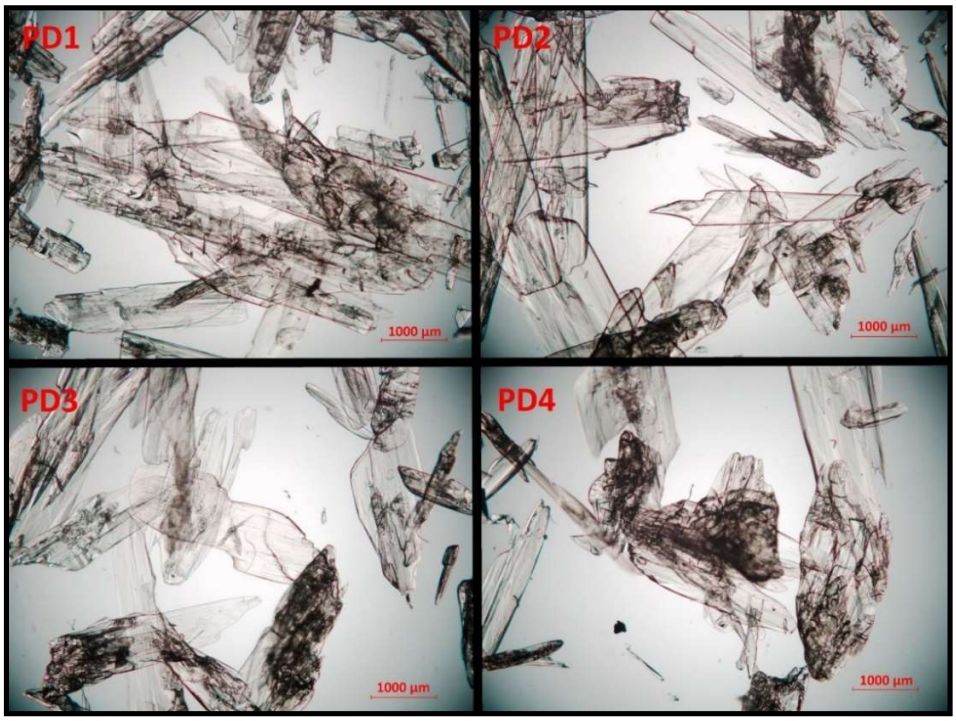
7.9.5.3 Type C Systems



Appendix Fig 7.100. Microscope images (x40) of PM-C1 crystals (0.5% Me-FA **15**) after each dissolution stage.

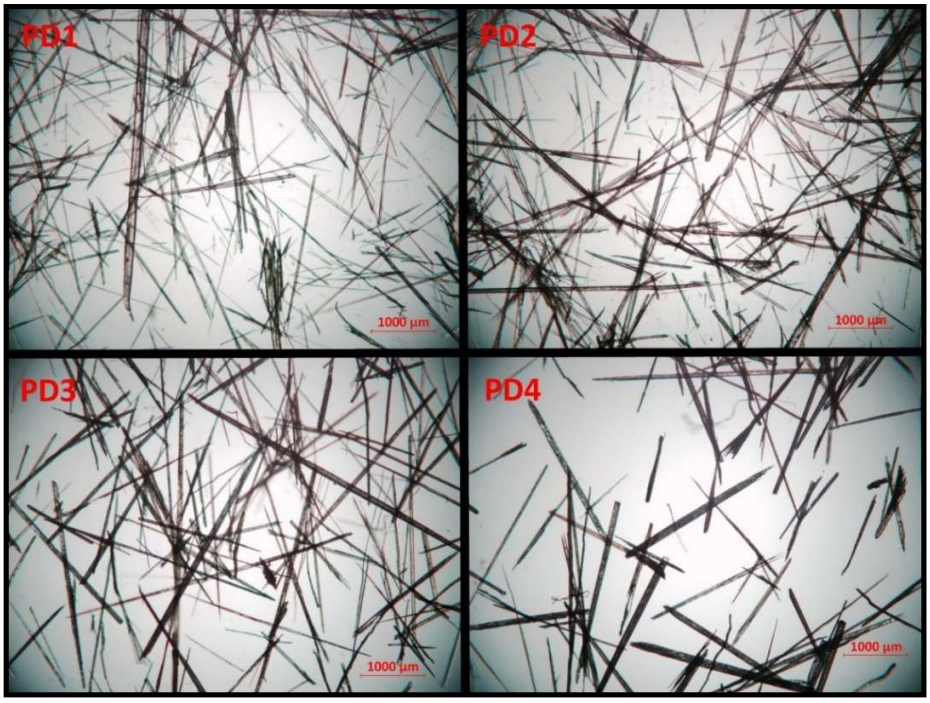


Appendix Fig 7.101. Microscope images (x40) of PM-C2 crystals (5% Me-FA **15**) after each dissolution stage.

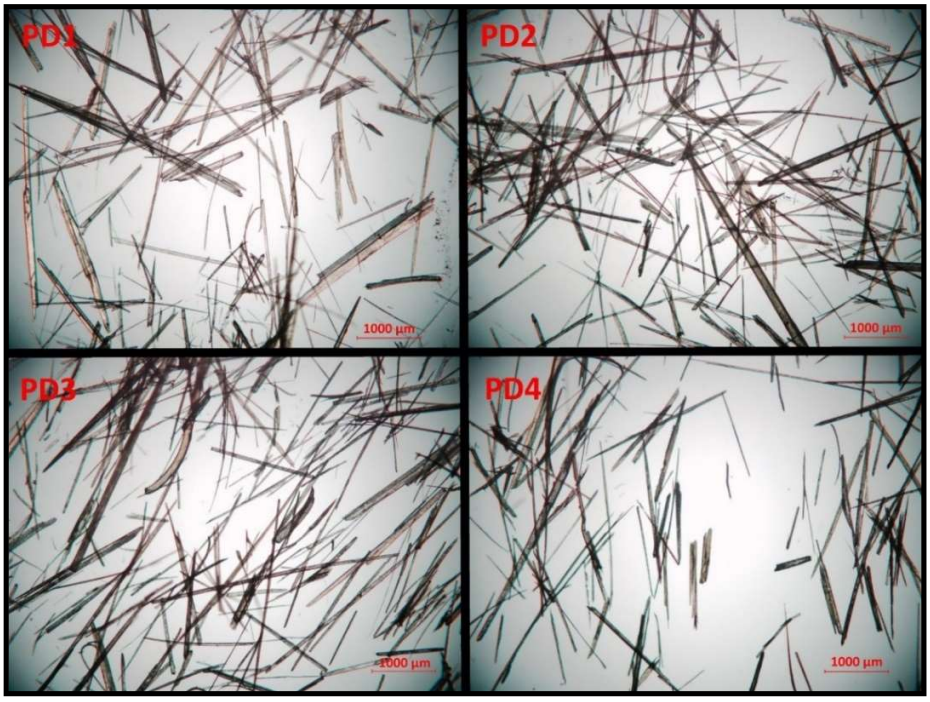


Appendix Fig 7.102. Microscope images (x40) of PM-C3 crystals (2% MF-FA **18**) after each dissolution stage.

7.9.5.4 Type D Systems



Appendix Fig 7.103. Microscope images (x40) of PM-D1 crystals (3% t-Bu-FA **19**) after each dissolution stage.



Appendix Fig 7.104. Microscope images (x40) of PM-D2 crystals (5% t-Bu-FA **19**) after each dissolution stage.

References

(1) International Conference on Harmonisation of Technical Requirements for Registration of Pharmaceuticals for Human Use (ICH). *Impurities in New Drug Substances Q3a(R2)*; 2006.
(2) *ICH M7 – Assessment and Control of DNA Reactive (Mutagenic) Impurities in Pharmaceuticals to Limit Potential Carcinogenic Risk*; 2021.
(3) McGovern, T.; Jacobson-Kram, D. *TrAC Trends Anal. Chem.* **2006**, *25* (8), 790–795.
(4) Pierson, D. A.; Olsen, B. A.; Robbins, D. K.; DeVries, K. M.; Varie, D. L. *Org. Process Res. Dev.* **2008**, *13* (2), 285–291.
(5) Datta, S.; Grant, D. J. W. *Nat. Rev. Drug Discov. 2004 31* **2004**, *3* (1), 42–57.
(6) Nagy, Z. K.; Fujiwara, M.; Braatz, R. D. *J. Process Control* **2008**, *18* (9), 856–864.
(7) Mullin, J. W. In *Crystallization*; Butterworth-Heinemann, 2001; pp 403–477.
(8) Mlinar, L.; Sinha, K.; Chaaya, E.; Nayak, S.; Cosbie, A. In *Chemical Engineering in the Pharmaceutical Industry*; John Wiley & Sons, Ltd, 2019; pp 787–797.
(9) Wilcox, R. F. In *Handbook of Downstream Processing*; Springer, Dordrecht, 1997; pp 417–455.
(10) Crowell, K. E. In *Handbook of Downstream Processing*; Springer, Dordrecht, 1997; pp 48–69.
(11) West, C. *TrAC - Trends Anal. Chem.* **2019**, *120*.
(12) Gottschalk, U. *Process Economic Drivers in Industrial Monoclonal Antibody Manufacture*; Gottschalk, U., Ed.; John Wiley & Sons, Ltd, 2017.
(13) Bhatia, A.; Chopra, S.; Nagpal, K.; Deb, P. K.; Tekade, M.; Tekade, R. K. In *Dosage Form Design Parameters*; Academic Press, 2018; Vol. 2, pp 31–65.
(14) Hansen, M. M.; Jarmer, D. J.; Arslantas, E.; DeBaillie, A. C.; Frederick, A. L.; Harding, M.; Hoard, D. W.; Hollister, A.; Huber, D.; Kolis, S. P.; Kuehne-Willmore, J. E.; Kull, T.; Laurila, M. E.; Linder, R. J.; Martin, T. J.; Martinelli, J. R.; McCulley, M. J.; Richey, R. N.; Starkey, D. R.; Ward, J. A.; Zaborenko, N.; Zweifel, T. *Org. Process Res. Dev.* **2015**, *19* (9), 1214–1230.
(15) Campeau, L.-C.; Chen, Q.; Gauvreau, D.; Girardin, M.; Belyk, K.; Maligres, P.; Zhou, G.; Gu, C.; Zhang, W.; Tan, L.; O'shea, P. D. *Org. Process Res. Dev* **2016**, *20*, 53.
(16) Deng, Y.; Xie, Q.; LaPorte, M. G.; Chasnoff, A. T. A.; Mortensen, M. A.; Patra, D.; Putrelo, S. A.; Antonovich, R. S.; Cao, H.; Yan, J.; Cooper, A. J.; Rippin, S. R.; Alexander, M. D.; Kumar, P. T.; Hendi, M. S.; Lee, Y. H.; Haimowitz, T.; Condon, S. M. *Org. Process Res. Dev.* **2016**, *20* (2), 242–252.
(17) Moynihan, H. A.; Horgan, D. E. *Org. Process Res. Dev.* **2017**, *21* (5), 689–704.
(18) Urwin, S. J.; Levilain, G.; Marziano, I.; Merritt, J. M.; Houson, I.; Ter Horst, J. H. *Org. Process Res. Dev.* **2020**, *24* (8), 1443–1456.
(19) Hendriksen, B. A.; Grant, D. J. W.; Meenan, P.; Green, D. A. *J. Cryst. Growth* **1998**, *183* (4), 629–640.
(20) Caspi, D. D.; Nordstrom, F. L. *Org. Process Res. Dev.* **2018**, *22* (7), 856–861.
(21) Teasdale, A.; Elder, D.; Chang, S. J.; Wang, S.; Thompson, R.; Benz, N.; Sanchez Flores, I. H. *Org. Process Res. Dev.* **2013**, *17* (2), 221–230.
(22) Tilley, R. J. D. In *Crystals and Crystal Structures*; Wiley, 2020; pp 1–19.
(23) Williams, J. H. In *Crystal Engineering How molecules build solids*; IOP Publishing, 2017.
(24) Brown, T. L.; Le May, E. H.; Bursten, B. E.; Murphy, C. J.; Langford, S. J.; Sagatys, D. *Chemistry. The Central Science: A Broad Perspective*, 2nd ed.; Pearson Australia: Front Forest, Australia, 2010.

(25) *A Dictionary of Chemistry*, 6th ed.; Daintith, J., Ed.; Oxford University Press, 2008.
(26) Bond, A. *Pharmaceutical Crystallography*; The Royal Society of Chemistry, 2019.
(27) Isomorphous crystals - Online Dictionary of Crystallography https://dictionary.iucr.org/Isomorphous_crystals (accessed 2021 -07 -06).
(28) Mcpazzo. File:UnitCell.png - Wikimedia Commons https://commons.wikimedia.org/wiki/File:UnitCell.png (accessed 2021 -11 -03).
(29) Mullin, J. W. In *Crystallization*; Butterworth-Heinemann, 2001; pp 216–288.
(30) Mullin, J. W. In *Crystallization*; Butterworth-Heinemann, 2001; pp 181–215.
(31) McGinty, J.; Yazdanpanah, N.; Price, C.; Horst, J. H. ter; Sefcik, J. In *The Handbook of Continuous Crystallization*; Royal Society of Chemistry, 2020; pp 1–50.
(32) Desiraju, G. R.; Vittal, J. J.; Ramanan, A. In *Crystal Engineering*; Co-Published with Indian Institute of Science (IISc), Bangalore, India, 2011; pp 77–97.
(33) Sear, R. P. *Journal of Physics Condensed Matter*. 2007, p 033101.
(34) Sear, R. P. *CrystEngComm* **2014**, *16* (29), 6506–6522.
(35) Mullin, J. W. (John W. In *Industrial Crystallization*; Springer US, 1976; pp 3–22.
(36) Erdemir, D.; Lee, A. Y.; Myerson, A. S. *Acc. Chem. Res.* **2009**, *42* (5), 621–629.
(37) Gibbs, J. W.; Bumstead, H. A.; Van Name, R. G.; Longley, W. R. **1928**.
(38) Wells, A. F. *London, Edinburgh, Dublin Philos. Mag. J. Sci.* **1946**, *37* (266), 184–199.
(39) Buckley, H. E. *Crystal Growth*; Chapman & Hall: London, 1952.
(40) Volmer, M.; Weber, A. *Zeitschrift für Phys. Chemie* **1926**, *119U* (1), 277–301.
(41) Noyes, A. A.; Whitney, W. R. *J. Am. Chem. Soc.* **1897**, *19* (12), 930–934.
(42) Lieth, R. M. A. *Preparation and Crystal Growth of Materials with Layered Structures*; Springer Netherlands, 1977.
(43) Gao, Z.; Rohani, S.; Gong, J.; Wang, J. *Engineering* **2017**, *3* (3), 343–353.
(44) Vu, T. T. L.; Hourigan, J. A.; Sleigh, R. W.; Ang, M. H.; Tade, M. O. *Comput. Aided Chem. Eng.* **2003**, *14* (C), 527–532.
(45) Warkentin, M.; Thorne, R. E. *J. Appl. Crystallogr.* **2009**, *42* (Pt 5), 944.
(46) Ó'Ciardhá, C. T.; Frawley, P. J.; Mitchell, N. A. *J. Cryst. Growth* **2011**, *328* (1), 50–57.
(47) Doki, N.; Kubota, N.; Yokota, M.; Kimura, S.; Sasaki, S. *J. Chem. Eng. JAPAN* **2002**, *35* (11), 1099–1104.
(48) Mullin, J. W. In *Crystallization*; Butterworth-Heinemann, 2001; pp 315–402.
(49) Tanoury, G. J.; Hett, R.; Kessler, D. W.; A. Wald, S.; Senanayake, C. H. *Org. Process Res. Dev.* **2002**, *6* (6), 855–862.
(50) Jones, P. G. *Chem. Br.* **1981**, *17* (5).
(51) Trastoy, B.; Lomino, J. V.; Wang, L.-X.; Sundberg, E. J. *Acta Crystallogr. Sect. F Struct. Biol. Cryst. Commun.* **2013**, *69* (Pt 12), 1405.
(52) Adam, M.; Wang, Z.; Dubavik, A.; Stachowski, G. M.; Meerbach, C.; Soran-Erdem, Z.; Rengers, C.; Demir, H. V.; Gaponik, N.; Eychmüller, A. *Adv. Funct. Mater.* **2015**, *25* (18), 2638–2645.
(53) Millar, S. Tips and Tricks for the Lab: Growing Crystals Part 3 https://www.chemistryviews.org/details/education/2538941/Tips_and_Tricks_for_the_Lab_Growing_Crystals_Part_3.html (accessed 2021 -11 -03).
(54) Lombard, J.; Smith, V. J.; Roex, T. le; Haynes, D. A. *CrystEngComm* **2020**, *22* (45), 7826–7831.
(55) Yu, Q.; Dang, L.; Black, S.; Wei, H. *J. Cryst. Growth* **2012**, *340* (1), 209–215.
(56) Schönherr, E.; Freiberg, M.; Hartmann, H. *Cryst. Res. Technol.* **1997**, *32* (8), 1041–1047.
(57) Ulrich, J.; Bülau, H. C. *Handb. Ind. Cryst.* **2002**, 161–179.
(58) Ostwald, W. *Zeitschrift für Phys. Chemie* **1897**, *22U* (1), 289–330.
(59) Burley, J. C.; Duer, M. J.; Stein, R. S.; Vrcelj, R. M. *Eur. J. Pharm. Sci.* **2007**, *31* (5), 271–276.
(60) McNaught, A. D.; A. Wilkinson. IUPAC. Compendium of Chemical Terminology, 2nd

ed. (the “Gold Book”) http://goldbook.iupac.org/html/M/M03940.html.
(61) Habit - Online Dictionary of Crystallography https://dictionary.iucr.org/Habit (accessed 2021 -11 -03).
(62) Klein, C. *Minerals and Rocks : Exercises in Crystal and Mineral Chemistry, Crystallography, X-Ray Powder Diffraction, Mineral and Rock Identification, and Ore Mineralogy*, 3rd ed.; Wiley, 2008.
(63) Mullin, J. W. In *Crystallization*; Butterworth-Heinemann, 2001; pp 1–31.
(64) Growing Quality Crystals – MIT Department of Chemistry https://chemistry.mit.edu/facilities-and-centers/x-ray-diffraction-facility/growing-quality-crystals/ (accessed 2021 -11 -03).
(65) López-Mejías, V.; Kampf, J. W.; Matzger, A. J. *J. Am. Chem. Soc.* **2012**, *134* (24), 9872–9875.
(66) Wang, I.-C.; Lee, M.-J.; Seo, D.-Y.; Lee, H.-E.; Choi, Y.; Kim, W.-S.; Kim, C.-S.; Jeong, M.-Y.; Choi, G. J. *AAPS PharmSciTech* **2011**, *12* (2), 764.
(67) Millar, S. Tips and Tricks for the Lab: Growing Crystals Part 1 https://www.chemistryviews.org/details/education/2532131/Tips_and_Tricks_for_the_Lab_Growing_Crystals_Part_1/ (accessed 2021 -11 -03).
(68) Polymorphism - Online Dictionary of Crystallography https://dictionary.iucr.org/Polymorphism (accessed 2021 -11 -05).
(69) Byrn, S. R.; Zografi, G.; Chen, X. S. In *Solid State Properties of Pharmaceutical Materials*; John Wiley & Sons, Ltd, 2017; pp 22–37.
(70) Frank, D. S.; Zhu, Q.; Matzger, A. J. *Mol. Pharm.* **2019**, *16* (8), 3720–3725.
(71) Lee, E. H.; Byrn, S. R. *J. Pharm. Sci.* **2010**, *99* (9), 4013–4022.
(72) Wu, H. B.; Chan, M. N.; Chan, C. K. *Aerosol Sci. Technol.* **2007**, *41* (6), 581–588.
(73) Lee, E. H. *Asian J. Pharm. Sci.* **2014**, *9* (4), 163–175.
(74) Morissette, S. L.; Soukasene, S.; Levinson, D.; Cima, M. J.; Almarsson, Ö. *Proc. Natl. Acad. Sci.* **2003**, *100* (5), 2180–2184.
(75) Lakshmi Prasanthi, N.; Sudhir, M.; Jyothi, N.; Sri vajrapriya, V. *Am. J. Adv. Drug Deliv.* **2016**, *04* (05), 58–63.
(76) Aldridge, S. *Chemistry World*. April 2007, pp 64–70.
(77) McCrone, W. C. *Polymorphism*; Interscience New York, 1965; Vol. 2.
(78) Cruz-Cabeza, A. J.; Reutzel-Edens, S. M.; Bernstein, J. *Chem. Soc. Rev.* **2015**, *44* (23), 8619–8635.
(79) Groom, C. R.; Bruno, I. J.; Lightfoot, M. P.; Ward, S. C. *Acta Crystallogr. Sect. B Struct. Sci. Cryst. Eng. Mater.* **2016**, *72* (2), 171–179.
(80) Beran, G. J. O.; Sugden, I. J.; Greenwell, C.; Bowskill, D. H.; Pantelides, C. C.; Adjiman, C. S. *Chem. Sci.* **2022**, *13* (5), 1288–1297.
(81) Reany, O.; Kapon, M.; Botoshansky, M.; Keinan, E. *Cryst. Growth Des.* **2009**, *9* (8), 3661–3670.
(82) Zhou, Q.; Fang, Z.; Li, J.; Wang, M. *Microporous Mesoporous Mater.* **2015**, *202* (C), 22–35.
(83) Manchanda, S.; Chandra, A.; Bandopadhyay, S.; Deb, P. K.; Tekade, R. K. In *Dosage Form Design Considerations: Volume I*; Elsevier, 2018; pp 773–831.
(84) Berkovitch-Yellin, Z.; Mil, J. Van; Addadi, L.; Idelson, M.; Lahav, M.; Leiserowitz, L. *J. Am. Chem. Soc.* **2002**, *107* (11), 3111–3122.
(85) Van Enckevort, W. J. P.; Los, J. H. *J. Phys. Chem. C* **2008**, *112* (16), 6380–6389.
(86) Blagden, N. *Powder Technol.* **2001**, *121* (1), 46–52.
(87) Tran, D. T.; Majerová, D.; Veselý, M.; Kulaviak, L.; Ruzicka, M. C.; Zámostný, P. *Int. J. Pharm.* **2019**, *556*, 383–394.
(88) Fiebig, A.; Jones, M. J.; Ulrich, J. In *Crystal Growth and Design*; American Chemical Society, 2007; Vol. 7, pp 1623–1627.

(89) Davey, R. J. *J. Cryst. Growth* **1976**, *34* (1), 109–119.
(90) Moynihan, H. A.; Armstrong, D. *CrystEngComm* **2018**, *20* (18), 2617–2633.
(91) Addadi, L.; Weinstein, S.; Gati, E.; Weissbuch, I.; Lahav, M. *J. Am. Chem. Soc.* **2002**, *104* (17), 4610–4617.
(92) Yan, S.; Xie, C.; Zhang, X.; Zhou, L.; Hou, B.; Huang, J.; Zhou, L.; Yin, Q. *ChemistrySelect* **2018**, *3* (8), 2293–2297.
(93) Ó'Meadhra, R.; Kramer, H. J. M.; Van Rosmalen, G. M. *AIChE J.* **1996**, *42* (4), 973–982.
(94) Pietsch, W. *Agglomeration in Industry: Occurrence and Applications*; wiley, 2008.
(95) Chow, A. H. L.; Chow, P. K. K.; Zhongshan, W.; Grant, D. J. W. *Int. J. Pharm.* **1985**, *24* (2–3), 239–258.
(96) Gielen, B.; Jordens, J.; Thomassen, L. C. J.; Braeken, L.; Gerven, T. Van. *Cryst. 2017, Vol. 7, Page 40* **2017**, *7* (2), 40.
(97) Nguyen, T. T. H.; Khan, A.; Bruce, L. M.; Forbes, C.; O'Leary, R. L.; Price, C. J. *Cryst. 2017, Vol. 7, Page 294* **2017**, *7* (10), 294.
(98) Peter, A.; de Paula, J. *Atkins' Physical Chemistry*, 8th ed.; Oxford University Press, 2006.
(99) Mullin, J. W. In *Crystallization*; Butterworth-Heinemann, 2001; pp 135–180.
(100) Matsuoka, M.; Ozawa, R. *J. Cryst. Growth* **1989**, *96* (3), 596–604.
(101) Zhan, Y. Z.; Du, Y.; Zhuang, Y. H. In *Methods for Phase Diagram Determination*; Elsevier, 2007; pp 108–150.
(102) Bernstein, L.; Kaufman, H. *Met. Powder Rep.* **2000**, *55* (4), 40.
(103) Smith, J. F. In *Methods for Phase Diagram Determination*; Elsevier, 2007; pp 1–21.
(104) Petrucci, R. H.; Herring, F. G.; Madura, J. D.; Bissonnette, C. *General Chemistry : Principles and Modern Applications*, 8th ed.; Prentice Hall: Upper Saddle River N.J., 2007.
(105) Sathisaran, I.; Dalvi, S. V. *Pharmaceutics* **2018**, *10* (3), 108.
(106) Lusi, M. *CrystEngComm* **2018**, *20* (44), 7042–7052.
(107) Wirth, D. D.; Miller, M. S.; Boini, S. K.; Koenig, T. M. *Org. Process Res. Dev.* **2000**, *4* (6), 513–519.
(108) *A Dictionary of Physics*, 6th ed.; Oxford University Press, 2015.
(109) Britannica., T. E. of E. "eutectic" https://www.britannica.com/science/eutectic (accessed 2021 -11 -04).
(110) Cherukuvada, S.; Nangia, A. *Chem. Commun.* **2013**, *50* (8), 906–923.
(111) Askeland, D. R.; Fulay, P. P. *Essentials of Materials Science & Engineering - SI Version.*; Cengage Learning: Boston, 2009.
(112) Co-crystal - Online Dictionary of Crystallography https://dictionary.iucr.org/Co-crystal (accessed 2021 -11 -05).
(113) Karimi-Jafari, M.; Padrela, L.; Walker, G. M.; Croker, D. M. *Cryst. Growth Des.* **2018**, *18* (10), 6370–6387.
(114) Sun, C. C. *Expert Opin. Drug Deliv. 10* (2), 201–213.
(115) Basavoju, S.; Boström, D.; Velaga, S. P. *Cryst. Growth Des.* **2006**, *6* (12), 2699–2708.
(116) Billot, P.; Hosek, P.; Perrin, M. A. *Org. Process Res. Dev.* **2013**, *17* (3), 505–511.
(117) Ranganathan, A.; Pedireddi, V. R.; Rao, C. N. R. *J. Am. Chem. Soc.* **1999**, *121* (8), 1752–1753.
(118) Kálmán, A.; Párkányi, L.; Argay, G. *Acta Crystallogr. Sect. B* **1993**, *49* (6), 1039–1049.
(119) Horgan, D. E.; Crowley, L. M.; Stokes, S. P.; Lawrence, S. E.; Moynihan, H. A. In *Advanced Topics in Crystallization*; InTech, 2015; pp 57–84.
(120) He, X.; Stowell, J. G.; Morris, K. R.; Pfeiffer, R. R.; Li, H.; Stahly, G. P.; Byrn, S. R. *Cryst. Growth Des.* **2001**, *1* (4), 305–312.
(121) Moynihan, H. A.; Armstrong, D. *RSC Adv.* **2019**, *9* (37), 21405–21417.
(122) Prasher, P.; Sharma, M. *Drug Dev. Res.* **2021**.
(123) Whitehouse, M. W. *Curr. Med. Chem.* **2005**, *12* (25), 2931–2942.

(124) Davis, A. P.; Grondin, C. J.; Johnson, R. J.; Sciaky, D.; Wiegers, J.; Wiegers, T. C.; Mattingly, C. J. *Nucleic Acids Res.* **2021**, *49* (D1), D1138–D1143.
(125) J.K. Aronson. *Meyler's Side Effects of Analgesics and Anti- Inflammatory Drugs*, 1st ed.; Elsevier Science, 2010.
(126) Mei, X.; August, A. T.; Wolf, C. *J. Org. Chem.* **2006**, *71* (1), 142–149.
(127) Pellón, R. F.; Carrasco, R.; Márquez, T.; Mamposo, T. *Tetrahedron Lett.* **1997**, *38* (29), 5107–5110.
(128) Schuster, C.; Julich-Gruner, K. K.; Schnitzler, H.; Hesse, R.; Jäger, A.; Schmidt, A. W.; Knölker, H. J. *J. Org. Chem.* **2015**, *80* (11), 5666–5673.
(129) Albaugh, P.; Fan, Y.; Mi, Y.; Sun, F.; Adrian, F.; Li, N.; Jia, Y.; Sarkisova, Y.; Kreusch, A.; Hood, T.; Lu, M.; Liu, G.; Huang, S.; Liu, Z.; Loren, J.; Tuntland, T.; Karanewsky, D. S.; Seidel, H. M.; Molteni, V. *ACS Med. Chem. Lett.* **2012**, *3* (2), 140–145.
(130) Abignente, E.; de Caprariis, P. *Anal. Profiles Drug Subst. Excipients* **1982**, *11* (C), 313–346.
(131) Dannenfelser, R. M.; Yalkowsky, S. H. *Sci. Total Environ.* **1991**, *109–110* (C), 625–628.
(132) Liu, Y.; Xu, S.; Zhang, X.; Tang, W.; Gong, J. *Cryst. Growth Des.* **2019**, *19* (12), 7175–7184.
(133) Delaney, S. P.; Smith, T. M.; Korter, T. M. *J. Mol. Struct.* **2014**, *1078*, 83–89.
(134) Gordon, A. J.; Ford, R. A. *The Chemist's Companion: A Handbook of Practical Data, Techniques, and References*; 1973.
(135) Tseng, C. C.; Baillie, G.; Donvito, G.; Mustafa, M. A.; Juola, S. E.; Zanato, C.; Massarenti, C.; Dall'Angelo, S.; Harrison, W. T. A.; Lichtman, A. H.; Ross, R. A.; Zanda, M.; Greig, I. R. *J. Med. Chem.* **2019**, *62* (10), 5049–5062.
(136) McConnell, J. F. *Cryst Struct Commun* **1973**, *3*, 459–461.
(137) Krishna Murthy, H. M.; Bhat, T. N.; Vijayan, M.; IUCr. *urn:issn:0567-7408* **1982**, *38* (1), 315–317.
(138) Jr. J., K. *Microscope* **1977**, *25* (1), 31–45.
(139) Hu, Y.; Wikström, H.; Byrn, S. R.; Taylor, L. S. *J. Pharm. Biomed. Anal.* **2007**, *45* (4), 546–551.
(140) Burger, A.; Ramberger, R. *Microchim. Acta 1980 731* **1980**, *73* (1), 17–28.
(141) Chen, X.; Stowell, J. G.; Morris, K. R.; Byrn, S. R. *J. Pharm. Biomed. Anal.* **2010**, *51* (4), 866–874.
(142) Maestrelli, F.; Rossi, P.; Paoli, P.; De Luca, E.; Mura, P. *J. Pharm. Biomed. Anal.* **2020**, *180*, 113058.
(143) Gerber, F.; Krummen, M.; Potgeter, H.; Roth, A.; Siffrin, C.; Spoendlin, C. *J. Chromatogr. A* **2004**, *1036* (2), 127–133.
(144) Cullity, B. D. *Elements of X-Ray Diffraction, 2nd Edition*, 2nd ed.; Addison-Wesley, 1978.
(145) Pungor, E. In *A Practical Guide to Instrumental Analysis*; CRC Press, 2020; pp 181–191.
(146) Coats, A. W.; Redfern, J. P. *Analyst* **1963**, *88* (1053), 906–924.
(147) Nernst, W.; Palmer, C. S. *Theoretical Chemistry from the Standpoint of Avogardro's Rule \& Thermodynamics*; Macmillan and Company, 1895.
(148) Retgers, J. W. *Zeitschrift für Phys. Chemie* **1890**, *5U* (1), 436–466.
(149) Laves, F. H. *Zeitschrift für Krist. - Cryst. Mater.* **1980**, *151* (1–2), 21–29.
(150) Crundwell, G. A.; Cowans, B. A.; Hopkins, J. A.; Grutzner, J. B.; Kahr, B. *J. Solid State Chem.* **1999**, *145* (1), 327–335.
(151) Schur, E.; Nauha, E.; Lusi, M.; Bernstein, J. *Chem. – A Eur. J.* **2015**, *21* (4), 1735–1742.
(152) Isostructural crystals - Online Dictionary of Crystallography https://dictionary.iucr.org/Isostructural_crystals# (accessed 2022 -03 -24).
(153) Romero, S.; Bustamante, P.; Escalera, B.; Cirri, M.; Mura, P. *J. Therm. Anal. Calorim.* **2004**, *77* (2), 541–554.
(154) Jain, A.; Shah, H. S.; Johnson, P. R.; Narang, A. S.; Morris, K. R.; Haware, R. V. *Eur. J.*

Pharm. Biopharm. **2018**, *132*, 83–92.
(155) Macrae, C. F.; Bruno, I. J.; Chisholm, J. A.; Edgington, P. R.; McCabe, P.; Pidcock, E.; Rodriguez-Monge, L.; Taylor, R.; van de Streek, J.; Wood, P. A. *J. Appl. Crystallogr.* **2008**, *41* (2), 466–470.
(156) Chem3D http://www.cambridgesoft.com/software/ChemDraw/ (accessed 2022 -01 -11).
(157) Streitwieser, A.; Taft, R. W. *Progress in Physical Organic Chemistry*; Wiley, 2007; Vol. 6.
(158) Karni, R.; Amarschwartz, A. WO 2021/059270 A2, 2021.
(159) Li, X. J.; Zeng, Z. Z. *Chem. Res. Chinese Univ.* **2006**, *22* (1), 6–10.
(160) López-Mejías, V.; Matzger, A. J. *Cryst. Growth Des.* **2015**, *15* (8), 3955–3962.
(161) Bondi, A. *J. Phys. Chem.* **1964**, *68* (3), 441–451.
(162) Todeschini, R.; Consonni, V. *Wiley-VCH* **2000**, *11*, 688.
(163) R.E.Banks. *Organofluorine Chemistry: Principles and Commercial Applications*; 1994.
(164) Gorelik, L.; Brickelmaier, M.; Lugovskoy, A. US 9.233,107 B2, 2016.
(165) Tsui, G. C.; Hu, J. *Asian Journal of Organic Chemistry*. Blackwell Pub 2019, pp 566–567.
(166) Ben-Naim, A. *Cooperativity and Regulation in Biochemical Processes*; Springer US, 2001.
(167) Yujie, R.; Fei, L. CN111346082, June 18, 2020.
(168) Cerretani, D.; Micheli, L.; Fiaschi, A. I.; Giorgi, G. *J.Chromatogr.B* **1996**, *678* (2), 365–368.
(169) What is Peak Fronting? Chromatography Today https://www.chromatographytoday.com/news/columns-lc/37/breaking-news/what-is-peak-fronting/31490 (accessed 2021 -07 -12).
(170) Núñez, O.; Lucci, P. In *Advances in Chemical Research*; C. Taylor, J., Ed.; Nova Science Publishers, 2014; pp 71–86.
(171) Dolan, J. A Guide to HPLC and LC-MS Buffer Selection https://www.hplc.eu/Downloads/ACE_Guide_BufferSelection.pdf (accessed 2021 -07 -12).
(172) Prichard, L.; Barwick, V. *Preparation of Calibration Curves A Guide to Best Practice*; 2003.
(173) Miller, J. N.; Miller, J. C. *Statistics and Chemometrics for Analytical Chemistry*, 5th ed.; Pearson Education, 2005.
(174) Givand, J. C.; Teja, A. S.; Rousseau, R. W. *AIChE J.* **2001**, *47* (12), 2705–2712.
(175) Alshehri, S.; Shakeel, F. *J. Mol. Liq.* **2017**, *240*, 447–453.
(176) Cayman Chemical. Product Information - Flufenamic Acid https://cdn.caymanchem.com/cdn/insert/21447.pdf (accessed 2022 -07 -18).
(177) Santen, R. A. Van. *J. Phys. Chem.* **2002**, *88* (24), 5768–5769.
(178) Burger, A.; Ramberger, R. *Mikrochim. Acta* **1979**, *72* (3–4), 273–316.
(179) Mao, C.; Pinal, R.; Morris, K. R. *Pharm. Res.* **2005**, *22* (7), 1149–1157.
(180) Perrenot, B.; Widmann, G. *Thermochim. Acta* **1994**, *234* (C), 31–39.
(181) Brittain, H. G.; Bruce, R. D. *Compr. Anal. Chem.* **2006**, *47*, 63–109.
(182) Otsuka, M.; Kaneniwa, N. *Chem. Pharm. Bull.* **1984**, *32* (3), 1071–1079.
(183) Waters. i-FIT, A Novel Method of Isotope Prediction Applied to Elemental Composition Analysis https://www.waters.com/waters/library.htm?locale=en_US&lid=1538125 (accessed 2022 -07 -29).
(184) Ullmann, F. *Berichte der Dtsch. Chem. Gesellschaft* **1903**, *36* (2), 2382–2384.
(185) Goldberg, I. *Berichte der Dtsch. Chem. Gesellschaft* **1906**, *39* (2), 1691–1692.
(186) Sperotto, E.; Klink, G. P. M. van; Koten, G. van; Vries, J. G. de. *Dalt. Trans.* **2010**, *39* (43), 10338–10351.
(187) Ma, D.; Cai, Q. *Acc. Chem. Res.* **2008**, *41* (11), 1450–1460.
(188) Monnier, F.; Taillefer, M. *Angew. Chemie - Int. Ed.* **2008**, *47* (17), 3096–3099.

(189) SV, L.; AW, T. *Angew. Chem. Int. Ed. Engl.* **2003**, *42* (44), 5400–5449.
(190) Beletskaya, I. P.; Cheprakov, A. V. *Coord. Chem. Rev.* **2004**, *248* (21–24), 2337–2364.
(191) Cohen, T.; Cristea, I. *J. Org. Chem.* **1975**, *40* (25), 3649–3651.
(192) Bethell, D.; Jenkins, I. L.; Quan, P. M. *J. Chem. Soc. Perkin Trans. 2* **1985**, No. 11, 1789–1795.
(193) Weston, P. E.; Adkins, H. *J. Am. Chem. Soc.* **2002**, *50* (3), 859–866.
(194) Aalten, H. L.; van Koten, G.; Grove, D. M.; Kuilman, T.; Piekstra, O. G.; Hulshof, L. A.; Sheldon, R. A. *Tetrahedron* **1989**, *45* (17), 5565–5578.
(195) Weingarten, H. *J. Org. Chem.* **2002**, *29* (12), 3624–3626.
(196) Hartwig, J. F.; Richards, S.; Barañano, D.; Paul, F. *J. Am. Chem. Soc.* **1996**, *118* (15), 3626–3633.
(197) Driver, M. S.; Hartwig, J. F. *J. Am. Chem. Soc.* **1997**, *119* (35), 8232–8245.
(198) Hartwig, J. F. *Pure Appl. Chem.* **1999**, *71* (8), 1417–1423.
(199) Wagaw, S.; Rennels, R. A.; Buchwald, S. L. *J. Am. Chem. Soc.* **1997**, *119* (36), 8451–8458.
(200) Huang, X.; Anderson, K. W.; Zim, D.; Jiang, L.; Klapars, A.; Buchwald, S. L. *J. Am. Chem. Soc.* **2003**, *125* (22), 6653–6655.
(201) Kwong, F. Y.; Klapars, A.; Buchwald, S. L. *Org. Lett.* **2002**, *4* (4), 581–584.
(202) Csuk, R.; Barthel, A.; Raschke, C. *Tetrahedron* **2004**, *60* (27), 5737–5750.
(203) Pretsch, E.; Bühlmann, P.; Badertscher, M. *Structure Determination of Organic Compounds: Tables of Spectral Data*, 3rd ed.; Springer Berlin Heidelberg, 2009.
(204) Wolf, C.; Liu, S.; Reinhardt, B. C. *Chem. Commun.* **2006**, No. 40, 4242–4244.
(205) Susumu Muto, A. I. US7626042 B2, 2003.
(206) **李文博**; **金立**诺; **郭**艳云; **霍**东升; **余勇**; 杨燕; **王建文**; **刘骞峰**. January 8, 2014.
(207) Hager, F. D. *Org. Synth.* **1941**, *1*, 544.
(208) Field, J. E.; Venkataraman, D. *Chem. Commun.* **2002**, *2* (4), 306–307.
(209) Huang, P. C.; Parthasarathy, K.; Cheng, C. H. *Chem. – A Eur. J.* **2013**, *19* (2), 460–464.
(210) Janke, J.; Villinger, A.; Ehlers, P.; Langer, P. *Synlett* **2019**, *30* (7), 817–820.
(211) Kaltenbronn, J. S.; Scherrer, R. A.; Short, F. W.; Jones, E. M.; Beatty, H. R.; Saka, M. M.; Winder, C. V.; Wax, J.; Williamson, W. R. N. *Arzneimittelforschung* **1983**, *14* (37), 621–627.
(212) Sowinski, F.; Yale, H. L. *J. Med. Pharm. Chem.* **1962**, *5* (1), 54–63.
(213) Inczedy, J.; Lengyel, T.; Ure, A. In *Orange Book; IUPAC Compendium on Analytical Nomenclature, Definitive Rules 1997*; Blackwell Science, 1998.
(214) Rome, K.; Mcintyre, A. *Cromatography today* **2012**, No. May/June, 52–56.
(215) Hammond, C. In *The Basics of Crystallography and Diffraction*; Oxford University Press, 2015; pp 252–282.
(216) Waguespack, L. *TA Instruments*. 2009.
(217) Steiner, T. *Angew. Chem. Int. Ed. Engl.* **2002**, *41* (1), 49–76.
(218) Gardiner, D. J.; Graves, P. R. *Practical Raman Spectroscopy*; Springer Berlin Heidelberg, 1989.
(219) Nernst, W. *Zeitschrift für Phys. Chemie* **1891**, *8U* (1), 110–139.
(220) Kitamura, M.; Nakai, T. *J. Chem. Eng. Japan* **1983**, *16* (4), 288–293.
(221) ImageJ https://imagej.nih.gov/ij/ (accessed 2021 -04 -28).
(222) Schneider, C. A.; Rasband, W. S.; Eliceiri, K. W. *Nat. Methods* **2012**, *9* (7), 671–675.
(223) PubChem. 2-(2-Ethylhexyloxy)ethanol (C10H22O2) https://pubchem.ncbi.nlm.nih.gov/compound/2-_2-Ethylhexyloxy_ethanol (accessed 2021 -04 -22).
(224) Kempkes, M.; Eggers, J.; Mazzotti, M. *Chem. Eng. Sci.* **2008**, *63* (19), 4656–4675.
(225) Vaccaro, A.; Šefčík, J.; Morbidelli, M. *Part. Part. Syst. Charact.* **2007**, *23* (5), 360–373.

(226) Vasanth Kumar, K.; Heffernan, C.; Ramisetty, K. A.; Howard, C. A.; Beloshapkin, S. *CrystEngComm* **2022**.